STUDIES ON THE INTERNALLY-HEATED STEAM TURBINE FIXED BLADE AND ITS INFLUENCE ON THE COST OF REPLACING ERODED BLADES

by

HAMEED KHALIL IBRAHIM AL-AZZAWI

Thesis submitted in accordance with the requirements of the University of Liverpool for the Degree of Doctor of Philosophy.

Department of Mechanical Engineering,
University of Liverpool.

July 1984.

ORIGINAL COPY TIGHTLY BOUND

To

My Wife Euhood

My Daughter Abeer

and to

My Son Bakir

Abstract

Erosion in a wet steam turbine (which commences with the deposition of nucleated fog droplets on the stator blades) is still a serious problem in the modern power stations especially nuclear and geothermal. A theoretical study is undertaken of the diffusive deposition of nucleated fog droplets on a low-pressure steam turbine blade operating between terminal conditions 0.233 bar, 3% wetness and 0.1 bar. Nucleation is assumed to occur at the entry to the blade passage and fog droplets in the diameter range 0.01-1.0 μm invade both concave and convex boundary layers in addition to the free stream. The size of droplets in the boundary layers are polydispersed whilst in the free stream they are monodispersed. Droplets in the boundary layer are subjected to diffusion and deposition.

The literature concerned with droplet generation, size measurement, diffusional deposition, phenomenon of thermophoresis and evaporation or condensation of large and small droplets is briefly discussed. A brief historical review is included of the erosion problem, the simulation methods used to find the distribution of droplet deposition on the surfaces of fixed blades and the ways of reducing or preventing erosion on the rotor blades.

An experimental investigation was carried out to study the effect of thermophoresis on the deposition of the particles on a heated blade surface of a large LP turbine stator. Prediction of the particle deposition on heated and on unheated surfaces using the whole thickness of the boundary gave satisfactory results.

The likelihood of interaction between the droplets is small

and the existence of the droplets has no effect on the development of the boundary layer. The characteristics of the boundary layer along the concave and convex surfaces were predicted using Head's entrainment method since the flow inside the blade passage was turbulent. Laminarisation occurs along both blade surfaces and it was found that there were two inverse transition points along each surface. Laminarisation has a great effect on the development of the boundary layer and on the heat transfer from the blade surface. If the blade surface temperature is raised above the adiabatic temperature by internal heating, the droplets in the boundary layer are subjected concurrently to thermophoresis and phase change. The amount of heat from the blade surface depends mainly on the degree of laminarisation and the size of entrained droplets. The boundary layers were divided into cells of 5 μm height-wise (y-axis) and varying magnitude flow-wise (x-axis). The effects of the coupled phenomena; evaporation/ condensation, diffusion (Brownian + eddy) and thermophoresis were traced using a comprehensive computer program for the complete fluid transit for blade temperatures of 66-85℃. Calculations show that deposition can be inhibited by a modest degree of heating (i.e. t_{wi} = 80℃) which for 1.0 μm entrained droplets is ∿ 2.1 kW per metre of blade length. Accordingly the mass flow rate of the heating steam, which is extracted at the entry of the penultimate stage, is about 0.11% of the mass flow rate of the working steam. However the mass flow of the boiler is increased by about 0.04% in order to recover the turbine output loss due to blade heating. The efficiency of the last stage was found to be increased by about 0.2% which is sufficient to increase the turbine output by about the same amount as the loss due to blade heating. A practicable proposal of designing the hollow diaphragm is presented.

The economic calculations show that investment in this blade heating method is profitable under all conditions. However, it is found that if the blade heating had been employed in the first generation of large turbines (i.e. in 1967), the investment would have resulted in a very large profit. Today the investment would generate a small profit with probability of success of 85% (or 99.9% if the increase in the last stage efficiency is considered) when uncertainty in the engineering and economic factors are taken into account. Finally, it is found that steam blade heating is the most promising method to prevent steam turbine erosion without engineering or economic risk.

Acknowledgements

I am indebted to the head of the department, Professor J. F. Norbury (and latterly Professor N. Jones) for allowing this work to be performed in the Steam Laboratory of the department.

I would like to express my gratitude and my appreciation to my supervisor, Dr. D. J. Ryley, Reader in Mechanical Engineering for the great deal of advice, support and encouragement given during the course. His suggestions, guidance, continuous help and moral support have been essential in the course of the work.

I also wish to express my gratitude and thanks to Mr. C. S. Wells, Senior Lecturer in the Department of Industrial Studies, joint-supervisor of this project, for his invaluable assistance and encouragement.

I gratefully acknowledge the assistance given by the following gentlemen:

Professor J. F. Norbury for a valuable discussion and assistance;

Professor J. S. Halliday, Dean of the Faculty of Engineering, for a useful discussion on this work;

Drs. H. Barrow and N. Carpenter for the helpful discussions;

Mr. F. J. Heymann (from Westinghouse Electric Corporation) and Dr. A. Konorski (Turbomachinery Institute, Gdansk) for their interest and for sending useful suggestions concerning this work;

Mr. V. T. Forster, Mr. H. Cox, Mr. F. R. Harris (from the General Electric Company) for their great help and for supplying the economic data. I am especially indebted to Mr. Harris.

Mrs. J. Irgin, I. Birnie, L. E. Beard and J. Lister (from the Central Electricity Generating Board) for their interest and for supplying the economic data;

Mr. P. Devenish, the electron microscopist in the Department of Metallurgy and Materials Science for his help with the use of the electron microscope facilities.

Mr. Eric Hughes in the Steam Laboratory for his great help with the experimental work.

All the staff in the Computer Laboratory for their useful assistance.

My sincere appreciation is directed to Dr. I. I. Owen for the helpful assistance and discussion concerning this work. I wish also to thank Mrs. M. Hemingway for typing the manuscript of this thesis.

The work described in this thesis was carried out in the Department of Mechanical Engineering, University of Liverpool over the period March 1981 to July 1984.

Financial aid granted by the IRAQI Government made this study possible. This is gratefully acknowledged.

Finally, I would like to thank my wife Euhood who, despite domestic duties, typed part of the master plates of this thesis.

H. K. Al-Azzawi

CONTENTS

List of Tables

List of Plates

Notation

A	Surface area, cross-section area, constant
$\bar{A}$	Hamaker constant
A_{CF}	Cash flow
a	Radius of the blade nose, year number
a_{th}	Thermal accommodation of molecules hitting the droplet
B	Displacement of the droplet due to Brownian motion, constant
C	Absolute velocity, constant
$\bar{C}$	Mean thermal velocity of the vapour molecules
CC	Capital cost
C_D	Discharge coefficient
C_E	Entrainment coefficient
C_f	Skin friction coefficient
C_m	Constant
Cp	Specific heat at constant pressure
C_s	Constant
C_t	Constant
Cv	Specific heat at constant volume
c	Condensation or evaporation coefficient, concentration of the droplets, chord length of the blade
D	Diffusion coefficient, average spacing of the adjacent droplets, nozzle diameter
D_p	Height of the blade passage
d	Droplet diameter = $2r$
d_a	Arithmetic average diameter = $2r_a$
dg	Geometric mean diameter = $2rg$
E	Constant
e	Coefficient of restitution, erosion depth

FC	Cost of coal
F_C	Cunningham correction
F_c	Correction factor for skin friction coefficient
$F_{d,s}$	Stokes drag force
F_ℓ	Heat transfer correction factor due to laminarisation
F_T	Thermophoretic force
F_θ	Correction factor for momentum thickness
f	Reciprocal of the mobility of a droplet or a partical, friction factor, function
f′	Inflation rate
fn	Frequency of occurrence of droplet
G	Mass flow rate per unit area
$\overline{G}$	Brownian mean velocity
G_B	Flashing parameter
Gp	Parameter for controlling the length of the step Δx
g	Acceleration of gravity
g_B	Flashing parameter
H	Shape factor = δ_1/θ
H_1	Shape parameter
H_{32}	Shape factor = δ_3/θ
h	Enthalpy
h_d	Deposition velocity coefficient
I	Electrical current, Index
IRR	Internal rate of return
i	Step along the y-axis, interest rate
i_r	Real rate of interest
J	Constant
j	Step along the x-axis
K	Thermal conductivity, dimensionless parameter

Kn	Knudsen number
k_B	Boltzmann's constant
L	Acceleration parameter
LE	Leading edge
ℓ	Length of the blade
ℓ'	Mean free path of the vapour phase
ℓ_B	Droplet mean free path
ℓ_{mx}	Prandtl mixing length
M	Mach number, maximum precipitated mass on the droplet surface
M_m	Molecular weight
m	Droplet mass
$\dot{m}$	Mass flow rate
m_{pm}	Mass of one molecule
N	Deposition rate
Ng	Number of steps along the x-axis
N_m	Number of droplet movements
NPV	Net present value
N_p	Specific number of the droplets
Nu	Nusselt number
n	Number of droplet, number of years, number of steps along x-axis
O_{hr}	Number of operating hours
P	Price of coal
PI	Profitability index
Pr	Prandtl number
PV	Present value of cash flow
p	Static pressure
$\dot{p}$	Expansion rate
Q	Volumetric flow rate

$\dot{Q}$	Rate of heat transfer
q	Specific heat transfer
q"	Heat flux
R	Radius, gas constant
Re	Reynolds number
Re_θ	Reynolds number based on the momentum thickness
r^+	Dimensionless droplet radius
r_{flash}	Maximum radius of droplet which escape flashing
S	Stopping distance, specific entropy
S^+	Dimensionless stopping distance
Sc	Schmidt number
S_D	Standard deviation
S_{DG}	Geometric standard deviation
Sh	Dimensionless mass transfer coefficient
St	Stanton number
s	Supersaturation ratio
T	Absolute temperature
TE	Trailing edge
T_{gm}	Modified vapour temperature
t	Time, temperature (℃)
U	Steam velocity outside the boundary layer, peripheral velocity
u	Steam velocity inside the boundary layer
u_*	Shear velocity
V	Velocity, electrical potential
V_i	Incidence velocity of the droplet
V_T	Thermophoretic velocity
v	Specific volume, flow velocity in the direction of y-axis
v_{pm}	Volume per molecule in the condensed phase
W	Work

We	Weber number
x	Position along the x-axis, dryness fraction
y	Wetness fraction, distance along y-axis
y^+	Dimensionless distance along y-axis
Z_o	Constant

Greek Symbols

α	Degree of dispersity, accommodation coefficient, wetness losses factor
α_m	Mass diffusivity
α_r	Heat transfer coefficient
β	Constant
γ	Specific heat ratio
Γ, Γ_θ	Pressure gradient parameter
δ	Thickness of the boundary layer, very small element
δ_1	Displacement thickness
δ_3	Energy thickness
δ_c, δ_d	Thickness of the diffusion boundary layer
δ_{sub}	Thickness of the boundary sublayer
$\varepsilon, \varepsilon_M$	Eddy viscosity of the gas or the vapour
ε_p	Eddy diffusivity of the particles or the droplets
ϵ	Shear stress parameter
λ	Translational part
μ	Dynamic viscosity
ν	Kinematic viscosity
η	Efficiency, dimensionless distance
ρ	Density
σ	Surface tension of the water
τ	Shear stress, turbulence level
τ_r	Relaxation time
τ_r^+	Dimensionless relaxation time
θ	Momentum thickness
Ψ	Ratio of the actual to the maximum condensate mass
φ	Angle of blade twisting, mass transfer parameter
Δ	Mass flow thickness, small element
Δ_2	Enthalpy thickness

Subscripts

a	Arithmetic
ac	Actual
av	Average
C	Centre, cell
C-r	Centre to the surface of the droplet
co	Corrected
cr,crit	Critical
d	Deposition, diffusion
e	Exit, ending
eq	Equilibrium
ev	Evaporation
exp	Expansion
f	Fluid
g	Gas, saturated vapour
i	Initial, incident
inc	Incompressible
int	Internal
is	Isentropic
ℓ	Liquid
m	Molecular, mean
max	Maximum
mm	Mass median
N	Nozzle
net	Net
p	Particle
ps	Partial supersaturation
r	Droplet, surface of the droplet, real

rel	Relative
S	Stopping distance, surface
s	Saturation, settling, subcooling, supersaturation, starting, isentropic
sptn	Supersaturation
sub	Sublayer
TE	Trailing edge
w	Wall
x	Along x-axis
0	Stagnation, absolute, zero pressure gradient
1,2,3..	Points
.	Rate
-	Average
∞	Free stream
$\rightarrow$	Vector
θ	Momentum thickness

CHAPTER ONE

INTRODUCTION

1.1 PRESENTING THE PROBLEM

The extensive development of world power generation based on nuclear and geothermal plants has highlighted the problems of creating and perfecting wet steam turbines. The problem of designing wet stages lies partly in the large peripheral velocities and partly in the increasing moisture content which is economically permissible in turbines of modern power stations. Blade erosion and low stage efficiency are the two main problems associated with wetness in steam turbines.

The process of steam expansion in turbines of this type (condensing steam turbines) usually begins from the saturation line or from a very small degree of superheat and lies in the two-phase domain of states. It should be borne in mind that problems of wetness apply to the last stages of both large low pressure turbines in fossil power plants and to the H.P. turbines found in nuclear and geothermal power plants.

The problem of reliably protecting rotor blades from erosion has not been solved, so the search for practical measures for reducing or preventing erosion remains one of the most important problems facing turbine designers.

The erosion process in the wet steam turbine commences with the deposition of nucleated fog droplets (0.01 - 1.0 μm diameter) on the stator blades. The mechanism which leads to this phenomenon has been subjected to extensive studies (1 to 10) in order to find ways of reducing or preventing erosion which is regarded as one of the factors limiting further

progress in design of modern turbines.

Very large turbines currently being designed and manufactured, typically produce 600 - 660 MW of electricity and have final stage moving blades approximately one metre long. In such turbines, blade replacement is undesirable from both an economic and a technical point of view. The cost of rotor replacement is high, since materials, manufacturing and outage costs attain a huge sum of loss costs. Therefore, the wet stages must be designed so that eroded blades need to be replaced only after an economically acceptable operational life. Many practical ideas have been suggested and used to reduce or prevent erosion of the moving blades. Some of these have been reviewed by Refs. (11 - 13) and some of the more recent methods will be presented in Chapter Three.

1.2 EROSION CYCLE

It is clear from the literature that the erosion rate depends on several factors:

(1) The velocity of impact of the water drops.

(2) The size of the drop.

(3) The mass of the impacting water.

(4) The impact angle and blade geometry.

(5) The geometry of the axial gap between the fixed and moving blades.

(6) The mechanical properties of rotor blades.

Figure 1.1 shows the erosion parameters and the effect of flow conditions on forming a water film.

Blade erosion in wet steam turbines is known to be preceded by the deposition of fog droplets (0.01 - 1.0 μm diameter) on the fixed blade surfaces. The fog droplets are small and move nearly at the steam

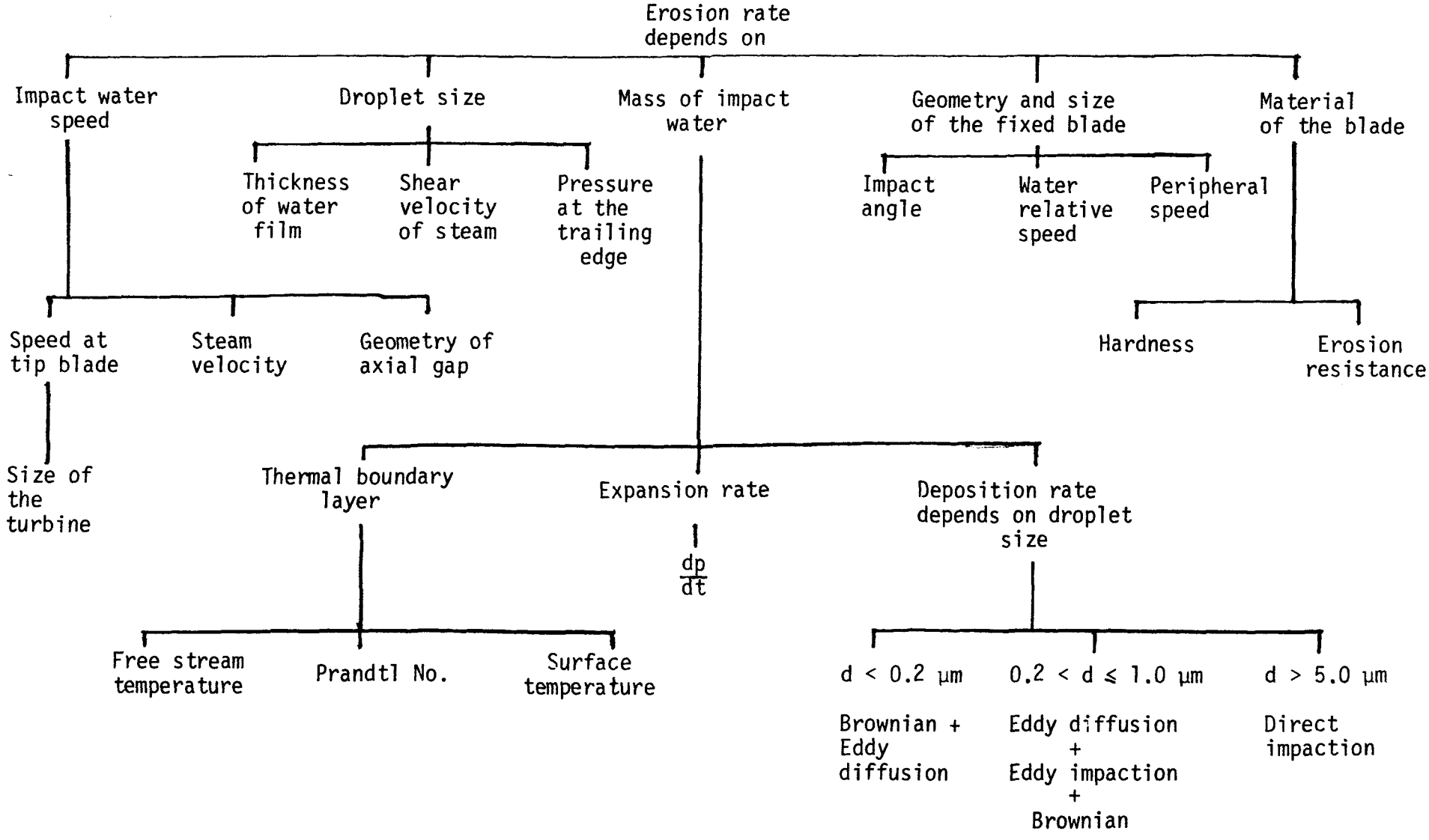

FIGURE 1.1 EROSION PARAMETERS

velocity and hence cannot cause damage directly. Due to rapid acceleration and sharp curvature encountered by the steam as it flows through the fixed blade passage, few of the fog droplets deposit by impact on the fixed and moving blade surfaces. A high proportion of the water deposited on the other surfaces of the turbine is successively re-entrained and re-deposited whilst further deposition of fog droplets occurs. The mechanisms promoting deposition depend on droplet size, on the nature of the flow and on the concentration of droplets in the free stream flow. The process of deposition has been studied in this work and by a number of investigators (2, 3, 4, 7, 14, 15). The investigations show that diffusion (eddy and Brownian) and eddy impaction are the main mechanisms of deposition of fog droplets on the blade surfaces where they subsequently form a water film.

The water deposited on the moving blades is centrifuged towards the casing whilst that deposited on the fixed blades moves across and along their surfaces towards the trailing edge under the action of fog impaction, steam drag and by the existing pressure gradient. Water eventually leaves the trailing edges of the fixed blades and breaks up to form a distribution of drops typically up to 2.0 mm in diameter. The calculation of the size of the largest drops in the flow depends upon a critical value of the Weber number for the drop (We_{cr}) and the ratio of time of motion of the drop at its relative velocity to the time required for deformation of the drop. From estimation of the time ratio and the critical Weber number (We_{cr} is considered to be in the range of 10 - 30), Kirillov and Faddeev (16) have given a formula for calculating the size of the largest drop in the flow:

$$r_{max} = \frac{0.5\,\sigma\ We_{cr}}{\rho_g\ V_{rel}^{\ 2}} \qquad (1.1)$$

The drops from the fixed blade trailing edge are insufficiently accelerated by the steam and therefore impinge onto the moving blade at a large inlet angle and at a relative velocity higher than the steam as shown in Figure 1.2. Analysis of the velocity triangles (Figure 1.2) reveals that the coarse drops strike the moving blades almost perpendicularly, resulting in an impact force large enough to cause erosion.

The continuous impaction of water drops onto the surface of the blade at high speed leads to cracking of the grain structure of the blade material followed by grains being removed and finally wholesale removal of material. The development of erosion on material specimens has been investigated in a number of test rigs (Refs. 16 to 27).

In general, erosion can be considered in three phases which are shown in Figure 1.3. Insignificant material is lost in the first phase; the second phase is characterised by the maximum rate of material loss which remains constant during a given period. For various reasons the erosion rate then decreases during the subsequent time of the third phase. The first and second phases are very short compared with usual turbine operating times, and therefore only the third phase is of relevance when the erosion of a turbine blade is evaluated.

The complexity of the processes which cause blade erosion make it extremely difficult to develop a general method for determination of the erosion rate in steam turbines.

1.3 PREVENTION OF EROSION

Heightened concern about steam turbine blade erosion arose in the early sixties because of the considerable increase in blade tip speed, up to 550 m/s was encountered, together with increased moisture levels in

nuclear and geothermal turbines. A reduction in erosion can be brought about by suitable adjustment of the erosion parameters.

The erosion can be modified by influencing the size of the droplets which are produced from the first nucleation by suitably locating the position of Wilson point along the expansion line. If nucleation occurs in the region of high expansion rate, the sizes of the created droplets are very small and vice-versa. Some investigators believed that nucleation with very fine droplets could reduce the destructive erosion. In the present work the author found the situation is not as simple as that, since very small droplets have a high tendency to deposit on blade surfaces by diffusion and they grow very quickly due to their large relative interface area with the vapour. However, supersaturation losses are small compared with those from bigger droplets, and fine droplets (0.01 - 0.1 μm diameter) can be easily eliminated by increasing the vapour temperature to be just above the local saturation temperature. Therefore, the size of fog droplets has a considerable effect on:

(1) The extent of supersaturation losses.

(2) The quantity of deposited water.

(3) The magnitude of heat input to the blade surfaces for evaporating the droplets.

The principal methods of reducing or diminishing the erosion are:

(1) Protecting the leading edge of the moving blades.

(2) Increasing the axial gap length.

(3) Decreasing the surface area of the fixed blade.

(4) Removing the deposited water mechanically from the fixed blade surfaces.

(5) Evaporating the fog droplet before deposition.

(6) Modifying the rotor blade leading edge in order to disperse the deposited water radially by centrifugal force.

(7) Increasing the absolute velocity of the coarse drops or atomisation of the large drops inside the axial gap.

(8) Using anti-erosion protection based on electrolytic chrome plating.

These methods will be discussed in Chapter Three in more detail.

1.4 THE PRESENT WORK

The present study is one of a series of projects which have comprised long term research programme at the University of Liverpool to investigate the deposition of fog droplets on fixed blade surfaces. The purpose is to establish an efficient method of discouraging or preventing deposition in order to overcome the erosion on the moving blade. These studies (3, 4, 7, 15), have employed experimental simulation techniques in which solid uranin particles have been injected into a flow of air over a test cascade of turbine stator blades. In the work reported herein, the technique used in Refs. (3, 4), were modified and used successfully to obtain experimental results. These results are compared with the earlier investigations and also with theoretical results developed in this thesis.

It was realised, however, that the works in references (3, 4) could not provide satisfactory simulation of the real steam case insomuch as the aerosol particles, unlike fog droplets, were not subjected to phase change. To complete the series, a theoretical study is now made of the behaviour of the fog within the boundary layer, treating

concurrently the principal coupled phenomena of droplet phase change, diffusive deposition and thermophoresis for different temperature of blade surface. The intention is to discourage fog droplets from alighting on the blade surface and hence suppress the formation of coarse water.

Realistic financial costs and operating data are established to investigate the balance between the saving in costs due to the need of an earlier re-blading of the rotor blade for unheated fixed blade, and the enhanced aggregate expenditure incurred by providing the additional equipment and fuel needed for heating the fixed blade.

The remainder of the thesis is divided as follows:

Chapter Two gives a brief survey concerning the mechanisms by which droplets are entrained in the steam flow and subsequently deposited on surfaces. Also included is a survey of the phenomenon of thermophoresis. In effect, this Chapter briefly examines the various theories of deposition of small particles and the theory which has been developed to study the effect of temperature gradients on the size and the movement of the droplets in the flow.

Chapter Three presents a comprehensive review of the methods which have been developed for measuring the deposition rate of fog droplets on the blade surfaces, and for controlling the erosion within the turbine. The survey considers most of the methods developed since 1964 up to the present time. Wood (11, 12), has made an excellent review of most of the methods used or suggested before 1965.

Chapter Four involves the experimental work for measuring the distribution of fog droplets on full scale fixed blade surfaces by using

a simulation method.. The sizes of the particles were measured using an electron microscope. The previous experimental technique, (3, 4, 7), for measuring the particle size and the deposition rate on adiabatic and heated surfaces have been modified slightly. Comparisons have been made between the experimental results of the present work and those from Ryley and El-Shobokshy (3) and Davies (4), when the incidence angle to the cascade is -15^{o} and Parker and Lee (7), when the incidence angle is zero.

The value of the thermal conductivity of the uranin particle was measured by using a convenient experimental method in order to analyse successfully the behaviour of the particles in the boundary layer on heated blade surfaces.

Chapter Five presents the theoretical analysis of the blade passage flow and predicts the boundary layer characteristics. It contains:

(1) Analysis of the flow field in the blade passage using a teledeltos paper technique.

(2) Prediction of the steam properties before and after the condensation shock.

(3) Prediction of the degree of relief of supersaturation along the passage, and outside the boundary layer.

(4) Prediction and theoretical analysis of the hydrodynamic boundary layer characteristics on the surface of the blade. The laminarisation phenomenon and its effect on mass transfer of the vapour has been taken into consideration.

(5) Correlation between the boundary layer parameters, the droplet geometry and the acceleration parameter.

Chapter Six involves the calculation of heat transfer from the blade surface to the wet steam flow. It contains:

(1) Prediction of the distribution of free stream temperature and heat transfer from the blade surfaces, and the effect of the droplet size on their values.

(2) Derivation of the equations for calculating the distribution of stagnation temperature in two-phase flow.

(3) Analysis of the effect of highly accelerated flows on the rate of heat transfer.

(4) Prediction of the variation of temperature profile of the wet steam inside the thermal boundary layer due to heating.

(5) Suggestions and discussions of the practical heating methods which can be employed for this purpose.

Chapter Seven is concerned with the mathematical model and the computer program for predicting the combined effects of phase change, diffusion and thermophoresis on the moving droplet. This involves:

(1) The size distribution of the fog droplets, shortly after nucleation, across the blade passage.

(2) Analysis of the behaviour of fog droplets inside the boundary layer which involves the mechanisms of droplet movement and phase change.

(3) A method for controlling the size of the conceptual cells inside the boundary layer.

(4) The numerical method and its translation into a computer program.

(5) The analysis of the theoretical results which trace the history of the fog droplets inside the boundary layer.

Chapter Eight considers the argument of the economics of the relative cost of re-blading for a conventional turbine, compared with the cost of additional instrumentation, equipment and fuel consumption for the new turbine with heated hollow blades. The information necessary to determine whether or not the heating method is attractive to the turbine manufacturer, includes:

(1) The minimum temperature of the blade surfaces.

(2) The heating method.

(3) The variation of the stage efficiency.

(4) The magnitude of heat consumption.

(5) The operating conditions of the actual turbine.

(6) The actual cost of fuel, re-blading, outage time and hollow diaphragm.

(7) The financial rate of interest and inflation.

Chapter Nine summarises the work and presents the main conclusions and suggestions for further work.

CHAPTER 2

GENERAL SURVEY

This Chapter presents a general survey of the literature concerned with the generation and size measurement of solid or liquid particles. The transfers of heat and mass in two phase flow need to be understood and a review of papers published during the last fifteen years regarding the phenomena of diffusion, thermophoresis and phase change is presented. The combined effect of diffusion and thermophoresis has been studied by many investigators (4, 28, 29, 30). This Chapter also discusses the studies of the behaviour of droplets under different flow conditions.

2.1 Generation and Size Measurement of Particles

Using wet steam with known initial droplet diameter and known flow parameters would permit an accurate study of the distribution of the deposition rate of fog droplets on turbine blade surfaces. Ryley and Parker (15) discussed the difficulties of using water droplets in steam for assessing the deposition rate on the blade surface. They recognised that a simulation method using solid particles representing the fog droplets might give acceptable results. This method, which is adopted by the others (3, 4, 7), requires information regarding the material and techniques for generating the solid particles. The most suitable material can be selected by taking into consideration the following points:

1. The solid particles must dissolve easily in water or in other liquids.
2. The solution has to emit a fluorescent light suitable for fluorimetric analysis.

3. The generated particles must not be absorbed by the blade surface.

4. The material must not be toxic, radioactive or harmful.

5. The material should not be expensive.

Wohlers et al (31) discussed the technical and economical advantages of some suitable tracer materials.

2.1.1 Generation of aerosol particles

A number of techniques are well known for generating controlled-size aerosol particles. In this section the methods of generating very small particles only are discussed. Some of the apparatus and techniques are as follows:

1. Condensation generators:

These rely on either self-nucleation or an external source of nucleation to produce submicron liquid particles.

(a) Self nucleation: Aerosol is produced when a saturated vapour is mixed with a cool dry gas stream, or by using a special design of a nozzle or set of nozzles to expand the steam rapidly with a certain value of expansion rate, $\dot{p}$, (14). The location of the nucleation and the sizes of the created particles are dependent on the degree of the supersaturation and the expansion rate, $\dot{p}$. Generally, this technique produces submicron particles with a diameter range 0.01 - 2.0 μm.

(b) External nucleation can be produced by a number of techniques and apparatus. A Sinclair and La Mer generator (32) was an early technique used to produce submicron liquid particles and has since been modified by many investigators; the details

can be found in Ref. (33). Fuchs and Sutugin (34) gave a comprehensive survey of most of these types of aerosol generators. Generally, highly monodispersed particles with $S_{DG} \approx 1.1$ can be produced by these methods and techniques. The sizes of the particles are mainly dependent on the evaporation temperature of the liquid used and the super-saturation ratio.

2. Generation of monodisperse aerosols by atomisation of suspensions

Solutions of different substances can be atomised mechanically under the action of hydraulic pressure, a centrifugal or aerodynamic forces. The liquid is drawn into narrow ligaments or films, which subsequently disintegrate into droplets under the action of the surface tension. The solid particles, therefore, can be produced by subsequent drying of the mist and this process should lead to highly monodisperse particles. Some of these techniques and apparatus are:-

(a) Atomiser Impactor

Developed by Whitby et al (35) for the testing of dust filter units and used by a number of investigators (3, 4, 7, 15). This technique is based on the atomisation of a dilute suspension and evaporation of the liquid droplets. The resultant aerosol cloud is composed of minute solid particles of the original solute. The size of the particles can be varied by altering the strength of the solution and the gap between the impactor plate and the casing of the impactor. A size range of 0.01 - 1.0 μm mass median diameter (moderately monodispersed with geometric standard deviation $S_{DG} < 1.5$) can be obtained from the atomiser impactor technique. This method has been used in the present work.

(b) Spinning disc atomiser

Different models of spinning disc atomisers have been modified and developed, (35). A dilute suspension is separated as a thin film on a sharp-edged small disc by the action of a centrifugal force. The liquid is spun off as a mixture of primary homogeneous droplets of $S_{DG} \approx 1.1$. Submicron solid particles remain from the evaporated droplets. Particle size can be varied by changing the solution strength, solution feed rate, size of the disc and the rotational speed.

(c) Vibrating orifice monodisperse aerosol generator

Designed by Berglund and Liu (36) to produce monodisperse aerosols. Production and size control of the particles can be achieved using this technique. El-Shobokshy (37) gave a good description of the generator components and the operation conditions. The generator is able to produce particles having a size range of 0.5 - 50 μm diameter.

3. Dispersion of monodisperse powders

Powders with any desired degree of dispersity can be prepared, although at a great expenditure of time and cost. The difficulties are:

1. The shape of the particle cannot be controlled.
2. Dispersion of the particles with $\bar{r} < 0.5$ μm is very difficult.
3. Humidity impairs the particle's dispersion considerably.

Therefore, this technique is not practicable for the generation and dispersion of submicron particles.

2.1.2 Particle size measurements

Numerous methods exist which can be used to measure the size of particles. These methods can be classified into four groups, namely:

1. Mechanical methods (direct and indirect measuring).

2. Electrical methods (indirect and automatic measuring).

3. Thermal methods (indirect measuring).

4. Photographic and optical techniques (direct and automatic measuring).

Each of these groups require special techniques and instruments to be used. Some of these methods are listed in the following table:

Method	Technique employed	Description	Size range	Reference number
MECHANICAL METHODS	Coated side systems	A sample of the liquid spray is collected on a glass slide coated with a material which records the drop size by mechanical deformation of the surface film. This deformation is then measured microscopically. The coating material may be: 1. Lamp black (kerosine flame). 2. White vaseline. 3. Magnesium oxide. This method depends on the coefficients of capture and impression.	Greater than 5.0 μm	38, 39 and 39a
	Cascade impactors technique	A set of orifices are used to increase the velocity of the flow, and arranged to obtain different impact velocity for different droplet sizes. The relative mass of sample on each stage can be obtained by gravimetric, chemical, microscope, etc. This method measures indirectly the size of the droplets.	Greater than 100 μm	40
	Sieve sizing	Used for large solid particles.	Greater than 50 μm	

Method	Technique employed	Description	Size range	Reference number
ELECTRICAL METHODS	Electrical mobility	By varying the voltage on a plate ion counter the current-voltage relation can be obtained when charged particles pass through. The analysis of the current-voltage curve by the method of tangents gives the mobility distribution of the particles. It is relatively easy to operate and can be applied to any aerosol that can be charged.	Submicron sizes	41
	Coulter counter	A device for particle counting and sizing which determines the number and size of particles suspended in electrically-conductive liquid.	Greater than 1.0 μm	38
	Charge spectrometer	The aerosol is injected through a small diameter tube into a laminar flow field, is deposited on two charged collecting plates or on a filter. The mass particle distribution is computed from the fluorescent dye distribution on the plates and the filter.	Submicron sizes	42
	Pulse counting technique	By recording voltage pulses produced when droplets short circuit the tips of two needles across which a potential is applied.	15-1000 μm	43 and 43a

Method	Technique employed	Description	Size range	Reference number
Electrical Methods (Cont.)	Electrostatic Technique	An electrically conducting liquid is used to produce droplets. The pulsation of the voltage of the probe can be recorded when the conducted drops strike it. It can be experimentally shown that the pulse height is proportional to the square of the diameter of the drops.	Very large drops	44
THERMAL METHODS	Freezing Method	A spray liquid is used through a very cold medium, in which the drops freeze into solid spheres. The freezing mediums may be alcohol immersed in a dry ice bath and liquid nitrogen. Direct photography followed by image analysis processing of the frozen drops may be employed.	Greater than 5.0 μm	38
	Evaporating Method	A special thermocouple technique has been used to measure the droplet size by measuring the temperature fall as the droplet collides with the hot junction. Heat is removed by evaporation from the junction. It is capable of detecting and measuring water droplets in air and steam flows even at high pressure and temperature. It can be modified by reducing the area of hot junction to measure smaller sizes of droplets.	3.0 - 1200 μm	45

Method	Technique employed	Description	Size range	Reference number
PHOTOGRAPHIC AND OPTICAL TECHNIQUES	Electromicroscopy	A sample of aerosol particles can be prepared on a glass slide and can be coated by carbon and shadowed by platinum metal. The slide is immersed in distilled water to remove the carbon film which contains the particles. A micro-mesh is used to prepare it for electronmicroscopy.	Submicron	3, 4, 7, 15
	Laser holography	The technique of recording an image of an object using the intensity, the wavelength and the phase of light reflected or transmitted by that object.	Greater than 5.0 μm	46
	Laser diffraction	Using the laser technique to detect small change in drop size distributions, especially in small drop populations. The method is based upon the forward diffractive scattering of parallel, monochromatic beam of light passing through a spray.	Greater than 2.0 μm	47, 48
	Light scattering techniques	The principle of this method is that when the light is incident upon a small droplet, some of the light is scattered, some is transmitted and the remainder absorbed. The proportions of the extinguished light absorbed within and scattered by the particle and the angular distribution of scattered light vary with particle size, shape and composition.	Greater than 1.0 μm	49, 50

Method	Technique employed	Description	Size range	Reference number
PHOTOGRAPH AND OPTICAL TECHNIQUES (Cont..)	Optical spot scanning	For counting and sizing, the particles are mounted on prepared slides. The detection system consists of a device such as a photo-electric scanning cell, combined with a high speed pulse counter.	Greater than 50 μm	50a

2.1.3 Statistical analysis of droplet size and population

Particles generated for the purpose of the present work are known to be nearly spherical (see Plates 4.1 and 4.2), but are polydisperse in size. In such a case, a single measurement concerning their size would be incomplete for defining the polydispersion. A mean diameter (statistical diameter) of the different sizes of the particles must be calculated in order to change the case of polydispersion to an equivalent monodispersion. There are many definitions for the mean diameter such as arithmetic, geometric, harmonic, number, surface, surface-volume and mass-median.

The choice of a suitable definition of mean diameter must be properly made, depending on the subject of the study. In the present work, we are dealing with the mass of particles or droplets depositing on a blade surface or suspended in the flow. The rate of deposition, or the rate of mass transfer, during condensation, or evaporation, is to be measured and calculated whilst the physical and thermal processes take place. It is therefore appropriate to use the mass-median diameter in this context as a part of the droplet or particle definition.

A. Calculation of mass-median diameter

The mass-median diameter can be obtained on the log-probability grid by plotting the values of cumulative percentage of mass against diameter, or by using the Hatch-Choate equation. The detail of calculation is presented in Chapter 4.

B. Frequency distribution

(i) Normal distribution (Gaussian):

If there are no effects imposing any conditions upon the droplet

size (coalescence, agglomeration or fracturing), the distribution will probably follow the normal distribution curve. If fn = frequency of occurrence of droplet diameter d, then

$$fn = \frac{\Sigma n}{S_D \sqrt{2\pi}} \exp \left[\frac{d - d_a}{2S_D^2} \right] \qquad (2.1)$$

where: d_a = arithmetic average diameter

Σn = total population

S_D = standard deviation = $\frac{\sqrt{\Sigma [n(d - d_a)^2]}}{\Sigma n}$

(ii) Skew distribution

In nearly all cases where wet steam is in flow, the agencies separating droplets from the flow and the different types of interaction between the droplets impose a "skew" size distribution. The skew frequency distribution may often be normalised by plotting fn against log(d). Then

$$fn = \frac{\Sigma n}{(\log S_{DG}) \sqrt{2\pi}} \exp \left[- \frac{\{\log(d) - \log(dg)\}^2}{2 \log^2(S_{DG})} \right] \qquad (2.2)$$

where dg = geometric mean diameter = $\exp \left(\frac{\Sigma n \log(d)}{\Sigma n} \right)$

S_{DG} = geometric standard deviation = $\exp \left[\sqrt{\frac{\Sigma [n\{\log(d) - \log(dg)\}^2]}{\Sigma n}} \right]$

C. Degree of dispersity (α)

It is important to find the degree of dispersity of each group of particle in order to use a convenient solution for the behaviour of the

particle in the flow. If the polydispersion is very high, it is not realistic to calculate the movement of the particles based on the mean diameter. The degree of dispersity is defined as

$$\alpha = \frac{S_D}{r_a} = \frac{\sqrt{\frac{\Sigma (r_i - r_a)^2}{\Sigma n}}}{r_a} \qquad (2.3)$$

where r_a = arithmetic average radius.

2.2 Phase Change between Droplet and Vapour

Thermodynamic equilibrium between the liquid and the vapour can exist if:

(i) The droplet size equals the critical size (i.e. $r = r_{crit}$). The critical radius of the droplet after spontaneous condensation can be calculated from Kelvin-Helmholtz equation:

$$r_{crit} = \frac{2\sigma}{\rho_\ell R T_g \ell n(s)} \qquad (2.4)$$

where $s = \frac{p_g}{p_s}$ = supersaturation ratio

σ = surface tension.

(ii) The temperature and pressure of the droplet are equal to the local temperature and pressure of the vapour, i.e.

$$p_g = p_s; \quad T_g = T_\ell$$

If in either a flow or a non-flow process the liquid and vapour are put out of mutual equilibrium, phase change will occur to restore it.

In some cases deformation of droplets may take place due to mechanical and thermal disequilibrium. The disequilibrium is a result of:

1. Bulk or local compression of wet steam.
2. Throttling of wet steam.
3. Bulk or local heating, stirring or agitation of wet steam.
4. Bulk or local expansion of wet steam.
5. Bulk or local cooling of wet steam.
6. Work extraction from wet steam.

Points 1, 2 and 3 promote evaporation and processes 4, 5 and 6 promote condensation.

Deformation of a droplet is due to aerodynamic forces and/or cavitation which act against the force of the surface tension, which tends to maintain the spherical shape. The effect of aerodynamic force is to disintegrate the larger drops into small drops. The resultant sizes can be determined by assuming a value for the Weber number, (We),

$$We = \frac{\rho_g V_{rel}^2 d}{\sigma} \tag{2.5}$$

Many investigators (25, 51, 52) have found that We has a value in the range of 10 - 30 under steam turbine operating conditions.

The cavitation or internal boiling is a result of reducing the droplet pressure below the saturation pressure,

$$p_\ell = p_\infty + \frac{2\sigma}{r} < p_s\ (T_\ell)$$

The large drop will be flashed into small drops due to increase of the size of the boiling bubbles inside the large drop which cause it to disintegrate. Gyarmathy (58) derived an expression for determining the maximum size r_{flash} of droplets which escape flashing,

$$r_{flash} = \sqrt{\left(\frac{K_f}{\rho_f \, Cv_f}\right) \frac{\Delta t}{G_B}} \qquad (2.6)$$

where Δt = time interval during which droplet is at risk

G_B = flashing parameter, determined from the parameter g_B

$$g_B = \frac{0.25}{\ell n \left(\frac{p_1}{p_2}\right)}$$ which is plotted against G_B in Ref. (53).

The state of the droplet and the vapour are characterised by the variables r, T_ℓ, T_r, T_g, u_ℓ, u_g, p_ℓ and p_g. The rate of phase change is a function of:

1. Number and size of droplet.
2. Degree of dispersion.
3. Supersaturation ratio.
4. Thermal relaxation times.
5. Heat transfer coefficient between the two phases.
6. Thermal conductivity of the two phases.
7. Flow velocity of the mixture.
8. The rate of latent heat transferred between the surface of the droplet and the vapour.

•

2.2.1 Phase Change between Large Drop and Vapour

The growth or evaporation of a large drop (Kn < 0.01) is independent on the Knudsen number (Kn), since it is considered as a continuum phenomenon. It is dependent on the Nusselt number (Nu), Reynolds number (Re), Mach number (M) and Prandtl number (Pr). The drop is assumed to be a liquid sphere. The heat transfer from the centre to the surface of the drop is by conduction and it is a function of the temperature distribution inside the drop t = t(r). If the surrounding steam is superheated therefore, there are two layers around the drop, a very thin saturated vapour shell (inner layer) and an infinite superheated vapour atmosphere (outer layer). However, if the surrounding steam is saturated, then only the saturated vapour layer is present. The temperature distribution inside and outside the drop is shown in Figure 2.1.

Gyarmathy (54) has formulated the growth or evaporation of a large drop in the form,

$$\frac{dr^2}{dt} = \frac{K_f \, Nu_H}{\rho_f \Delta h_{fg}} (T_r - T_{go}) + \frac{\dot{Q}_{int}}{4\pi r^2 \rho_f \Delta h_{fg}} \qquad (2.7)$$

where T_{go} = adiabatic wall temperature of the drop, defined by

$$T_{go} = T_g \left[1 + \frac{15}{16} (\gamma - 1) \, Pr \, M_{rel}^2 \right]$$

Nu_H = Nusselt number of heat transfer, defined by

$$Nu_H = \frac{\dot{Q}}{2\pi r K_f (T_{go} - T_\ell)}$$

$\dot{Q}$ = rate of heat transfer to or from the drop, defined as

$$\dot{Q} = \dot{m}\Delta h_{fg} + \dot{Q}_{int}$$

$\dot{m}$ = the rate of condensed or evaporated mass which is defined as

$$\dot{m} = 4\pi\rho_f r^2 \frac{dr}{dt}$$

r = drop radius

$\dot{Q}_{int}$ = the heat conduction rate, from or to the surface of the drop, which may be defined by Fourier's Law if there is no internal flow, or defined by Gyarmathy (54), as

$$\dot{Q}_{int} = m\, Cv_f \frac{dT}{dt} - \frac{m}{\rho_f}\frac{dp_\infty}{dt} - \dot{m}\, Cv_f\, (T_r - T_\ell)$$

Kirillov and Yablonik (55) have defined the rate of growth or evaporation of the large drop by assuming the surrounding steam as a large sphere with radius R containing one large drop with radius r. Therefore, the heat transfer between the two spheres (see any text book of heat transfer), is defined by

$$\dot{Q}_r = \frac{4\pi\, K_f\, (T_r - T_g)}{\frac{1}{r} - \frac{1}{R}} \qquad (2.8)$$

where $\dot{Q}_r$ = the heat rate from the surface of the drop to the surface of surrounding sphere (R).

The rate of growth or diminution of the drop, therefore, can be defined by the heat balance between $\dot{Q}_r$ and the latent heat as below:

$$\frac{dr^2}{dt} = \frac{2\, K_f\, (T_r - T_g)}{\Delta h_{fg}\, \rho_f} \qquad (2.9)$$

Mason (56) has derived a differential equation for the rate of growth or evaporation of the drop by using the respective laws of Fick and Fourier and employing the Clausius-Clapeyron equation,

$$\frac{dr^2}{dt} = \frac{\frac{p_g}{p_s} - 1}{\frac{\rho_f R T_g}{2\alpha_m p_s} + \frac{\Delta h^2_{fg} \rho_f}{2K_f R T_g^2}} \qquad (2.10)$$

where α_m = mass diffusivity

2.2.2 Phase change between small droplets and vapour

If Kn > 4, the carrier phase may be treated with respect to the droplet as having uniform temperature, steam velocity (no slip) and composition through space. Heat conduction, viscous shear and surface tension being properties of a continuum, lose physical relevance. Therefore, the transfer rate of heat and momentum must be expressed as the sum of the amounts of energy and momentum transferred individually by the molecules which collide with the droplets. Similarly, the mass transfer rate is the net difference in the total mass of vapour molecules condensing on and evaporating from the droplet. The heat capacity of the small droplet ($d \lesssim 1.0$ μm) is negligible compared with the amount of latent heat released by condensation. Therefore, the rate of phase change is governed by the rate at which the latent heat can be carried away between the surface of the droplets and the vapour. The heat transfer between a droplet and the vapour is driven by the temperature difference $(T_\ell - T_g)$ which controls the rate of latent heat released or accepted by the droplet, as seen in the equation

$$\dot{Q} = 4\pi r^2 \rho_f \frac{dr}{dt} \Delta h_{fg} \qquad (2.11)$$

A number of investigators have defined the rate of phase change using different approaches. Gyarmathy (14) used a continuum equation to define the rate of heat transfer using a heat transfer coefficient modified by using the kinetic theory,

$$\dot{Q} = A_r \alpha_r (T_r - T_g) \tag{2.12}$$

where α_r = heat transfer coefficient = $K_g / [r\{1 + \frac{2\sqrt{8\pi}}{1.5\, a_{th} Pr_g} (\frac{\gamma}{\gamma+1}) Kn\}]$,

and the rate of growth or evaporation of droplet is defined by,

$$\frac{dr}{dt} = \frac{\alpha_r}{\Delta h_{fg}\, \rho_f} (T_r - T_g) \tag{2.13}$$

The kinetic theory approach appears to be a realistic solution of phase change for very small droplets and it was adapted to steam turbine studies as early as the work of Stodola (57). Kirillov and Yablonik (55), Gyarmathy (58), Hill (59) and Bakhtar et al (60) have used a combined approach using thermodynamic and kinetic theories to trace the history of the changing characteristics of the fog droplets in different conditions of steam flow.

Kirillov and Yablonik (55) derived an equation for the rate of growth or evaporation of droplets having very small diameters compared with the mean free path (i.e. $d << \ell'$). This equation can be written as,

$$\frac{dr}{dt} = \frac{Cp\, \rho_g}{\Delta h_{fg} \rho_f} \sqrt{\frac{R\, T_g}{2\pi}} \; \frac{T_\ell - T_g}{1 - \frac{2\sigma}{r \Delta h_{fg} \rho_f}} \tag{2.14}$$

Gyarmathy (58) has expressed a differential equation for obtaining the growth or evaporation history of very small droplets ($Kn >> 1.0$),

$$\frac{dr}{dt} = c \frac{p_g}{\rho_f \sqrt{2\pi RT_g}} \left[1 - \frac{p_s(T_r)}{p_g} \sqrt{\frac{T_g}{T_r}} \exp\left(\frac{2\sigma}{r\rho_f RT_r}\right) \right] \tag{2.15}$$

where c = condensation or evaporation coefficient $\approx$ 1.0

σ = surface tension.

Moses and Stein (61) have used the law of droplet growth which is developed by Hill (59), and it is valid for Kn >> 1.0,

$$\frac{dr}{dt} = \frac{c(p_g - p_s)\, V_{pm}}{\sqrt{2\pi\, m_{pm}\, k_B\, T_g}} \tag{2.16}$$

where c = condensation coefficient $\approx$ 1.0

V_{pm} = volume per molecule in the condensed phase

k_B = Boltzmann's constant = 1.38×10^{-16} ergs/mole

m_{pm} = mass of one molecule.

Bakhtar et al (60) have given a general equation for droplet growth, or evaporation, based on the kinetic theory,

$$\frac{dr}{dt} = \frac{2}{3} \frac{Kn}{\rho_f\, (1+2.7\, Kn/c)} \sqrt{\frac{8}{\pi R}} \left[\frac{p_g}{\sqrt{T_g}} - \frac{p_s(T_\ell, r)}{\sqrt{T_\ell}} \right] \tag{2.17}$$

where $p_s(T_\ell, r)$ = saturation pressure, and is dependent on the saturation temperature and droplet size.

This equation covers all values of Knudsen number and has been selected for use in the present work, (Chapter 7).

Gardner (62) made a comprehensive analysis of the transfer of

energy, momentum and mass between a very small droplet (Kn > 4) and the surrounding vapour.

2.3 Deposition of Fog Droplets

It is very important to understand fully the deposition processes in order to predict the wetness losses and erosion in wet steam turbines. These processes depend on the droplet or particle size and on the nature of the flow. In a wet steam L.P. turbine spontaneous nucleation generates droplets having a small size (0.01 - 1.0 μm diameter or Kn > 0.2) and these droplets are subjected to phase change during the expansion process. Most of the droplets lie in the transition and molecular regions. Knowledge of the deposition rate will help the steam turbine designer to solve the erosion problem by various means, (Chapter 3). Bearing in mind the deposition process is the first stage of the erosion cycle, it is important to break the cycle at this stage rather than allowing it to continue for deposition to occur. This is the aim of this study. Therefore, it is necessary to understand the following points:

1. The cohesion and adhesion between the droplets themselves and between the droplets and the solid surfaces.

2. The mechanisms of deposition of droplets, within the range of the present work, on the blade surfaces.

2.3.1 Adhesion and cohesion of particles and droplets

The interaction between the fog droplets themselves may cause agglomeration due to the cohesion of the droplets. This only occurs if the cohesive force is greater than the force between the molecules of the droplets.

Smaller droplets (d < 0.5 μm) exhibit more violent Brownian motion than larger droplets, and have greater opportunity to collide with each other and to agglomerate. If the collision takes place between fog droplets and the internal surfaces of the turbine, the droplets will adhere to the surfaces and there is no chance for re-entrainment as found by Refs. (3, 4, 7, 15 and 63). However, if the collision force of a solid particle on the surface exceeds the adhesion force, the particles may re-entrain or bounce to the main flow. The results of these interactions have a great effect on the mechanism or the rate of deposition of small particles on surfaces.

There are many types of forces which contribute to the strength of the adhesive bond between the particles themselves and between the particles and the surfaces. These forces have been discussed in detail by Corn (64) and reviewed by El-Shobokshy (37). The forces and the factors influencing adhesion are:

1. Van der Waals forces. (Attraction force between molecules of particles themselves or particles and surfaces.

2. Electrostatic forces. (during generation of the particle electrostatic charges on the particles occur - The force depends on the charges and the distance between the particles or the particle and the surface.

3. Surface tension of absorbed surface films. (a wetted particle's surface as a result of humidity in the surrounding stream atmosphere, gives rise to forces due to surface tension which depend on the particle size and the temperature.

4. External force fields.

5. Factors influencing adhesion:

   (a) Particle and surface bulk material.

   (b) Surface contamination.

   (c) Nature of particle surface contact.

   (d) Temperature.

   (e) Approach to contact equilibrium.

2.3.2 Particle re-entrainment

Capture of particles or droplets by surfaces upon collision may occur. Possibilities of bouncing or re-entrainment also exist. Most of the theoretical and experimental studies published on particle deposition have found that small particles ($d \lesssim 1.0$ μm) are captured upon touching a surface. It was essential at the beginning of the present study to check whether the particles or droplets (0.01 - 1.0 μm diameter) used, will be captured by the blade surfaces upon contact or be re-entrained. This can be found from the results of other investigators. Two tests must be considered:

1. Before deposition:

Dunhneke (65) studied the mechanism of particle-surface collision. He found that there is a limiting value of incident velocity of the particle. If this limit is exceeded the particle may bounce and be re-entrained to the main flow. He derived the following equation for determining the maximum value of incident velocity:

$$V_{i,crit} = \frac{1}{d}\sqrt{\frac{\bar{A}}{\pi Z_o \rho_p}\left(\frac{1}{e^2} - 1\right)} \qquad (2.18)$$

where $V_{i,crit}$ = critical value of incident velocity

d = particle diameter

$\bar{A}$ = Hamaker constant

ρ_p = particle density

$Z_o = 4\overset{o}{A}$

e = coefficient of restitution = $\frac{V_{rebound}}{V_{incidence}}$ which is equal to 0.99 for solid particle.

2. After deposition:

Aerodynamic characteristics of the particle after being deposited on the surface must also be tested against the flow conditions. This test consists of calculating the drag on the deposited particles on surfaces when exposed to the steam flow. It has been considered that a particle adhering to a surface will be removed when the drag and lift forces exceed the adhering force. For small particles the lift force is negligible compared with the drag force. Therefore, the only force acting against the adhesion force is the drag force. Many investigators (3, 4, 7, 15) found for submicron particles, the maximum drag force acting on the deposited particles is very much lower than the forces required to dislodge the largest particle or droplet from the surface.

Theoretical work by Ryley (63) suggests that deposited fog droplets are unlikely to be re-entrained. From the study of capillarity forces he concluded that the residual energy in a deposited droplet is insufficient to cause detachment and the tangential forces are also too weak for the purpose.

2.3.3 Mechanisms of deposition

The mechanisms which are of concern to this work, plus others which may possibly be acting, will be discussed in this section.

1. Brownian motion:

This is a mechanism by which the particles or droplets within a purely laminar or stagnant flow are brought to the surface under the action of gas or vapour molecules colliding with the particle or droplet. This motion of suspended particles in a fluid was defined by Einstein as,

$$\bar{x}^2 = 2\,Dt \qquad (2.19)$$

where $\bar{x}^2$ = the mean square displacement of particle

t = the time taken for this displacement

D = diffusion coefficient of the particle, expressed by the equation

$$D = \frac{k_B\,T}{f}$$

k_B = Boltzmann constant

T = absolute temperature

f = reciprocal of the mobility of the particle.

This equation is valid only when all other external forces on the particle are absent, therefore, their continual motion will be random. When the particle path intercepts an interface, the particle will be deposited at the place of interception. Brownian motion increases with decreasing particle size and is negligible when Kn < 0.01 (i.e. in the continuum regime).

2. Diffusive deposition (motion due to concentration gradient):

Brownian motion does not change the mean concentration of the particles in an isolated aerosol cloud, provided there is no deposition of particles on the adjacent surfaces. If a concentration gradient exists normal to a surface, particles will migrate from the region of high concentration to the region with lower concentration. This migration due to the presence of a concentration gradient is known as diffusion. In stationary or flowing wet steam adjacent to an adiabatic surface, diffusion leads to the deposition of fog droplets from the steam (stagnant or flowing) to the blade surface. This deposition maintains a concentration gradient with the concentration of the droplets always being zero at the surface. The rate of transport or deposition of the droplets to the

surface in laminar or stagnant flow is equal to the product of the diffusion coefficient and the concentration gradient,

$$N = D \frac{dc}{dy} \tag{2.20}$$

The conditions for which this equation is valid are that the external forces (thermal, electrical, mechanical, etc.) are absent.

3. Eddy diffusion:

Fog droplets or small particles ($d < 1.0$ μm) closely follow the flow stream. In turbulent flow, these particles or droplets are brought near the surface by the action of eddies which exist in the turbulent boundary layer. This is followed by Brownian diffusion of the particle through the sublayer region. The effects of Brownian motion and concentration gradients, on the movement of the droplets outside the boundary sublayer, are negligible compared with the effect of eddies. However, Brownian motion is the dominant cause of droplet movement inside the sublayer.

Eddy diffusivity of the droplets of diameter less than 1.0 μm is assumed to be equal to the eddy viscosity of the flow. Therefore, the rate of deposition on the surfaces through turbulent flow can be written as in Refs. (4, 37, 66, 67, 68, 69, 70 and 71),

$$N = (D + \varepsilon) \frac{dc}{dy} \tag{2.21}$$

where $\varepsilon = \varepsilon_M = \varepsilon_p$

The boundary conditions are:

at $y = r$, $c = 0.0$

at $y = \delta$, $c = c_\infty$

The only modifications that can be made to this equation is the values of D and ε and this will be discussed later in this Chapter.

4. Eddy impaction:

In the turbulent flow, the large particles ($d > 1.0$ μm) may gain sufficient momentum from the turbulent eddies near the surface to be projected directly through the remaining distance to the surface (free flight) without responding to the molecular (Brownian) diffusion which will be negligibly small. The rate of mass transfer from the free stream to the surface, therefore, can be written in the form,

$$N = \varepsilon \frac{dc}{dy} \tag{2.23}$$

The boundary conditions are,

$$\text{at } y = S + r, \quad c = c_S$$

$$\text{at } y = \delta, \quad c = c_\infty$$

where S = stopping distance and it is determined by,

$$S = V_i \, \tau_r$$

τ_r = relaxation time = $\dfrac{\rho_p \, d^2}{18\mu}$

V_i = the incidence velocity which can be calculated from the equation given by Davies (72). The full derivation is presented in Ref. (37):

$$V_i = u_* \left[\tfrac{1}{2} \left(1 - \frac{r^+ + 10}{\tau_r^+}\right) + \left\{ \tfrac{1}{4} \left(1 - \frac{r^+ + 10}{\tau_r^+}\right)^2 + \frac{r^+}{\tau_r^+} \right\}^{\frac{1}{2}} \right] \tag{2.24}$$

where u_* = shear velocity

r^+ = dimensionless droplet radius = $\frac{ru_*}{\nu}$

τ_r^+ = dimensionless relaxation time = $\frac{\tau_r \, u_*^2}{\nu}$

5. Sedimentation of Aerosol Particles

Sedimentation is a continuum phenomenon and it is the mechanism of deposition of the particles when the flow is stagnant. When a spherical particle is freely falling it attains a terminal velocity at which the drag force on it is equal to its weight.

Falling particles are usually subject to bombardment from gas molecules due to Brownian motion. However, if it is assumed that the particle is rigid, falling independently, free from external influences and is of a size larger than the length of mean free path of the gas molecules and without inertia effects, its motion will lie in the Stokes regime. In such a case the Stokes drag will be:

$$F_d = 3\pi \mu V_s d \tag{2.25}$$

where V_s = the settling velocity.

This drag is equal to the weight of the particle and therefore,

$$3\pi \mu V_s d = \frac{\pi}{6} d^3 (\rho_p - \rho_g) g$$

where g = acceleration of gravity

$\rho_p >> \rho_g$

and hence the settling velocity is

$$V_s = \frac{\rho_p g d^2}{18\mu} \tag{2.26}$$

This equation is valid when the diameter of the particle is larger than the molecular mean free path and $Re_p = \frac{\rho_g V_s d}{\mu}$ should be less than 1.0.

If the particle size is comparable to the molecular mean free path (ℓ') the medium in this case cannot be regarded as a continuum and equation (2.26) is no longer valid. The particles will move faster than predicted because of the slip between them and the gas molecules. A Cunningham correction factor must then be used in equation (2.26), to take account of this slip, which has the form,

$$F_C = 1 + 2A\ Kn + 2B\ Kn\ e^{\frac{-C}{2Kn}} \qquad (2.27)$$

where A = 1.246, B = 0.42 and C = 0.87

Kn = Knudsen number = $\frac{\ell'}{2r}$

ℓ' = molecular mean free path = $\frac{1.5\ \mu\ \sqrt{RT}}{p}$

The final form of the settling velocity becomes,

$$V_s = \frac{\rho_p\ g\ d^2}{18\mu} F_C \qquad (2.28)$$

Ryley, Davies and El-Shobokshy (3, 4, 37) concluded that for submicron particles the contribution to deposition from settling compared with that due to eddy and Brownian diffusion, is very small and can be neglected. They found that the effect of sedimentation increases with increasing particle size and decreasing shear velocity.

2.3.4 Theory of thermophoresis

In the steady state, under the influence of a temperature gradient and friction the aerosol particles or droplets move with a variable velocity towards the region of lower temperature. This phenomenon is called thermophoresis and was first observed in 1870 by Tyndall. Since then many contributions and developments to the theory have been made by a great number of investigators. The nature of thermophoresis is that if a droplet or particle is within a vapour or gas which is subject to a temperature gradient, the force due to the molecular momentum change on the hot side hemisphere exceeds that on the cooler side hemisphere and the net force acts to propel the droplet down the temperature gradient. Therefore, the thermophoretic force depends on the temperature gradient through the medium, the pressure of the medium, the thermal conductivities of the droplet and of the medium and the droplet size.

The theory for small droplets ($d < 1.0$ μm) is well established through employing the kinetic theory, and those of intermediate and large droplets have been considerably improved in later years. In wet steam flow the droplets are always subjected to condensation or evaporation, depending on the flow conditions. Therefore the sizes of the droplets lie in the molecular and intermediate regions, and thus the predicted formulae for the thermophoretic force and velocity need to cover a wide range of Knudsen number. The theories of thermophoresis for small, intermediate and large droplets and the relevant contributions which have been made since the phenomenon became known, will be discussed in this Section.

1. Thermophoresis with small particles or droplets ($d < 1.0$ μm):

If $Kn > 1.0$, the particle presence does not considerably affect

the velocity distribution of the surrounding gas molecules. Therefore with no phase change between the droplet and the surrounding vapour, the forces on the moving droplet consisting of friction, thermophoretic and any other forces, can be determined by calculating the momentum transferred per unit time (the momentum transfer method). Most of the theories for the thermal forces on small particles ($d < 1.0$ μm) have been found, by many investigators, to be in good agreement with the experimental results.

The first theoretical treatment for thermophoresis was made by Einstein in 1924. Epstein (73), in 1929, repeated the derivation of the theoretical formula given by Einstein; the difference between the two formulae is the constant multiplier as shown in the equation, due to Epstein,

$$F_T = - 17.9 \frac{rK_g}{2K_g + K_p} p \frac{\ell'^2}{T} \nabla T \qquad (2.29)$$

where r = droplet radius in cms

p = pressure in dyne/cm^2

K_g, K_p = thermal conductivity of gas and particles

ℓ' = molecular mean free path

∇T = temperature gradient

Epstein's result has been found by Schaelt et al (74) and Derjaguin et al (75) to be in reasonably good agreement with experiments for particles of low thermal conductivity, but it underestimates the thermal force on particles of high thermal conductivity.

Waldmann (76) derived a new expression for the thermophoretic force based on the concepts of the kinetic theory, which is in the form,

$$F_T = -\left(\frac{32}{15} r^2 \lambda \nabla T\right)/\bar{C} \qquad (2.30)$$

where λ = translational part = $\dfrac{15\, k_B\, \mu}{4m}$

m = molecular mass

$\bar{C}$ = mean thermal velocity of the gas molecules = $\sqrt{\dfrac{8\, k_B\, T}{\pi\, m}}$

Later, Cha and McCoy (77) showed that the thermophoretic force for small droplets may be expressed as,

$$F_T = \frac{Kn}{2\sqrt{2}\, a_1 (1 + b_1 Kn)} \left[1 - \exp\left(-\frac{a_1}{2Kn}\right)\right] \sqrt{\frac{8}{3\pi}\, \phi\, b_1\, Kn\, \frac{K_g d^2}{d_m^2}}\, \nabla T \qquad (2.31)$$

where d_m = mean molecular diameter of the gas

d = particle diameter

$$a_1 = \sqrt{\frac{\pi\, \phi}{6(1 + b_1\, Kn)}}$$

b_1 = 3.23 when the thermal accommodation = 1.0

$\phi = 0.25\,(9\gamma - 5)\, Cv/R$

For the intermediate range of droplet size ($0.1 < Kn < 2.5$), a theoretical expression for the thermophoretic force has been given by Brock (78),

$$F_T = -18\pi\, \mu \sqrt{\frac{2R}{\pi T}}\, Kn\, C\, \nabla T \qquad (2.32)$$

where $C = \dfrac{\frac{K_g}{K_p} - 2\, C_t\, Kn}{(1 - 6\, C_m\, Kn)(1 - 2\,\frac{K_g}{K_p} - 4\, C_t\, Kn)}$

C_m, C_t are constants.

Talbot et al (79) modified Brock's formula, equation (2.32), in order for it to be applicable to a wide range of Knudsen number ($0 < Kn < \infty$). They obtained an equation for calculating F_T,

$$F_T = - \frac{12 \pi \mu \nu r C_s \left(\frac{K_g}{K_p} + 2 C_t Kn\right) \nabla T}{(1 + 6 C_m Kn)(1 + 2 \frac{K_g}{K_p} + 4 C_t Kn) \bar{T}} \qquad (2.33)$$

where $C_s = 1.14$, $C_t = 2.18$ and $C_m = 1.14$.

To obtain an expression for the thermophoretic velocity over the entire range of Knudsen number, Talbot et al (79) equated F_T from equation (2.33) to the Millikan drag formula, which has the form,

$$F_d = \frac{6 \pi \mu r V}{1 + 2 Kn (A + B \exp (- C/2Kn))} \qquad (2.34)$$

to give

$$V_T = - \frac{2 C_s \nu \left(\frac{K_g}{K_p} + 2 C_t Kn\right) \left[1 + 2 Kn (A + B \exp (- C/2Kn))\right] \nabla T}{(1 + 6 C_m Kn)(1 + 2 \frac{K_g}{K_p} + 4 C_t Kn) \bar{T}} \qquad (2.35)$$

where $A = 1.2$, $B = 0.41$ and $C = 0.88$.

Equation (2.35) has been used in the present work (Chapter 7) for determining the thermophoretic velocity since it is valid for the entire range of the expected sizes of the droplets.

2. Thermophoresis with large droplets (without phase change):

The presence of small particles has no influence on the distribution of the gas molecules around the particles. With large particles, however,

this influence must be taken into account. From such effects, discontinuities exist in the gas temperature (a jump) and the gas tangential velocity (slip) at the boundary with respect to temperature and velocity at the surface. The "jump" and the "slip" are dependent on the conditions and the nature of the flow.

Epstein (73) calculated the thermophoretic force on a larger particle by solving the Fourier heat conduction equation and the Navier-Stokes' flow equation. The expression was in the form,

$$F_T = - 6 \pi \mu r \frac{2 K_g}{5 (2 K_g + K_p)} \frac{K_g}{p} \nabla T \qquad (2.36)$$

Equation (2.36) is valid for $\frac{K_p}{K_g} < 10$.

Brock (80) modified Epstein's formula, equation (2.36), took into consideration the isothermal slip which was predicted by Maxwell, the effect of thermal conductivity, the effect of temperature jump at the gas-wall interface and a Knudsen number correction to obtain an expression for the thermophoretic velocity in the form,

$$V_T = - \frac{3}{2} \frac{\mu}{\rho_g T} \frac{(K_g + 2 C_t K_p Kn) F_C \nabla T}{(1 + 6 C_m Kn)(2 K_g + K_p + 4 C_t Kn)} \qquad (2.37)$$

where F_C = Cunningham correction factor

$= 2.25 Kn + 0.84 Kn \exp (- 0.435/Kn)$

Derjaguin and Talamov (81) improved Epstein's and Brock's formulae by taking into account the effect of temperature stress of the gas phase and the variation of the velocities of the gas molecules before striking the particle. They formulated the thermophoretic velocity in the simple form,

$$V_T = - \frac{1}{2} \frac{\mu}{\rho_g T} \frac{(8\ K_g - K_p)}{(2\ K_g + K_p)} \nabla T \qquad (2.38)$$

Cha and McCoy (77) simplified equation (2.31) to determine the thermophoretic force on particles which have diameter greater than 1.0 μm,

$$F_T = - 0.81 \sqrt{Kn^3}\ \frac{K_g\ d^2}{d_m^{\ 2}} \nabla T \qquad (2.39)$$

Work published by Gardner (62) and Byers and Calvert (82) suggest that in the slip flow regime ($0.5 < Kn < 2.5$), Brock's expression, equation (2.37), offers a reasonable prediction for the thermophoretic velocity of particles, whilst Derjaguin and Talamov's formula, equation (2.38), is more applicable in the regime where $Kn \ll 1$. Wood (30) used Cha's and McCoy's formula and found good agreement between the predicted and measured results for the deposition rate of $Mg(OH)_2$ particles on duct surfaces. However, the maximum size of the droplets used in the present work is about 1.0 μm. Therefore, only the thermophoresis theories for small and intermediate particle size will be used.

3. Thermophoresis in flow with phase change

The mixture of liquid and vapour is subject to phase change (either condensation or evaporation) if the temperature of the vapour is lower or higher than that of liquid phase (i.e. disequilibrium phenomenon). Let us concentrate on the flow of wet steam inside the boundary layer on a L.P. turbine guide blade. If the blade surface is cooler than the surrounding steam, the deposition of the existing droplets increases due to:

(i) The increase in the droplet size by condensation.

(ii) The effect of a thermophoretic force towards the blade surface.

However, if the blade surface is hotter than the surrounding steam as in the present work, evaporation of the droplets will occur as long as the temperature of the vapour is higher than the saturation temperature ($T_s(p)$). The deposition of the surviving droplets, which are at a distance from the blade surface, onto the heated surface will, therefore, be lower than that on an adiabatic surface and much lower than that on the cooled surface. The reasons for this are:

(i) The droplet size is reduced by evaporation and a dry region may be created along the blade surface.

(ii) The droplets are pushed away from the blade surface by the effect of thermophoresis.

Thermophoresis and the mechanisms of deposition are dependent, among the other things, on the droplet size. If the size of the droplet is very small ($d < 1.0$ μm), the droplet temperature is uniform at all times and under different flow conditions (i.e. heat capacity and heat conduction are not significant). Therefore, the theory of thermophoresis for small solid particles can be used by taking into consideration the change in droplet size and the variation in the temperature gradient due to condensation or evaporation. From the theory it can be seen that:

$$V_T = V_T \left(Kn, \frac{K_g}{K_p}, \frac{y\ K_g \left(\frac{dT}{dy}\right)_x}{\dot{m}\Delta h_{fg}}\right) \qquad (2.40)$$

where y = the distance along the normal axis

$\dot{m}$ = mass transfer between the liquid and vapour phases due to condensation or evaporation

$(\frac{dT}{dy})_x$ = the temperature gradient of the mixture along the normal axis, which is affected by the amount of mass and heat transfer between the two phases due to thermodynamic disequilibrium.

If the droplet size is large (d > 2 μm), the temperature of the centre of the droplet is either leading or lagging the temperature of the surface due to heating, cooling, or expansion of the flow. This may result in:

(i) Deformation of the droplet.

(ii) Flashing or disintegration of the droplet.

(iii) Unsteady heat flux inside the droplet.

The temperature of the droplet surface is not uniform as a result of different rates of condensation or evaporation to or from the surface and a reaction force, due to mass transfer, on the droplet may have considerable effect on the movement of the droplet. Therefore, the problem is extremely complicated in detail and no thermophoresis theory exists to deal with this complex situation at the present time.

Gardner (62) derived an expression for calculating the thermophoretic force on a small evaporating droplet which is stationary with respect to the vapour. This expression can be written in a form,

$$F_T = - 6\pi \mu r \left[\frac{\nabla T \, K_g}{\rho_g \, \Delta h_{fg}}\right] \Pi_2 \qquad (2.41)$$

where

$$\Pi_2 = \frac{4+4C_i\ Kn\left(\frac{K_p}{K_g}\right)\left[2+\frac{\pi}{24Kn^2}GH\right]+\frac{\pi}{18Kn^2}G\left[1+12C_m\ Kn\right]}{1+\frac{2}{H}\left[1+2\left(\frac{K_g}{K_p}\right)+4C_i\ Kn\right]\left[1+4C_m\ Kn\right]+\frac{\pi}{18Kn^2}G\left[1+4C_i\ Kn\right]\left[1+6C_m\ Kn\right]} \qquad (2.42)$$

$$G = \frac{\Delta h_{fg}\ M_m}{RT}$$

$$H = \frac{\mu\ \Delta h_{fg}}{K_p T}$$

M_m = molecular weight

$$C_i = \frac{5}{1+\gamma}\left(\frac{2-\alpha}{\alpha}\right)$$

α = accommodation coefficient $\approx$ 1.0

γ = specific heat ratio

$$C_m = \frac{2-\alpha}{\alpha}$$

For large particles (d > 2 μm), Gardner found that the last term in both the numerator and denominator of equation (2.42) dominate and gives $\Pi_2 \approx 1.0$. The large droplet will obey Stokes' law, and he suggested that the equilibrium velocity (thermophoretic velocity) will be

$$V_T = -\frac{K_g\ \nabla T}{\rho\ \Delta h_{fg}} \qquad (2.43)$$

Gardner's work (62) on the transfer of mass, momentum and energy between a very small droplet (Kn > 1) and the surrounded vapour is very useful and is a good contribution to understanding the behaviour of evaporating droplets in the flow.

2.3.5 Theory of diffusional deposition

For very small particles ($d < 1.0$ μm) the effects due to sedimentation, inertia impaction, eddy impaction and motion due to electrical and body forces are negligible. Brownian, concentration and eddy diffusion are the only mechanisms controlling the movement and the deposition of such particles or droplets onto adiabatic surfaces. If the surface temperature is different from that of the free stream, thermophoresis can have a considerable effect on the deposition rate of the particles. However, even if the surface temperature is equal to that of the adiabatic temperature (no heat transfer to or from the wall), the transfer of heat inside the flowing gas due to friction will create a temperature gradient through the boundary layer. The thermophoresis effect must therefore be taken into consideration even though its contribution will be small. In highly accelerated flows in adiabatic nozzles (steam and gas turbines), the effect of thermophoresis will be significant (Chapter 7).

It can be concluded that the effect of the thermophoresis on the particles should always be considered. Its effect depends on:

1. The size of the particle or droplet.
2. The temperature gradient through the boundary layer.
3. The thermal conductivities of the droplet and the medium.
4. The gas velocity.

Most investigators have ignored the effect of thermophoresis on the deposition rate of particles onto an adiabatic surface.

Broadly, deposition of small droplets falls into two main categories, depending on the nature of the flow. In the laminar flow,

Brownian motion and thermophoresis are the dominant phenomena, whilst in the turbulent flow, outside the boundary sublayer, eddy diffusion controls the movement of the particles. Thermophoresis in the turbulent flow is more effective in the sublayer, since $\frac{dT}{dy}$ is very high through it. The deposition rate is defined by the "deposition velocity" (V_{net}) which has the dimensions of velocity (m/s) and is the mass deposition rate per unit area per unit time divided by the mean concentration (c_∞).

$$V_{net} = \frac{N_{net}}{c_\infty} \tag{2.44}$$

This section will involve the study of the deposition of the particles from laminar and turbulent flow, with or without taking the thermophoresis into account.

(a) Diffusion through a laminar boundary layer:

In wet steam flow (without phase change) a hydrodynamic boundary layer and a particle concentration boundary layer will be built up on the blade surface. Feasible assumptions can be made to simplify the theoretical analysis,

1. The thickness of the diffusion layer is equal to that of hydrodynamic layer.

2. The concentration gradient behaves the same as the velocity gradient, and the boundary conditions are:
   at $y = 0.0$, $u = 0.0$ and $c = 0.0$
   at $y = \delta = \delta_d$, $u = U_\infty$ and $c = c_\infty$ where $\delta_d = \int_0^\infty \left(\frac{c_\infty - c}{c_\infty}\right) dy$.

3. The solution of mass transfer equations can be obtained from the similarity between momentum and mass transfer or heat and mass transfer. The equations of momentum, heat and mass transfer for

zero pressure gradient can be written in the forms:

(i) Momentum transfer equation

$$u \frac{\partial u}{\partial x} + v \frac{\partial v}{\partial x} = \nu \frac{\partial^2 u}{\partial y^2} \qquad (2.45)$$

(ii) Heat transfer equation

$$u \frac{\partial T}{\partial x} + v \frac{\partial T}{\partial y} = \frac{K_g}{\rho C_p} \frac{\partial^2 T}{\partial y^2} \qquad (2.46)$$

(iii) Mass transfer equation

$$u \frac{\partial c}{\partial x} + v \frac{\partial c}{\partial y} = D \frac{\partial^2 c}{\partial y^2} \qquad (2.47)$$

The solutions of momentum and heat transfer are well established in the text books, therefore, a similar solution can be obtained for the mass transfer due to the similarity between equations (2.45), (2.46) and (2.47). However, if a thermophoresis term is introduced into the mass transfer equation the solution will be more complicated. Therefore, the solution of the mass transfer equation can be divided into two main parts, with and without considering the effect of thermophoresis.

I. Diffusional deposition without thermophoresis:

Davies (83) has simplified the equation of mass transfer by assuming:

(1) One-dimensional flow along the horizontal axis (x), therefore the velocity v is negligible compared with the velocity u.

(2) The concentration gradient through the diffusion layer is shown

to be in the form

$$\frac{\partial^2 c}{\partial y^2} = \frac{c_\infty}{\delta_d^2} \tag{2.48}$$

(3) The concentration gradient along x-axis is linear and can be written in the form

$$\frac{\partial c}{\partial x} = \frac{c_\infty}{x} \tag{2.49}$$

(4) The velocity gradient through the hydrodynamic boundary layer $(\frac{du}{dy})$ is similar to $\frac{dc}{dy}$, therefore, he obtained a relation between the thicknesses of the hydrodynamic boundary layer (δ) and the diffusion layer (δ_d) as follows

$$U_d = U_\infty \frac{\delta_d}{\delta} \tag{2.50}$$

where U_d = the velocity at the edge of diffusion layer. Hence, equation (2.47) becomes

$$D \frac{c_\infty}{\delta_d^2} - \frac{c_\infty U_\infty}{x} \frac{\delta_d}{\delta} = 0.0 \tag{2.51}$$

or

$$\delta_d^3 = \frac{Dx\delta}{U_\infty} \tag{2.52}$$

(5) The flow is incompressible and with zero pressure gradient, the thickness of the laminar boundary layer is given by Ref. (84) as

$$\delta = \frac{\beta x}{\sqrt{Re_x}} \tag{2.53}$$

where β = constant which can have different numerical values, depending on the method used to solve the momentum equation. This value can be 3.464, 4.64 or 5.835.

(6) The rate of deposition can be defined as

$$N = D \frac{c_\infty}{\delta_d} \tag{2.54}$$

Therefore the deposition velocity ($V_d = \frac{N}{c_\infty}$) can be determined from equations (2.52), (2.53) and (2.54) in the form:

$$V_d = \frac{U_\infty}{\beta^{1/3}\, Sc^{2/3}\, Re_x^{1/2}} \tag{2.55}$$

where Sc = Schmidt number = $\frac{\nu}{D}$

Equation (2.55) was successfully applied by El-Shobokshy (37) and Davies (4).

The theory for heat transfer was originally presented by Squire (85) and has been employed by many investigators in their experimental work. Lee (86) has used a similar analysis to Squire's for mass transfer, and he obtained

$$Sh = \frac{0.5715}{\frac{\delta_d}{\ell}\sqrt{Re_\ell}} \tag{2.56}$$

and then,

$$\text{Percentage deposition/cm}^2 = \frac{h_d}{Q} \times 100 \tag{2.57}$$

where Sh = local dimensionless mass transfer coefficient

Q = volumetric flow rate

$h_d = Sh \frac{D}{\ell}$

ℓ = the length of the plate or the chord of the blade.

$\frac{\delta_d}{\ell}$ can be obtained from numerical integration of the following equations:

$$\frac{\delta_1}{\ell}\sqrt{Re_\ell} = \left[\left\{2.96 \int_0^{x/\ell} \left(\frac{U_\infty}{U_{\infty_2}}\right) d\left(\frac{x}{\ell}\right)\right\} / \left(\frac{U_\infty}{U_{\infty_2}}\right)^6\right]^{1/2} \tag{2.58}$$

and

$$\left(\frac{\delta_d}{\delta_1}\right)^2 \phi\left(\frac{\delta_d}{\delta_1}\right) = \left[0.386 \left(\frac{U_\infty}{U_{\infty_2}}\right)^4 \int_0^{x/\ell} \left(\frac{U_\infty}{U_{\infty_2}}\right) d\left(\frac{x}{\ell}\right) / Sc \int_0^{x/\ell} \left(\frac{U_\infty}{U_{\infty_2}}\right)^5 d\left(\frac{x}{\ell}\right)\right] \tag{2.59}$$

The function $\phi\left(\frac{\delta_d}{\delta_1}\right)$ is given by

$$\phi\left(\frac{\delta_d}{\delta_1}\right) = \frac{1}{0.8604} \int_0^\infty f\left(\frac{0.8604y}{\delta_1}\right) \left[1 - f\left(\frac{0.8604y}{\delta_1} \frac{\delta_1}{\delta_d}\right)\right] dy \tag{2.60}$$

where $f\left(\frac{0.8604y}{\delta_1}\right)$ is the Blasius distribution for velocity $\frac{u}{U_\infty}$

δ_1 is the displacement thickness.

Parker and Lee (7) plotted the values of $\left(\frac{\delta_d}{\delta_1}\right)^2 \phi\left(\frac{\delta_d}{\delta_1}\right)$ against $\frac{\delta_d}{\delta_1}$. Numerical integration of equation (2.59) gives the values of $\left(\frac{\delta_d}{\delta_1}\right)^2 \phi\left(\frac{\delta_d}{\delta_1}\right)$ along the blade surface. The corresponding values of $\frac{\delta_d}{\delta_1}$, therefore, obtained from the plot (published in Ref. (7)). The values of $\frac{\delta_1}{\ell}$ along the x-axis can be obtained from equation (2.58). Thus,

equation (2.56) gives the value of Sh to be used in equation (2.57) for determining the deposition percentage of the particle in flow with zero pressure gradient.

Parker and Lee (7) obtained a good agreement between the experimental results and the results from equation (2.57) for aerosol in the cascade of steam turbine stator blades. Equation (2.57) is better than equation (2.55) for predicting the deposition rate through a laminar flow in the actual turbine, since it is not simplified by many assumptions which are not justified for the flow in a real turbine.

II. Diffusional deposition with thermophoresis

The effect of thermophoresis on the deposition of small particles through a laminar flow was treated by Davies (4). He added the thermophoresis term to the deposition equation to predict the net deposition rate on the blade surfaces.

$$N_{net} = D \frac{dc}{dy} + V_T c \tag{2.61}$$

where N_{net} = the net deposition rate

V_T = thermophoretic velocity

$V_T c$ = mass transfer by thermophoresis.

The integration of equation (2.61) gives,

$$V_{net} = \frac{V_T}{1 - \exp(- V_T \delta_d / D)} \tag{2.62}$$

where V_{net} = the net deposition velocity.

The thickness of the diffusion layer can be obtained from:

1. Equation (2.53) when the flow has no pressure gradient.

2. Equations (2.58), (2.59) and (2.60) when the flow has a pressure gradient.

Expressions for V_T have been given by many investigators (73, 76, 77, 78 and 79). A suitable expression is that given by Talbot et al (79), equation (2.35), since it is valid for the entire range of Knudsen number (Kn).

(b) Diffusion through a turbulent boundary layer

The transfer of particles or droplets from a turbulent stream to a boundary wall has been studied by a number of investigators both theoretically and experimentally. The mechanisms of deposition fall into three main classes, depending on their size range. The smallest particle (Kn > 1.0 or d $\lesssim$ 1.0 μm) are deposited by diffusion analogues to the molecular (Brownian diffusion) and turbulent diffusion (eddy diffusion) process controlling gaseous mass transfer.

Deposition of particles in the intermediate size range (0.1 < Kn < 1.0 or 1 < d < 50 μm) may be calculated by considering a turbulent eddy diffusion or eddy impaction process in which the particles are assumed to acquire momentum towards the wall as a result of turbulence and the mass of the particle.

The largest droplets or particles (Kn < 0.1 or d > 50 μm) have a high inertia and are less readily deposited by the turbulent velocity component. This process is dependent on flow conditions, fluid and

droplet properties and it is known as turbulent impaction.

This section involves the history of developing the theory of deposition of particles in the range of $d < 2.0$ μm through the turbulent flow onto the surfaces. The published work on the deposition of large particles will be mentioned very briefly. The section is divided into two main studies, firstly the theory of deposition of small particles without taking thermophoresis into account, and secondly, the theory including the effect of thermophoresis on the deposition process.

For small particles or droplets a number of assumptions are made concerning the particles and the surrounding flow, these are:

1. The system (fluid + particles or droplets) is incompressible, two-dimensional and adiabatic.

2. Both phases are in equilibrium.

3. In a time-averaged sense, the system is in the steady state.

4. The droplets or the particles are rigid spheres.

5. No body or external forces act between particles, and no collisions occur.

6. There is no slip between the flow and the particles.

I. Diffusional deposition without thermophoresis

For adiabatic flow with low velocities, thermophoresis makes only a small contribution to the process of diffusional deposition and can therefore be neglected. The deposition flux through a turbulent flow, therefore, can be determined from equation (2.21),

$$N = (D + \varepsilon_p) \frac{dc}{dy}$$

The first difficulty that must be overcome in order to solve this equation is the determination of the turbulent diffusivity of the particles. For small particles ($d \leqslant 1.0$ μm) all the investigators in this field assume that the diffusivity of the particles and the viscosity of the fluid are identical, (i.e. $\varepsilon_p = \varepsilon_M$).

By adopting the classical approach of subdividing the boundary layer into three zones, (laminar, buffer and turbulent), some investigators assumed ε_M in laminar sublayer to be zero. Lin et al (69), found, however, that when $\varepsilon_p = \varepsilon_M = 0.0$, in the laminar sublayer, and equation (2.21) was integrated to obtain the deposition velocity coefficient, the theoretical results fell considerably below the experimental ones. In order to overcome this discrepancy they proposed the following variation of ε_M in the laminar sublayer,

$$\frac{\varepsilon_M}{\nu} = \left[\frac{y^+}{14.5}\right]^3 \tag{2.63}$$

This is purely empirical to align their model and experimental results. Substituting equation (2.63) into (2.21) and integrating gives them the equation of deposition velocity coefficient,

$$h_d = \frac{U_\infty}{\phi_d}\frac{f}{2} \tag{2.64}$$

where $$\phi_d = 1 + \sqrt{\frac{f}{2}}\left[\frac{14.5}{3}(Sc)^{2/3}F(Sc) + 5\ell n\left\{\frac{1 + 5.64\ Sc}{6.64(1 + 0.041Sc)}\right\} - 4.77\right] \tag{2.65}$$

$$F(Sc) = 0.5\ \ell n\left[\frac{\{1 + \frac{5}{14.5}(Sc)^{1/3}\}^2}{1 - \frac{5}{14.5}(Sc)^{1/3} + (\frac{5}{14.5})^2(Sc)^{2/3}}\right] + \sqrt{3}\ \tan^{-1}\left[\frac{\frac{10}{14.5}(Sc)^{1/3} - 1}{\sqrt{3}}\right] + \frac{\pi\sqrt{3}}{6} \tag{2.66}$$

f = skin friction coefficient

Lin et al (69) found, for their experimental conditions, that at a distance far away from the wall (outside the laminar sublayer) the mass transfer of the particles is less important and can therefore be neglected. El-Shobokshy (37) and Davies (4) in their simulation method to determine the deposition distribution of the fog droplets on L.P. steam turbine blades, have used the approach of Lin et al. Although they found a good agreement between their experimental results and the Lin et al model, the flow conditions and the particle properties used are not the same as those found in the actual turbine. Their results (theoretical and experimental) served only to give an indication about the behaviour of the fog droplets, but cannot truly describe the deposition distribution of fog droplets on the blade surfaces in the real turbine (more detail can be found in Chapter 7).

Davies (72), who did not assume a laminated structure for the boundary layer, also derived an empirical equation for ε_M based on his experimental results for pipe flow,

$$\frac{\varepsilon_M}{\nu} = \frac{(y^+)^{F_1}}{1000\left(\frac{2.5 \times 10^7}{Re}\right)^{F_2}} \qquad (2.67)$$

where $F_1 = 4 - (y^+)^{0.08}$

$$F_2 = \frac{y^+}{400 + y^+}$$

$$y^+ = y\, u_*/\nu$$

This equation is valid for a wide range of y^+ ($0 < y^+ \lesssim 500$).

The model of Friedlander and Johnstone (87) is similar to that of Lin et al except that the diffusion coefficient (D) was neglected in the laminar sublayer, buffer layer and turbulent core which is reasonable for

particles of more than 1.0 μm diameter.

Beal (66) used the theories of Friedlander-Johnstone and Lin et al in order to define a new equation of deposition flux of particles having a very wide range in size ($1 \times 10^{-3} < d < 30$ μm) in channel flow.

$$V_d = \frac{\bar{u}\sqrt{\frac{f}{2}}}{5\left[\left\{1 + \frac{10}{\nu h^+}(D-0.959\nu)\right\}\ell n\left\{\frac{D + 5.04\nu}{D+\nu(\frac{S^+}{5} - 0.959)}\right\} - \frac{10}{h^+}(6 - \frac{S^+}{5})\right] + \frac{1-13.73\sqrt{\frac{f}{2}}}{\sqrt{\frac{f}{2}}}} \qquad (2.68)$$

where h^+ = dimensionless channel spacing or pipe diameter

$$= \frac{h\,\bar{u}\sqrt{\frac{f}{2}}}{\nu}$$

S^+ = dimensionless stopping distance = $\frac{S\,\bar{u}\sqrt{\frac{f}{2}}}{\nu}$

f = friction factor.

Owen (88) proposed a simple formula for the deposition of particles in the intermediate size range, and it correlates well with the published experimental data, it is written in the form,

$$V_d = 4.5 \times 10^{-4}\ \tau_r^+ \qquad (2.69)$$

where τ_r^+ = dimensionless relaxation time = $\frac{u_*^2\ \tau_r}{\nu}$

τ_r = relaxation time = $\frac{m_p}{F_{d,s}} = \frac{\rho_p\ d^2}{18\mu}$

$F_{d,s}$ = Stokes drag force (valid only when $Re_p < 1.0$).

Sehmel (71) defined the eddy diffusivity of particles, in an intermediate size range, in terms of y^+ and τ_r^+ along the horizontal, vertical and ceiling surfaces as follows,

1. For horizontal surfaces,

$$\frac{\varepsilon_M}{\nu} = \psi \, (y^+)^{2.6} \, (\tau_r^+)^{1.2} \qquad (2.70)$$

where $\psi = 0.531 \exp (- 0.033 \, u_*)$

2. For vertical surfaces,

$$\frac{\varepsilon_M}{\nu} = 0.011 \, (u^+)^{1.1} \, (\tau_r^+)^{1.1} \qquad (2.71)$$

3. For ceiling surfaces,

a. when $u_* = 0.34$ m/s

$$\frac{\varepsilon_M}{\nu} = 0.0041 \, (y^+)^{1.3} \, (\tau_r^+)^{1.3} \qquad (2.72)$$

b. when $u_* = 0.75$ m/s

$$\frac{\varepsilon_M}{\nu} = 0.0087 \, (y^+)^{2.6} \, (\tau_r^+) \qquad (2.73)$$

These equations are generalised from the experimental results, and are valid for limited range of u_* and y^+ ($0.34 < u_* < 0.75$ m/s and $0.004 < y^+ < 15$).

McCoy and Hanratty (9) have plotted most of the available experimental results of dimensionless deposition velocity of particles, which have a wide range of sizes, against dimensionless relaxation time. They modelled these results using a number of empirical equations, depending on the particle size. These formulae are:

1. For small particles ($d < 1.0$ μm),

$$V_d = 0.086\ u_* \ Sc^{-0.7} \tag{2.74}$$

the deposition velocity is not dependent on relaxation time (τ_r).

2. For intermediate particle size ($1 < d < 10$ μm)

$$V_d = 3.25 \times 10^{-4}\ (\tau_r^+)^2 \tag{2.75}$$

3. For large particles ($d > 10$ μm)

$$V_d = 0.17\ u_* \tag{2.76}$$

the velocity of deposition appears to be relatively insensitive to the particle diameter and to the relaxation time. Equations (2.74), (2.75) and (2.76) are for predicting the deposition velocity of particles on the vertical surface only.

Crane (89) has studied the deposition flux of droplets, with intermediate and large sizes, on the wall of a wet steam turbine cross-over pipe.

The deposition of very large drops ($d > 150$ μm) on the walls has been investigated by Farmer et al (90). This range of sizes may be re-entrained into the steam flow from the water film which is deposited on the L.P. steam turbine fixed blade.

Rouhiainen and Stachiewicz (6) concluded that, for intermediate droplet sizes, the concept of Stokes' stopping distance is not valid under most flow conditions used in their work, ($Re_g < 3 \times 10^5$, $d > 10$ μm), since the effect of shear flow induced transverse lift forces on the particle and it cannot, therefore, be neglected.

Kubie (91) and Trela et al (8) have described the motion of large droplets in a turbulent flow. They presented two new models of droplet deposition on horizontal and vertical surfaces. They found a good agreement between the results from the theoretical models and their, and other experimental results.

Crane (2) has made a good survey on the movement of fog droplets in 500 MW L.P. steam turbine. He concluded that droplets with diameters below 0.5 μm cannot deposit on the leading edge and the concave surface by inertia impaction, since the collection efficiency is very low and is not significant.

II. Diffusional deposition with thermophoresis

The turbulent flow over smooth surfaces is often associated with high velocity gradients (along x and y axes) and a high temperature gradient due to friction. Therefore thermophoresis can have a great effect on the movement of the particles or droplets inside the boundary layer as a result of temperature gradient. The mechanism of thermophoresis is to drive the particles to or away from the surface, depending on the variation of the fluid temperature in the boundary layer region. In the case of heated surfaces, the combined effect of molecular and eddy diffusion on the small particles ($d < 1.0$ μm) will be opposed by the thermophoretic effect, which will be acting to repel the particles away from the region of higher temperature, (i.e. in the present case, the blade surface). The contribution of thermophoresis on the particle movement in the turbulent flow is lower than that in the laminar flow, since the effect of eddy diffusion exceeds that of Brownian diffusion in most cases.

El-Shobokshy (28) investigated the effect of thermophoresis on

the deposition flux of particles, for a range of sizes, on a horizontal pipe wall. The wall temperature was increased from 20°C up to 200°C. He found that:

1. When the wall temperature was increased by 30°C, the small particles ($0.1 < d < 1.0$ μm) were not deposited on the wall.

2. To prevent deposition of particles in the intermediate size range ($1 < d < 6$ μm), the wall temperature was increased by 80°C.

3. The large particles ($d \approx 100$ μm) are pushed away from the wall when the wall temperature was increased by 180°C.

His mathematical model consists of two equations, one for determining the deposition velocity and the other for calculating the thermophoretic velocity. He solved the two equations separately and then calculated the resultant velocity by adding the two velocities algebraically.

Vermes (29) studied the deposition of large particles ($Kn < 0.1$) on cooled gas turbine fixed blade. He found that when the blade is cooled to 593°C (the gas temperature is 1427°C), the deposition flux increased by 10 - 30 times due to the thermophoretic effect. The increase in the deposition is also dependent on the flow conditions of the gas.

Wood (30) investigated the deposition of molecules of acid vapour (H_2SO_4) and Mg $(OH)_2$ powder on the walls of flue ducts in oil-fired power stations. He found that the deposition flux increased by 7 - 12%, when the wall temperature was below that of the flue gas, as a result of thermophoresis. The benefits of thermophoresis in his case were:

1. It increased the deposition of Mg $(OH)_2$ powder on the duct wall

where it reacts with the deposited H_2SO_4 to produce harmless materials, therefore, preventing atmospheric pollution.

2. The wasted heat from the flue gas can be used in preheaters, therefore increasing the efficiency of the plant.

For small particles or droplets, a theoretical model for determining the combined effect of diffusion (Brownian + eddy) and thermophoresis on the movement of the particles in the turbulent flow was first established by Davies (4).

$$N = (D + \varepsilon_p) \frac{dc}{dy} + V_T c \qquad (2.77)$$

However, he used the empirical formula due to Lin et al for defining ε_p, in which he assumed the concentration gradient and the mass transfer due to thermophoresis and diffusion outside the laminar sublayer to be insignificant. From equation (2.77) one can see that the effect of thermophoresis is extended to the edge of the thermal boundary layer but $\frac{dc}{dy}$ is also significant through the remainder of the diffusion boundary layer. This can be seen from the comparison between Davies' theoretical and experimental results. The theoretical results of the net deposition are always below the experimental results, by a factor of six in some cases.

Most investigators neglected the transfer of mass outside the laminar sublayer. However in the present work, the combined effect of evaporation, diffusion and thermophoresis through the entire thickness of the turbulent boundary layer is taken into consideration.

Van Driest's model was used for defining the eddy diffusivity. Modification of that model was introduced since the flow in the actual turbine is subjected to relaminarisation. Therefore the flow conditions

and the boundary layer characteristics in the real steam turbine are entirely different from those studied by El-Shobokshy (37) and Davies (4). The effect of laminarisation of turbulent flow on the eddy viscosity and on the concentration gradient will be discussed in Chapter 7.

CHAPTER 3

RECENT METHODS FOR FINDING THE DISTRIBUTION OF WATER DEPOSITION ON LOW PRESSURE STEAM TURBINE BLADES AND FOR SUPPRESSING EROSION

3.1 Introduction

It is clear that the deposition and accumulation of fog droplets (0.01 - 1.0 μm diameter) are a principal cause of possible erosion. A series of investigations into the deposition mechanisms and mass distribution within the L.P. steam turbine have been carried out since the late sixties in the steam laboratory at the University of Liverpool. The aim of these studies has been to find a suitable method for controlling the deposition of droplets and hence erosion of the turbine blades.

There are many mechanical and thermal methods of controlling erosion. The main function of these methods is to reduce part or all of the cause of erosion; these methods are:

1. Provision of local hardened surfaces.
2. Increase of axial distance between the fixed and moving blades to allow longer time for droplet acceleration.
3. Reducing of blade surface area in order to minimise deposition. This method is not practical for modern turbines, since the extraction of energy from low pressure, low density steam requires large blade surface areas.
4. Extraction of deposited water from the blade surfaces.
5. Heating of the blade surface to evaporate the water which has deposited or to prevent the deposition of droplets in the flow.
6. Acceleration and/or atomisation of water drops during transport.

This Chapter presents a comprehensive review of the methods developed for measuring the deposition rate and for controlling the erosion within the turbine. Due to the long history of steam turbines, it is not practicable to give a complete review. For this reason the methods introduced here are those which have been employed since 1964.

3.2 The Deposition of Fog Droplets onto the Turbine Blade

Generally the deposition rate is a function of the droplet size and the nature of the flow of the medium (air, steam or any gas). Through the last stages of the steam turbine, the steam with a small initial degree of superheating, expands rapidly inside the saturation region, and the flow becomes supersaturated. Subsequently, self-nucleation takes place to form a large number of very fine droplets, usually called fog. The size and growth of the droplets depends upon the rate of expansion ($\dot{p}$). When this is low, relatively large droplets can be formed. However, for all values of ($\dot{p}$), the droplet sizes are in the range 0.01 - 1.0 μm in diameter. The means of deposition of these droplets on the blade surfaces may be:

1. Impact diffusion - at the stagnation point.
2. Eddy diffusion - inside the transition zone.
3. Brownian diffusion - inside the laminar flow.
4. Eddy plus Brownian diffusion and eddy impaction - inside the turbulent flow.

Ryley and Parker, El-Shobokshy and Davies (15, 37, 4), used a simulation method to find the rate of deposition of droplets on the blade surface. They used uranin particles of sizes 0.05 - 0.25 μm in diameter, and air as an entrainment medium. The methods are outlined below.

3.2.1 The Ryley-Parker method

The first simulated attempt to find the concentration distribution of deposited droplets on the blade surfaces of the steam turbine was made by Ryley and Parker (15). Blades were selected, similar to those used in a 500 MW steam turbine final stage, for testing. Uranin particles were used since they fluoresced and were more easily traced and handled and had density nearly the same as those of water. The extent of the deposition was found by fluorimetric measurements of a prepared reception surface mounted on the blade. Ryley and Parker found that for droplets of 0.145 μm mass median diameter, the integrated deposit for the whole blade was 0.03% by mass of incoming aerosol. At high turbulence flow, the high rate of deposition was due to the superimposition of the eddy and Brownian diffusion. This method, therefore, showed that the best position of the slot for extracting the deposited water was where there was a high concentration of deposited particles on the blade surface. The conclusion obtained from the results was that this optimum position was near the trailing edge on both sides of the blade.

3.2.2 The Parker-Lee method

Parker and Lee (7) modified the above method by using two baffles upstream of the test blades in order to find the effect of turbulence on the deposition. The tests with inlet turbulence levels 2.2%, 14% and 21%, showed that the distribution of deposition around the blade was generally the same. The turbulence levels have no effect on the rate of deposition of large particles (d_{mm} = 0.25 μm), but the deposition of smaller particles (d_{mm} = 0.07 μm) rapidly increased in proportion to the turbulence. The total deposition however, as a mass percentage of the incoming particles, was found to be 0.03%, a result

similar to that of the first method. Theoretical approaches have been made and it has been shown that these agree well with the experimental results.

Parker and Lee found that:

1. The deposition rate in the turbulent flow is greater than in the laminar flow by a factor of about 3.0.
2. The deposition rate increases as particle size decreases.
3. The use of the mass median diameter, for prediction, was found to give close agreement with observations.
4. There was no re-entrainment of the deposited particles to the main flow.
5. There was a high rate of deposition at stagnation points.

3.2.3 The Ryley-El-Shobokshy method

The deposition of submicron particles by a diffusion process onto steam turbine fixed blade, running at off-design conditions, was studied by Ryley and El-Shobokshy (3). Deposition tests were carried out with three different inlet velocities to the cascade (9.5, 11.2 and 13.0 m/s), for each value of particle size (0.07, 0.13, 0.19 and 0.24 μm). The technique adopted to record the deposition rate of the particles was the same as that used by Ryley and Parker (15).

Ryley and El-Shobokshy found that:

1. Any remaining electrostatic charge on the blade has a negligible effect on the deposition process.
2. The rebound energies of the particles, upon collision with the blade surface, were not enough to return them back to the main flow

if these particles were less than 0.9 μm in diameter. It was recommended that double-sided adhesive tape be used to record the deposition rate if the particles were greater than 0.9 μm in diameter.

3. On the convex surface, the total deposition was the same whether the incidence angle was equal to -15 degrees (off-design) or zero degrees (full load). But on concave surfaces, it varied.

4. For the submicron particles, the deposition rate is inversely proportional to the size of the particle for given turbulence levels and flow velocities.

5. There was close agreement between the experimental and theoretical results. Consequently, this method can be employed to study how much deposition would occur in the actual low-pressure steam turbine.

3.2.4 The Ryley-Davies method

In this method the arrangement of the apparatus and the techniques to find the distribution of the deposition on the blade surface were the same as those used by Ryley and El-Shobokshy (3).

Ryley and Davies (92) studied the effect of thermophoresis on the deposition of submicron particles. This method was the last one employed in a series of simulation method tests and it represented an improvement in the reduction of erosion damage. Davies had replaced three reinforced fibre-glass blades in the centre of the cascade by three semi-hollow aluminium blades. The metallic blades were heated at a rate of about 600 W/m^2 and the blade surface temperature was measured by 25 thermocouples mounted along the centre line of the blade.

Ryley and Davies found that:

1. The blade surface temperature increased slightly from the leading edge value to a maximum value at x/c = 0.3 and then decreased until it was almost constant towards the trailing edge.

2. The particles of less than 1.3 μm diameter were most likely to be captured upon collision with the blade surfaces.

3. The drag force on the largest particle (0.25 μm) was found to be negligible compared with the force required to dislodge it, thus confirming that re-entrainment was unlikely.

4. The deposition rate was reduced by between 30% to 90% at most positions on the heated blades.

5. The thermophoretic effect decreased in direct proportion to the particle size.

6. The experimental results of thermophoretic deposition exceeded the predicted results by about 6 times.

7. The simulation technique proved to be convenient, economical and easily monitored.

3.2.5 The limitations of the methods

1. The four simulation methods gave only a crude prediction of the distribution of droplets on the blade surfaces in the actual steam turbine, since by using air as a medium, the phenomenon of supersaturation had been largely ignored.

2. The probability of the droplet growing along the blade passage was not taken into consideration since solid particles were used.

3. Ryley and Davies (92) studied the diffusion and thermophoretic effects. However, in the real case evaporation occurs when a temperature gradient exists within the boundary layer.

4. The methods indicated reliably the effect of particles or droplet size on diffusion or thermophoretic processes, but the fact that droplet sizes are variable and may increase or decrease in the actual L.P. steam turbine had not been taken into consideration.

5. The thermal conductivities and densities of water and uranin are different so that for a given temperature gradient, the magnitude of thermophoretic forces on particles of the latter will also be different.

6. Simulation method gives reliable results when it is employed in other fields, rather than steam turbines, such as in the health, industrial and environmental, etc.

7. Although the velocity ratio $(\frac{U_{\infty 2}}{U_{\infty 1}})$ along the path of the fixed blades in simulation methods, is approximately the same as in the actual turbine (500 MW), the characteristics of the boundary layer and the nature of the flow will be different and it might give rise to laminarisation in the latter case. Therefore, a different level of deposition and of thermophoresis might be obtained.

8. The presence of a temperature gradient inside the boundary layer may relieve supersaturation, and superheated flow could be obtained near the blade surfaces in some areas.

3.3 Methods in use for Suppressing Erosion in L.P. Steam Turbines

Preventing or reducing erosion damage of the rotor blading by overcoming the cause of erosion, increases the life of a turbine and may improve stage efficiency. Many methods have been suggested to suppress the wetness. Wood (11) has an excellent survey of the methods proposed and used up to 1960. The principle most frequently used is the separation, by different mechanisms, of the water either from the surfaces of stationary blades or from the axial gap before the rotor blades. The most satisfactory method is that which will remove the greatest amount of deposited water without disturbing the main flow. Some of the methods developed increase the resistance of the leading edge of the rotor blades, others used a combination of surface hardening, water separation and blade heating. A comprehensive survey of the main methods of reducing or diminishing the effects of erosion has been compiled by Ryley (13).

3.3.1 Suction slot methods:

Many investigators have studied the characteristics of suction slots for water removed (such as the performance, location, number and dimensions) under different inlet conditions of the working steam or air/water flow. Some of these methods are presented here.

1. Vuksta (93) suggested a gutter on the convex side of each stator blade at its intersection with the outer ring. The gutter was intended to collect and draw away the water which otherwise formed a film on the convex surface of the blade. It communicated with the condenser through the passage in the ring. Recently, many investigators found that the suction slots on the concave are the most effective and efficient on reducing the accumulated water on the blade surface.

2. Skopek (94) used a system of 2 mm diameter holes and 2 mm wide slots on the concave surface. He observed that slots were 3 - 4 times more effective than the holes, and the slots adjacent to the trailing edge removed two-thirds of the total water drained. The slot efficiency was found to rise with the steam wetness, while that of the holes remained practically constant. Therefore, the slots were recommended rather than the holes for increasing the extraction efficiency.

3. Todd and Fallon (95), from the tests on a cascade of hollow blades, established the feasibility of water extraction by trailing edge suction slots. They also found that blowing superheated steam through the slots caused an accelerative effect on water stripped off the blade surfaces, but it was not economical. Therefore, blowing through the slot is an inferior method to extraction.

4. Brown Boveri & Co. Ltd. (96) proposed a different method to eliminate or reduce erosion on L.P. rotor blades. They introduced auxiliary steam into the steam path through one or more orifices in the stator or the rotor blades. The auxiliary steam is at a sufficiently high temperature to reduce or eliminate condensation in the steam path. The mixing of the auxiliary and working steam takes place as a result of expansion and turbulence. However, it appears that the effects of this method on the nozzle or rotor efficiency can be serious, since the boundary layers are disturbed.

5. Smith (97) built an accurate cascade of hollow blades for an experimental turbine to determine the best slot arrangement for water drainage. He concluded that a slot along the trailing edge

is superior to both convex and concave face slots when the blade is unstalled, and almost complete drainage seems possible, so long as the pressure in the hollow interior of the blade is kept below the static pressure at the trailing edge. The additional condensation due to cooling the internal surface of the blade in this method was not taken into consideration. Although he obtained encouraging results, the economics of the method and the change in the stage efficiency have not been studied.

6. Ryley and Parker (98) also used a hollow fixed blade from a low pressure turbine with a suction slot located in the trailing edge. Different inlet conditions of the steam were employed in order to test the slot performance under the actual conditions found in the L.P. steam turbine. They were successful in removing most of the water collected on the surfaces of stationary blades and in protecting the rotating blades from erosion damage. The investigation showed the effect of the shape of the slot lips on the efficiency of extraction. They found that part-rounded lips were the most satisfactory. When demonstrating this, the slot was never run full, but with a mixture of steam and water, so that although erosion was reduced, there were two losses:

(i) Thermodynamic losses due to the fact that extracted steam and water have a high enthalpy.

(ii) Aerodynamic losses and slot losses.

They observed condensation taking place due to a difference between the temperatures of the inner and outer surface of the blade when suction was applied. Internal insulation could improve this method by reducing the outer surface cooling.

7. Todd and Gregory (99) concluded from their tests on a 60 MW working turbine, that a significant reduction in wet steam erosion can be achieved by the use of trailing edge suction slots. Clearly a small penalty must be incurred due to the thickening of the blade trailing edge and the removal of steam. However, they observed no measurable loss in output because of the suction in the slot and no detrimental effect on moving blade vibration conditions. Also no benefit from the alternative scheme of injecting steam through the slot was observed.

A manufacturing process for a hollow blade has been proposed, which may encourage the turbine designer to employ one of these methods.

8. McAllister and Moore (100) investigated hollow fixed blades with slots distributed along the trailing edge and along concave and convex surfaces to communicate with the hollow cavity. Their results revealed that hollow blades with suitably disposed slots can remove water deposited on the blade surfaces. No accumulation of water occurred on the convex surface and hence a slot on this surface was ineffective. The trailing edge slot was as effective as the concave slot for flow velocity up to about M = 0.5 but decreased seriously at higher Mach numbers. A large L.P. turbine runs under supersonic flow conditions in the last stage; it therefore appears that the suction slot method becomes inefficient for modern turbine applications.

9. Kirillov et al (101) carried out their investigation on a full scale diaphragm with a different arrangement of slots along the blade surfaces. The diaphragm provided for moisture removal

through a system of slots in the leading edge of the blades on the convex surface side and through a slot on the concave surface at a distance of x/c = 0.38 from the trailing edge. Tests were carried out to measure the removed moisture from each group of slots independently. They concluded, from their experimental results, that:

(i) In all operation modes the slot on the concave side of the profile was found to be more effective than the group of slots on the leading edge.

(ii) The influence of regenerative extraction of steam on reducing the efficiency when the water is removed by slots on the leading edge, is greater than that by slots on the concave surface.

3.3.2 Internal blade heating methods:

Blade heating techniques have been considered as an alternative method for eliminating the erosion of the moving blade. The majority of the investigations into these techniques and studies of the benefits obtained have been carried out since the late sixties. Some of these investigations are listed below:

1. Konorski et al (102) have investigated, experimentally and theoretically, the effect of internally heating the stator blade for removing partially or completely the deposited water on the blade surfaces. They concluded that:

(i) The process is strongly affected by the heating system conditions; with high steam temperature it is possible to evaporate the entire water film.

(ii) The effect of heating with steam extracted from the stage directly preceding the heated one, is very poor.

(iii) The evaporation from the convex surface is higher than that from the concave surface.

2. Engelke (103) sought to ensure sufficient heating to evaporate any deposited drops before they had time to coalesce and form rivulets. He made a series of tests on steam-heated stationary blades, but no analytical work has been published up to the present time. Engelke found that there is a distinct difference in the erosion damage between the system in which moisture is removed through a suction slot, and that using the same blade but internally heated, to evaporate the moisture. The damage associated with internally heated blades is insignificant and much less than that using suction slots wherever located on the blade surface.

3. Venhoff (105) used the guide blade as a heat exchanger. The hollow blade was divided into two channels and they were connected together inside the guide blade by a transverse channel. The hot steam supplied flowed inwards through one of the radial channels inside the guide blade and through the transverse channel at the inner ring, the heating steam then flowed outwards through the other channel. He claimed that this method, with a satisfactory quantity of heat, can reduce the wetness in the steam turbine and improve the thermal efficiency of the stage, but no experimental or theoretical evidence has been presented.

4. Akhtar et al (106) demonstrated that a single blade in a steam tunnel could be kept clear of surface water by only a small amount

of heat. The blade surface temperature was adjusted to be greater than Leidenfrost temperature in order to obtain the phenomenon of Leidenfrost (critical heat flux) and thus enough heat to deflect and evaporate the main flow water droplets away from the blade surfaces. The analysis is based on the relationship between the pressure and temperature of the steam flow which is only valid for equilibrium flow; it is not valid for supersaturated flow which is the dominant flow in the real turbine. However, their results are very useful for the turbine designers and show that the internal heating method is successful if it is used before the formation of the water film along the guide blades. Also the results show this method is the only one which can be currently employed that causes no damage to the aerodynamic and thermal properties of the flow inside the blade passage, whilst preventing erosion of the rotor blade.

3.3.3 The combined effects of suction slot and internal heating

Kirillov et al (104) observed that about 20% of the deposited water separated from the fixed blade trailing edge whilst 80% of it did not separate. With the given arrangement of the slots up to 80% of the moisture moving in a film over the upper half of the fixed blade, could be removed. The remaining quantity of moisture has a small effect on the stage efficiency but can erode the moving blade. Therefore, Kirillov et al proposed a new method of removing the entire deposited water by using the combined effects of extraction and internal heating methods. A part of the deposited water can be removed through the slots arranged over the leading edge and the remaining moisture removed by evaporation on the surface of the blade or in a steam jet. The advantages claimed for the suggested methods are:

(i) A small amount of heat can be used to evaporate the remaining deposited water rather than trying to evaporate the total accumulated water on the blade surfaces.

(ii) Heating blade may increase the stage efficiency.

(iii) The rotor blades are absolutely protected from erosion.

There are also disadvantages of the method, as:

(i) The distribution of the deposited water on the blade surface has been reported to be maximum at or near the trailing edge, therefore, it is not possible to remove 1/2 - 2/3 of the deposited water through the slots along the leading edge.

(ii) There is no experimental confirmation (according to the author's knowledge) showing an increase in the stage efficiency by using this suggested method.

(iii) The hollow blade required for this method will be expensive to manufacture, since it combines two different protection techniques each of which will add to the cost.

3.3.4 Hardening and modifying the leading edge of the rotor blades:

Hardening of the leading edge of the rotor blade which is most vulnerable to erosion, is a well tried method and is widely used since the erosion is considered to be a dangerous feature. There are many proposals and investigations regarding the material for the shielding of the blade. Kazak et al (107) investigated a new method to increase the resistance of the rotor blade to erosion. The basic method can be outlined as follows:

(i) On the convex side of the inlet edge of the rotor blade is situated a flat piece inclined at an angle of 12 - 45^{o} to the front

of the cascade; it contains longitudinal grooves in order to split off the collected water towards the casing. A feature of the grooves, employed in this method, was that they were rounded in section.

(ii) Anti-erosion protection provided by electrolytic chrome plating plus induction hardening along the part of the leading edge which was expected to be seriously damaged, gave excellent results. They carried out a long test (over two years) to determine the resistance to erosion of the rotor leading edge with a new chromium plating. It was found that the resistance was about five times more than for the conventional design.

3.4 Conclusions

An appraisal has been made of the methods available for suppressing or removing moisture from the surfaces of the turbine fixed blades in order to decrease, or prevent, the erosion of the rotor blades. It can be concluded that:

1. The level of fog droplet deposition is nearly the same order of magnitude on the concave and convex surfaces.

2. There are two regions of high deposition rate, one the blade nose and near the trailing edge of the fixed blade.

3. Extraction of the deposited water can be achieved by arranging a series of slots on the nose, on the trailing edge and near the trailing edge along both surfaces.

4. The most effective slots are those along the trailing edge.

5. The dimensions and the number of the slots depend on the amount of the moisture in the flow, the accumulated water on the blade surface and the velocity of the flow.

6. Blowing steam through the slots to remove the water appears to have a detrimental effect on the nozzle. It is not an effective method.

7. Additional condensation occurs on the blade surface when using the suction method due to decreasing the blade surface temperature. The rate of condensation increases if the differential pressure between the interior and exterior of the blade is increased. A possible remedy can be achieved by insulating the internal surfaces of the blade. This, however, will increase the capital cost of the diaphragm and it does not appear to be economical.

8. The width of the slot in the trailing edge is limited, since if it is increased, the aerodynamic performance of the blade will be poor.

9. In large turbines, suction slot methods appear to be unsuccessful, since:

   (i) The extraction efficiency of the slot will be reduced, since the flow is supersonic.

   (ii) The aerodynamic losses are increased, therefore, the stage efficiency will decrease.

   (iii) The internal insulation of the blade is rather expensive.

   (iv) The slot, in any flow conditions, extracts only a part of the deposited water, therefore the danger of some erosion remains.

10. Hardening methods can increase the life of the rotor blade if the mechanical properties of the blade shield are satisfactory. To achieve a very good wear resistance property, it is necessary to use very expensive materials and manufacturing technique.

11. The combined use of blade hardening and suction slot methods may increase the life of the turbine but may prove to be too expensive.

12. Methods employing interstage superheating cannot be used in nuclear and geothermal power plants, since the steam sources generate saturated steam.

13. The internal heating method gives unsatisfactory results when it is used to evaporate a water film. However it is an efficient method when used to prevent initial deposition of the water droplets on the blade surface.

14. The benefits of using heating methods are:

    (i) No additional condensation occurs unlike the suction slot method.

    (ii) The aerodynamic losses will be reduced, since the thickness of the trailing edge is not affected.

    (iii) The thermodynamic losses due to wetness can be reduced.

    (iv) Prevention of deposition can be achieved by using a relatively small amount of heat (to be discussed in detail in Chapter 8).

    (v) It may be economically attractive (the economics analysis of the method will be presented in Chapter 8).

15. The heating method is the only feasible method at the present time for preventing erosion of the rotor blades in the modern turbine.

16. The heating method can be improved by using more heat for surfaces with high deposition rates and less heat for those with low deposition rates, i.e. matching the heat rate to the duty required.

CHAPTER 4

PARTICLE DEPOSITION ON BLADE SURFACES

4.1 Introduction

Suspended droplets or particles entrained in a moving fluid may be deposited on a surface by different mechanisms; the operating mechanisms may be:

1. molecular diffusion
2. turbulent diffusion
3. diffusiophoresis (due to concentration gradient)
4. thermophoresis
5. sedimentation
6. electric mobility
7. inertial impaction
8. eddy diffusion impaction

} not of significant magnitude in comparison with others in the present situation.

Depending upon the size of the particles, one or more of these mechanisms are operative at any time. Experimental work has been done on particles with mass-median diameter of order of 0.186 and 0.135 μm which are produced from 5% and 3% uranin solutions. The contribution of this analysis is to predict the wetness losses and erosion, then, the reduction of them by internally heating turbine blades. Also to correlate the effect of different variables acting together on the particle. The experimental test technique was described in detail by El-Shobokshy (37) and by Davies (4) and can be successfully repeated. It was also the intention to compare the results obtained with those evaluated from theories of diffusional deposition on unheated and heated surfaces.

4.2 Particle Generation and Size Measurement

4.2.1 Generation of submicron particles:

The method employed in this work was used successfully by Ryley and Parker (15) in the pioneering work for this investigation. The same technique was also repeated by El-Shobokshy (37) and Davies (4).

The reasons for using this method are:

1. The generated particles are easy to trace and detect, so that exact masses can be determined.
2. The particles dissolve easily in pure water, and the solution emits fluorescent light of sufficient intensity to be detected by fluorimetric analysis.
3. It is highly sensitive, simple to prepare and handle.
4. The particles are not absorbed by the surface.
5. When the particles are discharged into the atmosphere, they present no health hazard or harm to the environment.

There are different types of apparatus for producing a continuous supply of solid aerosols, such as the spinning disc atomiser, the vibrating orifice monodisperse aerosol generator and atomisation of a solution by an atomiser impactor generator. The principle involved here is the atomisation of a solution of an appropriate chemical compound in distilled water or methylated spirit. The liquid droplets are then evaporated leaving behind minute particles of the original solute. The atomiser-impactor generator was used in this work and was maintained and operated for the condition as in Ref. (4), but because of maintenance and cleaning, the gap between the impactor plate and the case was slightly changed so that the same solution strength was used by Davies produced different particle sizes. He found from a 5% uranin solution, the particle

diameter was 0.25 μm, whilst in this work it was 0.186 μm. Fig. 4.1 shows the processes of producing particles and injecting them into the wind tunnel.

4.2.2 Particle size measurement

Many methods exist for measuring the size of the droplet or the particle, e.g. direct particle measuring methods of which one was used in the present work. There also exists indirect particle measuring methods and automatic counting and sizing methods (details in Chapter 2).

The technique of electron microscopy was found to be the most useful and has been described in detail in Refs. (15, 37). The sampling process involved diffusional deposition of particles on a glass slide of dimensions 25 x 75 mm in preparation for coating and shadowing. The method of preparation of the sample was slightly different from the method which has been used in Refs. (4, 37).

Basically, the procedure consisted of the following routine:

1. The glass slide was washed by tap water using a detergent solution.
2. The slide was placed in a beaker which was filled with de-ionised water and a few drops of soap, then the beaker was placed inside an ultrasonic cleaner (bath) for 15 minutes in order to obtain a very clean surface.
3. The slide was kept inside a desiccator overnight to be completely dried.
4. The aerosol particle generator was started, the sonic jet ion generator was switched on, and the set left running for about 10 minutes to obtain the steady state for all the parts. The glass slide was placed horizontally inside the aerosol pipe, between

the holding chamber and the exit valve for half an hour. The valves were set up as in Ref. (37). The particles were deposited on the glass surface and then the slide was ready for coating by carbon and shadowing to obtain a good photograph.

(I) The carbon coating, shadowing process and preparation of the specimen for electron microscopy

The method used for coating and shadowing in the present work was more accurate than that used previously, and was economic both in time and cost.

The procedure was as follows:

1. The prepared sample was placed in a vacuum coating unit.

2. Two 6 mm diameter carbon electrodes of hard grade were prepared, one electrode had a sharpened point and the other had a small circular groove on the blunt end. They were placed under the bell jar of the coating unit.

3. A v-shaped tungsten wire was connected to the electrical circuit of the vacuum unit as a resistance element, and a very small piece of platinum or gold was attached to it as the material to be used in the shadowing process, in order to improve the appearance of the particle under the electron microscope.

4. The glass slide was positioned at an angle of 90^{o} with the carbon electrode and an angle of 20^{o} with the tungsten wire.

5. The bell jar was then placed in position and the unit was kept running overnight to bring the pressure within the bell jar down to 10^{-6} mm Hg.

6. The unit's power was adjusted to supply the carbon electrodes with

10 amps and 50% input voltage. This process was continued for 15 seconds to obtain a perfect thin carbon film covering for the particles.

7. The unit was left for 15 minutes to recover the vacuum of 10^{-6} mm Hg in order to shadow the particles.

8. The unit's power was then readjusted to supply 30 - 40 amps with exposure time around 15 seconds to evaporate the piece of platinum over corresponding small sectors, of each particle's surface.

9. The unit was brought back to atmospheric pressure very slowly in order to avoid destroying the thin carbon film and the shadowing. The glass slide was then removed from the vacuum unit.

10. The slide was tipped carefully at an angle of about 45^{o} in de-ionised water, the carbon film left the glass and floated on the water surface. Electron microscope grids (3 mm diameter) were used to catch a small piece of carbon film, using very fine tweezers. About 25 grids and 21 photographs were taken for 5% and 3% uranin solutions.

The advantages of this method were as follows:

(a) The carbon film was saved from contamination, since shadowing was done at the time of coating the sample.

(b) The time, the effort and the cost were about 50% of those from the method in Refs. (37, 4).

(c) In this method the carbon film kept the shape and the size of the particles unchanged during the preparation of the electron microscope grids.

From the 21 photographs, the counting and sizing of the particles for statistical analysis was more accurate than from 5 photographs for each

solution used in Refs. (37, 4).

(II) Particle size calculation (statistical analysis)

The generated particles for the purpose of this work are clearly spherical as indicated in plates (4.1) and (4.2), but were polydisperse in size, therefore the mean diameter and the size distribution (geometric standard deviation) must be stated together with the nature of the size distribution.

There are many statistical definitions for the mean diameter. Some of these are: arithmetic, geometric, number, surface, surface-volume and mass-median. Obviously, the most useful mean diameter for the present work, where the mass of the particles are required, is the mass-median. The distribution of the polydisperse particles is not of normal or Gaussian form, but is skewed, rising steeply at the small-size side, then decreasing more slowly at the large-size side. For this distribution to be normalised, one can plot the size logarithmically. In this case the geometric mean diameter is a measure of the particle size, and larger and smaller particles will be distributed equally about its value. The normal probability equation as applied to the size distribution, is:

$$F(d) = \frac{\Sigma n}{\sqrt{2\pi}\ \log S_{DG}} \exp\left\{ - \frac{\left[(\log(d) - \log(dg) \right]^2}{2\ (\log\ (S_{DG}))^2} \right\}$$

where F(d) is the frequency of occurrence of particles with diameter d,

Σn is the total number of particles,

dg is the geometric mean diameter and defined by

$$\log dg = \frac{\Sigma n\ \log(d)}{\Sigma n}$$

and S_{DG} is the geometric standard deviation given by

$$\log(S_{DG}) = \sqrt{\frac{\Sigma n\ (\log(d) - \log(dg))^2}{\Sigma n}}$$

If the cumulative percentage of number of particles up to various stated sizes is plotted against diameter on logarithmic-probability paper, then theoretically a straight line should be obtained. The median size can then be directly obtained by reading the diameter corresponding to the value of 50% on the probability scale. The median size is the geometric mean in the above case whereas a direct plot of cumulative frequency against diameter would yield the arithmetic mean. The geometric standard deviation also can be obtained from the graph using the two values of diameter corresponding respectively to probabilities of 84.13% and 50%, and using the result given from the probability equation:

$$S_{DG} = \frac{84.13 \text{ percent size}}{50 \text{ percent size}}$$

Similarly, if the cumulative percentage of mass is plotted, the mass median diameter can be obtained. Table 4.1 shows the analysis performed for particles produced from 5% uranin solution. The number line on Fig. 4.2 is plotted using data in columns1 and 5 from Table 4.1, whilst the "mass line" is plotted using data in columns 1 and 9 from the same Table. Hatch and Choate developed and simplified the expressions to relate the median diameter to the other parameters of the particle distribution such as geometric mean diameter and geometric standard deviation. They considered the frequency of particles between two diameters differing infinitesimally, then:

$$dF(d) = \frac{\Sigma n}{\sqrt{2\pi}\ \log(S_{DG})} \exp\left\{ - \frac{(\log(d) - \log(dg))^2}{2\ (\log S_{DG})^2} \right\} \log\ (\frac{d_2}{d_1})$$

By integrating the above equation:

$$\log d_a = \log dg + 1.51 (\log S_{DG})^2$$

$$\log d_{mm}{}^3 = \log dg^3 + 10.362 (\log S_{DG})^2$$

where: d_a is the arithmetic mean diameter

d_{mm} is the mass-median diameter

4.3 Description of the Experimental Rig

The experimental rig consists of two main parts, the particle generator and the wind tunnel. Figure 4.1 shows in detail the relevant components of the aerosol generator which were explained earlier. The wind tunnel as shown in Fig. 4.3 originally designed by Ryley and Parker (15) was low speed and open circuit. It was constructed to provide a maximum air velocity (at full load) of about 60 m/s at exit from a cascade of six full-size blades (five blade passage). The blades were made of reinforced fibre-glass and mounted on one of the two acrylic resin windows, the other was removable for access to the cascade. Filtered air was drawn into the test cascade from a contraction unit. The filters were used before the entry of the contraction unit to reduce the impurities from the inlet air flow. The dimensions of the wind tunnel, the work section and the blade are shown in Figure 4.3 and Figure 4.4. The shape of the passage between the blades was convergent-parallel and is shown in Figure 4.5. The air flow through the tunnel could be controlled by means of a damper in the fan discharge duct. The injector pipe for the aerosol particles was located at the top centre of the contraction unit at a distance of about 15 cm below the honeycomb and the top filters. The exhaust air from the cascade passed through a reservoir containing diffusing

passages having a bank of glass-fibre filters to absorb the outlet aerosol particles from the cascade before the air was discharged outside the laboratory through a 600 m^3/min suction fan. In 1972, work was done by Parker and Lee (7) under design conditions with the blade at zero incidence angle. Three years later, El-Shobokshy set up the apparatus in order to work under off-design conditions, hence the incidence angle of the flow was negative. Later, Davies extended that work in Ref. (37), with the incidence angle kept unchanged. In the present work the two experimental configurations (design and off-design) were both employed. Because the aerodynamic performance of the wind tunnel under the condition of zero incidence angle has been studied by Parker and Lee (7) and under off-design condition by El-Shobokshy (37) and repeated successfully by Davies (4), it is permissible to use their experimental results of the boundary layer around the cascade blade.

In the present study theoretical calculations were made to predict the boundary layer characteristics. The methods which were used here will be presented in Chapter 5. It was found that:

(i) For zero incidence angle:

(a) Along the concave surface:

1. The laminar boundary layer starts from $x/c = 0.0$ and finishes at $x/c = 0.75$.
2. The transition point is at $x/c = 0.75$.
3. The turbulent flow continues from the transition point until the exit of the blade passage.

(b) Along the convex surface:

1. The laminar flow extends along $0.0 < x/c < 0.55$.
2. The transition point is at $x/c = 0.55$.

3. The turbulent flow is from x/c = 0.55 until the exit of the passage.

(ii) For negative incidence angle (-15^{o}):

(a) Along the concave surface:

1. The laminar flow is along $0.0 \leqslant x/c < 0.2$.
2. The separation point is at x/c = 0.2.
3. The turbulent flow is between x/c = 0.2 and the trailing edge.

(b) Along the convex surface:

1. The laminar boundary layer starts from x/c = 0.0 and finishes at x/c = 0.65.
2. The transition point is at x/c = 0.65.
3. The turbulent flow is along $0.65 < x/c \leqslant 1.0$.

In the latter work, Davies replaced three reinforced fibre-glass blades by metallic (90% aluminium) ones. They were hollow blades, each one containing three separate channels of different sizes, as shown in Fig. 4.6, so they could be heated internally, by using hot air, in order to study the effect of thermophoresis on the deposition rate. The heating system which produced the hot air for heating the blades is illustrated in Fig. 4.7.

4.4 Temperature Distribution at Inlet to the Cascade and around the Blade

The temperature distribution at the inlet, 10 cm upstream of the blades, was measured using a thermocouple on a traversing mechanism. Temperature measurements were taken for each inlet velocity (13.0, 11.2 and 9.5 m/s) at constant fuel gas pressure and constant mass flow rate of heating air. The inlet temperature distribution is uniform with a value

just above atmospheric temperature, as shown in Fig. 4.8. There were 25 thermocouples mounted on the surface of the blade in order to indicate temperature distribution around the test blade. Figure 4.9 shows that the distribution of the temperature for different incidence conditions are very similar, since the local heat input to both surfaces are nearly equal. The curve for the convex surface is slightly higher than that of the concave surface between the leading edge and half way downstream, since there is more heat transfer from the convex surface. The temperature distribution up to 40% of the chord length from the trailing edge was much lower than for the remaining part of the blade, since channel (1) is of smaller cross-section than that of (2) or (3), hence heat input is less. Thermal equilibrium was also confirmed by checking the reading of the thermocouples every 20 minutes.

4.5 Deposition Test Procedure

The experimentation was divided into two main parts, firstly deposition on an unheated blade and secondly, deposition on an internally heated blade.

4.5.1 Deposition rate on the surfaces of unheated blade

The procedure for measuring the deposition rate on the unheated surface was as follows:

1. It was necessary to measure the level of background contamination (tunnel and filter) which existed in the air drawn through the wind tunnel. The sampling probe (illustrated in Fig. 4.10) was inserted in a position about 20 cm above the cascade inlet and the "millipore" filter (which had a pore size of 0.8 μm) placed in position (Fig. 4.10). The probe was then connected to the pump

via a flowmeter. The removable cascade window was placed in position, and the tunnel set to run at an appropriate speed. The pump was run during a timed period of 4 - 6 minutes with the particle generator off, the flow rate through the probe being kept constant. The sampling process was, in a few cases, isokinetic.

2. The filter paper was removed from the probe and immersed into the fluorimeter test tube containing 4 ml of de-ionised water for about 10 minutes to dissolve off any trapped particles.

3. The fluorimeter should be started at least one hour before use. The adequate standard solution was between 0.1 - 0.2 μg/ml for background contamination measurements. From the fluorimeter readings and knowing the flow rate the background concentration could be calculated.

4. 1, 2 and 3 were repeated for actual particle deposition but this time with different strengths of standard solution, the strengths depending on the concentration of dissolved particles.

5. The concentration of particles in the blade passage can be found by traversing the sampling probe along the centre line of the blade passage.

6. The deposition rate on the unheated blade was measured by the same technique as was used by El-Shobokshy and by Davies. Basically, the procedure was:

   a. The third blade in the cascade was cleaned using acetone or methylated spirit whilst in position.
   b. The adhesive aluminium tape (2.5 cm width) was also cleaned by acetone.

c. The tape then was wrapped around the central portion of the blade.

d. The metallic blade, the tape and the corners of the window were earthed in order to eliminate any electrostatic charges that might occur due to the air flow over the blade.

e. The tunnel and particle generator were operated for a period of one hour. Then the wind tunnel and particle generator were stopped.

f. Using a sharp knife the tape was cut into (19) 3 cm pieces while the tape was on the blade, since the presence of the thermocouples prevented its removal.

Then, using fine tweezers, the pieces were peeled from the blade and wrapped around glasware and placed inside the fluorimeter tube which contained 4 ml of de-ionised water.

g. The standard solution, about 5 μg/ml, was selected for use in the fluorimeter in order to find the concentration of the deposited particle on each piece of the tape.

Before each particle deposition determination, the background contamination had to be found by repeating without particle injection. It was then a simple matter to find the deposition rate of the particles by subtracting the amount of background contamination from the deposition record of the particles.

4.5.2 Deposition rate on the surfaces of the heated blade

The test blade surface, tape and wind tunnel were prepared as in the above procedure, this time with the hot air delivery tubes from the mixing manifold connected to the blades. The air and gas flow rates to

the heater were adjusted and the heater started. When thermal equilibrium had been achieved between the blade surface and the surround air (whilst the tunnel was running), the aerosol particles were then injected into the tunnel. After 60 minutes the tunnel and the heater were stopped and deposition analysed as for the unheated blade. In Refs. (37) and (4), there were general precautions observed during the deposition experiments which should be noted before any experimental work is carried out. During the experimental work, it was also necessary to clear any bubbles from the fluorimeter tube.

4.6 Deposition Results for the Unheated Blade

During maintenance and cleaning of the particle generator, it was found that:

1. The four atomisers had rusted.
2. The small holes through the two impactor plates were blocked by dried particles and rust.
3. The valve between the holding chamber and the wind tunnel was jammed.

After cleaning and repairing the apparatus the position of the impactor plate had changed slightly. The particle size is affected by the adjustment of the gap between the impactor plate and the case of the impactor, and by the strength of the solution. In this work 5% and 3% uranin solutions were used to produce particles having a mass-median diameter of the order of 0.186 μm and 0.135 μm respectively. These are different from those reported in Refs. (37), (4) and (7) for the same strength of uranin solutions, since the position of the impactor plate was changed. However, there was very good agreement with Whitby's results

which are presented in Fig. (4.11). El-Shobokshy, Davies and Parker and Lee obtained particles with mass-median diameter about 0.186 μm from 1% uranin solution and 0.135 from 0.5% solution. However, the deposition depends on the particle size and the flow conditions only and not upon the strength of the solution. For a 0.186 μm particle diameter, deposition measurements were made in this work for blade Reynolds number (Re_1) of 1.65×10^5, 1.95×10^5 and 2.25×10^5 corresponding to cascade inlet velocities of 9.5, 11.2 and 13.0 m/s. For 0.135 μm particles measurements were only made for an inlet velocity of 13.0 m/s. The deposition results were classified into two groups, firstly for an inlet incidence angle equal to 0.0 degree (full load running) and secondly, for a negative incidence angle equal to - 15 degrees (partial load or off-design running). Figures (4.12) - (4.14) show the deposition rate measured along the blade surfaces for the cascade running at full load. Figures (4.15) - (4.17) show the measured deposition rate along the blade surfaces when the incidence angle to the cascade is - 15 degrees.

The background contamination was taken into consideration. All the results presented in this section and the following sections in this Chapter, show the measured deposition without background contamination. The net deposition values were obtained by subtracting the amount of background contamination from the measured value of particle deposition. The deposition velocity at any point along the blade surfaces can be determined by dividing the local rate of net deposition by the corresponding concentration,

$$V_d = \frac{\text{net deposition rate } (\mu g/cm^2/h)}{\text{concentration } (\mu g/ml)}$$

The accuracy of the experimental results depends on:

1. The accuracy of measuring the background contamination.

2. The technique used to prepare the samples and recording the results.

3. The care taken during the experiment.

4. The duration of the experiment:

   (a) A long period (not less than one hour), should give better results; however it was noticed that the pressure inside the atomiser decreased slowly and affected the particle generation (i.e. the rate of generation is decreasing).

   (b) Measuring the deposition rates over a short period produced inadequate results.

The results of the deposition rate for zero incidence angle are presented as a percentage of the aerosol passing through the blade passage in a zone 1 pitch wide by 1 cm deep to enable comparison with those of Parker and Lee.

4.6.1 Discussion of the deposition results for zero incidence angle

(a) Discussion

The results shown in Figures (4.12) - (4.14) demonstrate clearly that diffusional deposition plays an important role for submicron diameter particles. The deposition rates inside the laminar flow along the concave surface ($0.05 < x/c < 0.6$) and the convex surface ($0.05 < x/c < 0.6$) are of similar magnitude and consequently the deposition is reasonably uniform in distribution. At $x/c > 0.7$ along the concave surface and $x/c > 0.6$ along the convex, the deposition increases rapidly due to the combined effects of eddy and Brownian diffusion. The increase in the deposition rate along the concave surface is higher than that along the convex. The high deposition rate along the blade nose is due

to the effect of eddy impaction inside the stagnant flow. The total deposition along the concave surface is nearly equal to that along the convex. The total mass of the deposited particles along the blade surfaces for particle sizes of 0.135 μm (Fig. 4.12) is higher than that for particle sizes of 0.186 μm (Fig. 4.13) when the flow conditions are the same. For the same particle size and different flow velocity, the total deposited mass on the blade surfaces for flow velocity 13 m/s, is higher than when the flow velocity is 9.5 m/s. More detail about the deposition process is presented in the next section, (4.6.2).

(b) Comparison between the present results and those due to Parker and Lee

Parker and Lee (7) have recorded the distribution of the deposition rate along the blade surfaces using the same flow conditions and the same apparatus as the present work. Figures (4.12) and (4.13) show that there is a good agreement between the present results and Parker's and Lee's results when the flow is laminar and a moderate agreement when the flow is turbulent. In general the present results show a lower rate of deposition than those of Parker and Lee when the boundary layer is laminar, whilst in turbulent flow ($x/c > 0.8$ along concave surface and $x/c > 0.6$ along convex surface), the deposition rate in the present work is higher.

4.6.2 Discussion of the deposition results when the incidence angle is - 15^{o} (off-design condition)

(a) Discussion

From Figures (4.15) - (4.17), it is noticed that the total mass of deposited particles on the concave surface is always higher than that on the convex surface by 20 - 25%. According to the characteristics of

the boundary layer the process of deposition can be divided into three main regions:

1. On the nose of the blade, the deposition rate is much higher than on the adjacent points at both sides of the blade. This is due to the thickness of the boundary layer being very small. This means that the concentration thickness is also very small, and the concentration gradient $\frac{dc}{dy}$ will have a higher value in the diffusion equation,

$$N = D \frac{dc}{dy}$$

2. Inside the laminar flow, as the boundary layer grows thicker downstream, it implies also an increase in the concentration boundary layer thickness, so that the value $\frac{dc}{dy}$ will fall. The deposition rate will then decrease continuously further downstream due to the growth of the velocity boundary layer. This phenomenon can be noted on the concave surface between $x/c = 0.0$ and $x/c = 0.2$, and on the convex surface between $x/c = 0.0$ and $x/c = 0.55$, as shown in Figures 4.15 - 4.17.

3. Inside the turbulent flow, along the concave surface at $x/c > 0.2$, and along the convex surface at $x/c > 0.55$, the presence of eddies increase the deposition rate on the blade surfaces. The turbulent boundary layer grows in thickness causing an increase in turbulence intensity, therefore, the deposition rate increases uniformly up to the trailing edge on both surfaces.

For the same particle size the deposition rate decreases with decreasing flow velocity, since the thickness of the boundary layer will be increased as seen in Figs. 4.15 - 4.17 for flow velocities equal to

13, 11.2 and 9.5 m/s respectively.

(b) Comparison between the present results and those of El-Shobokshy (37) and Davies (4)

The flow conditions, the droplet size and the experimental procedure used were the same as those in Refs. (37) and (4), therefore, a good comparison should be obtained between the three sets of results (the present, El-Shobokshy's and Davies' results). The pattern of the deposition curves are almost the same, as shown in Figs. 4.15 - 4.17. The present results have a good agreement with the results due to Davies' and considerable agreement with El-Shobokshy's results. The distribution of the deposition rate in this work is always higher than those in Refs. (37) and (4) along the blade surfaces. The best agreement between the three sets of results is achieved when the flow velocity is 13 m/s, as shown by Fig. 4.15. The reasons for the small discrepancy in the results may be:

1. the droplet size is not exactly equal to that used by El-Shobokshy and Davies, the difference in the mass-median diameter is about 3%.

2. using a different uranin solution density to produce the same size of the particles, may increase the concentration of the particles in the flow stream;

3. there may be statistical reasons. Mass-median diameter is only a statistical diameter and can be made up in many ways. A given value does not define the size distribution function for population.

4.7 Deposition Results for Heated Blade Surfaces

The mass flow rate of the heating air inside the hollow blade was adjusted for each chamber in order to reduce the temperature difference between the leading edge temperature and the trailing edge temperature. It was impossible to achieve a constant blade surface temperature, since the hollow blade chambers are different in size and furthermore there is no room for a heating chamber near the trailing edge. The difference between the maximum and minimum temperature of the blade surface was about 20% of the maximum temperature, and that was the least difference which could be obtained in the present work.

The experimental work for measuring the deposition rate along the heated surface was carried out for two values of incidence angle (zero and - 15^{o}). For zero incidence angle the inlet flow velocities were 13.0 m/s and 9.5 m/s; two droplet mass-median diameters were also used (0.135 μm and 0.186 μm). Figure 4.18 shows the distribution of the deposition rate when the droplet size is 0.135 μm and the inlet flow velocity is 13.0 m/s. Figures 4.19 and 4.20 illustrate the deposition rate along the heated surface for a droplet size of 0.186 μm and when the inlet flow velocities are 13.0 and 9.5 m/s. The results of net deposition are shown as a percentage of the aerosol passing through the blade passage.

For negative incidence angle (- 15^{o}), measurements of the net deposition were carried out for three inlet velocities, 13.0, 11.2 and 9.5 m/s (Re_1 = 2.25 x 10^5, 1.95 x 10^5 and 1.65 x 10^5) and using particles having a mass-median diameter of the order of 0.186 μm. Figures 4.21 - 4.23 show the results of the three experiments.

The background contamination was taken into consideration for the whole set of experiments, and it was in the order of 40 - 65% of the

particle deposition rate. The effect of thermophoresis on the deposition results is shown as a percentage reduction in the deposition rate of the isothermal blade surface and presented in Figs. 4.24 - 4.26. The reduction was in the range 60 - 95%. Most of the experiments were repeated more than twice, since one test was considered insufficient to establish the deposition rate. Moreover, two tests for the unheated and heated surface under the same flow conditions were made in the same day, in order to overcome the effects of the weather on the background contamination.

4.7.1 Discussion of the results for a zero incidence angle

The effect of thermophoresis on the deposition of particles (0.135 and 0.186 μm) on the blade surfaces is displayed on Figures 4.18 - 4.20. The deposition patterns for heated blade and for unheated blade surfaces are almost identical for all flow conditions and particle properties, but the total mass of deposition was considerably different. The total mass of deposition for the large particle (0.186 μm) was less than that for the small particle (0.135 μm) for the same flow conditions by about 30%, as shown in Figs. 4.18 and 4.19. The rate of deposition increases with decreasing particle size within the range 0.1 - 1.0 μm diameter. This observation is supported by the theory of diffusional deposition where the thermophoretic effect is seen to increase with increasing droplet size (Chapters 2 and 7).

In spite of the relatively high temperature gradient at the transition point the increased particle transport due to simultaneous laminar and turbulent diffusion resulted in high rate of deposition. The effect of thermophoresis on the nose and the trailing edge of the blade is less than that along the blade surfaces; the reasons for this are:

1. The mechanism of deposition on the blade nose is a combination of Brownian, impact diffusion and concentration gradient, whilst in the laminar flow along the blade surfaces the mechanisms is that of Brownian diffusion and concentration gradient through the boundary layer.

2. The concentration layer along the leading edge is very small compared with that along the blade surface, since the boundary layer starts from the leading edge. This gives $\frac{dc}{dy}$ a very high value in the stagnation region and therefore causes a high deposition rate in the diffusion equation.

3. The flow near the trailing edge is turbulent and has a turbulence level much higher than that far from the trailing edge. Therefore, deposition rate increases since it is a combination of eddy and Brownian diffusion.

4. The temperature difference between the blade surface and flow temperatures at the trailing edge is smaller than that along the blade surfaces. Therefore the effect of the thermophoresis is less at the trailing edge.

The flow velocity has no considerable effect on the deposition process on the heated or unheated blade as shown in the experimental results since the variation in the available velocity is relatively small and any effect cannot be seen clearly (as shown in Figures 4.19 and 4.20).

4.7.2 Discussion of the results for an incidence angle of - 15^0

(a) Discussion

The cascade was arranged to run at off-design conditions (- 15^0 inlet angle). The distribution of deposition rate along the blade was

measured for this arrangement and compared the results with the results obtained by Davies (4). The deposition patterns for zero and - 15^{o} incidence angles are almost identical, but the value of deposition rate is different in magnitude, since the flow conditions and the heat transfer rates are different in both cases. The values of the residual deposition on the nose and the trailing edge of the blade are maximum, the reasons are the same as those discussed in the previous section (4.7.1), but the local magnitude of the deposition rates are different. Figures 4.21 - 4.23 show the net deposition distribution (diffusion + thermophoresis) along the blade surfaces for particles having a mass-median diameter of 0.186 μm and for inlet velocities of 13.0, 11.2 and 9.5 m/s.

(b) Comparison between the present results and those of Davies

To permit a valid comparison it was necessary to make the flow and thermal conditions identical with those of Davies for the same particle size. Therefore the temperature distribution along the blade surface was adjusted to keep it the same as in the previous work. It can be observed from Figs. 4.21 - 4.23 that the deposition rate was significantly higher everywhere on the blade surface by about five times (as average) compared with those obtained in Ref. (4), the reasons for this are probably,

1. The concentration distribution of the particles (of this work) in the potential flow is higher than that of Davies'.

2. The polydispersion in sizes of the particles which have a mass-median diameter of 0.186 μm was different from that of the previous work as shown in Table 4.1. The number of very small particles is higher in the present work, it means higher diffusion and lower thermophoretic force. However the pattern of the deposition distributions are generally similar.

4.7.3 Discussion of the reduction in particle deposition due to thermophoresis for zero and - 15° incidence angle

Figures 4.24 - 4.26 show the percentage reduction in particle deposition due to heating for an incidence angle of zero. Figures 4.27 to 4.29 show the same for an incidence angle of - 15°.

For a zero incidence angle the reduction was in the range of 60 - 95% for all flow conditions and different droplet size. For the same droplet size and different flow conditions, the reduction for low velocity is higher than that in high velocity, (Figs. 4.25 and 4.26). For the same flow conditions and different droplet size, it can be seen that there is a significant difference in the reduction of the deposition rate (Figs. 4.24 and 4.25). The maximum reduction in the deposition of the particle occurred between x/c = 0.35 and x/c = 0.75 along the concave and along the convex surface.

For - 15° incidence angle the reduction in the deposition of the particles (0.186 μm) is shown in Figs. 4.27 - 4.29 for inlet velocities 13.0, 11.2 and 9.5 m/s respectively. When the flow inlet velocity decreases the reduction increases (Figs. 4.27 - 4.29). The reduction for the three inlet velocities was in the range of 60 - 97%.

The agreement between the present results and Davies' results is significant and the scatter in the results is low (the maximum difference is about 40%). The results along the concave surface have better agreement with Davies' results than those along the convex surface.

In general the reduction in the deposition of the particle on the blade surfaces when the incidence angle is zero is higher than that when the incidence angle is - 15°. The reasons are:

1. The development of the boundary layer is different.

2. The heat transfer and the temperature profile are different.

3. Aerodynamic losses in the flow with zero incidence angle are less than those in the flow with - 15^{o} incidence angle.

4. The turbulence levels are different.

It can be concluded that for the geometry and conditions used here the thermophoresis is more effective in reducing the deposition rate when the steam turbine is running at full load than when it is running at partial load. The results displayed here cannot be safely applied to other blade geometries and flow conditions where the extent of the zones of stagnation laminar boundary layers and turbulent boundary layers may differ.

4.8 Thermal Conductivity of the Uranin Particle

To apply successfully the analysis of the theoretical study of the effect of thermophoresis on the deposition of the solid particles on the blade surfaces, a value for the thermal conductivity of the uranin was required. According to the author's knowledge, this value is not available in the published literature or from conventional sources, Refs. (109 - 112). However, recently Al-Azzawi and Owen (108) have published the value of the thermal conductivity of the uranin (K_p). The aim of this section therefore is twofold: firstly, to provide a value for the thermal conductivity of uranin, which may be of general interest and not only to those researching in the field of aerosol physics; and secondly, to present a simple and convenient experimental method for determining the thermal conductivity of such materials.

4.8.1 Experimental apparatus and procedure

The thermal conductivity of a material is essentially a function of its substance, temperature, and internal geometric structure, but is independent of the external geometric shape (i.e. sphere, cube, etc.). Therefore, by arranging that the test specimen has the same internal structure as the uranin particle of interest, the thermal conductivity becomes a function of temperature only. The uranin particles used in the aerosol simulation experiments are produced by atomising a water/uranin solution. After the water evaporates in the air stream a small uranin particle remains, the internal structure of the particle, particularly the void fraction, will be a function of its drying rate. The uranin test pieces which were used to measure the thermal conductivity were produced from a strong water/uranin solution which was allowed to dry out at room temperature, i.e. at the same temperature as the aerosol particle, to produce a similar internal structure.

The experimental apparatus used is shown in Fig. 4.30. With this arrangement two uranin samples could be simultaneously investigated. Each sample was located on the opposite surface of the slab of good insulating material. Mounted on each side of the insulating material was a copper coated laminated sheet with dimensions 140 mm x 140 mm. Some of the copper film was peeled off the outer surface of each sheet to leave a central area, 60 mm x 60 mm, as a heating element. Five thermocouples were mounted on the heating surface to measure the surface temperature of the uranin sample. Two wires were connected to the ends of each heating element to enable the voltage across it to be measured. The two heating elements were connected in series by heavy copper wires to enable a relatively large current to be drawn from the power supply. A wooden frame with internal dimensions, 60 mm x 60 mm was placed over each heating

element. The uranin test pieces were then individually cast into these frames to produce solid blocks, one being 6.4 mm thick and the other 7.15 mm. These were designated block 1 and block 2 respectively. Five thermocouples were then attached to the outer surfaces of the test pieces.

The above arrangement permitted two uranin blocks of different thickness to be exposed to one-dimensional steady-state conduction. The electrical current through the copper heating elements was measured together with the potential differences across each to yield the power supplied to each block. The experimental procedure was as follows:

(i) Starting with a low current and low voltage, the copper films were heated. Air was continuously blown over the outer surfaces of the test blocks to assist the heat transfer and to increase the measured temperature difference between the inner and outer surfaces. Steady state conditions were maintained for 30 minutes, during the following 120 minutes the electrical inputs and surface temperatures were measured and recorded three times. These values were averaged.

(ii) The electrical load was increased and (i) repeated to produce a total of ten sets of data. The maximum current drawn was 136 A.

(iii) The maximum temperature to which the blocks could be heated was limited by the tendency of the material to soften at temperatures above about $70^{o}C$.

4.8.2 Results and discussion

Assuming that the electrical energy supplied to the heating elements is conducted through the uranin test blocks as heat rate, $\dot{Q}$, then

$$\dot{Q} = I\ V$$

where I and V are the measured current and potential difference for each heating element.

Fouriers equation for one-dimensional steady-state conduction reduces to:

$$\dot{Q} = - K_p A \frac{\Delta T}{\Delta x}$$

where K_p = thermal conductivity of the uranin

A = cross-sectional area normal to heat flux

$\Delta T/\Delta X$ = temperature gradient through test block.

Since A and ΔX are geometric constants the thermal conductivity will be a function of the ratio $\dot{Q}/\Delta T$. A linear relationship indicates a constant value of K_p whilst a curvilinear relationship indicates that K_p is temperature dependent. The variation of the heat rate through the two main uranin blocks as a function of the temperature difference measured across them, is shown in Fig. 4.31. The derived values for the thermal conductivity as a function of the mean bulk temperature in the blocks $\bar{T}$, is shown in Fig. 4.32. These values were calculated using the slope measured between consecutive points in Fig. 4.31.

Figures 4.31 and 4.32 clearly show that the thermal conductivity of the uranin has a constant value up to an average test block temperature of about $55^{o}C$ after which it is seen to decrease. At the higher average temperatures the heated surface temperature was as much as $90^{o}C$ and the test blocks were beginning to soften. The apparent temperature dependency of the thermal conductivity at higher temperature is therefore more likely to be the result of a change in the structure of the material. For the temperature range in which the uranin can be sensibly used as a solid material, the thermal conductivity has a constant value of about 0.43 W/mK.

The errors involved in the experiment were estimated to be in the order of 2%. These were mainly due to voltage fluctuations from the thermocouples and a slight variation in the thickness of the test blocks after solidification. The scatter in the results of Fig. 4.32 reflect this error. A least squares regression analysis in the linear portion of Fig. 4.31 would give a single value for the corresponding section of Fig. 4.32. The individual data points and their scatter were retained and plotted in Fig. 4.32, however, as a demonstration of the experimental consistency

4.8.3 Conclusions

To complement a long term research programme involving experimental and theoretical aerosol techniques, it has been necessary to find the thermal conductivity of uranin (fluorecein sodium). Two solid uranin test blocks were manufactured by allowing a strong water/uranin solution to dry out and solidify. The blocks were exposed to one-dimensional steady-state conduction by heating one surface using electrically heated copper elements. The experimental method was found to be very satisfactory and produced a constant value for the thermal conductivity of uranin of 0.43 W/mK.

CHAPTER 5

THEORETICAL ANALYSIS OF THE BLADE PASSAGE FLOW

5.1 Introduction

In this Chapter, the passage geometry of the steam turbine fixed blade is analysed and compared with that in the actual turbine. Section 5.3 is concerned with the electrical field analogy technique and how it was employed to locate the flow properties along the blade surfaces. The points on the blade surfaces were projected on the blade chord.

The terminal conditions are studied in section 5.4 and they were provided by the G.E.C. for an existing 500 MW turbine. The Gyarmathy method (114) for predicting the properties of the steam before or after the condensation shock was employed, since the nucleation was assumed to have occurred shortly before the entry of the blade passage.

The degree of relief of the supersaturation was predicted for the existing range of the droplets (0.01 - 1.0 μm) by using the Ryley method (115) with modifications for this work, and the thermodynamic losses as a function of the droplet size are studied in detail in section 5.5.

The remaining part of the Chapter involves the analysis of the boundary layer and flow acceleration along the concave and convex surfaces. Head's entrainment method was successfully employed to predict the characteristics of the turbulent boundary layer. The same method has been used by many steam turbine designers. In section 5.6.8, the laminarisation phenomenon, and its effect on the transfer of the mass and the developing of the turbulent boundary layer, was studied and analysed in detail.

The last section of this Chapter contains the discussion of the results and analyses the correlation between the boundary layer parameters, the droplet geometry and the acceleration parameter.

5.2 Nozzle Geometry

The passage between the two turbine blades forms a convergent-divergent nozzle. The dimension and the passage shape (Fig. 5.1) used in this work were adopted for several reasons:

1. They are similar to the mid-radius section of the final stage fixed blade found in the full scale turbine.

2. The reaction is assumed to be equal to 50%.

3. Steam and air tests have already been made using this blade shape in connection with other research projects, Refs. (15, 7, 3, 4).

El-Shobokshy (37) and Davies (4) used a convergent-parallel nozzle as a passage between consecutive blades. Therefore, Mach number could not exceed 1.0. In the present work a modification was made to obtain a convergent-divergent nozzle, in order to allow the flow to expand and become supersonic, as in the existing modern turbine, Fig. 5.2 shows the distribution of the cross-sectional area of the passage. The area in respect to the concave surface is maximum at $x/c = 0.3$, then decreases up to $x/c = 0.9$. At $0.9 < x/c < 1.0$ the passage cross-sectional area increases to form the divergent section. Beyond $x/c = 1.0$ the flow is bounded only by the convex surface as the preceding blade end.

5.3 Electrical Analogy Field Plot

This method consists of establishing in a uniformly conductive sheet a field of electrical potential and current flow that is an analogue representation of the actual gas flow field to be investigated. By plotting equipotentials of the conduction field, or by measuring the potentials at selected points, information is obtained and converted, by known scaling factors, to the required parameters of the actual field.

The output of the application of the conductive sheet analogue is determined by the nature of the analogue representation. The current and potential distributions in a uniformly conductive sheet between prescribed potential boundaries are essential of a two-dimensional Laplacian form. The two-dimensional flow can be forced into one-dimensional flow, in order to define the flow belocity (U_∞) as a polynomial of x. The procedure of using a teledeltos paper technique consists of:

1. The shape of the cascade (two blades) was drawn on the conducting paper. The scale used in the present work was 1 : 1.

2. The blade shapes were painted using a conducting silver paint, this ensured that the surfaces are equipotential on each blade profile (Fig. 5.3a).

3. A midpotential stream line was taken as the locus of centres of successive circles drawn tangentially to each boundary of the blades. It was painted in order to be used as a second boundary condition with either the concave or the convex side (Fig. 5.3b).

4. The conducting paper was cut along a straight line perpendicular to the mid-stream line for some distance upstream and downstream of the cascade. The inlet and exit angles are known. The other side of the paper were cut parallel to the mid-stream line. The edges so produced were painted using the conducting paint to form two outer streamlines as shown in Fig. 5.3c.

5. A relative potential difference was applied equal to 100 units between the two outer streamlines.

6. The mid-stream line was located using a probe at a potential equal to 50 units, this was compared with the guessed mid-stream line. If

the difference was found to be significant the boundary conditions should be changed, and the procedure should be repeated until the difference was not considerable and could be neglected. The other streamlines were located by adjusting the galvanometer, (Fig. 5.3d).

7. The velocity potential lines were located by:

   (a) cutting the shape of the cascade out of a new conducting paper by making two holes to represent the two blades, Fig. 5.3e;

   (b) repeating point (4) without painting;

   (c) painting two lines perpendicular to the flow at a distance upstream and downstream of the cascade, Fig. 5.3f;

   (d) applying a relative potential difference equal to 100 units between the two painted lines;

   (e) adjusting the galvanometer to read between zero and 100 units to locate a velocity potential line for each reading, Fig. 5.3g.

8. The two plots (streamlines and velocity potential lines) were superimposed to produce the final plot, Fig. 5.3h.

5.4 The Terminal Conditions

The first nucleation within the flow passage will occur at a location which may be approximately found by the method proposed by Gyarmathy (14). If the continued expansion is very rapid, the supercooling will be greater and dependent on the balance between the expansion rate and the heat and mass transfer around the fog droplets. Furthermore, if the expansion rate is large enough for the degree of the supercooling to reach a level where spontaneous nucleation sets in again, a second generation of

fog droplets will be produced. It may be followed by a third nucleation. There is no standard position within a stage where nucleation occurs and therefore a feasible set of assumptions have been chosen for this work to avoid further complicating an already complex problem.

It has been assumed that:

1. The first nucleation occurred shortly before the blade entry, so that the entering steam is an equilibrium mixture of saturated vapour and grown droplets.

2. The pressure and the velocity at the inlet of the blades passage were taken from the real turbine conditions (G.E.C.) and equal to 0.233 bar absolute and 80.0 m/s respectively.

3. The wetness fraction is equal to 3%. this is reasonable for the first nucleation.

4. The entrained droplets are monodispersed in size with a diameter in the range 0.01 - 1.0 μm (Refs. 58, 113).

5. No second nucleation occurs during the flow through the nozzle.

6. There is no slip between the droplets and the vapour, since they are very fine and can follow the stream lines.

5.4.1 Condensation shock calculations

The supersaturated steam is rapidly expanded in the L.P. turbine. The temperature falls and therefore at a certain temperature (subcooling temperature $\approx 40^{o}C$) the unstable flow tends to seek equilibrium. The phenomenon which allows the steam to find equilibrium is called a condensation shock. The thermodynamic properties are changed after the shock such as an increase in pressure and decrease in enthalpy. In the

present work, Gyarmathy's method for calculating the conditions of the steam before and after the shock was adopted (114).

The steam flow is such that perfect supersaturation prevails before the shock and perfect thermodynamic equilibrium exists after it. The method is to solve the continuity, momentum and energy equations simultaneously.

(i) The continuity equation:

$$\frac{U_{\infty 2}}{U_{\infty 1}} = x_2 \left(\frac{h_2/h_1}{p_2/p_1}\right) \tag{5.1}$$

(ii) The momentum equation:

$$\frac{\gamma}{\gamma - 1} \frac{U^2_{\infty 1}}{h_1} \left\{ \frac{U_{\infty 2}}{U_{\infty 1}} - 1 \right\} = 1 - \frac{p_2}{p_1} \tag{5.2}$$

(iii) The energy equation:

$$h_1 + \frac{1}{2} \left\{ U^2_{\infty 1} - U^2_{\infty 2} \right\} = h_2 - (1 - x_2)\, h_{fg}\,(p_2) \tag{5.3}$$

From the three equations a formula for $(U_{\infty 2}/U_{\infty 1})$ can be found.

$$\frac{U_{\infty 2}}{U_{\infty 1}} = 1 - \frac{\dfrac{h_2}{h_1} - 1 + \dfrac{h_{fg}(p_2)}{h_1} \left\{ \dfrac{p_2/p_1}{h_2/h_1} - 1 \right\} - \dfrac{\gamma - 1}{\gamma} \left\{ \dfrac{p_2}{p_1} - 1 \right\}}{\dfrac{h_{fg}(p_2)}{h_1} \dfrac{p_2/p_1}{h_2/h_1} - \dfrac{1}{2} \dfrac{\gamma - 1}{\gamma} \left\{ \dfrac{p_2}{p_1} - 1 \right\}} \tag{5.4}$$

Therefore, there are only three unknowns: either the inlet conditions p_1, $U_{\infty 1}$, h_1 or the conditions after the shock p_2, $U_{\infty 2}$ and h_2. The variation in the pressure, temperature, velocity and enthalpy due to the condensation shock were found to be very small and could be neglected. The pressure

was changed by 0.02%, the velocity by 0.12% and the enthalpy by 0.015%.

5.5 Treatment of Metastability

Nucleation takes place when the expansion line crosses the Wilson line, this was assumed to occur at the entry to the nozzle. The droplet size produced was in a range of 0.01 - 1.0 μm. The expansion rate is the parameter which can specify the droplet size. The higher the expansion rate, the smaller the droplet size. At the nucleation point thermodynamic equilibrium is rapidly re-established by the mutual adjustment of the temperature of the droplet and the steam. The flow will then expand inside the nozzle where the steam temperature will drop below the saturation temperature, the flow then changes to supersaturated flow. The equations and the formulae applied to the supersaturated steam are the same as for the superheated flow except the values of the isentropic exponent (γ) have a different range. The governing equations are:

(i) Equation of state:

$$p\, v^{\gamma} = \text{const.} \qquad \text{in which } \gamma = 1.31 \text{ when } y = 0.03 \text{ kg}_{\ell}/\text{kg}_{s}$$

(ii) The enthalpy change:

$$h = y_s\, h_f + (1 - y_s)\, h_g - Cp\, \Delta T_s \tag{5.5}$$

where ΔT_s = the subcooling temperature

y_s = wetness fraction of the supersaturated flow

h_f, h_g = the enthalpy of saturated liquid and vapour.

It was recognised, however, that condensation would continue to occur on the existing dispersed droplets within the core flow giving partial or full relief to the rising supersaturation. The process for relieving of supersaturation is thus seen to be a complex combination of the frequency of production of nuclei and of heat and mass transfer around them. The method, which is described in Ref. (115), was modified and used in the present work. In the absence of foreign matter, there is only one surface for heat and mass transfer and it is the droplets surface. The area of this surface depends on the size and the number of the droplets. For the same wetness fraction, the smallest size of droplets have the greater aggregate surface area for exchanging the heat and the mass between the two phases.

For steam which is initially wet as in the present work, it is to be expected that expansion will still promote supersaturation within the dry saturated content, but that the presence of the liquid will provide internal surface upon which condensation and relief of supersaturation may proceed. The rate of relieving the supersaturation depends on the dimensions of available internal area and the degree of disequilibrium. Therefore the stability of the expanded steam can be calculated by employing a step-by-step method through the nozzle.

The step length, Δx, was selected as a variable along the nozzle. Δx was allowed to decrease through the nozzle and at the region near the throat, could be reduced to a half of the initial value. This change in the step length was done in order to match the rapid change in the flow parameters at and near the throat. The formulae which control the step length could be written as:

$$\Delta x = x(j + 1) - x(j) \tag{5.6}$$

$$x(j+1) = x(j) + x_{gp}\, Gp^{Ng-j} \tag{5.7}$$

$$x_{gp} = (x_e - x_i)\left\{\frac{1+Gp}{1+Gp^{Mg}}\right\} \tag{5.8}$$

where $Mg = Ng - 1$

x_i = a value of the inlet x

x_e = a value of the exit x

$Gp > 1.0$ in the present work Gp is taken to be equal to 1.02

Ng = number of steps

Gp and Ng are the control parameters by which the step length can be specified.

The rate of droplet growth equation which is used in this work was derived by Young (116) and can be written as:

$$\frac{dr}{dx} = \frac{2}{3}\sqrt{\frac{8}{\pi R}}\;\frac{Kn\;\bar{p}}{\rho_f\,\bar{U}_\infty\,(1+2.7\;Kn)}\left\{\frac{1}{\sqrt{T_{gm}}} - \frac{1}{\sqrt{T_s}}\right\} \tag{5.9}$$

where $\rho_f = 1000.0$ kg/m^3

$R = 461.5$ J/kg K

$\bar{U}_\infty$ = the average velocity at the centre of the step length Δx in m/s

$\bar{p}$ = the average pressure at the centre of the step length Δx in bar

T_{gm} = the modified vapour temperature in ^oK

T_s = saturation temperature appropriate to $\bar{p}$ in ^oK.

Equation (5.9) can be rewritten in the form:

$$\frac{dr}{dx} = \frac{4.952\ Kn\ \tilde{p}}{\bar{U}_\infty\ (1 + 2.7\ Kn)} \left\{ \frac{1}{\sqrt{T_{gm}}} - \frac{1}{\sqrt{T_s}} \right\} \tag{5.10}$$

and the new droplet size $r(j + 1) = r(j) + (dr/dx)\ \Delta x$, the total precipitated mass can be calculated from

$$m = (4/3)\pi\ \rho_f \left\{ (r(j + 1))^3 - (r(j))^3 \right\} N_p \tag{5.11}$$

where N_p = the specific number of the droplets.

$$N_p = \frac{y}{\frac{4}{3}\pi\ \rho_f\ (r(1))^3}$$

The ratio of the actual condensed mass (m) to the maximum condensed mass when the flow is fully reverted to equilibrium (M) is defined as

$$\psi = m/M$$

Therefore,

$$T_{ac} = T_{gm} + \psi\ (T_s - T_{gm}) \tag{5.12}$$

where T_{ac} and $r(j + 1)$ are the actual temperature and droplet size after partial or full relief of supersaturation. Figure 5.4 shows the temperature distribution of the wet steam for different droplet sizes. The flow is supersaturated when the droplet size is greater than 1.0 μm. The wetness fraction distribution behave the same as the temperature distribution for a certain droplet size as shown in Fig. 5.5. The supersaturation losses are presented in Fig. 5.6. The losses are seen to increase with the increasing of the size of the entrained droplet.

There is a large drop in the temperature of the vapour at $x/c > 0.9$, and a small reduction in the saturation temperature. Therefore, there is a rapid increase in the subcooling temperature at $x/c > 0.9$ and hence a sudden increase in the supersaturation losses at the same x/c. The losses are maximum when the droplet size is 1.0 μm and zero when its size is less than 0.01 μm.

5.6 Boundary Layer Velocity Calculation

The boundary layer parameters have a great effect on the movement and growth or diminishing of the fog droplets inside the boundary layer. Therefore, a good prediction of the boundary layer characteristics gives a more accurate analysis of the droplets behaviour.

There are many practical methods for solving the boundary layer equations. A method was selected which was able to:

(i) match the nature of the flow without further complicating the analysis;

(ii) be sufficiently accurate;

(iii) produce acceptable results quickly.

The flow along the blade surface was divided into four regions:

(1) Stagnation flow, along the blade nose only.

(2) Laminar flow:

(a) with zero pressure gradient; along the concave surface for a short distance from the end of stagnation flow.

(b) With pressure gradient; along the convex surface for a very short distance from the end of stagnation flow.

(3) Transition flow; treated as a point and not as a region.

(4) Turbulent flow:

(a) with zero pressure gradient; along the concave surface starting from the transition point and ending at the entrance to the blades passage.

(b) with pressure gradient; along both surfaces for flow inside the passage.

The boundary layer calculations were done on the basis of the following assumptions:

(1) The flow is dry, i.e. single phase, since the droplets are very fine and have no effect on the developing of the boundary layer.

(2) The blade surfaces are smooth.

(3) The flow along the surface is adiabatic.

(4) The blade surfaces are flat, since the thickness of the boundary layer is very small compared with the blade curvature, i.e. $\delta << \text{blade radius}$.

(5) The flow is incompressible, but modification was undertaken for C_f, θ and δ_1 when the Mach number (M) was greater than 0.3.

(6) The flow is homogeneous, since the water droplets are very fine. They cannot maintain, for very long, a significant relative speed in relation to the steam, the developed drag force quickly cancels this slip. They therefore obey the general movement of the flow of the steam.

5.6.1 Calculation of free stream velocity

The flow inside the nozzle is supersaturated. From the previous section the degree of supersaturation is a function of droplet size, and hence there are many possible flow regimes, starting from full supersaturation and finishing with equilibrium. The equilibrium flow as a result of full reversion contains very fine droplets with a range of sizes less than 0.1 μm. Therefore, the treatment of all flow regimes can be the same by using the ideal equation of state and the gas dynamic equations for a shock-free monophase nozzle flow to find the flow parameters.

(1) Continuity equation: $\dot{m} = \rho U_\infty A$

(2) Equation of perfect gas: $p = \rho RT$

(3) Poisson relation for temperature, pressure and density:

$$T(j+1) = T(j) \left[\frac{p(j+1)}{p(j)} \right]^{\frac{\gamma - 1}{\gamma}} \tag{5.13}$$

$$\rho(j+1) = \rho(j) \left[\frac{p(j+1)}{p(j)} \right]^{\frac{1}{\gamma}} \tag{5.14}$$

(4) Energy equation: $T_o = T + \frac{U_\infty^2}{2Cp}$ (5.15)

Figure 5.7 shows the velocity distribution along the core of the passage. It is rapidly increasing towards the throat and very slowly increasing after the throat (located at x/c = 0.92 along the concave surface).

5.6.2 Boundary layer characteristics

The main parameters of the boundary layer, which are used in the following sections for theoretical analysis, can be stated as follows:

(1) The overall boundary layer thickness δ can be obtained when $\frac{u}{U_\infty} \approx 0.995$.

(2) Displacement thickness δ_1 is defined by

$$\delta_1 = \int_0^\infty (1 - \frac{u}{U_\infty})\, dy \tag{5.15}$$

(3) Momentum thickness θ which measures the flux of momentum defect within the boundary layer as compared with the inviscid flow, and may be defined by

$$\theta = \int_0^\infty \frac{u}{U_\infty} (1 - \frac{u}{U_\infty})\, dy \tag{5.16}$$

(4) Mass flow thickness $\Delta = \delta - \delta_1$ is defined by

$$\Delta = \int_0^\delta \frac{u}{U_\infty}\, dy \tag{5.17}$$

(5) Shape factor H is defined by $H = \frac{\delta_1}{\theta}$

(6) Shape parameter H_1 may be defined by $H_1 = \frac{\Delta}{\theta}$

(7) Skin friction coefficient C_f is defined by

$$C_f = \frac{\tau_w}{\frac{1}{2}\rho U_\infty^2} \tag{5.18}$$

(8) Entrainment coefficient C_E is defined by

$$C_E = \frac{1}{U_\infty} \frac{d}{dx} \int_0^\delta u\, dy \tag{5.19}$$

(9) Shear velocity u_* is given by

$$u_* = \sqrt{\frac{\tau_w}{\rho}} \tag{5.20}$$

5.6.3 Flow analysis around the blade nose

The nose of the blade is considered as a cylinder with radius equal to 10.6 mm. The potential flow theory was applied on the flow past the nose of the blade in order to calculate the velocity distribution. The ideal velocity at any point around the cylinder in non-viscous, irrotational flow with radius R was calculated by:

$$U_\infty = -\frac{U_{max}}{2}\left[-\frac{a^2}{R^2}\cos(2\phi) - 1\right] \tag{5.21}$$

where ϕ = the angle measured from the stagnation point

$a = R$

U_{max} = maximum velocity = 80.0 m/s

The stagnation point was estimated to be the intersection point of the centre line of the blade with the nose surface. For zero incidence angle, the concave surface forms 25% of the perimeter of the nose as does the convex surface. Blasius' exact solution (84) was adopted to calculate the boundary layer characteristics of a stagnated flow. The method defines the displacement and momentum thickness, shear stress and shape factor as follows:

(1) $\delta_1 = 0.648\sqrt{\frac{\nu}{dU_\infty/dx}}$ displacement thickness

(2) $\theta = 0.292\sqrt{\frac{\nu}{dU_\infty/dx}}$ momentum thickness

(3) $\tau_w = 1.233\,\mu U_\infty\sqrt{\frac{dU_\infty/dx}{\nu}}$ wall shear stress

(4) $H = \frac{\delta_1}{\theta} = 2.21$ shape factor.

The method was applied from the stagnation point up to 25% of the perimeter of the nose along the concave and convex surfaces ($x/c = 0.032$).

5.6.4 Boundary layer equations of laminar flow

The laminar flow was assumed to be incompressible and two-dimensional steady flow over a flat plate. The main governing equations are those of continuity and momentum, which can be written as follows:

(1) Continuity equation

$$\frac{\partial u}{\partial x} + \frac{\partial v}{\partial y} = 0 \tag{5.22}$$

(2) Momentum equation in x-direction

$$u \frac{\partial u}{\partial x} + v \frac{\partial u}{\partial y} = - \frac{1}{\rho} \frac{\partial P}{\partial x} + \nu \left[\frac{\partial^2 u}{\partial x^2} + \frac{\partial^2 u}{\partial y^2} \right] \tag{5.23}$$

(3) Momentum equation in y-direction

$$u \frac{\partial v}{\partial x} + v \frac{\partial v}{\partial y} = - \frac{1}{\rho} \frac{\partial P}{\partial y} + \nu \left[\frac{\partial^2 v}{\partial x^2} + \frac{\partial^2 v}{\partial y^2} \right] \tag{5.24}$$

The boundary conditions are

a. $u = v = 0.0$ at $y = 0.0$

b. $u = U_\infty$ at $y > \delta$

c. $\frac{\partial^2 u}{\partial x^2} << \frac{\partial^2 u}{\partial y^2}$

d. The pressure in a direction normal to the boundary layer can be taken equal to that outside the boundary layer, i.e. $\frac{dp}{dy} = 0.0$.

e. $v << u$

Now equations (5.23) and (5.24) can be simplified and rewritten in the form:

$$u \frac{\partial u}{\partial x} + v \frac{\partial u}{\partial y} = - \frac{1}{\rho} \frac{\partial p}{\partial x} + \frac{\partial^2 u}{\partial y^2} \qquad (5.25)$$

Equations (5.22) and (5.25) can be considered to be the appropriate boundary layer equations without affecting the accuracy of the results. It is not practicable to solve equations (5.22) and (5.25) in these forms. Hence, Von Karman integrated them between $y = 0.0$ and $y = \infty$ for constant x, and gave a more convenient expression which is known as the Momentum Integral Equation,

$$\frac{\tau_w}{\rho} = \frac{d}{dx} (U_\infty^2 \theta) + U_\infty \frac{dU_\infty}{dx} \delta_1 \qquad (5.26)$$

5.6.5 Laminar boundary layer analysis

There are many practical methods for solving the momentum integral equation. Pohlhausen's method and Thwaites' method were employed for zero and non-zero pressure gradient. The details of the two methods can be found in Appendix 5A. On the concave surface, the flow is stagnated in the range $0.0 < x/c < 0.032$ and then laminar with constant free stream velocity until $x/c = 0.136$. On the convex surface the stagnated flow is followed by laminar flow with variable free stream velocity (favourable pressure gradient) in the range $0.032 < x/c < 0.1$.

5.6.6 Prediction of the transition point

The starting point of transition was assumed to be the point of starting the turbulent flow, since the flow is very complicated inside the transition region. Recently Abu-Ghannam and Shaw (117) have investigated experimentally the nature of the transition under different conditions. They have formulated their model to predict the points of transition, and it showed good agreement with their experimental results. Their empirical formula gives the values of Re_θ at the starting and finishing points of the transition for zero and non-zero pressure gradient.

(1) Zero pressure gradient

$$Re_{\theta s} = 163.0 + \exp (6.91 - \tau) \tag{5.27}$$

$$Re_{\theta e} = 2.667\ Re_{\theta s} \tag{5.28}$$

(2) Non-zero pressure gradient

$$Re_{\theta s} = 163.0 + \exp \left\{ F(\Gamma_\theta) - \frac{F(\Gamma_\theta)}{6.91} \tau \right\} \tag{5.29}$$

where $F(\Gamma_\theta) = 6.91 + 2.48\ \Gamma_\theta - 12.27\ (\Gamma_\theta)^2$

$$\Gamma_\theta = \frac{\theta}{\nu} \frac{dU_\infty}{dx}$$

The location of the transition point is a function of the values of the turbulence level and Reynolds number based on the momentum thickness. Parker and Lee (7) conducted a series of experiments using a blade cascade almost identical to that used in the present work. They measured the turbulence intensity at the cascade entry and found it to be 2.2%.

In this work the flow inlet velocity is about five times that used by Parker and Lee and relaminarisation may occur, since highly

accelerated flow was used. Therefore, it is reasonable to assume the turbulence level, τ, to be in the range 2.0 - 2.5%.

It was found that:

(1) On the concave surface, equation (5.27) was used to determine the starting point of the turbulence, since the upstream flow has zero pressure gradient until x/c = 0.3. The position of the transition point was at x/c = 0.136.

(2) On the convex surface, equation (5.29) was adopted to predict the location of the transition point, since the flow has negative pressure gradient. The position at which the turbulent flow started was predicted at x/c = 0.11.

5.6.7 Turbulent boundary layer analysis

The nature of the flow inside the blade passage is turbulent except on the convex surface at x/c < 0.11 where the flow is laminar. The starting point of the turbulent flow along both surfaces are given in the previous section.

It is still difficult to find an analytical solution of the Navier-Stokes equations for turbulent flow. The equations of the boundary layer were simplified in section 5.6.4 for laminar flow, and were adapted for turbulent flow with using the flow velocities u, v as the average velocity in x and y directions. It was still found to be impossible to obtain an analytical solution to the problem. The existing solutions are based on experimental and analytical formulae. One of the most convenient methods employed is Head's entrainment method, (118), although other methods have been tried, such as that due to Curle and Davies (119), which

gave inadequate results for the purpose of the present work. The Head entrainment method was used by steam turbine designers, (120), therefore, it appeared to be the best choice for this research. The method predicts the turbulent boundary layer parameters by a simultaneous forward integration of the two main equations:

(1) Von Karman momentum integral equation which can be written as:

$$\frac{d\theta}{dx} = \frac{C_f}{2} - (H + 2) \frac{\theta}{U_\infty} \frac{dU_\infty}{dx} \tag{5.30}$$

(2) Head entrainment equation may be written as:

$$\frac{d\Delta}{dx} = C_E - \frac{\Delta}{U_\infty} \frac{dU_\infty}{dx} \tag{5.31}$$

where $\Delta = H_1 \theta$.

The entrainment equation can be rewritten in a form:

$$\theta \frac{dH_1}{dx} = C_E - H_1 \left\{ \frac{C_f}{2} - (H + 1) \frac{\theta}{U_\infty} \frac{dU_\infty}{dx} \right\} \tag{5.32}$$

Appendix 5B shows the details of the method.

The two main equations, (5.30) and (5.32) with auxiliary equations were solved numerically by using the Runge-Kutta method. The numerical method needs the initial values of θ, H_1 and the free stream velocity distribution along the x-axis. The computer program for solving the differential equations of the Head method is presented in Appendix 7D as part of the main program.

The boundary sublayer is defined by setting the value of y^+ equal to 7.8.

$$y = \frac{y^+ \nu}{u_*}$$

$$y_{sub} = 7.8 \frac{\nu}{u_*} \tag{5.33}$$

5.6.8 Laminarisation

When the acceleration of the flow is severe enough, the originally turbulent layer undergoes a reversion towards laminar. This phenomenon has been given different names such as "laminarisation", "reverse transition", "inverse transition" and "relaminarisation". The first name is used in the present work. The location point of laminarisation has been found experimentally by many investigators, (121 - 124). The predicted value of that point in Ref. (121) was in a good agreement with the experimental one, and it was in the range when $L_{cr} \approx 3.0 \sim 4.0 \times 10^{-6}$. Laminarisation can be achieved as long as $L > L_{cr}$, where $L = \frac{\nu}{U_\infty^2} \frac{dU_\infty}{dx}$, the acceleration parameter. This parameter has been derived from the Momentum Integral Equation, as shown in Appendix 5C. The momentum equation in the form of Re_θ can be written as:

$$\frac{dRe_\theta}{dx} = \frac{4}{5} \frac{U_\infty}{\nu} \left[\frac{0.016}{Re_\theta^{0.25}} - 3.55\, Re_\theta \frac{\nu}{U_\infty^2} \frac{dU_\infty}{dx} \right] \tag{5.34}$$

The critical value of Re_θ can be obtained by setting $\frac{dRe_\theta}{dx} = 0.0$, and equation (5.34) gives

$$L_{cr} = \frac{4.507 \times 10^{-3}}{(Re_\theta)_{cr}^{1.25}}$$

In section 5.6.6, the value of $(Re_\theta)_{cr} \approx 280.0$ when the turbulence level was assumed to be $\approx 2.0\%$. Therefore, the critical value of the acceleration parameter is equal to 3.9×10^{-6} and thus the value of L can define the

nature of the flow. For $L > L_{cr}$, equation (5.34) gives $\frac{dRe_\theta}{dx} < 0$ or $\frac{d\theta}{dx} < 0$; this means that there is a reduction in Re_θ and θ values with increasing x when the flow represents laminarisation. Back, Cuffel and Massier (122) have found that the local mass flux can exceed the free stream value, and for this situation the boundary layer displacement is not outward from the wall, but inward in the accelerated flow, i.e. $\frac{d\delta_1}{dx} < 0$. When laminarisation occurs ($L > L_{cr}$), the equations of laminar flow can be employed to define the boundary layer as long as $L > L_{cr}$. For $L < L_{cr}$ the flow reverts to its turbulent nature and there is no significant reduction in the turbulence level.

In this work $\frac{dU_\infty}{dx}$ based on the concave surface was found to be in the range of about 100 - 200 at x/c = 0.33, then steeply increased to about 8,000 at x/c = 0.93, then suddenly decreased to about 3,000 at x/c = 0.935 and finally it decreased gradually to about 50 at x/c = 1.0. The values of $\frac{dU_\infty}{dx}$ based on the convex surface were started from about 300 at x/c = 0.11, then increased to a maximum value about 10,000 at x/c = 0.52, and then decreased suddenly to about 3,000 at x/c = 0.53, $\frac{dU_\infty}{dx}$ then decreased gradually until the exit of the passage to the value of about 50 at x/c = 0.6. The values of (L) were calculated along x/c for concave and convex surfaces are presented in Fig. 5.8.

It was observed that:

(1) There are three forward transitions and two reverse transitions along both surfaces.

(a) Forward transition; along the concave surface at x/c = 0.33, 0.7 and 0.94 and along the convex surface at x/c = 0.1 , 0.42 and 0.53.

(b) Reverse transition; along the concave surface at $x/c = 0.35$ and 0.91 and along the convex surface at $x/c = 0.11$ and 0.46.

(2) The flow acceleration along the convex surface is higher than that along the concave. Therefore, about 75% of the turbulent flow along the convex surface is laminarised, and about 50% of the turbulent flow along the concave surface is laminarised.

(3) The variation of U_∞ and $\frac{dU_\infty}{dx}$ as the main parameters of L can be compensated, since the increase in U_∞ was gradual, whilst the change in $\frac{dU_\infty}{dx}$ values were rapid. Hence, the forward transition is sometimes close to the inverse transition as shown in Fig. 5.8.

It may be noticed from this section that the prediction of the boundary layer characteristics of the full or partial laminarised flow can be found by employing one of the laminar flow methods. However, there is much evidence from some investigators, listed below, who have shown that the prediction of high accelerated flow can be done accurately by using a method of predicting a turbulent boundary layer rather than a laminar method.

(1) Donald et al (121) have found a good agreement between their experimental data of the temperature and velocity profiles inside an accelerated flow boundary layer, with the predicted results using a 1/7th power law.

(2) Cebeci et al (125) have shown that the numerical solution of the turbulent boundary layer on a flat plate can give satisfactory results for a highly accelerated flow with or without heat transfer.

(3) Back, Massier and Cuffel (123) have shown that the measured velocity distribution in accelerated flow agrees well with the law of the wall relation.

(4) Back, Cuffel and Massier (122) have observed the values of the shape factor $H = \delta_1/\theta$ and $H_{32} = \delta_3/\theta$ for the accelerated flow are in fair agreement with the predicted results from solving the integral form of the momentum and energy equations for a turbulent boundary layer.

(5) Jones and Launder (124) have concluded that turbulence model may be applied to the prediction of a strongly accelerated boundary layer flow. This model has been shown to be remarkably successful in predicting the hydrodynamic and thermal consequences of the acceleration.

5.6.9 Discussion of the results

The nature of the flow inside the blade passage can be seen from the previous sections, and it is turbulent for:

(1) the entire length along the concave side;

(2) about 95% of the length along the convex surface.

Therefore it is necessary to focus attention only on the turbulent boundary layer results inside the blade passage.

Figure 5.9 shows the variation of the momentum thickness along both surfaces. On the concave surface, θ is decreasing until $x/c = 0.94$, then increasing to the exit. $\frac{d\theta}{dx}$ starts with high negative values and then at about $x/c = 0.7$, $\frac{d\theta}{dx}$ has a small negative value or may be zero, since $L \sim L_{cr}$ at that position. Then at $x/c > 0.94$, $L < L_{cr}$ and $\frac{d\theta}{dx}$ acquires

positive values. On the convex surfaces, the momentum thickness gradually decreases from x/c = 0.11 to x/c = 0.23. Then θ is nearly constant up to x/c = 0.35, followed by a gradual decrease up to x/c = 0.47. Afterwards, a rapid drop in θ value is seen up to x/c = 0.52, since L increases rapidly at $0.47 < x < 0.53$. When $x/c > 0.52$, θ is rapidly increasing until the exit of the passage, since the values of L are dropping sharply at the same x/c. In general the momentum thickness along the concave surface was thicker than that along the convex.

The shape factor H was not affected as much as the momentum thickness by the laminarisation parameter. It can be observed that H was decreasing rapidly until x/c = 0.45 along the concave surface and x/c = 0.2 along the convex surface. Then the value of the shape factor was kept constant at H = 1.25 in the range $0.45 < (x/c)_{concave} < 0.95$ and at H = 1.3 in the range $0.2 < (x/c)_{convex} < 0.55$. At $(x/c)_{concave} > 0.95$ and $(x/c)_{convex} > 0.55$, the shape factor was increased gradually, since the nature of the flow changed to laminar due to laminarisation. Figure 5.10 shows the distribution of the shape factor along the concave and convex surfaces.

The shear velocity along both surfaces was seen to be increasing gradually to the maximum value about 28.0 m/s. Then it decreases rapidly at x/c = 0.05 from the passage exit due to the sudden change from laminarised flow to high turbulent flow as illustrated in Fig. 5.11.

It is well known that the friction factor of a laminar flow is higher than that of a turbulent flow. Thus, it can be observed that the distribution of the friction factor along both surfaces behaves nearly the same as the acceleration parameters, as seen in Fig. 5.12.

The thickness of the boundary layer was thinning steeply along both surfaces for the first 35% of the working length due to rapid increase

in the acceleration parameter. Then, for the remaining length, δ was building up slowly, but when $(x/c)_{concave} > 0.95$ and $(x/c)_{convex} > 0.55$ there was a steep increase in δ since there was a sudden change in the nature of the flow as shown in Fig. 5.13.

The distribution of the boundary sublayer thickness was predicted from equation (5.33). If μ is assumed constant, δ_{sub} is a function of the specific volume v_∞ and the shear velocity u_* only. The values of v_∞ is nearly constant up to $(x/c)_{concave} = 0.75$ and $(x/c)_{convex} = 0.35$, (Fig. 5.14), and u_* was increased gradually, therefore, δ_{sub} was decreasing smoothly. At $(x/c)_{concave} > 0.95$ and $(x/c)_{convex} > 0.55$, δ_{sub} was increasing slowly, since u_* was decreased and $\frac{dU_\infty}{dx}$ was about zero along both surfaces. Figure 5.15 shows the δ_{sub} distribution along both surfaces.

CHAPTER 6

PREDICTION OF SURFACE HEAT FLUX AND THERMAL PROFILE OF WET BOUNDARY LAYER AND A STUDY OF THE BLADE HEATING METHODS

6.1 Introduction

This Chapter contains the prediction methods used to find the distribution of free stream temperature, surface temperature and the surface heat flux. The energy equation for ideal single phase flow can be written in the form

$$T_o = T + \frac{U^2}{2\,Cp}$$

and it was found unacceptable for two phase flow. A new formula for defining the recovery temperature in two phase flow, regardless of the stability of the phases, was derived in section 6.3.

The difference in the wall temperature between the inlet and the exit of the blade passage was found experimentally. Section 6.4 covers the calculation of the wall temperature along the blade surfaces.

The wall heat flux into the turbulent boundary layer was predicted by employing Ambrok's method, (section 6.5). The laminarisation has a great effect on reducing the surface heat flux into the turbulent boundary layer along the concave and convex surfaces. According to the knowledge of the author, there is nothing published about how the designers of wet steam turbines deal with the effects of wetness and laminarisation on heat transfer. Section 6.5.3 contains a theoretical analysis of the laminarisation phenomenon and the effect on the transfer of the heat. In section 6.6, the effect of the physical form of existing wetness on

the heat transfer and the temperature profile in the boundary layers is considered.

The heating methods were discussed briefly in section 6.7. More discussion about the steam heating method is presented in Chapter 8. Finally, the last section involves the discussion of the results of heat transfer and the relation between the laminarisation, the droplet size, the nature of the flow and the amount of heat flux from the blade surfaces.

6.2 The Distribution of Free Stream Temperature

The free stream temperature of wet steam flow is dependent on the degree of relieving of the supersaturation. In the existing droplet range 0.01 - 1.0 μm, the flow was either partially supersaturated or in equilibrium as analysed in detail in section 5.5. The internal heat transfer between the two phases has no effect on the developing free stream velocity and boundary layer. Figure 5.4 shows the distribution of the static free stream temperature along the concave and convex surfaces. The curves are very similar, regardless of the temperature values. It can be seen that the subcooling temperature, ΔT_s, which is defined by

$$\Delta T_s = T_s - T_\infty \qquad (6.1)$$

is higher when the droplet size is bigger, as illustrated in Fig. 6.1. Therefore, the possibility of a second nucleation when the initial droplet size is less than 1.0 μm is low, and could be insignificant when the droplet size is less than 0.5 μm, since the highest ΔT_s is below 30^oC and along a very short distance from the exit of the blade passage.

6.3 The Recovery Temperature

In section 5.6.1, the energy equation

$$T_o = T + \frac{U^2}{2\,Cp} \tag{6.2}$$

was used to calculate the free stream velocity, where it was valid for isentropic single phase flow. Two phase flow, however, is influenced by:

(1) mass and heat exchange between the two phases;

(2) partial or full relief of the supersaturation;

(3) losses due to the existence of the supersaturation.

Therefore, equation (6.2) must be modified to be used with such complicated flows.

The flow of the steam is either partially supersaturated or in equilibrium, and for the same point in the saturation region, the specific enthalpy for the two flows should be equal. For partially supersaturated flow, the specific enthalpy may be defined by:

$$h_{ps} = h_g - y_{ps}\, h_{fg} - Cp\, \Delta T_{ps} \tag{6.3}$$

and for equilibrium flow:

$$h_e = h_g - y_e\, h_{fg} \tag{6.4}$$

The energy equation can be written in terms of the enthalpy:

$$h_o = h + \frac{U_\infty^2}{2} \tag{6.5}$$

If h in equation (6.5) is substituted by h_{ps} in equation (6.3), this yields:

$$h_o = h_g - y_{ps}\, h_{fg} - Cp\, \Delta T_{ps} + \frac{U_\infty^2}{2} \tag{6.6}$$

If $h_o = Cp\ T_o$, therefore, equation (6.6) can be rewritten as:

$$T_o = \frac{h_g - y_{ps}\ h_{fg}}{Cp} - \Delta T_{ps} + \frac{U_\infty^2}{2\ Cp} \tag{6.7}$$

If h in equation (6.5) is substituted by h_e from equation (6.4), the energy equation becomes

$$T_o = \frac{h_g - y_e\ h_{fg}}{Cp} + \frac{U_\infty^2}{2\ Cp} \tag{6.8}$$

Equations (6.7) and (6.8) define the adiabatic temperatures of the two phase flows and T_o must be the same value in both cases. Thus from equations (6.7) and (6.8) can be derived the same equation which was given by Gyarmathy (14):

$$y_{ps} = y_e - \frac{Cp\ \Delta T_{ps}}{h_{fg}} \tag{6.9}$$

It may be concluded that equation (6.7) is the general equation for defining the adiabatic temperature outside the boundary layer, regardless of the degree of relief of the supersaturation.

For the flow inside the boundary layer, the adiabatic temperature is dependent on the nature of the flow and the value of the Prandtl number (Pr). In wet steam flow, Pr approaches unity, and it is feasible to assume the value of the recovery factor to be equal to 1.0 for laminar and turbulent flows.

6.4 The Wall Temperature

The temperature of the wall can be assumed constant for flow along a flat plate. In the present work the wall temperature decreased from the leading edge to the trailing edge for both blade surfaces. The

temperature at the trailing edge was found experimentally using the simulation method to be approximately equal to 80 - 90% of the temperature (T_{wi}) at the entrance of the working length along both surfaces.

Therefore a straight line or curve fit can be employed to define the wall temperature along the concave and convex surfaces. There is little difference in the results between the two fitting methods, and hence a straight line fit was adopted, which can be mathematically formulated as follows:

$$T_w(x) = T_o + (T_{wi} - T_o) \left\{ \frac{T_{TE}}{T_{wi}} \left(\frac{\sum_{i=1}^{i=n} \Delta x}{x_e} \right) \right\} \qquad (6.10)$$

where n = number of steps

Δx = step length

x_e = value of x at the blade exit

T_{wi} = wall temperature at the entrance to the blade passage.

Figure 6.2 shows the distribution of the wall temperature for different initial T_{wi} and when $\frac{T_{TE}}{T_{wi}} = 0.8$.

6.5 Prediction of Heat Transfer

The advantage of relief of the supersaturation is to raise the value of the free stream temperature. The larger the initial entrained droplet the lower is the free stream temperature which gives a higher heat transfer from the blade surfaces. Some assumptions were made to simplify the problem of heat transfer, as follows:

(1) The blade surfaces were assumed to be flat plates, since the thickness of the thermal boundary layer is negligible compared with the blade curvature.

(2) The thicknesses of the thermal and velocity boundary layers are equal in magnitude, since the Prandtl number was assumed equal to 1.0.

(3) Turbulent Prandtl number is equal to 1.0.

(4) Incompressible two-dimensional flow.

(5) The flow is steady and homogeneous.

6.5.1 Heat transfer in laminar flow

The laminar flow along the concave surface was outside the working passage. Along the convex surface the laminar flow was inside the passage and occupied about 5% of the working length. The heat transfer to the laminar flow can be calculated by solving the energy differential equation which for incompressible flow, can be written as:

$$\frac{q_w''}{\rho_\infty U_\infty Cp(T_w-T_\infty)} = \frac{d\Delta_2}{dx} + \Delta_2 \left[\frac{1}{U_\infty}\frac{dU_\infty}{dx} + \frac{1}{\rho_\infty}\frac{d\rho_\infty}{dx} + \frac{1}{Cp(T_w-T_\infty)}\frac{d[Cp(T_w-T_\infty)]}{dx} \right] \quad (6.11)$$

Equation (6.11) can be simplified, since the laminar flow along the concave surface has a zero pressure gradient, i.e. $\frac{dU_\infty}{dx}$, $\frac{d\rho_\infty}{dx}$, $\frac{dT_\infty}{dx}$ and $\frac{dT_w}{dx}$ are all zero. Furthermore, the flow along the convex surface is laminar for only a short distance from the entrance of the blade passage. Along this distance the variation in U_∞, ρ_∞, T_∞ and T_w is very small and can be neglected.

Therefore equation (6.11) is reduced to:

$$\frac{q_w''}{\rho_\infty U_\infty Cp\ (T_w - T_\infty)} = \frac{d\Delta_2}{dx} \quad (6.12)$$

From the definitiion of Stanton number, St,

$$St = \frac{q_w''}{\rho_\infty U_\infty Cp\ (T_w - T_\infty)} \quad (6.13)$$

so that equation (6.12) becomes:

$$St_x = \frac{d\Delta_2}{dx} \tag{6.14}$$

where $\Delta_2 = \dfrac{\int_0^\infty u\,(T - T_\infty)\,dy}{U_\infty\,(T_w - T_\infty)}$

Kays (132) has solved equation (6.14) and found.

$$St_x = \frac{C_1\,\mu^{0.5}\,G_x^{C_2}}{\sqrt{G_x^{C_3}\,x}} \tag{6.15}$$

where $C_1 = 0.332$, $C_2 = 0.475$, $C_3 = 1.96$, $G_x = \rho_\infty U_\infty$. Substituting the values of C_1, C_2 and C_3 in equation (6.15) gives:

$$St_x = 0.332 \sqrt{\frac{\mu}{x\,G_x}} \tag{6.16}$$

The heat transfer per unit area can be calculated by substituting St_x from equation (6.16) into equation (6.13),

$$q_w'' = 0.332\,Cp\,(T_w - T_\infty) \sqrt{\frac{\mu\,G_x}{x}} \tag{6.17}$$

And hence, equation (6.17) was used for calculating the heat transfer rate in the laminar boundary layers along both blade surfaces.

6.5.2 Heat transfer in turbulent flow

There are a number of methods which may be applied to predict the heat transfer between the blade surface and the turbulent flow. The chosen method would have to contend with:

(1) low and high accelerated flow;

(2) varying wall temperatures,

(3) variable free stream temperatures.

The method due to Ambrok and modified by Moretti and Kays (133) may be used for calculating the heat transfer through a turbulent boundary layer with variable free stream and wall temperatures, and variable free stream velocity. The method requires the solution of the integral energy equation. The solution is given in detail in Appendix 6A, and leads to

$$St_x = \frac{0.0295\,(t_w - t_\infty)^{0.25}\,\mu^{0.2}}{\left[\int_0^x (t_w - t_\infty)^{1.25}\,G\,dx\right]^{0.2}} \qquad (6.18)$$

which can be solved numerically.

For highly accelerated flows the value of St_x was modified, since the turbulence level and the rate of heat transfer are reduced. The heat transfer correction factor is defined by St_x from equation (6.18) and the acceleration parameter, L, (Ref. (133)).

$$F_\ell = 1 - 165\,(\frac{L}{St_x}) \qquad (6.19)$$

F_ℓ must be calculated at (100 - 200) θ upstream of the application point. Then, the corrected value of St_x can be defined by:

$$(St_x)_{co} = F_\ell\, St_x \qquad (6.20)$$

6.5.3 Effect of laminarisation on the heat transfer within the turbulent boundary layer

Laminarisation has a considerable effect in reducing the rate of

heat and mass transfer inside the turbulent boundary layer. The respective flows along the concave and convex surfaces each have more than one reverse-transitions, therefore the nature of the flow was continually changed. Many authors (134 - 138) have comprehensively studied the phenomenon of laminarisation. They have found that a laminar method could be used for laminarised flow to predict the temperature profile and heat transfer. If a turbulent method is adopted a correction must be made to allow for the laminarisation.

In the present work a turbulent method was used. The necessary correction was made by using the empirical formula proposed by Moretti and Kays (133), (equation (6.20)). From the definition of F_ℓ in equation (6.19), equation (6.20) can be rewritten as:

$$(St_x)_{co} = St_x - 165\ L \tag{6.21}$$

Substituting equation (6.13) into (6.21) gives

$$(q_w")_{co} = q_w" - 165\ L\ \rho\ Cp\ U_\infty\ (T_w - T_\infty) \tag{6.22}$$

From the definition of L and the adiabatic temperature T_0 in equation (6.2) and the flow assumed to be ideal, equation (6.22) can be written in the form,

$$(q_w")_{co} = q_w" + \frac{82.5\ \gamma R}{(\gamma-1)} \left[\mu\ \frac{(T_w - T_\infty)}{(T_0 - T_\infty)}\ \frac{dT_\infty}{dx} \right] \tag{6.23}$$

when $\gamma = 1.31$, $R = 461.5\ \frac{J}{kg\ K}$ and $\mu \approx 1.1 \times 10^{-5}\ \frac{kg}{ms}$, equation (6.23) becomes

$$(q_w")_{co} = q_w" + 1.77 \left\{ \frac{T_w - T_\infty}{T_0 - T_\infty}\ \frac{dT_\infty}{dx} \right\} \tag{6.24}$$

If the value of T_w is close to the value of the adiabatic temperature T_o, such that $\frac{T_w - T_\infty}{T_o - T_\infty} \approx 1.0$, equation (6.24) indicates that the laminarisation correction for heat transfer depends on the free stream temperature gradient $\frac{dT_\infty}{dx}$. A high temperature gradient produces a reduction in the heat transfer from the wall into the turbulent boundary layer. The range of $\frac{dT_\infty}{dx}$ can be defined from the acceleration parameter (L). Therefore L should be written in terms of the temperature and the temperature gradient. L can be written in term of pressure gradient by substituting $\frac{dU_\infty}{dx}$ with $\frac{dp}{dx}$ by using the Navier-Stokes equations outside the boundary layer.

$$L = - \frac{\nu}{U_\infty^3} \frac{1}{\rho} \frac{dp}{dx} \tag{6.25}$$

For ideal flow p can be defined by the temperature

$$p = p_o \left(\frac{T_\infty}{T_o}\right)^{\frac{\gamma}{\gamma-1}}$$

and

$$\frac{dp}{dx} = - \frac{\gamma R \rho_\infty}{\gamma-1} \frac{dT_\infty}{dx} \tag{6.26}$$

Substituting equation (6.26) into equation (6.25) gives

$$L = - \frac{\gamma R}{\gamma-1} \frac{\nu}{U_\infty^3} \frac{dT_\infty}{dx} \tag{6.27}$$

By re-arranging and multiplying the right-hand-side by $\frac{T_\infty}{T_\infty}$, equation (6.27) can be rewritten as

$$L = - \frac{1}{\gamma-1} \frac{1}{M_\infty^2 \, Re_x} \frac{\frac{dT_\infty}{T_\infty}}{\frac{dx}{x}} \tag{6.28}$$

Knowing the range of (L), the local range of the temperature gradient can be found from equation (6.28).

Therefore for highly accelerated flows, the reduction in heat transfer from the wall into the boundary layer depends on the degree of laminarisation. The higher the value of L ($L > L_{crit}$), the greater the reduction in the heat transfer for turbulent flow. Figures 6.3 and 6.4 show the degree of reduction in the heat transfer and the correlation with L along the concave and convex surfaces for the extreme values of d and T_{wi}.

6.6 The Effect of Wetness on the Heat Transfer and the Temperature Profiles inside the Boundary Layer

The physical form of the existing wetness is a principal factor affecting the heat transfer calculations. There are many possible forms of the water inside the steam flow and on the blade surfaces.

(1) The water may exist as a thin film along the blade surfaces.

(a) If the water film covers the whole surface of the blade, the wall temperature will be equal to the local saturated temperature regardless of the nature and the characteristics of the flow above the surface. Konorski (102) has studied this problem by heating the blade surface to evaporate the deposited water.

(b) If the water film is discontinuous, the wall temperature will fluctuate between the local saturated temperature and the temperature of the heating steam. The heat transfer through the surface free from the deposited water will be affected by the properties of the flow of the steam, while they have no effect on the covered surface. This case may occur in the real turbine and it is not easy to study theoretically.

(2) If the blade surface is free from collected water as may occur early in the wet regime in the L.P. turbine; the transfer of heat is affected by the size of the existing entrained water droplets. A droplet whose diameter is less than 2.0 μm is considered to be small whilst droplet diameters about this or greater is considered large and is referred to as coarse water.

(a) Large droplets

The flow with large droplets is not homogeneous, in other words the flow is non-Newtonian. This kind of flow has its own formulae and equations for thermal and velocity boundary layers. The behaviour of large droplets will be explained later.

(b) Small droplets

The flow can be correctly assumed to be homogeneous, as explained in the previous Chapter, section 5.6. The temperature of the droplet is assumed to be equal to the saturated temperature at the local pressure since the time lag for the heat transfer between the centre and the surface of the droplet is very small compared with the expansion time of the steam, (Δt_{exp}). Δt_{exp} found to be about 650 μs. The time lag between the temperatures at the centre and at the surface of the droplet was defined by Gyarmathy, (58),

$$\Delta t_{c-r} = \frac{(T_c - T_r)_{t=0}}{\left[\frac{-d(T_c - T_r)}{dt}\right]_{t=0}} \qquad (6.29)$$

Neglecting the heat conduction inside the droplet Carslaw (140) has found analytical solution for Δt_{c-r},

$$\Delta t_{c-r} \approx \frac{\rho_f \, Cp_f \, r^2}{K_f} \tag{6.30}$$

where $\rho_f = 1000.0 \text{ kg/m}^3$

$Cp_f = 4180 \text{ J/kg K}$

and $K_f = 0.645 \text{ W/m K}$

Therefore, equation (6.30) can be rewritten as

$$\Delta t_{c-r} = 6.48 \times 10^6 \, r^2 \tag{6.31}$$

And thus for the extreme sizes of fog droplet, Δt_{c-r} can be defined from equation (6.31).

(i) For droplet diameter = 1.0 μm,

$\Delta t_{c-r} = 1.62$ μs or $\Delta t_{c-r} = 0.25\%$ of Δt_{exp}.

(ii) For droplet diameter = 0.01 μm,

$\Delta t_{c-r} = 1.62 \times 10^{-2}$ μs or $\Delta t_{c-r} = 0.0025\%$ of Δt_{exp}.

Therefore, the time lag in internal droplet temperature change can be neglected.

The temperature profile inside the boundary layer is a function of heat transfer along the y-axis. The heat exchange between the two phases may increase or decrease the transportation of heat along x-axis, since it depends on whether condensation or evaporation is taking place. It was seen that if the length steps along the x and y axes were very small, the effect of phase change on the temperature profile through the boundary layer was insignificant and the error did not exceed 0.1%.

The heat transfer value along the x-axis was affected by the phase change inside the boundary layer. It was reduced with the evaporation of

the droplets and increased with the condensation of the vapour. The rate of evaporation was found to be maximum at the entrance of the passage and reduced slowly along the blade surfaces.

6.7 The Choice of Heating Method

There are three principal methods which can be considered; electrical, hot air and saturated steam. The selection of the appropriate method is dependent on many technical and economical parameters, e.g.

(1) Effectiveness.

(2) The technical problems; designing, manufacturing, installing and operating.

(3) Economics.

(4) Reliability.

(5) Safety.

6.7.1 Electrical method

This method is effective since the blade surface temperature can be controlled. It has a number of disadvantages, however.

(1) It is very difficult to insulate the electrical coils from the turbine body. The presence of the wetness in the low pressure turbine make conditions dangerous.

(2) It is not economical compared with the other methods, since it needs higher capital costs. The running cost is greater than that for steam heating since the quantity of heat used in the steam heating method may not exceed 50% of that for the electrical method.

(3) It is not safe.

(4) It is not easy to design and manufacture.

(5) It is not reliable.

6.7.2 Hot air method

This method is safe providing there is no escape of air into the working steam. It is easy to design the auxiliary components and the blade. The same manufacturing processes are employed for designing the blade internally heated by air or steam. The disadvantages of this method are:

(1) Oxidation may take place when air escapes into the wet steam in the L.P. turbine.

(2) It is not efficient, since the heat transfer coefficient for the air is less than that for the steam.

(3) It is not economical, since it needs high capital and running costs.

(a) The capital cost consists of the costs of the blade, heat exchanger, small air pump and piping.

(b) The running cost is higher than in the electrical or steam heating method, since it has less efficiency.

(4) It is not reliable.

6.7.3 Steam method

This method has been tested experimentally. Many investigators have adopted this method in experiments on a real turbine and on a simulated turbine, (Refs. 103, 104, 106). The advantages of this method are:

(1) It is more efficient than the other methods, since the latent enthalpy of the saturated steam is very high.

(2) It is safe and reliable.

(3) It is economical compared with the others, more details in Chapter 8.

(4) The hollow diaphragm was already designed by G.E.C., Ref. (139). The design and the manufacturing processes are not complicated, the details have been published in Ref. (99). The suggested path of the heating steam and the condensate from the extraction point in the turbine to the main water feeding pipe will be discussed in detail in Chapter 8.

(5) Controlling the blade surface temperature can be obtained only by adjusting the pressure of the saturated heating steam. Therefore, the operating process will be easier than for the other methods.

6.8 Discussion of the Heat Transfer Results

Heat transfer from the blade surfaces in the internally heated blade is critically dependent on the nature of the boundary layer, the size of the entrained droplets, the laminarisation, the degree of supersaturation and the expansion rate. The net rate of heat transfer along the flow path may increase or decrease depending on whether condensation or evaporation occurs within the boundary layer. As long as the vapour static temperature is higher than the local saturation temperature, evaporation is the dominant phenomenon, otherwise the condensation is dominant and the latent heat will be liberated into the flow.

The effect of laminarisation on the rate of heat transfer in the turbulent flow can be seen in Figures 6.3 and 6.4. The maximum reduction in heat transfer may be equal to 50% at $x/c = 0.2$ along the

convex surface and to 40% at x/c = 0.4 along the concave surface. In general the reduction in heat transfer from the convex surface is higher than that from the concave surface due to higher acceleration. The droplet size has a small influence on the developing value of heat transfer correction factor (F_ℓ) with constant initial wall temperature and can be neglected (Fig. 6.3). For constant droplet size the variations of the initial wall temperature (T_{wi}) have a considerable effect on F_ℓ. It can be observed from Fig. (6.4), that a small reduction in heat transfer occurs for low T_{wi} (i.e. $T_{wi} \approx T_o$). This is a good advantage for an unheated blade, since more heat can be generated from the friction between the blade and the flow itself. If there is a significant relative velocity between the droplets and the vapour, the turbulence level may acquire a higher value than that in flow with zero relative velocity, since the droplets in the first case could be considered as trip wires to increase the turbulence, regardless of the mechanical losses. The increase of F_ℓ when the initial wall temperature drops to nearly the adiabatic temperature, was about 2 - 3%. The pattern of F_ℓ is seen to be the mirror image of the pattern of L.

The Stanton number (St) distribution was affected by the value of F_ℓ, so that St behaves the same as F_ℓ. Figure (6.5a and 6.5b) show the distribution of St for each droplet size with $t_{wi} = 85^oC$. The variation in St due to the change in the droplet size is considerable only at x/c < 0.25 from the end of the working length. The increase in droplet size gives an increase in the Stanton number. The values of St along the convex surface were less than that along the concave surface when x/c > 0.1 from the inlet to the passage, and higher at x/c < 0.1. The sudden reduction in St at x/c = 0.05 from the exit of the passage is due to a sudden increase in L (i.e. highly laminarised flow).

Figures (6.6 - 6.9a and b) illustrate the distribution of St for different droplet size (i.e. 0.01 - 1.0 μm) and the initial wall temperature t_{wi} = 80, 75, 70 and 66°C respectively. From these figures it can be seen that the droplet size has more effect on the value of St when t_{wi} was decreasing, e.g. a considerable change in St value at x/c > 0.1 from the inlet of the working length along both surfaces when t_{wi} = 66°C (Figures (6.9a and 6.9b), while this occurs at x/c > 0.25 when t_{wi} = 85°C (Figures (6.5a and 6.5b).

The accumulated heat transfer along both surfaces for the whole range of droplet size and different initial wall temperature can be seen in Figs. 6.10 - 6.14; the different distribution of heat in each figure has shown that the droplet size is a significant variable.

The effect of the droplet size was significant along the second half of the working length. For the same droplet size and wall temperature the extent of heat transfer from the concave surface was approximately equal to that from the convex surface, since the laminarisation has more effect along the convex surface. Therefore the total heat from the blade surfaces could be calculated by multiplying the total heat from the concave surface by two.

The maximum heat transfer from one side of the blade was found about 1.0 kW per one metre of the blade length, when the droplet size was maximum (d = 1.0 μm) and t_{wi} = 85°C (Fig. 6.10). The minimum heat was about 0.2 kW per one metre of the blade length, when the droplet size was minimum (d = 0.01 μm) and t_{wi} = 66°C (Fig. 6.14). The predicting of maximum heat will be used in Chapter 8 for calculating the fuel cost.

CHAPTER 7

THE PARAMETERS AND DEVELOPMENT OF THE MATHEMATICAL MODEL

7.1 INTRODUCTION

This Chapter presents the mathematical model which describes the behaviour of the fog droplet inside the boundary layer. The possible size distribution of the generated droplets from the nucleation process is given in section 7.2. The analysis of the kinds of interaction between the droplets is considered in section 7.3. Sections 7.4 and 7.5 involve the parameters of the theoretical model. These parameters are the transfer of heat and mass between the two phases, diffusion and thermophoresis. The theoretical results are presented in section 7.8. A very large number of figures have been produced; it was considered that there were too many to be introduced in this thesis, therefore

1. A selected number of plots have been considered which are adequate to give a clear picture of the situation concerning the droplets in the flow.
2. The sizes of some plots were reduced to a quarter without losing the detail of the curves.

Comparisons of some theoretical results with the available experimental data were made in order to verify the theoretical model (section 7.10). The theoretical model is based on a few acceptable assumptions. These are:

1. There is no second nucleation inside the passage.
2. The entrained droplets are monodisperse in size.
3. There is no rotation of the droplet.

4. The heat capacity of the droplet can be neglected.

5. The eddy diffusivity of the droplet is equal to the eddy viscosity of the vapour.

6. There is no slip between the droplet and the vapour.

7. The density of the liquid phase is constant and it is equal to 1000 kg/m^3.

7.2 DISTRIBUTION OF DROPLET SIZE

In the present work it is assumed that nucleation occurs shortly before entry to the passage and therefore the droplet distribution is size-monodisperse at entry. In the general case spontaneous nucleation may take place anywhere along the blade passage. If so, the distribution of the droplet size at the nucleation position is not monodisperse. Small droplets will form in free stream flow whilst large droplets will form inside the boundary layer, due to the different value of the expansion rate ($\dot{p}$) inside and outside the boundary layer. It is well known that the size of the new droplet depends on the expansion rate and the nucleation onset pressure. At the nucleation point the onset pressure can be assumed constant along the normal axis (y), therefore the size of the droplet is mainly dependent on the value of the expansion rate ($\dot{p}$). For a given onset pressure, the expansion rate can be defined inside and outside the boundary layer as follows

(a) Outside the boundary layer:

The general definition of $\dot{p}$ is

$$\dot{p} = -\frac{1}{p}\frac{dp}{dt} = -\frac{1}{p}\frac{dp}{dx}\frac{dx}{dt} \qquad (7.1)$$

where $\frac{dx}{dt} = U_\infty$ (free stream velocity).

From the Navier-Stokes equation, $\frac{dp}{dx}$ can be written in terms of U_∞

$$\frac{dp}{dx} = - \rho U_\infty \frac{dU_\infty}{dx} \tag{7.2}$$

Therefore, equation (7.1) can be rewritten in the form

$$\dot{p} = \frac{\rho}{p} U_\infty^2 \frac{dU_\infty}{dx} \tag{7.3}$$

Equation (7.3) shows that, at any position x along the passage ρ, p, U_∞ and $\frac{dU_\infty}{dx}$ are constant. Therefore $\dot{p}$ is constant at a given x, and thus the new droplets will be monodisperse in size.

(b) Inside the boundary layer

Within the boundary layer the term $\frac{dx}{dt}$ in equation (7.1) is a function of the distance from the blade surface (y),

$$\frac{dx}{dt} = u(y)$$

$\frac{dp}{dx}$ is determined from equation (7.2).

Therefore equation (7.1) becomes

$$\dot{p} = \frac{\rho}{p} u(y) U_\infty \frac{dU_\infty}{dx}$$

At a given (x), ρ, p, U_∞ and $\frac{dU_\infty}{dx}$ are constant, and thus $\dot{p}$ is only a function of u(y)

$$\dot{p}(y) = (C)_x \frac{u(y)}{U_\infty} \tag{7.4}$$

where $(C)_x = \frac{\rho}{p} U_\infty^2 \frac{dU_\infty}{dx} = \dot{p}_\infty$

Substituting $(C)_x$ in equation (7.4) gives,

$$\frac{\dot{p}(y)}{\dot{p}_\infty} = \frac{u(y)}{U_\infty} \tag{7.5}$$

From the 1/7th power law $\frac{\dot{p}(y)}{\dot{p}_\infty}$ can be written in terms of y and δ

$$\frac{\dot{p}(y)}{\dot{p}_\infty} = \left(\frac{y}{\delta}\right)^{1/7} \tag{7.6}$$

where δ is the boundary layer thickness.

It can be concluded that

1. The distribution of $\dot{p}$ inside the boundary layer is the same as that of the velocity.

2. Different droplet sizes may be produced through the boundary layer, large droplets near the surface and small droplets at the edge of the boundary layer.

3. The significance of the dispersion of the droplet size depends on the thickness of the boundary layer. The dispersion is considered only for a thick boundary layer, and neglected for a thin boundary layer.

4. Statistical analysis must be used for finding a mass-median diameter of the droplets, when the dispersion in droplet size is significant.

In the present study the dispersion in the size of the droplet can be neglected, since the nucleation occurred before the entry to the passage. It can also be neglected when the nucleation occurs at the entry, where the thickness of the boundary layer is very small relative to the height of the passage. If the nucleation takes place after the throat, the dispersion in droplet size must be taken into consideration. In spite of the probability of dispersion in droplet size, the range of droplet size

was found to lie within 0.01 - 1.0 μm.

7.3 ANALYSIS OF THE BEHAVIOUR OF FOG DROPLETS IN THE BOUNDARY LAYER

The motion of the fog droplets inside the boundary layer is a function of the physical and geometrical properties of the droplets, the nature of the flow and the geometry of the blade passage. The mechanisms which govern the droplet motion are influenced by the droplet size and the nature of the flow. The fog droplet in the boundary layer is subjected to the following effects which act concurrently.

1. Mutual collision, bouncing or mutual fracture.
2. Flow-wise drift by vapour propulsion.
3. Phase change.
4. Reaction, due to uneven mass transfer.
5. Brownian diffusion.
6. Diffusive deposition; in the laminar and turbulent flows.
7. Thermophoresis.
8. Adhesion forces.
9. Eddy diffusion.
10. Body and electrical forces.
11. Eddy impaction.
12. Inertia impaction.
13. Sedimentation.

Effects of 2, 4, 10, 11, 12 and 13 are negligible since the size of the droplets studied in this Chapter are submicron. These effects are examined in the literature survey (Chapter 2). Wall roughness effects

are not included in this study.

7.3.1 Mutual collision, bouncing and mutual fraction

Interaction between fog droplets is due to the eddies of the turbulence, Brownian motion and the inter-droplet spacings. The space between the droplets is a function of droplet size and the wetness fraction. In low pressure steam turbines the inter-droplet spacing may be ten times larger than that in high pressure turbines for the same wetness fraction. The three effects on the droplet's interaction can be stated as follows:

(a) Configuration of the droplets inside the boundary layer

The distribution of the droplets in the flow is mostly random. For the sake of analysis, however, it is necessary to assume that the spacing complies with a specific configuration. In the present work a proposal (5) due to Ryley was employed. He considered that each droplet could be located at the intersection points of a rhombohedral lattice. Therefore the local population density can be calculated, provided the droplets are monodisperse in size. The expression to define the lattice ratio in terms of interglobular distance and droplet size for low pressure was derived by Ryley:

$$R = \frac{D}{d} = 9.0 \left[\frac{x\, v_g}{1-x} \right]^{1/3} \qquad (7.7)$$

The expression is applicable to the flow with fog droplets only where no slip occurs between the liquid and the vapour. The full analysis for the derivation of equation (7.7) is presented in Appendix (7A).

The general value of R was found to be in the range 50 - 100, which means the relative distance between the droplets is large. The evaporation has a considerable effect on increasing the value of R, since

it reduces the wetness fraction and the droplet size. The local value of R sometimes deviates from the mean value due to a reduction in the droplet size.

Figures 7.1 - 7.3 show the local distribution of R inside the boundary layer when the initial wall temperature (t_{wi}) is maximum ($85^{o}C$). It can be noticed from the results at $y > 100$ μm, that when the evaporation or the condensation are not considerable, the local R is nearly constant along the concave and convex surfaces. The rapid increase in R for droplets near to the blade surface is due to a high evaporation rate as shown in Table 7.1.

TABLE 7.1 - THE CONDITIONS OF THE MAXIMUM LATTICE RATIO (R)

Figure number	d_i μm	y μm	surface	R_{max}	$(\frac{x}{c})$ from the LE (completely evap.)
7.1	1.0	50.0	concave	600	0.45
7.2	0.5	50.0	concave	120	0.35
7.2	0.5	50.0	convex	4000	0.23
7.2	0.5	100.0	concave	1200	0.47
7.3	0.1	100.0	concave	—	0.33
7.3	0.1	100.0	convex	12000	0.15
7.3	0.1	280.0	concave	200	0.35

Table 7.1 shows that evaporation dramatically increases the inter-spacing distance between the droplets to about 12,000 times the droplet diameter.

If the wall temperature is reduced to about the adiabatic temperature (t_{wi} = 66°C) the evaporation depends on the energy dissipation due to friction. Figures 7.4 - 7.6 shows the distribution of the lattice ratio when t_{wi} is equal to 66°C. For a droplet size equal to 1.0 μm, the phase change is not considerable when the droplets are at a distance $y > 50$ μm from the blade surface and R has a small range (60 - 80), as shown in Figure 7.4. The range of R is always bigger for droplets on the concave surface than that on the convex surface. Figure 7.5 illustrates an increase in the range of R along both surfaces when d_i equal to 0.5 μm. Figure 7.6 shows that there is a complete evaporation of the droplets at different locations inside the boundary layer, and R_{max} may exceed 20,000. From Figures 7.4 - 7.6 the history of the effect of droplet size can be seen as the lattice ratio increases due to decreasing the droplet size. For the same initial droplet size, the wall temperature has no effect on the lattice ratio when the droplets are far from the surface, as shown by a comparison between Figures 7.1 and 7.4.

(b) Droplet interaction due to Brownian motion

The motion of a particle due to a large number of collisions with the vapour molecules is called the thermal or Brownian motion. It was recognised by Fuchs (126) that the particle acquires a velocity perpendicular to its original direction due to the bombarding vapour molecules. The distance along which the droplet moves before changing its direction is called the apparent mean free path and defined by Fuchs as

$$\ell_B = \bar{G}\tau_r \qquad (7.8)$$

where $\bar{G}$ is Brownian mean velocity and can be expressed in terms of the temperature and the droplet mass thus

$$\bar{G} = \sqrt{\frac{8\overline{G^2}}{3}} \qquad (7.9)$$

and $\overline{G^2} = \frac{3K_B T_f}{m_p}$ where $m_p = \frac{4}{3}\pi r^3 \rho_f$

Equation (7.9) can be rewritten in the form

$$\bar{G} = \sqrt{\frac{6K_B T_f}{\pi r^3 \rho_f}} \tag{7.10}$$

τ_r in equation (7.8) is the relaxation time; the time during which the droplet travels a distance equal to the apparent mean free path. τ_r can be defined by

$$\tau_r = \frac{m_p}{6\pi\mu r} = \frac{2r^2\rho_f}{9\mu} \tag{7.11}$$

Equation (7.10) is valid only for fog droplets in a molecular size range.

The equation of droplet mean free path can be rewritten by substituting equations (7.10) and (7.11) into equation (7.8),

$$\ell_B = \frac{1}{\mu}\sqrt{\frac{8rK_B T_f \rho_f}{27\pi}}$$

where $K_B = 1.381 \times 10^{-23}$ J/K

$\rho_f = 1000.0$ kg/m^3

Substituting the value of K_B into the above equation gives

$$\ell_B = \frac{3.6 \times 10^{-11}}{\mu}\sqrt{rT_f} \tag{7.12}$$

The saturation temperature has a small effect on the droplet mean free path, since the difference between the square root of the maximum and minimum temperature is less than 2.5%. Therefore ℓ_B is mainly a function of droplet size. The droplet size range of interest in this work is

0.01 - 1.0 μm. It can be shown that the value of ℓ_B for a droplet which has a diameter of 1.0 μm is nearly ten times that for a droplet which has a diameter of 0.01 μm, thus ℓ_B can be written in the term of r only,

$$\ell_B \propto \sqrt{r} \tag{7.13}$$

Figures 7.7 - 7.9 show the apparent mean free path distribution along the concave and convex surfaces with initial wall temperature equal to 85°C. It can be seen that there is a sharp drop in the value of ℓ_B for droplets close to the blade surfaces and ℓ_B reduces very slowly or sometimes increases due to condensation for droplets (1.0 μm) at a distance $y > 100$ μm from the blade surfaces (Fig. 7.7). For droplet sizes less than 0.5 μm in diameter the droplets at $y = 100$ μm along the concave surface and $y < 100$ μm along the convex surface do not survive due to evaporation and their sizes are comparable with the molecular size (Fig. 7.8). Figures 7.10 - 7.12 display the variation of ℓ_B along x/c for droplet diameters 1.0, 0.5 and 0.1 μm and the initial wall temperature nearly equal to the adiabatic temperature. Fig. 7.10 shows that the value of ℓ_B is nearly constant along y, when condensation takes place or when the evaporation is very slow. However, when the droplet size is reduced or the surface of heat and mass transfer is increased, the evaporation of the droplet near to the surface is significant even when the wall temperature is close to the adiabatic temperature, (Figs. 7.11 and 7.12).

The local ratio of droplet mean free path to the droplet diameter is nearly constant for the surviving droplets along both surfaces regardless of the initial wall temperature and the location of the droplet inside the boundary layer, as shown in Figs. 7.13 - 7.18.

The relaxation time is conceived to be the time taken for the droplet to travel a distance equal to ℓ_B (and it may change its direction).

The number of movements of the droplet within a certain distance depends on,

(1) the relaxation time of the droplet,

(2) the length of the interval distance,

(3) the velocity of the steam.

The maximum length of the interval distance is 4 mm and the minimum velocity is 85 m/sec, therefore the maximum time for the droplet to travel Δx_{max} is 47 μs. The relaxation time (equation (7.11)) for survival of a droplet ($d < 0.1$ μm) is about 0.06 μs. Thus, the maximum number of droplet movements N_m can be calculated by

$$N_m = \frac{t}{\tau_r} = 783$$

The least probable movement of the droplet can be shown by imagining two similar droplets in the same location from the blade surfaces moving toward each other, as seen in the figure below.

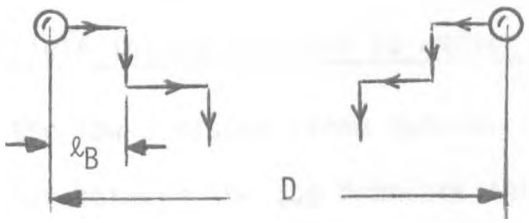

Each droplet will share half the moving distance, i.e. it is the same situation as assuming one of the droplets to be fixed and the other moving towards it in one direction, thus

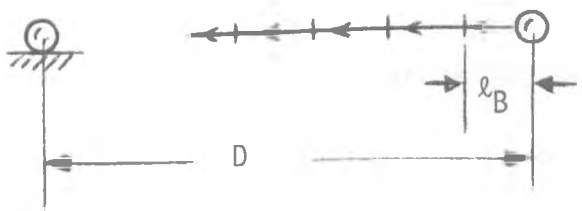

Therefore if $N_m > \frac{D}{\ell_B}$, collision will occur and there is insufficient information to determine whether agglomeration or bouncing will take place. The possibility of interaction between the droplets does not exist when the droplet size is greater than 0.1 (Figs. 7.19, 7.20, 7.22 and 7.23). It is perhaps possible along the first 30% of the working length when the droplet size is less than or equal to 0.1 μm, and even if agglomeration does occur the resulting particle will be harmless to the rotor blade since it has no chance to deposit on the nozzle blade surfaces, (Figs. 7.21 and 7.24). Figures 7.19 - 7.24 show that, for surviving droplets, the value of (D/ℓ_B) is nearly constant for each droplet size regardless of the temperature of the blade surface.

Recently, Kantola (127) has found experimentally that agglomeration of the droplet occurred immediately after nucleation onset in his shock tube; in the present situation, however, there is no chance of interaction between the droplets, but there is such a probability when the droplets are very fine for a short distance from the entry to the passage.

(c) Droplets interaction due to eddies of turbulence

In the low pressure steam turbine fixed blade passage, the chance of interaction between the fog droplets can be neglected for the following reasons:

1. The intensity of the turbulence is assumed to be 2.0 - 2.5% and is too low to produce significant interaction.
2. The laminarisation reduces the turbulence to a very low level along the blade passage.
3. The initial wetness fraction is 3%, and is very low.

4. The expansion rate near the throat of the passage was sufficiently high as to cause a further reduction in the population density of the droplets, since it is inversely proportional to the specific volume of the flow.

5. Crane (128) found very little increase in the droplet size due to coalescence for a low pressure flow with 4% wetness. This small increase in droplet size is probably due to condensation rather than coalescence. He did not mention the thermodynamic conditions of the flow. He also found that there was no coalescence between droplets in flow with turbulence levels less than 2%.

According to Crane's information there is no chance for coalescence to take place in the present situation. However, other types of intereaction may occur, such as bouncing. Chapters 5 and 6 showed that the flow is laminarised along more than 50% of the working length of the passage, and it is therefore reasonable to treat the flow as being laminar. Therefore the effect of turbulence is reduced and the principal cause of collisions between the droplets is that of Brownian motion. The analysis of this situation has been presented in point (b).

It can be concluded from Kantola (127) and Crane (128) that there is no possibility of obtaining mutual fracture between the droplets due to interaction since there was no recording of a reduction in the droplet size. An increasing or constant droplet size was observed in their findings. A mutual fracture might occur between large droplets due to a reduction in the surface tension influence with the increasing of the droplet diameter. However for very small droplets ($Kn > 4$) there is no experimental information (according to the author's knowledge) about the surface tension, since it is a continuum phenomenon whilst the treatment of the behaviour of the

droplets should be within a molecular region. Therefore, the value of the inter-molecular force inside the droplet will determine whether bouncing, coalescence or mutual fracture will occur. The inter-molecular force inside a very small droplet (Kn > 4) is probably decreased by decreasing the size of the droplet since the number of molecules are less. Thus it can be concluded that the collision between very small droplets (Kn > 4) may result with coalescence, since

(i) the cohesion force increases by decreasing the droplet size;

(ii) a reduction in the number of the droplets is associated with increase in the size of the droplet, has been recorded by Kantola (127).

7.3.2 Phase change

On unheated L.P. steam turbine fixed blades, the phase change is that of condensation and the process may be divided into three regions:

1. Expansion of dry steam and increased supercooling.
2. Spontaneous condensation at maximum supercooling.
3. Droplet growth and disappearance or partial disappearance of supercooling. It proceeds by depositing some of these droplets on the blade surfaces.

The first region cannot be changed or modified. The second region is too complicated to control. Whilst designers can calculate the position of maximum supercooling or the nucleation point inside the nozzle for certain turbine conditions, they cannot easily allow for the case when the turbine is run at partial load. Therefore the third region is the main subject in the present work. This process can be controlled by using heated blades. The nature of the phase change mainly depends on the droplet size and the temperature difference between the vapour and the liquid.

When the temperature of the blade surface reduces below the local saturation temperature a very rapid growth can be expected in the size of the fog droplets which are in the vicinity of the surface. Accordingly, this may lead to large droplets with diameters greater than 2.0 μm. On the contrary, when the temperature of the blade surface is increased above the local saturation temperature, high evaporation will occur. The survival droplet from evaporation may have diameters below 0.01 μm.

In this work a wide range of droplet sizes can be obtained and it depends on the degree of heating and flow conditions of the wet steam. Therefore, it is necessary that the phase change between the large droplets and the surrounding vapour is to be considered as well as that of the small droplets.

(a) Phase change of large droplets

The growth or evaporation of a droplet with $r > \ell'$ is determined on the basis of the amount of heat removed from or added to it. There are four types of heat transfer between the two phases and can be listed as:

1. Heat conduction within the droplet. This is very rapid for the expected sizes in the present work, which are less than 3.0 μm.
2. Heat capacity of the droplet which can be neglected for such sizes of droplets.
3. Heat conduction from or to the surface of the droplet, assuming there is no relative movement between the vapour and the droplets.
4. Latent heat due to mass transfer.

The balance between the heat conduction (point 3) which is in the form

$$\dot{Q} = 4\pi r K_{\ell} (T_{\ell} - T_g(r)) \qquad (7.14)$$

and latent heat (point 4) which is in the form

$$\dot{Q} = h_{fg}\, d\dot{m} \tag{7.15}$$

where $$d\dot{m} = 4\pi\rho_{\ell}\, r^2 \frac{dr}{dt} \tag{7.16}$$

gives the rate of growth or evaporation of large droplets (equation 2.9) as following,

$$\frac{dr^2}{dt} = \frac{2K_{\ell}\,(T_{\ell} - T_g(r))}{h_{fg}\,\rho_{\ell}} \tag{7.17}$$

Whether droplet growth or evaporation occurs is dependent on the vapour temperature T_g being lower or higher than the droplet temperature. It can be seen from equation (7.17) that the rate of change in the droplet radius is proportional to $\sqrt{t}$ and not t. It should also be borne in mind that the heat transfer inside the droplet has been neglected.

(b) Phase change of small droplet

When the droplet has a radius (r) less than the mean free path (ℓ'), the phase change between the droplet and the surrounding steam is evaluated on the basis of the molecular kinetic theory. Therefore the transfer rate of heat or momentum must be expressed as the sum of the amounts of energy or momentum transferred individually by the molecules which collide with the droplet. Similarly, the mass transfer rate is the net difference in the total mass of vapour molecules condensing on and evaporating from the droplet. The net transfer of mass can be formulated using the kinetic theory of gases as:

$$\frac{dm}{dt} = r^2\, c \sqrt{\frac{8\pi}{R}} \left[\frac{p_g}{\sqrt{T_g(r)}} - \frac{p(T_{\ell}, r)}{\sqrt{T_{\ell}}} \right] \tag{7.18}$$

where c = coefficient of condensation or evaporation and can be assumed to be unity (c = 1.0).

Equation (7.18) can be used for a very wide range of Knudsen number, when a correction factor is included. In the present work, the correction factor $\frac{8\ Kn}{3(1 + 2.7\ Kn)}$ used by Young (116) was adopted, and thus equation (7.18) becomes

$$\frac{dm}{dt} = \frac{8\ r^2\ Kn}{3(1 + 2.7\ Kn)} \sqrt{\frac{8\pi}{R}} \left[\frac{p_g}{\sqrt{T_g(r)}} - \frac{p(T_\ell, r)}{\sqrt{T_\ell}} \right] \tag{7.19}$$

The full derivation of equation (7.19) is presented in Appendix 7B.

To find the rate of droplet growth or evaporation, the mass rate can be written in the term of r and $\frac{dr}{dt}$, equation (7.16),

$$m = \frac{4}{3} \pi \rho_\ell\ r^3$$

$$\frac{dm}{dt} = 4\pi \rho_\ell\ r^2 \frac{dr}{dt} \tag{7.20}$$

If equation (7.20) is substituted into equation (7.19) the variation in the droplet size due to a temperature difference between the droplet and the vapour can be determined as,

$$\frac{dr}{dt} = \sqrt{\frac{32}{9R\pi}} \frac{Kn}{\rho_\ell(1 + 2.7\ Kn)} \left[\frac{p_g}{\sqrt{T_g(r)}} - \frac{p(T_\ell, r)}{\sqrt{T_\ell}} \right] \tag{7.21}$$

or

$$\frac{dr}{dx} = 4.952 \frac{Kn}{\bar{u}(1 + 2.7\ Kn)} \left[\frac{p_g}{\sqrt{T_g(r)}} - \frac{p(T_\ell, r)}{\sqrt{T_\ell}} \right] \tag{7.22}$$

where ρ_ℓ = 1000 kg/m^3

R = 461.5 J/kg K

It is assumed that the vapour pressure p_g is equal to the droplet pressure ($p(T_\ell, r)$ since there is no information (according to the author's knowledge), about the increase in droplet pressure due to the surface tension of the fog droplet. The droplet temperature is assumed to be equal to the saturation temperature at the local pressure ($T_s(p)$). Therefore equation (7.22) becomes

$$\frac{dr}{dx} = 4.952 \frac{Kn\ p_s}{\bar{u}(1 + 2.7\ Kn)} \left[\frac{1}{\sqrt{T_g(r)}} - \frac{1}{\sqrt{T_s}} \right] \qquad (7.23)$$

where p_s = the saturation pressure in bar.

The main difference between equation (7.17) and (7.21) is that the latter describes the change in the droplet radius, whilst the former describes the change in the square of the radius. The rate of increase or decrease in the size of a small droplet is higher than that of large droplets, since it is proportional to time t for the small droplet, whilst for the large droplet it is proportional to the square root of time ($\sqrt{t}$).

The rate of heat transfer from or to a large or small droplet can be determined from:

$$\dot{Q} = (h_{fg})_r \frac{dm}{dt} \qquad (7.24)$$

where $(h_{fg})_r$ is the latent heat of vapourisation from or to the droplet.

$(h_{fg})_r = h_{fg} + \frac{4\sigma_r}{3\rho_f r}$ where $\frac{4\sigma_r}{3\rho_f r}$ = capillary term used with very small droplets only,

or

$$(h_{fg})_r = h_{fg}\left(1 + \frac{\frac{4\sigma_r}{3\rho_f r}}{h_{fg}}\right) \qquad (7.25)$$

σ_r is the surface tension of the droplet. For a very small droplet the surface tension lies below its bulk value. The formula for the surface tension of liquid as a function of radius has been obtained by Annis et al (129), as

$$\sigma_r = \sigma_\infty \left[\frac{1}{1 + \frac{2J}{r}}\right] \qquad (7.26)$$

where J = constant for a given liquid, and it is approximately equal to the inter-molecular spacing ($J \approx 1 \times 10^{-10}$ m),

σ_∞ = surface tension of plane interface.

In the present situation, the maximum value of the term $[(4\sigma_r/3\rho_\ell r)/h_{fg}]$ was calculated to be 1×10^{-4}, so that it can be neglected without significantly affecting the accuracy of calculating $\dot{Q}$. Therefore, the latent heat of vapourisation from and to a droplet ($(h_{fg})_r$) is equal to that from and to the plane surface (h_{fg}), and equation (7.25) becomes,

$$(h_{fg})_r = h_{fg} \qquad (7.26a)$$

and equation (7.24) becomes

$$\dot{Q} = h_{fg}\frac{dm}{dt} \qquad (7.27)$$

where $\frac{dm}{dt}$ can be calculated from equation (7.20) and h_{fg} can be found from steam tables.

The change in the wetness fraction can be calculated from the rate of change of the droplet size and the flow rate of the vapour,

$$\Delta y = \frac{4\pi \rho_\ell N_p \Delta r^3}{\rho_g A \bar{u}} \qquad (7.28)$$

where N_p = number of droplets per unit length of the blade

A = cross section area of the blade passage

$\bar{u}$ = average velocity of the flow.

The results will be presented and discussed later in this Chapter.

7.3.3 Brownian motion

The movement of small droplets ($d \lesssim 1.0$ μm) will be influenced by impacting vapour molecules and thus maintained in a state of continuous random motion. The effect of Brownian motion diminishes when the droplet size increases and can be neglected for droplets with Knudsen number (Kn) less than 0.01. In the absence of turbulence (in laminar flow) and with the uniform concentration the movement of the fog droplet is mainly affected by Brownian motion.

Thermal (Brownian) motion of droplets suspended in a vapour is expressed by the following equations derived by Einstein,

$$\overline{B^2} = 2D(r)t \qquad (7.29)$$

$$D(r) = \frac{k_B T_s(p)}{f} \qquad (7.30)$$

where $D(r)$ = the diffusion coefficient of the droplet

T_s = the absolute droplet temperature

f = the drag at unit velocity, or the reciprocal of the droplet mobility = $\frac{6\pi r\mu}{F}$

F = the Cunningham slip factor, which is defined by many investigators. A recent expression for F was given by Annis et al (129) in the form,

$$F = 1 + Kn\left[\,1.558 + 0.173 \exp\left(\frac{-0.769}{Kn}\right)\,\right] \qquad (7.31)$$

In the turbulent flow the diffusion coefficient was found to be very small, compared with the eddy diffusivity ($D(r) << \varepsilon_p$), therefore $D(r)$ can be neglected outside the laminar sub-layer without affecting the accuracy of the calculations.

7.3.4 Thermophoretic force

The thermophoresis phenomenon exists even when the blade surface is adiabatic since temperature recovery occurs at the surface promoting a local temperature gradient along the vertical axis. In adiabatic stagnant flow, the thermophoretic force can be neglected. The magnitude of the thermophoretic force increases with increasing temperature gradient and droplet size. Therefore the benefits of heating the blade surface are:

1. Reducing the droplet size or reducing the rate of growth of the droplet.
2. Increasing the thermophoretic force to propel the droplet away from the surface and thus discourage deposition.

The calculation of the thermophoretic force and velocity can be achieved by using an empirical formula which was derived by Talbot et al (79).

(1) The thermophoretic force, using Brock's original formula, is

$$F_T(r) = \frac{12\pi\mu\nu r C_s \left[\frac{K_g}{K_p} + 2C_t\, Kn\,\right]\left[\frac{(\nabla T)_x}{\bar{T}}\right]}{\left[\,1 + 6\, C_m Kn\,\right]\left[\,1 + 2\,\frac{K_g}{K_p} + 4\, C_t Kn\,\right]} \qquad (7.32)$$

(2) The thermophoretic velocity is

$$V_T(r) = \frac{2C_s\nu \left[\frac{K_g}{K_p} + 2C_t Kn\right]\left[1 + 2\,Kn\,(A + B\,e^{(-2CKn)})\right]\left[\frac{(\nabla T)_x}{\bar{T}}\right]}{\left[1 + 6\,C_m Kn\right]\left[1 + 2\frac{K_g}{K_p} + 4\,C_t Kn\right]} \qquad (7.33)$$

where C_s, C_t, C_m, A, B and C are constants whose values are 1.14, 2.18, 1.14, 1.2, 0.41 and 0.88 respectively.

Substituting the value of the constants in equation (7.32) and (7.33), gives:

1. Thermophoretic force

$$F_T(r) = \frac{43\,\mu\nu r \left[\frac{K_g}{K_p} + 4.36\,Kn\right]\frac{\left(\frac{dT}{dy}\right)_x}{\bar{T}}}{\left[1 + 6.84\,Kn\right]\left[1 + 2\frac{K_g}{K_p} + 8.72\,Kn\right]} \qquad (7.34)$$

2. Thermophoretic velocity

$$V_T(r) = \frac{2.28\nu \left[\frac{K_g}{K_p} + 4.36\,Kn\right]\left[1 + 2\,Kn\,(1.2 + 0.41\,e^{1.76\,Kn})\right]\frac{\left(\frac{dT}{dy}\right)_x}{\bar{T}}}{\left[1 + 6.84\,Kn\right]\left[1 + 2\frac{K_g}{K_p} + 8.72\,Kn\right]} \qquad (7.35)$$

where $\bar{T}$ = the average temperature at x.

Equations (7.34) and (7.35) are valid for the entire range of Knudsen number ($0 \lesssim Kn \lesssim \infty$). It can be observed from the above two equations that $F_T(r)$ and $V_T(r)$ are not sensitive to the variation of K_g/K_p, e.g. the increasing of K_g/K_p from 0.01 to 1.0 gives an increase in V_T of less than 2%. Reducing the droplet size by evaporation has two opposing effects, firstly

to propel the droplets away from the surface by thermophoresis and secondly to increase the droplet motion towards the surface by Brownian force. Therefore the net effect depends on the temperature profile and the nature of the flow.

7.3.5 Diffusive deposition

The deposition of fog droplets (0.01 - 1.0 μm) is dependent on many factors:

1. The nature of the flow; laminar or turbulent.
2. The distribution of the droplet concentration along the vertical axis (y-axis).
3. The temperature of the blade surface and the temperature and velocity profile inside the boundary layer.
4. The geometry of the blade passage.
5. The size and the temperature of the droplets.

The mechanism of droplet deposition is determined by the nature of the boundary layer, i.e. laminar or turbulent, therefore, there are two situations to consider:

(a) Diffusive deposition in laminar flow

It is believed that in the last stage of a steam turbine the friction is sufficient to produce a thermophoretic force on a small droplet even with an unheated blade. Therefore an accurate formula for calculating the rate of mass transfer must include the thermophoresis term. This can be compared in magnitude with other terms in order to determine the significance of the thermophoresis effect. The net droplet diffusion is the difference between the diffusion (due to concentration

gradient and Brownian motion) and the thermophoretic diffusion, this can be formulated as:

$$N = D(r) \frac{dc}{dy} + V_T(r)c \tag{7.36}$$

where $D(r) \frac{dc}{dy}$ = the mass transfer due to concentration gradient and Brownian diffusion (-ve in y direction),

$V_T(r)c$ = the mass transfer due to thermophoresis (-ve in y direction),

$\frac{dc}{dy}$ = the concentration gradient which can be determined by the 1/7th power law (+ve in y direction).

Equation (7.36) may be integrated with the following boundary conditions,

$c = 0$ at $y = 0$

$c = c_\infty$ at $y > \delta_c$

where δ_c = the concentration boundary layer thickness and can be taken as equal to that of the velocity boundary layer (δ). The solution of equation (7.36), therefore, can be written as

$$V_{net} = \frac{V_T(r)}{1 - \exp\left(-\frac{V_T(r)\,\delta}{D}\right)} \tag{7.37}$$

where V_{net} = the residual velocity of the droplet (-ve in y direction).

The details for deriving equation (7.37) can be found in Appendix 7C.

In the present study, the effective working length of the laminar flow is very short and may be less than 6% of the total length along the convex surface. The flow is entirely turbulent inside the working length of the passage. Therefore, the laminar flow can be neglected and the

flow inside the passage is considered to be turbulent only.

(b) Diffusive deposition in turbulent flow

The turbulent flow was divided into two regions, laminar sublayer and turbulent. The mechanism of diffusive deposition in the sublayer is dominated by Brownian diffusion, concentration gradient and thermophoresis, whilst in the turbulent core, the eddy diffusion is the dominant effect. The diminishing of the concentration and thermophoretic effects is due to the decreasing of the gradient of the concentration $(\frac{dc}{dy})$ and the temperature $(\frac{dT}{dy})$. The mathematical form of mass transfer from the turbulent flow to the surface may be written as

$$N = (D(r) + \varepsilon_p) \frac{dc}{dy} + V_T(r)\, c \qquad (7.38)$$

where $(D(r) + \varepsilon_p) \frac{dc}{dy}$ = the mass transfer due to eddy diffusion, Brownian diffusion and concentration gradient (-ve in y direction),

ε_p = the eddy diffusivity which is equal to the eddy viscosity $(\varepsilon_M) = \varepsilon$

The eddy diffusivity can be found by using the Van Driest model (130). The final expression from the integration of equation (7.38) is

$$V_{net} = \frac{V_T(r)}{1 - \exp\left(- V_T(r) \int_0^{\infty} \frac{dy}{\varepsilon + D}\right)} \qquad (7.39)$$

and can be solved numerically. Greater detail may be found in Appendix 7C.

7.4 The Numerical Method

In order to formulate the problem in mathematical terms a step-by-step method was used (131) in the present work. A number of assumptions were made to simplify the problem.

1. The effect of the blade curvature relative to the boundary layer thickness was neglected.
2. Nucleation occurred at the entry to the passage therefore the size of the generated droplets is initially monodispersed.
3. The entire flow inside the passage is turbulent, despite that for a very short distance from the entry, the flow was laminar.

In general the local conditions will vary with reference to deposition, phase change and droplet concentration both in the flow-wise (x) and the normal (y) directions. During the time that the droplet travels along the blade passage, there are many changes in the droplet properties along both the x and y axes and also in its behaviour such that changing in size, velocity, temperature, diffusivity, thermophoretic force and turbulence.

7.4.1 Choice of the cell sizes

The boundary layer was divided axially and vertically into a grid of rectangular cells stationary in space and parallel to the flow plane. Ryley and Al-Azzawi (131) divided the boundary layer into cells having the same size which is 4 mm flow-wise (x-direction), 5 μm normal to the flow and unity in the direction of blade length. In the present work, the flow-wise step was variable, i.e. it was decreasing along the passage, and it was very small at the throat (a point of rapid change in the dynamic and thermodynamic properties of the droplets and the associated

vapour (see section 5.5 for calculating the length of the flow-wise steps (Δx)). The width and the height of the cells was kept the same as in the previous work (5 μm and unity respectively). Figure 7.25 shows the boundary layer cells.

7.4.2 The analytical procedure

It is not practicable to represent each droplet by a cell, even if the size of the droplet is the maximum (1.0 μm). Therefore to simplify the problem, a set of droplets is assumed to have common physical and geometric properties and to populate a cell. The droplets within a given cell are at all times monodisperse in size, move as set and are subject to the same changes. The number of droplets in each cell in the first column can be determined from:

$$N_p(i,1) = \frac{y(i,1)\ A_C\ (i,1)}{\frac{4}{3}\ \pi\ \rho_f\ r^3(i,1)\ v(i,1)} + \left[N_C\ (i+1,1) - N_C\ (i-1,1) \right] \qquad (7.40)$$

where y = the initial wetness fraction = 0.03 kg_f/kg_s

A_C = the volume of the cell per unit of blade length

$= 5 \times 10^{-6}\ \Delta x(i,j)\ m^3$/unit length of the blade length

ρ_f = the density of the water = 1000 kg/m^3

v = the specific volume of the wet steam

r_i = the initial droplet radius in metres

N_C = the number of the droplets transferred into/from the cell due to diffusion and thermophoresis

Substituting $y(i,1)$, $A_C(i,1)$ and ρ_f in equation (7.40) gives

$$N_p(i,1) = \frac{3.581 \times 10^{-11}\ \Delta x(i,1)}{v(i,1)\ r^3\ (i,1)} + \left[N_C(i+1,1) - N_C(i-1,1) \right] \qquad (7.41)$$

Starting from the known values of droplet size (r(i,1)), wetness fraction (y(i,1)) and the entry steam conditions, the droplet population, phase change (normally evaporation) and the net motion from diffusion and thermophoresis are calculated for each cell sequentially out to the edge of the boundary layer. At each vertical position i, the net axial concentration between adjacent cells is calculated over the time step $\Delta t(i,j) = \frac{\Delta u_{av}}{\Delta x(i,j)}$ and thus the droplet concentrations at the upstream faces of the cell (j + 1, (i, i + 1, i + 2 ....., i + n)) are obtained, therefore, the number of droplets in the cells of the remaining columns (i.e. j > 1) can be written in the form

$$N_p(i,j) = N_p(i,j-1) + [N_C(i+1,j) - N_C(i-1,j)] \qquad (7.41a)$$

The method used is:

1. Initialise droplet size (r(i,1)), pressure (p(i,1)), velocity (u(i,1)), temperature ($T_g(i,1)$), droplet temperature ($T_\ell(i,1)$), wetness fraction (y(i,1)) and the distance along the concave and convex surfaces (x(i,1)).

2. Calculate the step length $\Delta x(i,j)$ or step time $\Delta t(i,j)$.

3. Calculate the concentration in each cell in the first column (from the blade surface up to the edge of the boundary layer).

4. Calculate the rate of heat and mass transfer.

5. Calculate the new droplet size.

6. Calculate the movement of the new droplet due to diffusion and thermophoresis.

7. Calculate the new concentration of the polydispersed droplets.

8. Calculate the mass-median diameter of the droplets in each cell in the column in order to restore the monodispersion of the droplets.

9. The properties of the droplets and the steam upstream of the cells in the second column are calculated in points 1 to 8.

10. Repeat 1 - 9 for each column ($\Delta x(j)$) to the exit of the blade passage.

For the set of droplets within each cell (i,j) inside the boundary layer the following quantities are calculated: droplet size, droplet temperature, droplet velocity, droplet concentration, rate of phase change, rate of heat transfer, droplet position as a result of the coupled effects of diffusion and thermophoresis and mass-median diameter of the population comprising the original and immigrant droplets within a cell. The history of the changing group was traced until either all the droplets were evaporated or the residual population was discharged with the boundary layer leaving the nozzle. High accuracy can be achieved by subdividing the step length Δx into a number of smaller step lengths δx, and the properties of the droplet and the vapour can be found by using the linear interpolation method within the large step length Δx.

7.5 The Computer Program and the Main Equations

There are two similar programs for the concave and convex surfaces. The difference between the two programs is the location of the droplet and the steam properties. The concave computer program has covered the study of the droplet and vapour history along the entire length of the passage along the concave surface ($0.3 < x/c \leq 1.0$), while the convex program has done so for the working length along the convex surface ($0.1 < x/c \leq 0.6$). Therefore an explanation of one of the two programs suffices to describe the variation in droplet geometry and properties inside the blade passage.

The computer program (Appendix 7D) consists of many steps of calculations and it can be stated as follows:

1. Curve-fit for the calculated free stream velocity (U_∞):

In order to locate the flow properties along the concave and convex surface, the distribution of the free stream velocity should be known. The values of the properties can be defined for any point along the x-axis by using the cubic-spline method. This method is suitable for a complicated distribution of any properties along the co-ordinates. The curve of the free stream velocity was divided into twelve small pieces and applying the cubic-spline method for each piece and the whole curve without loosing the continuity of the distribution. The summation error was in order of 5×10^{-3}, and it is very small and it may be considered negligible. Special sub-routines from the computer library in the University of Liverpool were used in this stage, (the detail in Appendix 7D).

2. Calculation of the flow-wise step length

The step length was chosen according to the distribution of the properties of the flow (p, T, U, ...). The gradient of the properties was changed slowly for the first 30% of the working length and changed rapidly for the remaining length up to the exit of the passage. Therefore, the step length was stated with a long step (4 mm) and reduced up to the point of rapid change in the flow parameters, to a length of 1.0 mm. The formulae and the derivation of the method were presented in section 5.5. The equation governing the length of the step is

$$\Delta x(j) = \left[(x_e - x_i) \left\{ \frac{1 + Gp}{1 + Gp^{Mg}} \right\} \right] \; Gp^{(Ng - j)} \qquad (7.42)$$

3. The distribution of the wall temperature

The temperature of the blade surface was assumed constant (131), but actually it is variable along the concave and convex surface. The variation of the surface temperature is due to the blade geometry and the velocity distribution which has an effect on the transfer of heat from the blade. The difference between the inlet and the exit wall temperature was assumed to be 20% of the inlet wall temperature, since there is not enough room for heating steam near the trailing edge. The wall temperature was determined from this equation:

$$T_w(j) = T_o + (T_w(1) - T_o)\left[1 - \frac{j-1}{Ng}\right] \tag{7.43}$$

4. Calculation of the actual flow properties

The steam was assumed to be supersaturated. The flow diminished the instability by the transfer of heat and mass between the two phases. The flow properties were affected by the amount of relief of the supersaturation which is dependent on the droplet size (full details in section 5.5). Therefore the actual condition of the steam at any point along the working length was determined by using the following equations:

$$T_{ac}(j) = T_{is}(j) - \psi(j)\,(T_s(j) - T_{is}(j)) \tag{7.44}$$

$$y_{ac}(j) = y_{eq}(j) - \frac{Cp(j)(T_s(j) - T_{ac}(j))}{h_{fg}(j)} \tag{7.45}$$

$$(\Delta W_{sptn}(j))_{loss} = -293\,Cp(j)\left[\log_e\left(1 + \frac{T_s(j) - T_{ac}(j)}{T_s(j)}\right) + \frac{T_s(j) - T_{ac}(j)}{T_s(j)}\right] \tag{7.46}$$

5. Calculation of the heat flux from the blade surfaces

The transfer of heat from the blade surface to a dry flow was calculated first. Then the modification of the heat flux due to evaporation or condensation was done during the rest of the program. A modification to Stanton number due to high acceleration of the flow was made at this stage. The main equation used for the calculation of heat flux is as follows:

$$St(j) = \frac{0.0295\ (T_w(j) - T_\infty(j))^{0.25}\ \mu(j)^{0.2}}{\left[\int_0^x (T_w(j) - T_\infty(j))^{1.25}\ \rho(j)\ U_\infty(j)\right]^{0.2}} \qquad (7.47)$$

The denominator of equation (7.47) was integrated numerically using the trapezoidal method. The sub-routine for numerical integration was selected from the Computer Library in the University of Liverpool.

6. Boundary layer calculations

The flow was assumed adiabatic and the curvature of the blade compared with the thickness of the boundary layer was neglected. The Head entrainment method was used to calculate the boundary layer characteristics. It is simply the solution of two differential equations and three algebraic equations; these equations are:

$$\frac{\Delta\theta(j)}{\Delta x(j)} = \frac{C_f(j)}{2} - (H(j) + 2)\ \frac{\theta(j)}{U_\infty(j)}\ \frac{\Delta U_\infty(j)}{\Delta x(j)} \qquad (7.48)$$

$$\theta(j)\ \frac{\Delta H_1(j)}{\Delta x(j)} = C_E(j) - H_1(j) \left\{ \frac{C_f(j)}{2} - (H(j) + 1)\ \frac{\theta(j)}{U_\infty(j)}\ \frac{\Delta U_\infty(j)}{\Delta x(j)} \right\} \qquad (7.49)$$

$$C_E(j) = 0.0299\ (H_1(j) - 3)^{-0.6169} \qquad (7.50)$$

$$\left(\frac{C_f(j)}{C_{f_o}(j)} + 0.5\right)\left(\frac{H(j)}{H_o(j)} - 0.4\right) = 0.9 \qquad (7.51)$$

$$H(j) = 1 + 1.12\left[H_1(j) - 2 - \sqrt{(H_1(j) - 2)^2 - 3}\right]^{0.915} \qquad (7.52)$$

The five main equations were solved numerically by using Runge-Katta method. The method is well established. The velocity distribution through the boundary layer is determined by the following equations:

(i) Inside the boundary sub-layer

$$u(i,j) = u_*(j)\, y^+(i,j) \qquad (7.52a)$$

(ii) Outside the boundary sub-layer

$$u(i,j) = u_*(j)\left[2.5\ \ell n\left\{y^+(i,j) - 5.3\right\} + 5.50927\right] \qquad (7.52b)$$

7. Dividing the boundary layer into rectangular cells

The flow-wise length of the cell was determined in stage 2 and the height is set in this stage and is 5.0 μm. The cells are stationary in the flow and each one contains a group of monodisperse droplets. The temperature and the velocity of the flow inside each cell were taken as the average of the temperatures and velocities at the boundary of the cell.

8. Calculation of the rate of diminishing or growth of the droplets in each cell

The reduction or increase in the droplet size is dependent on whether the vapour temperature is higher or less than the droplet temperature (saturation temperature at local pressure). The rate of evaporation or

condensation is determined by the following differential equation,

$$\frac{\Delta r}{\Delta x}(i,j) = \frac{5.0\ Kn(i,j)\ p_s(j)}{u_{av}(i,j)\ [1 + 2.7\ Kn(i,j)]} \left[\frac{1}{\sqrt{T_{av}(i,j)}} - \frac{1}{\sqrt{T_s(j)}} \right] \qquad (7.53)$$

and the variation of the wetness fraction was determined from,

$$y(i,j) = \frac{4188.8\ N_p(i,j)\ r(i,j)^3}{\rho_g(j)\ A_C(i,j)} \qquad (7.54)$$

The rate of mass transfer from or to the cell is calculated from,

$$\frac{\Delta m}{\Delta t}(i,j) = -\frac{\Delta y}{\Delta x}(i,j)\ U_m(j)\ \rho_g(j) \qquad (7.55)$$

and the rate of heat transfer from or to the cell is calculated from,

$$\frac{\Delta Q}{\Delta t}(i,j) = \frac{\Delta m}{\Delta t}(i,j)\ h_{fg}(j) \qquad (7.56)$$

9. The probability of droplet collision

If the droplet moves a distance exceeding the inter-space distance between two droplets, then collision will take place. Therefore, the main equations are:

(a) The apparent (droplet) mean free path was defined by the expression,

$$\ell_B(i,j) = 3.609 \times 10^{-11}\ \frac{\sqrt{r(i,j)\ T_s(j)}}{\mu_g(j)} \qquad (7.57)$$

(b) The inter-space distance between the adjacent droplets was determined by,

$$D_p(i,j) = 18.0\, r(i,j) \left\{ \frac{1 - y(i,j)}{y(i,j)\, \rho_g(j)} \right\}^{1/3} \qquad (7.58)$$

Thus, if $(\frac{\ell_B}{D_p})(i,j) > 1.0$ the collision must occur, otherwise there is no collision between the droplets.

10. Calculation of diffusion coefficient and thermophoretic velocity

The size of the droplets is within the molecular and transition regions, therefore Brownian diffusivity is a considerable term. The diffusion coefficient was calculated from,

$$D(i,j) = \frac{k_B T(i,j) \{1 + Kn(i,j)(1.558 + 0.173 \exp(-0.769/Kn(i,j)))\}}{18.85\, r(i,j)\, \mu_g(j)} \qquad (7.59)$$

The thermophoretic velocity which opposes the diffusion toward the wall, and can be determined from the equation which covers the whole range of Knudsen number, can be written as

$$V_T(i,j) = \frac{2C_s\nu(\frac{K_g(j)}{K_p(j)} + 2C_t\, Kn(i,j))[1 + 2\, Kn(i,j)\{A+B \exp(\frac{C}{2Kn(i,j)})\}](\frac{\Delta T}{\Delta y}(i,j))}{(1 + 6\, C_m Kn(i,j))(1 + 2\, \frac{K_g(j)}{K_p(j)} + 4\, C_t Kn(i,j))\, T_{av}(i,j)} \qquad (7.60)$$

11. Calculation of the net diffusive velocity due to Brownian motion, eddy diffusivity and thermophoresis

When the droplets subjected to a phase change are moving, at the mean time they have a net velocity due to Brownian diffusion, eddy diffusion and thermophoresis. The group of droplets has a centre of movement

which is located on the centre of the cell. The moved distance of the centre determines the number of the droplets which move to the adjacent cells. The governing equation of the net velocity was written in the form,

$$V_{net}(i,j) = \frac{V_T(i,j)}{1 - \exp\left(-V_T(i,j) \int_0^y \frac{dy}{D(i,j)\,\varepsilon_p(i,j)}\right)} \tag{7.61}$$

The integral term was solved numerically and the eddy diffusivity (viscosity) was determined by using Van Driest model,

$$\varepsilon_M(i,j) = \ell_{mx}^2(i,j)\,\frac{\Delta u}{\Delta y}(i,j) = \varepsilon_p(i,j) \tag{7.62}$$

$$\ell_{mx}(i,j) = 0.4\,y(i)\left[1 - \frac{1}{\exp\left\{\frac{y(i)u_*(j)(30.175\,\Gamma(j) + 1)}{25\nu(j)}\right\}}\right] \tag{7.63}$$

$$\Gamma(j) = \frac{\nu(j)\,U_\infty(j)\,\frac{\Delta U_\infty}{\Delta x}(j)}{u_*^3(j)} \tag{7.64}$$

The range of calculation is $y(i) = 0.0$ to $y(i) = \delta$ for each $\Delta x(j)$ along the concave and convex surfaces.

12. Calculation of the new size of the droplets

The droplets in the cells of the second column will be polydisperse in size and a new concentration due to the effects of phase change, diffusion and thermophoresis on the droplets in the cells of the first column. The polydispersion in the droplet size is not very high since the immigrant droplets come from the adjacent cells. To obtain

monodispersion of the droplet size in the cells of the second column, a mass-median diameter was found for each group of droplets in each cell. This statistical analysis is based on a Hatch-Choate expression and auxiliary equations:

(a) The Hatch-Choate equation for a mass-median diameter is,

$$d_{mm}(i,j) = 3\sqrt{10^{\left[\log(dg^3(i,j)) + 10.362\ \{\log\ (S_{DG}(i,j))\}^2\right]}} \qquad (6.65)$$

(b) Geometric standard deviation,

$$S_{DG}(i,j) = 10^{\left[\sqrt{\frac{\Sigma N_p\ \{\log\ (d(i,j)) - \log\ (dg(i,j))\}}{\Sigma N_p}}\right]} \qquad (6.66)$$

where $$dg(i,j) = 10^{\left[\frac{\Sigma N_p\ \log\ (d(i,j))}{\Sigma N_p}\right]}$$

13. Plotting the results

There are no numerical results presented in this work. All the results were plotted either along the length-wise (horizontal) x-axis or the vertical y-axis. The plot program will not be shown in Appendix 7D since it is standard and it is very long for presentation.

7.6 Range of the Calculations

The calculations of the variation of the droplet parameters were made for flows along the concave and convex surfaces of a steam turbine fixed blade. The results have been obtained for the following ranges of parametric variables for the droplet and the vapour:

1. Droplet size

Nucleation produces very small droplets in the range of 0.01 - 1.0 μm diameter. Five sizes were selected, within this range, for entrained entry droplets, d_i equal to 0.01, 0.05, 0.1, 0.5 and 1.0 μm.

2. The temperature of the blade surfaces

The surface temperature along the concave and convex surfaces will be non-uniform, since the flow velocity increases considerably towards the trailing edge. Thus the blade surface temperature will decrease along both blade surfaces. The initial surface temperature (t_{wi}) can be adjusted for the present calculations. Five values of t_{wi} have been set between 66 - 85°C, viz. 66, 70, 75, 80 and 85°C for heating. In some cases t_{wi} is set to be equal to and less than the adiabatic temperature in order to find the deposition rate of the droplets when,

(i) the blade is unheated,

(ii) the suction slot method is used for blade surface drainage.

3. Droplet path height

The changes in the vapour and droplet characteristics along the stream lines (droplet paths) adjacent to the blade surface are greater than those along paths far from the surface (y > 100 μm). Therefore, seven levels of height, y equal to 20, 25, 30, 40, 50, 100 and 170 μm from the convex surface and 20, 25, 30, 40, 50, 100 and 280 μm from the concave surface have been selected.

7.7 Limitations of the Mathematical Model

The present calculation method is valid for a certain range of properties and conditions of droplets and vapour. The method can be made

more general by introducing new parameters and new boundary conditions. This can easily be done since the computer program is not complicated and has been developed in sections. The calculated results are obtained from the present method assuming the following conditions:

1. The flow of the steam inside the passage is one-dimensional and turbulent.
2. The temperature of the blade surface must not fall below the local free stream temperature for heat transfer calculations.
3. The fog droplets in the wet steam mixture are either monodispersed or can be represented by a suitable average radius.
4. The diameter of the droplet inside the flow must not be greater than 2.0 μm.
5. There is no slip between the droplet and the surrounding vapour.
6. The effect of the rotation of the droplet on its movement is not significant.
7. The vapour phase behaves as a perfect gas.
8. No second nucleation occurs.
9. Re-entrainment of the liquid phase does not take place.
10. Droplet interaction is not taken into account.

7.8 The Theoretical Results

The study of the variation in the vapour and droplet parameters due to the changing blade surface temperature produces a very large number of results. Only the plots which are considered necessary to give a clear picture of the situation with the droplets inside the boundary layer are presented here. In some cases the results for only the lowest and

highest blade surface temperatures are presented in order to restrict the size of this thesis.

At the inlet to the passage, five droplet sizes (0.01, 0.05, 0.1, 0.5 and 1.0 μm diameter) have been used for each value of the initial blade surface temperature (t_{wi} = 66, 70, 75, 80 and 85^{o}C). Therefore, twenty-five cases have been considered in order to cover all the possible conditions in the actual steam turbine. However the results of droplets with a diameter of 0.01 μm are not shown, since complete evaporation always occurs at $t_{wi} > t_{o}$.

Figures 7.26 and 7.27 show the distribution of the temperature difference between the vapour and droplet (Δt_{gf}) through the boundary layer. A positive value of Δt_{gf} ($\Delta t_{gf} = t_{g} - t_{f}$) means evaporation is occurring whilst a negative value indicates condensation.

The history of the change in the droplet size inside the boundary layer, due to heating, along both blade surfaces is shown in Figures 7.28 - 7.47. Five droplet paths at y equal to 30, 40, 50, 100 and 280 μm along the concave surface and at y equal to 30, 40, 50, 100 and 170 μm along the convex surface were selected. Figures 7.48 and 7.49 display the distribution of the droplet size through the boundary layer (i.e. across the stream lines) for initial droplet sizes of 1.0 and 0.5 μm.

The values of the local wetness fraction, along the stream lines, inside the boundary layer along both blade surfaces are plotted in Figures 7.50 - 7.69. The location of the droplet paths from the blade surfaces, along which the wetness fraction is calculated, are the same as those for droplet size in Figures 7.28 - 7.47. The distribution of wetness fraction along the y-axis can be seen in Figures 7.70 and 7.71 for entrained

droplet sizes of 1.0 and 0.5 μm.

Figures 7.72 - 7.91 show the mass transfer between the droplet and the surrounding vapour along the concave and convex surfaces. The mass flux is calculated for a group of identical droplets inside the boundary layer cell. The calculations were made along five droplet paths, y equal to 20, 30, 50, 100 and 280 μm along the concave surface and 20, 30, 50, 100 and 170 μm along the convex surface. The increased or diminished droplet mass through the boundary layer is shown in Figures 7.92 and 7.93.

The variations of the local thermophoretic velocity (V_T) of the droplet along three stream lines (y equal to 50, 100 and 280 μm along the concave surface and 50, 100 and 170 μm along the convex surface) inside the boundary layer can be seen in Figures 7.94 - 7.116. For initial surface temperatures greater than the adiabatic temperature, the values of V_T have been plotted in Figures 7.94 - 7.114. For t_{wi} about equal to or less than the adiabatic temperature, the values of V_T are shown in Figures 7.115 - 7.116.

Figures 7.117 - 7.122 show the distribution of Knudsen number (Kn), diffusion coefficient (D) and dimensionless relaxation time (τ_r^+) along the y-axis on the concave surface. The sizes of the entrained droplets are 1.0 and 0.5 μm and the values of t_{wi} are 66 and 85°C.

The net deposition velocity (V_{net}) which is due to combined effect of thermophoresis and diffusion is calculated along both blade surfaces. The values of V_{net} along three droplet paths inside the boundary layer are plotted in Figures 7.123 - 7.145. Figures 7.123 - 7.143 show the values of V_{net} when $t_{wi} \geq 66^oC$, whilst Figures 7.144 and 7.145 display the values

of V_{net} along the concave surface when the initial surface temperature is equal to 64, 64.5, 65.0, 65.2 and 65.5^{o}C. The variation of the local values of V_{net} along the y-axis on the concave surface when d_i is equal to 1.0 and 0.5 μm are plotted in Figures 7.142 - 7.145.

The values of the rate of deposited water on the concave and convex surfaces when the blade surface temperature is about equal to or less than the adiabatic temperature, are displayed in Figures 7.146 - 7.153. Two curves can be seen along both blade surfaces, one for the distribution of the local rate of deposition and the other for the accumulated value of the rate of deposited mass of the droplets. The value of the rate of deposited mass is presented in μg/cm^2/h.

Figures 7.154 - 7.193 show the interface line between the fog cloud and the dry steam due to heating the concave and convex surfaces of the fixed blade. The local values of the boundary sublayer thickness are also plotted to enable a comparison with the thickness of the dry region.

7.9 Discussion of the Theoretical Results

After the nucleation, the steam is no longer pure vapour, but contains a fog which consists of very small droplets (0.01 - 1.0 μm diameter). If this fog is subjected to a progressive expansion along the unheated blade water will precipitate onto the interface by condensation of the vapour since the surface of the fog droplets is the only one available for the transferring of heat and mass between the two phases. The amount of deposited condensate is mainly dependent on the total area of the blade surface and the temperature difference between the two phases. The exchange of mass and energy takes place as soon as the deviation from thermodynamic equilibrium occurs. The adverse effects of the fog droplets in the steam

turbine are due to:

1. Their presence as the starting point of the erosion process.

2. The increase in the thermodynamic losses.

3. The increase in the aerodynamic losses.

4. The production of the electrostatic charge on the blade and on the main turbine shaft.

The present heating method may be the only one by which these effects can be prevented or reduced. If the blade surface is heated to a temperature above the saturation temperature, thermodynamic equilibrium can be recovered only when the mass of the droplet reduces and the latent heat transfers from the vapour to the droplet. If the size of the droplet reduces below the critical size, the droplet will be naturally evaporated completely.

The temperature difference between the two phases (Δt_{gf}) can define the direction of the transfer of mass and heat between the vapour and the droplet. If Δt_{gf} is negative it means the flow is supersaturated and condensation is the way to restore equilibrium. However, if it is positive it indicates that the vapour is hotter than the droplet and evaporation is required to obtain thermodynamic equilibrium between the two phases. The values of Δt_{gf} when the initial surface temperatures are 66 and 85^{o}C and the size of the entrained droplets are in the range of 0.01 - 1.0 μm diameter, are plotted in Figures 7.26 and 7.27. When the initial size of the droplet is 1.0 μm and t_{wi} equals 85^{o}C, the value of Δt_{gf} along $(x/c)_{concave} \gtrsim 0.59$ becomes negative at $y \gtrsim 50$ μm. However, when the initial size of the droplet decreases the region of the negative Δt_{gf} (condensation) decreases until it becomes zero if the droplet size is equal to and less than 0.01 μm. Therefore, with the smallest size of droplet, the transfer of heat and mass

between the droplet and the vapour is controlled by evaporation only, as long as $t_{wi} \geq t_o$ (Figures 7.26e and 7.27e). If t_{wi} reduces to 66°C, Δt_{gf} becomes negative at $(x/c)_{concave} \gtrsim 0.37$ and $y \gtrsim 40$ μm when the initial droplet size is 1.0 μm. Therefore, one can conclude that the region of condensation (negative Δt_{gf}) or that of evaporation (positive Δt_{gf}) is dependent on:

1. The size of the entrained droplet. Larger droplets increase the condensation region, for the same value of t_{wi} (Figs. 7.26a and 7.27a).

2. The temperature of the blade surface. Higher temperatures give a greater region of evaporation (when the size of the droplet is the same), this can be seen by comparing all the plots in Figure 7.26 with those in Figure 7.27.

Figures 7.28 - 7.47 display, for various values of y (vertical distance), the variation in radius of a set of droplets with initial diameters of 1.0, 0.5, 0.1 and 0.05 μm during the x-transit of the concave and of the convex boundary layers. For each size of the entrained droplet five initial temperatures for the blade surface were used (66, 70, 75, 80 and 85°C). Droplets inside the cells adjacent to the heated blade surfaces are seen to evaporate completely and this can be confirmed from the results in Figures 7.48 and 7.49. More remote droplets on both surfaces evaporate by varying degrees but some droplets which are far from the surface survive and grow as the nozzle exit is approached, since Δt_{gf} becomes negative as a consequence of the diminishing core flow temperature. From the five stream lines, along which the size of the droplet are traced on both blade surfaces, for t_{wi} increasing from 66 to 85°C and for a constant initial droplet size (d_i), it can be observed that:

1. $\frac{dr}{dx}$ decreases substantially along the stream lines which are close to the blade surface, since Δt_{gf} is positive and at its maximum.

2. The rate of evaporation is always greater than the rate of condensation.

3. The reduction in the size of a droplet along the convex surface is always lower than that along the concave surface. This is because,

   (i) the laminarisation region on the convex surface is greater;

   (ii) the flow velocity is higher along the convex surface.

4. For $d_i > 0.1$ μm, the change in the droplet size is not significant when the path of the droplet is at $y \gtrsim 280$ μm along the concave surface and when it is at $y \gtrsim 170$ μm along the convex surface as shown in Figs. 7.28 - 7.39.

5. For $d_i \lesssim 0.1$ μm, the rate of evaporation or condensation is very high, even though Δt_{gf} is low, since the total droplet surface area is very large, (Figs. 7.40 - 7.47). The initial total surface area of the droplets (per unit mass of the steam and per unit length of the blade) for $d_i = 1.0$ μm is 180 m^2 and for $d_i = 0.1$ μm is 1800 m^2 when the initial wetness fraction is equal to 0.03.

Figures 7.48 and 7.49 give a satisfactory picture regarding the variation of the droplet size through the boundary layer, at constant x, along the concave surface. The decrease (evaporation) or the increase (condensation) in the droplet size occur smoothly, since the Δt_{gf} and u(y) distribution through the boundary layer is smooth. The distribution of droplet radius along the y-axis on the heated surface can be formulated

in a simple fitting formula, as follows:

$$r(y) = r_i \left(\frac{y - \delta_{ev}}{\delta - \delta_{ev}}\right)^{1/4}$$

where δ_{ev} = the thickness of dry region

δ = the thickness of the boundary layer.

The local values of wetness fraction (y) change very rapidly particularly when the initial size of the droplet is less than 0.5 μm and greater than 0.01 μm as shown in Figures 7.50 - 7.69. By arranging for the nucleation to occur when the expansion rate ($\dot{p}$) is maximum the droplets produced will be very small, therefore, it was believed that the contained water would be less and hence the quantity of deposited water would be reduced from which the erosion on the rotor blade could be expected to be reduced. In fact, only the first part of the statement about creating small droplets when $\dot{p}$ is high is strictly true, the remainder of the statement is correct only when the size of the created droplets is less than 0.05 μm (Figures 7.65 - 7.69). However, when the nucleation generates droplets having a size greater than or equal to 0.05 μm, in the last stage of unheated blade, the situation is as follows:

1. The supersaturation is not fully relieved inside the blade passage. Therefore, for constant inlet wetness fraction y_i = 3%, if d_i reduces and Δt_{gf} is negative, the local wetness fraction is increased dramatically to more than three times y_i as seen in Fig. 7.60. Thus, when the blade is unheated the worst situation is when $d_i \approx 0.1$ μm.

2. The number of the generated droplets increases very rapidly, i.e. the total surface area of the droplets is increased, (e.g. the total

droplet surface area increases about 20 times when d_i is reduced from 1.0 μm to 0.05 μm). Thus when Δt_{gf} is negative there is a large surface area for heat to transfer from the droplets to the vapour and a very large amount of condensed vapour precipitates onto the droplets.

3. The advantages of creating small droplets are only realised when the heating method is used. This is because when the value of Δt_{gf} is positive, or nearly equal zero, the effect of the droplet surface area will increase the rate of evaporation or reduce the rate of condensation. Therefore, a very small value of Δt_{gf} (positive) is sufficient to create a dry region on the blade surface as shown in Figs. 7.55, 7.60 and 7.65.

4. The smaller the size of the droplets the lower are the thermodynamic losses due to supersaturation. Therefore, the generation of small droplets ($d > 0.01$ μm) has a number of both advantages and disadvantages. A superposition of the two effects is necessary to find the optimum size of droplets which should be obtained from the nucleation.

The variation of the local wetness fraction along the vertical axis at five positions on the concave surface is shown in Figures 7.70 and 7.71. The value of the wetness fraction at y adjacent to the wall is very small and in most cases it is zero; it then increases very rapidly at y far from the surface, since here the rate of evaporation is very low or zero and in some cases, condensation occurs (Fig. 7.71).

The local rates of mass transfer between the droplets and the vapour inside the boundary layer on the blade surfaces are displayed in Figs.(7.72 to 7.93). The maximum rate of mass transfer (evaporation) always occurs at the

entrance of the blade passage for a very short distance. Further into the passage the rate of evaporation or condensation for $d_i > 0.05$ μm changes slowly, or in some cases, is zero due to the complete evaporation of the droplet or due to $\Delta t_{gf} = 0.0$. The reasons for this are that at the entry of the blade passage the total surface area of the droplets is maximum and $\Delta t_{gf} > 0.0$ inside the boundary layer, as shown in Figs. 7.72 - 7.81. The net accumulative value of mass transfer along the concave and convex surfaces at $y \lesssim 100$ μm is always equal to or greater than zero for all sizes of entrained droplets ($d_i > 0.01$ μm) and when $t_{wi} > t_o$. However at $y > 100$ μm, the net accumulative mass change is either equal to or less than zero. If the initial size of the droplet is in the range of $0.05 \lesssim d_i \lesssim 0.1$ μm and the droplet is far from the blade surface (near the edge of the boundary layer), and if Δt_{gf} is very small at the entrance and less than zero further down, then the rate of condensation increases rapidly until shortly before the exit, as seen in Figs. 7.82 and 7.87. The reasons for this are:

1. The evaporation along a very short distance from the entrance causes only a very small reduction in the droplet size. Therefore, the change in the total surface area is not significant.

2. The remaining droplets are subject to $\Delta t_{gf} < 0.0$ at $x/c > 0.45$ along the concave surface and at $x/c > 0.15$ along the convex surface until the throat of the passage.

3. Beyond the throat, the supersaturation is quickly relieved and hence the temperature difference between the droplet and the vapour is reduced and in some cases is reduced to zero.

The change in the droplet mass along the y-axis at five positions along the x-axis on the concave surface is shown in Figs. 7.92 and 7.93. It

can be observed that at the entrance to the blade passage there is a considerable decrease in the droplet mass along the y-axis. From a short distance after the entrance until the exit, the increase or decrease in the mass of the remaining droplets is not significant along the y-axis, since Δt_{gf} is very small at these positions when the droplets exist.

The transfer of enthalpy between the droplet and the vapour is the latent enthalpy which is transferred from the droplet when Δt_{gf} is negative and accepted by the droplet when Δt_{gf} is positive. The value of the increase or decrease in the latent enthalpy of the droplet is calculated from the change in the droplet mass and h_{fg},

$$\dot{Q}_{gf}(i,j) = \dot{m}_r(i,j)\ h_{fg}(j)$$

The value of h_{fg} is dependent on the value of the pressure. The pressure of the mixture flow is reduced from 0.233 bar to 0.1 bar and the corresponding values of h_{fg} are 2392 and 2350 kJ/kg. The reduction in the value of h_{fg} is very small (about 1.75%) and it can be taken as constant. Then the variation of $\dot{Q}_{gf}$ is a function of $\dot{m}_r$ only, so that the behaviour of the change of droplet enthalpy along the x and y-axes on both blade surfaces is the same as that for $\dot{m}_r$.

The distribution of the local thermophoretic velocity along three stream lines inside the boundary layer of the concave and convex surfaces are shown in Figs. 7.94 - 7.116. It is seen that droplets travelling near the wall acquire a higher thermophoretic velocity (Figs. 7.94 - 7.103). For each surface the three curves are similar in form but V_T varies in magnitude with y. On the convex surface the curves rise slowly up to about x/c = 0.3 whilst on the concave surface they rise slowly to about x/c = 0.7 if the initial droplet size is in the range of $d_i \gtrsim 0.5$ μm. The rapid increase

in V_T thereafter ($0.3 < x/c < 0.54$ along the convex surface and $0.7 < x/c < 0.94$ along the concave surface) is due to an increase in the droplet size by condensation coupled with a rising temperature gradient $(\frac{dT}{dy})_x$. If the diameter of the entrained droplets (d_i) is equal to or less than 0.1 μm (Figs. 7.104 - 7.112) the change in the value of V_T along both surfaces is always slow except for a small fluctuation at the throat due to a very rapid increase in $(\frac{dT}{dy})_x$. The reduction in V_T after the throat is a result of very fast relief of the supersaturation which causes a rapid reduction in $(\frac{dT}{dy})_x$.

When the blade surface temperature is constant and five sizes of the entrained droplets are employed, it can be seen that the value of V_T falls with the decreasing size of the droplet. This can be noticed by comparing the three curves on each surface in Figs. 7.94, 7.99 and 7.104 for $t_{wi} = 66^oC$ or in Figs. 7.95, 7.100 and 7.105 for $t_{wi} = 70^oC$ and also for $t_{wi} = 75$, 80 and 85^oC. The variation of V_T along the y-axis for a droplet, $d_i = 1.0$ or 0.5 μm, on the concave surface is plotted in Figs. 7.113 - 7.116. The positive values of V_T obtained when $t_{wi} < t_o$ along a very short distance of y from the surface, are due to the values of $(\frac{dT}{dy})_x$ being positive. However, when $t_{wi} \geq t_o$ or at y far from the surface in the case of $t_{wi} < t_o$, the thermophoretic velocity acquires a negative value (i.e. away from the surface) or a zero value. Furthermore it can be observed that the droplets near to the surface have a low thermophoretic velocity despite $(\frac{dT}{dy})_x$ being a maximum since the size of the droplets are reduced rapidly as the result of evaporation. However, droplets far from the surface which are larger than those adjacent to it, have a high thermophoretic velocity even though the temperature gradient $(\frac{dT}{dy})_x$ is very low. The local value of V_T is nearly constant at y far from the surface; the reasons for this are:

1. The local value of Knudsen number (Kn) at y far from the surface is constant for each position on the x-axis, as shown in Figs. 7.117 and 7.118.

2. $(\frac{dT}{dy})_x$ and $(\frac{du}{dy})_x$ are very small at y far from the surface.

The distributions of the diffusion coefficient (D) and the dimensionless relaxation time (τ_r^+) at five values of x along the y-axis are plotted in Figs. 7.119 - 7.122. There is a sudden increase in the value of D at the interface line between the droplets and dry regions, this is followed by a rapid decrease to an almost constant value as seen in Figs. 7.119 and 7.120. The fluctuation in the local value of D is a result of evaporation, since D is increased by decreasing the droplet size. The size of the droplet at the interface line is the smallest size and therefore the greatest value of D always occurs at that line. The variation in the droplet size at y far from the surface is very small and hence the change in the value of D at that y is not significant and D may be considered to be constant. The height of the fluctuation is dependent on the rate of evaporation, i.e. on the blade surface temprature; when t_{wi} decreases the length of the fluctuation decreases until it reaches a minimum at t_{wi} equal to the adiabatic temperature.

The value of τ_r^+ along the y-axis is proportional to d^2, since u_*, ν and ρ_g are constant at constant x. Therefore the behaviour of the curves of τ_r^+ (Figs. 7.121 and 7.122) are the same as those of the droplet radius (Figs. 7.48 and 7.49). In the present work the relaxation time is based on Stokesian drag only.

The net deposition velocity (V_{net}) is mainly dependent on the thermophoretic velocity, the diffusion coefficient, the eddy diffusivity and

the relaxation time (if the size of the droplet is large (i.e. d > 3 μm)). The local values of V_{net} along three droplet paths on both blade surfaces are plotted in Figs. 7.123 - 7.141. The size of the droplets in the present work cannot exceed 2.0 μm, so that the effect of relaxation time can be considered as insignificant. To simplify the analysis of the variation of V_{net} along the x-axis, the boundary layer can be divided into two regions:

I. Far from the blade surface (y > 100 μm)

The value of D is nearly constant, therefore the change in V_{net} values are due to the variation of V_T and ε_p values only. The local values of V_{net} along the upper curves on both blade surfaces (i.e. at $y_{concave}$ = 280 μm and y_{convex} = 170 μm) are nearly zero for ∿ x/c = 0.15 from the entry, since:

1. The flow is laminarised (i.e. the values of ε_p are reduced).
2. Thermophoretic velocity is increased due to increasing the droplet size and increasing the temperature gradient.

When the eddy diffusivity (ε_p) increases (i.e. the laminarisation factor decreases) V_{net} increases until shortly before the throat of the passage even though V_T increases because the eddies of the turbulent flow become stronger and appear to be the dominant effect on the movement of the droplet. At the throat V_{net} is rapidly decreased since the flow is suddenly laminarised; this is followed by a steep increase in V_{net} shortly after the throat when the flow becomes turbulent. The reduction in V_{net} for a distance of x/c = 0.05 before the exit is a result of the rapid decrease in ε_p. This is due to a corresponding decrease in $\frac{dU_\infty}{dx}$. Furthermore the value of V_T also decreases. When the surface temperature increases the local value of V_{net} increases (seen by comparison between Figs. 7.123 and 7.138). This is due to:

1. The local values of V_T are decreasing when the droplets are subjected to evaporation rather than condensation.

2. The values of ε_p in the two figures are the same, therefore thermophoresis is the most influential effect.

II. Near to the blade surface ($y < 100$ μm)

When the droplet path is very close to the interface line between the wet and dry regions, the droplets have a minimum possible size and therefore a maximum value of diffusion coefficient (D). The values of V_T may also be high due to a high temperature gradient. Although the values of ε_p are not as high as those at a distance far from the blade surface this still appears to be the dominant factor, since:

1. The effect of the possibly high value of D will be opposed by the effect of a high value of V_T.

2. The boundary sublayer is thinning along the x-axis and its thickness is very small, therefore, the values of ε_p are not very small when the droplets are outside the boundary sublayer.

For each surface the three curves are similar in form but V_{net} varies in magnitude with y. When the values of V_{net} become zero no net force acts and the droplet moves parallel to the surface locally or complete evaporation occurs.

The local values of V_{net} at y far from the surface are nearly constant since the change in the droplet size, the temperature gradient, the diffusion coefficient and the eddy diffusivity are not considerable. However, the variation of V_{net} close to the wall is defined by the change in D and V_T as shown in Figs. 7.142 - 7.145.

The values of V_{net} along the concave surface are always greater than the corresponding values on the convex surface since ε_p along the concave surface is higher than that along the convex surface.

When the blade surface temperature is about equal to or less than the adiabatic temperature as occurs in the case of an unheated blade or when a suction slot drainage method is employed, deposition of droplets on the surface will take place. The rate of the deposition is a function of droplet size, blade surface temperature and the expansion rate of the flow. When the initial size of the droplet is maximum (i.e. droplet diameter equal to 1.0 μm in the present work) the distributions of the rate of the deposited mass of the water when the blade surface temperature is equal to 64, 64.5, 65.0, 65.2 and 65.5°C are shown in Figs. 7.146 - 7.150. There are two curves along each surface one for the local value of the deposition rate (dashed curve) and the other for the accumulated value (solid curve).

The deposition rate is equal to the average concentration of the droplet ($\mu g/m^3$) multiplied by the net deposition velocity (V_{net}). The change of the droplet concentration along the x-axis is very small, therefore the variation in the value of the rate of deposition is due to the change in V_{net} along the x-axis. The mass of the deposited water increases by decreasing the temperature of the surface (Figs. 7.146 - 7.150) since:

1. The $(V_T)_{av}$ is decreasing and in the case of very low surface temperature (i.e. t_w less than the free stream temperature) V_T becomes positive (i.e. towards the surface). Thus the two factors, diffusion and thermophoresis, combine to force the droplet to deposit on the surface (i.e. increase V_{net}) in the case of $t_w(x) < t_\infty(x)$.

2. The free stream concentration of the droplets ($\mu g/m^3$) increases as a result of additional condensation.

The local and accumulated values of the rate of deposition increase along both blade surfaces when $t_w < t_o$ as shown in Figs. 7.146 and 7.147. However, when $t_w \approx t_o$ the local value of the deposition rate becomes zero after a short distance from the entry along the concave surface as a result of evaporation, whilst along the convex surface, it increases until the exit of the passage (Figs. 7.148 and 7.149). This phenomenon has been observed experimentally by Gyarmathy and Meyer (141) inside a Laval nozzle when they noticed a dry region above the nozzle surface along the divergent section. If $t_w = t_o + 0.3$, the local values of the deposition along both surfaces become zero after a very short distance from the entry as shown in Fig. 7.150. The total deposited mass is decreased by increasing the surface temperature and it becomes zero when $t_w \gtrsim t_o + 1.0$.

The quantity of deposited water when $t_w < t_o$ along the concave surface is greater than that along the convex surface. The maximum value of the local deposition rate occurs near to the trailing edge (Fig. 7.146). If the temperature of the surface is set to be equal to 32^oC, as may occur when the pressure inside the hollow blade is equal to the condenser pressure (0.05 bar), the local and total deposition rate of droplets of 0.1 μm are greater than those of droplets of 0.5 μm and those of droplets of 1.0 μm (Figs. 7.151 - 7.153). This is due to the difference in the rate of growth of the droplet which is higher in the case of 0.1 μm droplets. Flow with droplet diameters less than 0.1 μm may reach thermodynamic equilibrium quickly and therefore there is no chance for the droplet to grow. Thus generating small droplets ($0.1 \lesssim d_i < 1.0$ μm) will reduce the supersaturation losses but may increase the erosion of the rotor blade due to increasing the deposited water on the surface of the fixed blade.

Figures 7.154 - 7.193 are drawn to provide a visual indication of the location of the fog "cloud base" (dashed curve) as the nozzle passage is traversed. Fog droplets existing "above" the cloud base are shown conventionally as dots. The clear space immediately above the surface implies the absence of droplets and therefore of diffusive deposition and the shape and extent of this space profile depends upon the initial size of the droplet and the rate of heat input. It also differs for given conditions whether the surface considered is convex or concave. On each surface, if the surface temperature is constant, the interface line (cloud base) is located more distant from the surface if the initial size of the droplets decreases (e.g. see Figs. 7.154 - 7.157). It is also clear that for constant d_i, the thickness of the dry region increases with the increasing of the surface temperature, e.g. Figs. 7.154, 7.162, 7.170, 7.178 and 7.186) when d_i = 1.0 μm. Clearly the theoretical minimum heat input is that required to lift the cloud base marginally from the entire blade surface from entry to the passage onwards to its exit. In the present work, the practicable surface temperature and minimum heat input is that when the thickness of the dry region is about that of the boundary sublayer. This occurs when $t_{wi} = 80^{o}C$ as shown in Figs. 7.162 and 7.166.

Furthermore, the effect of generating dry region on the fixed blade surface may extend beneficially in the improving of the rotor passage efficiency by preventing the generation of coarse water from the fixed blade surface and relatively reducing the wetness fraction due to heating. Thus, internally heated blade will result in:

1. preventing erosion of the rotor blades,
2. reducing thermodynamic and aerodynamic losses in the L.P. turbine.

7.10 Prediction of the Rate of Deposition of Solid Particles and a Comparison Between the Theoretical and Experimental Results

The theoretical model has been modified to calculate the rate of deposition of a solid particle. The change was made by removing the evaporation term. The size of the particle and the distribution of the particle concentration inside the blade passage were given in Chapter 4. The temperature of the surface and the velocity of the flow are the only factors which control the rate of deposition, since the size of the solid particle is constant. Therefore, the results of deposition can be divided into two groups: on an unheated surface and on a heated surface. The calculations were made for the particle deposition on the concave surface only.

7.10.1 Results of particle deposition on an unheated surface

The flow conditions and the particle properties are the same as those given in Chapter 4 in the present thesis and also given by Davies (4) and El-Shobokshy (37). Three inlet velocities 13.0, 11.2 and 9.5 m/s were used. The theoretical results of deposition and the experimental results from the present work and those due to Davies and El-Shobokshy are in acceptable agreement as shown in Figs. 7.194 - 7.196. The agreement becomes better when the inlet velocity decreases. When the inlet velocity is maximum, in the present range equal to 13.0 m/s, the predicted results along $x/c > 0.5$ are always greater than the measured (Fig. 7.194). This is possibly because the effect of laminarisation is not taken into consideration for this range of velocities.

7.10.2 Results of particle deposition on a heated surface

The temperature of the blade surface was taken as the average values of temperature along the concave surface and are given in Chapter 4. The

conditionsof the flow (velocity and temperature) and the physical properties of the particles in the theoretical model are the same as those measured in the experimental rig. The agreement between the local values of the rate of deposition from the theory and the experiment are acceptable, (Figs. 7.197 - 7.199). However, the accumulated values of the deposited mass on the heated surface from the theory and the experiment are in a very good agreement. The results from Davies' test along the first half of the passage are in better agreement with theory than those of the present work, but those from the present work are in better agreement along the second half.

It can be concluded that:

1. Using the whole thickness of the boundary layer for calculating the deposition rate gives more realistic results than if only the thickness of the sublayer is considered.

2. The agreement between the theoretical and experimental results suggests that the part of the present model for predicting the movement of the particles (diffusion and thermophoresis) is the more reliable model.

3. Laminarisation of the turbulent boundary layer should be checked and its effect must be considered for flow with high velocity.

CHAPTER 8

THE ECONOMIC EVALUATION OF THE PREVENTION OF EROSION BY BLADE HEATING

8.1 Introduction

This Chapter is concerned with the economic evaluation of the blade steam heating method. A large number of engineering and economic data must be prepared before using the economic theory. Section 8.2 involves the calculations of all the required engineering factors such as the efficiencies of the diaphragm, the rotor, the penultimate stage, the last stage and the quantity of additional coal required for blade heating. In section 8.3 alternative practicable designs for the hollow diaphragm are described. The economic data such as the rates of inflation and interest and the costs of the hollow diaphragm, the rotor, the fuel and the outage are described in section 8.4. Two types of data for two economic decisions are presented: if the C.E.G.B. had decided to use the heating method in 1967 (Case I) for the first large coal stations and if they had decided in 1982 (Case II) for a modern power station. Therefore the economic data must cover the past period, from 1967 to 1983 (which are actual data) and future period from 1982 on (which are estimated data).

If the heating method is not used, reblading of the damaged rotor is likely to be required once during the life of a large turbine. The C.E.G.B. estimated the life of the rotor to be about fifteen years when blade heating is not employed.

The economic methods for appraising the investment in the heating method are explained in section 8.5. Two economic techniques - the net present value (NPV) and the internal rate of return (IRR) - are each used for the two cases (Case I and Case II). The present analysis is made for a turbine in a large coal power station; the significance for a turbine in a nuclear station will be discussed later in this Chapter. Section 8.6

presents the economic results in two stages: firstly results based on single value best estimates assuming certainty, and secondly the effect on those results of variations in the estimated economic data. In this way uncertainty in these data can be tested. Finally the discussion of the economic results and conclusions will be presented in section 8.7.

8.2 Prediction of the Stage Efficiency and Thermodynamic Changes in the Turbine due to Blade Heating

There are a number of engineering factors which must be defined and calculated in order to determine the additional coal required for the heating and for recovering the output losses from the turbine.

8.2.1 Nozzle efficiency:

The passage of the stator blade forms a non-symmetrical convergent-divergent nozzle (passage). It is very difficult to determine accurately the effiency of the fixed blade passage, since the actual conditions of the flow at the exit are not known. There are three approaches for finding an approximate value for the efficiency of the passage:

(i) From the boundary layer calculations

The flow at the exit of the passage is turbulent; therefore the velocity distribution through the boundary layer can be simply represented by the seventh power law. The mean velocity, therefore, can be calculated by integrating the velocity (u(y)) along the y-axis (perpendicular to the blade surface) as follows

$$U_m = \frac{\int_0^{y=\delta} u(y)dy}{\delta} = \frac{U_\infty \int_0^{\delta} \left(\frac{y}{\delta}\right)^{1/7} dy}{\delta} = \frac{7}{8} U_\infty \qquad (8.1)$$

where δ = the boundary layer thickness.

Hence, there are two different flows inside the passage - the flow of the boundary layer along both blade surfaces and the free stream flow. The average velocity (actual) of these flows can be determined by using the values of the boundary layer thickness along the concave and convex surfaces (Chapter 5). Thus the actual velocity is

$$U_{ac} = \frac{U_m (\delta_{concave} + \delta_{convex}) + U_\infty [A_{passage} - (\delta_{concave} + \delta_{convex})]}{A_{passage}} \quad (8.2)$$

where $A_{passage}$ = the passage area per mm length of blade.

The boundary layer thicknesses along both surfaces at the exit of the passage are very similar,

$$\delta = \delta_{concave} = \delta_{convex} \approx 1.0 \text{ mm.}$$

The cross-sectional area of the passage at the exit section is equal to 21.5 mm^2/mm length of the blade. The exit velocity of the free stream (U_∞) is equal to 510.0 m/s. Therefore, U_{ac} = 504 m/s.

From the definition of the nozzle efficiency,

$$\eta_N = \frac{h_i - h_e}{h_i - h_{es}} = \frac{U_{e,ac}^2 - U_{i,ac}^2}{U_{es}^2 - U_{i,ac}^2} \quad (8.3)$$

Where, $U_{i,ac}$ = the inlet velocity = 80.0 m/s

$U_{e,ac}$ = the actual velocity at the exit = 504.0 m/s

U_{es} = the isentropic velocity at the exit = 510.0 m/s.

Hence the efficiency of the blade passage is calculated to be 97.6%.

(ii) From the calculated value of the discharge coefficient:

Ryley and Barrow (142) have defined the discharge coefficient

for a nozzle as the actual area divided by the ideal area,

$$C_D = \frac{A_{ac}}{A_{ideal}}$$

For circular nozzle, $A_{ac} = \frac{\pi}{4} (D_N - 2\,\delta_1)^2$

$$A_{ideal} = \frac{\pi}{4} D_N^2$$

where δ_1 = the displacement thickness at the exit of a nozzle

D_N = the diameter of the nozzle at the exit section.

For the blade passage, $A_{ac} = \ell_B \left\{ D_P - \left((\delta_1)_{concave} + (\delta_1)_{convex} \right) \right\}$

$$A_{ideal} = \ell_B D_P$$

where ℓ_B = the length of the blade

D_P = the height of the passage = 21.5 mm

$(\delta_1)_{concave}$, $(\delta_1)_{convex}$ = the displacement thickness along the concave and convex surfaces.

In the present work $(\delta_1)_{concave} + (\delta_1)_{convex} = 0.275$ mm.

Therefore, the discharge coefficient of a nozzle having a uniform geometry can be written in terms of D and δ_1

$$C_D = \frac{(D - 2\,\delta_1)^2}{D^2} \tag{8.4}$$

or when the blade passage is used C_D can be defined as

$$C_D = \frac{A_{ideal} - \left[(\delta_1)_{concave} + (\delta_1)_{convex} \right] \ell_B}{A_{ideal}} \tag{8.5}$$

The efficiency may be defined in terms of C_D as

$$\eta_N \approx C_D^2 \tag{8.6}$$

Hence, on this basis, the efficiency of the passage is equal to 97.5%.

(iii) Direct estimation of the nozzle efficiency:

Forster (120) suggested that the value of the efficiency of the passage is about 97% when dry steam passes the blade. Dixon (143) also expected the efficiency of the blade passage to be about 97%.

Thus the three estimations of the efficiency of the blade passage suggest that a common value of η_N is about 97%. Therefore, this value has been adopted as the nozzle efficiency in the present work.

8.2.2 Heat input

The rate of transfer of heat from the blade surface was found to be mainly dependent on the size of the entrained droplets when the initial surface temperature is constant, as described in Chapter 6. The larger the droplet size the greater is the rate of heat transfer from the blade surface to the flow inside the passage and hence the greater the heat input required from the heating steam. It has been shown in Chapter 7 (section 7.9) that the practical minimum initial temperature of the blade surface (t_{wi}) is 80°C. This temperature is sufficient to ensure that a layer of dry steam will form on the surfaces of the guide blades and thereby prevent water in the steam from contacting the guide blade surfaces. In the present range of droplet sizes the maximum initial diameter of the droplets is 1.0 μm. Therefore, Fig. 6.11 gives the rate of heat transfer from both blade surfaces when the initial surface temperature is 80°C and the droplet size is 1.0 μm. This estimate corresponds to the maximum heat input required

and hence also to the maximum operating cost for the economic evaluation. The total heat transfer from the surface of a single guide blade is equal to 2.06 kW per metre of blade length. Several investigators have stated that first nucleation produces droplets with an average size less than 1.0 μm. The economic evaluation which follows is therefore based on a conservative prediction of the engineering conditions.

8.2.3 Characteristics and properties of the heating steam

The following assumptions can be made for the flow of the heating steam inside the hollow blade.

1. The steam flow is stagnant.
2. The flow of the condensate is two-dimensional.
3. The steam is saturated vapour.
4. The internal blade surface is smooth.
5. The effect of the blade curvature on the movement of the condensed vapour film is negligible.

The governing equations of the characteristics and the properties of the condensate are:

(i) Continuity equation

$$\frac{du}{dx} + \frac{dv}{dy} = 0 \tag{8.7}$$

or

$$\dot{m} = \int_0^{\delta} \rho u \, dy \tag{8.8}$$

(ii) Momentum equation

$$\rho_\ell \left(u \frac{\partial u}{\partial x} + v \frac{\partial u}{\partial y}\right) = \mu_\ell \frac{\partial^2 u}{\partial y^2} - (\rho_\ell - \rho_g) \, g \sin\phi \tag{8.9}$$

where ϕ is the angle of the condensate flow with the horizontal.

(iii) Energy equation

$$\rho_\ell \, Cp \left(u \frac{\partial t}{\partial x} + v \frac{\partial t}{\partial y}\right) = K_\ell \frac{\partial^2 t}{\partial y^2} \tag{8.10}$$

(iv) Heat balance equation

$$K_\ell \frac{\partial t}{\partial y} = \frac{\partial \dot{m}}{\partial x} h_{fg} \tag{8.11}$$

Nusselt has simplified the system of equations by neglecting the convective transport and considering the density of the condensate to be much greater than density of the vapour. In this way equations (8.9) to (8.11) simplify to:

$$\mu_\ell \frac{\partial^2 u}{\partial y^2} = \rho_\ell \, g \sin\phi \tag{8.12}$$

$$K_\ell \frac{\partial^2 t}{\partial y^2} = 0 \tag{8.13}$$

$$K_\ell \frac{t_s - t_w}{\delta_\ell} = \frac{\partial \dot{m}}{\partial x} h_{fg} \tag{8.14}$$

The boundary conditions are:

at $y = 0$; $u = 0$ and $t = t_w$

at $y = \delta_\ell$; $\mu_\ell \frac{du}{dy} = \mu_g \frac{du}{dy}$.

However $\mu_g << \mu_\ell$; therefore $\mu_\ell \frac{du}{dy} = 0$ and $t = t_s$.

The integration of equation (8.12) subject to the boundary conditions gives the velocity distribution in the condensate layer,

$$u(y) = \frac{g \, \rho_\ell \sin\phi}{\mu_\ell} \left(\delta y - \frac{1}{2} y^2\right)_\ell \tag{8.15}$$

From equations (8.8), (8.14) and (8.15), the distribution of the thickness of the condensate layer can be determined.

$$\delta_\ell(x) = \left[\frac{4\ \mu_\ell\ K_\ell\ (t_s - t_w)\ x}{g\ \rho_\ell^{\ 2}\ h_{fg}\ \sin\phi} \right]^{1/4} \tag{8.16}$$

The mean velocity $(U_m)_\ell$ of the condensate flow can be found from equation (8.15)

$$U_m = \frac{\int_0^{\delta_\ell} u(y)\ dy}{\delta_\ell} = \frac{g\rho_\ell\ \delta_\ell^{\ 2}\ \sin\phi}{3\mu_\ell} \tag{8.17}$$

The mass flux of the condensate flow, therefore, can be defined as

$$\dot{m}_\ell = \rho_\ell\ U_m\ A_\ell = \frac{g\rho_\ell^{\ 2}\ \delta_\ell^{\ 3}\ A_S}{3\mu_\ell} \tag{8.18}$$

where A_ℓ = cross-section area of the condensate flow

A_S = internal blade surface area per unit length of blade.

The mass flux can also be defined in terms of the input heat and the latent heat of condensation:

$$\dot{m}_\ell = \frac{\dot{Q}}{h_{fg}} \tag{8.19}$$

The heat input is given in the previous section. Therefore equations (8.18) and (8.19) can be solved iteratively to find $\dot{m}_\ell$ by assuming the thermodynamic conditions of heating steam. Hence, the properties of the heating steam can be determined. It was found that most internal surfaces of hollow blades have an angle ϕ greater than 60^o. Setting the angle ϕ equal to 60^o gives a conservative value for $\dot{m}_\ell$ (when the blade surface temperature is 80^oC). For a single blade $\dot{m}_\ell$ was found to be 9.5×10^{-4} kg/s.

8.2.4 Reduction in work and efficiency of the L.P. turbine due to heating

As a result of additional heat input through the guide blades, two types of losses may result:

(i) loss due to extraction of steam for heating before the penultimate stage;

(ii) loss due to a possible reduction in the efficiency of the last stage.

To calculate these losses the efficiencies of the last and penultimate stages must first be determined. Figure 8.1 shows the thermodynamic process of the flow along the heated and unheated blade inside the last two stages.

(i) Penultimate stage efficiency

The flow during the penultimate stage is dry; therefore at the midheight section of the blade the losses are only aerodynamic losses. Bakhtar (113) and Forster and Cox (120) have estimated the value of dry efficiency to be about 93%. The enthalpy drop through the stator and the rotor passages of the penultimate stage can be assumed to be the same as that through the stator and the rotor passages of the final stage. Therefore the rotor efficiency can be determined. The details of the calculation are presented in Appendix 8A and the calculated rotor efficiency is about 91%.

(ii) The final stage efficiency

There are two thermodynamic losses: firstly that due to an increase in the enthalpy of the flow along the guide blade because of blade heating and secondly, that due to wetness. In Chapter 7 the prevention of the occurrence of coarse water and erosion, and the relative reduction in the wetness fraction, were discussed. These factors result in an increase in

the rotor efficiency and hence possibly also an increase in the stage efficiency. The calculations of the efficiencies of the passages of unheated and heated blades are presented in Appendix 8A, and shown an increase in the efficiency of the last stage of about 0.2%.

(iii) The reduction in the turbine output

Increasing the last stage efficiency results in an increase in the output of the last stage. In Appendix 8A it can be seen that the work gain from improving the last stage efficiency is nearly equal to the loss due to extracting heating steam at the entry to the penultimate stage for blade heating. However to consider the most pessimistic case, the work gained is not taken into account. Therefore the reduction in the turbine output due to employing blade heating can be determined as follows:

1. If the turbine has 3 L.P.s (as in a 500 MW or old version of 660 MW turbine), the loss in the output is

$$\Delta W_{loss} = \left[\Delta \dot{m}_{\substack{\text{heating} \\ \text{steam}}} (\Delta hn)_{\substack{\text{last two} \\ \text{stages}}} \right]_{\text{one diaphragm}} \times 6 = 193 \text{ kW.}$$

2. If the turbine has 2 L.P.s (as in a modern turbine), the loss in the output of the turbine is,

$$\Delta W_{loss} = \left[\Delta \dot{m}_{\substack{\text{heating} \\ \text{steam}}} (\Delta hn)_{\substack{\text{last two} \\ \text{stages}}} \right]_{\text{one diaphgragm}} \times 4 = 129 \text{ KW.}$$

Accordingly the boiler mass flow has to be increased (by $(\delta \dot{m})_{boiler}$) in order to recover the loss in the output of the turbine due to blade heating. $\delta \dot{m}_{boiler}$ is less than the mass flow rate of heating steam ($\Delta \dot{m}$) since it (i.e. $\delta \dot{m}_{boiler}$) will do work due to expand through the H.P. and I.P. turbines and the first three stages of the L.P. turbines. The increase in

the mass flow rate of the boiler ($\delta\dot{m}_{boiler}$) to provide blade heating but no overall change in the work output from the turbine compared with a conventional turbine, is calculated as:

1. If the turbine has 3 L.P.s; $\delta\dot{m}_{boiler} = 0.185$ kg/s
   $\Delta\dot{m} = 0.285$ kg/s

2. If the turbine has 2 L.P.s; $\delta\dot{m}_{boiler} = 0.122$ kg/s
   $\Delta\dot{m} = 0.19$ kg/s

Full details can be found in Appendix 8A.

8.3 The Steam Heating Method

In Chapter 6 the steam heating method was identified as the most practicable compared with the other methods (hot air, electrical or hot oil). The advantages of using saturated steam as the heating fluid are:

1. It does not need complicated auxiliary equipment.
2. There is less technical risk such as leaking, rust and corrosion which may exist with the other methods.
3. The hollow diaphragm for steam heating, is very similar to that designed by the G.E.C. (139). Therefore there is no extra cost for designing a new diaphragm.
4. The heat capacity of the steam is higher than that for the other fluids, e.g. under the same thermodynamic conditions the heat capacity of steam is greater than that of air by about 16 times.

The suggested design of the heating steam and the condensate return systems is as follows:

(i) The heating steam is drawn from the flow of the working steam at the entry to the penultimate stage. The steam conditions will be 137°C, 0.86 bar and 40°C superheat.

(ii) At the entry to the hollow diaphragm, the steam should be close to saturation. However, using superheated steam from the tapping point directly into the hollow blades results in an increase in the heat input to the blade of about 4%. This increase is due to the difference between the heat capacity of the superheated steam (h = 2780 kJ/kg) and that for saturated steam (h_g = 2675 kJ/kg), and it is acceptable in the present work. Otherwise a heat exchanger must be used to reduce the conditions of the superheated steam to saturation to recover this small increase in the enthalpy of the heating steam.

(iii) It has been suggested, in Ref. (106), that the heating steam should enter the hollow diaphragm from the upper end and leave the diaphragm as condensate from the lower end, as shown in Fig. 8.2a. The heating steam is supplied to the top of the hollow diaphragm (point 1), passes around the upper semi-circular duct in the casing and then through the blades (path 2) towards the inner semi-circular ring of the upper half (point 3). The steam and the condensate are collected in the inner semi-circular ring of the lower half (point 4). They then flow through the blades towards the outer semi-circular duct of the lower half (point 5). The condensate is then drawn through the lowest point (point 6).

(iv) An alternative to the Akhtar et al proposal would be to feed the two halves of the diaphragm with the same quality of steam as illustrated in Fig. 8.2b. The upper half will be supplied by heating steam from the upper outer ring (channel 2), whilst the lower half from the lower inner ring. This can be described as follows:

1. The upper outer ring can be divided into two channels, channel 2 and channel 3. These channels must be designed so that the amount of steam from the entrance (point 1) can be divided into two nearly equal halves for heating the upper and lower halves of the diaphragm.

2. The blades in the upper half receive steam from channel 2. The condensate will be collected in the upper inner ring.

3. Through the tubes (channel 5) inside the first and the last blades of the lower half, the condensate (from the upper half) can be drawn into the lower outer ring (channel 6). The path of the condensate flow is kept separate from the steam as shown in Fig. 8.2c.

4. The blades in the lower half are supplied by steam from channel 3 through the first and the last blades in the upper half (channel 4). The heating steam will be distributed from the lower inner ring to the blades of the lower half.

5. The condensate from the lower half will accumulate in the lower outer ring (channel 6) and mix with that from the upper half.

6. The total condensate from the diaphragm will discharge through the exit (lowest point or point 7) to the feed pipe.

(v) The condensate from the lower end of the diaphragm will be put back into the main feed water pipe before the condenser pump, in order to extract all the available energy from it.

The differences between the two suggested heating methods in (iii) and (iv) are:

1. The Akhtar proposal is less complicated to design.

2. The heating operation in the new alternative is more efficient than that by Akhtar et al, since the same quality of steam is supplied to both upper and lower blades resulting in a uniform blade surface temperature. Therefore less heating steam will be required to achieve the same minimum blade surface temperature for avoiding deposition of the fog droplets.

8.4 Calculation of Costs and Benefits of Blade Heating

This section examines the costs and the benefits associated with adopting the proposed blade heating design for a new turbine. The following section (8.5) describes how the quantified costs may be compared to arrive at an economic decision.

The cash flows in and out of the operating company that result solely from the investment are shown for each year of the turbine life in Fig. 8.3 and are listed as follows:

(i) Potential benefits

Adopting blade heating will avoid any reblading during the turbine life. However without blade heating (as in the conventional turbine) it is likely that the last row of L.P. rotor blades will have to be replaced at least once (at about the half life which is year 15). Two costs would then be incurred:

1. The cost of new blades to replace the eroded ones.
2. The outage cost, which is the extra cost of running a marginal, lower efficiency station while the reblading is carried out.

(ii) Costs of achieving these savings

The additional costs of building and running a new turbine with hollow diaphrams in the last stages for fixed blade heating are:

1. The capital cost which is the differential cost between the new hollow diaphragm and a conventional one, and associated pipework and instrumentation.

2. The running cost which is the cost of the additional fuel used to heat the fixed blade. It is assumed that the heating of the blades will be stopped at year 32 (i.e. eight years before the end of the turbine life) since erosion can be accepted for the remaining life of the turbine.

The balance between the costs in (i) and (ii) will determine the sign and the magnitude of the value of the investment. Two economic cases will be considered and analysed in the present work:

Case I

As though a decision had been made to adopt hollow blade heating for a 500 MW set due to start operation in 1967. During the 1960's a large number of 500 MW turbines having one H.P., one I.P. and three L.P.s were ordered. A turbine bought then will now have reached its half life when reblading is assumed to be required. Therefore all cost information up to reblading is based on published data.

Case II

As though a decision was taken in 1982 for a 660 MW turbine having one H.P., one I.P. and two L.P.s for which all economic data must be estimated.

8.4.1 The capital cost of hollow blade diaphragms

G.E.C. (139) and C.E.G.B. (144) have estimated the costs of a solid (conventional) and a hollow (new) diaphragm. The cost of a single solid

diaphragm for 660 MW L.P. turbine is £110,000 (price in 1982). The expected cost of a hollow diaphragm with steam and condensate piping and instrumentation is about twice the cost of the conventional diaphragm. Therefore the differential cost will be about £110,000 (price in 1982). This is the capital cost (CC) of the investment decision. To study the 1967 decision of using the blade heating, the capital cost must be determined for that year by deflating the cost in 1982 to 1967 prices. The inflation rate for the diaphragm capital cost has been estimated using published price indices (material and fuel index and wages index) for the Electrical Engineering Industry. The total costs of that industry (Ref. (145)) are made up of:

Material and fuel	58%
Wages	28%
Other costs	14%

Therefore the diaphragm cost is assumed to have moved in line with the indices for "material and fuel" and "wages", weighted 2/3 and 1/3 respectively.

The values of the indices of the material and fuel for electrical machinery are obtained from Ref. (146) whilst those for wages are published in Ref. (147).

The average index can thus be determined from

$$I_{av} = \frac{2}{3} I_{material} + \frac{1}{3} I_{wages} \qquad (8.20)$$

where I_{av} = average index; $I_{material}$ = material index; I_{wages} = wages index. The inflation rate, for year (a + 1) therefore, can be defined as

$$f'_{av}(a+1) = \left(\frac{I_{av}(a+1)}{I_{av}(a)} - 1\right) \times 100\% \qquad (8.21)$$

Figure 8.4 shows the variation of the three indices over the last sixteen years whilst the values of the resulting inflation rate for electrical machinery capital costs are listed in Table 8.1.

The future cost of a new diaphragm may be less than that estimated merely by inflating present costs for the following reasons:

(i) improvements in manufacturing technology;

(ii) a cheaper material can be used, since erosion is being prevented.

These factors have not been taken into account in the present work.

8.4.2 The running cost

The only running cost is the cost of fuel (coal) for blade heating. This cost can be calculated from the following equation:

$$FC(a) = \dot{Q}_{coal}\ P_{coal}(a)\ O_{hr}(a) \times 3600 \qquad (8.22)$$

where $FC(a)$ = cost of the coal in year a (£)

$P_{coal}(a)$ = price of coal in year a (£/kJ)

$O_{hr}(a)$ = number of operating hours in year a

$\dot{Q}_{coal}$ = the required amount of heat from the coal (kW).

The parameters of equation (8.22) can be determined as follows:

(i) The heat required from the coal to the heating steam is equal to the enthalpy of the heating steam divided by the boiler efficiency.

$$\dot{Q}_{coal} = \frac{h_{fg} \times \delta\dot{m}_{boiler}}{\eta_{boiler}} \qquad (8.23)$$

(ii) The price of coal which is given by:

1. C.E.G.B. (148) over the past sixteen years.

2. C.E.G.B. (149) over next fifty years.

The future price of coal is influenced by world economic development and other energy prices. For the United Kingdom economy, the C.E.G.B. have described five alternative scenarios for U.K. economic development, prepared in the context of three world economic background cases: potentially high, medium and low levels of economic growth. Ref. (149) describes estimated U.K. energy supplies and prices, U.K. energy demands and C.E.G.B. electricity supplies consistent with the scenarios up to the year 2030. Prices are in real terms; therefore prices in money terms which are required for the present work can be estimated by inflating prices from Ref. (149). The five scenarios A, B, C, D and E for the U.K. economy which have been developed present differing estimates of economic activity both in terms of composition and level. These estimates vary according to factors such as resource utilisation, degree of success of economic policy, rates of increase in productivity and demand, and world economic development. The cases of B, C and D are consistent with more than one outcome for the world economy whilst cases A and E are consistent only with the case of high and low world economic growth respectively. Details of the conditions of the scenarios can be found in Ref. (149) and these are presented in Appendix 8B.

The actual and predicted prices of coal (in money terms) over the life of the steam turbine can be seen in Fig. 8.5 when scenarios A and E are used and inflation rates of 7% and 11% are assumed for the period 1982 up to the end of the turbine life. The inflation rate has a great effect on the estimated (future) price of the coal.

(iii) The number of operating hours each year ($O_{hr}(a)$).

Four power stations - Ferrybridge - C (in the north-east), Eggborough (in the north-east), West Burton (in the midlands) and one designed for the future - were selected to study the economics of the blade

heating method. The annual operating hours of the first three power stations for the past sixteen years have been published in Ref. (148). The number of running hours of a power station is dependent on the following inter-related factors:

1. The size of the power station compared with the latest current design.
2. The efficiency of the power station.
3. The demand factor for electricity.
4. The age of the power station.

Bartlett (150) has given a typical distribution of annual operating hours over the life of a turbine. This is an American source of information in the 1950's; no equivalent British information has been found. Using this distribution in Ref. (150), the annual running hours for the remaining life of the existing power stations and for a future one have been estimated. However the total (actual and estimated) operating hours for each station are nearly equal, being in the range 167,000 - 170,000 hours (i.e. the difference between the maximum and minimum total operating hours is about 1.8%). The total operating hours of a typical coal station was given by the C.E.G.B. (144) to be in the range 150,000 - 200,000 hours.

Table 8.1 shows the actual and estimated coal price and annual operating hours over the life of the four turbines in the four power stations.

8.4.3 The cost of the reblading

G.E.C. (139) has given the cost of the blades of the last L.P. rotor for a 660 MW turbine as £101,000 (price in 1982). This value was confirmed

by the C.E.G.B. in the north-west (144). Reblading was expected by the G.E.C. to be required in about year fifteen of the turbine's life. Blade heating may lead to cost savings for a future turbine for the following reasons:

(i) The problem of erosion can be overcome. Therefore, cheaper materials can be used for manufacturing the rotor blade.

(ii) The aerodynamic and thermodynamic parameters of the passages of the last rotor blades will be improved due to suppression of the coarse water and reduction of wetness fraction. Thus the cost of output energy will be lower since the rotor efficiency will be increased.

(iii) The belt drainer for removal of coarse water will no longer be necessary thereby reducing the cost of the turbine.

8.4.4 Cost of the outage time during reblading

If any particular station has to be taken out of service for reasons other than lack of demand then the power it would have provided must be supplied by the "marginal station" which is less efficient. The outage cost is therefore the additional cost of running the lower efficiency station. The C.E.G.B. in the north-west have estimated the running cost of nuclear, coal and oil stations as:

- Nuclear about £10/MW h (1982 prices)
- Coal about £18/MW h (1982 prices) for a 500 or 660 MW turbine and about £22/MW h (1982 prices) for the older and smaller turbines
- Oil about £25/MW h (1982 prices).

Therefore the outage cost of a 660 MW turbine of a nuclear power station replaced by a coal station will be about £10/MW h (i.e. about £160,000/day), and that for a modern coal station replaced by an older station will be about £2-4/MW h (i.e. £32,000 - £63,000/day for a 660 MW turbine and £25,000 - £50,000/day for a 500 MW turbine).

In 1982 Harris (151) gave the cost of one day's loss of generation from a 660 MW steam turbine to be about £270,000 for a nuclear power station and about £60,000 for a coal power station; the last figure is also quoted by the C.E.G.B.

The efficiency of the marginal station depends on the electricity demand (during the winter lower efficiency stations have to be run to meet the demand). Therefore the outage cost varies during the year. Outage costs are lowest during the summer period and hence maintenance work including reblading would normally be carried out then. Recently Wronski and Wilson (152) from the C.E.G.B. have published the outage cost in winter and summer time for a 500 MW turbine in a coal station. The figures are £60,000 and £42,000 per day in winter and summer respectively. For the economic evaluation a figure of £50,000/day is used as the outage cost for a 660 MW turbine and £40,000/day for a 500 MW turbine. For a number of reasons (to be discussed later), the present work is concerned only with a steam turbine in a coal power station rather than in a nuclear station.

According to the C.E.G.B. (144), the downtime for reblading is about fourteen weeks and is distributed as follows:

(i) Two weeks for dismantling the turbine. This is considered to be part of the turbine inspection.

(ii) Eight weeks are required to repair a rotor damaged by erosion or to replace it with a new rotor. Of this, four weeks is usually taken for inspection and repair of other parts of the turbine. Therefore the remaining four weeks period is considered to be the outage time which could be saved if reblading is avoided by using blade heating.

(iii) Four weeks for re-assembling the turbine.

8.4.5 The C.E.G.B.'s cost of borrowing

The C.E.G.B.'s cost of borrowing over the past sixteen years has been calculated from the total borrowing at the year end and the interest charged for that year; these are published by C.E.G.B. in Ref. (153).

$$\text{Interest rate } i(a) = \frac{\text{interest paid during year a}}{\text{total borrowing at the end of year a}} \times 100\% \qquad (8.23a)$$

Figure 8.6 shows the interest rate from equation (8.23a) and (for comparison) the bank lending rate, from Ref. (154), over the first sixteen years of the 1967 turbine. The figure also shows the linear regression line for the bank lending rate over the period; it can be seen that the C.E.G.B. borrowing rate remained about 3% below this line over the whole period. It is likely that the present and future governments will expect the C.E.G.B. to pay interest closer to the market rates.

8.5 The Economic Method of Investment Appraisal

In its simplest form the method assumes the investment is risk free and all cash flows are certain. The effect of uncertainty will be examined later in this Chapter. The approach is to identify and estimate the cash outlays and benefits associated with the investment and to compare these

to establish whether a net profit or loss would be produced. The cash flows over the life of the project must be converted to constant value terms, since the pound of next year will not have the same value as that of today. A pound received now is more valuable than a pound to be received one year from now because of investment possibilities that are available for today's pound. If the pound received is used now for consumption, it means that the owner is giving up the option of more than one pound's worth of consumption in a year's time. Therefore, a sum of money (A_{CF}) now is held to have the same value as the sum $A_{CF}(1 + \frac{i}{100})$ one period from now. In other words, the assumption is that the exchange rate between money now and money one period in the future is the same as the ratio of 1 to $(1 + \frac{i}{100})$ one period hence. For that reason future receipts should always be converted into equivalent present values in order to compare them with present receipts and to determine whether the investment yields more cash than would alternative uses of the same amount of money (such as lending or depositing in the bank). There are two techniques which are commonly used in the appraisal of investment projects: the net present value and the internal rate of return.

8.5.1 Net present value method (NPV)

This is the classical economic method of investment appraisal; it is widely discussed in the text books such as Refs. (155, 156). The value of future money is not the same as that of present money. The present value (PV) of any sequence of future cash flows is found by discounting at the firm's discount rate all future net cash flows to their present value equivalent. The discount rate is the cost of capital or the interest rate in the present work.

$$PV = \frac{A_{CF1}}{(1+i_1)} + \frac{A_{CF2}}{(1+i_1)(1+i_2)} + \cdots\cdots + \frac{A_{CFn}}{(1+i_1)(1+i_2)\cdots(1+i_n)} \quad (8.24)$$

where $i_1, i_2 \ldots i_n$ = discount rate (divided by 100%) at year 1, 2, ... n.

$A_{CF1}, A_{CF2} \ldots A_{CFn}$ = the net cash flow during year 1, 2, ... n.

n = the life of the project in years.

If the discount rate is uniform over the life of the project, equation (8.24) becomes,

$$PV = \frac{A_{CF1}}{(1+i)} + \frac{A_{CF2}}{(1+i)^2} + \ldots \frac{A_{CFn}}{(1+i)^n} \tag{8.25}$$

Equation (8.25) can more conveniently be written as

$$PV = \sum_{a=1}^{a=n} \frac{A_{CFa}}{(1+i)^a} \tag{8.26}$$

The net present value (NPV) is determined by subtracting the initial investment outlay (A_{CF0}) of the project from the cumulative present value of the cash flows.

$$NPV = \sum_{a=1}^{a=n} \frac{A_{CFa}}{(1+i)^a} - A_{CF0} \tag{8.27}$$

If the NPV is positive, the project is profitable.

An index of profitability commonly quoted in economic texts is defined as:

$$PI = \frac{\text{PV of all benefits}}{\text{PV of investment cost}} \tag{8.28}$$

If the profitability index (PI) is greater than one, the project generates profit. The bigger the value of PI the greater the profit the investment earns. It can be interpreted as the benefit earned (at present value) by each unit of money invested.

8.5.2 Internal rate of return method (IRR)

The internal rate of return (yield) is defined as the rate of

discount which reduces the cash flows from the project to a present value equal to the investment cost of the project. Stated another way, it means the discount rate which results in a zero NPV. Therefore, the internal rate of return (IRR) can be calculated from the following equation:

$$\left[\frac{A_{CF1}}{(1+IRR)} + \frac{A_{CF2}}{(1+IRR)^2} + ... \frac{A_{CFn}}{(1+IRR)^n} \right] - A_{CFO} = 0 \qquad (8.29)$$

This equation can be solved iteratively by substituting various values of IRR until one is found which satisfies the condition of the equation. This iteration can be done most efficiently by a graphical solution. The NPV of the project is calculated for various trial values of the discount rate (i) and the two are then plotted. The point of intersection of the curve with i-axis gives the value of IRR, as shown in Fig. 8.7.

8.5.3 Application of these appraisal methods to a conventional project

The most common form of investment has cash flows as follows:

1. Capital cost which is at year zero of the project life.
2. Benefits (cash inflows) over the life of the project (year 1 to n).

Therefore, the sign of the cash flow changes only once, i.e. from - ve to + ve as illustrated in Fig. 8.8a. This distribution of cash flows will give one value for IRR only. For example, the life of a project is five years and the cash flows in money terms are as follows:

	Year 0	Year 1	Year 2	Year 3	Year 4	Year 5
Cash flow (£)	-1000	+250	+250	+250	+250	+250

The economic evaluation of this investment can be obtained by using the NPV or the yield method. Assume the market interest rate is 10%; we find that (using equations (8.27), (8.28) and (8.29)) NPV = - £52.3, PI = 0.95

and IRR = 7.2%. These results indicate that the project is not profitable, and the incurred loss is £52.3 (at year 0 values).

However, it is common for benefits to be constant in "real" terms, and consequently for them to rise in line with inflation, e.g. for an inflation rate of 8%:

Year :	0	1	2	3	4	5
Cash flow (real terms) £ :	-1000	250	250	250	250	250
Cash flow (money terms)£ :	-1000	250(1.08) = 270	250(1.08)^2 = 292	250(1.08)^3 = 315	250(1.08)^4 = 340	250(1.08)^5 = 367

The real rate of interest is defined as

$$i_r = \frac{1 + i}{1 + f'} - 1 \qquad (8.30)$$

Therefore when i = 10%, f' = 8%, $i_r \approx 2\%$.

The appraisal must be carried out either in money terms for both the cash flows and the interest rate, or in real terms for both; the results will be identical by either method.

The result of the second example (whether working in "money" or "real" terms) is : NPV = + £183.5, PI = 1.18 and IRR = 15.5%. It can be seen that in this case the investment is profitable, making a profit of £183.5 (at year zero values). The yield is in "money" terms and it is higher than the market discount rate (which is also in money terms). The yield in "real" terms is 6.9%.

It is found that one change of sign of the cash flows over the life of the project will give a unique value of the yield (IRR) and thus for a cash flow distribution of that type the economic evaluation is straight forward by using equations (8.27), (8.28) and (8.29).

For cash flow distributions that change sign twice (e.g. as a result of a negative cash flow in the last year of the project in order to close-down the project), there are two mathematical solutions for IRR. In general, n changes of sign give n mathematical solutions. Some writers (e.g. (155)) suggest that this can be resolved by discounting the negative cash flows forward to earlier years using the normal market discount rate (i) until the accumulated final year cash flow becomes positive. This can be explained better by giving an example. Asssume a project has four years life and the cash flow distribution is

Year	:	0	1	2	3	4
Cash flow (£):		-500	+400	+400	+250	-500

The discount rate is 10%. The procedure to change this distribution of cash flows with two changes of sign to a distribution with one change of sign in order to calculate the yield is:

1. Discount year 4 to year 3 and calculate the equivalent cash flow in year 3 which is - £204.5 (i.e. 250 - 500/1.1).

2. Equivalent cash flow is still negative, so discount it to year 2. Therefore the equivalent cash flow in year 2 is + £214 (i.e. + 400 - 204.5/1.1).

3. Equivalent cash flow is now positive. Hence calculate the single value of IRR for the following cash flow:

Year	:	0	1	2
Cash flow (£):		-500	+400	+214

The yield is found to be about 16.7%. There is only one change of sign and therefore this is the only solution for IRR.

This procedure can be interpreted as follows. The surplus benefit earned in year 2 is £400 - 214 = £186. This is invested at 10%. The year 3 benefit of £250 is added to it for investment, thereby together yielding £500 in year 4 to fund the outflow required in that year. Note that a value of i = 25% applied to the original cash flows gives NPV equal to zero, but this is a false solution since, by definition, surplus benefits from years 2 and 3 cannot be invested elsewhere at 25% to yield the sum required for the year 4 outflow. It is necessary to apply this procedure to the present project.

8.5.4 Application of the appraisal methods to this project

In the present proposal the cash flows, as seen in Fig. 8.3, are all outflows until year 15; then very large benefits in year 16 are followed by further outflows (running costs) for the rest of the project. Thus there are two changes of sign of the cash flows - from negative to positive and from positive to negative. Whilst the calculation of NPV is straight forward, the calculation for yield will result in two mathematical values and even a meaningful value is likely to be false as shown in the previous section. To simplify the problem, the distribution of the cash flows can be modified to give only one change of sign like a conventional investment. The modification is made as follows:

1. By making provision for the running costs from year 1 up to year 15 in the year 0 investment, in addition to the diaphragm cost (Fig. 8.8b). The cash flows from year 1 to year 15 are discounted by the actual (for Case I) or estimated (for Case II) interest rates.

2. By making provision for the running costs from year 16 up to year 32 out of the net benefits received in year 16 (Fig. 8.8b). The cash flow from year 17 to year 32 are discounted by the assumed interest rate (i).

Therefore the cash flows of the present project will consist of a large capital cost in year 0 in order to obtain a benefit in year 16. The modified distribution of the cash flows will give a single value of the yield. This approach also seems to give the most satisfactory interpretation for the profitability index (rather than treating all running costs as negative benefits). Negative cash flows can be regarded as either additional investments or as negative benefits. Consequently there is no indisputable way of defining PI for all distributions of cash flow.

8.6 The Results

There are two groups of results: firstly those based on best estimates of the economic parameters and secondly those which test uncertainty associated with the costs.

8.6.1 The results without sensitivity testing

Two cases are considered here:

Case I (1967 decision): The parameters for economic evaluation of the project are assumed as follows:

1. Ferrybridge - C power station has been selected. Its first year of operation was 1967; at that time a number of 500 MW turbines were already in use. The results for the other power stations studied (Eggborough and West Burton) are not shown in this work because they are very similar - the only difference between the three stations being the number of annual operating hours (bearing in mind the difference between the total operating hours for each station is less than 2%).

2. The inflation rate from 1983 up to the end of the turbine life is assumed to be constant at 7%. Domestic inflation has fallen from a peak of 28% in 1974 to 5.2 in April 1984. Government policy is

to use monetary controls to continue this fall. The Government predicts that the inflation rate will be below 5% for the next four years. A recent report by the Liverpool Research Group in Macroeconomics (157) have predicted the inflation rate to be below 4% for the next four years. A recent report on the Channel Link (158) by a major Anglo-French banking consortium assumes an average infaltion rate of 9% for the next eight years.

Now that the U.K. has its own oil and the demand for oil has fallen, it seems unlikely that steep rises in inflation such as those experienced in 1974 and 1979 will be repeated. It is therefore felt that a figure of 7% for the inflation rate (as an average of the values of inflation rates from Refs. (157, 158)) is both realistic and reasonably conservative.

3. The interest rate is assumed to be 9% for the period between 1983 and the end of the turbine life. In the long run we would expect the interest rate to be slightly higher than the inflation rate, in order that investors receive a positive real rate of return that would encourage them to invest rather than spend on consumption. For the Channel Link (158), an interest rate of 13% was assumed i.e. a real interest rate of 4%. The Government (159) in 1978 set a target real rate of return for the Nationalised Industries of 5% (this was set when inflation was running at 10.75%). The Liverpool Research Group in Macroeconomics (157) predicts a rate of interest of below 7%, i.e. a real rate of interest of less than 3%. For this study we have assumed a 2% real rate of return over and above the 7% inflation figure i.e. an interest rate of 9%.

4. Scenario C is used to define the future price of coal since it is the most likely one, and the one used by the C.E.G.B. for the Sizewell-B inquiry.

Figure 8.9 shows the cumulative net present value over the life of the project (costs discounted to 1967). The net present value for the whole project life is therefore £300,000. This is the extra wealth created by investing about £160,000 (£108,000 for hollow diaphragms and £52,000 "earmarked" to pay running costs up to year 15). The net benefit is about £460,000 (£570,000 for the rotor and outage cost savings in year 16 from which must be "earmarked" about £110,000 to pay running costs for years 16 to 32); all costs are in 1967 prices. The corresponding profitability index is about 2.9. The internal rate of return for this project is 15% and the "real" internal rate of return is ((1.15/1.07) - 1) = 7.5%.

Case II (1982 decision): For a future station the economic parameters were assumed as follows:

1. The inflation rate is constant and equal to 7%.
2. The interest rate is constant and equal to 9%.
3. Scenario C is employed to define the future price of coal.
4. The distribution of the annual operating hours is the same as the Bartlett American distribution, Ref. (150).

The distribution of the cumulative present value (1982 costs) over the life of the future station is illustrated in Fig. (8.10). The net present value of the project is found to be just less than £0.5m; this is the net profit produced by investing about £0.7 m (£0.44m for hollow diaphragms and £0.26m "earmarked" to pay running costs up to year 15). The net benefit is about £1.2 m (£1.4 m for the net benefits in year 16 from which must be "earmarked" about £0.2m to pay running costs for years 16 to 32). All the costs are in 1982 prices. The profitability index

is about 1.7. The yield (IRR) is about 12½% and the "real" internal rate of return is about 5%.

8.6.2 The results of sensitivity testing

Uncertainty has a great effect on the investment decision. Therefore, uncertainty in estimating the outlay and cost savings must be taken into account in order to evaluate more comprehensively whether the blade heating is economic or not. In the previous study we have used the best estimates for all costs and we will refer to these as the "base case" for Case I and Case II. We can now examine the effect of a variation in each cost on the net present value, whilst all other parameters keep their base case values.

8.6.2a Case I (1967 decision)

1. The price of coal:

The price of coal during the past sixteen years (from 1967 to 1982) was taken from the C.E.G.B. quoted costs. The future price of coal in real terms depends upon the scenarios described in section 8.4.2. The widest range of future prices can be studied by using the extreme cases of the scenarios which are A and E. Scenario A price is about 15% above that from scenario C whilst the price from scenario E is about 10% below that from C. Use of scenario A would result in an increase in the present value of the running costs over the life of the turbine of about £25,000 (1967 prices); this would reduce the NPV of the project by about 8%.

2. Inflation and interest rates:

Figures 8.11 - 8.13 show the effect of the variation of future inflation on the cumulative present value over the life of the project. If the interest rate is kept constant at 5% (Fig. 8.11) an increasing inflation rate results in decreasing the present value of the project since the coal costs will be increasing in money terms. As has been explained,

all cash flows up to and including year 15 are based on actual costs. The estimate of future inflation therefore only affects costs after year 15 (i.e. only the coal costs). If the interest rate (i) is high then the reduction in the NPV will be much less (Fig. 8.13). On the other hand if inflation is held constant, an increase in the interest rate results in an increase of the NPV of the project. As long as the real rate of interest ($i_r = \frac{1 + i}{1 + f} - 1$) is positive, the variation of inflation and interest rates has little effect on the NPV as shown in Fig. 8.14. However if i_r is negative, the NPV is sensitive to the change in the values of interest and inflation rates. It can be seen that the NPV is positive even when the value of i_r is very low (i.e. $i_r < -4\%$).

The project becomes unprofitable (PI < 1) at a real rate of interest less than - 6% (Fig. 8.14). However as explained in section 8.6 it is unlikely that the average real rate of interest would be negative when looking at periods of more than 15 - 20 years.

If the inflation rate is greater than the interest rate (i.e. $i_r < 0$) the running costs from year 16 up to year 32 would be higher than the base case, leading to a lower profitability of the project. For positive values of the real rate of interest, inflation has little effect on the values of NPV and PI and hence on the economic decision.

3. Diaphragm cost: If the cost of the hollow diaphragm is higher than that given by the G.E.C., the NPV will be reduced by the amount of the increase in the diaphragm cost. The uncertainty in this cost could be as great as 50%. Therefore, the maximum reduction in the NPV of the project would be about £50,000. This would reduce the NPV by less than 20%.

4. Outage cost: This is defined by two factors,

(i) cost of one MW h : The additional cost of one MW h from a steam

turbine in a marginal coal power station is between £2 and £4. If the outage time is constant (four weeks), the reduction in the outage cost is about 40% when the minimum cost of outage is used (£2/MW h) . Therefore, the NPV will be decreased by about £130,000 (i.e. about 45%).

(ii) Outage time: Four weeks is given by the C.E.G.B. as the additional outage time needed to replace or repair the damaged rotor after about 15 years running. If the outage cost is kept at £3.3/MW h, then it is not until an outage time of only half a week is reached that the NPV falls to zero, assuming a real rate of interest of 2%. The period of outage time would always be greater than this unless some other major overhaul task was also being carried out at the same time on the turbine. This would seem unlikely.

5. Reblading cost: If the uncertainty in the rotor cost is about 50% (higher than the actual cost), the NPV would be reduced by about £90,000 (i.e. about 30%) assuming i_r equal to 2%. However, using the blade heating technique the required rotor could be cheaper than the existing one. Therefore the maximum reduction in the NPV is likely to be less than 30%.

8.6.2b Summary of the sensitivity analysis of Case I

The effect of uncertainty on the NPV can be seen summarised as follows:

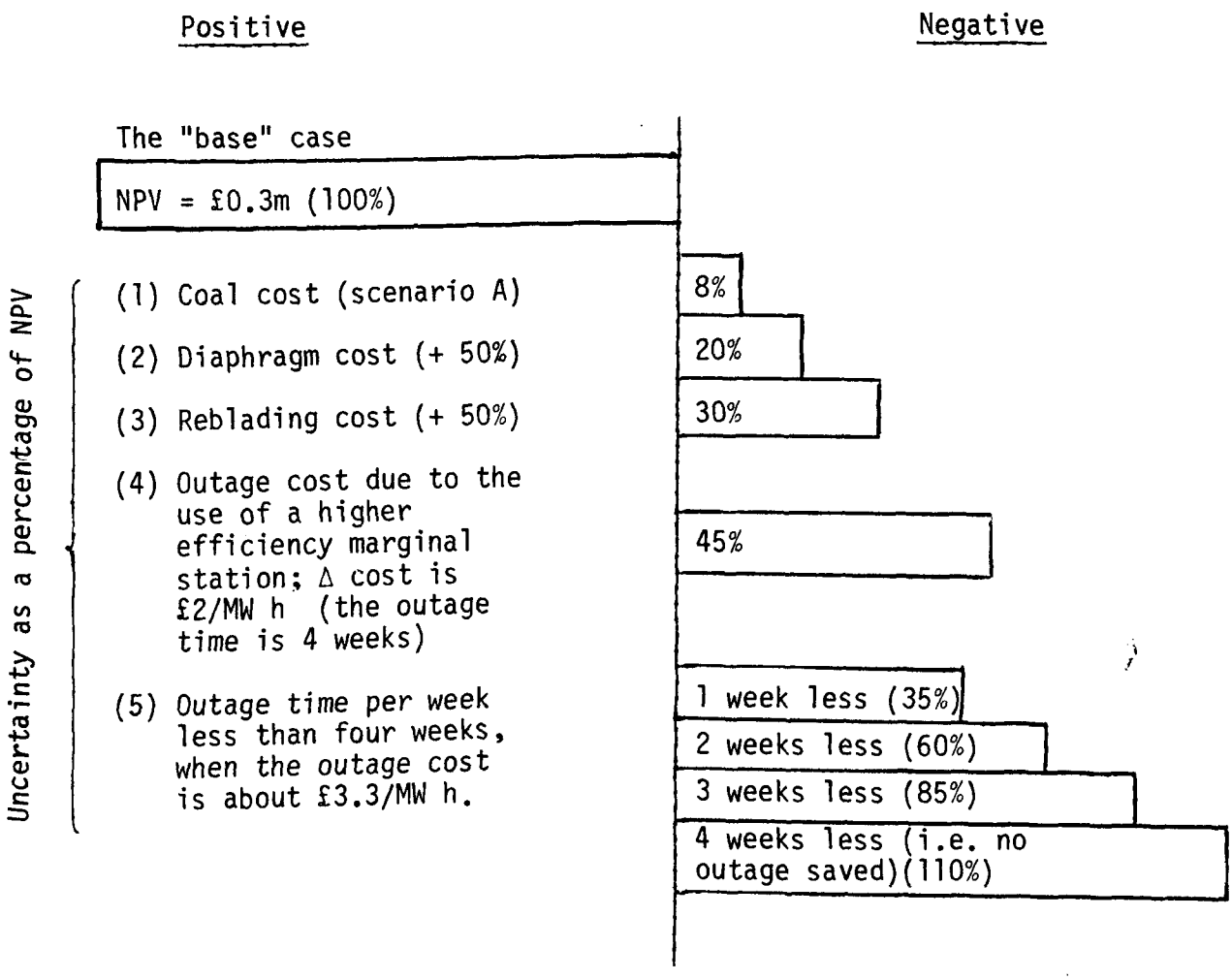

From this summary, the following points can be concluded:

(i) Consider all the factors except the duration of outage; profitability is only at risk if, at the time of reblading, demand is very low and few high efficiency stations are shut down. Under these two circumstances the marginal station would be a relatively efficient one, producing power at perhaps only about £2/MW h more expensively than the station being rebladed. Otherwise positive NPV seems relatively certain.

(ii) The overwhelming factor affecting profitability is the duration of outage attributable only to the reblading. This was discussed in detail in section 8.6.2a. It is left to the C.E.G.B.'s engineers to examine their records of downtime durations and to assess the likelihood of an outage duration less than four weeks that could put profitability in some doubt.

8.6.2c Case II (1982 decision)

1. The price of coal: The predicted"real"price was taken from the five scenarios given by the C.E.G.B. The change in the coal price has a greater effect on the NPV of the 1982 decision than that of the 1967 decision since the cost of coal will affect costs during the whole life of the project except the last eight years. Scenario A gives a maximum possible price of coal. The maximum increase in coal cost results in the maximum decrease in the NPV which is about £0.11m when the real interest rate is 2% (bearing in mind that the NPV of the base case is about £0.5m), i.e. the reduction in the NPV of the project due to using scenario A is about 25%.

2. Inflation and interest rate: Inflation has a major effect on the money values of the coal cost, reblading cost and the outage cost. An increase in f' results in an increase in the money costs of reblading, outage and coal. Because the cost savings are larger than the outlay costs, an increase in inflation will appear to increase the NPV of the project as shown in Figs. 8.15 - 8.17. If the inflation rate is kept constant, an increase in the interest rate will result in a decrease in the NPV of the project. An increase in the real rate of interest results in a decrease in the NPV and the NPV will change its sign from positive to negative at i_r equal to 5.5% when scenario A is used and at i_r equal to 6.5% when scenario E is used as shown in Fig. 8.18. The profitability index

also decreases with increasing real rate of interest (Fig. 8.18). The PI is one at i_r equal to 5.5% when scenario A is used and at i_r equal to 6.5% when scenario E is used. Therefore, if i_r is greater than 5.5% the project will not be profitable. However it is unlikely that the average i_r will be as large as this in the long run. The shapes of the curves of Fig. 8.18 are different from those in Fig. 8.14 because of the major effect of discounting the future benefits. The shape of the curves in Fig. 8.18 are similar to those that would be obtained for a conventional investment (see section 8.5.3). The rising curves of Fig. 8.14 are untypical since inflation assumptions apply only after the benefit of year 15 has been received.

3. Diaphragm cost: If the uncertainty in the cost of the hollow diaphragm is 50%, the NPV of the project would be reduced by a maximum of about £0.2m (i.e. about 40%).

4. Outage cost: This consists of two factors:

(i) Outage cost of one MW h: this cost was given by the C.E.G.B. to be in the range of £2-4/MW h. A figure of £50,000/day (equal to £3.15/MW h) was used as the outage cost in the base case. Therefore if the minimum cost is used (£2/MW h) the reduction in the total outage cost will be 36% provided the outage time is constant (4 weeks). This uncertainty will cause a possible reduction in the NPV of the project of about £0.37 m (1982 prices), i.e. about 75%. A reduction in the outage cost of this size seems unlikely as discussed before (section 8.4.4).

(ii) Outage time: If the outage time is less than four weeks, the outage cost will be decreased and hence the NPV of the project will be reduced too. If the outage cost is kept at £3.15/MW h, then it is

not until an outage time of only 2.5 weeks is reached that the NPV falls to zero assuming a real rate of interest of 2%. The likelihood of the outage time being less than four weeks was also discussed in section 8.6.2a.

5. Reblading cost: If the cost of reblading is 50% higher than estimated, the NPV will be reduced by about £0.15m (i.e. about 30%).

8.6.2d Summary of the sensitivity results of Case II

The results of uncertainty in the costs and the benefits can be presented as a percentage of the NPV of the project as follows:

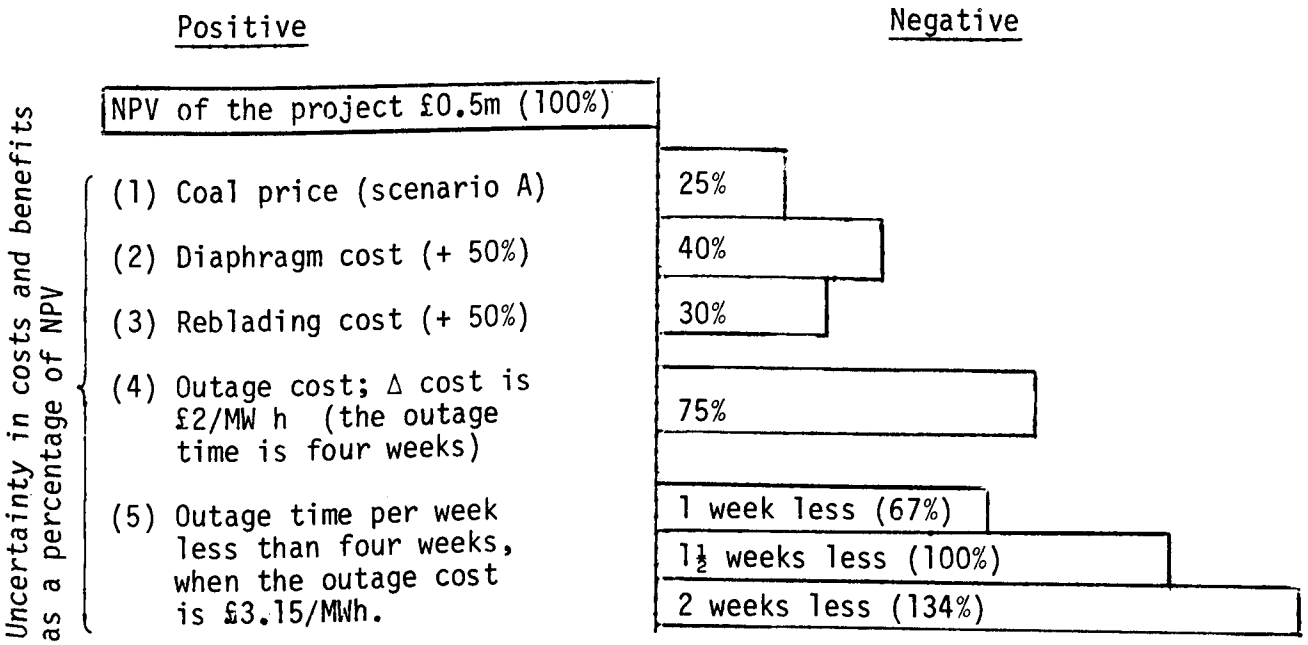

From this summary one can see that a combination of uncertainty of outage costs plus one factor from the rest, is enough to make the project unprofitable. However the probability of occurrence of all these uncertainties is not unity; therefore there is doubt about the outcome of the project.

To clarify the situation, statistical analysis can be used to

help reach an economic decision. Extreme values of each factor have been identified in section 8.6.2a and b according to the G.E.C., the C.E.G.B. and the other information. We have some confidence in the values of inflation (7%) and the real interest rate (2%). The values of uncertainty in the costs and benefits which have previously been discussed are probably too pessimistic and can be modified as follows:

1. Reblading cost: The cost was given by the G.E.C. They are continuing manufacturing 500 MW and 660 MW turbines. Therefore, the cost of reblading was based on actual costs and the uncertainty is probably less than 1% which is negligible compared with the other costs.

2. Diaphragm cost: A similar diaphragm was manufactured by the G.E.C. to use the suction slots method to drain the collected water on the blade surface. However they were unable to give us an estimate for the cost of a new hollow diaphragm for blade heating. They suggested a factor of two between a conventional and a hollow blade; therefore a 50% higher cost has a considerable change of occurrence.

3. Coal prices: The description of scenario A in Appendix 8B seems to represent an extremely optimistic outlook for the U.K. economy and is therefore unlikely to be achieved. Therefore the percentage reduction in the NPV previously quoted (8% for case I and 25% for case II) must be regarded as very pessimistic.

4. Outage cost: It is difficult to estimate the uncertainty of the duration and the cost of outage since although the base case data were given by the C.E.G.B., the G.E.C. doubted whether there would be any long outage time attributable specifically to reblading.

Therefore we assume that there is about a 5% chance of the outage cost being at or below the minimum figure (£2/MW h) and also a 10% chance of the outage time being less than 2½ weeks.

In this section the possibility of these uncertainties is defined in statistical terms such as standard deviation (S_D) and probability. The statistical analysis is an attempt to assess how the uncertainty in costs and benefits may affect the profitability of the investment.

Let us assume that the probability of occurrence of a particular value of a cost can be described by a normal distribution having a mean equal to the value of the cost used in the base case. The sensitivity analysis assumed an extreme, pessimistic value for the cost, and its effect on NPV has been calculated. The value of the standard deviation of the distribution of effect on NPV is estimated by assessing how extreme was the value chosen, e.g. if the likelihood of a more extreme value occurring is 10% then the value is 1.25 standard deviations from the mean. For example - for the coal price, if it is felt that the chance of a price in excess of even scenario A is about ½%, then there is a ½% chance of the NPV being reduced by £0.125m.

From any statistical text book, a normal distribution table shows that a 15.9% chance of being exceeded corresponds to one standard deviation, 6.7% chance represents 1.5 S_D, 2.3% represents 2.0 S_D, 0.6% represents 2.5 S_D and 0.1% chance represents 3 S_D . Hence a £0.125m reduction in the NPV (Scenario A coal price) can be written in S_D terms as follows:

$$£0.125m \approx 2.5\ S_D$$

Therefore, S_D (coal price) = £0.05m.

Estimates of standard deviation for the other costs are shown in Table 8.2.

TABLE 8.2

ASSESSMENT OF THE COMBINED EFFECT OF THE UNCERTAINTIES OF THE COSTS AND BENEFITS ON THE NPV OF THE 1982 PROJECT

Cost	Extreme case	Reduction of NPV due to extreme case £m	Likelihood of extreme case being exceeded (%)	Number of standard deviations from base case	Standard deviation of NPV reduction	$S_D^2 \times 10^{-3}$
Coal price	Scenario A	0.125	0.5	2.5	0.05	2.5
Diaphragm cost	Base case + 50%	0.2	2	2.1	0.095	9.025
Reblading cost	Base case + 50%	0.15	0.5	2.5	0.06	3.6
Outage cost	£2/MW h	0.375	5	1.6	0.234	54.75
Outage time	2½ weeks	0.5	10	1.2	0.416	173.05

$\Sigma S_D^2 = 0.243$; $\sqrt{\Sigma S_D^2} = 0.492$

Therefore the number of S_D is $\frac{0.5}{0.492} = 1.02$

The corresponding probability is 15%.

The standard deviation of all costs and benefits combined can therefore be determined by summing the variances (variance = S_D^2) for all costs and benefits and taking the square root. The probability of the 1982 project having a NPV less than zero can therefore be found from normal distribution tables at $(\frac{0.5}{0.492})$ standard deviations away from the mean. Accordingly the probability is about 15%. This result means that the chance of profitability is 85%.

8.7 Discussion of the Economic Results

This study deals with the future, about which we can never be certain. The economic theory is oriented towards accept/reject decisions based on a given set of conditions and assumptions. Inflation rate, discount rate, capital cost, coal price, annual operating hours, reblading cost and outage cost are all uncertain and they fundamentally affect the economic decision. Simple economic theory assumes certainty; best estimates for all the data are used in the calculations to arrive at a provisional decision. Then all the assumptions must be tested to find out the circumstances which might change the decision. Thus a decision can be made with more confidence that includes consideration of the consequences when important variables are different from those expected. The economic decision is based on the net present value (NPV) and the internal rate of return (IRR), both expressed as a function of the real rate of interest.

Inflation rose steeply in 1974 and 1979 because of the crisis in oil supplies and prices; these are mainly influenced by political considerations. Furthermore the growth in the world economy has been very low during the 1970s because there was failure to make any significant improvements in the extent of co-operation between world countries. It

seems unlikely that future inflation will rise as steeply as before and it may well be kept in single figures because:

1. The price of oil is currently nearly constant or slowly decreasing in the real terms.

2. United Kingdom and some other countries have recently become oil producers; therefore the supply and the price of oil is more controllable than before.

3. A commercial agreement was reached recently between the producers and the consumers of oil; this may lead to better co-operation between world countries.

4. The efficiency of power stations is continuing to improve so that the amount of fuel required is going down.

5. Other demands for energy are not rising as fast as they were during the early 1970 s because of the development of more energy-efficient processes, and projects to reduce energy losses.

6. Political and socio-economic reasons such as:

   (a) Monetarist policies.

   (b) New realism in wage settlements from improved management - employee co-operation, etc.

Therefore an average inflation rate of 7% seems realistic for the next 20 - 30 years. The real rate of interest in the long run can reasonably be assumed equal to 2%, i.e. the market interest rate is slightly higher than the inflation rate, giving a positive real rate of return for the investor.

Assuming certainty in the costs and the benefits of the investment, profit would be expected if the decision had been made in the 1967 case

and the 1982 case. The net profit of case I (about £1m in 1982 prices) is higher than that of case II (which is about £0.5m in 1982 prices). The yield and the profitability index for the project in case I are higher than those in case II, suggesting that the earlier investment was the more attractive.

The revised figures for uncertainty in section 8.6.2d suggest a new economic decision. In case I the combination of the worst values of costs and benefits (excluding the possibility of outage time less than four weeks) will result in a reduction in the NPV of about 60%, and the profitability index will reduce to about 1.1. Thus if blade heating had been adopted in 1967 a profit would be expected from the investment under all conditions. In case II the combined effect of uncertainty in all costs and benefits has a low probability (about 15%) of making the investment unprofitable. However this small chance of unprofitability must be considered carefully when a project for a new power station is being studied.

The blade heating method used in a turbine of a nuclear station would give better economic results for the following reasons:

1. The outage cost, which is about 70% of the cost savings, is about three times the outage cost for a coal power station.

2. The running cost, which is the fuel cost, forms about 50% of the total outlay cost. The published cost of nuclear fuel (relative cost/kJ) is about 0.6 of the coal cost.

Figure 8.19 shows the distribution of the costs and the benefits of the blade heating in a nuclear power station and in a coal station, for a decision made in 1982. The economic results of adopting blade heating in a nuclear power station can be listed as follows:

		Nuclear	Coal	
1.	NPV is about	£1.5m	£0.5	(in 1982 prices)
2.	PI is about	3.5	1.8	
3.	Yield is about	23%	13%	

The increase in the cost savings and the decrease in the outlay costs will result in an increase in the NPV of the project for a nuclear station of about 3 times that for a coal station. Therefore the nuclear station gives better results (more profitability) in the economic evaluation. A truly objective economic analysis cannot be made on a turbine in a nuclear station, since nuclear fuel costs are influenced by political and strategic factors (e.g. the production of plutonium).

The results show that if the decision to proceed with blade heating in a conventional station had been made in 1967, the project would be expected to be profitable, generating new wealth approximately equal in value about twice the original investment after repayment of that investment. If the decision was to be taken today, the element of uncertainty would have a great influence.

The analysis and sensitivity testing suggest that,

(i) investment in blade heating for a nuclear station is highly likely to be very profitable;

(ii) investment in blade heating for a coal station in 1967 would very likely have proved profitable;

(iii) investment in blade heating made now for a new coal-fired station is perhaps 85% likely to prove profitable.

If the increase in the efficiency of the last stage is taken into consideration, it means that the fuel cost would be very small and could be neglected. The net present value would therefore be increased by about 80%.

Thus the chance of unprofitability in case II would be reduced to about 0.1% corresponding to 3 S_D. Therefore, when W_{gain} (due to an increase in the last stage efficiency) is taken into account, a decision taken today is highly likely to be profitable.

However the steam heating method may well not be adopted by manufacturers and generating companies although the economic results are encouraging. The reason for this is that the payback period is too long; the investor normally wants to see his return within a reasonably short period (i.e. less than five years) whereas this investment requires him to wait fifteen or more years. A shorter payback period is required because:

(i) the longer the project is, the greater is the uncertainty about economic data (particularly the rates of inflation and interest), supply and demand, political influences and so on, and hence the greater the uncertainty about the final profitability, and

(ii) the investor will be unwilling to sink funds into a project if his business might not survive long enough to be able to reach the benefits.

Therefore a project of this duration would probably not be acceptable for a commercial company but it may be acceptable for a far-seeing public utility since it is able to make much longer term decisions.

The final decision on the economic value of blade heating for the control of erosion lies of course with the operating company. Their engineers must obtain and evaluate the latest data for the parameters described in this study and then assess whether the probability of profitability and length of payback are acceptable for their business.

CHAPTER 9

GENERAL SUMMARY AND CONCLUSIONS

9.1 General Summary

The method of internally heating the L.P. turbine fixed blades to prevent erosion of the rotor blade was first proposed in the late sixties. A number of experimental investigations, by using a simulation technique in order to understand the process of droplet deposition on the blade surface, have been carried out. However, no theoretical study concerning the performance of the heating method has been made, up to the present time. Therefore a theoretical investigation has been undertaken in order to understand the physical, the mechanical and the thermodynamic properties of the droplets inside a real turbine when heating or cooling of the blade surface is considered. In addition to this the experimental studies have also advanced the theoretical investigations in the field of wet steam flow.

The present work may be divided broadly into four parts:

1. Part One

This part consists of the first three Chapters. A general description and presentation of the erosion problem has been given in Chapter 1. Following this, Chapter 2 involves a review of the previous work which are concerned with:

(a) Generation and size measurement of the particles or droplets.

(b) The theories of evaporation and condensation between the droplets and the surrounding vapour.

(c) The theory of thermophoresis and its development.

(d) The mechanisms of deposition of the particles or droplets on the blade surface.

Chapter 3 gives a brief review and discussion of the previous methods used to:

(a) measure the deposition rate of the particles on the concave and convex surfaces of the L.P. steam turbine fixed blade;

(b) reduce or prevent erosion of the rotor blade.

Thus an extensive theoretical background and a historical review of the existing methods for suppressing the wetness or preventing erosion have been presented in this part.

2. Part Two

This part involves an experimental investigation (Chapter 4) into the generation and size measurement of particles and their deposition onto unheated and heated surfaces. Solid particles were produced using an atomiser-impactor generator and samples of the particles were analysed using the technique of electron microscopy. Statistical analyses were undertaken and particle mass-median diameters 0.135 and 0.186 μm, corresponding to uranin solutions of 3% and 5%, were obtained. The geometric standard deviation of the particles varied from 1.4 to 1.5. The apparatus and the main experimental work were described. Two arrangements for the wind tunnel were employed in order to obtain two incidence angles (two turbine loads) for the flow which were zero (full load) and - 15 degrees (part load). For each incidence angle the particle size, the inlet velocity and the concentration of particles entering the blade cascade and in the test blade passage were obtained, after which deposition measurements were carried out on the unheated blade. The blade was then internally heated (the temperature of the surface was controlled by adjusting the flow rate of the heating air) and the deposition measurements were repeated. The experimental results of this work

were compared with those from Refs. (4, 15, 37). To predict the result of deposition on the heated blade the value of the thermal conductivity of the uranin should be known. Using a standard procedure, the thermal conductivity of the uranin was measured within the range of the test temperature ($20 < t < 65^{o}C$) and was found to be equal to 0.43 W/m K.

3. Part Three

A theoretical investigation to predict the characteristics and properties of the vapour and the droplets inside the blade passage was carried out. This study was presented in Chapters 5, 6 and 7 as follows:

(a) Chapter 5 involves the calculation and analysis of the geometry of the blade passage, the relief of supersaturation, the developing of the boundary layer and the effect of laminarisation on the transfer of mass of the vapour between the potential and friction flows. The flow was assumed to be one-dimensional, steady and to be a perfect gas. The free stream velocity was predicted, by using the isentropic relationship between pressure and temperature, by using the energy equation. A teledeltos paper technique was used to:

(i) locate an estimated stagnation point;

(ii) determine the distribution of the velocity, temperature and pressure along the free stream line on the concave and convex surfaces;

(iii) define the shape of the stream and potential lines inside the blade passage in order to simplify the problem to one-dimensional flow for the purpose of calculating the properties of the flow outside the boundary layer.

The relief of the supersaturation was found as a function of the size of the entrained droplets. The effect of the condensation shock at the entry of the passage on the properties of the steam (pressure, temperature, velocity and enthalpy) was also taken into account.

The turbulent flow along the concave surface was found to start before the entry of the passage, whilst it was found to start at $x/c \approx 0.1$ along the convex surface. Therefore the flow inside the passage was considered as a turbulent flow since there is a very short laminar flow at the entry of the passage on the convex surface.

(b) Chapter 6 contains the prediction and analysis of the heat transfer from the blade surface into the wet steam flow. The size of the entrained droplets has a considerable effect on the amount of heat transfer from both blade surfaces. The reduction in the rate of heat transfer due to laminarisation was calculated. A formula for determining the adiabatic temperature of the wet steam flow was derived and presented in this Chapter. The effect of phase change on the temperature profile inside the thermal boundary layer was checked.

(c) Chapter 7 involves the theory of the behaviour of the evaporating/condensing droplet along the hot/cold surfaces, inside the boundary layer. Dispersion in droplet size inside the boundary layer was studied in detail.

This Chapter is the main Chapter in the thesis since it contains the

developed theory which is used in the present work. This theory can be divided into a number of stages as follows:

(i) The possibility of interactions between the droplets such as collision, bouncing and mutual fracture.

(ii) The growth or diminution of the fog droplets inside the vapour which is dependent on the temperature difference between the droplet and the vapour (Δt_{gf}). The theory of large droplets ($d > 2$ μm) was also taken into consideration since it may be possible to obtain such sizes of droplet when condensation is the dominant phenomenon.

(iii) The transfer of heat between the droplets and the vapour was determined as a latent heat exchange between the two phases.

(iv) The mechanisms of the movement of droplets smaller than 2.0 μm were studied and formulated into a mathematical model. A new model for deposition of fog droplets from the turbulent flow was devised by considering the thickness of the diffusion layer to be equal to the thickness of the velocity boundary layer. The Van Driest model was used to define the eddy viscosity (or eddy diffusivity of the droplet).

(v) The effect of thermophoresis on the movement of the droplet was determined by using the empirical formula due to Talbot et al (79).

(vi) The combined effects of evaporation/condensation, diffusion and thermophoresis were formulated mathematically. The net deposition velocity was determined from equation (7.39) which can be solved numerically.

(vii) The numerical method was the same as that used by Ryley and Al-Azzawi (131) except the size of the cell inside the boundary layer and the temperature of the surface are not constant. This modification enables the present method to be used for predicting the deposition of the particles in the simulated method. The size of the cell can be adjusted to any selected size.

(viii) The computer program was made from individually tested stages in order to be understandable.

4. Part Four

The final part involves the economic study of the steam heating method (Chapter 8). Information and data about the costs of the diaphragm, the rotor and the outage time were collected from the C.E.G.B. and the turbine manufacturer (G.E.C.). The ways of determining the interest rate, the inflation rate, the operating hours over the life of the turbine and the prices of the coal were presented. The annual quantity of the coal for heating the fixed blade was determined from the following factors.

(a) The value of a practicable blade surface temperature.

(b) The value of the heat transfer rate from the surface of the blade in order to maintain the temperature of the surface as in (a).

(c) The efficiency of the stator, the rotor, the penultimate stage and the final stage in order to find the change in the output of the turbine due to heating the diaphragm.

(d) The quantity of recovered work when the additional steam from the boiler passes through the H.P., I.P. and the first three stages of the L.P. turbines.

The details of the operation of the heating were presented. Two economic methods: the net present value and the yield, were used for appraising the investment in the heating method. Two decisions were examined:

(i) if the heating method has been used in 1967 when the first 500 MW steam turbine was employed;

(ii) if the C.E.G.B. used a new 660 MW turbine in 1982 with the heating method.

The time of employing the heating method had a great influence on the economic decisions.

9.2 Conclusions

The conclusions from the experimental and theoretical investigations can be summarised as follows:

1. The problems of growth or diminution of the fog droplets, diffusion through the laminar and turbulent flows and thermophoresis as a separate phenomenon were well understood. Davies (4) had calculated the deposition rate of solid particles due to the combined effect of diffusion and thermophoresis. However no attempt had been made to study the combined effect of diffusion and thermophoresis on the deposition of growth or diminishing droplets onto the blade surface as may occur in the flow inside the final stage of a low pressure steam turbine.

2. Submicron particles with a low polydispersion in size and having a geometric standard deviation of 1.4 to 1.5 can be produced from the atomiser-impactor generator. The electrostatic charges arising within the aerosol cloud fed to the wind tunnel were minimised by

means of the sonic-jet ion generator. Also the blade was earthed during the experimental running time to remove the remaining charge and the charge caused at the solid/air interface during the particle transportation inside the wind tunnel. The use of the mass-median diameter in the theoretical study appeared to best represent the size of the particle and produced good agreement between the theoretical and experimental results (Chapter 7).

The change in the total deposition of the particle when the incidence angle was changed from - 15^{o} to zero degrees is not considerable. This is true for the present experimental work when the flow velocity is low and the nature of the flow will not be significantly different from that of zero incidence angle.

3. There are more than one transition points along the concave and convex surfaces. Along the concave surface transition from laminar to turbulent flow occurred at x/c = 0.3, 0.69 and 0.945 whilst along the convex surface it occurred at x/c = 0.1, 0.455 and 0.57. The laminarised flow is considered as turbulent flow for determining the velocity and temperature profile. However, for the purpose of heat and turbulence calculation, the effect of laminarisation was taken into account. The thickness of the concave surface boundary layer is always greater than that of the convex surface.

4. The relief of supersaturation increases with the decreasing size of droplets generated by spontaneous condensation on the basis of constant wetness fraction (constant Wilson point). Supersaturated steam containing droplets with diameters less than 0.05 μm is restored to thermodynamic equilibrium before the throat of the passage. Thus the thermodynamic loss due to supersaturation

increases with an increasing droplet size and it was found to be equal to zero when the initial size of the droplets was nearly equal to or less than 0.01 μm since the supersaturation is completely relieved shortly after the entry to the passage. The rate of increase of the supersaturation loss is almost constant when the size of the droplets are greater than 0.5 μm, as shown in Figure 5.6.

5. If the nucleation takes place shortly before the entry of the passage the effect of the condensation shock on the properties of the steam, such as velocity, temperature, pressure and enthalpy is not significant. The increase in the pressure and the decrease in the velocity, the temperature and the enthalpy due to the condensation shock were found to be less than 0.2%.

6. It is reasonable to assume the supersaturated steam to be a perfect gas. However the definition of the stagnation temperature for the supersaturation flow is not the same as that for a perfect gas. A new equation therefore has been introduced for the stagnation temperature of wet steam flow (equation (6.8)).

7. The effect of acceleration on reducing the transfer of heat from the blade surface into the turbulent wet steam flow is very considerable, particularly when the flow is highly accelerated at the middle of the passage. It was found that a reduction of as much as 50% in heat transfer, below that typical of a turbulent boundary layer, occurs at $x/c = 0.2$ along the convex surface. The greater reduction in the heat transfer takes place at the throat of the passage, except for a very short distance on the convex surface only ($0.15 < x/c < 0.28$) where the maximum reduction occurs.

8. There is a possible second nucleation if the size of the droplets from the first nucleation have a diameter greater than 0.5 μm. The second nucleation could probably occur at or shortly after the throat since:

   (a) the subcooling temperature has a maximum value at the throat $\Delta T_s > 37^oC$;

   (b) it has been found by a large number of investigators that nucleation can take place only inside the divergent section.

   Therefore the convergent section, which forms about 93% of the blade passage is free from a second nucleation. In any case, in the present work the effect of a second nucleation can be neglected since the problem becomes very complicated and also the remaining length of the passage after the anticipated second nucleation is very short (about 7% of the passage length).

9. The amount of heat transfer from the blade surface into the flow is increased by increasing the size of the entrained droplets on the basis of the same surface temperature. The total value of heat transfer from the convex surface is about the same as that from the concave surface.

10. The droplets which are produced from nucleation are monodispersed in size inside the potential flow and are polydispersed in size inside the boundary layer. It is found that inside the boundary layer larger droplets are generated near to the surface since the variation of the expansion rate ($\dot{p}$) inside the boundary layer is similar in shape to the velocity profile. If the thickness of the boundary layer is large compared with the height of the blade passage, the polydispersion in the droplet size must be taken into account.

A statistical analysis was used to determine the average size of the entrained droplets.

11. The interaction between the fog droplets is due to Brownian motion and eddies of the turbulence only. It is found that no interaction can take place between droplets having a diameter greater than 0.1 μm. However there is a possible chance of interaction between the very small droplet ($d \lesssim 0.1$ μm) due to Brownian motion along about 30% only of the passage from the entry. The most probable result of interaction may be coalescence. The effect of the eddies on the interaction in the present work can be neglected since the turbulence intensity was low, less than or equal to 2.2%. When heating is used the surviving droplets have a diameter less than 0.1 μm are far from the surface and are thus harmless if coalescence does take place.

12. Droplets smaller than 0.1 μm cannot survive inside the boundary layer when the surface temperature is greater than the adiabatic temperature. The reason for this is that the available surface area for heat and mass transfer is the maximum for the present range of the droplet sizes (0.01 - 1.0 μm diameter).

13. When the blade surface temperature is nearly equal to the adiabatic temperature, droplets greater than 0.5 μm are deposited along the convex surface. The evaporation which takes place near to the surface has no considerable effect on reducing the rate of deposition. The reasons for this are:

(a) Droplets near to the convex surface will not evaporate completely but will produce very small droplets. These fine droplets possess high diffusion coefficient.

(b) The concentration gradient near to the wall (inside the boundary sublayer) is very high.

(c) The temperature gradient is not very high when the temperature of the surface is not greater than the adiabatic temperature. Therefore the effect of thermophoresis is minor compared with that from the diffusion.

Thus insufficient evaporation leads to an increase in the net velocity (diffusion + thermophoresis) of the droplets towards the surface.

14. On the concave surface, even when the surface temperature is about equal to the adiabatic temperature, the droplets along the stream lines which are very close to the surface cannot survive. This is because:

(a) The local concentration gradient of the droplets $(\frac{dc}{dy})$ along the concave surface is less than that along the convex surface, since the thickness of the convex boundary layer is less than that of the concave.

(b) The effect of laminarisation on the transfer of heat from the concave surface is less than that from the convex surface.

(c) The local transient time along the stream line at the same distance from the concave and convex surface is always higher along the concave surface. Therefore the droplets have more time to evaporate on the concave surface.

15. It was believed that reducing the size of the generated fog droplets by adjusting the position of the nucleation in the conventional

turbine might result in a reduction of the rotor blade erosion. The present results indicate that this is true only when the size of the droplets can be reduced below 0.05 μm in diameter, since thermodynamic equilibrium will then be restored shortly after nucleation and thus,

(i) there will be no further growth in the droplet size;

(ii) the low temperature difference between the vapour and the droplet near to the surface (Δt_{gf}), due to friction, is sufficient to evaporate completely the droplets.

However, when the diameter of the created droplets is in the range of 0.1 - 1.0 μm, the subcooling temperature (ΔT_s) along the passage is always greater than zero. Therefore the smaller the size of the droplets, the greater the amount of vapour which will condense on the droplets. This results in a greater amount of water depositing onto the blade surface thus increasing the damage to the rotor blade by erosion. The reasons for this process are:

(a) For the same initial wetness fraction, smaller droplets have a greater total surface area for transfer of mass and heat between the two phases.

(b) Smaller droplets have a higher tendency for diffusion and have lower thermophoretic velocities to push the droplets away from the surface on the basis of the same surface temperature. Therefore the droplets will acquire a higher net deposition velocity towards the surface.

16. The distance between the surface of the blade and the fog cloud base (i.e. the thickness of the dry layer) increases by increasing the

temperature of the surface ($t_w > t_o$) and/or decreasing the size of the droplets from nucleation. The minimum practicable temperature of the surface is assumed to be that which produces a dry layer thickness which is about equal to the boundary sublayer thickness. This temperature has been found to be equal to 80°C (i.e. about 15°C above the adiabatic temperature). Accordingly, the minimum amount of heat from the blade surface to the wet steam flow is about 2.06 kW per meter of the blade length. The mass flow rate of the heating steam inside the hollow blade, as a percentage of the mass flow rate of the working steam, is as low as 0.11%.

17. It can be concluded that using the entire thickness of the boundary layer for calculating the net deposition (diffusion + thermophoresis) velocity improves the theoretical deposition analysis. This is confirmed by the good agreement between the experimental deposition results of this work and those due to Davies (4) and El-Shobokshy (37) with those from the theoretical work on an unheated surface. A good agreement can also be seen between the experimental results of the net deposition rate and those from the present theoretical work on a heated surface; bearing in mind that the theoretical results due to Davies (4) are in poor agreement with his experimental results, since he used only the boundary sublayer for his calculations.

18. The simulation methods using solid particles in an air flow through the blade passage for measuring the deposition rate of fog droplets on unheated and heated blade surfaces, cannot give entirely reliable and rational results for the real turbine. The reasons are as follows:

(a) Evaporation or condensation from or to the fog droplets ($d \lesssim 0.1$ μm) has a great influence on the rate of deposition.

(b) The variation in the values of the thermophoretic velocity and diffusion coefficient of the solid particles are dependent on the temperature gradient ($\frac{dT}{dy}$) only, whilst those of droplets are also dependent on the variation of the droplet size.

(c) The properties of the wet steam flow are affected by the degree of supersaturation, the rate of transfer of heat and mass between the two phases and the location of the nucleation inside the passage. These factors are not present in the case of solid particles or with water spray droplets in air.

(d) The phenomenon of laminarisation is very significant in the real steam flow and it will not exist in simulated flow which has a low velocity. The laminarisation has a great effect on reducing the amount of deposited droplets on the blade surface.

19. It has been found that there are many disadvantages in using suction slot methods. These can be listed as follows:

(a) If the hollow blade is connected to the condenser, it means that the pressure inside the blade will be nearly equal to that of the condenser (i.e. 0.05 bar). The corresponding saturation temperature is about 32^{o}C which is below the adiabatic temperature by about 33^{o}C. This cooling process will result in more condensation and will create a thermophoretic force on the droplets towards the blade surface. Therefore the rate of deposition of droplets will increase

dramatically as a result of increasing the net deposition velocity and increasing the concentration gradient of the water in the flow (concentration defined by $\mu g/m^3$).

(b) If the nucleation creates very small droplets (d = 0.1 μm) the combination of the high level subcooling inside the boundary layer and the very large total surface area of the droplets results in a very large amount of condensate vapour and thus a higher deposition rate may be expected (Fig. 7.153). This may cause a reduction in the efficiency of the slots, since they may be designed for a particular flow condition. Thus the reduction in the erosion achieved by using a suction slot method is not as much as that which might be anticipated.

It can be concluded therefore that a suction slot method may not be effective unless all the possible conditions and properties of the vapour flow and the droplets are taken into account when designing the slots. Furthermore, improving this method will only have a limited effect on reducing the erosion and consequently on extending the life of the rotor. However employing the steam heating method can prevent any erosion by deposited water on a fixed blade by using only a very small amount of heating steam. Therefore, the steam heating method appears to be the most promising amongst the known methods available.

20. The analytical method here developed is applicable in principle to the flow beyond the first nucleation wherever this occurs. It is unlikely, however, that an attempt would be made to heat rotor blading and in any case moving blades tend to be self-draining

by centrifuging. Notwithstanding the suppression of coarse water generation which would occur after a heated fixed blade ring, it is unlikely that the beneficial effect of heating would extend much beyond the adjacent moving ring.

Any stator blade heating would be done by steam tapped from upstream in the turbine. It would be saturated or with a small degree of superheating at the pressure appropriate to the surface temperature required.

21. Investment in the heating method is found to be economic over the life of the turbine when the long term values of the inflation and interest rates were assumed equal to 7% and 9% respectively. Two cases can be considered:

(i) If the heating method had been employed in 1967 for three existing power stations, Ferrybridge-C, Eggborough and West Burton, the C.E.G.B. might make a profit of about two times of the initial cost (capital cost) when the future interest and inflation rates are moderate (i.e. $i = 9\%$ and $f' = 7\%$ or the real interest rate is 2%). However, the blade heating method is profitable for a wide range of real interest rate values. The practical range of the real rate of interest lays between - 5% and + 5% and the corresponding profit between about one to three times of the capital cost.

(ii) If the decision to invest was made in 1982, it has shown that profitability can be secured only when assuming certainty in the costs and the benefits of the investment and the real interest rate is less than 5%. The project can make a profit nearly equal to the capital cost when the rates of interest and

inflation are equal to 9% and 7%.

It can be concluded that the earlier the decision is taken by the C.E.G.B. to use the blade heating method, the greater the profit which can be obtained. If the decision was to be taken today, the element of uncertainty would have a great influence. However if the improvement in the last stage efficiency, due to heating, is taken into consideration the project will be profitable under all conditions.

22. The efficiency of the last stage is found to be increased slightly (about 0.2%) due to suppressing the coarse water on the fixed blade surface and decreasing slightly the wetness fraction. Finally it can be concluded that the steam heating method appears to be the best to prevent erosion of the rotor blade without economic risk and undue additional engineering construction.

9.3 Suggestions for Further Work

The results of the theoretical investigation indicate that the steam heating method can be used successfully in the early stage of the erosion cycle to prevent any deposition of the entrained droplets on the blade surface and thus prevent the erosion on the rotor blade. The economic results show that the proposed method is financially very attractive to the manufacturers and to the investors. However, before the idea can be strongly recommended for use in a production steam turbine it would be necessary to undertake an experimental investigation in order to verify the theoretical results. It is recommended, for reliable results, that the experimental work should be done on a real L.P. steam turbine since all the simulation methods in the field are not very accurate. A measurement of the turbulence intensity can be made to find the effect of laminarisation on the transfer of heat and mass inside the boundary layer and also on the deposition rate of the droplets when $t_w \lesssim t_o$.

A theoretical and experimental investigation could usefully be undertaken to study the effect of a second nucleation on the droplet population and on the amount of evaporation or deposited water. It would also be interesting to:

1. Study the distribution of the sizes of the droplets, which are generated by nucleation, inside the boundary layer.

2. Study the effect of the variation of the blade incidence angle on the performance of the heating method.

3. Study the effect of blade curvature on the development of the boundary layer and on the movement of the droplets which are near to the surface.

REFERENCES

1. Gardner, G.C.

"Events leading to erosion in the steam turbine", Proc. Inst. Mech. Engrs., Vol. 178, Part 1, pp. 593-624, (1963-64).

2. Crane, R.I.

"Deposition of fog drops on low pressure steam turbine blades", Int. J. Mech. Sci., Vol. 15, pp. 613-631, (1973).

3. Ryley, D.J. and El-Shobokshy, M.S.

"The deposition of fog droplets by diffusion onto steam turbine guide blades", 6th Int. Heat Transfer Conf., Toronto, Paper EC-14, pp. 85-90, (Aug. 7-11, 1978).

4. Davies, J.B.

"The effect of thermophoresis on the deposition of fog droplets on L.P. turbine fixed blades", Ph.D. Thesis, University of Liverpool, (1980).

5. Ryley, D.J.

"The behaviour of nucleation fogs within the nozzle boundary layer in the wet steam turbine", J. Mech. Engg. Sci., Vol. 13, No. 3, pp. 190-199, (1971).

6. Rouhiainen, P.O. and Stachiewicz, J.W.

"On the deposition of small particles from turbulent streams", J. Heat Transfer, Transactions of the ASME, Vol. 92, pp. 169-177, (1970).

7. Parker, G.J. and Lee, P.

"Studies of the deposition of sub-micron particles on turbine blades", Proc. Instn. Mech. Engrs., Vol. 186, 38/72, pp. 519-526, (1972).

8. Trela, M., Zembik, J. and Durkiewicz, B.

"Droplet deposition on a flat plate from an air/water turbulent mist flow", Int. J. Multiphase Flow, Vol. 8, No. 3, pp. 227-238, (1982).

9. McCoy, D.D. and Hanratty, T.J.

"Rate of deposition of droplets in annular two-phase flow", Int. J. Multiphase Flow, Vol. 3, pp. 319-331, (1977).

10. Ganic, E.N. and Mastanaiah, K.

"Investigation of droplet deposition from a turbulent gas stream", Int. J. Multiphase Flow, Vol. 7, pp. 401-422, (1981).

11. Wood, B.

"Wetness in steam cycles", Proc. Instn. Mech. Engrs., Vol. 174, No. 14, pp. 491-534, (1960).

12. Wood, B.

"Wetness in steam turbines : A general progress survey", Proc. Instn. Mech. Engrs., Vol. 180, Part 30, pp. 1-12, (1965-66).

13. Ryley, D.J.

"The present status of erosion studies in the wet steam turbine", Prace Instytutu Maszyn Przeplywowych, Zeszy 42-44, Nadbitka, Poland, pp. 241-253, (1969).

14. Gyarmathy, G.

"Basis of the theory of wet steam turbine", Ph.D. Thesis, E.T.H., Zurich, (1960).

15. Ryley, D.J. and Parker, G.J.

"Equipment and techniques for studying the deposition of sub-micron particles on turbine blades", Proc. Instn. Mech. Engrs., Vol. 184, Part (3C), p. 45, (1969-70).

16. Kirillov, I.I. and Faddeev, I.P.

"Erosion of blades of turbines operating on wet steam", Teploenergetika, Vol. 18, No. 9, pp. 50-53, (1971).

17. Smith, A.

"Physical aspects of blade erosion by wet steam in turbines", Phil. Trans. of the Royal Society of London, Vol. 260, pp. 209-215, (1966).

18. Heymann, F.J.

"High speed impact between a liquid drop and a solid surface", J. Appl. Physics, Vol. 40, No. 13, pp. 5113-5122, (1969).

19. Somm, E.

"A mean of estimating the erosion hazard in L.P. steam turbine", Brown Boveri Rev., Vol. 10, pp. 458-472, (1971).

20. Krzyzanowski, J., Weigle, B. and Severin, H.

"Semi-empirical criterion of erosion threat in modern steam turbine", J. of Engg. for Power, Transactions of the ASME, Vol. 4, pp. 1-6, (1971).

21. Krzyzanowski, J.

"On the erosion rate - Droplet size relation for an experimental stand with a rotating sample", The University of Michigan, Report No. UMICH 03371-17-T, (1972).

22. Heymann, F.J.

"On the prediction of erosion in steam turbines", 6th Conf. on Steam Turbines of Large Output, Plzen, Czechoslovakia, (Sept. 1975).

23. Perel´man, R.G.

"A method of calculating the erosion strength of moist steam turbine blades", Probl. Prochn., Vol. 5, pp. 595-604, (1977).

24. Radik, S.V.

"Erosion characteristics of wet steam turbine stages", Energomashinostroenie, Vol. 11, pp. 25-29, (1977).

25. Krzyzanowski, J. and Szprengiel, Z.

"The influence of droplet size on the turbine blading erosion hazard", J. Engg. for Power, Transactions of the ASME, Vol. 100, pp. 561-565, (1978).

26. Pollard, D. and Lord, M.J.

"An evaluation of L.P. steam turbine blade erosion", Instn. Mech. Engrs., Steam Turbines for the 1980's, Paper C259/79, pp. 413-419, (1979).

27. Vitale, D.

"Erosion test of steam turbine blade material", Power Engineering, Vol. 86, No. 1, pp. 54-55, (1982).

28. El-Shobokshy, M.S.

"A method for reducing the deposition of small particles from turbulent fluid by creating a thermal gradient at the surface", The Canadian J. Chem. Engg., Vol. 59, pp. 155-157, (1981).

29. Vermes, G.

"Thermophoresis - Enhanced deposition rate in combustion turbine blade passage", Trans. of the ASME, J. Engg. for Power, Vol. 101, pp. 542-548, (1979).

30. Wood, N.B.

"The mass transfer of particles and acid vapour to cooled surface", J. Inst. of Energy, Vol. , pp. 76-93, (1981).

31. Wohlers, H.C., Kass, T.E. and Johnson, K.R.

"Fluorescent dyes as airborne tracer material", A.S.T.M. Tech. Publ., No. 281, p. 15, (1959).

32. Sinclair, D. and LaMer, V.K.

Chem. Rev. Vol. 44, p. 245, (1949).

33. Kerker, M., Matijevic, E., Nicolaon, G. and Cooke, D.D.

"Preparation of liquid aerosols and their particle size analysis by light scattering" - Session 2, pp. 153-160, in "Assessment of Airborne Particles" (Eds. Mercer, T.T., Morrow, P.E. and Stöber, W.) Charles C. Thomas Publisher, (1972).

34. Fuchs, N.A. and Sutugin, G.

"Generation and use of monodisperse aerosols" - in "Aerosol Science" (Ed. Davies, C.N.). London and New York, Academic (Publisher), (1966).

35. Whitby, K.T., Lundgren, D.A. and Peterson, G.M.

"Homogeneous aerosol generators", Int. J. Air Wat. Pollut., Vol. 9, p. 263, (1965).

36. Berglund, R.N. and Liu, B.Y.H.

"Generation of monodisperse aerosol standards", Environ. Sci. Technol., Vol. 7, p. 147, (1973).

37. El-Shobokshy, M.S.

"Diffusional deposition of fog droplets onto L.P. steam turbine guide blades at off-design conditions", Ph.D. Thesis, University of Liverpool, (1975).

38. McCreath, C.G. and Beer, J.M.

"A review of drop size measurement in fuel sprays", Appl. Energy, Vol. 2, pp. 3-15, (1976).

39. Ryley, D.J. and Fallon, J.B.

"Size sampling of steam-borne water droplets", Proc. Instn. Mech. Engrs., Vol. 180, Part 30, pp. 23-38, (1966).

39a. Kolb, B.

"Measuring the size of the droplets in wet steam", The Brown Boveri Review, Vol. 49, No. 7/8, pp. 350-359, (1962).

40. May, K.R.

J. Sci. Inst., Vol. 22, p. 187, (1945).

41. Hurd, F.K. and Mullins, J.C.

Coll. Sci., p. 1791, (1962).

42. Whitby, K.T. and Peterson, C.M.

"The electrical neutralisation and particle size measurement of dye aerosol", A.C.S. Meeting, Atlantic City, N.J., Sept. 12-14, (1962).

43. Pye, J.W.

J. Inst. Fuel, p. 253, (1971).

43a. Gardiner, J.A.

"Measurement of the drop size distribution in water sprays by an electrical method", Instrument Practice, Vol. 18, pp. 353-356, (1964).

44. Steen, W.M. and Chatterjee, A.

"A technique for measuring the size and number of droplets", J. Phys. E. Sci. Inst., Vol. 13, pp. 1020-1021, (1970).

45. Van Passen, C.A.A.

"Thermal droplet size measurements using a thermocouple", Int. J. Heat Mass Transfer, Vol. 17, pp. 1527-1548, (1974).

46. Tshudi, T., Herziger, G. and Engel, A.

"Particle size analysis using computer synthesised holograms", App. Optics, Vol. 13, No. 2, pp. 245-247, (1974).

47. Cornillault, J.

"Particle size analyser", J. Appl. Optics, Vol. 11, pp. 265-268, (1972).

48. Jasuja, A.K.

J. Engg. for Power, Vol. 101, pp. 250-258, (1979).

49. Williams, I. and Hedley, A.B.

Report on the Progress of Applied Chemistry, Vol. 57, pp. 635-668, (1972).

50. Deich, M.E., Tsiklauri, G.V., Shanin, V.K. and Danilin, V.S.

"Investigation of flows of wet steam in nozzle", Thermal Engg., Vol. 16, pp. 102-107, (1972).

50a. Azzopardi, B.J.

"Measurement of drop size", United Kingdom Atomic Energy Authority, A.E.R.E.-R 8667, April (1977).

51. Moore, M.J., Langford, R.W. and Tipping, J.C.

"Research at CERL on turbine blade erosion", Proc. Inst. Mech. Eng., Vol. 182, Part 3H, p. 61, (1968).

52. Puzyrewski, R. and Krzeczkowski, S.

"Some results of investigation on the break-up of a film of water and the motion of drops of water in the aerodynamic wake", Prace Instytutu Maszyn Przeplywowych, Nos. 29-31, pp. 21-43, (1966).

53. Moore, M.J., Sieverding, C.H. (Eds.)

"Two-phase steam flow in turbines and separators", U.S.A., Hemisphere Publishing Corporation, (1976), pp. 38-39.

54. Gyarmathy, G.

"The spherical droplet in gaseous carrier streams : Review and analysis", Hemisphere Publishing Corporation, Washington and London, (1980).

55. Kirillov, I.I. and Yablonik, R.M.

"Fundamentals of the theory of turbines operating on wet steam", NASA TT F-611, (1970).

56. Mason, B.J.

Proc. Phys. Soc., B64, p. 773, (1951).

57. Stodola, A.

"Steam and gas turbines", Berlin, Springer-Verlag Publishing, (1924).

58. Gyarmathy, G.

"Condensation in flowing steam" in "Two-phase Steam Flow in Turbines and Separators", (Eds. Moore, M.J. and Sieverding, C.H.), U.S.A., Hemisphere Publ. Corp., (1976).

59. Hill, P.G.

"Condensation of water vapour during supersonic expansion in nozzles", J. Fluid Mech., Vol. 25, pp. 593-620, (1966).

60. Bakhtar, F., Ryley, D.J., Tubman, K. and Young, J.B.

"Nucleation steadies in flowing high pressure steam", Proc. Instn. Mech. Engrs., Vol. 189, Paper No. 41/75, pp. 427-436, (1975).

61. Moses, C.A. and Stein, G.D.

"On the growth of steam droplet formed in a laval nozzle using both static pressure and light scattering measurements", in "Condensation in High Speed Flows", (Ed. Pouring, A.A.), New York, ASME Publishing, pp. 1-26, (1977).

62. Gardner, G.C.

"Force on a small spherical evaporating particle in its pure vapour due to motion and temperature gradient", Chem. Engg. Sci., Vol. 23, pp. 29-40, (1968).

63. Ryley, D.J.

"The adhesion of small droplets to blades and other internal surfaces in wet steam turbines", Conf. on Steam Turbine of Large Output, Plzen, Czechoslovakia, Sept. (1975).

64. Corn, M.

"Adhesion of particles" in "Aerosol Science" (Ed. Davies, C.N.), London and New York, Academic Press, (1966).

65. Dahneke, B.

"The capture of aerosol particles by surfaces", J. Colloid Interface Sci., Vol. 37, No. 2, p. 342, (1971).

66. Beal, S.K.

"Deposition of particles in turbulent flow on channel or pipe walls", Nuclear Sci. & Engg., Vol. 40, pp. 1-11, (1970).

67. Davies, C.N.

"Brownian deposition of aerosol particles from turbulent flow through pipes", Proc. Roy. Soc., Series A, Vol. 290, pp. 557-562, (1966).

68. Valha, J.

"Liquid phase movement in the last stages of large condensing steam turbine", Proc. Instn. Mech. Engrs., Vol. 184, Part 3(III), p. 70, (1969-1970).

69. Lin, C.S., Moulton, R.W. and Putnam, G.L.

"Mass transfer between solid wall and fluid streams - Mechanism and eddy distribution relationships in turbulent flow", Ind. Engr. Chem., Vol. 45, No. 3, pp. 636-646, (1953).

70. Gardner, G.C.

"Deposition of particles from a gas flowing parallel to a surface", Int. J. Multiphase Flow, Vol. 2, pp. 213-218, (1975).

71. Sehmel, G.A.

"Particle eddy diffusivities and deposition velocities for isothermal flow and smooth surfaces", Aerosol Sci., Vol. 4, pp. 125-138, (1973).

72. Davies, C.N.

"Deposition of aerosol from turbulent flow through pipes", Proc. Roy. Soc., Series A, Vol. 289, p. 235, (1966).

73. Epstein, P.

"Zur theorie des radiometers", Z. Phys., Vol. 54, p. 537, (1929).

74. Schadt, C.F. and Cadle, R.D.

J. Phys. Chem., Vol. 65, p. 1689, (1961).

75. Derjaguin, B.V., Storozhilova, A.I. and Rabinovich, Y.I.

J. Colloid Interface Sci., Vol. 21, p. 35, (1966).

76. Waldmann, L.

Z. Naturf., Vol. 14a, p. 589, (1959).

77. Cha, C.Y. and McCoy, B.J.

Phys. Fluids, Vol. 17, pp. 1376-1380, (1974).

78. Brock, J.R.

J. Colloid Sci., Vol. 23, p. 448, (1967).

79. Talbot, L., Cheng, R.K., Schefer, R.W. and Willis, D.R.

"Thermophoresis of particles in a heated boundary layer", J. Fluid Mech., Vol. 101, Part 4, pp. 737-758, (1980).

80. Brock, J.R.

J. Colloid Sci., Vol. 17, p. 768, (1962).

81. Derjaguin, B.V. and Talamov, Yu.

"Thermophoresis of large aerosol particles", J. Colloid Sci., Vol. 20, p. 555, (1965).

82. Byers, R.L. and Calvert, S.

"Particle deposition from turbulent streams by means of thermal force", I. & E.C. Fundamentals, Vol. 8, No. 4, p. 646, (1969).

83. Davies, C.N.

"Aerosol Science", London and New York, Academic Press Publishing, pp. 407-417, (1966).

84. Schlichting, H.

"Boundary layer theory", London, McGraw Hill Book Company, 7th Ed., pp. 201-206, (1979).

85. Squire, H.B.

"Heat transfer calculation for aerofoils", Aeronaut. Res. Coun. Tech. Report R & M, No. 1986, (1942).

86. Lee, P.

"The deposition of small water droplets on stationary L.P. steam turbine blades", M.Eng. Thesis, University of Liverpool, (1970).

87. Friedlander, S.K. and Johnstone, H.F.

"Deposition of suspended particles from turbulent gas stream", Indust. Engg. Chem., Vol. 49, p. 1151, (1951).

88. Owen, P.R.

"Pneumatic transport", J. Fluid Mech., Vol. 39, p. 307, (1969).

89. Crane, R.I.

"Some aspects of wet steam flow in turbine cross-over pipe", Int. J. Mech. Sci., Vol. 20, pp. 237-246, (1978).

90. Farmer, R., Griffith, P. and Rohsenow, M.W.

"Liquid deposition in two-phase flow", J. Heat Transfer, Transaction of the ASME, Vol. 92, pp. 587-594, (1970).

91. Kubie, J.

"Settling velocity of droplets in turbulent flows", Chem. Engg. Sci., Vol. 35, pp. 1787-1793, (1980).

92. Ryley, D.J. and Davies, J.B.

"The effect of thermophoresis on the deposition of fog droplets on low pressure steam turbine guide blades", Int. J. of Heat and Fluid Flow, Vol. 4, No. 3, p. 161, Sept. (1983).

93. Vuksta, T. Jr.

"Tangential blade velocity and secondary flow field effect on steam turbine exhaust-blade erosion", ASME, Paper 63-WA-238, Nov. (1963).

94. Skopek, J.

"Removal of water from the fixed blades of a steam turbine", Strojirenstvi, CEGB Translation, Vol. 14, No. 11, pp. 828-833, (1964).

95. Todd, K.W. and Fallon, J.B.

"Erosion control in the wet steam turbine", I.Mech.E. Symposium on Wet Steam, Vol. 180, Part 30, Paper No. 26, pp. 50-64, (1966).

96. Brown Boveri & Co. Ltd.

"Improvements in and relating to steam turbines and method of operating the same", British Patent, No. 1, 074, 762, (1967).

97. Smith, A.

"The influence of moisture on the efficiency of a one-third scale model low pressure steam turbine", I.Mech.E. Symposium on Wet Steam, Vol. 180, Part 30, Paper No. 10, pp. 39-50, (1966).

98. Ryley, D.J. and Parker, G.J.

"The removal of water from low pressure steam turbine blades by trailing-edge suction slots", I.Mech.E. Thermodynamics and Fluid Mechanics Convention, Paper No. 9, pp. 94-104, March (1968).

99. Todd, K.W. and Gregory, B.

"An experiment on erosion control, using a 60 MW steam turbine", I.Mech.E. Thermodynamics and Fluid Mechanics Convention, Paper No. 31, pp. 297-309, (1968).

100. McAllister, D.H. and Moore, C.T.

"Water drainage from a cascade of hollow slotted low pressure turbine blades", I.Mech.E. Thermodynamics and Fluid Mechanics Convention, Paper No. 38, pp. 357-366, (1968).

101. Kirillov, V.I., Nakhman, Yu., Matveenko, V.A., Volchkov, V.I., Ryzhkov, V.K., Parkhomov, V.A. and Eremeev, A.M.

"Investigation of moisture removal within the passage of the last stage of a low pressure cylinder, with 960 mm moving blade", Thermal Engg., Vol. 28, No. 2, pp. 104-106, (1981).

102. Konorski, A.

"Steam drying in condensing turbine by internal preheating method utilising own steam", Gdansk, Prace Instytutu Maszyn Prezeplywowych, pp. 305-311, (1962).

103. Engelke, W.

"Operating experience of wet steam turbine" in "Two-phase Steam Flow in Turbines and Separators", (Eds. Moore, M.J. and Sieverding, C.H.), Mc-Graw Hill Book Co., pp. 305-311, (1976).

104. Kirillov, I.I., Nosovitskii, A.I. and Shpenzer, G.G.

"Moisture removal by separation and evaporation in wet turbine stages", Teploenergetika (Translated from Russian), Vol. 17, No. 8, pp. 40-42, (1970).

105. Venhoff, F.

"Improvements in or relating to multistage steam turbines and installations thereof", British Patent No. 995, 643, (1965).

106. Akhtar, M.S., Black, J. and Swainton, M.J.C.

"Prevention of steam turbine blade erosion using stator blade heating", Inst. Mech. Engrs. Proc., Vol. 191, 17/77, pp. 355-361, (1977).

107. Kazak, M.A., Kirillov, I.I., Faddeev, I.P., Okolov, V.K. and Radik, S.V.

"New method of erosion protection for turbine stage vanes", Energomashinostroenie, No. 3, pp. 32-34, (1977).

108. Al-Azzawi, H.K. and Owen, I.

"Measuring the thermal conductivity of uranin", Int. J. Heat and Fluid Flow, Vol. 5, No. 1, pp. 57 - 59, 1984.

109. C.R.C. Limited

"Handbook of Chemistry and Physics", Published by C.R.C. Press, 59th Edition, (1978-1979).

110. B.D.H. Chemical Limited

Private communication, (1983).

111. Kaye, G.W.C. and Laby, T.H.

"Tables of physical and chemical constants and some mathematical functions", Longman Group Ltd., London, (1973).

112. Literature survey in chemical abstract (subjects index).

Published by the American Chemical Society, Volumes 76-95, (1972 - 81).

113. Young, J.B. and Bakhtar, F.

"*Steam turbines for large power outputs*", Lecture Series, 1980-6, V.K.I. for Fluid Dynamics, April 21-25 (1980).

114. Gyarmathy, G.

"Condensation shock diagrams for steam flow", Forsch. Ing. Wes., Vol. 29, No. 4, pp. 105-114, (1963).

115. Ryley, D.J.

"Phase equilibrium in low pressure steam turbine", Int. J. Mech. Sci., Vol. 3, pp. 28-46, (1961).

116. Young, J.B.

"Nucleation in high pressure steam and flow in turbines", Ph.D. Thesis, University of Birmingham, (1973).

117. Abu-Ghannam, B.J. and Shaw, R.

"Natural transition of boundary layers - The effects of turbulence, pressure gradient and flow history", J. Mech. Engg. Sci., Vol. 22, pp. 213-228, (1980).

118. Green, E.J.

"Application of Head's entrainment method to the prediction of turbulent boundary layers and wakes in compressible flow", R.A.E. TR 72079, June (1972).

119. Curle, N. and Davies, H.J.

"Modern fluid dynamics", Part (1), D. Van Nostrand Co. Ltd., London, (1968).

120. Cox, H. and Forster, V.T.

Private communication, G.E.C., (1983).

121. Donald, R.B., James, F.S. and Anne, K.G.

"Laminarisation of a turbulent boundary layer as observed from heat transfer and boundary layer measurements in conical nozzles", NASA, TN D-4788, (1968).

122. Back, L.H., Cuffel, R.F. and Massier, P.F.

"Laminarisation of a turbulent boundary layer in nozzle flow-boundary layer and heat transfer measurements with wall cooling", J. Heat Transfer, Vol. 92, pp. 333-344, Aug. (1970).

123. Back, L.H., Cuffel, R.F. and Massier, P.F.

"Laminarisation of a turbulent boundary layer in nozzle flow", AIAA J. Vol. 7, No. 4, pp. 730-733, April (1969).

124. Jones, W.P. and Launder, B.E.

"The prediction of laminarisation with a two-equation model of turbulence", Int.J. Heat and Mass Transfer, Vol.15, pp. 301-314, (1972).

125. Cebeci, T., Smith, A.M.O. and Mosinskis, G.

"Solution of the incompressible turbulent boundary layer equations with heat transfer", J. of Heat Transfer, Vol.92, pp. 133-143, Feb. (1970).

126. Fuchs, N.A.

"The mechanics of aerosols", Pergamon Press Ltd., London, p. 183, (1964).

127. Kantola, R.A.

"Condensation in steam turbine", Electrical Power Res. Inst., Coal Combust. Syst. Div., Rep. EPRI-CS-2528, (1982).

128. Crane, R.I.

"Drop coalescence and deposition in turbulent wet steam pipe flows", Int. J. Heat and Fluid Flow, Vol. 3, No. 1, pp. 13-20, (1982).

129. Annis, B.K., Malinauskas, A.P. and Mason, E.A.

"Theory of drag on neutral of charged spherical aerosol particles", Aerosol Science, Vol. 3, No. 1, pp. 55-64, (1972).

130. Van Driest, E.R.

"On turbulent flow near a wall", J. Aero. Sci., Vol. 23, pp. 1007-1012, (1956).

131. Ryley, D.J. and Al-Azzawi, H.K.

"Suppression of the deposition of nucleated fog droplets on steam turbine stator blades by blade heating", Int. J. Heat and Fluid Flow, Vol. 4, No. 4, pp. 207-216, (1983).

132. Kays, W.M.

"Convective heat and mass transfer", McGraw-Hill Publishing Co. Ltd., (1966).

133. Moretti, P.M. and Kays, W.M.

"Heat transfer to a turbulent boundary layer with varying free stream velocity and varying surface temperature - An experimental study", Int. J. Heat and Mass Transfer, Vol. 8, pp. 1187-1202, (1965).

134. Back, L.H., Massier, P.F. and Gier, H.L.

"Convective heat transfer in a convergent-divergent nozzle", Int. J. Heat and Mass Transfer, Vol. 7, pp. 549-568, (1964).

135. Back, L.H., Massier, P.F. and Cuffel, R.F.

"Some observations on reduction of turbulent boundary layer heat transfer in nozzles", AIAA J., Vol. 4, No. 12, pp. 2226-2229, Dec. (1966).

136. Back, L.H., Massier, P.F. and Cuffel, R.F.

"Flow phenomena and convective heat transfer in a conical supersonic nozzle", J. Spacecraft and Rocket, Vol. 4, No. 8, pp. 1040-1047, Aug. (1967).

137. McEligot, D.M., Coon, C.W. and Perkins, H.C.

"Relaminarisation in a tube", Int. J. Heat and Mass Transfer, Vol. 13, pp. 431-433, (1970).

138. Back, L.H.

"Acceleration and cooling effects in laminar boundary layers - Subsonic, transonic and supersonic speed", AIAA J., Vol. 8, No. 4, pp. 794-802, April (1970).

139. Harris, F.R. (Chief Engineer, G.E.C. Rugby)

Private communication, (1983).

140. Carslaw, H.S. and Jaeger, J.C.

"Conduction of heat in solids", 2nd Edition, Clarendon, Oxford, (1959).

141. Gyarmathy, G. and Meyer, H.

"Spontaneous condensation, Part 2. Influence of the expansion rate on the fog formation in supersaturated steam", V.D.I., Forschungscheft 508, (1965).

142. Ryley, D.J. and Barrow, H.

"Discharge coefficient of an elementary steam nozzle", The Engineer, pp. 338-340, Aug. 29 (1958).

143. Dixon, S.L.

University of Liverpool, Private Communication, (1983).

144. Irgin, J., Birnie, I., Beard, L.E. and Lister, J.

C.E.G.B. North-Western Region Headquarters, Private Communication, (1982).

145. Report on the Census of Production - Summary table, CSO - Business Monitor, (1971).

146. Price Indices of Materials and Fuel, CSO - Monthly Digest of Statistics, Nos. 325-445, (1973-1983).

147. Wages Indices, CSO - Economic Trends, Nos. 257-351, (1975-1983).

148. Statistical Year Book, C.E.G.B., (1967-1983).

149. U.K. Economic Scenarios and Energy Demand, C.E.G.B. - Statement of Case, Sizewell-B Power Station - Public Inquiry, Appendix D, pp. 223-236, April (1982).

150. Bartlett, R.L.

"Steam turbine performance and economics", McGraw-Hill Book Company, New York, pp. 248-258, (1958).

151. Harris, F.R.

"Designing for quality - Large steam turbines", in "Quality Assurance in Design". Symposium (Joint I.Mech.E./I.Chem.E.), University of Manchester Institute of Science & Technology, Published by I.Mech.E., pp. 13-19, 23 Feb. (1982).

152. Wronski, G. and Wilson, R.G.

"Modernisation of control systems to maintain plant reliability and economy in a flexible operating regime", Proc. Instn. Mech. Engrs., Vol. 197A, Paper No. 85/83, Sept. (1983).

153. Annual Report and Accounts, C.E.G.B., (1967-1983).

154. Interest Rate - Security Prices and Yields, CSO - Economic Trends, No..352, pp. 64-66, (1983).

155. Merrett, A.J. and Sykes, A.

"The finance and analysis of capital projects", Longman Group Limited, London, (1963).

156. Bierman, H. and Smidt, S.

"The capital budgeting decision", Macmillan Publishing Co., New York, (1980).

157. Mathews, K. and Minford, P.

"Recent developments and forecasts", Quarterly Economic Bulletin, Liverpool Research Group in Macroeconomics, Vol. 5, No. 1, pp. 10-16, March (1984).

158. The Channel Link Report, Anglo-French Banking Consortium led in the U.K. by National Westminster Bank, May (1984).

159. The Nationalised Industries - The Financial and Economic Framework. The White Paper Cmnd 7131, March (1978).

APPENDIX 5A

POHLHAUSEN'S AND THWAITES' METHOD

The method is basically an approximate solution of the integral momentum equation,

$$U_\infty^2 \frac{d\theta}{dx} + (2\theta + \delta_1) U_\infty \frac{dU_\infty}{dx} = \frac{\tau_w}{\rho} \qquad (5A.1)$$

By assuming a suitable form for the velocity profile the boundary layer thicknesses can be calculated.

Pohlhausen has assumed a polynomial of the fourth degree for the velocity function in terms of the dimensionless distance from the wall, $\eta = \frac{y}{\delta(x)}$, as follows

$$\frac{u}{U_\infty} = f(\eta) = a\eta + b\eta^2 + c\eta^3 + d\eta^4 \qquad (5A.2)$$

The boundary conditions for solving equation (5A.1) can be listed in order to determine the four constant a, b, c and d.

(1) When $y = \eta = 0$

$$\nu \frac{\partial^2 u}{\partial y^2} = \frac{1}{\rho} \frac{dp}{dx} = - U_\infty \frac{dU_\infty}{dx}$$

(2) At $y = \delta$ or $\eta = 1.0$

$$u = U_\infty$$

and $$\frac{du}{dy} = 0.0, \quad \frac{\partial^2 u}{\partial y^2} = 0.0$$

Introducing a new dimensionless quantity λ

$$\lambda = \frac{\delta^2}{\nu} \frac{dU_\infty}{dx} = - \frac{dp}{dx} \frac{\delta}{\mu U_\infty / \delta}$$

The following expression for the four constants can be obtained from

$$a = 2 + \frac{\lambda}{6}; \quad b = - \frac{\lambda}{2}; \quad c = - 2 + \frac{\lambda}{2}; \quad d = 1 - \frac{\lambda}{6}$$

and hence the velocity profile

$$\frac{u}{U_\infty} = (2\eta - 2\eta^3 + \eta^4) + \frac{\lambda}{6} (\eta - 3\eta^2 + 3\eta^3 - \eta^4) \qquad (5A.3)$$

From the definitions of δ_1 and θ, the displacement and momentum thicknesses can be written in terms of λ

$$\frac{\delta_1}{\delta} = \frac{3}{10} - \frac{\lambda}{120}; \quad \frac{\theta}{\delta} = \frac{1}{63} \left(\frac{37}{5} - \frac{\lambda}{15} - \frac{\lambda^2}{144}\right)$$

Similarly, the viscous stress at the wall, $\tau_w = \mu \left(\frac{du}{dy}\right)_{y=0}$ is given by

$$\tau_w = \frac{\mu U_\infty}{\delta} (2 + \frac{\lambda}{6}) \qquad (5A.4)$$

The momentum equation can be rewritten by multiplying the two sides of the equation by $\frac{\theta}{\nu U_\infty}$

$$\frac{U_\infty \theta}{\nu} \frac{d\theta}{dx} + (2 + H) \frac{\theta^2}{\nu} \frac{dU_\infty}{dx} = \frac{\tau_w \theta}{\mu U_\infty} \qquad (5A.5)$$

Introducing a dimensionless parameter

$$k = \frac{\theta^2}{\nu} \frac{dU_\infty}{dx} = z \frac{dU_\infty}{dx} \text{ where } z = \frac{\theta^2}{\nu}$$

Therefore, k, H and $\frac{\tau_w \theta}{\mu U_\infty}$ can be written in terms of λ as follows

$$k = \left(\frac{37}{315} - \frac{\lambda}{945} - \frac{\lambda^2}{9072}\right)^2 \lambda,$$

$$H = \frac{\delta_1}{\theta} = \frac{\frac{3}{10} - \frac{\lambda}{120}}{\frac{37}{315} - \frac{\lambda}{945} - \frac{\lambda^2}{9072}} = f_1(k)$$

and

$$\frac{\tau_w \theta}{\mu U_\infty} = (2 + \frac{\lambda}{6})(\frac{37}{315} - \frac{\lambda}{945} - \frac{\lambda^2}{9072}) = f_2(k)$$

Hence the momentum equation can be written in terms of λ

$$U_\infty \frac{dz}{dx} = F(k) \qquad (5A.6)$$

where

$$F(k) = 2f_2(k) - 4k - 2kf_1(k)$$

Equation (5A.6) is a non-linear differential equation of the first order for $z = \frac{\theta^2}{\nu}$ as a function of the current length co-ordinate x. The form of the function F(k) is complex and Thwaite has plotted F(k) against k. He found F(k) can be approximated quite closely by the straight line

$$F(k) = 0.47 - 6k$$

In this manner equation (5A.6) reduces to

$$U_\infty \frac{dz}{dx} = 0.47 - 6k \qquad (5A.7)$$

From the definitions of z and k equation (5A.7) can be rewritten as

$$\theta^2 = \frac{0.47\nu}{U_\infty^6} \int_0^x U_\infty^5 \, dx \qquad (5A.8)$$

The solution of equation (5A.8) is not complicated and gives the value of θ along x and then k can be calculated. The values of H, λ and $f_2(k)$ are

listed in many fluid dynamics text books.

For flow with zero pressure gradient, equation (5A.8) can be simplified to

$$\theta = 0.68\sqrt{\frac{\nu x}{U_\infty}} \qquad (5A.9)$$

The other parameters can be calculated by setting $\frac{dU_\infty}{dx} = 0.0$.

APPENDIX 5B

THE HEAD ENTRAINMENT METHOD

The method was employed to predict the turbulent boundary layer parameters. The boundary layer parameters at the inlet to the turbulent flow should be known in order to predict the distribution of θ, δ and C_f along the x-axis. Head has proposed a solution to the problem by the simultaneous forward integration of the Von Karman momentum integral equation, which can be written

$$\frac{d\theta}{dx} = \frac{C_f}{2} - (H + 2)\frac{\theta}{U_\infty}\frac{dU_\infty}{dx} \qquad (5B.1)$$

and the entrainment equation, an expression for the streamwise rate of change the mass flow thickness

$$\frac{d\Delta}{dx} = C_E - \frac{\Delta}{U_\infty}\frac{dU_\infty}{dx}; \quad \text{where } \Delta = H_1\,\theta \qquad (5B.2)$$

Equation (5B.2) can be written in terms of H_1 and shape factor, H

$$\theta\frac{dH_1}{dx} = C_E - H_1\left(\frac{C_f}{2} - (H + 1)\frac{\theta}{U_\infty}\frac{dU_\infty}{dx}\right) \qquad (5B.3)$$

To integrate these equations it is necessary to express the parameters H, C_E and C_f in terms of H_1, θ and the local properties of the external flow.

1. Skin friction relations

Head has employed the empirical of Spalding and Chi to define the skin friction of flow with zero pressure gradient C_{fo}

$$C_{fo} = \frac{0.012}{\log_{10}(Re_\theta - 0.64)} - 0.00093 \qquad (5B.4)$$

Then, taking the Clauser shape parameter for flow with zero pressure gradient H_0,

$$H_0 = \frac{1}{\left(1 - 6.8\sqrt{\frac{C_{fo}}{2}}\right)} \qquad (5B.5)$$

For the flow with pressure gradient C_f is no longer a function of Reynolds number only. The formula of Ludwig and Tillmann was adopted to define C_f in terms of H and Re_θ

$$\left(\frac{C_f}{C_{fo}} + 0.5\right)\left(\frac{H}{H_o} - 0.4\right) = 0.9 \qquad (5B.6)$$

2. Entrainment and shape parameter relations

The Head empirical correlation between C_E and H_1 was written as

$$C_E = 0.0299\,(H_1 - 3.0)^{-0.6169} \qquad (5B.7)$$

The relation between H and H_1 was derived by Coles and can be written as

$$H = 1 + 1.12\left(H_1 - 2 - \sqrt{(H_1 - 2)^2 - 3}\right)^{0.915} \qquad (5B.8)$$

or

$$H_1 = 2 + 1.5\left(\frac{1.12}{H-1}\right)^{\frac{1}{0.915}} + 0.5\left(\frac{H-1}{1.12}\right)^{\frac{1}{0.915}} \qquad (5B.9)$$

Therefore C_f, C_E and H can be defined in terms of H_1 and substituted in equations (5B.1) and (5B.3), after which only two unknown θ and H_1 are available for two equations. Equations (5B.1) and (5B.2) were solved numerically by using Range-Kutta method.

The values of C_f and θ were corrected for compressible flow, since the Mach number exceeded unity. The expressions can be written in forms

$$\theta = \frac{\theta_{inc}}{F_\theta}; \quad \text{where } F_\theta = 1 + 0.056\ M^2$$

and

$$C_f = \frac{(C_f)_{inc}}{F_c}; \quad \text{where } F_c = \sqrt{1 + 0.2\ M^2}$$

APPENDIX 5C

ACCELERATION PARAMETER

The integral momentum equation can be written in the following form

$$\frac{d\theta}{dx} + \left[\left(\frac{H + 2}{U_\infty}\right) \frac{dU_\infty}{dx}\right] \theta = \frac{\tau_w}{\rho_\infty U_\infty^2} \qquad (5C.1)$$

Multiplying equation (5C.1) by $\frac{\rho_\infty U_\infty}{\mu}$ and re-arranging yields

$$\frac{dRe_\theta}{dx} + (H + 1) \frac{Re_\theta}{U_\infty} \frac{dU_\infty}{dx} = \frac{\tau_w}{\mu U_\infty} \qquad (5C.2)$$

The shear stress parameter ε and the pressure gradient parameter Γ are given by the following equations

$$\varepsilon = \frac{\tau_w}{\rho_\infty U_\infty^2} Re_\theta^{1/4} \qquad (5C.3)$$

$$\Gamma = \frac{\theta}{U_\infty} \frac{dU_\infty}{dx} Re_\theta^{1/4} \qquad (5C.4)$$

Multiplying equation (5C.2) by $Re_\theta^{1/4}$ and substitution of equations (5C.3) and (5C.4) gives the following alternate form of the momentum equation:

$$\frac{dRe_\theta^{5/4}}{dx} = \frac{5}{4} \frac{\rho_\infty U_\infty}{\mu} \left[\varepsilon - (H + 1)\ \Gamma\right] \qquad (5C.5)$$

The group of terms inside the brackets in equation (5C.5) was found to be dependent on Γ and can be expressed as follows:

$$\frac{5}{4} \left[\varepsilon - (H + 1)\ \Gamma\right] = 0.016 - 3.55\ \Gamma \qquad (5C.6)$$

Substitution of equations (5C.6) and (5C.4) into equation (5C.5) yields the equation for the momentum thickness Reynolds number distribution in the nozzle:

$$\frac{dRe_\theta^{5/4}}{dx} + 3.55 \frac{Re_\theta^{5/4}}{U_\infty} \frac{dU_\infty}{dx} = 0.016 \frac{\rho_\infty U_\infty}{\mu} \qquad (5C.7)$$

Equation (5C.7) can be readily solved for the change in Re_θ with distance x to give

$$\frac{dRe_\theta}{dx} = \frac{4}{5} \frac{U_\infty}{\nu_\infty} \left(\frac{0.016}{Re_\theta^{1/4}} - 3.55\, Re_\theta \frac{\nu_\infty}{U_\infty^2} \frac{dU_\infty}{dx}\right) \qquad (5C.8)$$

In highly accelerated flow in a nozzle $\frac{dRe_\theta}{dx}$ attains a negative value thus indicating a reduction in Re_θ with increasing distance x. If the value of Re_θ becomes sufficiently low, laminarisation of the boundary layer is postulated to occur. The critical Reynolds number at which laminarisation occurs will be assumed equal to the critical value for forward transition on a flat plate $(Re_\theta)_{crit} \approx 360$ or $(Re_\theta)_{crit} \approx 300$ in the present work. After substitution of $(Re_\theta)_{crit}$ into equation (5C.8) the critical value of acceleration parameter $L = \frac{\nu_\infty}{U_\infty^2} \frac{dU_\infty}{dx}$ can be calculated.

The critical value of L was found to be equal to 3.9×10^{-6} in this work.

APPENDIX 6A

HEAT TRANSFER INSIDE THE TURBULENT BOUNDARY LAYER

The method for calculating heat transfer through a turbulent boundary layer with a variable free stream velocity and wall temperature was suggested by Ambrok. Ambrok's method involved the solution of the integral energy equation only. The energy equation (equation (6.11)) can be written in the form

$$\frac{\dot{q}_w''}{Cp} = \frac{d}{dx} \left[\Delta_2 G_\infty (t_w - t_\infty)\right] \qquad (6A.1)$$

where G_∞ and Δ_2 have been defined in section 6.5.

For constant free stream velocity and constant properties;

$$\frac{dU_\infty}{dx} = \frac{d\rho_\infty}{dx} = \frac{d(t_w - t_\infty)}{dx} = 0.0,$$

hence energy equation can be reduced to equation (6.12)

$$\frac{\dot{q}_w''}{\rho U_\infty Cp (t_w - t_\infty)} = \frac{d\Delta_2}{dx} \qquad (6A.2)$$

The first group of terms on the left side of equation (6A.2) is the definition of Stanton number, St. Therefore equation (6A.2) can be rewritten in terms of St_x as the following

$$St_x = \frac{d\Delta_2}{dx} \qquad (6A.3)$$

Equation (6A.3) is valid only for flow with zero pressure gradient and constant properties of the flow.

It can be started with some convenient expressions for heat transfer through a constant surface temperature, constant free stream velocity boundary

layer, in order to simplify the energy equation to a practicable form for calculating the heat rate into a flow with variable surface temperature and free stream velocity. The constant surface temperature, constant free stream velocity Stanton number can be expressed in the form,

$$St_x = C\ Re_x^{-n} \tag{6A.4}$$

where C and n are constants.

If equation (6A.4) substitutes into equation (6A.3) and integrate along x yields

$$\Delta_2 = \frac{C\ U_\infty^{-n}}{\nu^{-n}} \frac{x^{(1-n)}}{1-n} \tag{6A.5}$$

Therefore, St_x can be defined in terms of the Reynolds number based on Δ_2 rather than x.

$$St = C \left(\frac{1-n}{C}\right)^{\left(\frac{n}{n-1}\right)} Re_{\Delta_2}^{\left(\frac{n}{n-1}\right)} \tag{6A.6}$$

and thus St in equation (6A.6) is expressed in terms of local parameters and is not associated with plate length. The fundamental assumption of the method is simply that this relation is valid regardless of any variation in free stream velocity, surface temperature and fluid properties. Equation (6A.6) can be written in terms of the local surface heat flux and substituted into equation (6A.1). After some algebraic manipulation the following differential equation results:

$$\left(\frac{1-n}{C}\right)^{\left(\frac{2n-1}{n-1}\right)} \mu^{\left(\frac{n}{1-n}\right)} G_\infty (t_w - t_\infty)^{\left(\frac{1}{1-n}\right)} dx = d\left[G_\infty \Delta_2 (t_w - t_\infty)\right]^{\left(\frac{1}{1-n}\right)} \tag{6A.7}$$

Integration of equation (6A.7) between zero and x, and substituting the definition of St_x, yields

$$St_x = \frac{C\ (t_w - t_\infty)^{\left(\frac{n}{1-n}\right)} \mu^n}{\left[\int_0^x (t_w - t_\infty)^{\left(\frac{1}{1-n}\right)} G_\infty\ dx\right]^n}$$

where $C = 0.0295\ Pr^{-0.4}$, Pr = 1.0 and n = 0.2.

Thus

$$St_x = 0.0295 \frac{(t_w - t_\infty)^{0.25} \mu^{0.2}}{\left[\int_0^x (t_w - t_\infty)^{1.25} G_\infty\ dx\right]^{0.2}} \tag{6A.8}$$

Equation (6A.8) was used to calculate the surface heat flux along the blade surface.

The value of St_x from equation (6A.8) was corrected for laminarised flow as follows:

$$(St_x)_{co} = F_\ell\ St_x \tag{6A.9}$$

where F_ℓ is the heat transfer correction factor and can be defined by

$$F_\ell = 1 - 165 \left(\frac{L}{St_x}\right)$$

The turbulence in the boundary layer covering any fixed point along the surface is apparently generated from the surface at various points upstream. Thus the Stanton number depression incorporated in the factor F_ℓ may be observed for some distance after acceleration has ceased, and F_ℓ should be evaluated about (100 - 200) momentum thicknesses (θ) upstream of the point of application.

APPENDIX 7A

DETERMINATION OF THE LATTICE RATIO

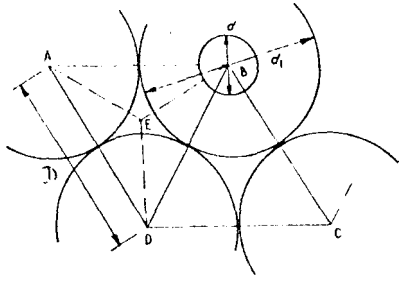

GEOMETRY OF LATTICE RATIO

Volume of complete liquid sphere = $\frac{\pi}{6} d_1^3$ for spheres in contact.

Thus $\frac{\text{volume rhombohedron}}{\text{volume liquid}} = \frac{1}{0.74} = \frac{6k\ D^3}{d_1^3\ \pi}$

For touching droplets $R = \frac{D}{d_1} = 1$

Whence $\frac{1}{0.74} = \frac{6k}{\pi}$

Therefore $k = 0.71$.

For small droplets, diameter d, situated at each lattice point, for wet steam mixture,

$$\text{Mass of vapour} = (0.71\ D^3 - \frac{\pi d^3}{6})\ \rho_g$$

$$\text{Mass of liquid} = \frac{\pi d^3}{6}\ \rho_f$$

$$\text{Dryness fraction, } x = \frac{\text{mass of vapour}}{\text{mass of vapour + mass of liquid}}$$

$$\text{Therefore } x = \frac{(0.71\ D^3 - \frac{\pi}{6} d^3)\ \rho_g}{(0.71\ D^3 - \frac{\pi}{6} d^3)\ \rho_g + \frac{\pi}{6} d^3\ \rho_f} \qquad (7A.1)$$

Setting $R = \frac{D}{d}$, and re-arranging equation (7A.1) gives

$$R = 0.9 \left[\frac{\rho_g - x(\rho_g - \rho_f)}{(1 - x)\ \rho_g}\right]^{1/3} \qquad (7A.2)$$

For low pressure $\rho_g << \rho_f$ and $\rho_f \approx 1000\ kg/m^3$, whence equation (7A.2) becomes

$$R = 9 \left[\frac{x}{(1 - x)\ \rho_g}\right]^{1/3} \qquad (7A.3)$$

APPENDIX 7B

EQUATION OF PHASE CHANGE

In the range of molecular regimes, the mass transfer is connected to the kinetic theory. The calculation is based on the number of molecules reaching the droplet N_{mg} or the number of molecules leaving the droplet N_{mf}. These numbers can be formulated from the kinetic theory of gases:

$$N_{mg} = \frac{p_g}{\sqrt{2\pi\, m_m\, k_B\, T_g}} \tag{7B.1}$$

$$N_{mf} = \frac{p(T_f,r)}{\sqrt{2\pi\, m_m\, k_B\, T_f}} \tag{7B.2}$$

The net rate of increasing or decreasing the droplet mass is given by

$$\frac{dm}{dt} = A_p\,(\alpha_g\, m_m\, N_{mg} - \alpha_f\, m_m\, N_{mf}) \tag{7B.3}$$

where α_g = accommodation coefficient of condensing the molecules vapour

α_f = accommodation coefficient of evaporating the molecules liquid

m_m = mass of a molecule

A_p = surface area of the droplet = $4\pi r^2$

The values of α_g and α_f are not far from unity. From Clapeyron's equation, $p = \rho RT$ and equation (7B.1), it can be obtained

$$m_m\, N_{mg} = \frac{1}{4}\,\rho_g \sqrt{\frac{8R\,T_g}{\pi}} \tag{7B.4}$$

Similarly, the term $N_{mf}\, m_m$ can be determined as

$$N_{mf}\, m_m = \frac{1}{4}\,\rho_f \sqrt{\frac{8R\,T_f}{\pi}} \tag{7B.5}$$

By substituting equations (7B.4) and (7B.5) into equation (7B.3) gives

$$\frac{dm}{dt} = r^2 \sqrt{8\pi r}\left[\rho_g \sqrt{T_g} - \rho_f \sqrt{T_f}\right] \tag{7B.6}$$

Using Clapeyron's equation and re-arranging equation (7B.6) to obtain

$$\frac{dm}{dt} = r^2 \sqrt{\frac{8\pi}{R}}\left[\frac{p_g}{\sqrt{T_g}} - \frac{p(T_f,r)}{\sqrt{T_f}}\right] \tag{7B.7}$$

Equation (7B.7) is valid for droplets with radius (r) less than the mean free path (ℓ'). For a wide range of Knudsen number ($Kn = \ell'/2r$), equation (7B.7) should be modified by multiplying it by a correction factor, or Cunningham correction. There are many expressions for the correction factor, and in the present work, Young (116) has derived the phase change equation, and found the correction factor to be $\frac{Kn}{1 + 2.7\ Kn}$. Therefore the final form of phase change equation can be obtained by introducing the correction factor,

$$\frac{dm}{dt} = \frac{r^2\ Kn}{1 + 2.7\ Kn}\sqrt{\frac{8\pi}{R}}\left[\frac{p_g}{\sqrt{T_g}} - \frac{p(T_f,r)}{\sqrt{T_f}}\right] \tag{7B.8}$$

and thus, equation (7B.8) can be applied for all ranges of Knudsen number.

APPENDIX 7C

THERMOPHORESIS IN DIFFUSIONAL DEPOSITION

(a) Laminar boundary layer

The mass transfer equation is given by equation (7.36)

$$N = D \frac{dc}{dy} + V_T c \qquad (7C.1)$$

which can be written as

$$\frac{dc}{N - V_T c} = \frac{dy}{D} \qquad (7C.2)$$

to be integrated with the boundary conditions:

$c = 0$ at $y = 0$

$c = c_\infty$ at $y \geqslant \delta_c$

where $\delta_c = \delta$, the concentration boundary layer thickness

δ = the hydrodynamic boundary layer thickness

$$\therefore \int_0^{c_\infty} \frac{dc}{N - V_T c} = \int_0^{\delta} \frac{dy}{D}$$

$$- \left[\frac{1}{V_T} \ln (N - V_T c) \right]_0^{c_\infty} = \frac{\delta}{D}$$

$$\ln = (1 - \frac{V_T c_\infty}{N}) = - \frac{V_T \delta}{D}$$

$$\therefore \frac{V_T}{V_{net}} = 1 - \exp (- \frac{V_T \delta}{D})$$

$$V_{net} = \frac{V_T}{1 - \exp (- \frac{V_T \delta}{D})} \qquad (7C.3)$$

where $V_{net} = \frac{N}{c_\infty}$ = the net deposition velocity.

(b) Turbulent boundary layer

Equation (7.38) which describes the mass transfer with thermophoresis through the turbulent boundary layer, is:

$$N = (D + \varepsilon_p) \frac{dc}{dy} + V_T c \qquad (7C.4)$$

which can be written as

$$\frac{dc}{N - V_T c} = \frac{dy}{D + \varepsilon_p} \qquad (7C.5)$$

to be integrated with the boundary conditions:

$c = 0$ at $y = 0$

$c = c_\infty$ at $y = \delta_c = \delta$

$$\int_0^{c_\infty} \frac{dc}{N - V_T c} = \int_0^{\delta} \frac{dy}{D + \varepsilon_p}$$

After the integration, it becomes

$$\ln (1 - \frac{V_T c_\infty}{N}) = - V_T \int_0^{\delta} \frac{dy}{D + \varepsilon_p} \qquad (7C.6)$$

and therefore the net deposition velocity can be defined as

$$V_{net} = \frac{V_T}{1 - \exp (- V_T \int_0^{\delta} \frac{dy}{D + \varepsilon_p})} \qquad (7C.7)$$

The droplet eddy diffusivity (ϵ_p) is equal to the flow viscosity (ϵ) which can be defined by using the Van Driest model

$$\epsilon_p = \epsilon = 0.4\, y \left[1 - \frac{1}{\exp\left\{\frac{y u_* \,(30.175\,\Gamma + 1)}{25\,\nu}\right\}} \right] \qquad (7C.8)$$

where Γ = the pressure gradient parameter = $\dfrac{\nu\, U_\infty \dfrac{dU_\infty}{dx}}{U_\infty^{\,3}}$

Substituting equation (7C.8) into equation (7C.7) yields

$$V_{net} = \frac{V_T}{1 - \exp\left[- V_T \int_0^\delta \frac{dy}{D + 0.4\, y \left\{1 - \exp\left(\frac{y u_* \,(30.175\,\Gamma + 1)}{25\,\nu}\right)\right\}} \right]} \qquad (7C.9)$$

Equation (7C.9) can be solved numerically to calculate the net deposition velocity (V_{net}).

THE COMPUTER PROGRAM

```
      EXTERNAL FCN,FUN1,FUN9,FUN10
      INTEGER I,M,NCAP,IWGHT,NCAP2,NCAP3,NCAP7,J,TRAIL,J2,M2,R,R2,R5
C-----------------------------------------------------------------------
      REAL AUE(80),AQO(80),AST0(80),AV1(80),ATE(80),AXX(80),AC11(80),
     1 DIF50(80),DIF100(80),DIF280(80),AVT(300),ADIFF(300),DIFEL(80),
     2 VTY50(80),VTY100(80),VTY280(80),AVVV(300),VVV50(80),VTBL(80),
     3 VVV100(80),VVV280(80),MFP50(80),MFP100(80),MFP280(80),VVBL(80),
     4 KNY50(80),KNY100(80),KNY280(80),TIM50(80),TIM100(80),RYBL(80)
     5 ,TIM280(80),RY30(80),RY40(80),RY50(80),RY100(80),RY280(80),
     6 WET100(80),WET40(80),WET50(80),WET30(80),WET280(80),WETBL(80)
     7 ,MEV20(80),MEV30(80),MEV50(80),MEV100(80),MEV280(80),MEVBL(80),
     8 QEV20(80),QEV30(80),QEV50(80),QEV100(80),QEV280(80),QEVBL(80),
     9 SS,XARG,FIT,RES,X1(200),Y1(200),W1(200),C(80),WORK1(200),RB(80)
      REAL WORK2(4,50),K(80),S(4),Y11(300),U11(600),T11(300),TSUB(80)
      LOGICAL MIDPT,MID
      REAL MUX,KTH,D01AHF,P(80),TSAT(80),DFDX,HFG(80),EP,YYE(80),YYS(80)
     1 ,YSFUL(80),YSUB(80),DELW(80),TTW(80),MACH,VNET(80),RADP(6),
     2 TWAL1(6),DDPCP(300),RDDPMF(300),RDPD(300),REMFPD(300),RDD50(80),
     3 RPD50(80),RPD100(80),RPD280(80),RDP50(80),RDE100(80),RDE280(80),
     4 RDD100(80),RDD280(80),PMF100(80),PMF280(80),AXX1(80),AXX2(80),
     5 AXX3(80),AXX4(80),AXX5(80),AXX6(80),AXX7(80),AXX8(80),AXX9(80)
      REAL CIN(6),COMM(5),CON(3),COUT(14),SOL(3),W(3,9),MEVAP(300),
     1 Y(2),CONST(3),WETPN(300),KNN(300),MFP(300),KG1,KP1,Y22(300),
     2 TOL,H,X,XEND,T0,CFT,H000,CF,UE,DUE,ME,TE,VE,RETH,HF,HDA,X5(300),
     3 TS1(300),CRTIM(300),QEVAP(300),WETF(300),DUEE(200),AREX(80),
     4 AACCP(80),ACFT(80),ADL(80),ABLT(80),AUSH(80),AEM(300),AHF(80),
     5 AD2(80),AEM50(80),AEM100(80),AEM280(80),DTDY(300),R66(300)
      REAL R11(300),YB1(300),DMO(300),DMO40(80),DMO50(80),DMO100(80),
     1 DMO280(80),TSE(80),TSFUL(80),QON(80),QEVXT(80),QQO(300),QQOX(80)
     2 ,A0(80),VVV(300),C11(300),DN1(300),DML(80),FST0(80),RT(300),
     3 EMP(300),PMP50(80),RT50(80),XGP(80),Y33(600),YBJ(600),X7(80),
     4 SCH50(80),SCH100(80),SCH280(80),VVV30(80),AC50(80),AC100(80),
     5 AC280(80),DEFMAS(80),TOTMAS(80)
      COMMON/EULROD/ X,H,T0,DISP,TE,UE,DUE,HDA,HF,CF,CFT,RETH,VE,V1,
     1DYNV,REX
      COMMON/BAKER/EP,DIFFC,USH,VSVE,BLT,EMFC,EMF9
      COMMON/ABEBBE/TW,RADIN1,TEMPE,DENS,AAUU
      ZERO=0.0
      ANS=ZERO
      A1=.088
      NLIMIT=0
      EPSI=1.0E-05
      N4=2
      N1=3
      N2=9
      CIN(1)=1.0
      Y(1)=4.33-4
      Y(2)=3.76
      CIN(2)=2.0
      DO 1 I=3,6
      CIN(I)=ZERO
    1 CONTINUE
C
```

```
      DO 2 L=1,5
      COMM(L)=ZERO
    2 CONTINUE
      DO 3 L=1,3
      CONST(L)=ZERO
    3 CONTINUE
      EEEE=1.0306
      GGG3=1.0808
      CALL PAPER(1)
      READ(4,2999)RADIN,TWW1
 2999 FORMAT(F12.10,F7.2)
      TAD=338.2005
      DO 8 L=1,300
      R11(L)=RADIN
      R66(L)=RADIN*EEEE
      WETP(L)=0.03
    8 CONTINUE
      RADIN1=RADIN*EEEE
      EPWET=0.03
      TOL=1.0E-05
      WRITE(6,198)TOL
C
C-----CALCULATION OF THE FREE STREAM VELOCITY
C
   20 READ(5,99,END=1111)M
      READ(5,98,END=2222)NCAP,IWGHT
      NCAP2=NCAP+2
      NCAP3=NCAP+3
      NCAP7=NCAP+7
      IF(NCAP.EQ.1)GO TO 40
      READ(5,97,END=3333)(X(J),J=5,NCAP3)
   40 DO 18 R=1,M
      IF(IWGHT.NE.1)GO TO 60
      READ(5,96,END=4444)X1(R),Y1(R)
      W1(R)=1.0
      GO TO 18
   60 READ(5,95,END=5555)X1(R),Y1(R),W1(R)
   18 CONTINUE
      IFAIL=0
      CALL E02BAF(M,NCAP7,X1,Y1,W1,K,WORK1,WORK2,C,SS,IFAIL)
      IF(IFAIL.NE.0) GO TO 500
      WRITE(6,996)SS
      MIDPT=.FALSE.
C-----CALCULATING THE STEP LENGTH AND STEP TIME
      M2=2*M-1
      R=0
      XGP(1)=0.09
      GP=1.02
      NG=80
      NG=NG-1
      XGP2=(0.275-XGP(1))*((1.0-GP)/(1.0-GP**NG))
      UUEE(1)=80.0
C
C                                  319
```

```
      DO 339 R2=2,NG
      JG=R2-1
      XGP(R2)=XGP(JG)+XGP2*GP**(NG-R2)
      DXGP=XGP(R2)-XGP(JG)
      X7(JG)=XGP(JG)
      X7(R2)=XGP(R2)
      IF(.NOT.MIDPT)GO TO 280
      XARG=.5*(X7(R)+X7(R+1))
      IFAIL=0
      CALL E02BBF(NCAP7,K,C,XARG,UE2,IFAIL)
      IF(IFAIL.NE.0)GO TO 260
      WRITE(6,995)XARG,UE2
      GO TO 320
  260 WRITE(6,994)XARG
      GO TO 320
  280 R=R+1
      IFAIL=0
      CALL E02BBF(NCAP7,K,C,X7(JG),UE2,IFAIL)
      IF(IFAIL.NE.0) GO TO 300
      GO TO 320
  300 WRITE(6,993)R,XARG
  320 MIDPT=.NOT.MIDPT
  339 CONTINUE
      TQEV=ZERO
      ICOUNT=0
      TAQQ=ZERO
      TQQM=ZERO
      ANS=ZERO
      SQQQX=ZERO
      TTTMAS=ZERO
      DO 340 R2=1,75
      R5=R2+1
C
C-----CALCULATION OF THE BLADE SURFACE TEMPERATURE

      IF(TWW1.GE.TAD)TTW(R2)=TAD+(TWW1-TAD)*(1.0-(0.2*(R2-1))/74.0)
      IF(TWW1.LT.TAD)TTW(R2)=TWW1
      TW=TTW(R2)
      X=X7(R2)
      DXGP=X7(R2+1)-X7(R2)
      DUE=(UUEE(R5)-UUEE(R2))/DXGP
      UE=UUEE(R2)
      AUE(R2)=UUEE(R2)
      AUE(R2+1)=UUEE(R2+1)
C
C-----CALCULATION OF THE ACTUAL FLOW PRPERTIES DUE TO RELIEVING OF THE
C     SUPERSATURATION
C
      TO=338.2
      E=A1+R2*H
      TSFUL(1)=336.5
      TSE(1)=336.5
C
C                                  320
```

```
      TSAT(1)=336.5
      TSUB(1)=336.5
      P(1)=0.233
      TSFUL(P2+1)=10-AUE(R2+1)**2/3840.0
      P(P2+1)=P(P2)*((TSFUL(P2+1)/TSFUL(P2))**4.03)
      TSB(P2+1)=TSUB(P2)*((P(P2+1)/P(P2))**0.24812)
      DYNV=(0.408*((TSUB(P2)-273.0+80.0)/2.0)+80.5)*9.40E-08
      SPE=-4.70264*P(P2+1)**2+3.24697*P(P2+1)+0.373111
      SPG=11.4297*P(P2+1)**2-7.66602*P(P2+1)+8.14867
      IF(P(P2).LT.0.158) ROF=1.0/((0.10024+8.0E-03*P(P2))*100.0)
      IF(P(P2).GE.0.158) ROF=1.0/((0.100636+5.4545E-03*P(P2))*100.0)
      IF(P(P2).LE.0.15) KTH=(19.5+15.0*P(P2))*1.0E-03
      IF(P(P2).GT.0.15) KTH=(19.4714+8.5714*P(P2))*1.0E-03
      IF(P(P2+1).LE.0.16) TSAT(P2+1)=-562.0*P(P2+1)**2+304.25*P(P2+1)+
     *20.9632+273
      IF(P(P2+1).GE.0.16) TSAT(P2+1)=-250.0*P(P2+1)**2+209.75*P(P2+1)+
     *28.1954+273
      HFG(P2)=2502.72-2.4242424*(TSAT(R2)-273.0)
      HFG(P2+1)=2502.72-2.4242424*(TSAT(P2+1)-273.0)
      TSTEG=0.5*(TSAT(P2+1)+TSFUL(P2+1))
      V1=6.5*((336.5/TSFUL(P2))**3)
      DENS=1.0/V1
      RR(1)=RADIN
      AKN=1.632E-04*DYNV*SQRT(TSTEG)/(P(P2)*RR(P2))
      DROPN=7.1b197E-06/(RADIN**3)
      SSS=7.65
      YYE(P2+1)=1.0-(SSS-SIG)/SPG
      IF(YYE(P2+1).LT.0.03) YYE(P2+1)=0.03
      YYE(1)=.03
      YYS(1)=ZERO
      IF(ICOUNT.EQ.1)GO TO 67
      TSTS=0.5*(TSAT(P2+1)+TSAT(P2))
      AAUE=0.5*(AUE(P2+1)+AUE(P2))
      SSS1=(1.0/SQRT(TSB(P2+1)))-(1.0/SQRT(TTS))
      DUDX1=AAUE*(1.0+2.7*AKN)
      DYDX1=((4.952*AKN*P(P2+1))/DUDX1)*SSS1
      DDR=DYDX1*DXGF
      RR(P2+1)=RR(P2)+DDR
      YYS(P2+1)=4.1888*1000.0*(RR(P2+1)**3-RR(P2)**3)*DROPN
      XFAC=YYS(P2+1)/YYE(P2+1)
      TSUB(P2+1)=TSB(P2+1)+XFAC*(TSAT(P2+1)-TSB(P2+1))
      IF(TSUB(P2+1).GE.TSAT(P2+1)) ICOUN1=1
      IF(TSUB(P2+1).GE.TSAT(P2+1)) TSUB(P2+1)=TSAT(P2+1)
      IF(TSUB(P2+1).GE.TSAT(P2+1)) YYS(P2+1)=ZERO
      IF(TSUB(P2+1).GE.TSAT(P2+1)) RR(P2+1)=RR(P2)
      GO TO 65
67    TSUB(P2+1)=TSAT(P2+1)
      YYS(P2+1)=ZERO
      RR(P2+1)=RR(P2)
5     CONTINUE
      ATE(1)=TSUB(1)
```



```
      ATE(R5)=TSUB(P2+1)
      TE=ATE(R2)
      TETE=TE
      YSFUL(P2)=(YYE(R2)-(1.915*(TSAT(R2)-TSFUL(P2)))/HFG(R2))*100.0
      YSUB(R2)=(YYE(R2)-(1.915*(TSAT(R2)-TSUB(R2)))/HFG(R2))*100.0
      IF(YSFUL(R2).LT.3.0)YSFUL(R2)=3.0
      IF(YSUB(P2).LT.3.0)YSUB(P2)=3.0
      YYE(P2)=YYE(R2)*100.0
      IF(YYE(R2).LT.3.0)YYE(R2)=3.0
      DELT=(TSAT(R2)-TSUB(R2))/TSAT(R2)
      DELS=-1.915*(ALOG(1.0-DELT)+DELT)
      DELW(R2)=DELS*293.0
C
C-----CALCULATION OF THE HEAT TRANSFER FROM THE BLADE SURFACE
C
      AO(R2)=X7(P2)
      EO=X7(P2+1)
      ANSO=1.0955*((TTW(1)-336.5)**1.25)
      X=X7(R2)
      IFAIL=0
      ANS=ANS+D01AHF(X7(P2),X7(R2+1),EPSR,N,RELERR,FUN1,NLIMIT,IFAIL)
      IF(IFAIL.GT.0)GO TO 500
      DYNV=(0.408*((TSFUL(R2)-273.0+80.0)/2.0)+80.5)*9.40E-08
      VE=V1*DYNV
      CP=1855.0+.8572*(TE+TTW(R2))/2.0
      VEVE=VE
      BANS=ANS+ANSO
      STO=.0295*((TTW(R2)-TE)**.25)*DYNV**.2/(BANS**.2)
      PSTO(R2)=1.0-165.0*(VE*DUE/(STO*UE**2))
      EMFC=PSTO(P2)
      IF(R2.GT.1)STO=PSTO(R2-1)*STO
      ASTO(R2)=STO*1000.0
      AV1(P2)=V1
      SV1=AV1(1)
      QQOX(P2)=SQQOX+CP*AUE(1)*(TTW(1)-ATE(1))*ASTO(1)*X7(1)/SV1/1.0E06
      SQQOX=SQQOX+CP*AUE(R5)*(TTW(R2)-ATE(R5))*ASTO(R2)*DXGF/V1/1.0E06
      AQO(P2)=QQOX(P2)
C
C-----CALCULATION OF THE BOUNDARY LAYER CHARACTERISTICS AND THE DISTRIB-
C     TIONS OF THE VELOCITY AND TEMPERATURE INSIDE THE BOUNDARY LAYER
C
      IFAIL=0
      X3=X7(R2)
      X4=X7(P2+1)
      XX=X3
      AXX(R2)=XX/0.27
      CALL D02PAF(X3,X4,N4,Y,CIN,TOL,FCN,COMM,CONST,COUT,W,N1,N2,IFAIL)
      IF (IFAIL.GT.0) GO TO 500
      ACCP=VE*DUE/(UE**2)
      AACCP(P2)=ACCP*EEEE
      MACH=UE/SQRT(1.31*461.5*TE)
      FRFAC=SQRT(1.0+0.2*MACH**2)
      DL2FAC=1.0+0.056*MACH**2
C
C
```

```
      CFT=CFS/12FAC
      ACFT(P2)=CFT*1000.0
      REX=UE*X/VE
      USH=SQRT(CFT*UE**2)
      DL=7.8*VE/USH
      EE=VE*UE*DUE/(UE**3)
      ADL(P2)=DL*1.0E05
      IF(P2.GT.0.1) UEPS=0.12*UE
      IF(P2.GT.0.2) UEPS=0.01*UE
      IF(P2.GT.0.5) UEPS=0.0005*UE
      IF(P2.GT.0.9) UEPS=0.0001*UE
      IF(P2.GT.0.99) UEPS=0.00001*UE
      IF(P2.GT.0.999) UEPS=0.000001*UE
      IF(P2.GT.0.62) UEPS=0.0001*UE
      DO 1112 J5=2,600
      J5=J5-1
      YB3(J5)=5.0E-06*J5
      YB3(J5)=YB3(J5)*USH/VE
      IF(YB3(J5).LE.DL) U11(J5)=USH*YB3(I5)
      IF(YB3(J5).GT.DL) U11(J5)=USH*(2.5*ALOG(YB3(J5)-5.3)+5.5092?)
      IF((UE-U11(J5)).LT.UEPS) BLT=YB3(J5)
      IF((UE-U11(J5)).LT.UEPS) GO TO 1113
 1112 CONTINUE
 1113 CONTINUE
      ABL(P2)=BLT*1000.0
      AUSH(P2)=USH
      AREX(P2)=REX*1.0E-05
      AD2(P2)=Y(1)*1.0E04/DI2FAC
      AHF(P2)=HF
      TS1(1)=TTW(P2)
      Y11(1)=5.0E-07
      U11(1)=0.01
      Y22(1)=2.5E-06
      T11(1)=TTW(P2)
      QEVX=ZERO
      TQNET=ZERO
      TQQQ=ZERO
      SUMVT=ZERO
      SVNET=ZERO
      ENTTG=ZERO
      SUMVT=ZERO
      SMAD=ZERO
      TEVAP=ZERO
      DO 1444 L=2,50
      M=L-1
      Y11(L)=5.02-06*M
      T11(L)=TTW(P2)+(TO-TTW(P2))*(U11(L)/UE)+(TE-TO)*((U11(L)/UE)**2)
      DDTDDY=(T11(L)-T11(M))/5.0E-06
      IF((Y11(L)-DL).LT.5.0E-06) DTDYDL=DDTDDY
 1444 CONTINUE
C
C                                  323
```

```
C-----DIVIDING THE BOUNDARY LAYER INTO RECTANGULAR CELLS AND LOCATING
C     THE FLOW PROPERTIES
C
      DO 5 I=2,60
      J=I-1
      R66(J)=R11(J)*EEEE
      Y11(I)=5.0E-06*J
      Y22(J)=Y11(I)-2.5E-06
      YB1(I-1)=Y11(I-1)*USH/VE
      YB1(I)=Y11(I)*USH/VE
      T11(I)=TTW(P2)+(TO-TTW(P2))*(U11(I)/UE)+(TE-TO)*((U11(I)/UE)**2)
      UL=7.8*USH
      TL=TTW(P2)+(TO-TTW(P2))*(UL/UE)+(TE-TO)*((UL/UE)**2)
      EE1=0.8571428
      DUDY=(U11(I)-U11(J))/(Y11(I)-Y11(J))
      DTDY(J)=(T11(I)-T11(J))/5.0E-06
      AAA=EXP(Y22(J)*USH/(26.0*VE))
      XLE=0.4*Y22(J)*(1.0-(1.0/AAA))
      EM=(XLE**2)*DUDY*EMFC
      EE=EM
      TS1(I)=T11(I)
C
C-----CALCULATION OF THE RATE OF DIMINISHING OF GROWTH OF THE DROPLETS
C     IN EACH CELL
C
      TAV=0.5*(TS1(I-1)+TS1(I))
      UAV=0.5*(U11(I-1)+U11(I))
      XSEC=5.0E-06*DXGP
      MFP(I-1)=32.223827E-05*DYNV*SQRT(TAV)/P(P2)
      IF(R66(I-1).LE.ZERO)KNN(I-1)=ZERO
      IF(R66(I-1).GT.ZERO)KNN(I-1)=MFP(I-1)/(2.0*R11(I-1))
      TRTTM(J)=DXGP/UAV
      IF(R66(I-1).LE.ZERO)C11(I-1)=ZERO
      IF(R66(I-1).GT.ZERO)C11(I-1)=INT(3.581E-11*DXGP/((RADIN**3)*V1))
C-----CALCULATION OF THE EFFECT OF WETNESS ON THE TEMPERATURE PROFILE
      DO 12 K1=1,5
      TAV=0.5*(TS1(I-1)+TS1(I))
      IF(R66(I-1).LE.ZERO)DRDX=ZERO
      SSSS=(1.0/SQRT(TAV))-(1.0/SQRT(TTSS))
      UUUU=UAV*(1.0+2.7*KNN(J))
      IF(R66(I-1).GT.0.)DRDX=((4.952*KNN(J)*P(P2))/UUUU)*SSSS
      DR=DRDX*DXGP
      R11(J)=R11(J)+DR
      R66(J)=EEEE*R11(J)
      IF(R66(J).LE.ZERO)R11(J)=ZERO
      IF(R66(J).LE.ZERO)FAC1=ZERO
      IF(R66(J).GT.ZERO)FAC1=4188.8*C11(I-1)*V1*R11(I-1)**3
      WETFN(J)=FAC1/XSEC
      DWETF=WETF(J)-WETFN(J)
      AMDOTC=(2.0/3.0)*5.0E-06*UE/V1
      MEVAP(J)=DWETF*AMDOTC
      QEVAP(J)=MEVAP(J)*HFG(R2)*1000.0
      QEVX=QEVX+QEVAP(I-1)
C
C                                  324
```

```
      IF(Y11(I).GE.DL)TG2=T11(1)
      IF(Y11(I).LE.DI)TG2=TS1(1)-QEVX*Y11(I)/KTH
      IF(ABS(TS1(I)-TG2).LE.1.0E-03)GO TO 13
      TS1(I)=TG2
   12 CONTINUE
      WETF(J)=WETFN(J)
C
C-----DETERMINING THE POSSIBILITY OF DROPLET COLLISION
C
      IF(R66(I-1).GT.ZERO)KNN(I-1)=EMP(I-1)/(2.0*R11(I-1))
      BK=1.381E-23
      IF(R66(J).GT.ZERO)RI(J)=222.22*R11(J)**2
      IF(R66(J).GT.ZERO)EMP(J)=3.609E-11*SQRT(R11(J)*TSAT(62))/DYNV
      IF(R66(I-1).LE.ZERO)EMP(J)=ZERO
      IF(R66(J).GT.ZERO)
     1DDROP(J)=18.0*R11(J)*(((1-WETF(J))*V1/WETF(J))**0.33334)
      IF(R66(J).GT.0.0)DDED(J)=DDROP(J)/(2.0*R11(J))
      IF(R66(J).GT.0.0)EMPRED(J)=EMP(J)/(2.0*R11(J))
      IF(R66(J).LE.ZERO)RED(J)=1.0
      IF(R66(J).LE.ZERO)EMPRED(J)=1.0E-03
      IF(R66(J).LE.ZERO)DDROP(J)=1.0E-10
      IF(R66(J).GT.ZERO)RDDEMP(J)=DDROP(J)/EMP(J)
      IF(R66(I-1).LE.ZERO)RDDEMP(J)=1.0
      IF(R66(I-1).LE.ZERO)FF=ZERO
C
C-----CALCULATION OF THE DIFFUSION COEFFICIENT OF THE FOG DROPLETS
C
      IF(R66(J).GT.ZERO)FF=1.0+KNN(J)*(1.558+0.173*EXP(-0.769/KNN(J)))
      IF(R66(I-1).GT.ZERO)DIFFC=BK*T11(I)*FF/(18.849556*R11(I-1)*DYNV)
      IF(R66(I-1).LE.ZERO)DIFFC=1.0E-15
      ADIFF(I-1)=DIFFC*1.0E15
      IF(R66(I-1).LE.ZERO)DIFFC=1.0E-15
      IF(R66(I-1).LE.ZERO)KNN(I-1)=ZERO
C
C-----DETERMINING THE NET DEPOSITION VELOCITY OF THE DROPLET DUE THE
C     COMBINED EFFECT OF DIFFUSION ( BROWNIAN+EDDY ) AND THERMOPHORESIS
C
      EPSR=1.0E-05
      NLIMIT=0
      IFAIL=0
      Y11(I+1)=Y11(I)+5.0E-06
      Y11(I+2)=Y11(I+1)+5.0E-06
      IF(Y11(I).LE.DI)ENTIG=ENTIG+D01AHF(Y11(I),Y11(I+1),EPSR,N,RELERR
     1,FUN9,NLIMIT,IFAIL)
      IF(Y11(I).GT.DI)ENTIG=ENTIG+D01AHF(Y11(I),Y11(I+1),EPSR,N,RELERR
     1,FUN10,NLIMIT,IFAIL)
      KG1=.019
      KP1=.630
      CC=.88
      CCS=1.14
      CCT=2.18
      CCM=1.14
C
C                                  325
```

```
      AA=1.2
      BB=0.41
      AEM(I-1)=EM
      AEM50(I2)=AEM(11)/VE
      AEM100(I2)=AEM(21)/VE
      AEM280(I2)=AEM(57)/VE
      IF(R66(J).GT.0.0)FAC2=2.0*CCS*VE*(KG1/KP1+CCT*2.0*KNN(J))
      IF(R66(J).GT.ZERO)FAC3=1.+2.0*KNN(J)*(AA+BB*EXP(-CC/(2.0*KNN(J))))
      IF(R66(I-1).LE.ZERO)FAC3=ZERO
      FAC4=DTDY(J)/T11(J)
      FAC5=1.0+6.0*CCM*KNN(I-1)
      FAC6=1.0+2.0*KG1/KP1+4.0*CCT*KNN(I-1)
      IF(R66(I-1).GT.ZERO)AVT(J)=FAC2*FAC3*FAC4/(FAC5*FAC6)
      SUMVT=SUMVT+AVT(J)*5.0E-06
      AVT(J)=SUMVT/Y11(I)
      IF(R66(I-1).LE.ZERO)AVT(J)=ZERO
      AVVX=-AVT(J)*ENTIG
      IF(R66(J).GT.ZERO)FAC7=1.0-EXP(AVVX)
      CPUV=7.1619724E-06/((FADIN**3)*V1)
      IF(R66(J).GT.ZERO)VVV(J)=AVT(J)/FAC7
      IF(R66(I-1).LE.ZERO)VVV(J)=ZERO
      SVNET=5.0E-06*VVV(J)+SVNET
      VNET(I2)=VVV(J)
      VELT=AVT(J)
      IF(R66(J).LE.ZERO)YEVAP=Y11(I)
      IF(R66(J).LE.ZERO)TEVAP=TEVAP+(DXGP/U11(I))*5.0E-06
      IF(TEVAP.EQ.ZERO)TEVAP=1.0
      SRAD=SRAD+R11(J)*5.0E-06
      RNET=SRAD/Y11(I)
    5 CONTINUE
C
C-----CALCULATION THE MASS MEDIAN DIAMETER OF THE DROPLETS IN EACH CELL
C
      DO 6 I2=1,57
      J2=59-I2
      DN1(J2)=INT(C11(J2)*VVV(J2)*TRTIM(J2)/5.0E-06)
      IF(R66(J2-1).LE.ZERO)GO TO 662
      CCCC=C11(J2-1)+DN1(J2)
      BBBB=ALOG10(R11(J2))
      BBBB1=ALOG10(R11(J2-1))
      ALRG=(DN1(J2)*BBBB+C11(J2-1)*BBBB1)/CCCC
      AISD=SQRT(((C11(J2-1)*((BBBB1-ALRG)**2))+(DN1(J2)*((BBBB-ALRG)**2)
     1))/CCCC)
      RG=10.0**ALRG
      ALRM3=ALOG10(RG**3)+10.362*ALSD**2
      RM3=10.0**ALRM3
      RM=EXP(0.33334*ALOG(RM3))
      R11(J2-1)=RM
      C11(J2-1)=CCCC
      DN1(J2-1)=INT(C11(J2-1)*VVV(J2-1)*TRTIM(J2-1)/5.0E-06)
      C11(J2-1)=C11(J2-1)-DN1(J2-1)
      DML(I2)=4188.8*R11(1)**3*DN1(1)*3.6E09
    6 CONTINUE
  662 C11(J2-1)=DN1(J2)
C
                                  326
```

```
C-----CALCULATION OF LOCAL AND CUMULATIVE DEPOSITED WATER ON THE BLADE
C     SURFACES
C
      IF(YEVAP.GT.ZERO)TEVAP=TEVAP/YEVAP
      YYMST=VMET(52)*TEVAP
      YYDEP=YYMET-YEVAP
      IF(YYDEP.GT.ZERO)VVDEP=YYDEP/TEVAP
      IF(YYDEP.LE.ZERO)VVDEP=ZERO
      IF(YEVAP.LE.ZERO)VVDEP=VMET(52)
      DEPTP=VVDEP*CFUV
      DEPMAS(52)=4188.8*3.6E05*DPET**3*DEPTP
      TOTMAS=ICTMAS+DEPMAS(52)
      ICTMAS(52)=TOTMAS
   33 IF(C.GE..275) GO TO 500
  340 CONTINUE
  500 WRITE(6,193)IFAIL,CIN(1)
      STOP
   99 FORMAT(I3)
   98 FORMAT(2I2)
   97 FORMAT(12F6.4/7F6.4)
   96 FORMAT(F7.5,E10.2)
   95 FORMAT(F7.5,E10.2,F5.3)
  996 FORMAT(/27H RESIDUAL SUM OF SQUARES = ,E20.5)
  995 FORMAT(5X,2(2X,E20.5))
  994 FORMAT(5X,E20.5,23H ARGUMENT OUTSIDE RANGE)
  993 FORMAT(5X,I3,E20.5,23H ARGUMENT OUTSIDE RANGE)
  198 FORMAT(1X,15HTHE TOLERANCE= ,E14.6)
  193 FORMAT(1X,7HIFAIL= ,I2,3X,7HCIN(1)=,F6.2)
 1111 STOP 1
 2222 STOP 2
 3333 STOP 3
 4444 STOP 4
 5555 STOP 5
      END
C
C-----SUBROUTINE FOR THE BOUNDARY LAYER CALCULATION
C
      SUBROUTINE FCN(T,Y,F)
      REAL T,X,TO,CF,CFT,H000,HDA,UE,DUE,ME,TE,VE,RETH,HF,DISP
      REAL F(2),Y(2)
      COMMON /EUHOD/ X,H,TO,DISP,TE,UE,DUE,HDA,HF,CF,CFT,RETH,VE,V1,
     1DYNV,REX
      RETH=Y(1)*UE/VE
      REX=UE*X/VE
      CF=.072/(REX**.2)
      H000=1.0/(1.0-6.8*SQRT(CF/2.0))
C
C                                  327
```

```
      HDA=1.0+1.12*(Y(2)-2.0-SQRT((Y(2)-2.0)**2-3.0))**.915
      HF=HDA
      CFT=(CF/2.0)*(.9*H000/(HDA-.4*H000)-.5)
      DISP=Y(1)*HF
      F(1)=CFT-(HF+2.0)*((Y(1)*DUE)/UE)
      F(2)=(1.0/Y(1))*((.0299/((Y(2)-3.0)**.6169))-Y(2)*(CFT-(HF+
     1  1.0)*((Y(1)*DUE)/(1.0*UE))))
      RETURN
      END
C
C-----FUNCTION FOR THE HEAT TRANSFER CALCULATION
C
      REAL FUNCTION FUN1(X)
      COMMON/ABEERB/TW,RACIN1,TETE,DENS,AAUU
      REAL X,UE
      FUN1=((TW-TETE)**1.25)*DENS*AAUU
      RETURN
      END
C
C-----FUNCTIONS FOR THE NET DEPOSITION CALCULATIONS
C
      REAL FUNCTION FUN9(YY)
      REAL YY,AAA,XLE,EM,FFF
      COMMON/EUHOD/ X,H,TO,DISP,TE,UE,DUE,HDA,HF,CF,CFT,RETH,VE,V1,
     1DYNV,REX
      COMMON/BAKER/FF,DIFFC,USH,VEVE,BLT,EMFC,EMF9
      AAA=EXP((YY*USH*(30.175*PP+1.0))/(25.0*VE))
      XLE=0.4*YY*(1.0-(1.0/AAA))
      EM=(XLE**2)*USH**2/VEVE
      EM=EM*EMFC
      EMF9=EM
      FUN9=1.0/(DIFFC+EM)
      RETURN
      END
      REAL FUNCTION FUN10(YY)
      REAL YY,AAA,XLE,EM
      COMMON/EUHOD/X,H,TO,DISP,TE,UE,DUE,HDA,HF,CF,CFT,RETH,VE,V1,
     1DYNV,REX
      COMMON/BAKER/FF,DIFFC,USH,VEVE,BLT,EMFC,EMF9
      AAA=EXP((YY*USH*(30.175*PP+1.0))/(25.0*VE))
      XLE=0.4*YY*(1.0-(1.0/AAA))
      EM=(XLE**2)*((2.5*USH**2)/(YY*USH-5.3*VEVE))
      EM=EM*EMFC
      EMF9=EM
      FUN10=1.0/(DIFFC+EM)
      RETURN
      END
C
C                                  328
```

APPENDIX 8A

DETERMINATION OF THE LAST STAGE EFFICIENCY AND THE LOSS IN OUTPUT DUE TO BLADE HEATING IN A MODERN TURBINE

It is assumed that the enthalpy drop across the stator and rotor of the penultimate stage is the same as that across the stator and rotor of the last stage. Knowing the terminal conditions of the stator and the rotor of the last stage enables us to plot the thermodynamic process inside the last two stages, as shown in Fig. 8.1. Process 1 - 3 is the expansion through the penultimate stage whilst process 3 - 5 is that through the last stage.

I. Calculation of the Efficiency of the Rotor of the Penultimate Stage

The flow through the penultimate stage is dry steam; therefore a stage efficiency (η_{1-3}) of 93% can be used as discussed in section 8.2. The enthalpy drop across the last stage is about 205 kJ/kg and this is the assumed enthalpy drop across the penultimate stage. Knowing the thermodynamic conditions at point 1 (p_1 = 0.86 bar and h_1 = 2750 kJ/kg) and at point 3 (p_3 = 0.233 bar and h_3 = 2544 kJ/kg), the conditions at point 2 can therefore be defined by finding the conditions at point 3ss

$$\eta_{1-3} = \frac{h_1 - h_3}{h_1 - h_{3ss}} = 0.93$$

$$h_{3ss} = 2750 - \frac{205}{0.93} = 2530 \text{ kJ/kg}$$

From the steam table the entropy at point 3ss (S_{3ss}) is 7.62 kJ/kg K. Figure 8.1 shows that $S_1 = S_{2s} = S_{3ss} = S_{4ss} = S_{5ss}$ and the pressure at point 2 is 0.45 bar. Therefore, h_{2s} can be found (from S_{2s} and p_2) to be 2636 kJ/kg. The enthalpy at 2 (h_2) can therefore be calculated from the definition of the nozzle efficiency

$$\eta_{1-2} = \frac{h_1 - h_2}{h_1 - h_{2s}} = 0.97$$

$\therefore\ h_2 = 2750 - 0.97\ (2750 - 2636) = 2642$ kJ/kg.

From the steam table S_2 and h_{3s} are found to be 7.63 kJ/kg K and 2535 kJ/kg respectively. The rotor efficiency therefore can be calculated:

$$\eta_{2-3} = \frac{h_2 - h_3}{h_2 - h_{3s}} = \frac{2642 - 2544}{2642 - 2535} = 0.91$$

II. Calculations of the Efficiencies of the Stator and the Rotor of the Last Stage

The flow inside the last stage is wet; therefore the efficiency of the dry flow must be modified according to the degree of wetness since the presence of the wetness reduces the efficiency. The wetness fraction at 3, 4a and 5a were found to be 3.0%, 6.4% and 9% kg/kg respectively. If a dry region can be created on the blade surface and spontaneous nucleation produces only very small droplets, the wetness losses will be minimised. They can then be neglected when compared with losses resulting from coarse water in the flow and on the blade surface. One of the earliest empirical corrections to stage efficiency to account for wetness loss was that of Baumann (53),

$$\eta_{wet} = \eta_{dry}\ (1 - \tfrac{1}{2}\alpha y_e)$$

where α = 1.4 for a stage

α = 0.7 for half stage.

This can be used to define the efficiency of the stator and the rotor when the steam is wet.

$$\eta_{3-4a} = 0.97\ (1 - 0.5 \times 0.7 \times 0.047) = 0.954$$

and hence h_{4a} can be calculated, knowing η_{3-4a} and h_{4s};

$$h_{4a} = h_3 - \eta_{3-4a} (h_3 - h_{4s}) = 2544 - 0.954 (2544 - 2425)$$

$$= 2430 \text{ kJ/kg}$$

When heating is employed the process 3 - 4a no longer defines the flow inside the stator since the exit enthalpy (h_{4a}) will be changed to $(h_d)_{dry}$ and increased by the amount of the heat input from the internal surface of the blade. The new enthalpy (h_{4H}) can be calculated from $(h_4)_{dry}$ and the heat input:

$$(h_4)_{dry} = h_3 - (\eta_{3-4a})_{dry} (h_3 - h_{4s}) = 2544 - 0.97 (2544 - 2525)$$

$$= 2428.7 \text{ kJ/kg.}$$

$$h_{4H} = (h_4)_{dry} + 2.3 = 2431 \text{ kJ/kg.}$$

The efficiency of the heated nozzle (η_{3-4H}) can be calculated from

$$\eta_{3-4H} = \frac{h_3 - h_{4H}}{h_3 - h_{4s}} = 0.951$$

The reduction in the efficiency of the passage of the stator due to heating is

$$(\Delta\eta)_{nozzle} = \eta_{3-4H} - \eta_{3-4a} = 0.3\%$$

From the steam chart h_{5Hs} = 2336 kJ/kg, S_{4H} = 7.66 kJ/kg K. The wetness fraction is reduced by about 0.1% because of heating. The efficiency of the passage of the blade rotor can be calculated using the Baumann equation

$$\eta_{4a-5a} = \eta_{2-3} (1 - 0.5 \times 0.7 \times y_{5a}) = 88.5\%$$

Because there is no coarse water from the stator when blade heating is employed the losses in rotor efficiency due to wetness can be assumed to be about ¾ of those when blade heating is not used. Therefore the rotor

efficiency, η_{4H-5H}, is

$$\eta_{4H-5H} = \eta_{2-3} (1 - 0.5 \times 0.75 \times 0.7 \times y_{5H}) = 89.1\%$$

Therefore the gain in rotor efficiency due to heating can be calculated:

$$(\Delta\eta)_{rotor} = \eta_{4a-5a} - \eta_{4H-5H} = 0.6\%$$

The enthalpy at the exit of the last stage without or with the blade heating method can be determined:

$$h_{5a} = h_{4a} - \eta_{4a-5a} (h_{4a} - h_{5as}) = 2347 \text{ kJ/kg}$$

$$h_{5H} = h_{4H} - \eta_{4H-5H} (h_{4H} - h_{5Hs}) = 2346 \text{ kJ/kg}$$

where h_{5as} and h_{5Hs} were determined from the steam chart (h-s diagram). Hence the change in stage efficiency can be calculated:

$$\eta_{3-5a} = 93.0\% \text{ and } \eta_{3-5H} = 93.2\%$$

$$(\Delta\eta)_{stage} = + 0.2\%$$

This indicates that blade heating will increase the efficiency of the last stage by about 0.2%. The importance of this figure is that there is no decrease in the stage efficiency due to heating the stator blade.

III. Calculations of the Change in the Turbine Output

The output of the turbine is affected by two factors:

1. Loss due to the extraction of blade heating steam from the entry to the penultimate stage. It is calculated from the following equation:

$$\Delta W_{loss} = \Delta\dot{m} \left[(\Delta h\, \eta)_{\text{penultimate stage}} + (\Delta h\, \eta)_{\text{last stage}} \right]$$

$$= 9.5 \times 10^{-4} (205 \times 0.94 + 189 \times 0.93) = 0.36 \text{ kW per passage.}$$

2. Work gain due to increase in the last stage efficiency

$$\Delta W_{gain} = (\dot{m} - \Delta\dot{m})(\Delta\eta\ \Delta h)_{\text{last stage}}$$

$$= (0.88615 - 9.5 \times 10^{-4}) \times 0.002 \times 189 \approx 0.3 \text{ kW per passage.}$$

The calculations have shown that this loss is closely matched by the gain due to the increased efficiency of the last stage. When considering the worst situation ΔW_{gain} is not taken into account for the economic evaluation of the blade heating method.

The loss due to steam extraction is:

(a) If the turbine has 3 L.P.s

$$\Delta W_{loss} = (\Delta W_{loss})_{\text{one passage}} \times \text{number of passages} \times \text{number of turbine exhausts} = 0.36 \times 99 \times 6 = 193 \text{ kW.}$$

(b) If the turbine has 2 L.P.s

$$\Delta W_{loss} = 0.36 \times 99 \times 4 = 129 \text{ kW}$$

IV. Calculations of the Quantity of the Additional Steam to Recover the Loss in the Output of the Turbine

The additional steam required from the boiler ($\delta\dot{m}_{boiler}$) is less than $\Delta\dot{m}_{blade}$ (9.5×10^{-2} kg/s per diaphragm) since it will produce work when it passes through the H.P., I.P. and the first three stages of the L.P. (which consists of five stages). To calculate $\delta\dot{m}_{boiler}$ we consider a notional small turbine having the same efficiency as the H.P. and I.P. turbines (about 85%), which receives $\delta\dot{m}_{boiler}$ of steam at the H.P. inlet conditions and expands it to the conditions at the entry to the penultimate stage of the L.P. turbine. Therefore there are two sources of work which

recover the loss in the output of the turbine.

1. Work from the notional turbine if its steam mass flow is $\delta\dot{m}_{boiler}$:

$$(\Delta W)_{\substack{\text{notional}\\\text{turbine}}} = \dot{m}_{boiler}\ (\Delta h\ \eta)_{\substack{\text{notional}\\\text{turbine}}} \qquad (8A.1)$$

2. Work from the last two stages of the L.P. turbine when $\delta\dot{m}_{boiler}$ expands through them, is calculated from,

$$(\Delta W)_{\substack{\text{last 2}\\\text{stages}}} = \delta\dot{m}_{boiler}\ (\Delta h\ \eta)_{\substack{\text{last 2}\\\text{stages}}} \qquad (8A.2)$$

The total recovery work is therefore,

$$W_{recovery} = (\Delta W)_{\substack{\text{notional}\\\text{turbine}}} + (\Delta W)_{\substack{\text{last 2}\\\text{stages}}} = \delta\dot{m}_{boiler} \left\{(\Delta h\ \eta)_{\substack{\text{notional}\\\text{turbine}}} + (\Delta h\eta)_{\substack{\text{last 2}\\\text{stages}}}\right\} \qquad (8A.3)$$

Equation (8A.3) can be solved iteratively by assuming $\delta\dot{m}_{boiler}$ until $W_{recovery}$ equal to W_{loss} (W_{gain} is neglected for considering the worst case).

It is found that the value of $\delta\dot{m}_{boiler}$ is;

(a) 0.122 kg/s when the turbine has 2 L.P.s and

(b) 0.185 kg/s when the turbine has 3 L.P.s.

In other words to design a complete turbine have two L.P.s, with blade heating, that would give the same work output as an equivalent conventional turbine;

(i) the boiler mass flow would have to be increased by 0.122 kg/s;

(ii) *the mass flow through each H.P. and I.P. turbine would then be* 0.122 and 0.061 kg/s respectively (the I.P. being double flow) higher than for a conventional turbine. The mass flow rate through the first three stages of each L.P. turbine would be about 0.03 kg/s higher;

(iii) 0.095 kg/s would then be extracted from each of the four L.P. streams for blade heating;

(iv) the mass flow rate through the last two stages of each L.P. turbine would then be about 0.065 kg/s lower than for a conventional turbine.

Similarly for designing a three L.P. turbine with blade heating the mass flow rate through the H.P., I.P. and L.P. turbines will be as follows:

(i) The boiler mass flow rate should be increased by 0.185 kg/s.

(ii) The mass flow rate through the H.P. turbine would be increased by $\delta\dot{m}_{boiler}$ which is 0.185 kg/s.

(iii) The mass flow rate through each I.P. turbine would be increased by about 0.092 kg/s. Through the first three stages of each L.P. turbine, the mass flow rate would then be increased by about 0.031 kg/s.

(iv) 0.095 kg/s would then be extracted from each of the six L.P. turbines for blade heating (the point of extraction is at the entry to the penultimate stage).

(v) The mass flow rate through the last two stages of each L.P. turbine would be lower than for a conventional turbine by about 0.064 kg/s.

APPENDIX 8B

U.K. ECONOMIC SCENARIOS

Before explaining the various scenarios for the U.K. economy which is highly affected by the development of the world economy, the C.E.G.B. has defined three alternative cases of world economic activity referred to as the High, Medium and Low cases; they are described as follows:

(a) High Growth

This case assumes that there will be rapid re-establishment of world financial order and discipline and that there will be an associated high degree of co-operation between industrialised, developing and oil exporting countries. Economic growth, while not quite achieving the rate of the 1950s and 1960s, recovers substantially towards these levels.

(b) Medium Growth

In this case both the degree of co-operation and the extent of reform in the international financial area are more limited and achieved on a more protracted time scale than in the high growth case. Moderate economic growth is assumed, substantially below the levels of the 1950s and 1960s but somewhat better than most recent experience.

(c) Low Growth

This case assumes that there is a failure to make any significant improvements in the extent of co-operation between countries, that the stability of the world financial system deteriorates and that, partly as a result, economic growth is very limited.

The C.E.G.B. analysis of the U.K. scenarios has assumed differing degrees of success for economic policy together with different levels of

economic activity. These scenarios are described by the C.E.G.B. as follows:

1. Scenario A - High economic growth based on services

Assumes a development of the economy which is relatively rapid but favouring services, a high regard for the environment and rapid progress on energy conservation. This scenario entails a substantial improvement in the efficiency of U.K. manufacturing industry through concentration on modern, technologically advanced, high value-added products. The scenario is associated with the high world economy growth case.

2. Scenario B - High economic growth based on manufacturing

Reflects successful economic development along traditional lines based on recovery and expansion of both traditional heavy and new technologically advanced manufacturing industries. The rate of growth, which is judged to be near the plausible maximum, still remains somewhat below that achieved in the 1950s and 1960s. This scenario is associated with the medium world economic growth case.

3. Scenario C - Medium economic growth

This scenario does not assume a high degree of either success or failure. It presumes mixed fortunes in overcoming the problems which have been evident in the U.K. for the last 10 - 20 years. It relates broadly to a continuation of the economic trends underlying the Electricity Supply Industry's Adopted Demand Estimates of October 1981. This scenario is associated with the medium world economic growth case.

4. Scenario D - Stable low economic growth

In this case de-industrialisation and a declining level of economic activity occur in the first half of the period to 2000, while in the second half the economy stagnates. It is assumed that this occurs as a

by-product of economic, industrial and environmental policy and that it represents an acceptable outcome to a majority of the population. Personal living standards are maintained through a reduction in the need for investment because of the declining industrial base and, in the long term, through returns on investment overseas. This scenario is associated with the medium world economic growth case.

5. Scenario E - Unstable low economic growth

This case presumes that de-industrialisation occurs by accident rather than design and that there would be a general lack of co-operation with consequent social differences, volatility of policy and an inability to overcome economic conflicts. This scenario is associated with the low world economic growth case.

TABLE 4.1 - DETERMINATION OF MASS-MEDIAN DIAMETER FOR 5% URANIN SOLUTION

Previous Work (4)		Present Work								
		1	2	3	4	5	6	7	8	9
Mid-range diameter μm	% in range	Mid-range diameter μm	No.	Cumul-ative	% in range	% Cumul-ative	d^3	nd^3	% in Range	% Cumul-ative
0.025	0	0.025	0	0	0.0	0.0	1.56×10^{-5}	0.0	0.0	0.0
0.075	7.9	0.05	14	14	1.1	1.1	1.25×10^{-4}	1.75×10^{-3}	0.02	0.02
0.125	15.8	0.075	105	119	8.26	9.36	4.22×10^{-4}	4.43×10^{-2}	0.51	0.53
0.175	19.8	0.125	282	401	22.19	31.55	1.95×10^{-3}	0.5507	6.34	6.87
0.225	25.3	0.15	325	726	25.55	57.1	3.37×10^{-3}	1.097	12.63	19.5
0.275	18.2	0.175	413	1139	32.5	89.6	5.36×10^{-3}	2.213	25.5	45.0
0.325	5.9	0.25	88	1227	6.9	96.5	1.56×10^{-2}	1.375	15.84	61.0
0.375	3.2	0.35	28	1255	2.2	98.7	4.29×10^{-2}	1.2	13.8	74.6
0.425	2.0	0.45	9	1264	0.7	99.4	9.11×10^{-2}	0.82	9.44	84.1
0.475	1.4	0.55	5	1269	0.4	99.8	0.166	0.832	9.58	93.7
0.525	0.4	0.65	2	1271	0.2	100.0	0.275	0.549	6.32	100.0

It gives,

$dg = 0.1522$ μm, $S_{DG} = 1.442$, $d_a = 0.166$ μm, $d_{mm} = 0.1861$ μm and $\alpha = 0.05$.

TABLE 8.1

Actual (from 1967 to 1983) and Assumed (from 1983 to 2023) Values of Inflation Rate, Coal Prices (in money terms up to 1983 and in REAL terms thereafter) and annual Operating Hours for Ferrybridge-C, Eggborough and West Burton .

Year number	Year	Inflation rate (%)	Coal Prices (P/GJ)					Annual Operating Hours			Future operating hours	
			Scenario A	Scenario B	Scenario C	Scenario D	Scenario E	Ferrybridge-C	Eggborough	West Burton	year	operat. hours
0	1967	0.0	18.9	18.9	18.9	18.9	18.9	2365.20	-------	2219.00	1983	3066
1	1968	7.97	18.8	18.8	18.8	18.8	18.8	3460.20	3460.20	4936.26	1984	6132
2	1969	8.55	18.9	18.9	18.9	18.9	18.9	3407.64	2277.60	3479.08	1985	6175
3	1970	10.78	19.6	19.6	19.6	19.6	19.6	2531.64	2093.64	3530.28	1986	6219
4	1971	6.88	22.5	22.5	22.5	22.5	22.5	3880.68	4555.20	3363.84	1987	6263
5	1972	7.23	25.8	25.8	25.8	25.8	25.8	3864.91	4257.36	3267.48	1988	6307
6	1973	14.72	27.2	27.2	27.2	27.2	27.2	3828.12	3871.92	3577.04	1989	6290
7	1974	28.57	30.8	30.8	30.8	30.8	30.8	3889.44	5369.88	4108.44	1990	6270
8	1975	19.64	54.2	54.2	54.2	54.2	54.2	3968.28	6245.88	3731.76	1991	6220
9	1976	20.15	67.9	67.9	67.9	67.9	67.9	6351.00	5904.24	5711.52	1992	6263
10	1977	13.86	79.4	79.4	79.4	79.4	79.4	5194.68	6894.12	4765.44	1993	6245
11	1978	10.75	93.4	93.4	93.4	93.4	93.4	6070.68	5448.72	5548.04	1994	6160
12	1979	13.93	119.9	119.9	119.9	119.9	119.9	6517.44	6123.24	5893.73	1995	6080
13	1980	14.86	123.2	123.2	123.2	123.2	123.2	6789.00	5877.96	6289.68	1996	5300
14	1981	7.99	147.4	147.4	147.4	147.4	147.4	5291.04	6727.68	6789.00	1997	4850
15	1982	8.31	174.6	174.6	174.6	174.6	174.6	6333.48	6403.56	6158.28	1998	4670
16	1983	7.0	180.0	180.0	180.0	180.0	180.0	5080.80	5080.80	5080.80	1999	4470
17	1984	7.0	190.0	185.0	185.0	180.0	180.0	4993.20	4993.20	4993.20	2000	4340
18	1985	7.0	201.0	189.0	189.0	180.5	180.0	4905.60	4905.60	4905.60	2001	4200
19	1986	7.0	210.0	193.0	193.0	181.5	180.0	4791.72	4791.72	4791.72	2002	4120
20	1987	7.0	221.0	200.0	199.0	182.5	180.0	4704.12	4704.12	4704.12	2003	4030
21	1988	7.0	230.0	207.0	201.0	184.0	181.0	4599.00	4599.00	4599.00	2004	3980
22	1989	7.0	239.0	213.0	207.0	186.5	183.0	4511.40	4511.40	4511.40	2005	3900
23	1990	7.0	248.0	220.0	210.0	188.0	187.0	4397.52	4397.52	4397.52	2006	3780
24	1991	7.0	255.0	230.0	215.0	190.0	180.0	4309.92	4309.92	4309.92	2007	3670
25	1992	7.0	260.0	240.0	220.0	192.5	193.0	4204.80	4204.80	4204.80	2008	3590
26	1993	7.0	268.0	250.0	223.0	196.0	200.0	4117.20	4117.20	4117.20	2009	3420
27	1994	7.0	271.0	263.0	229.0	199.0	208.0	4029.60	4029.60	4029.60	2010	3240
28	1995	7.0	275.0	280.0	232.0	201.0	213.0	3942.00	3942.00	3942.00	2011	3070
29	1996	7.0	279.0	293.0	238.0	206.0	220.0	3828.12	3828.12	3828.12	2012	2950
30	1997	7.0	282.0	309.0	241.0	210.0	228.0	3723.00	3723.00	3723.00	2013	2760
31	1998	7.0	287.0	321.0	247.0	214.0	234.0	3635.40	3635.40	3635.40	2014	2670
32	1999	7.0	290.0	332.0	250.0	219.0	240.0	3547.80	3547.80	3547.80	2015	2580
33	2000	7.0	299.0	342.0	255.0	224.0	246.0	3442.68	3442.68	3442.68	2016	2565
34	2001	7.0	305.0	350.0	260.0	230.0	250.0	3328.80	3328.80	3328.80	2017	2450
35	2002	7.0	312.0	354.0	265.0	237.0	253.0	3241.20	3241.20	3241.20	2018	2365
36	2003	7.0	321.0	360.0	270.0	243.0	257.0	2794.44	2794.44	2794.44	2019	2270
37	2004	7.0	330.0	364.0	278.0	250.0	260.0	2163.72	2163.72	2163.72	2020	2075
38	2005	7.0	340.0	369.0	282.0	256.0	263.0	1971.00	1971.00	1971.00	2021	1880
39	2006	7.0	350.0	371.0	290.0	262.0	267.0	1795.80	1795.80	1795.80	2022	1710
40	2007	7.0	359.0	376.0	298.0	270.0	270.0	1314.00	1314.00	1314.00	2023	1314
								TOTAL	TOTAL	TOTAL		total
								167116.3	168884.5	170228.3		170005

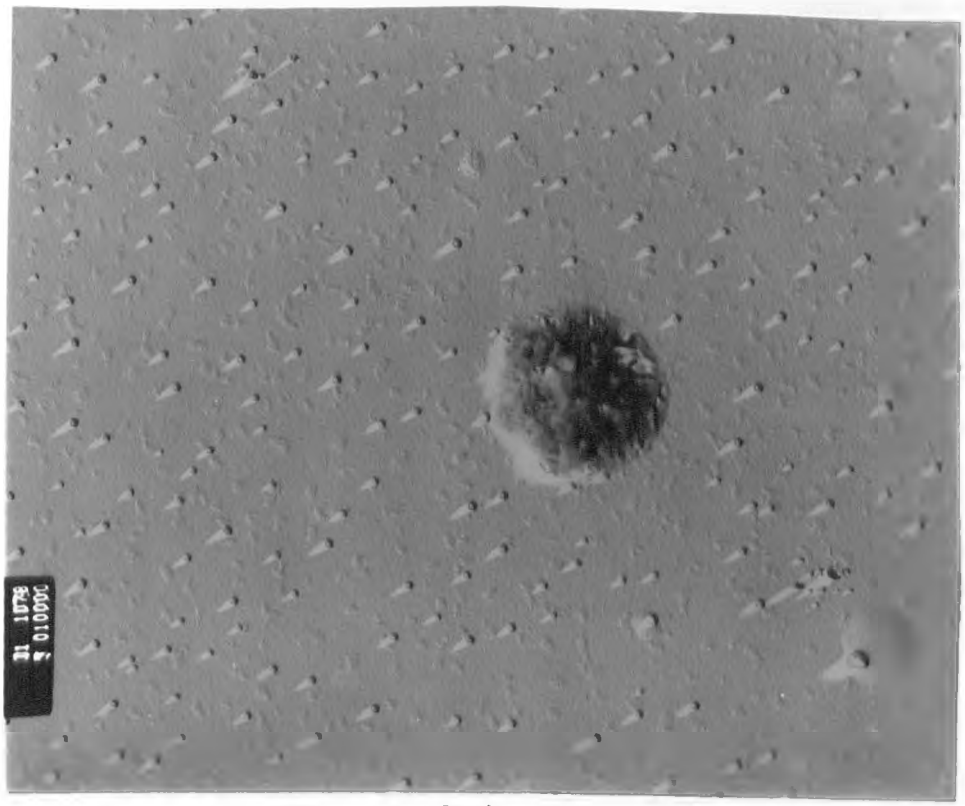

Plate 4.1: Electron Microscope photograph of Particles produced from 3% Uranin solution. Magnification= x 10,000 .

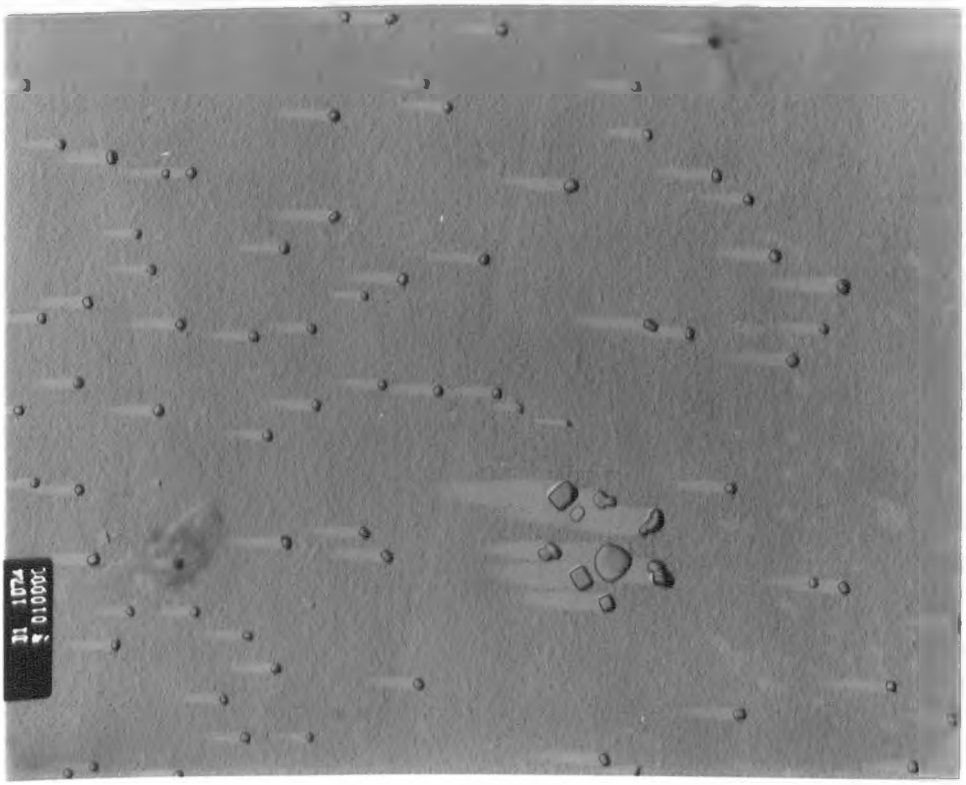

Plate 4.2: Electron Microscope photograph of Particles produced from 5% Uranin solution. Magnification= x 10,000 .

KEYS FOR THE FIGURES OF CHAPTER 7

In Figures 7.1-7.24, 7.28-7.47, 7.50-7.69, 7.72-7.91, 7.94-7.112, and 7.123-7.141 the Pattern of the Curves defines the Locations of the Droplets from the Blade Surface, as follows;

Pattern	Distance from the blade surface, y (um)
.....	20
-----------	30
----------	40
---------	50
--------	100
-.-.-.-.-	170
———	280

In Figures 7.26, 7.27, 7.48, 7.49, 7.70, 7.71, 7.92, 7.93, 7.113-7.122, 7.142-7.145 the Pattern of the Curves defines the Locations of calculation along the concave surface, as follows;

Pattern	Distance from the front stagnation point, x/c
----------	0.35
--------	0.59
— — — —	0.80
-.-.-.-.-	0.92
———	0.99

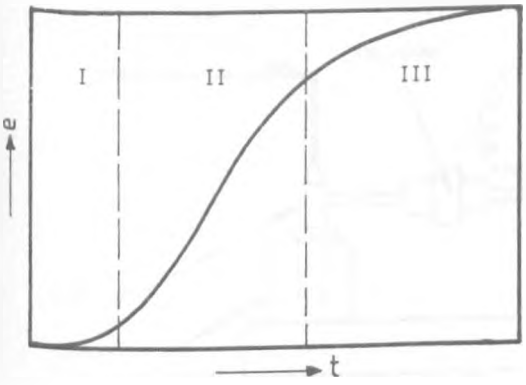

t = service life
e = erosion depth
I, II, III= time zones

FIGURE 1.3 EROSION WITH RESPECT TO TIME

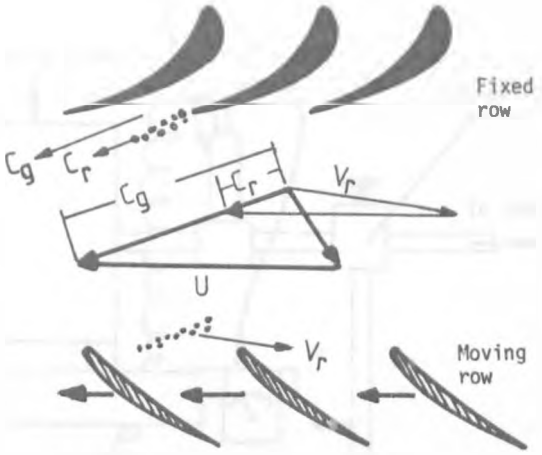

C_g = absolute steam velocity
C_r = absolute water velocity
U = peripheral velocity
V_r = relative water velocity

FIGURE 1.2 VELOCITIES IN A LOW PRESSURE STAGE

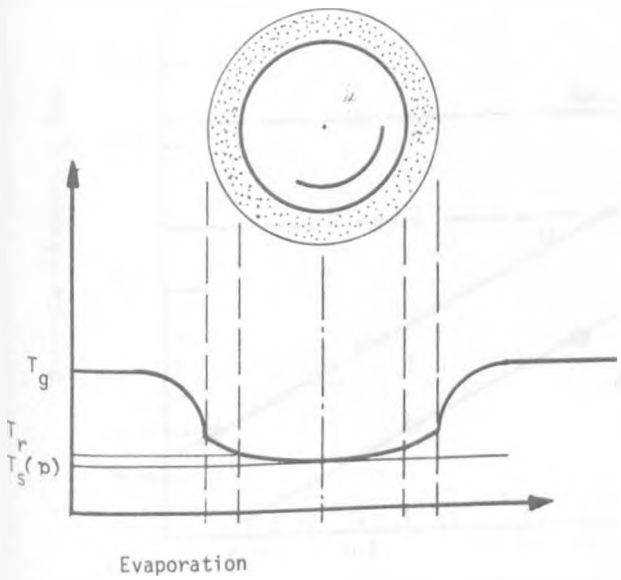

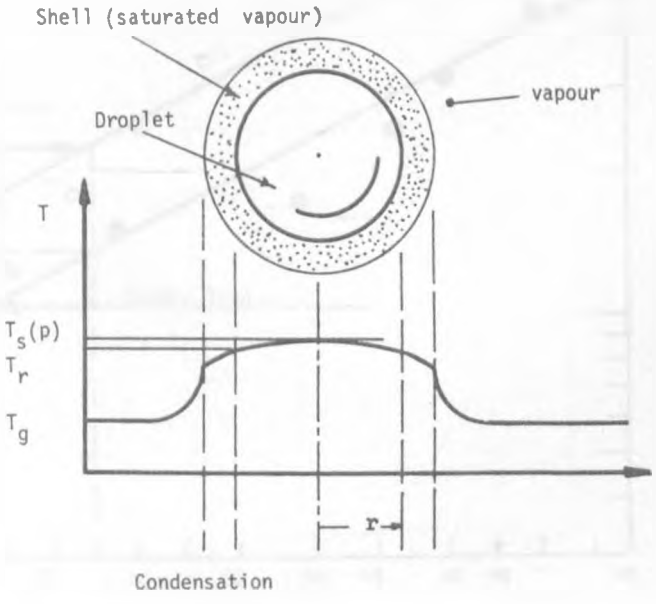

FIGURE 2.1 TEMPERATURE FIELD INSIDE AND OUTSIDE THE LARGE DROPLET WHEN IT EXISTS IN SUBCOOLED OR SUPERHEATED VAPOUR

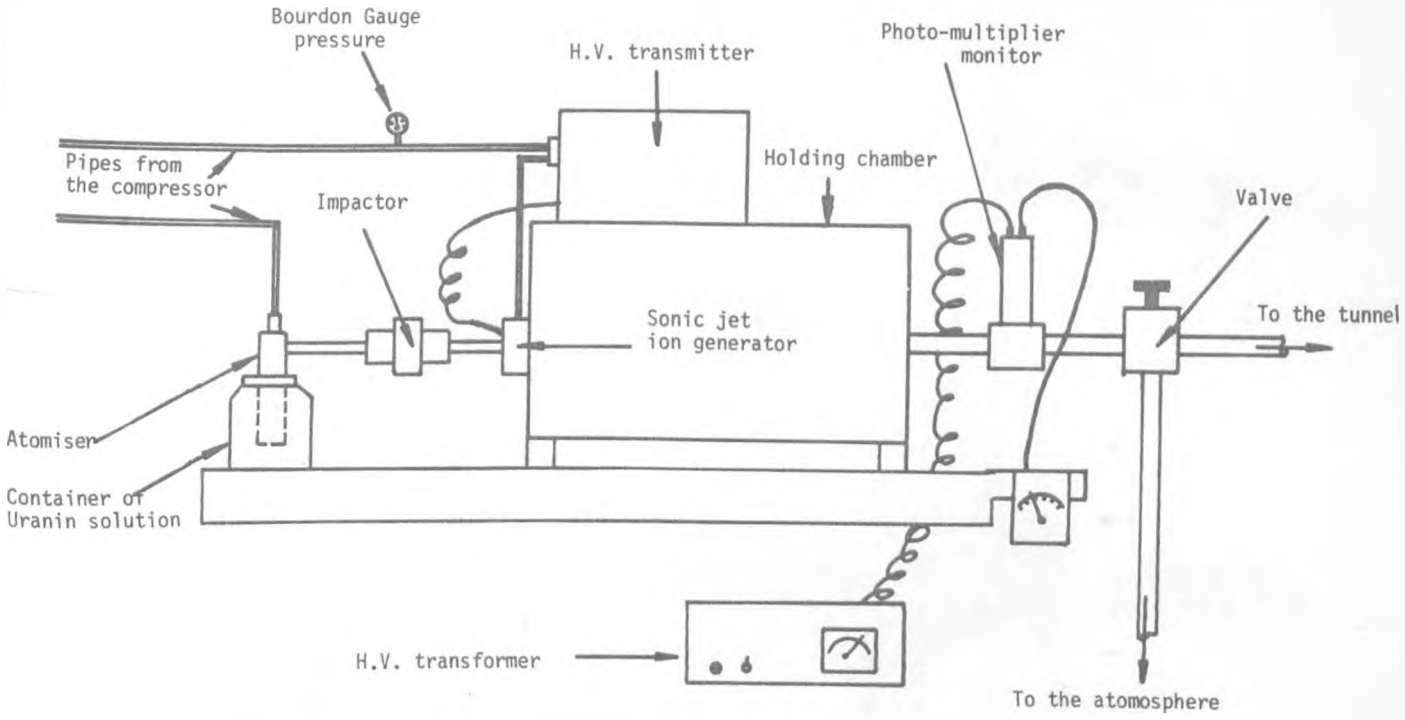

FIGURE 4.1 THE AEROSOL GENERATOR

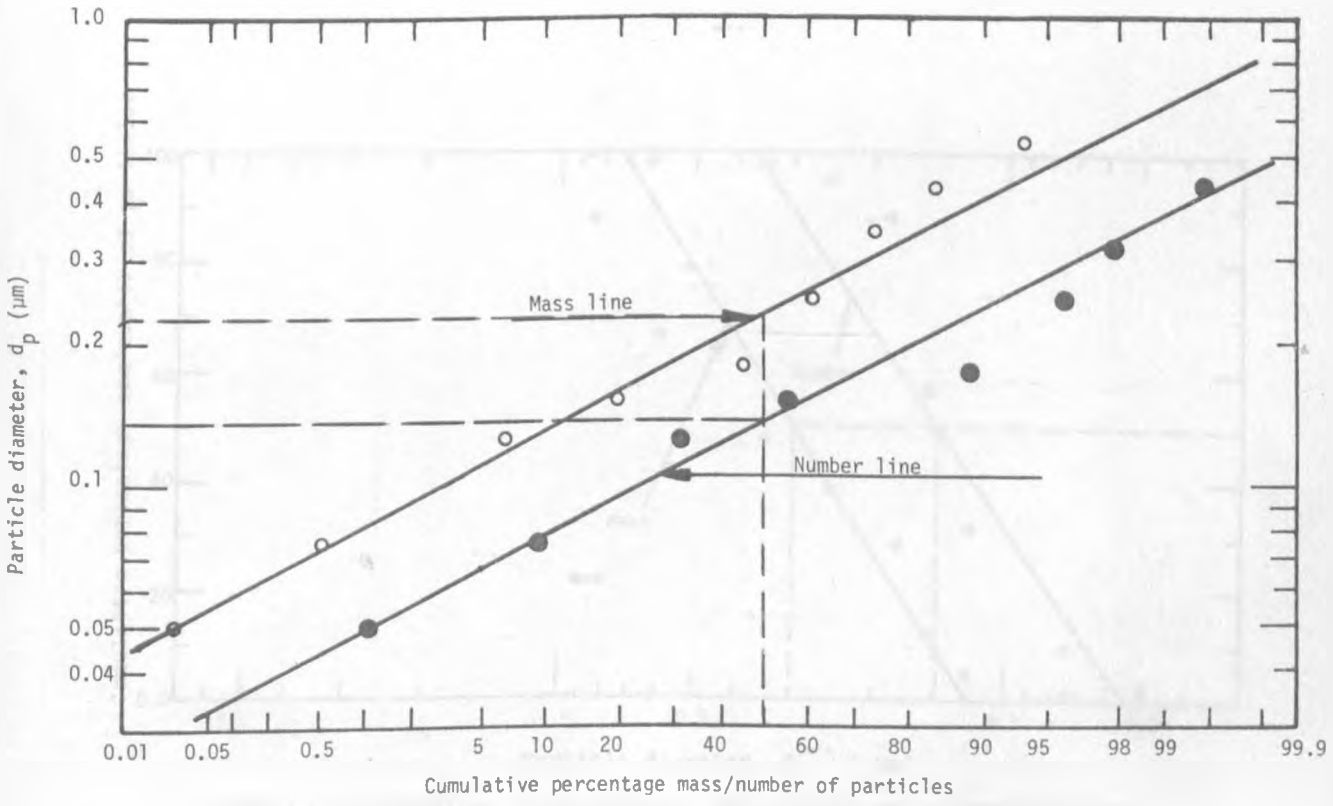

FIGURE 4.2 DETERMINATION OF MASS/GEOMETRIC MEAN DIAMETER FOR 5% URANIN SOLUTION

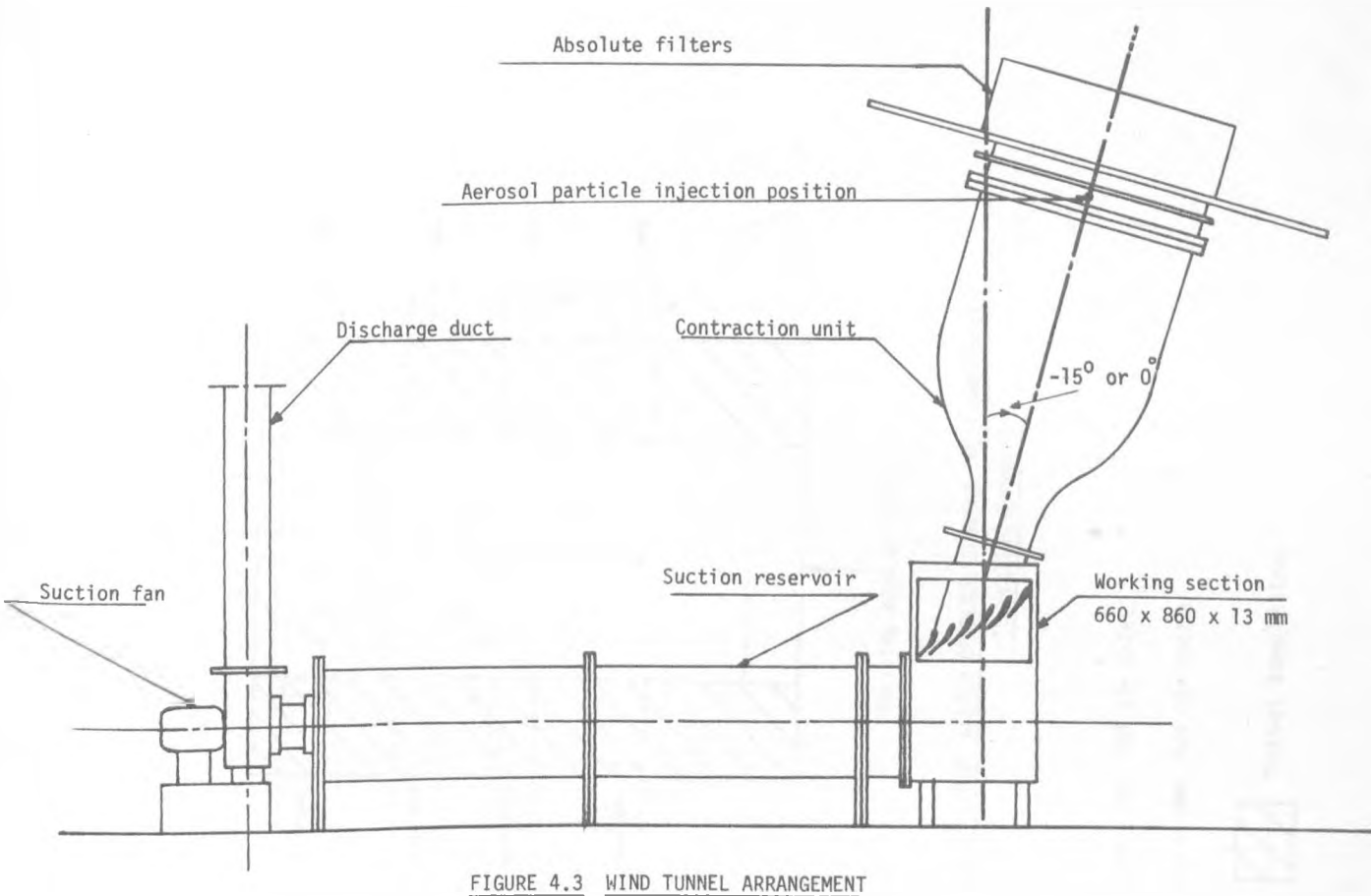

FIGURE 4.3 WIND TUNNEL ARRANGEMENT

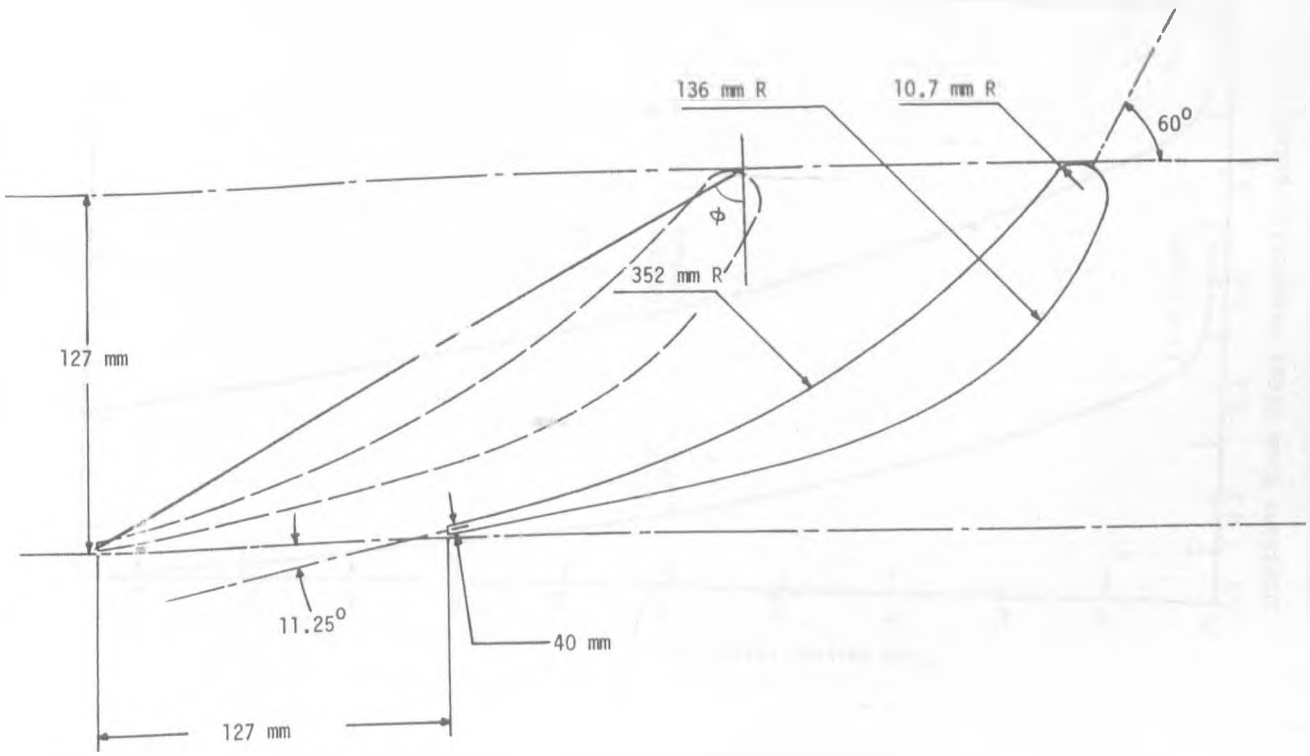

FIGURE 4.4 TEST BLADE PROFILE

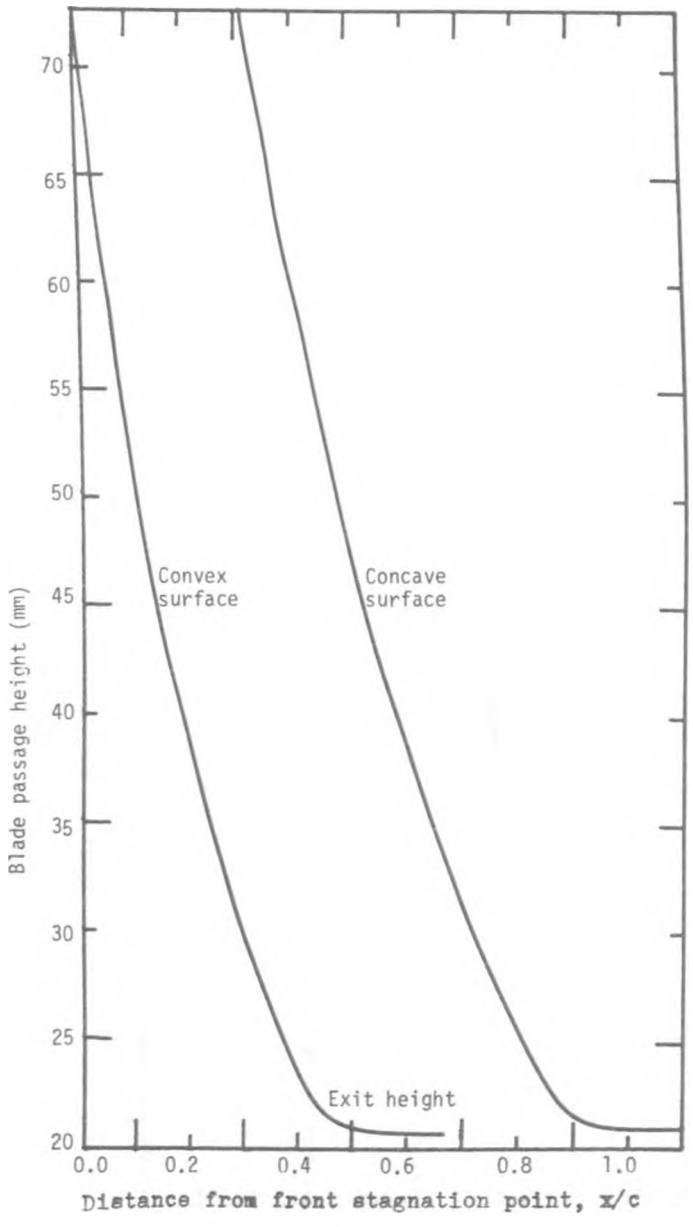

FIGURE 4.5 VARIATION OF THE BLADE PASSAGE HEIGHT

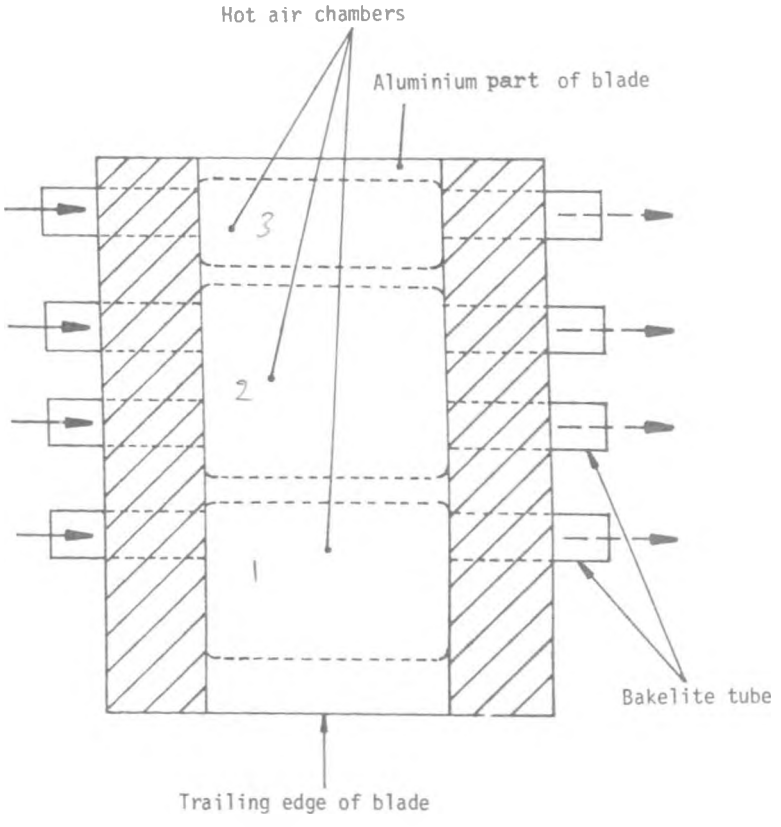

FIGURE 4.6 SKETCH OF BLADE SHOWING INLET AND OUTLET TO HEATING CHAMBERS

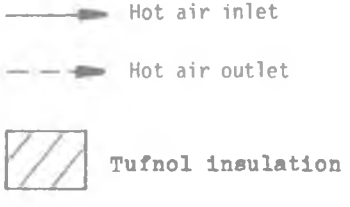

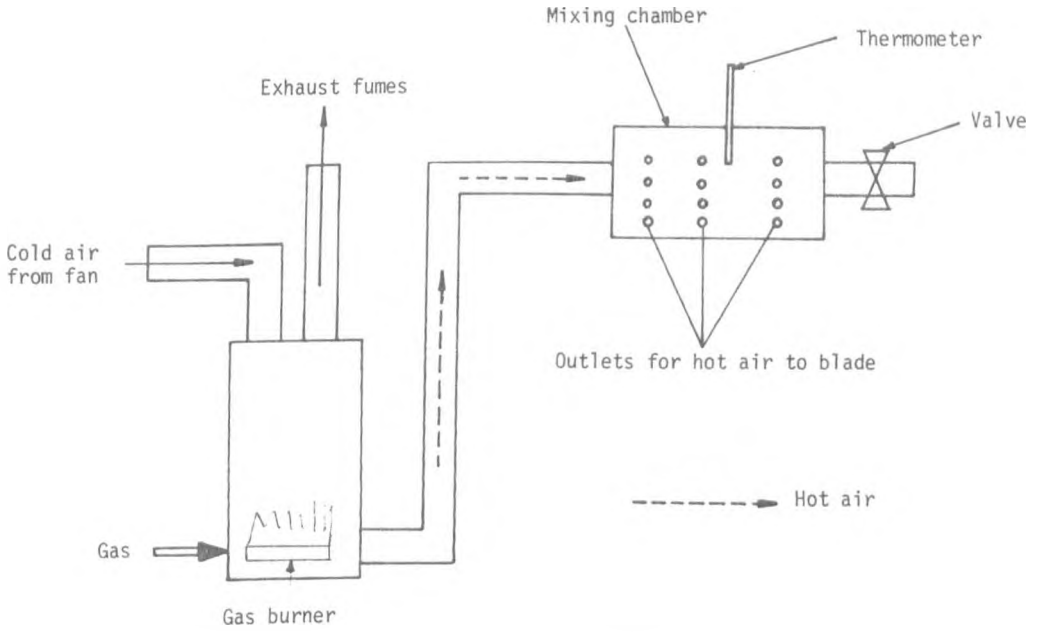

FIGURE 4.7 SCHEMATIC LAYOUT OF HEATING SYSTEM

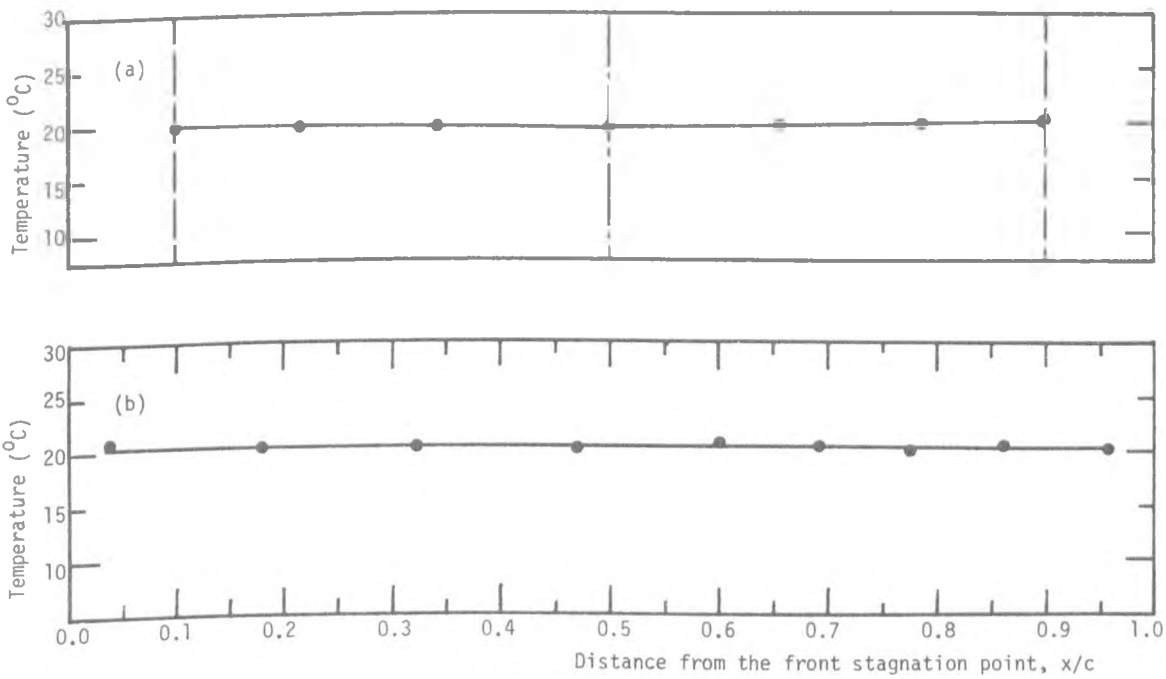

FIGURE 4.8 (a) TEMPERATURE DISTRIBUTION UPSTREAM FROM THE ENTRY TO THE BLADE PASSAGE

(b) DISTRIBUTION OF THE FREE STREAM TEMPERATURE INSIDE THE BLADE PASSAGE

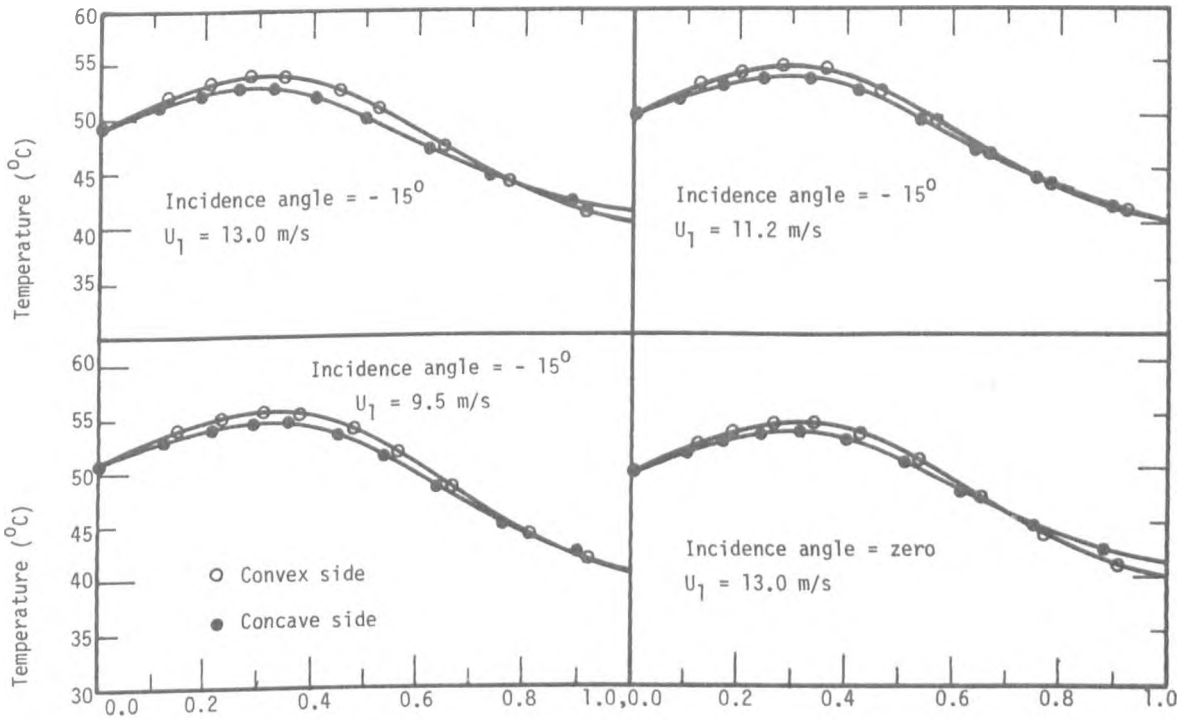

FIGURE 4.9 DISTRIBUTION OF THE BLADE SURFACE TEMPERATURE

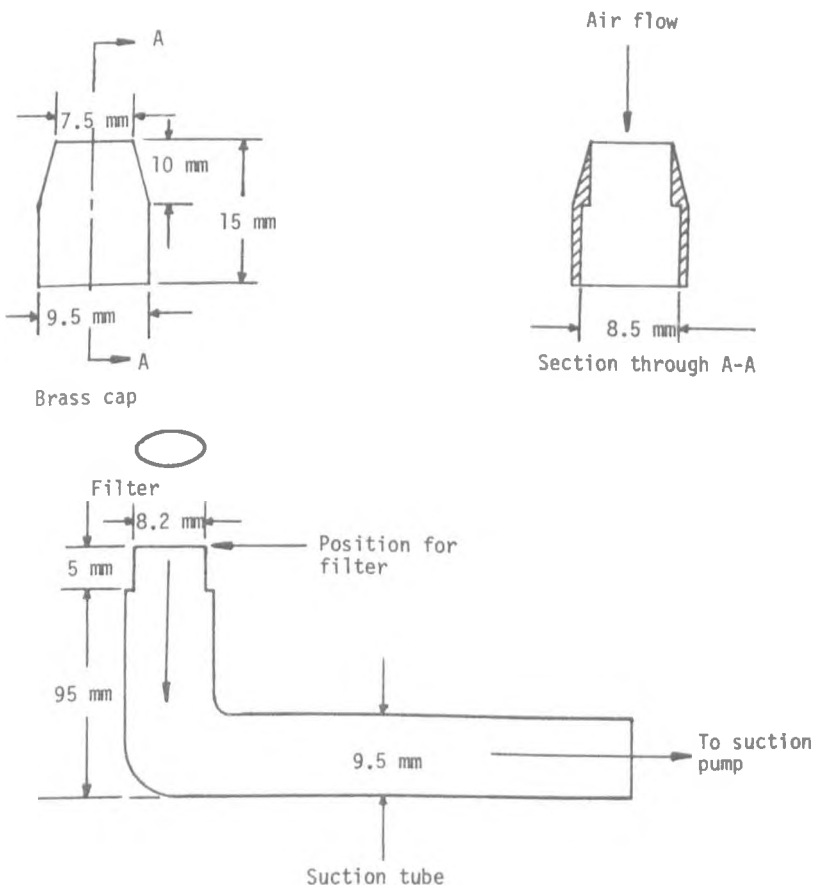

FIGURE 4.10 PROBE FOR MEASURING PARTICLE CONCENTRATION

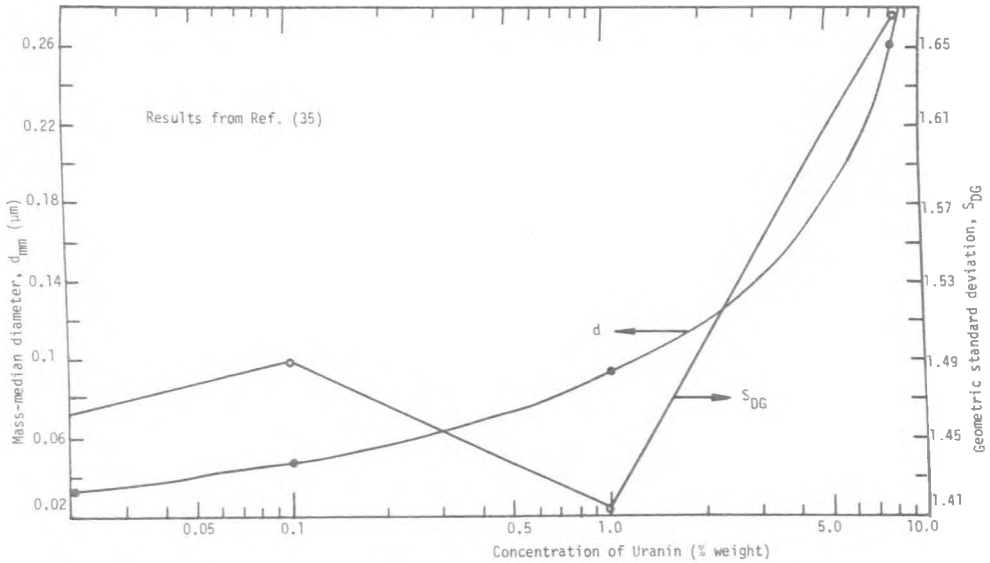

FIGURE 4.11 VARIATION OF PARTICLE STATISTICAL CHARACTERISTICS WITH THE STRENGTH OF THE URANIN SOLUTION

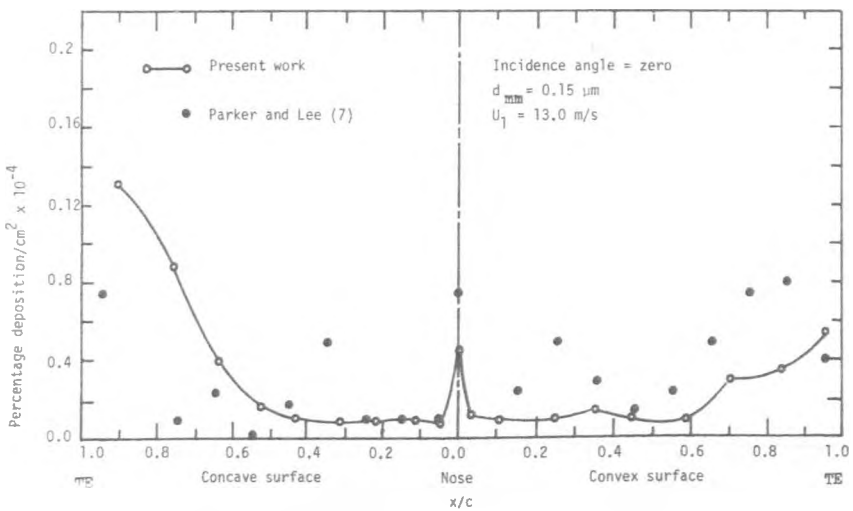

FIGURE 4.12 DEPOSITION DISTRIBUTION ON THE UNHEATED BLADE SURFACES

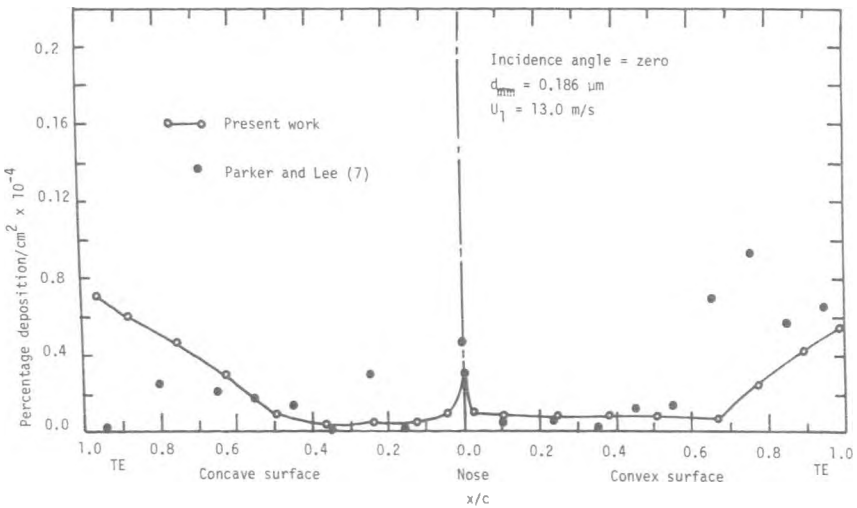

FIGURE 4.13 DEPOSITION DISTRIBUTION ON THE UNHEATED BLADE SURFACES

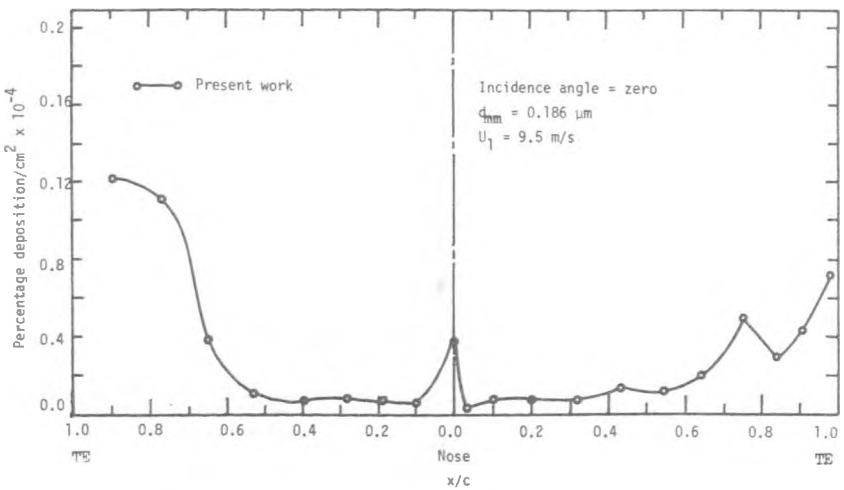

FIGURE 4.14 DEPOSITION DISTRIBUTION ON UNHEATED BLADE SURFACES

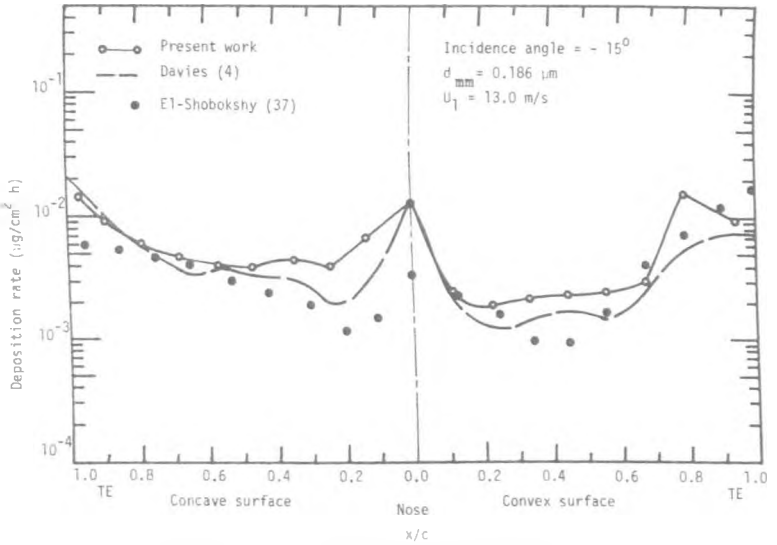

FIGURE 4.15 DEPOSITION DISTRIBUTION ON UNHEATED BLADE SURFACES

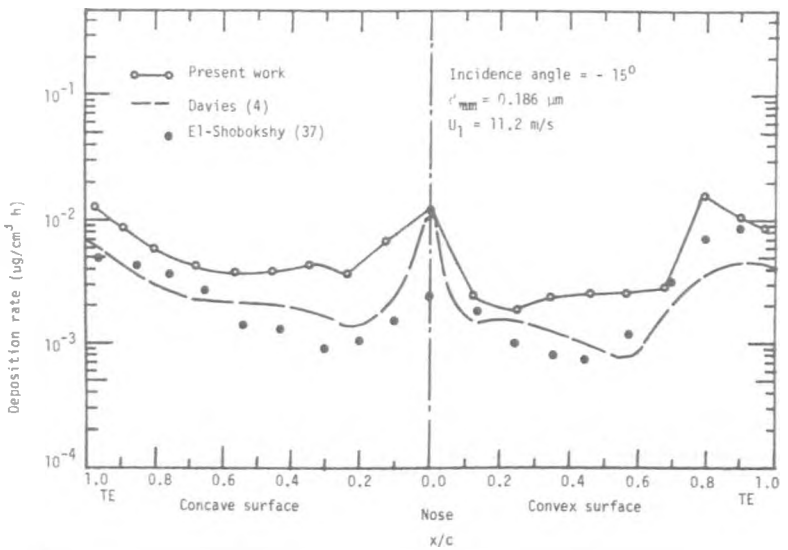

FIGURE 4.16 DEPOSITION DISTRIBUTION ON UNHEATED BLADE SURFACES

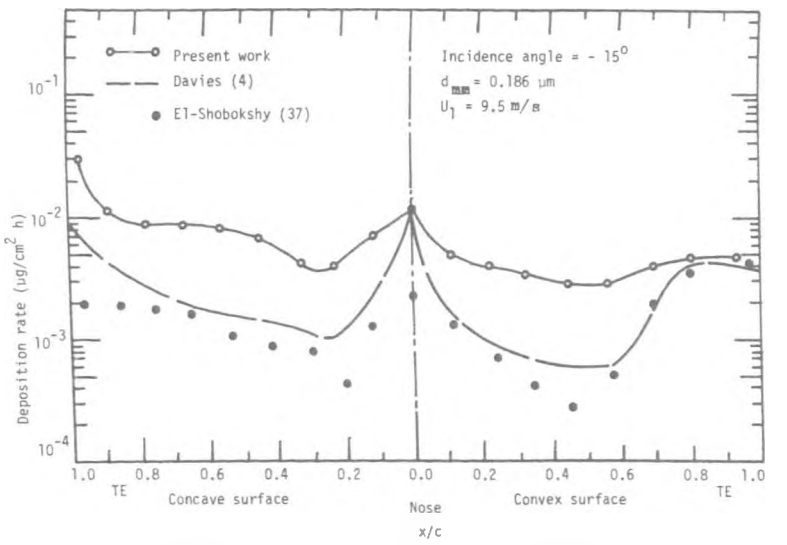

FIGURE 4.17 DEPOSITION DISTRIBUTION ON UNHEATED BLADE SURFACES

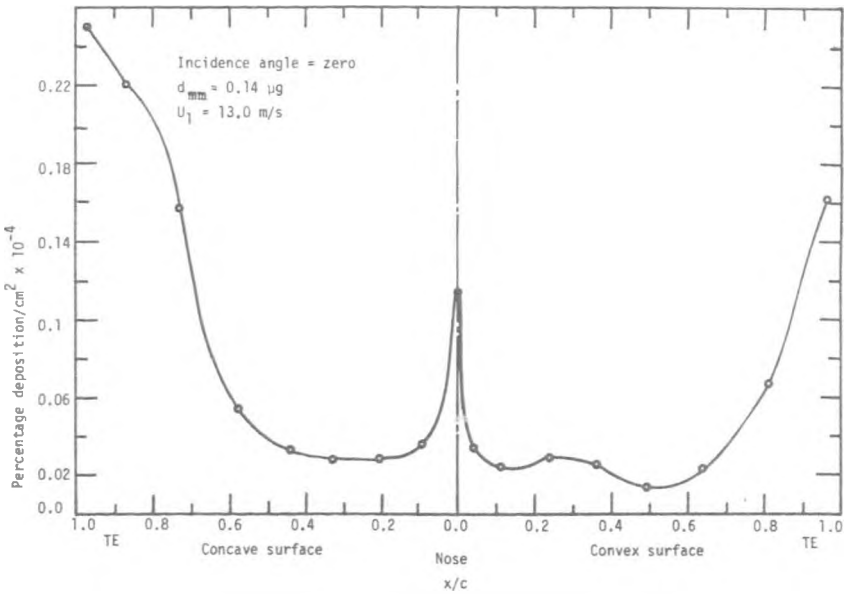

FIGURE 4.18 DEPOSITION DISTRIBUTION ON HEATED BLADE SURFACES

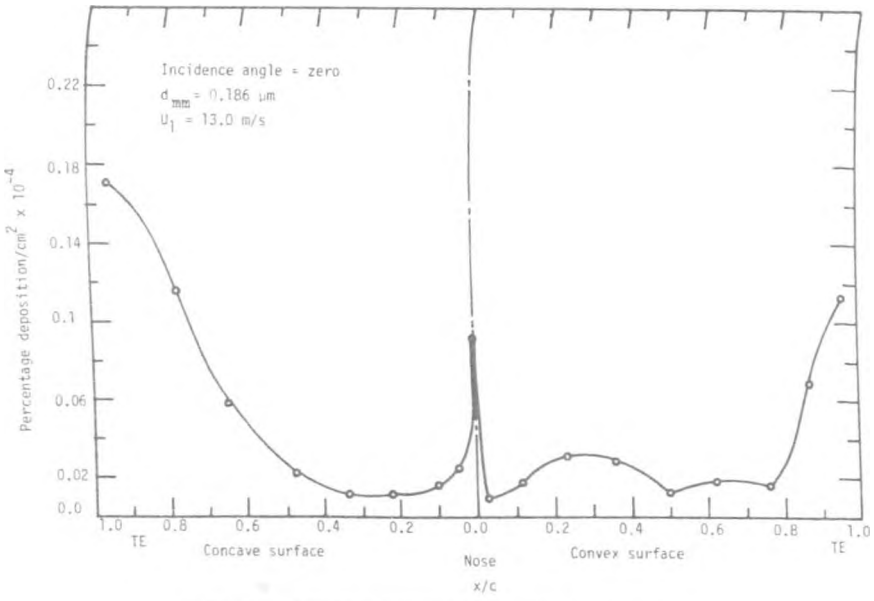

FIGURE 4.19 DEPOSITION DISTRIBUTION ON HEATED BLADE SURFACES

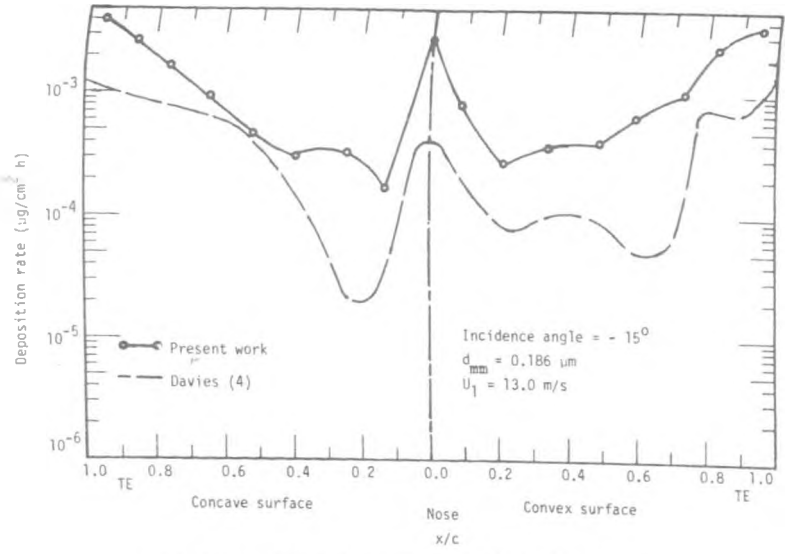

FIGURE 4.21 DEPOSITION DISTRIBUTION ON HEATED BLADE SURFACES

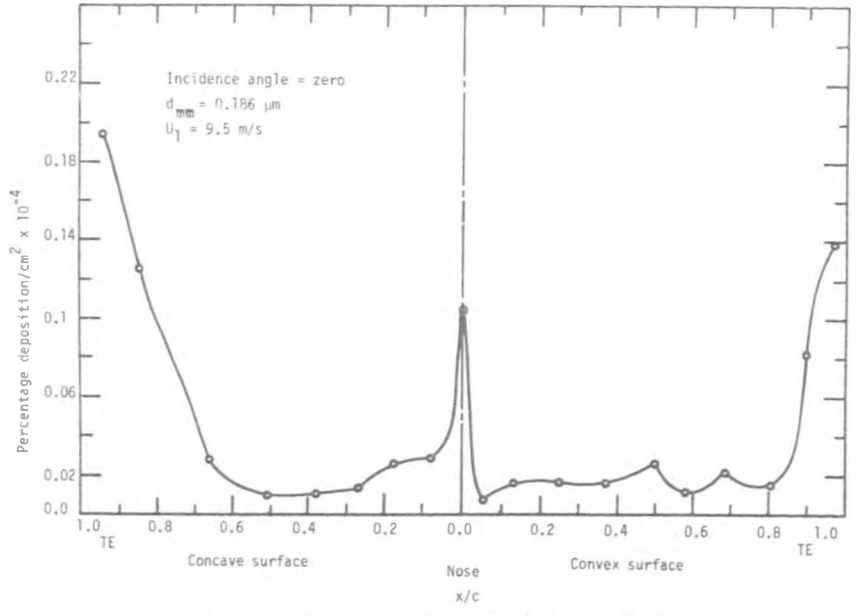

FIGURE 4.20 DEPOSITION DISTRIBUTION ON HEATED BLADE SURFACES

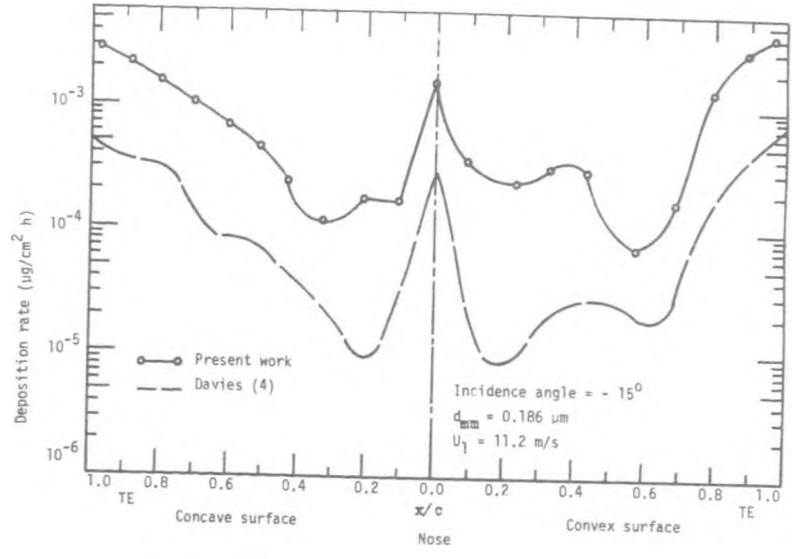

FIGURE 4.22 DEPOSITION DISTRIBUTION ON HEATED BLADE SURFACES

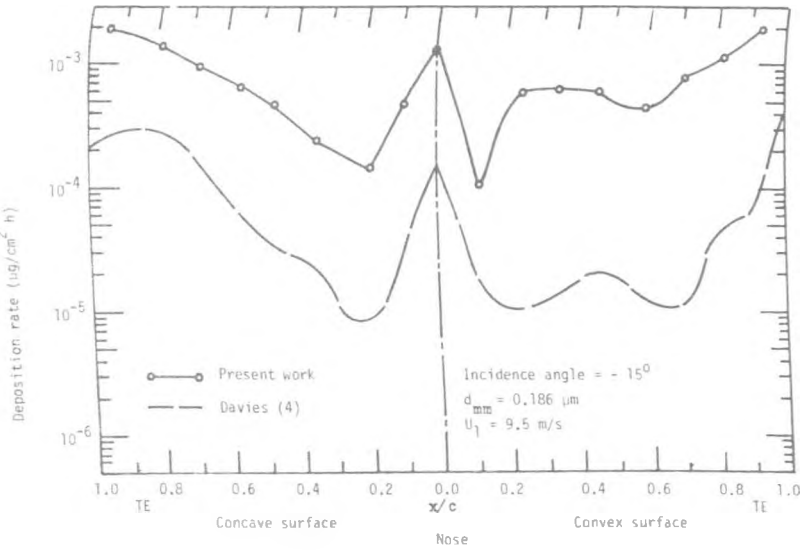

FIGURE 4.23 DEPOSITION DISTRIBUTION ON HEATED BLADE SURFACES

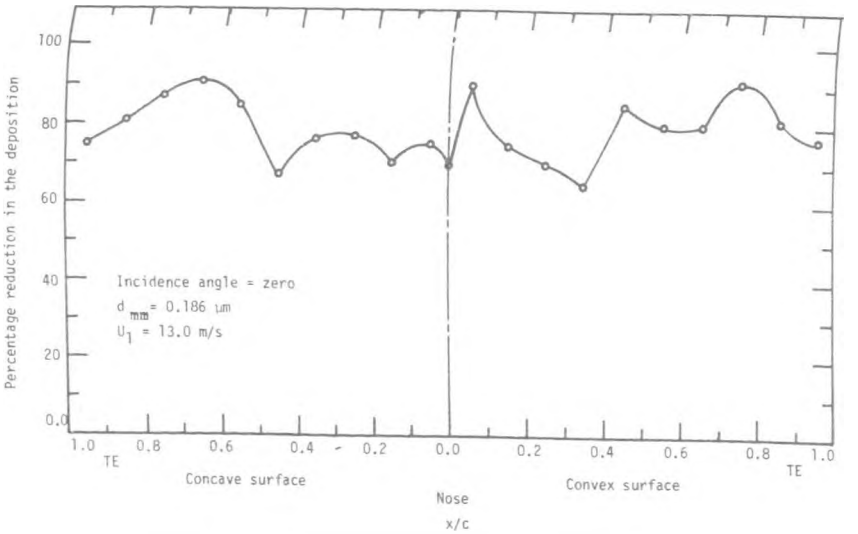

FIGURE 4.25 THE REDUCTION IN THE DEPOSITION OF THE PARTICLES DUE TO HEATING

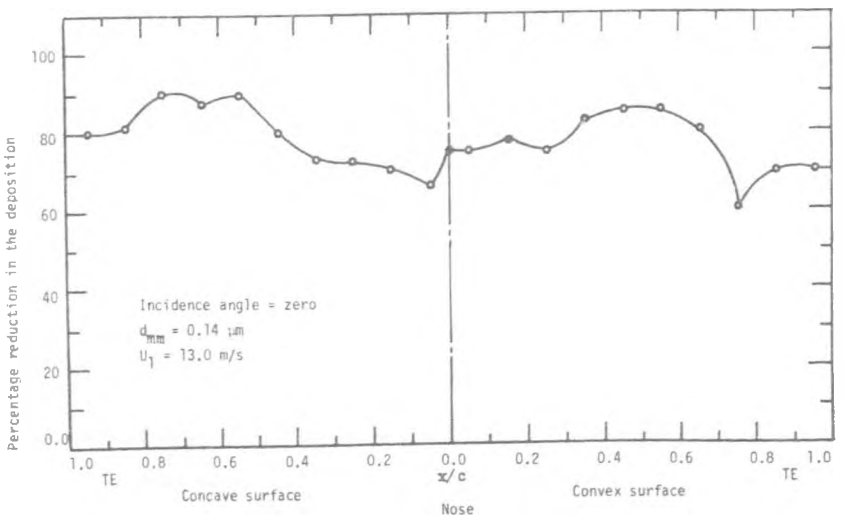

FIGURE 4.24 THE REDUCTION IN THE DEPOSITION OF THE PARTICLES DUE TO HEATING

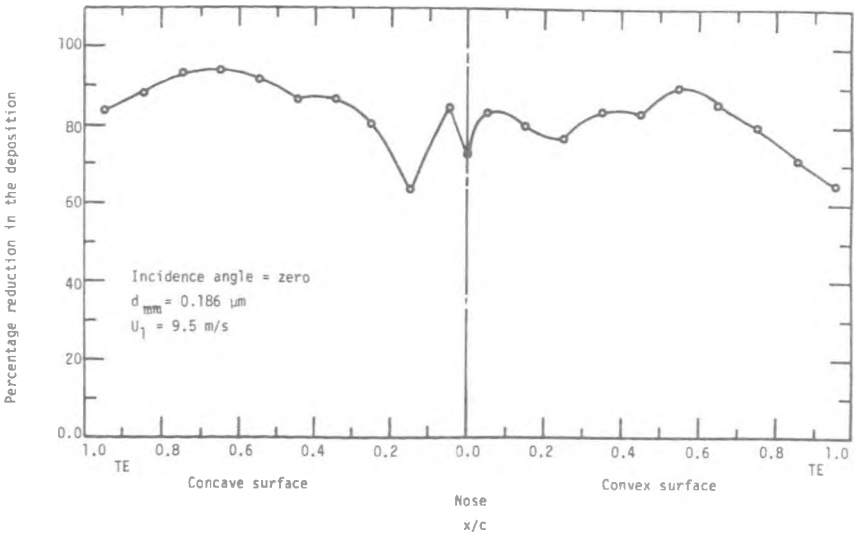

FIGURE 4.26 THE REDUCTION IN THE DEPOSITION OF THE PARTICLES DUE TO HEATING

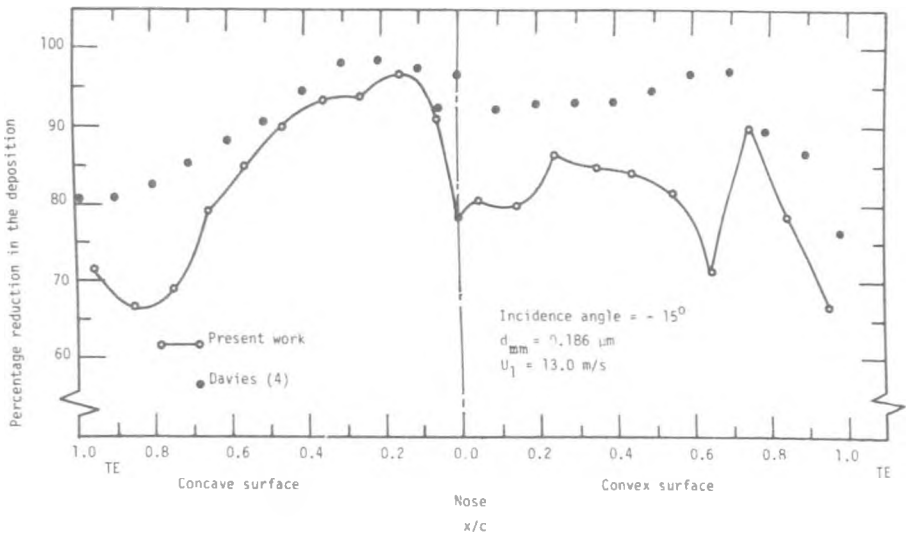

FIGURE 4.27 THE REDUCTION IN THE DEPOSITION OF THE PARTICLES DUE TO HEATING

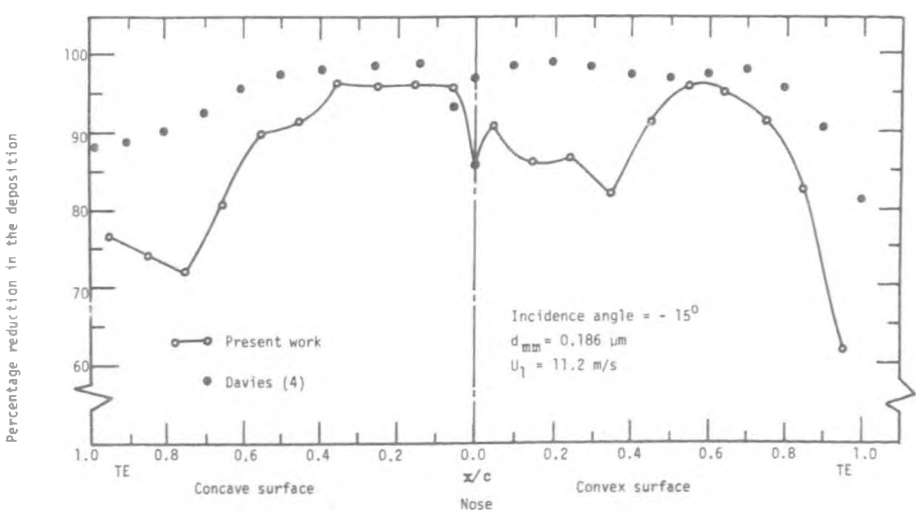

FIGURE 4.28 THE REDUCTION IN THE DEPOSITION OF THE PARTICLES DUE TO HEATING

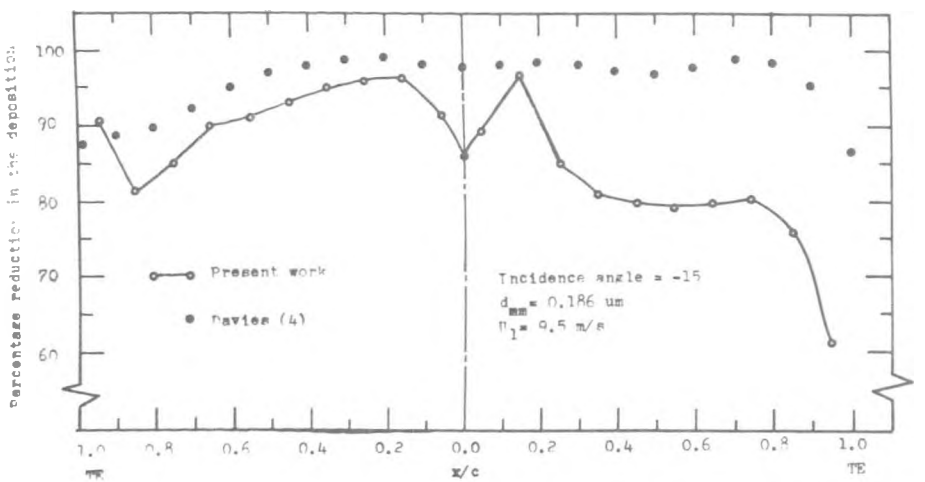

FIGURE 4.29 THE REDUCTION IN THE DEPOSITION OF THE PARTICLES DUE TO HEATING

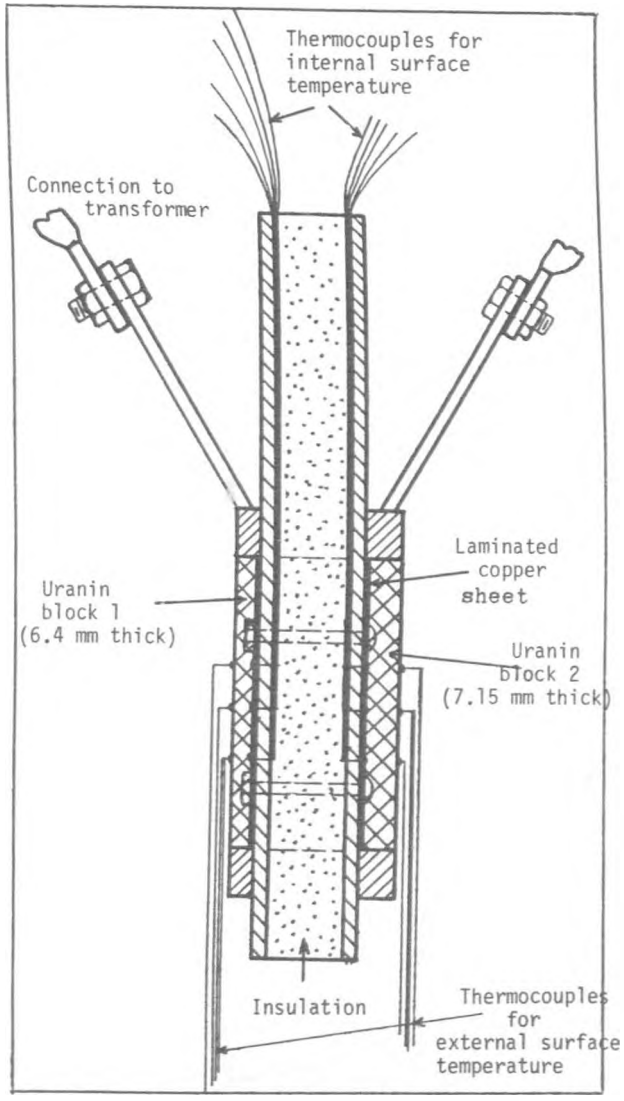

FIGURE 4.30 CROSS-SECTION OF THE EXPERIMENTAL APPARATUS FOR MEASURING THE THERMAL CONDUCTIVITY OF THE URANIN

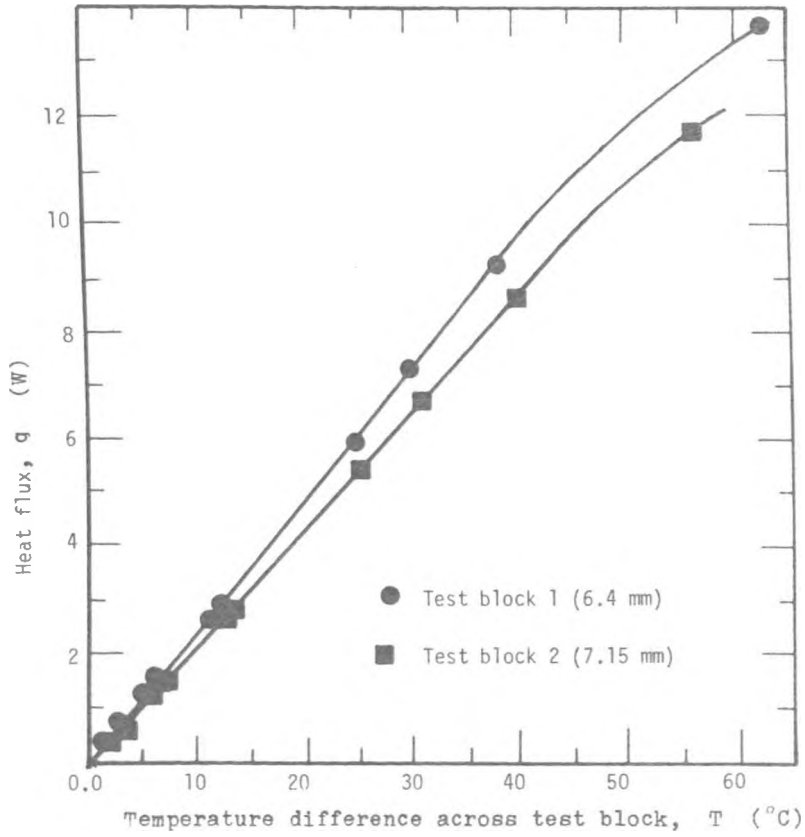

FIGURE 4.31 VARIATION OF HEAT FLUX THROUGH TEST BLOCKS WITH TERMPERATURE DIFFERENCE

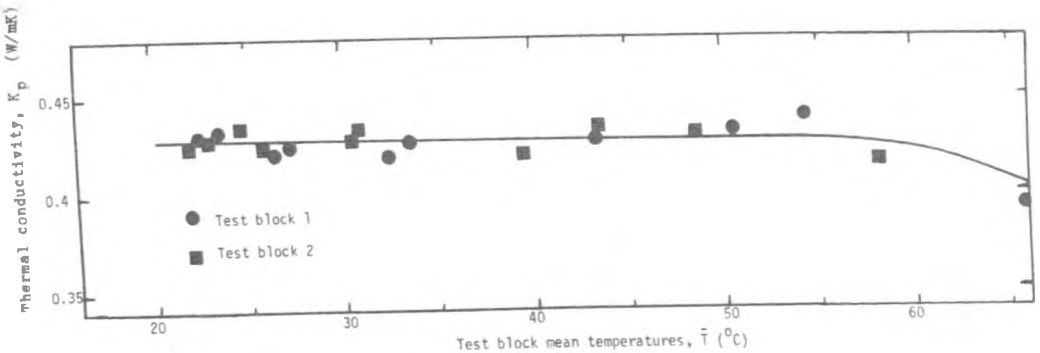

FIGURE 4.32 THERMAL CONDUCTIVITY OF SOLID URANIN

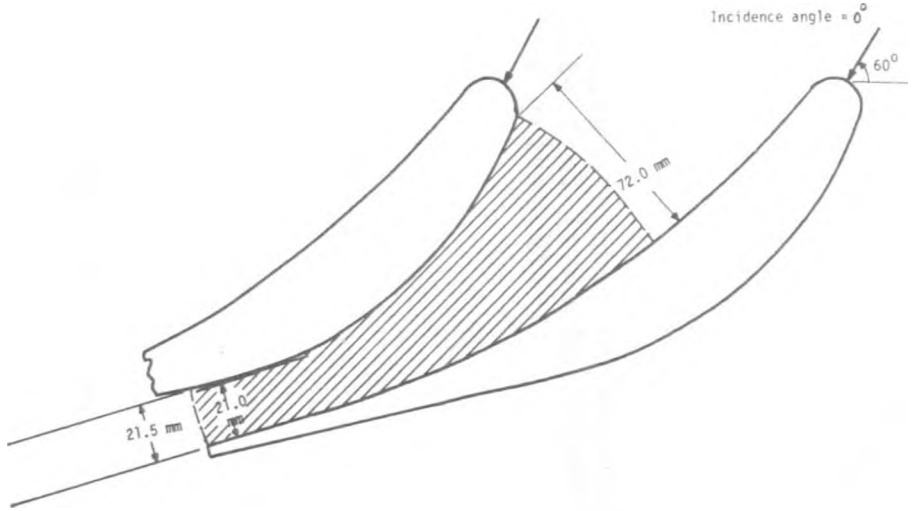

FIGURE 5.1 BLADE PASSAGE PROFILE

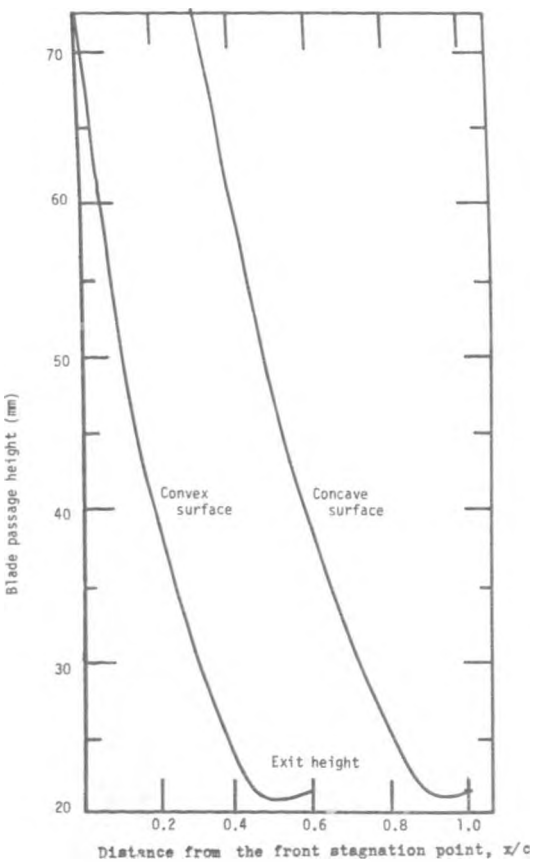

FIGURE 5.2 DISTRIBUTION OF THE BLADE PASSAGE HEIGHT

(a) Paint the shape of the cascade.

(b) Assume the midpotential line.

(c) Cut teledeltos paper perpendicular to upstream and downstream flow and paint two outer streamlines.

(d) Locate a number of streamlines inside the blade passage by adjusting the galvanometer.

(e) Cut the shape of the cascade out

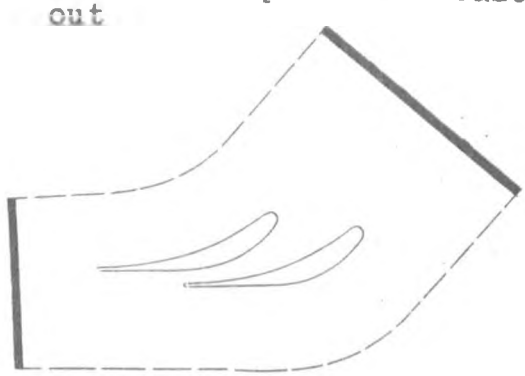

(f) Cut teledeltos paper perpendicular to upstream and downstream flow and paint the edges.

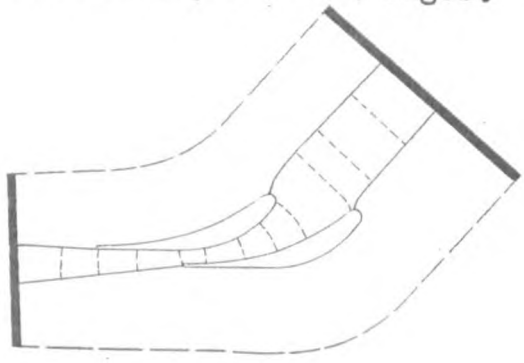

(g) Locate a number of velocity potential lines by adjusting the galvanometer.

(h) Superimpose the two plots of figures d and g.

Figure 5.3 : Illustrating the Method of Potential Plotting.

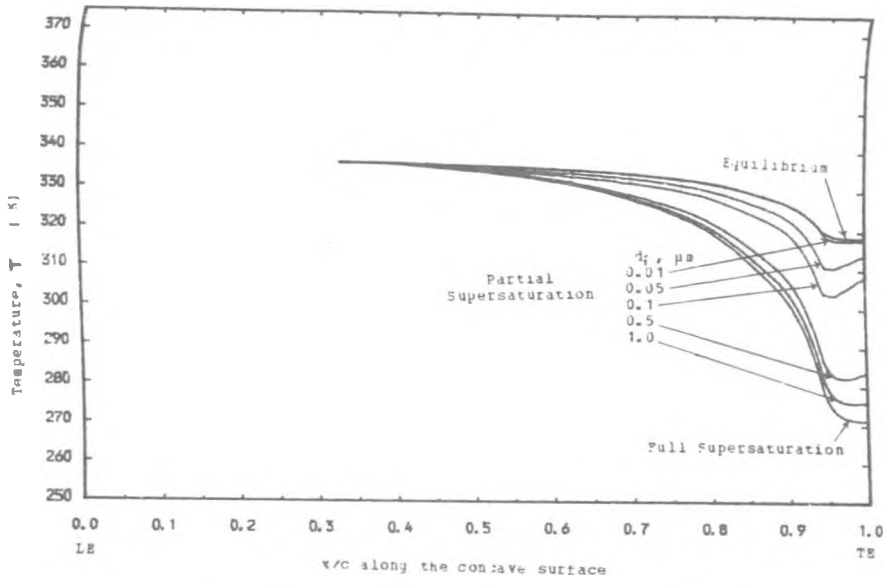

Figure 5.4 : Distribution of Free Stream Temperature for a Range of Droplet Sizes.

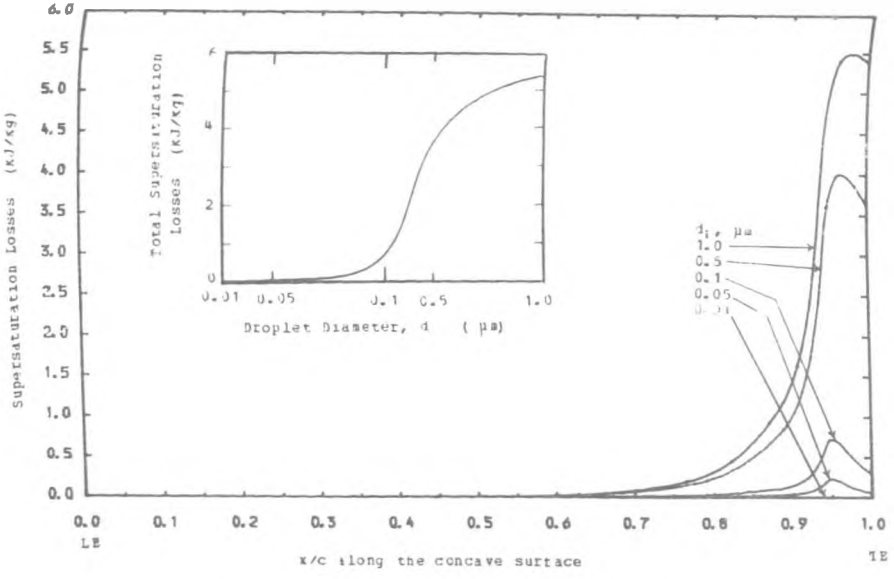

Figure 5.6 : Distribution of Supersaturation Losses for a Range of Droplet Sizes.

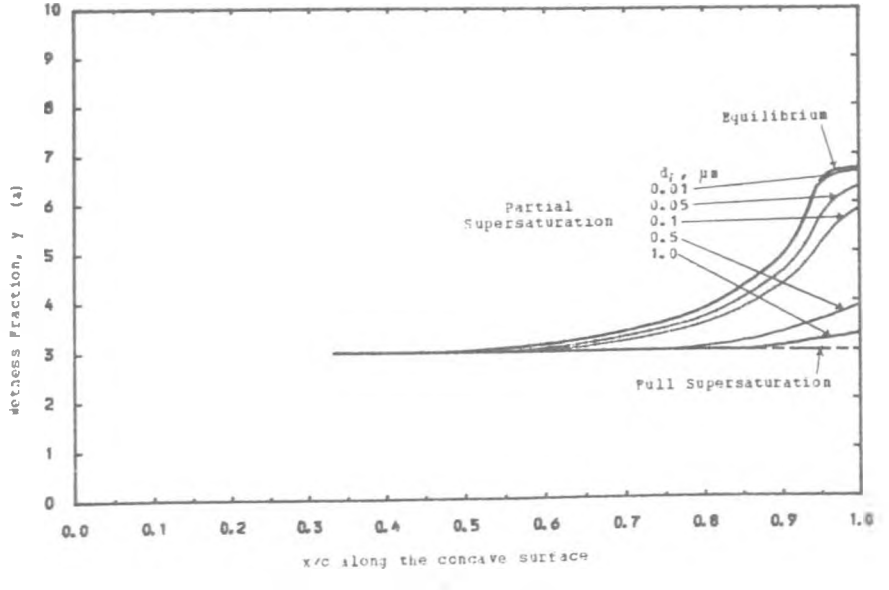

Figure 5.5 : Distribution of Wetness Fraction outside the Boundary Layer for a Range of Droplet Sizes.

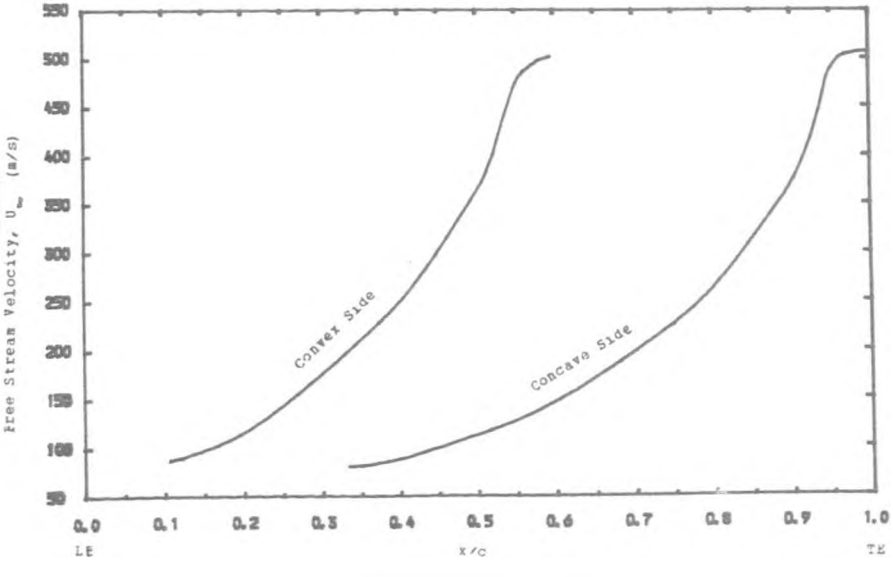

Figure 5.7 : Distribution of the Free Stream Velocity along the Blade Surfaces.

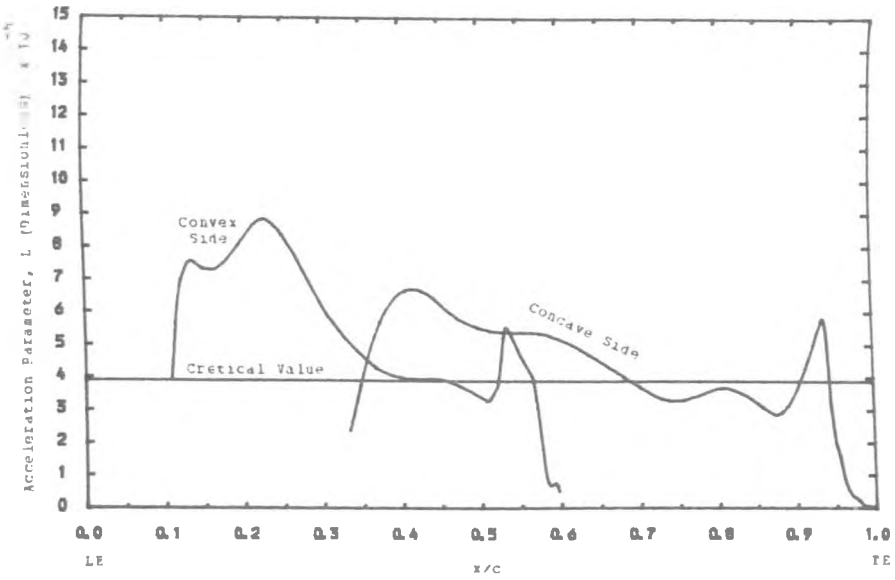

Figure 5.9 : Distribution of the Acceleration Parameter along the Blade Surfaces.

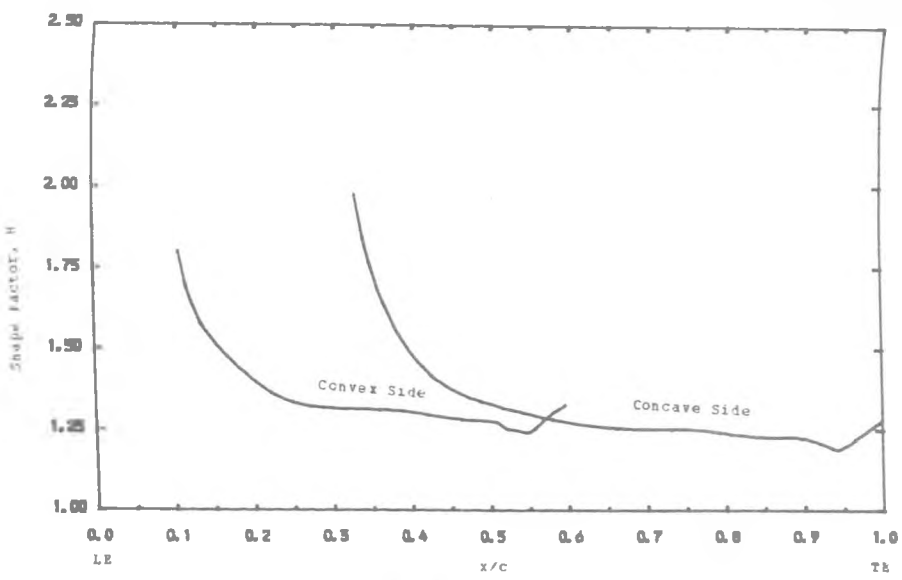

Figure 5.10 : Variation of the Shape Factor along the Blade Surfaces.

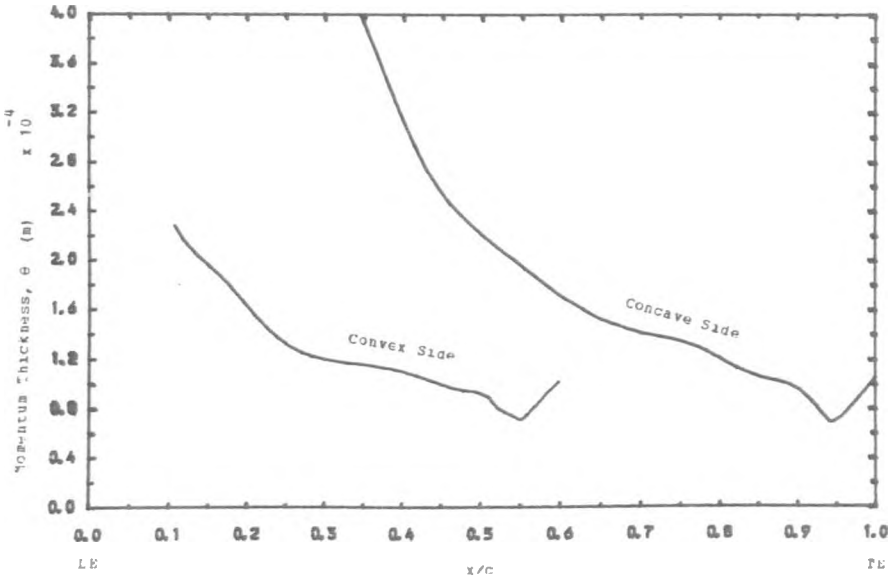

Figure 5.8 : Variation of the Momentum Thickness along the Blade Surfaces.

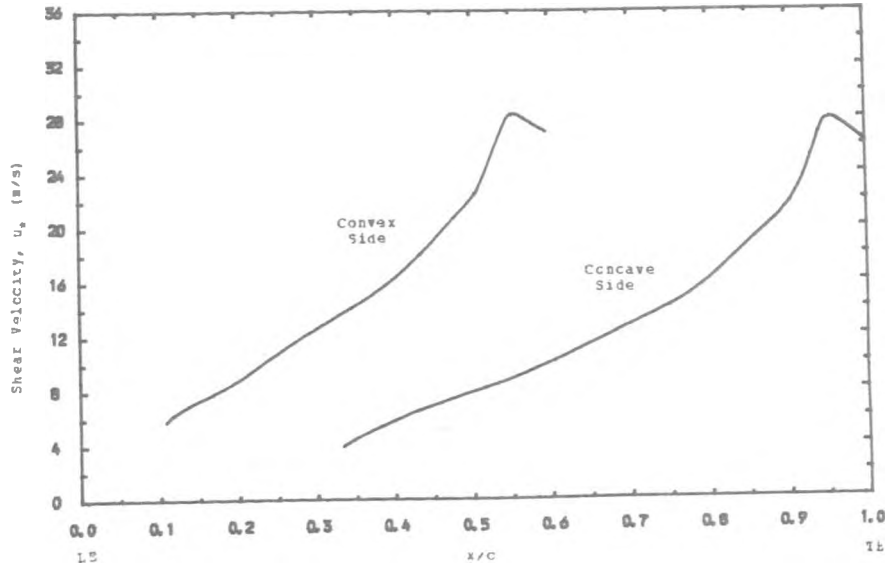

Figure 5.11 : Variation of the Shear Velocity along the Blade Surfaces.

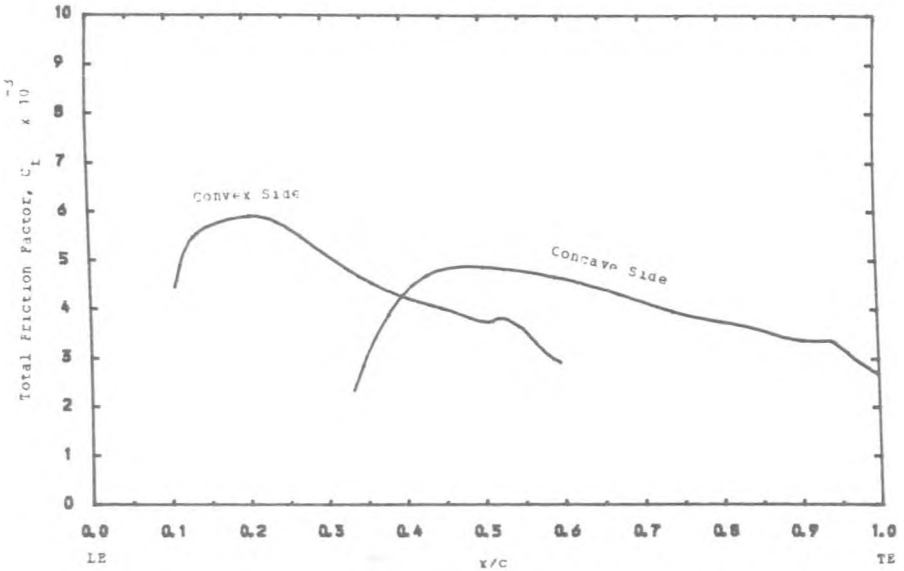

Figure 5.12 : Variation of the Total Friction Factor along the Blade Surfaces.

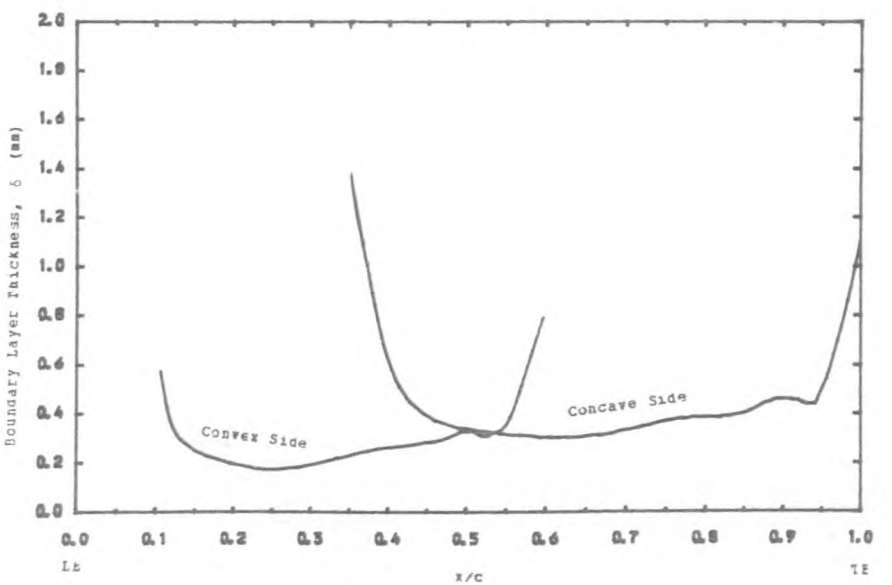

Figure 5.13 : Variation of the Boundary Layer Thickness along the Blade Surfaces.

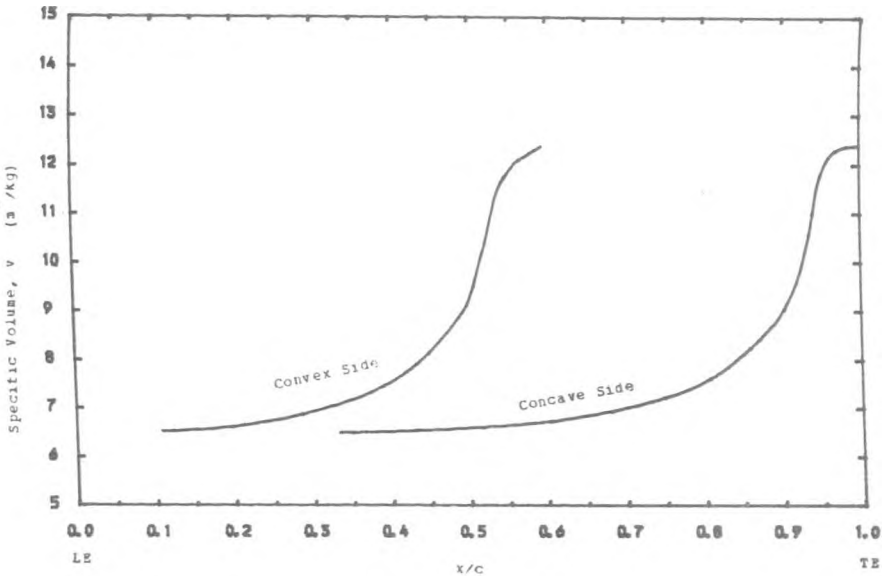

Figure 5.14 : Variation of the Specific Volume along the Blade passage.

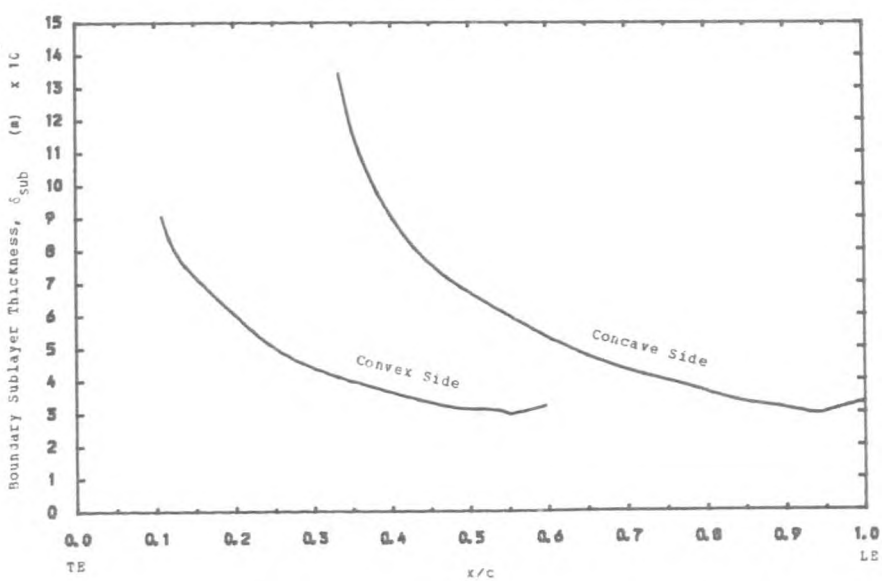

Figure 5.15 : Variation of the Boundary Sublayer Thickness along the Blade Surfaces.

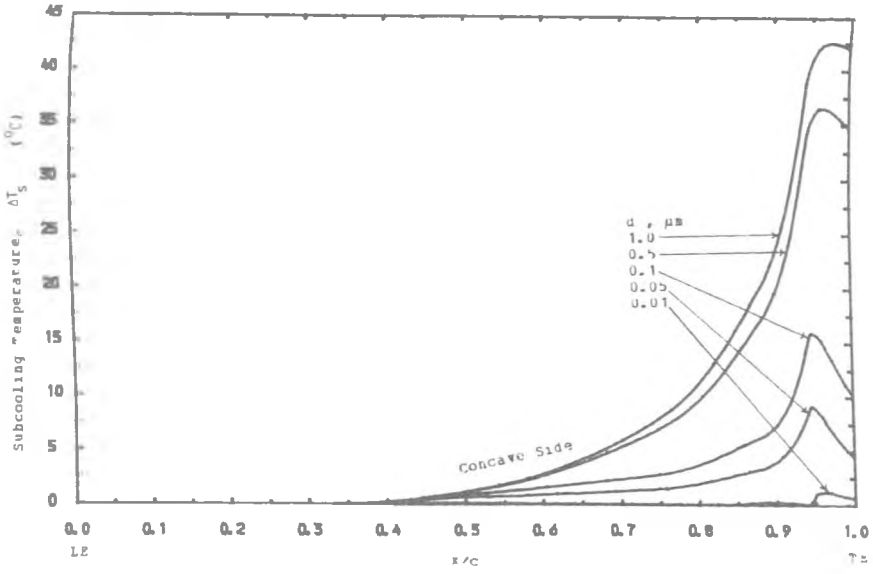

Figure 6.1 : Distribution of Subcooling Temperature along the Blade Passage for a Range of Droplet Sizes.

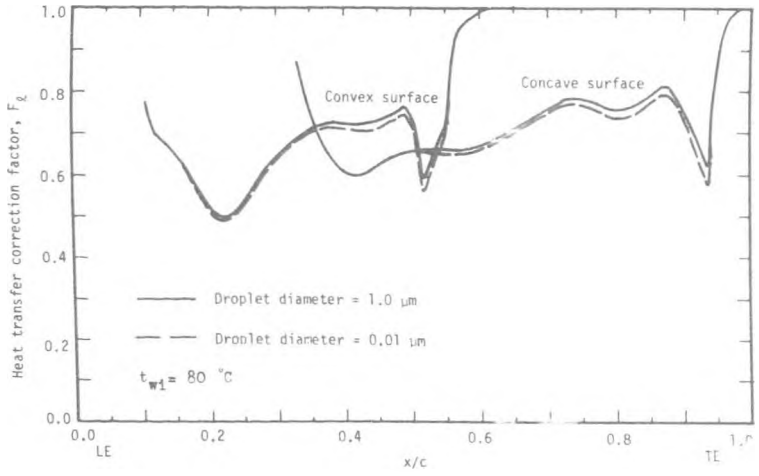

FIGURE 6.3 VARIATION OF HEAT TRANSFER CORRECTION FACTOR DUE TO LAMINARISATION ALONG THE BLADE SURFACES.

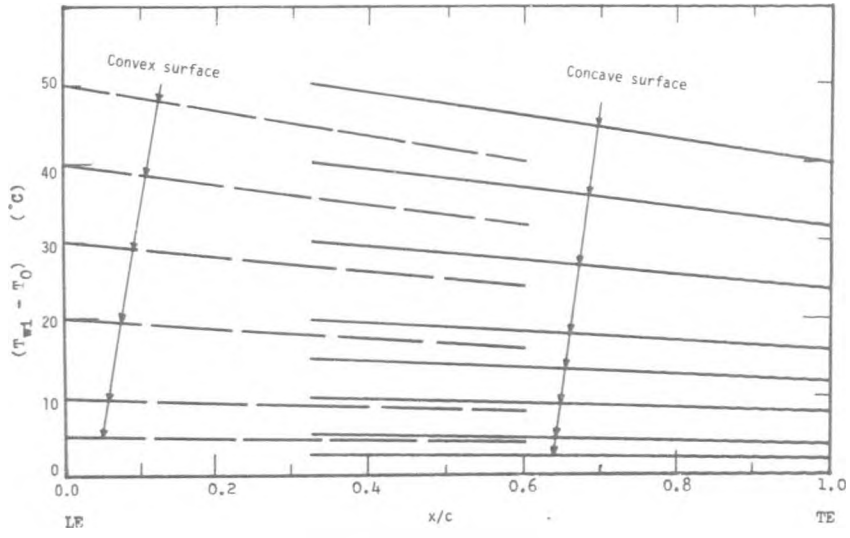

FIGURE 6.2 DISTRIBUTION OF SURFACE TEMPERATURE ALONG THE BLADE SURFACES FOR A RANGE OF INITIAL SURFACE TEMPERATURES

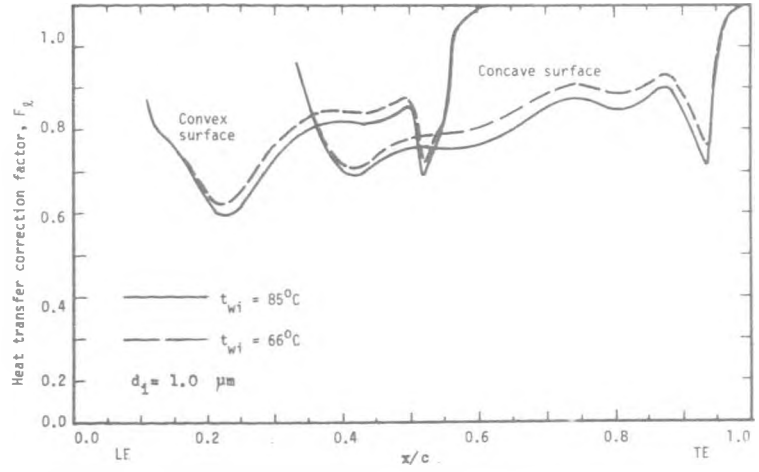

FIGURE 6.4 VARIATION OF HEAT TRANSFER CORRECTION FACTOR DUE TO LAMINARISATION ALONG THE BLADE SURFACES

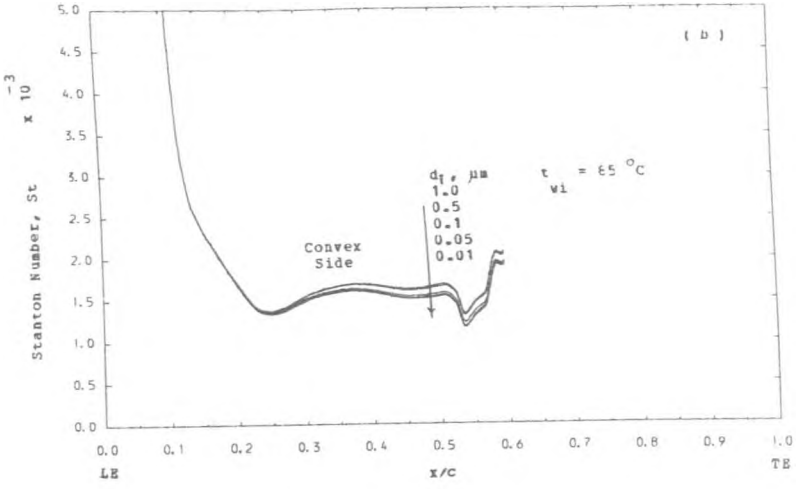

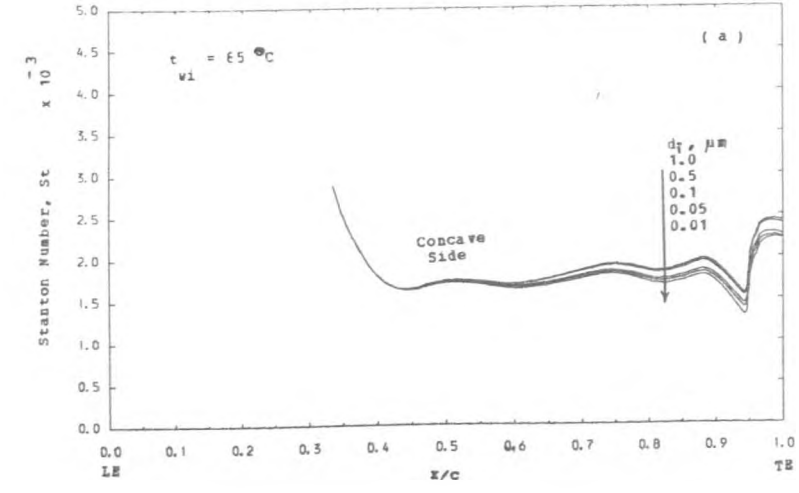

Figure 6.5 : Variation of Stanton Number along the Blade Surfaces for a Range of Droplet Sizes.

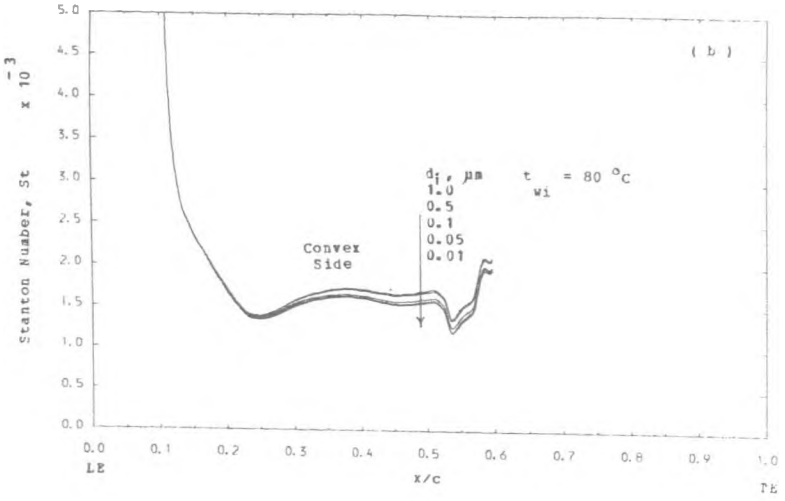

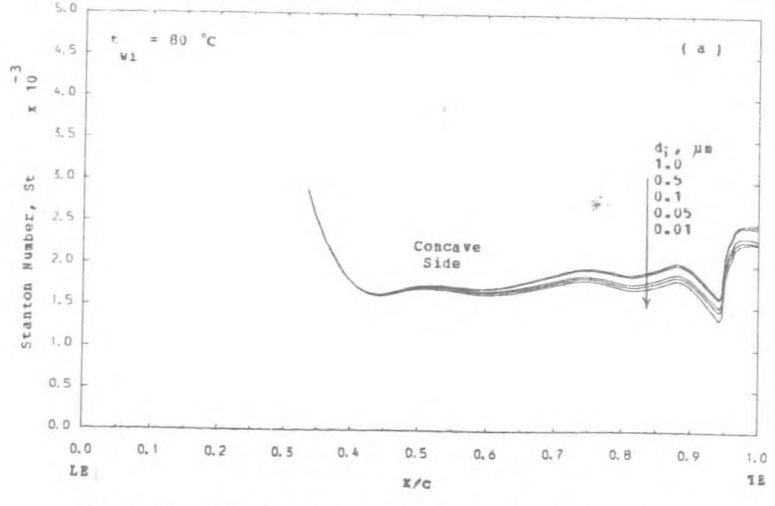

Figure 6.6 : Variation of Stanton Number along the Blade Surfaces for a Range of Droplet Sizes.

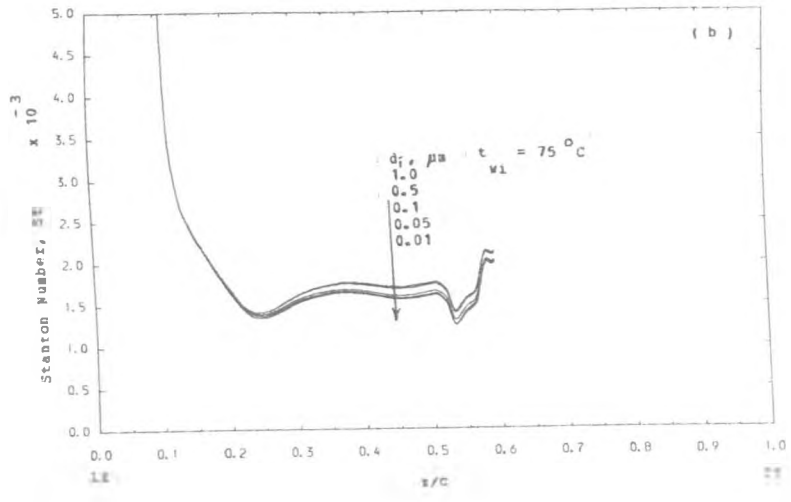

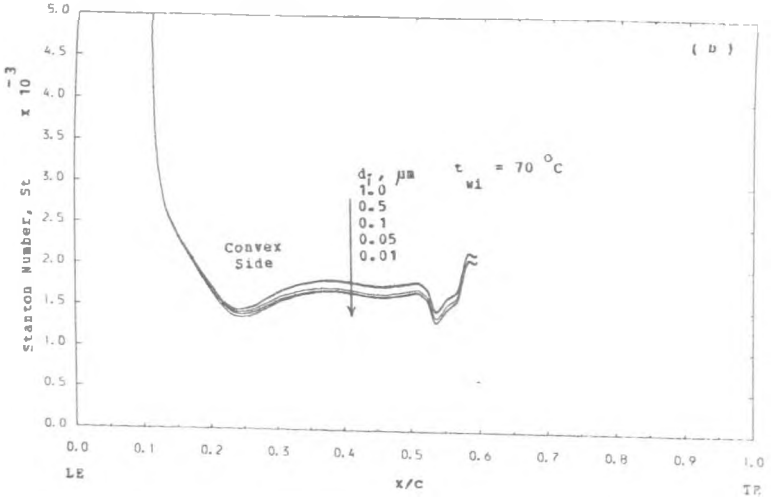

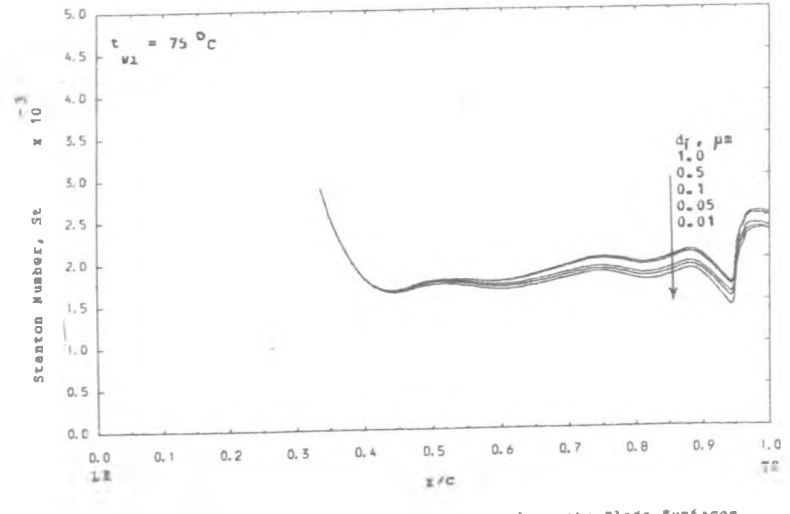

Figure 6.7 : Variation of Stanton Number along the Blade Surfaces for a Range of Droplet Sizes.

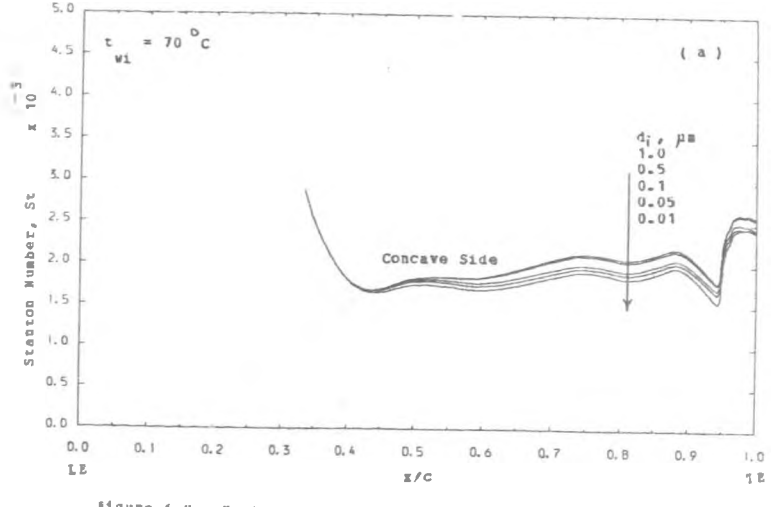

Figure 6.8 : Variation of Stanton Number along the Blade Surfaces for a Range of Droplet Sizes.

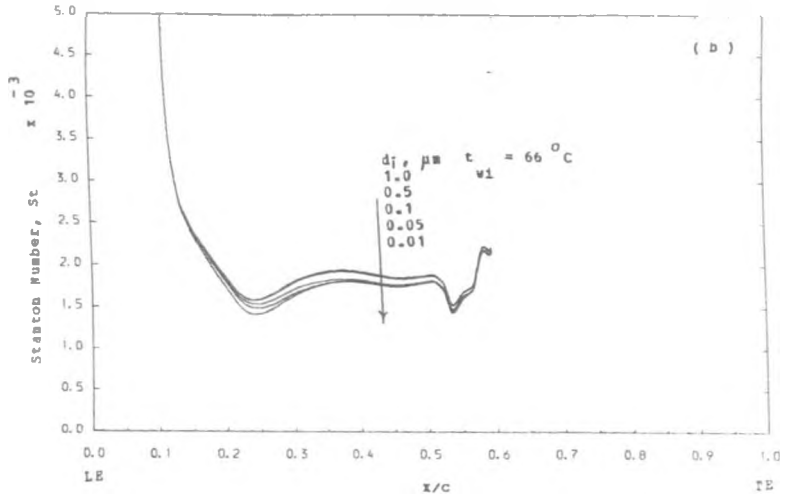

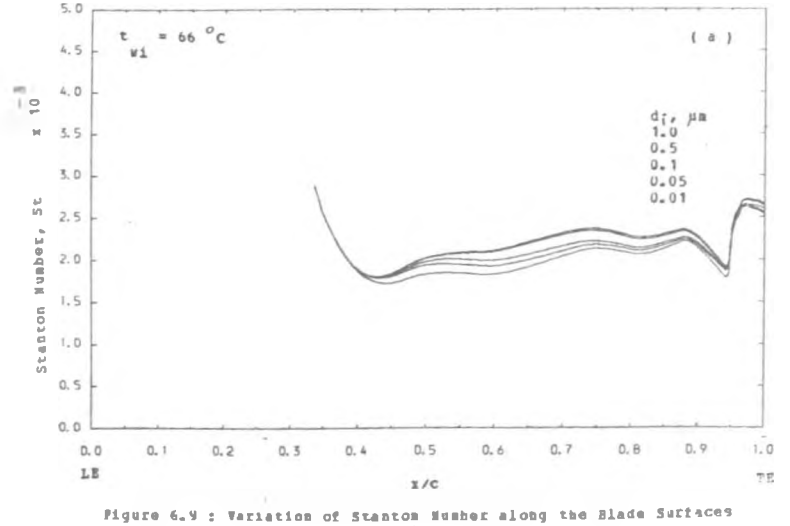

Figure 6.9 : Variation of Stanton Number along the Blade Surfaces for a Range of Droplet Sizes.

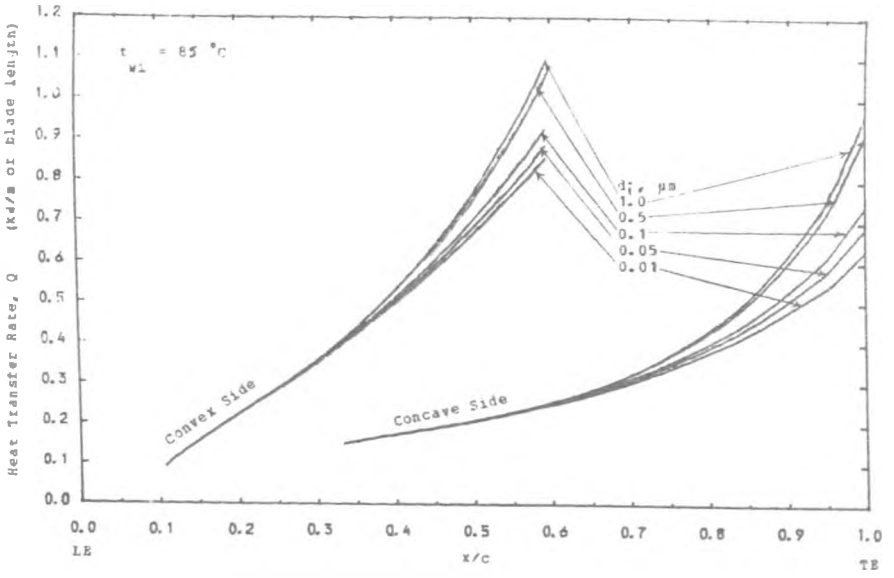

Figure 6.10 : Variation of the Total Heat Transfer Rate along the Blade Surfaces for a Range of Droplet Sizes.

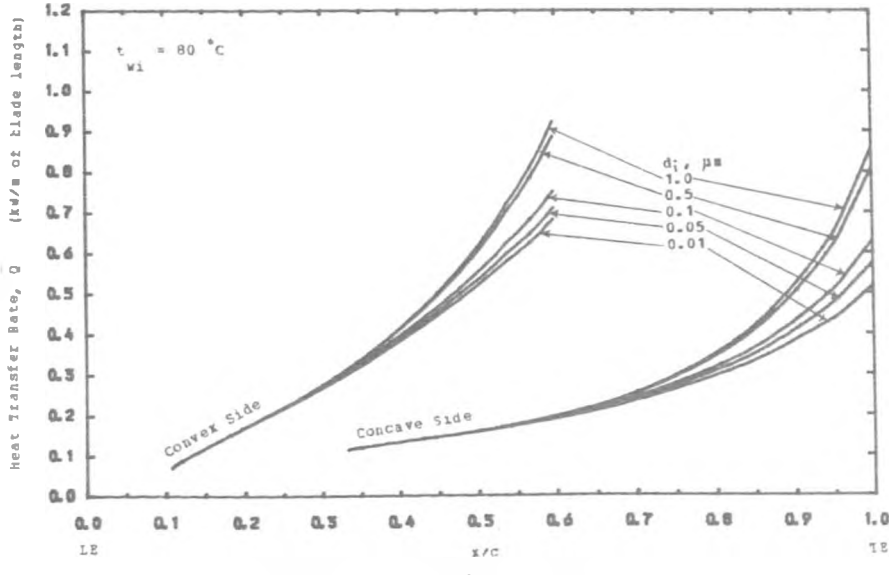

Figure 6.11 : Variation of the Total Heat Transfer Rate along the Blade Surfaces for a Range of Droplet Sizes.

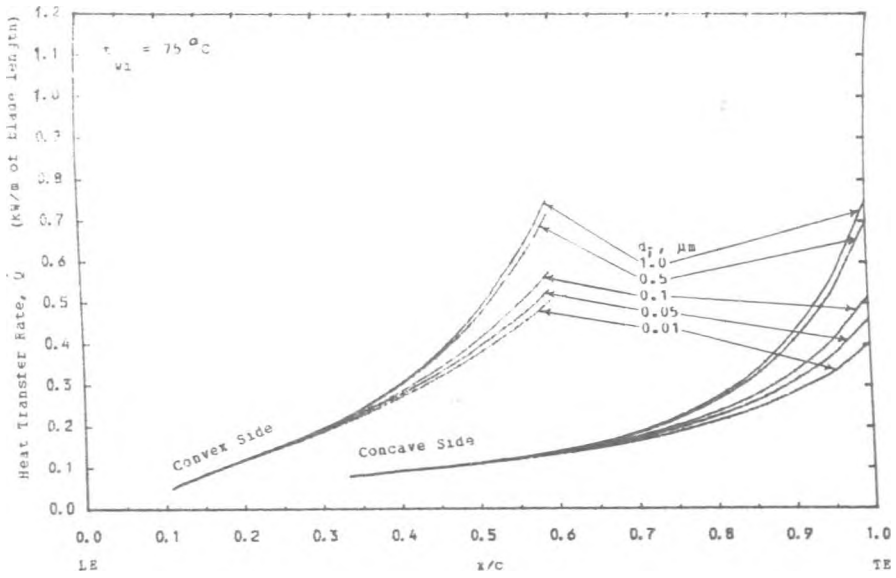

Figure 6.12 : Variation of the Total Heat Transfer Rate along the Blade Surfaces for a Range of Droplet Sizes.

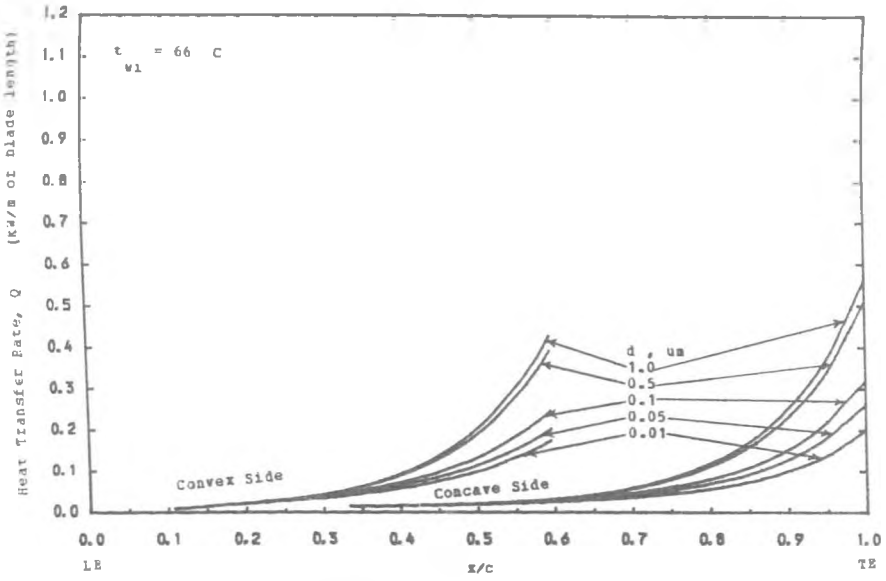

Figure 6.14 : Variation of the Total Heat Transfer Rate along the Blade Surfaces for a Range of Droplet Sizes.

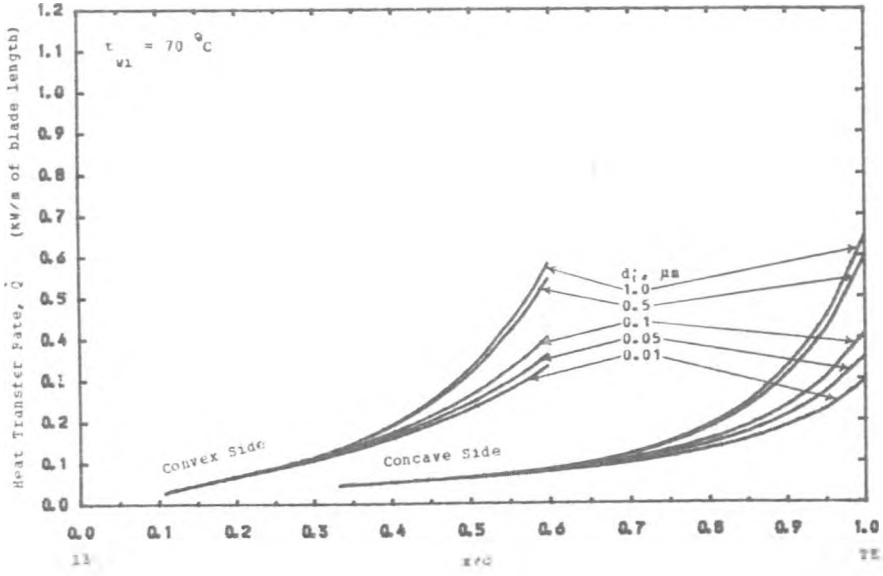

Figure 6.13 : Variation of the Total Heat Transfer Rate along the Blade Surfaces for a Range of Droplet Sizes.

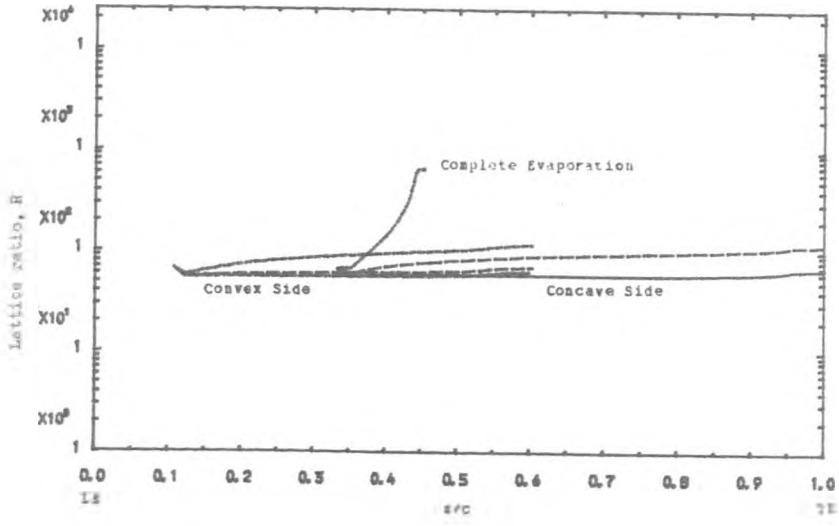

Fig. 7.1 : Distribution of Lattice Ratio inside the Concave and Convex Boundary Layer at Different Distance from the Blade Surface when t_{wi} = 85 °C and d_i = 1.0 μm .

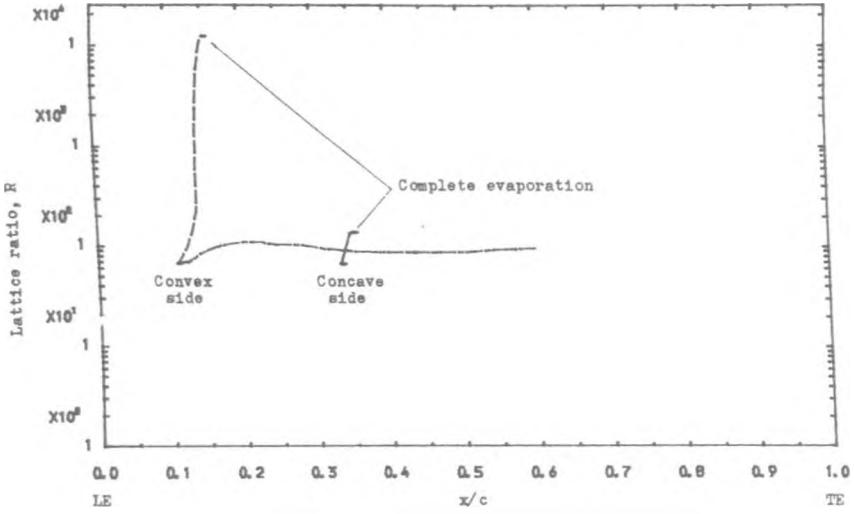

Fig. 7.3 : Distribution of Lattice Ratio inside the Concave and Convex Boundary Layer at Different Distance from the Blade Surface when t_{wi} = 85 °C and d_i = 0.1 μm .

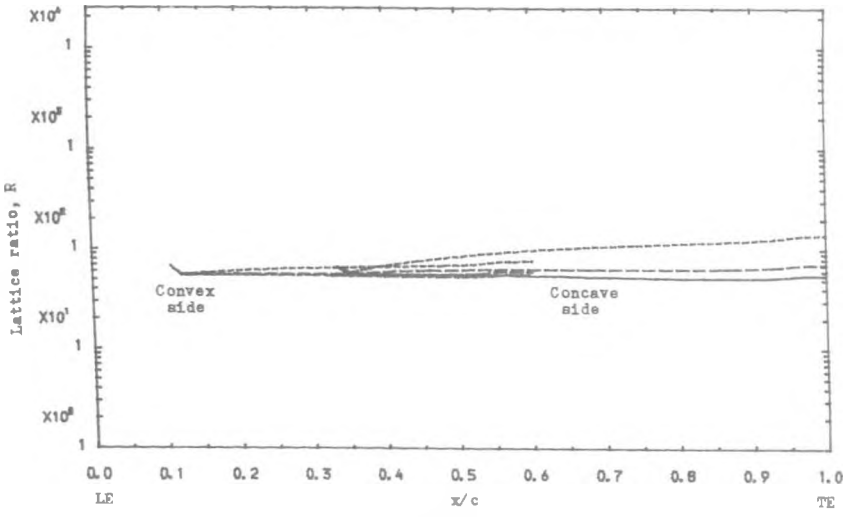

Fig. 7.5 : Distribution of Lattice Ratio inside the Concave and Convex Boundary Layer at Different Distance from the Blade Surface when t_{wi} = 66 °C and d_i = 0.5 μm .

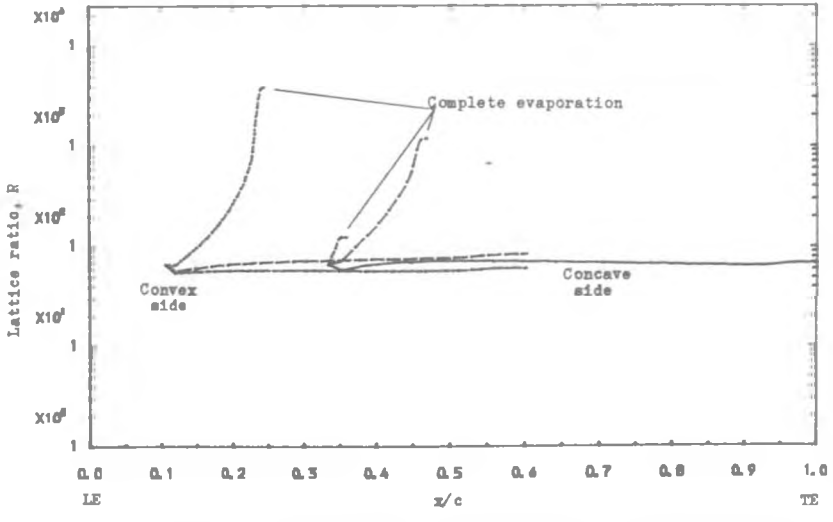

Fig. 7.2 : Distribution of Lattice Ratio inside the Concave and Convex Boundary Layer at Different Distance from the Blade Surface when t_{wi} = 85 °C and d_i = 0.5 μm .

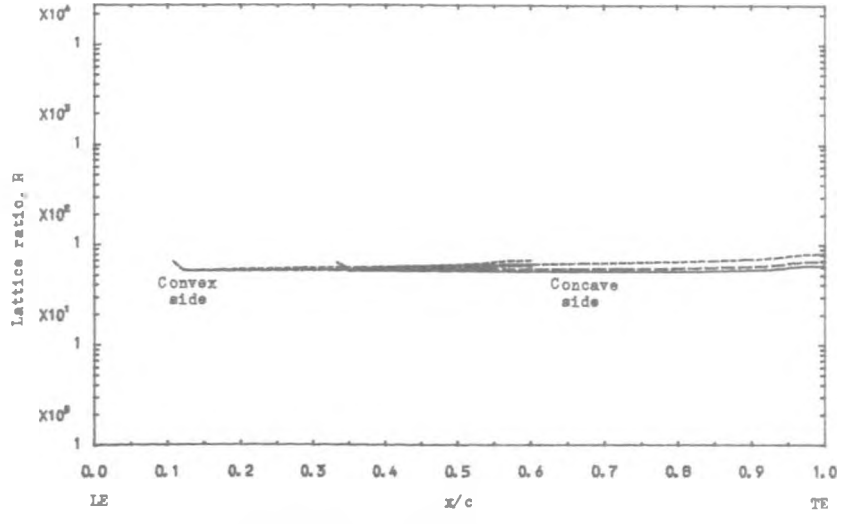

Fig. 7.4 : Distribution of Lattice Ratio inside the Concave and Convex Boundary layer at Different Distance from the Blade Surface when t_{wi} = 66 °C and d_i = 1.0 μm .

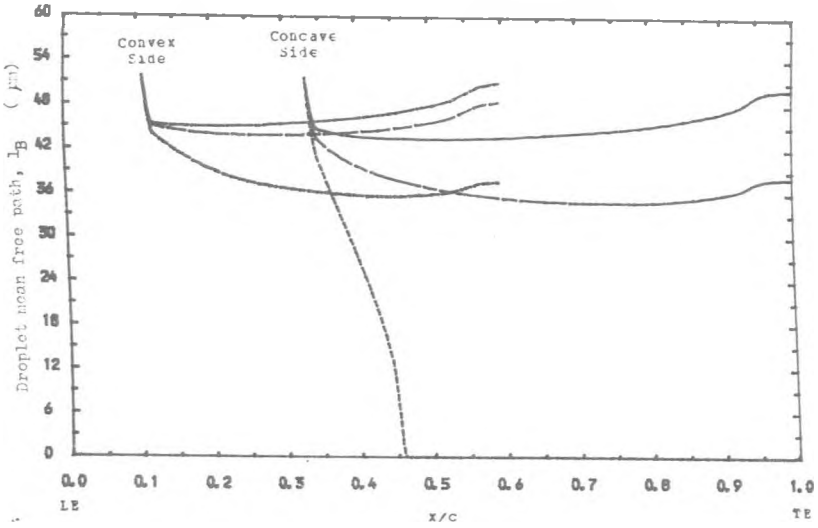

Fig. 7.7 : Variarion of Droplet Mean Free Path inside the Concave and Convex Boundary Layer at Different Distance from the Blade Surface when t_{wi}= 85 °C and d_i= 1.0 μm.

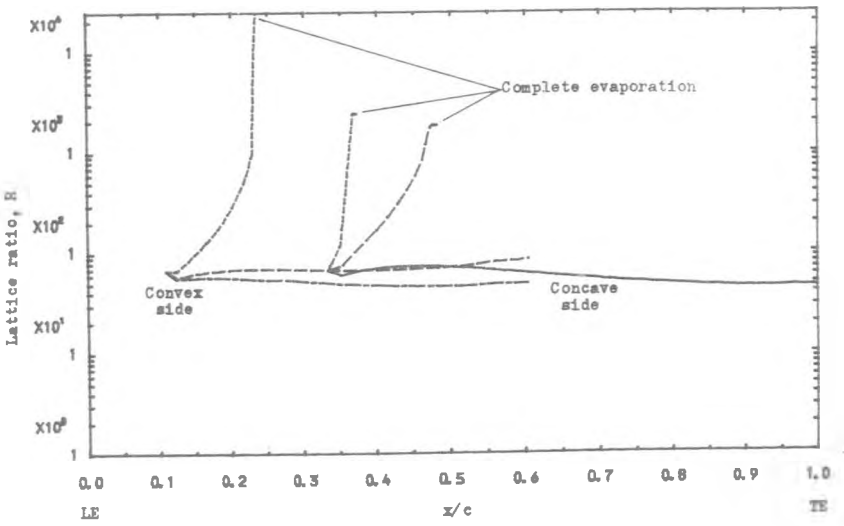

Fig. 7.6 : Distribution of Lattice Ratio inside the Concave and Convex Boundary Layer at Different Distance from the Blade Surface when t_{wi}= 66 °C and d_i= 0.1 μm .

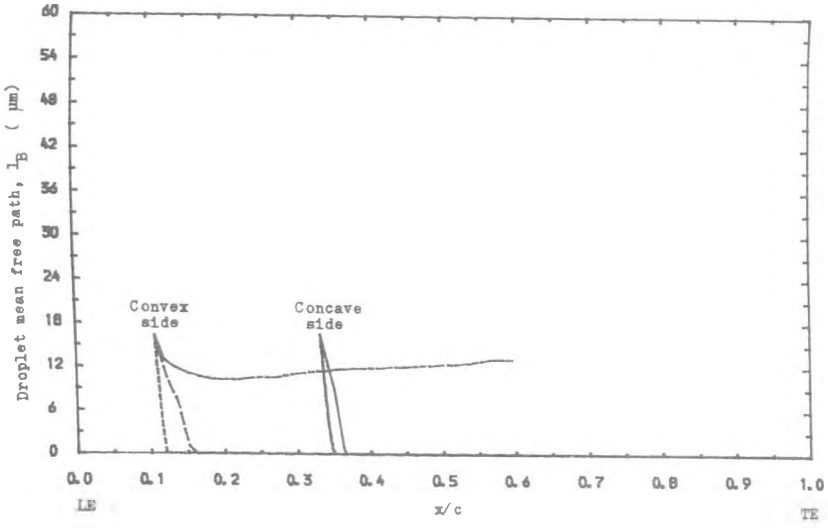

Fig. 7.9 : Variation of Droplet Mean Free Path inside the Concave and Convex Boundary Layer at Different Distance from the Blade Surface when t_{wi}= 85 °C and d_i= 0.1 μm .

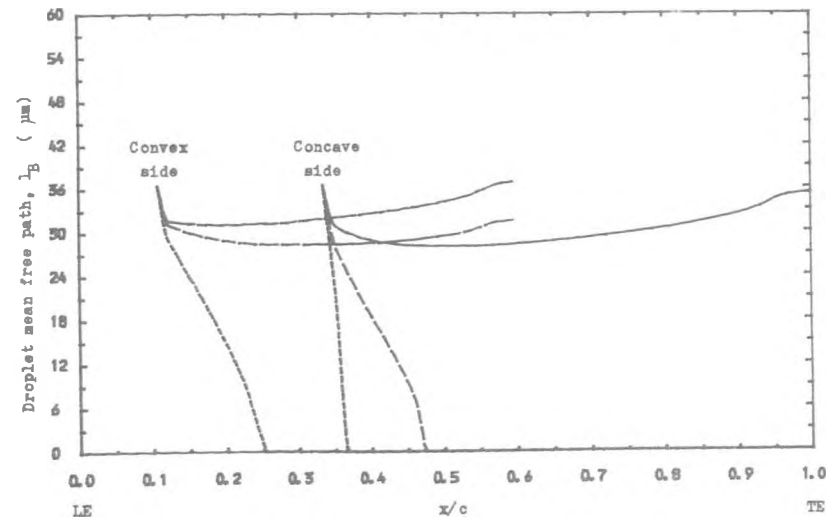

Fig. 7.8 : Variation of Droplet Mean Free Path inside the Concave and Convex Boundary Layer at Different Distance from the Blade Surface when t_{wi}= 85 °C and d_i= 0.5 μm .

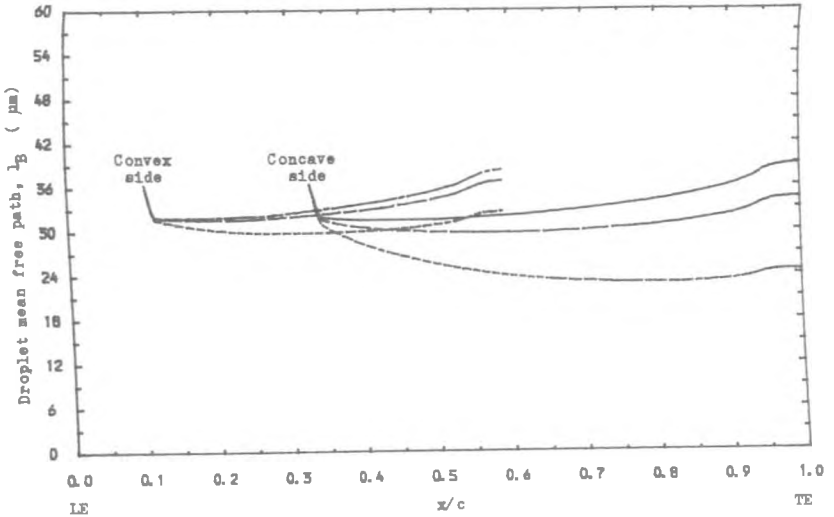

Fig. 7.11 : Variation of Droplet Mean Free Path inside the Concave and Convex Boundary Layer at Different Distance from the Blade Surface when t_{wi} = 66 °C and d_i = 0.5 μm .

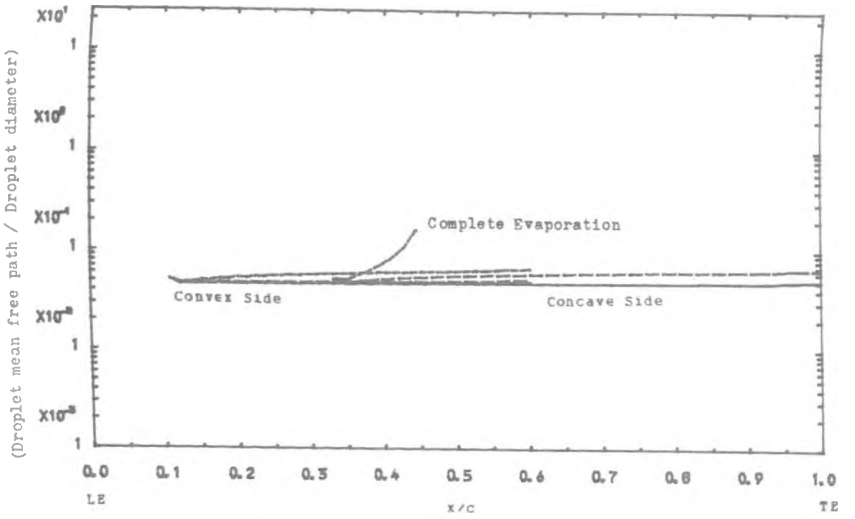

Fig. 7.13 : Variation of the Ratio of Droplet Mean Free Path to Droplet Diameter inside the Concave and Convex Boundary Layer at Different Distance from the Blade Surface when t_{wi} = 85 °C and d_i = 1.0 μm.

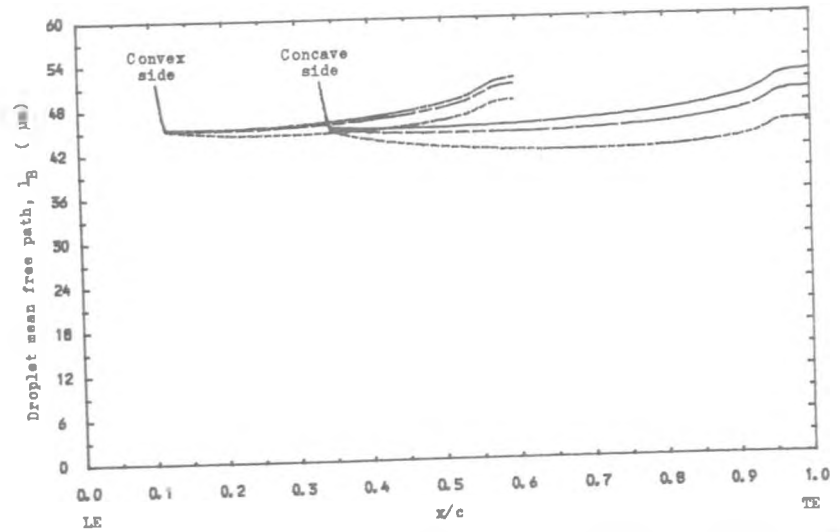

Fig. 7.10 : Variation of Droplet Mean Free Path inside the Concave and Convex Boundary Layer at Different Distance from the Blade Surface when t_{wi} = 66 °C and d_i = 1.0 μm .

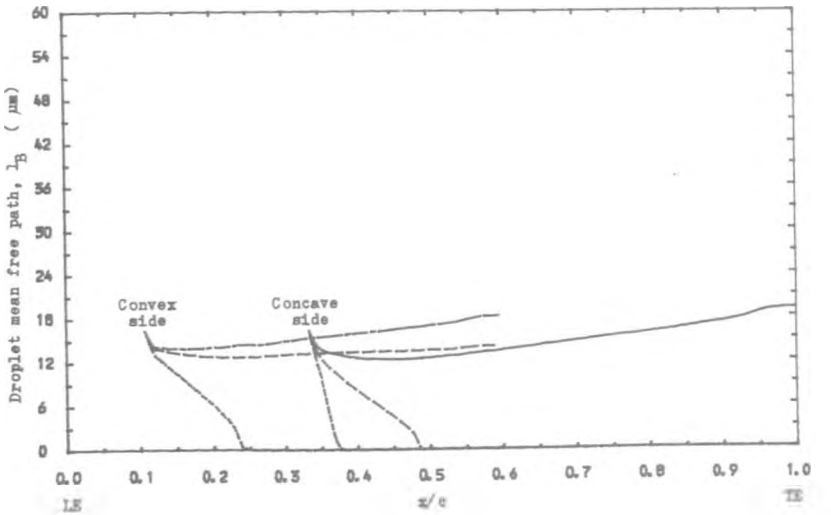

Fig. 7.12 : Variation of Droplet Mean Free Path inside the Concave and Convex Boundary Layer at Different Distance from the Blade Surface when t_{wi} = 66 °C and d_i = 0.1 μm .

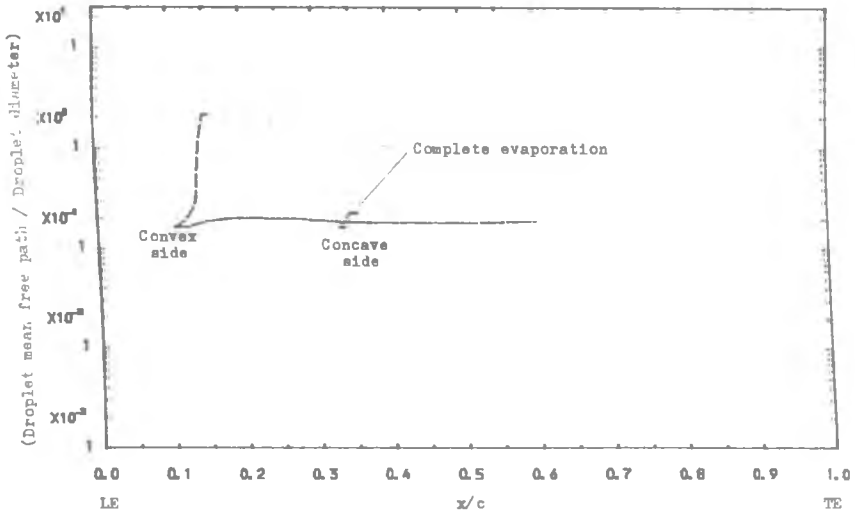

Fig. 7.15 : Variation of the Ratio of Droplet Mean Free Path to Droplet Diameter inside the Concave and Convex Boundary Layer at Different Distance from the Blade Surface when t_{wi}= 85 °C and d_j= 0.1 μm

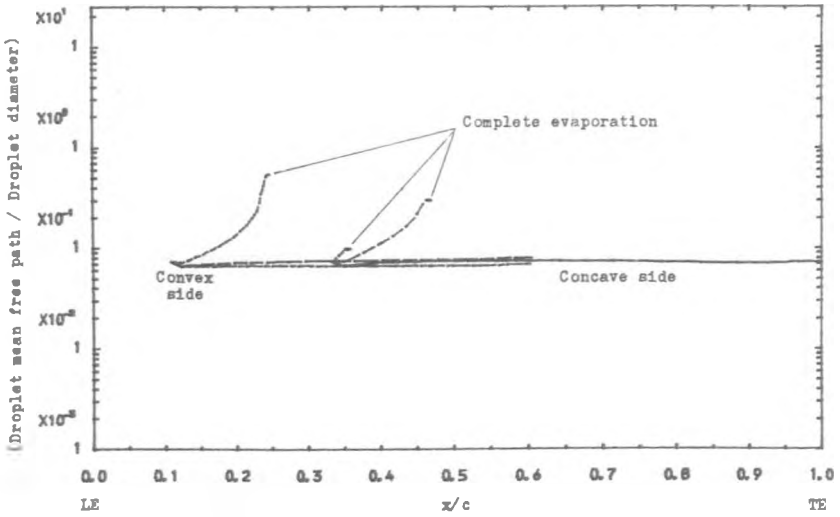

Fig. 7.14 : Variation of the Ratio of Droplet Mean Free Path to Droplet Diameter inside the Concave and Convex Boundary Layer at Different Distance from the Blade Surface when t_{wi}= 85 °C and d_j= 0.5 μm .

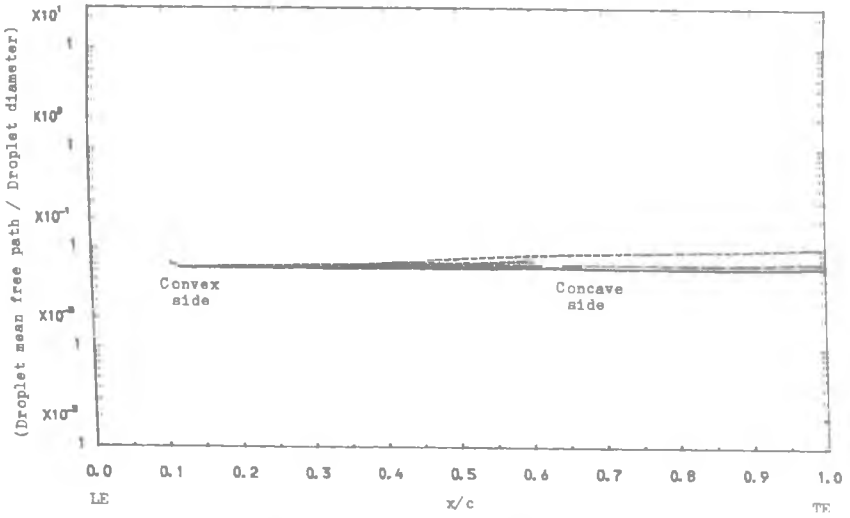

Fig. 7.17 : Variation of the Ratio of Droplet Mean Free Path to Droplet Diameter inside the Concave and Convex Boundary Layer at Different Distance from the Blade Surface when t_{wi}= 66 °C and d_j= 0.5 μm .

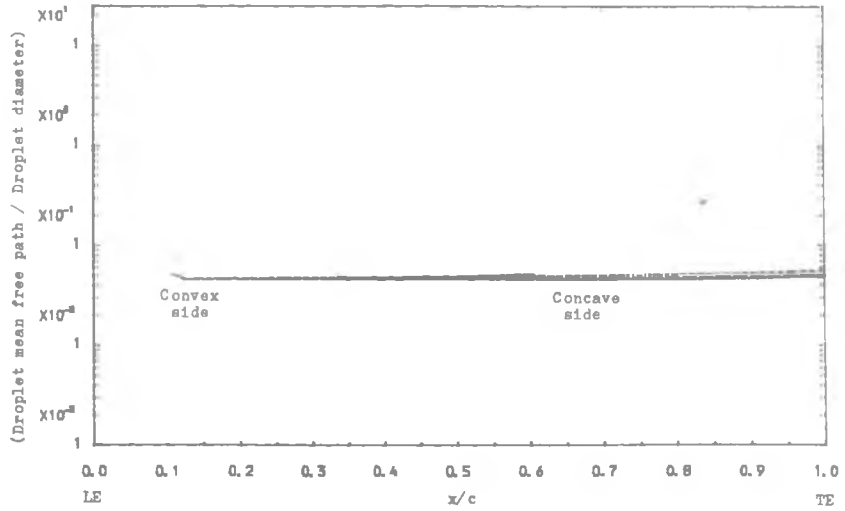

Fig. 7.16 : Variation of the Ratio of Droplet Mean Free Path to Droplet Diameter inside the Concave and Convex Boundary Layer at Different Distance from the Blade Surface when t_{wi}= 66 C and d_j= 1.0 μm .

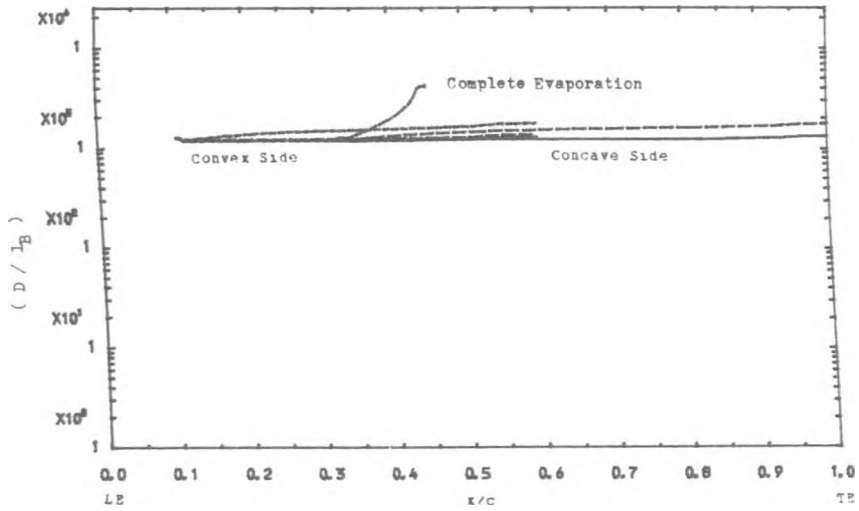

Fig. 7.19 : Variation of the Ratio of Distance between Adjacent Droplets to Droplet Mean Free Path inside the Concave and Convex Boundary Layer at Different Distance from the Blade Surface when t_{wi}= 85 °C and d_i= 1.0 μm.

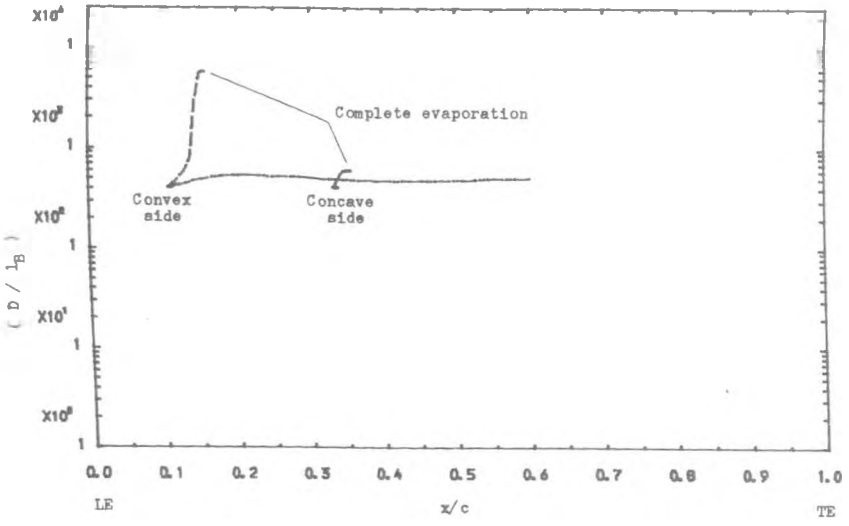

Fig. 7.21 : Variation of the Ratio of Distance between Adjacent Droplets to Droplet Mean Free Path inside the Concave and Convex Boundary Layer at Different Distance from the Blade Surface when t_{wi}= 85 °C and d_i= 0.1 μm .

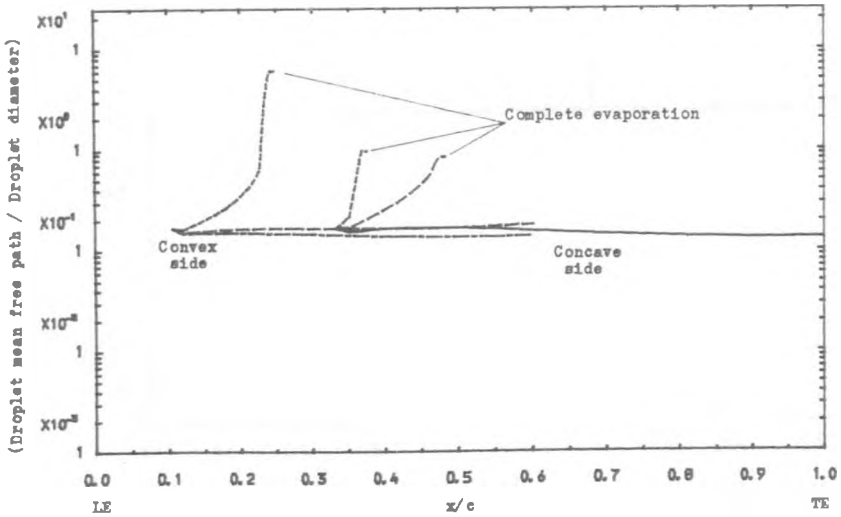

Fig. 7.18 : Variation of the Ratio of Droplet Mean Free Path to Droplet Diameter inside the Concave and Convex Boundary Layer at Different Distance from the Blade Surface when t_{wi}= 66 °C and d_i= 0.1 μm .

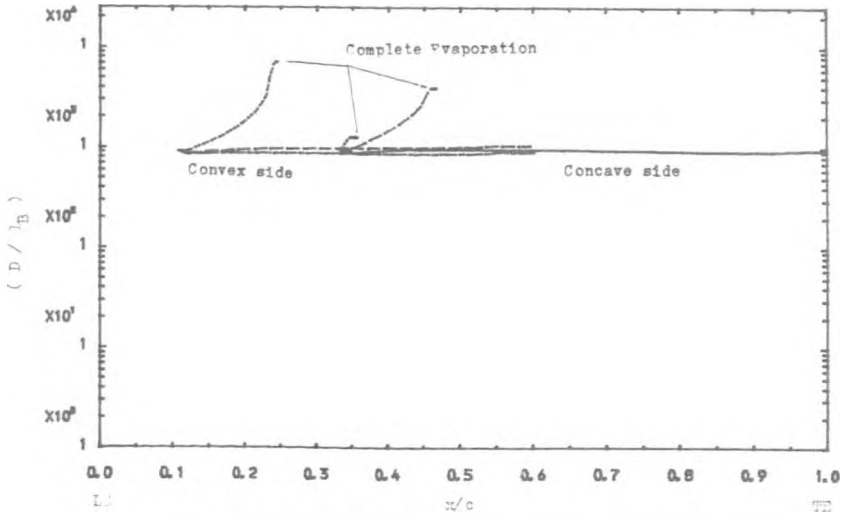

Fig. 7.20 : Variation of the Ratio of Distance between Adjacent Droplets to Droplet Mean Free Path inside the Concave and Convex Boundary Layer at Different Distance from the Blade Surface when t_{wi}= 85 °C and d_i= 0.5 μm.

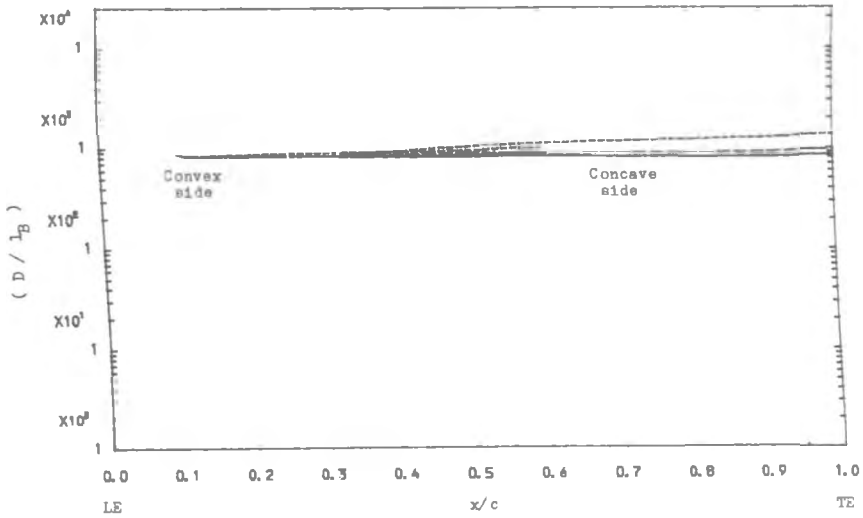

Fig. 7.23 : Variation of the Ratio of Distance between Adjacent Droplets to Droplet Mean Free Path inside the Concave and Convex Boundary Layer at Different Distance from the Blade Surface when t_{w1}= 66 C and d_i= ^.5 μm .

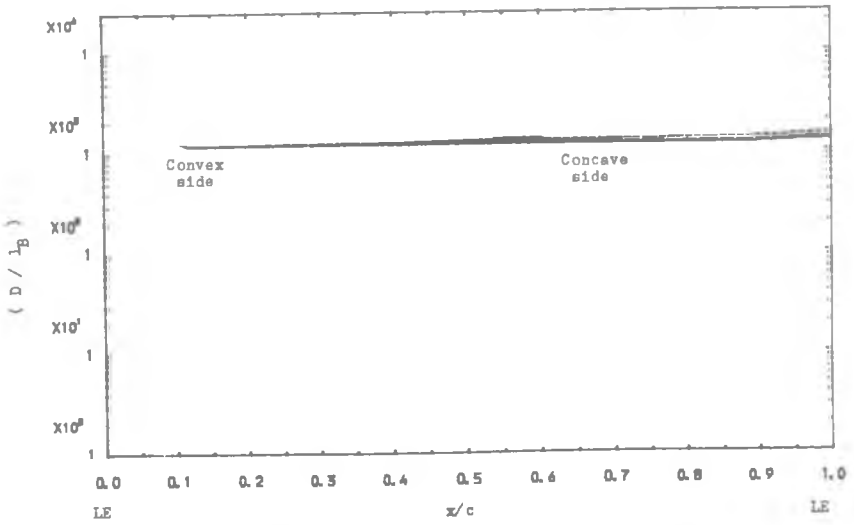

Fig. 7.22 : Variation of the Ratio of Distance between Adjacent Droplets to Droplet Mean Free Path inside the Concave and Convex Boundary Layer at Different Distance from the Blade Surface when t_{w1}= 66 °C and d_i= 1.0 μm .

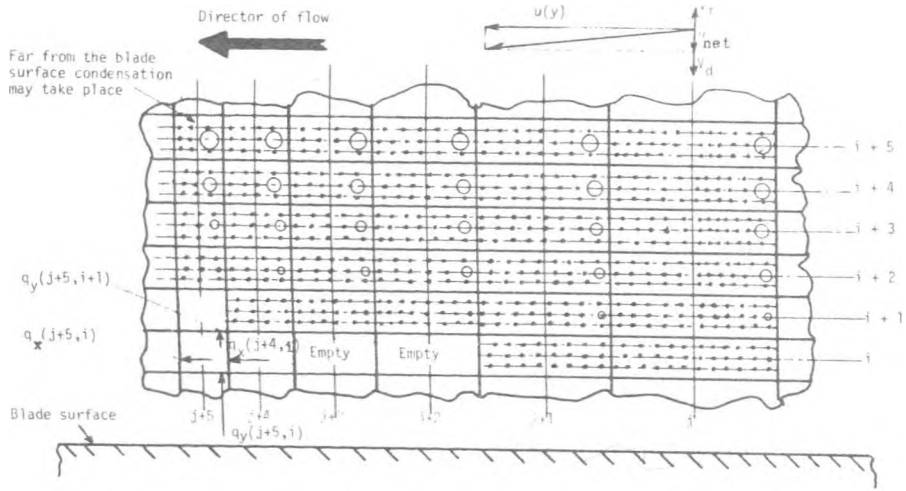

FIGURE 7.25 NOTATION FOR BOUNDARY LAYER CELLS, MASS AND HEAT TRANSFER

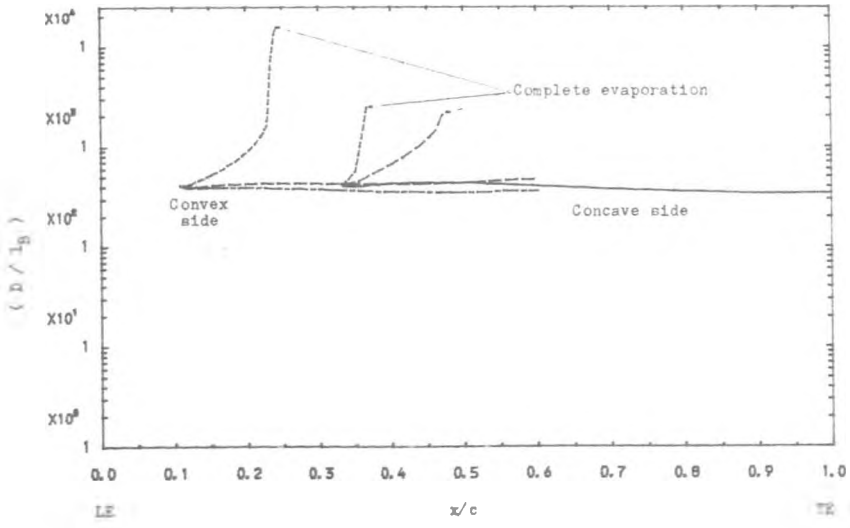

Fig. 7.24 : Variation of the Ratio of Distance between Adjacent Droplets to Droplet Mean Free Path inside the Concave and Convex Boundary Layer at Different Distance from the Blade Surface when t_{w1}= 66 °C and d_i= 0.1 μm .

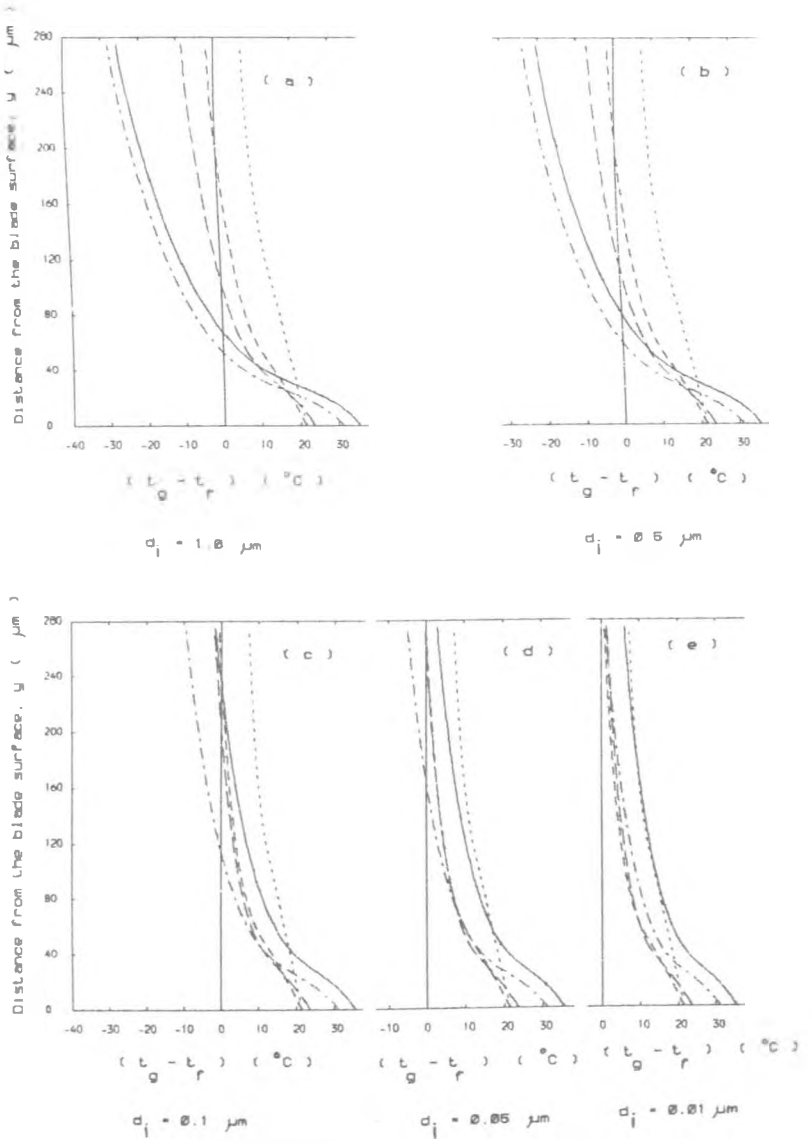

Figure 7.26 : Distribution of Temperature Difference between the Vapour and the Droplet inside the Boundary Layer along y-axis, for a Range of Droplet Sizes, when t = 85 °C.

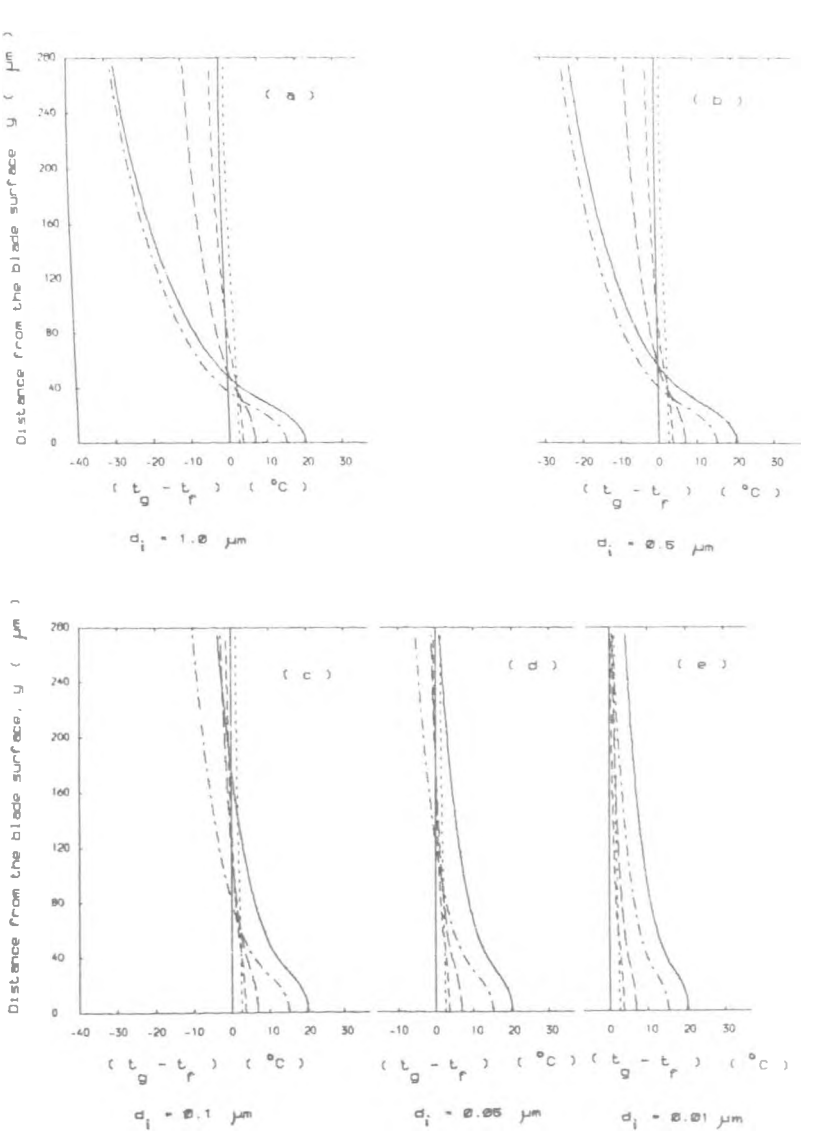

Figure 7.27 : Distribution of Temperature Difference between the Vapour and the Droplet inside the Boundary Layer along y-axis, for a Range of Droplet Sizes, when t = 66 °C

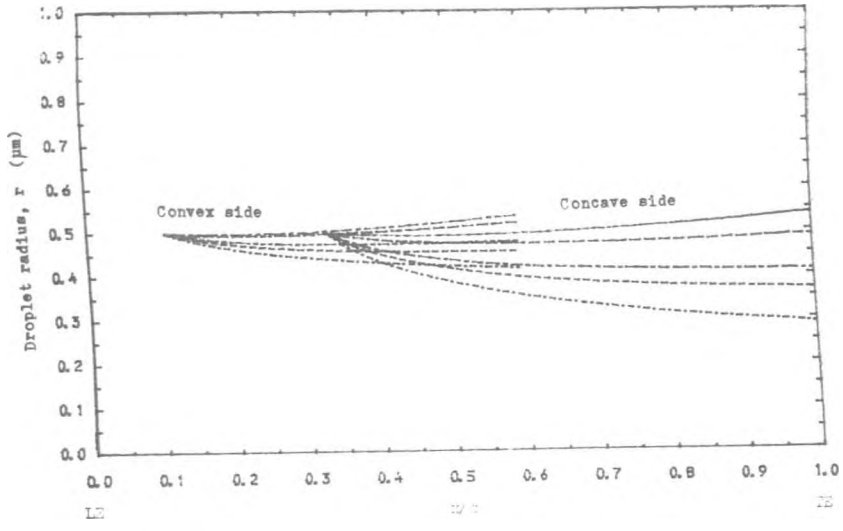

Fig. 7.28 : Variation of Droplet Radius inside the Concave and Convex Boundary Layer at Different Distance from the Blade Surface when t_{wi} = 66 °C and d_i = 1.0 μm.

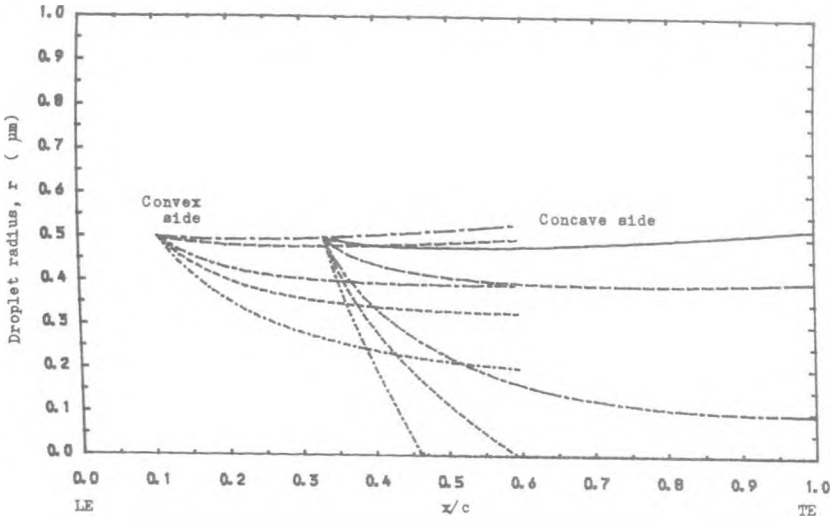

Fig. 7.30 : Variation of Droplet Radius inside the Concave and Convex Boundary Layer at Different Distance from the Blade Surface when t_{wi}=75 °C and d_i=1.0 μm .

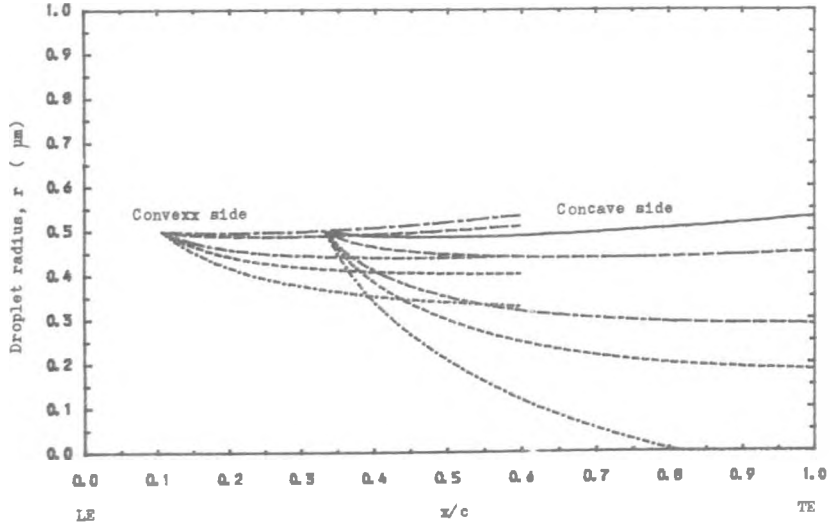

Fig. 7.29 : Variation of Droplet Radius inside the Concave and Convex Boundary Layer at Different Distance from the Blade Surface when t_{wi}= 70 °C and d_i= 1.0 μm .

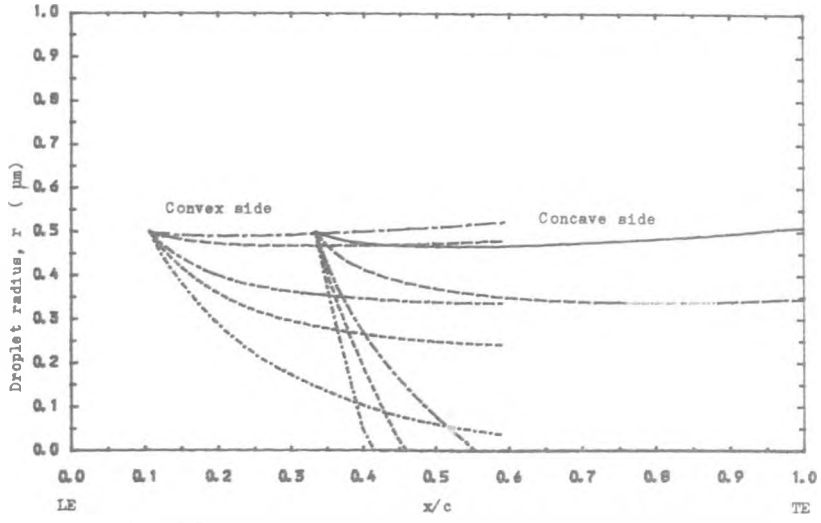

Fig. 7.31 : Variation of Droplet Radius inside the Concave and Convex Boundary Layer at Different Distance from the Blade Surface when t_{wi}= 80 °C and d_i= 1.0 μm .

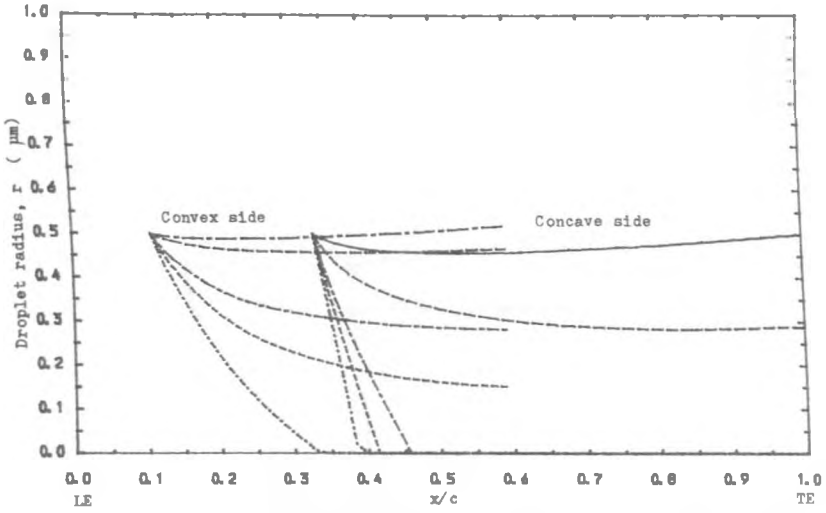

Fig. 7.32: Variation of Droplet Radius inside the Concave and Convex Boundary Layer at Different Distance from the Blade Surface when t_{wi}=85 °C and d_i=1.0 μm .

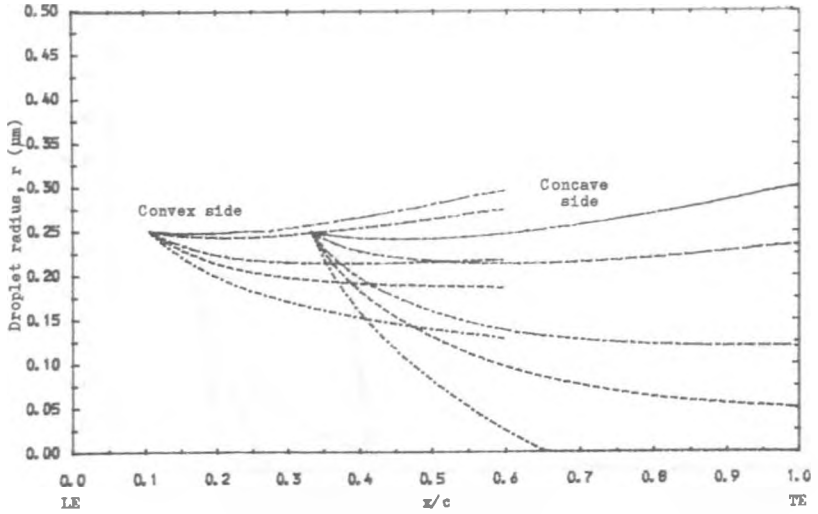

Fig. 7.33: Variation of Droplet Radius inside the Concave and Convex Boundary Layer at Different Distance from the Blade Surface when t_{wi}= 66 °C and d_i= 0.5 μm .

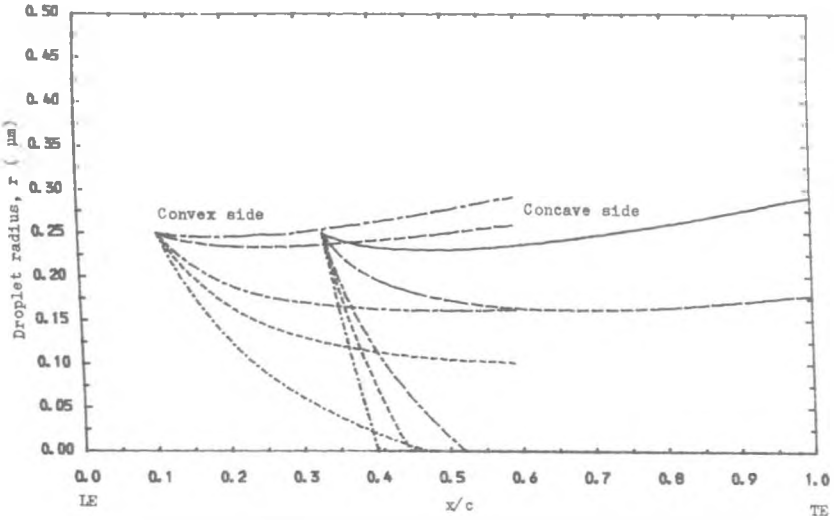

Fig.7.34: Variation of Droplet Radius inside the Concave and Convex Boundary Layer at different Distance from the Blade Surface when t_{wi}=70 °C and d_i= 0.5 μm .

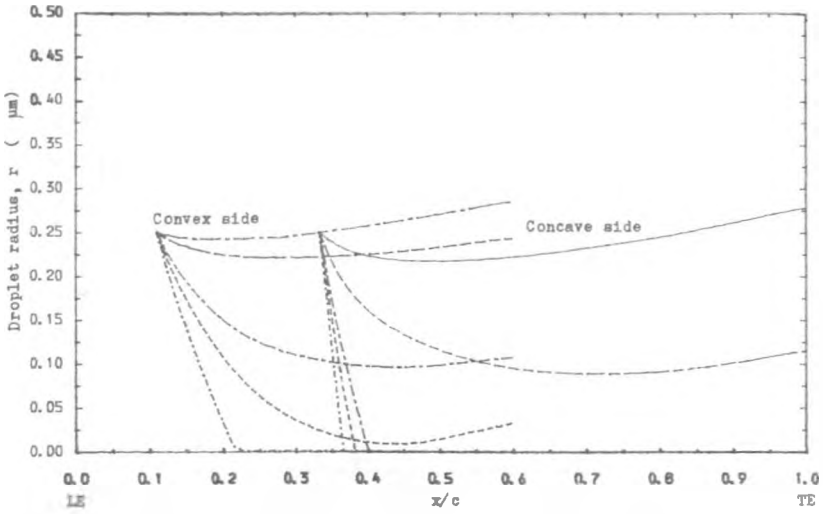

Fig. 7.35 : Variation of Droplet Radius inside the Concave and Convex Boundary Layer at Different Distance from the Blade Surface when t_{wi}=75 °C and d_i= 0.5 μm .

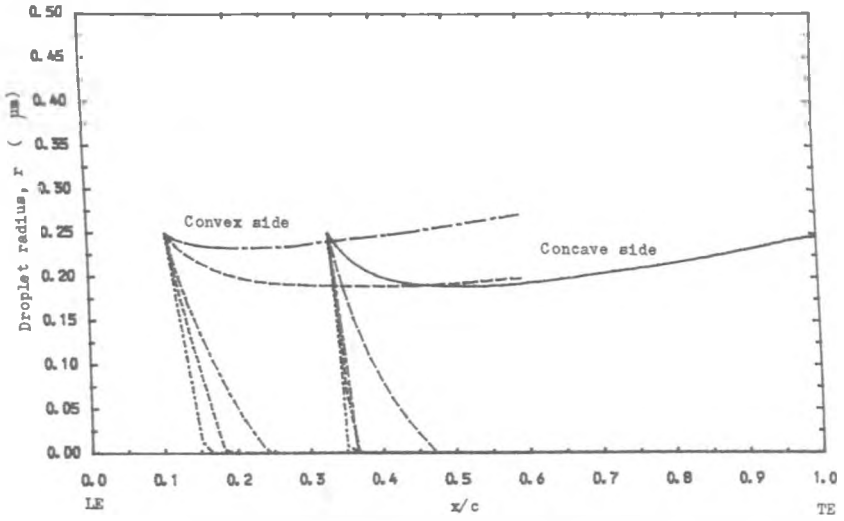

Fig. 7.37 : Variation of Droplet Radius inside the Concave and Convex Boundary Layer at Different Distance from the Blade Surface when t_{wi}= 85 °C and d_i= 0.5 μm .

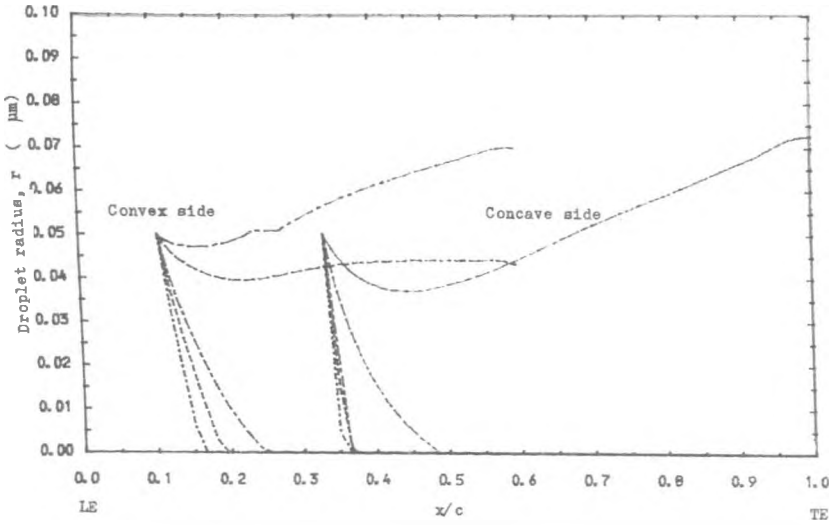

Fig. 7.38 : Variation of Droplet Radius inside the Concave and Convex Boundary Layer at Different Distance from the Blade Surface when t_{wi}= 66 °C and d_i= 0.1 μm .

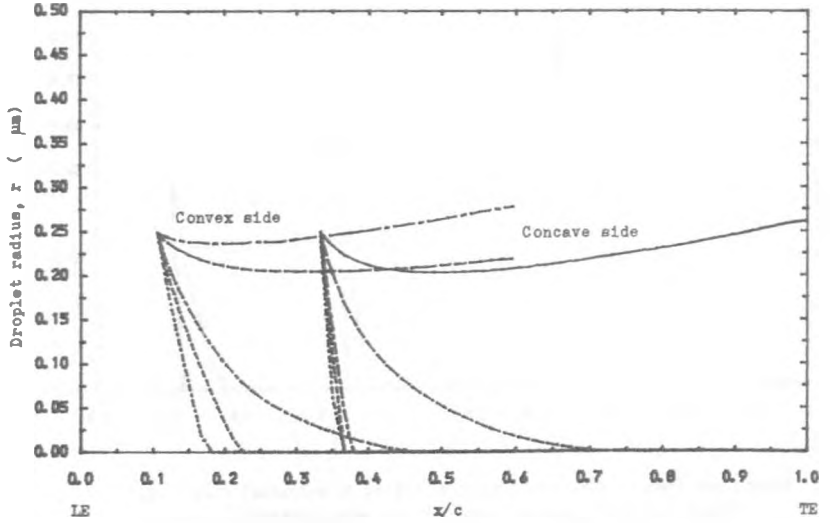

Fig.7.36 : Variation of Droplet Radius inside the Concave and Convex Boundary Layer at Different Distance from the Blade Surface when t_{wi}= 80 °C and d_i= 0.5 μm .

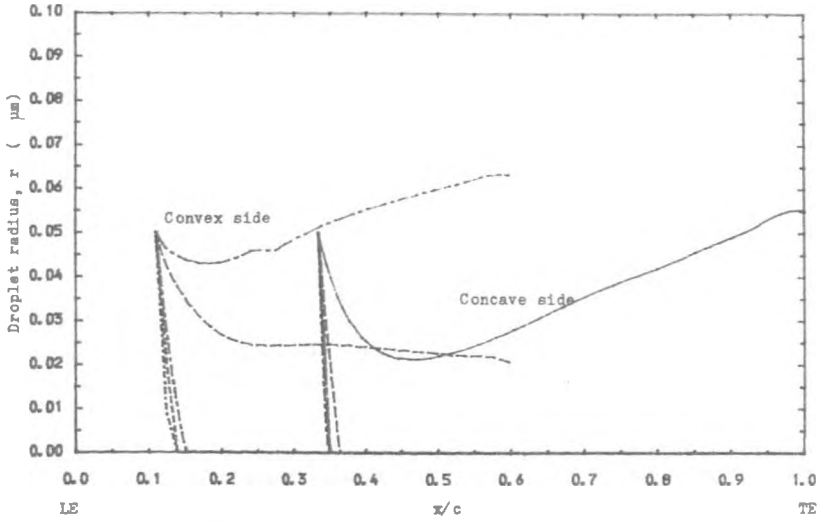

Fig. 7.39 : Variation of Droplet Radius inside the Concave and Convex Boundary Layer at Different Distance from the Blade Surface when t_{wi}=70 °C and d_i= 0.1 μm .

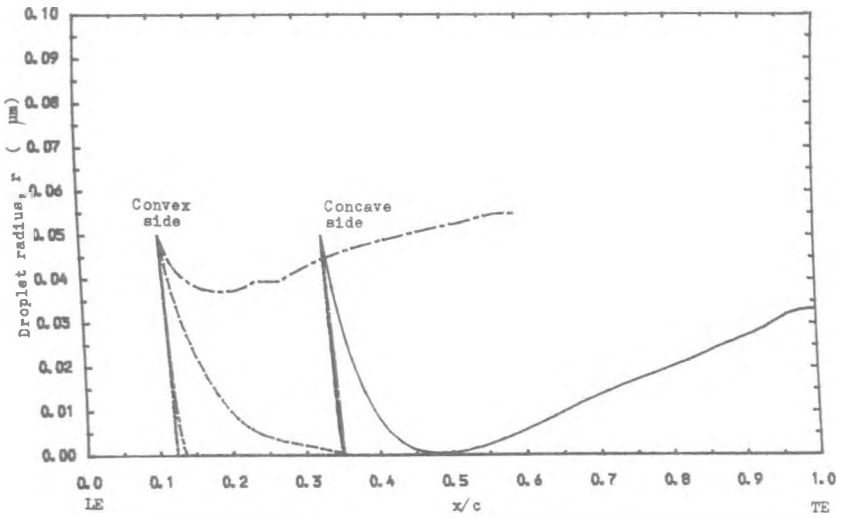

Fig. 7.40 : Variation of Droplet Radius inside the Concave and Convex Boundary Layer at Different Distance from the Blade Surface when t_{wi}= 75 °C and d_i= 0.1 μm .

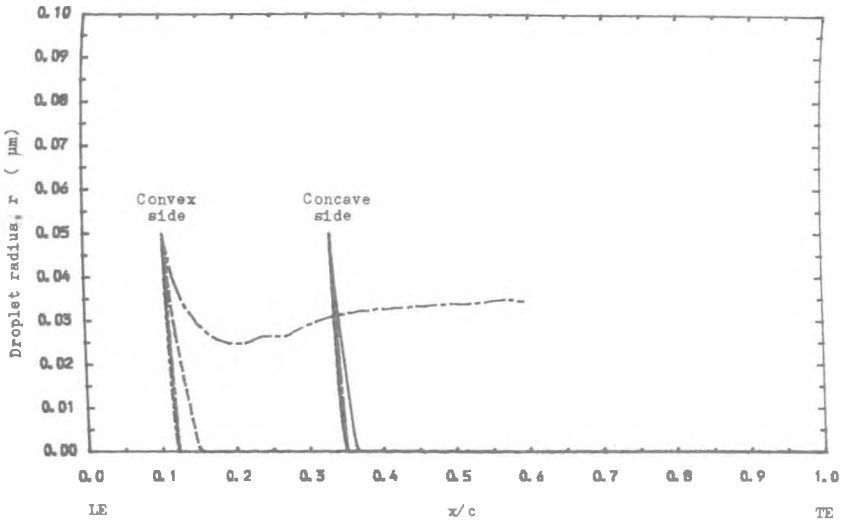

Fig. 7.42 : Variation of Droplet Radius inside the Concave and Convex Boudary Layer at Different Distance from the Blade Surface when t_{wi}= 85 °C and d_i= 0.1 μm .

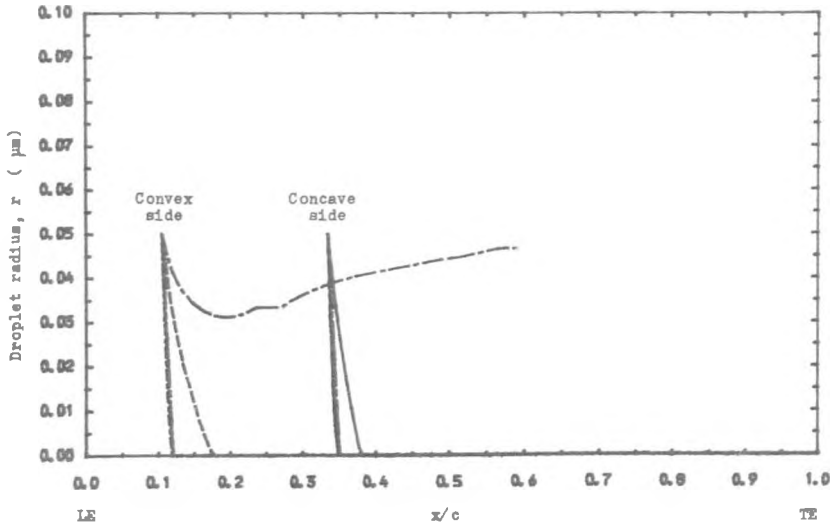

Fig. 7.41 : Variation of Droplet Radius inside the Concave and Convex Boundary Layer at Different Distance from the Blade Surface when t_{wi}= 80 °C and d_i= 0.1 μm .

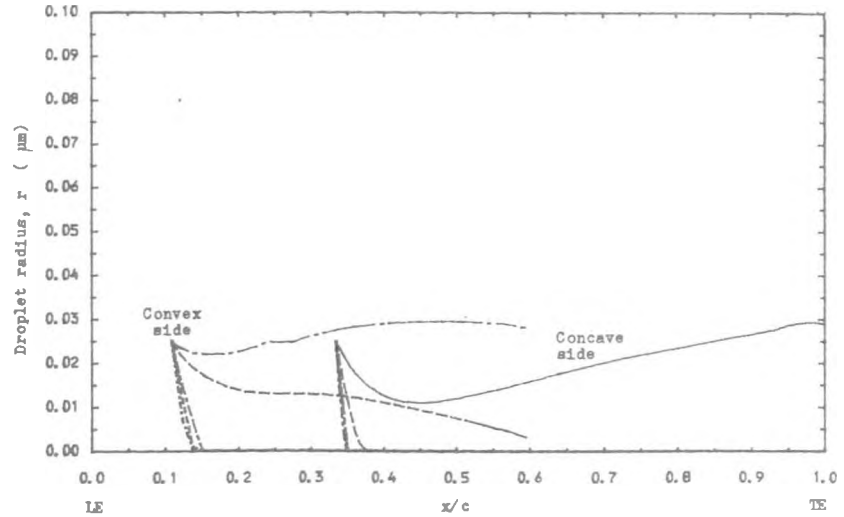

Fig. 7.43 : Variation of Droplet Radius inside the Concave and Convex Boundary Layer at Different Distance from the Blade Surface when t_{wi}= 66 °C and d_i= 0.05 μm .

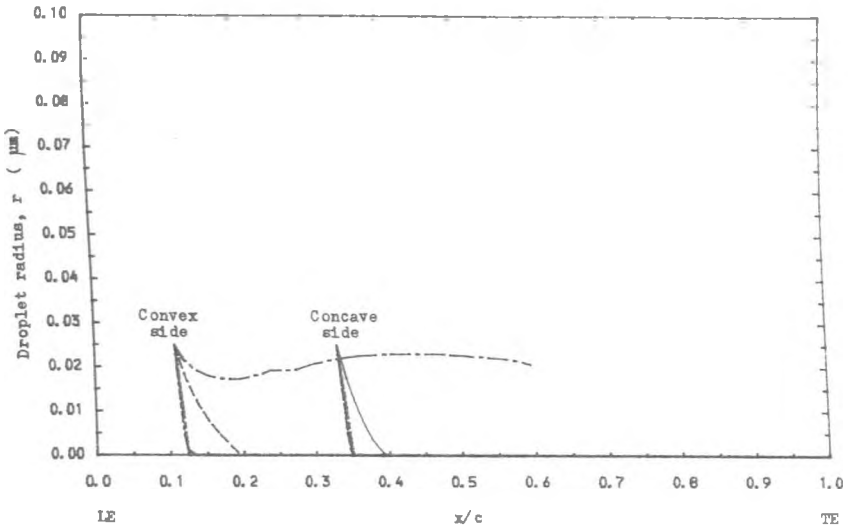

Fig. 7.44 : Variation of Droplet Radius inside the Concave and Convex Boundary Layer at Different Distance from the Blade Surface when t_{wi} = 70 °C and d_i = 0.05 μm .

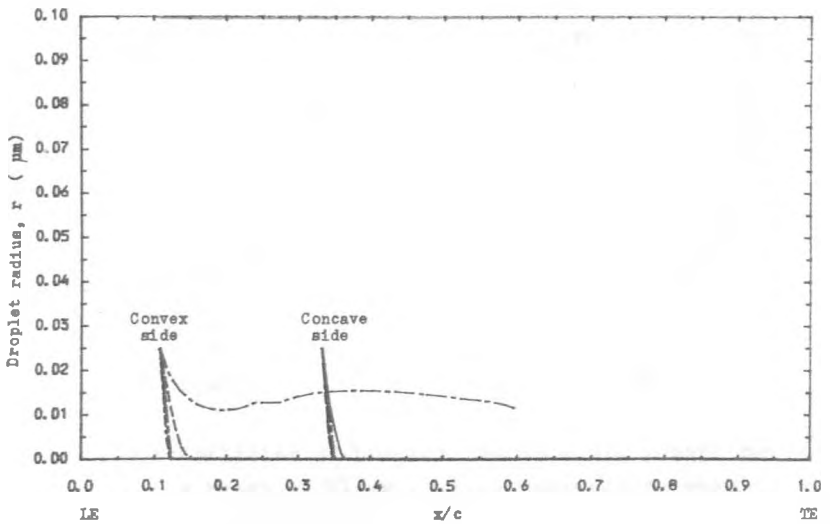

Fig. 7.45 : Variation of Droplet Radius inside the Concave and Convex Boundary Layer at Different Distance from the Blade Surface when t_{wi} = 75 °C and d_i = 0.05 μm .

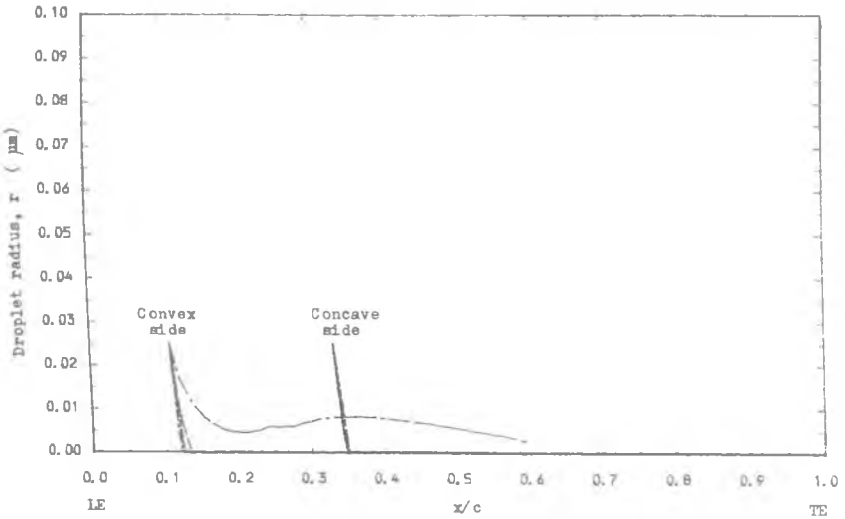

Fig. 7.46 : Variation of Droplet Radius inside the Concave and Convex Boundary Layer at Different Distance from the Blade Surface when t_{wi} = 80 °C and d_i = 0.05 μm .

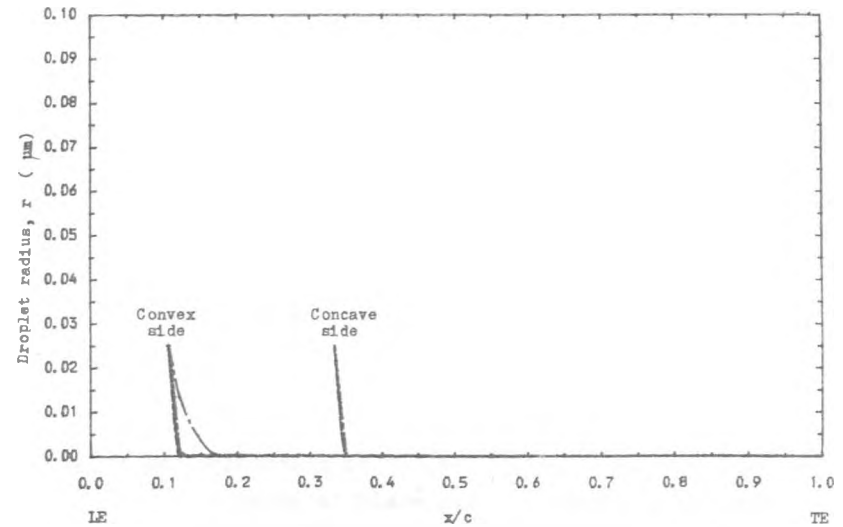

Fig. 7.47 : Variation of Dro plet Radius inside the Concave and Convex Boundary Layer at Different Distance from the Blade Surface when t_{wi} = 85 °C and d_i = 0.05 μm .

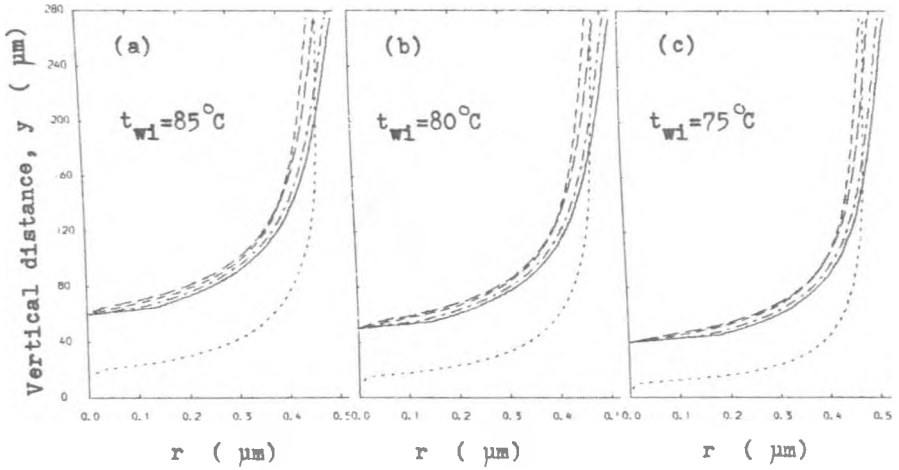

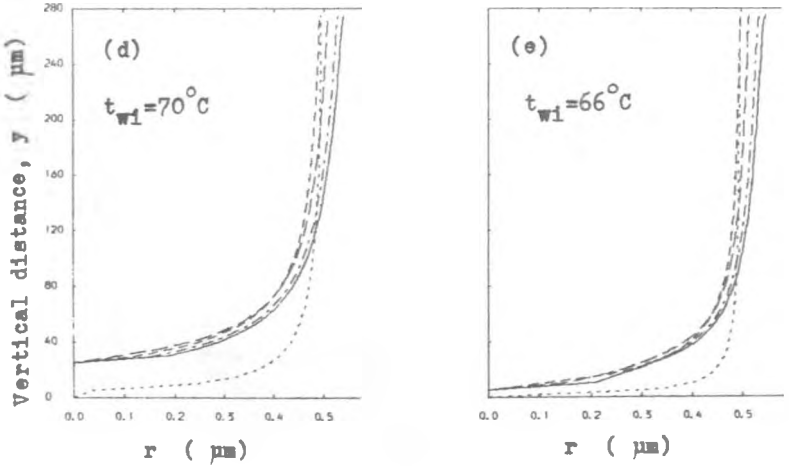

Fig. 7.48 : Variation of Droplet Radius along y-axis for a range of Blade Surface Temperature when d_1= 1.0 μm .

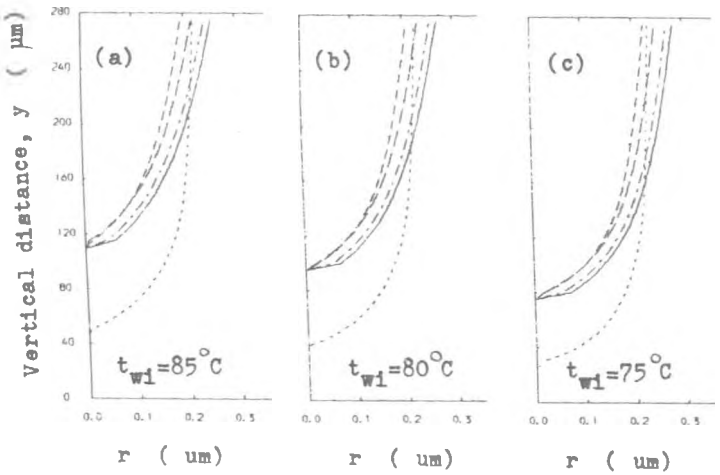

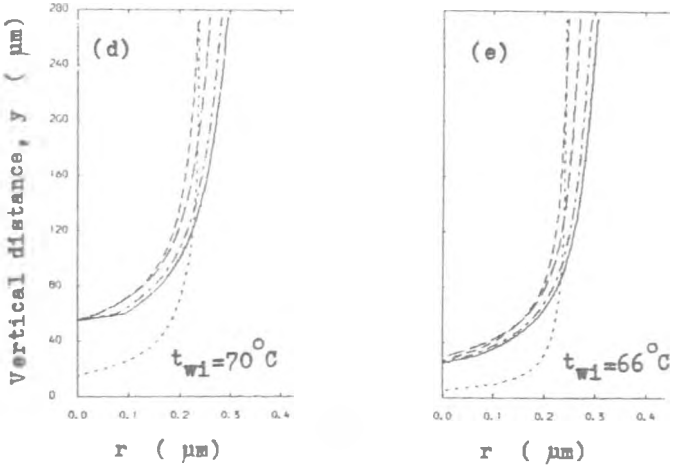

Fig. 7.49 : Variation of Droplet Radius along y-axis for a range of Blade Surface Temperatures when d_1= 0.5 μm .

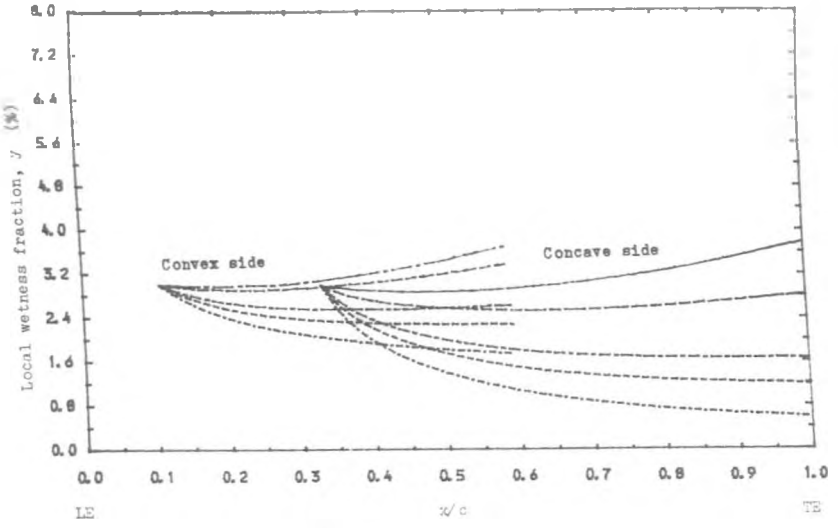

Fig. 7.50 : Variation of Local Wetness Fraction inside the Concave and Convex Boundary Layer at Different Distance from the Blade Surface when t_{wi} = 66 °C and d_i = 1.0 μm.

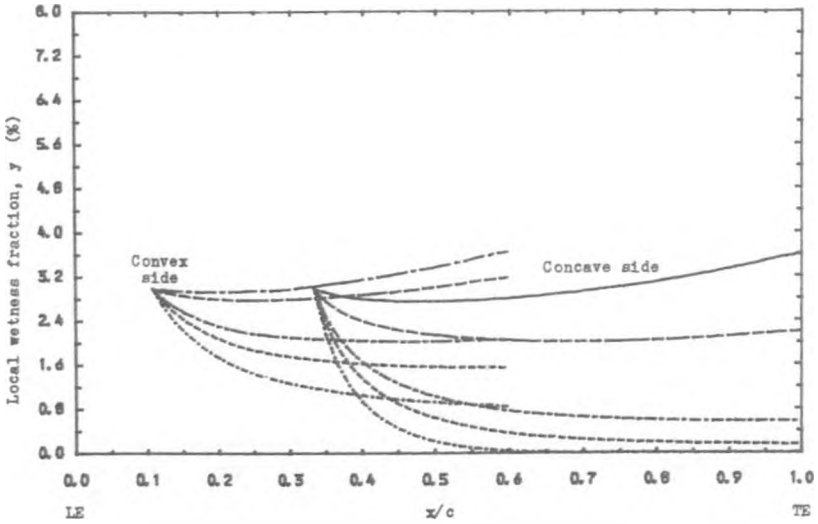

Fig 7.51 : Variation of Local Wetness Fraction inside the Concave and Convex Boundary Layer at Different Distance from the Blade Surface when t_{wi} = 70 °C and d_i = 1.0 μm .

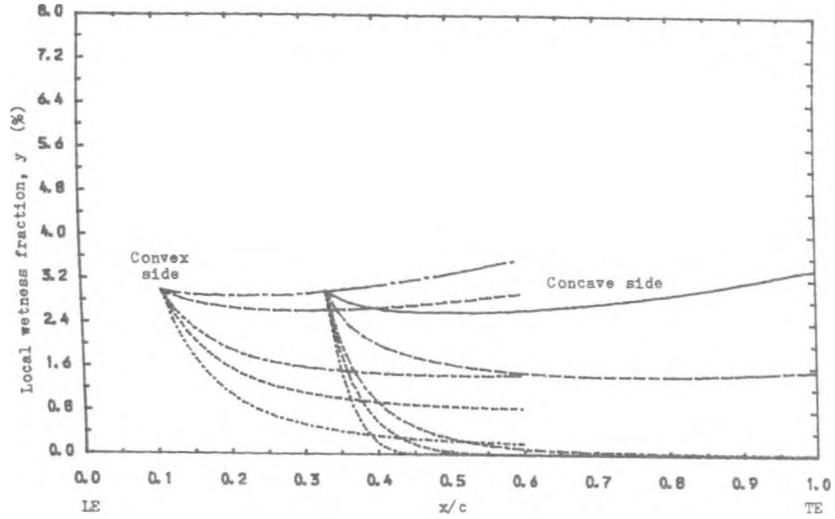

Fig. 7.52 : Variation of Local Wetness Fraction inside the Concave and Convex Boundary Layer at Different Distance from the Blade Surface when t_{wi} = 75 °C and d_i = 1.0 μm .

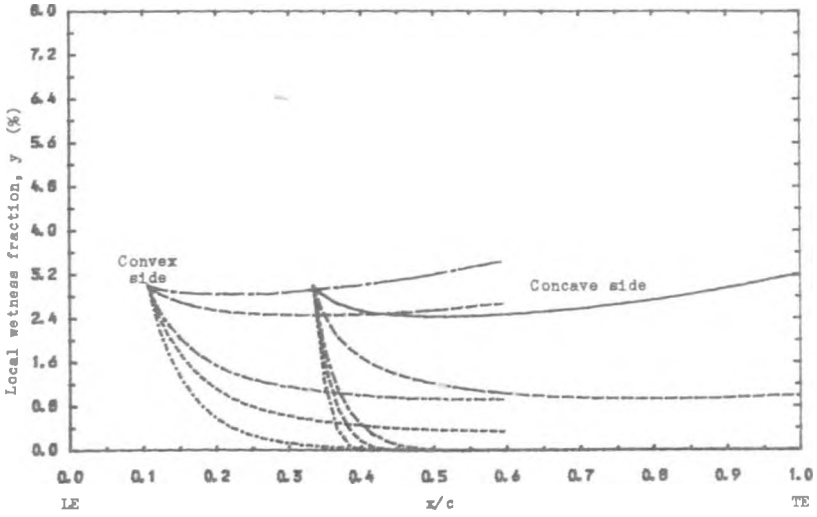

Fig. 7.53 : Variation of Local Wetness Fraction inside the Concave and Convex Boundary Layer at Different Distance from the Blade Surface when t_{wi} = 80 °C and d_i = 1.0 μm .

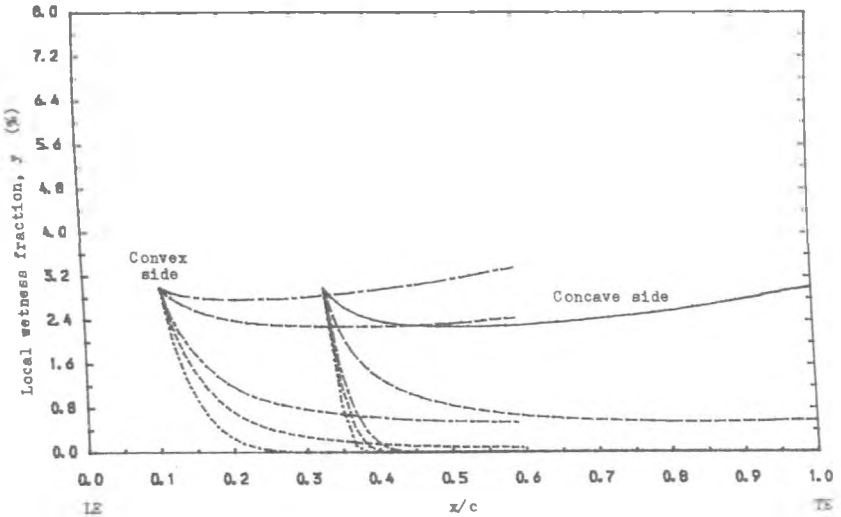

Fig.7.54 : Variation of Local Wetness Fraction inside the Concave and Convex Boundary Layer at Different Distance from the Blade Surface when t_{w1}= 85 °C and d_1= 1.0 μm .

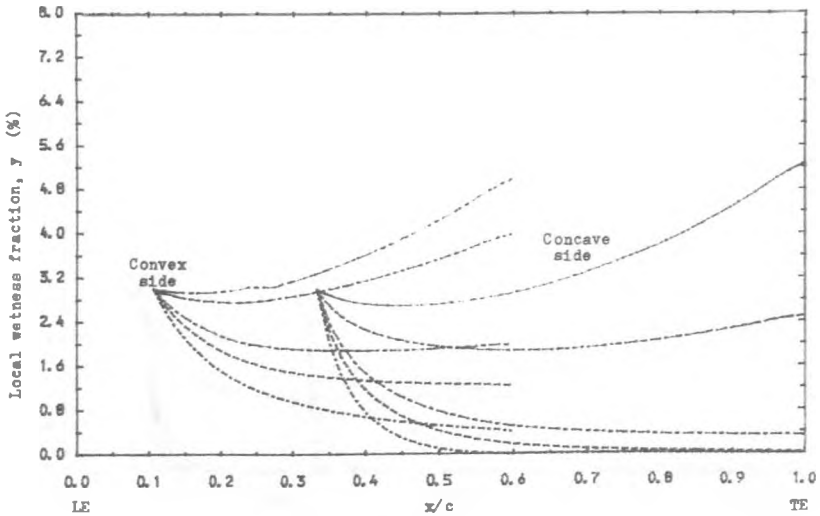

Fig. 7.55 : Variation of Local Wetness Fraction inside the Concave and Convex Boundary Layer at Different Distance from the Blade Surface when t_{w1}= 66 °C and d_1= 1.0 μm .

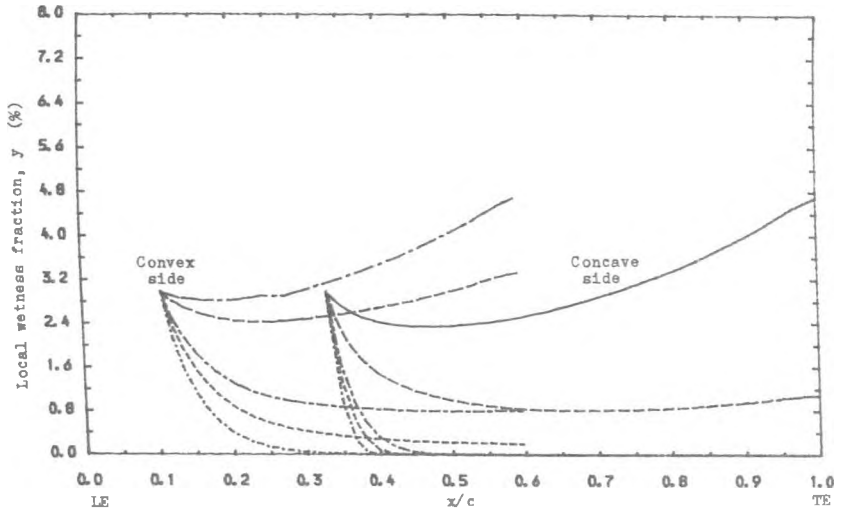

Fig. 7.56 : Variation of Local Wetness Fraction inside the Concave and Convex Boundary Layer at Different Distance from the Blade Surface when t_{w1}= 70 °C and d_1= 0.5 μm .

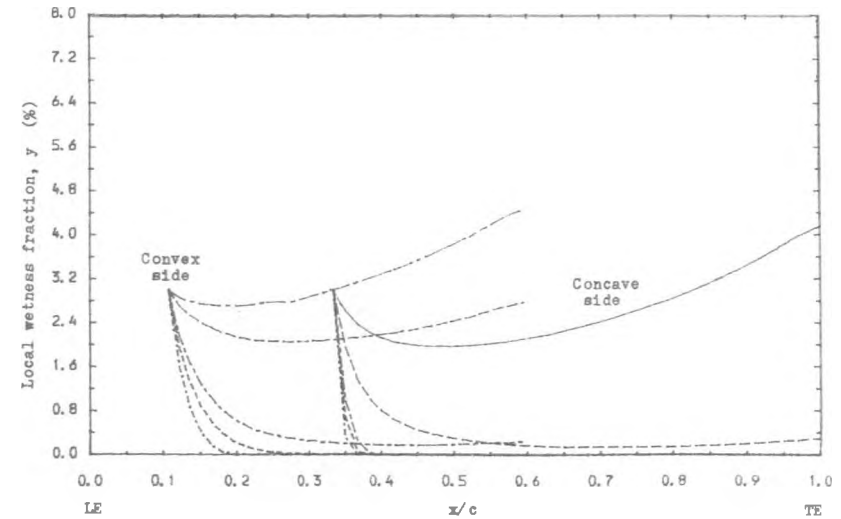

Fig. 7.57 : Variation of Local Wetness Fraction inside the Concave and Convex Boundary Layer at Different Distance from the Blade Surface when t_{w1}= 75 °C and d_1= 0.5 μm .

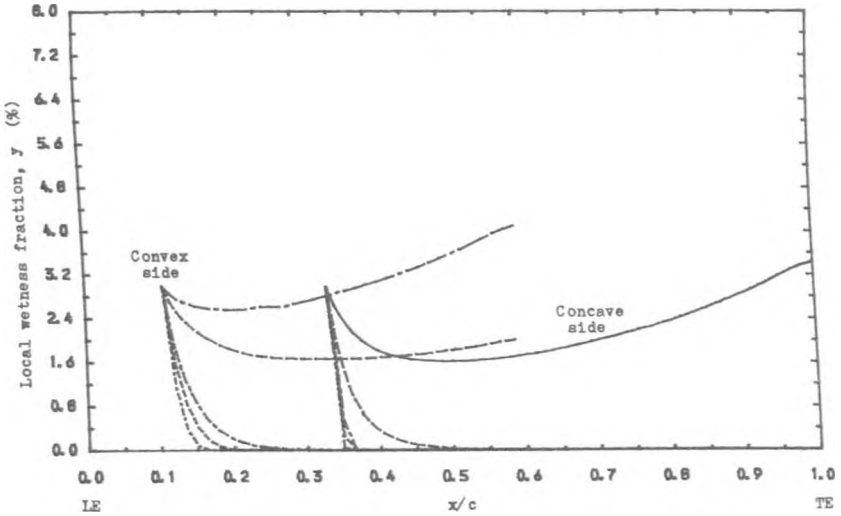

Fig. 7.58 : Variation of Local Wetness Fraction inside the Concave and Convex Boundary Layer at Different Distance from the Blade Surface when t_{wi} = 80 °C and d_i = 0.5 μm .

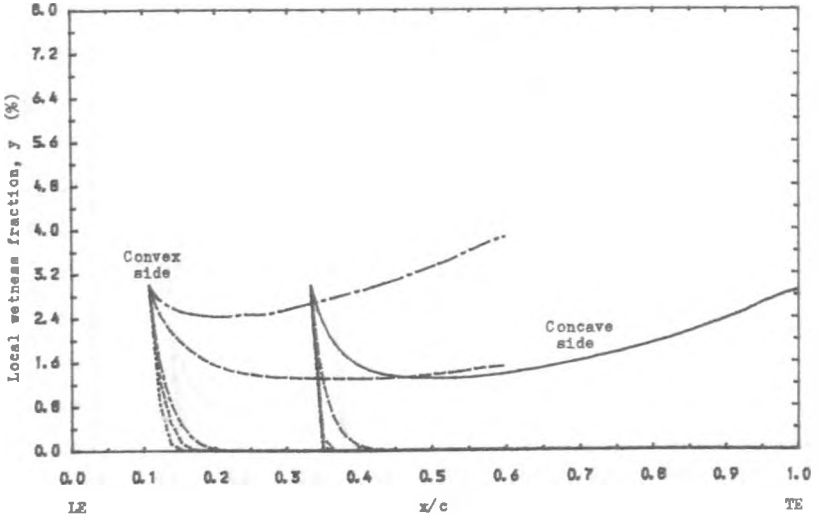

Fig. 7.59 : Variation of Local Wetness Fraction inside the Concave and Convex Boundary Layer at Different Distance from the Blade Surface when t_{wi} = 85 °C and d_i = 0.5 μm .

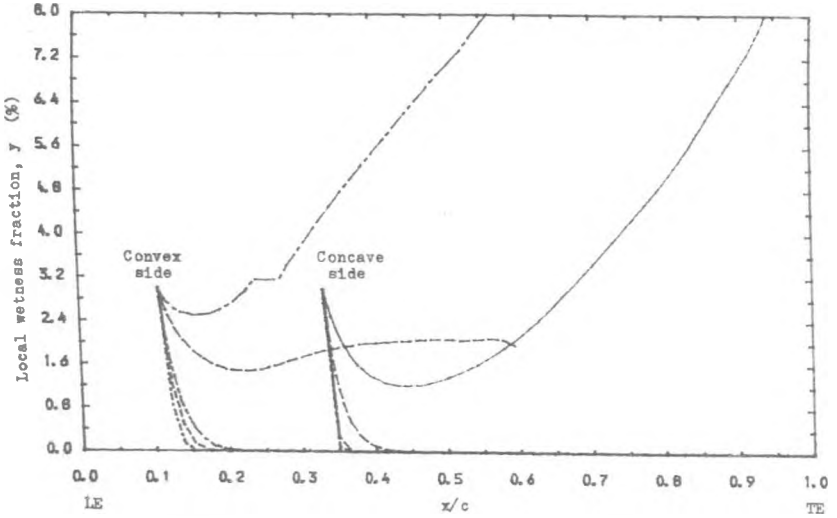

Fig. 7.60 : Variation of Local Wetness Fraction inside the Concave and Convex Boundary Layer at Different Distance from the Blade Surface when t_{wi} = 66 °C and d_i = 0.1 μm .

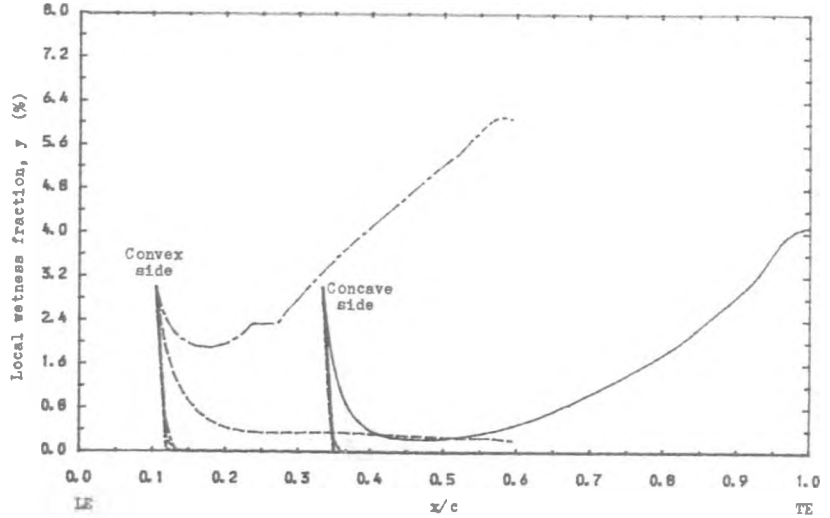

Fig. 7.61 : Variation of Local Wetness Fraction inside the Concave and Convex Boundary Layer at Different Distance From the Blade Surface when t_{wi} = 70 °C and d_i = 0.1 μm .

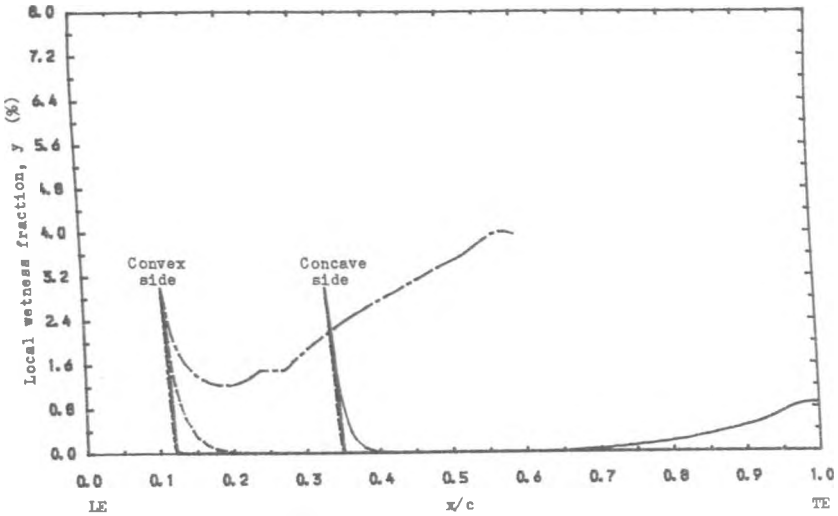

Fig. 62 : Variation of Local Wetness Fraction inside the Concave and Convex Boundary Layer at Different Distance from the Blade Surface when t_{w1}= 75 °C and d_i= 0.1 μm .

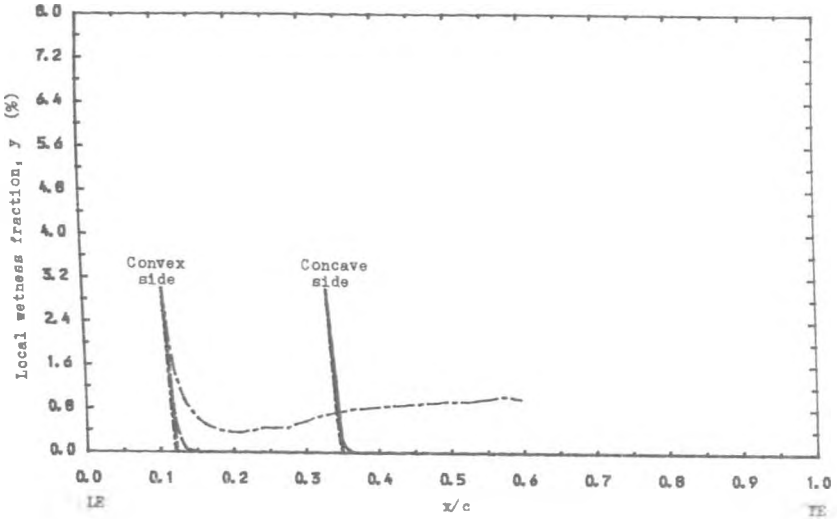

Fig. 7.64 : Variation of Local Wetness Fraction inside the Concave and Convex Boundary Layer at Different Distance from the Blade Surface when t_{w1}= 85 °C and d_i= 0.1 μm .

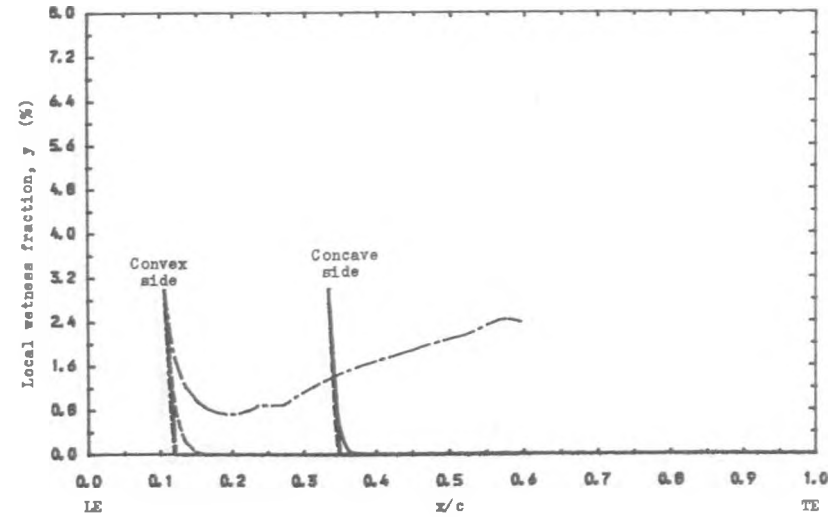

Fig. 7.63 : Variation of Local Wetness Fraction inside the Concave and Convex Boundary Layer at Different Distance from the Blade Surface when t_{w1}= 80 °C and d_i= 0.1 μm .

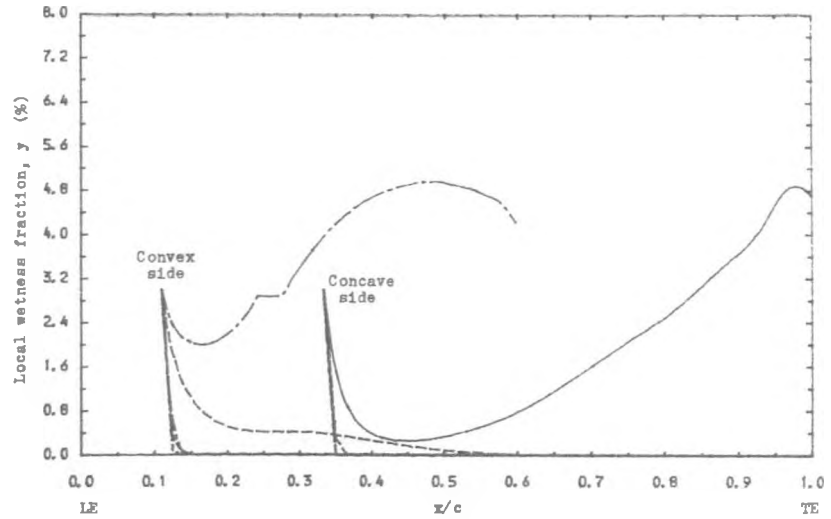

Fig. 7.65 : Variation of Local Wetness Fraction inside the Concave and Convex Boundary Layer at Different Distance from the Blade Surface when t_{w1}= 66 °C and d_i= 0.05 μm .

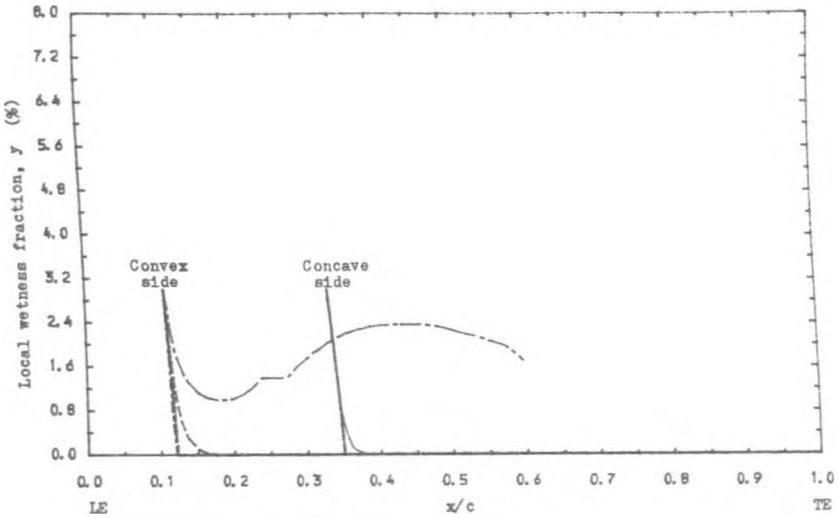

Fig. 7.66 : Variation of Local Wetness Fraction inside the Concave and Convex Boundary Layer at Different Distance from the Blade Surface when t_{wi} = 70 °C and d_i = 0.05 μm .

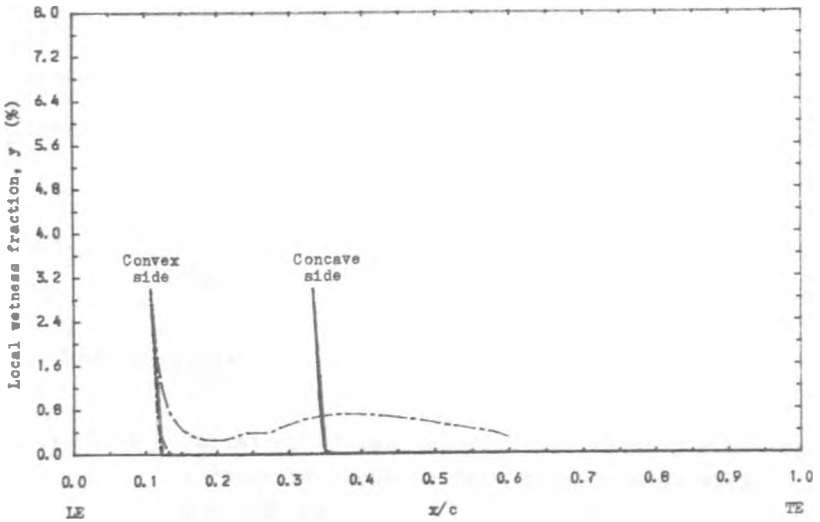

Fig. 7.67 : Variation of Local Wetness Fraction inside the Concave and Convex Boundary Layer at Different Distance from the Blade Surface when t_{wi} = 75 °C and d_i = 0.05 μm .

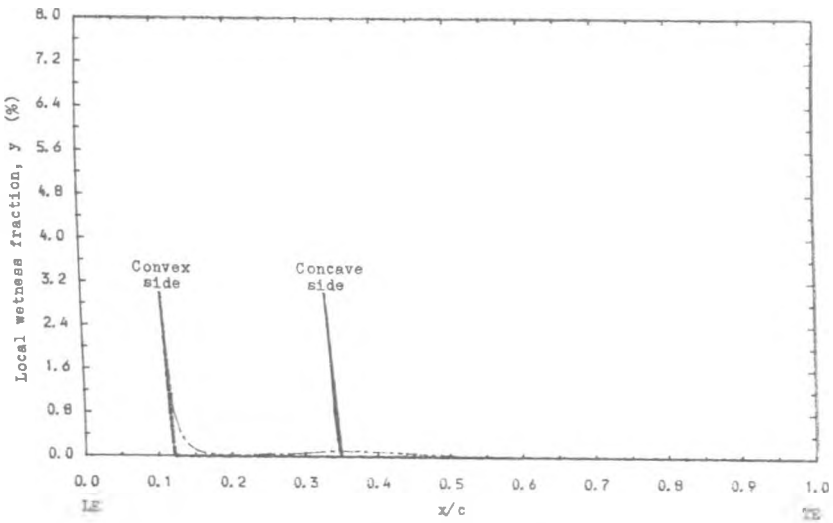

Fig. 7.68 : Variation of Local Wetness Fraction inside the Concave and Convex Boundary Layer at Different Distance from the Blade Surface when t_{wi} = 80 °C and d_i = 0.05 μm .

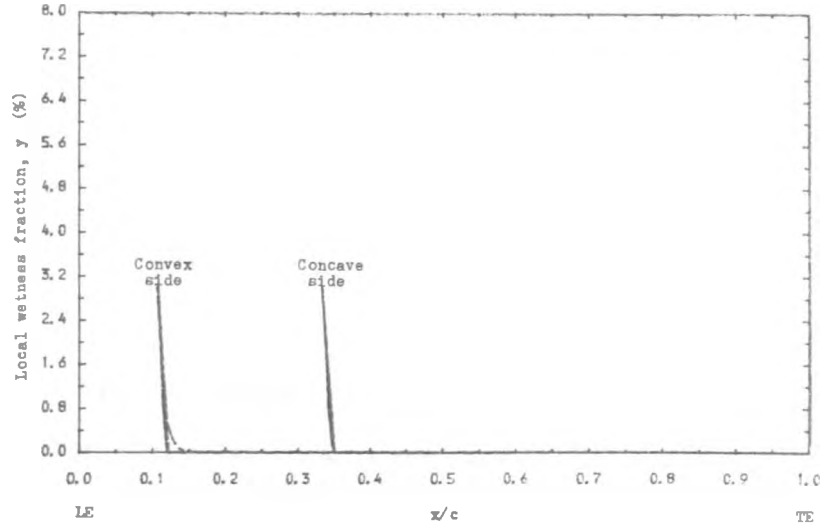

Fig. 7.69 : Variation of Local Wetness Fraction inside the Concave and Convex Boundary Layer at Different Distance from the Blade Surface when t_{wi} = 85 °C and d_i = 0.05 μm .

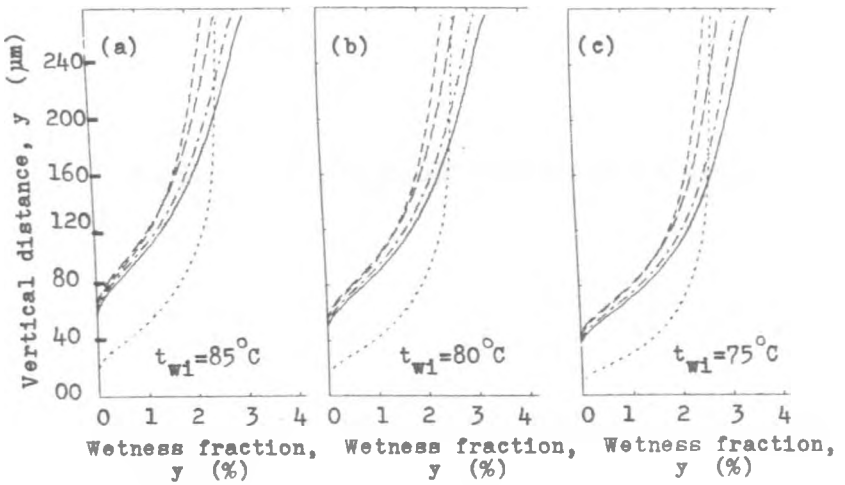

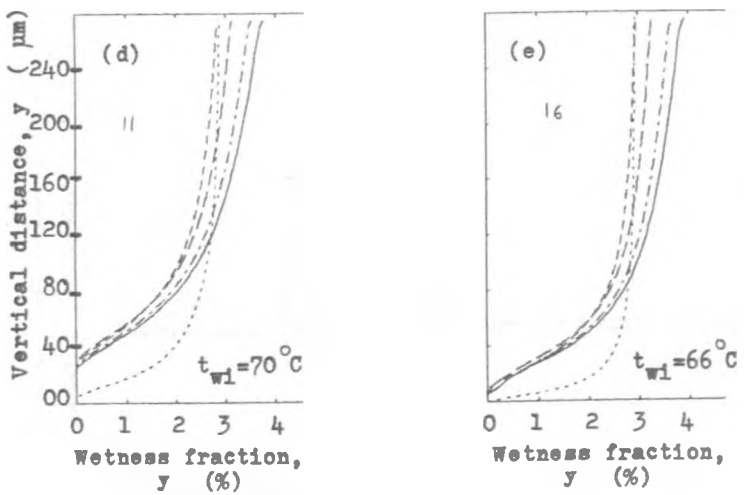

Fig. 7.70 : Variation of wetness fraction along y-axis for a range of Blade Surface Temperatures when d_1= 1.0 μm .

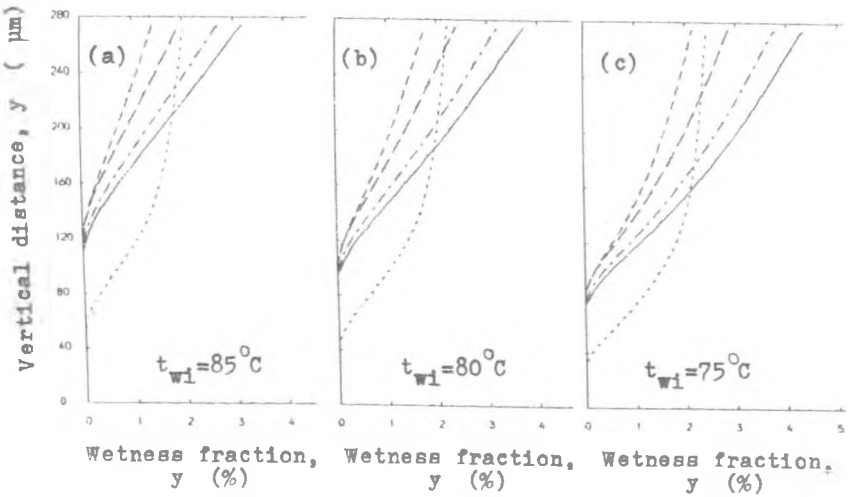

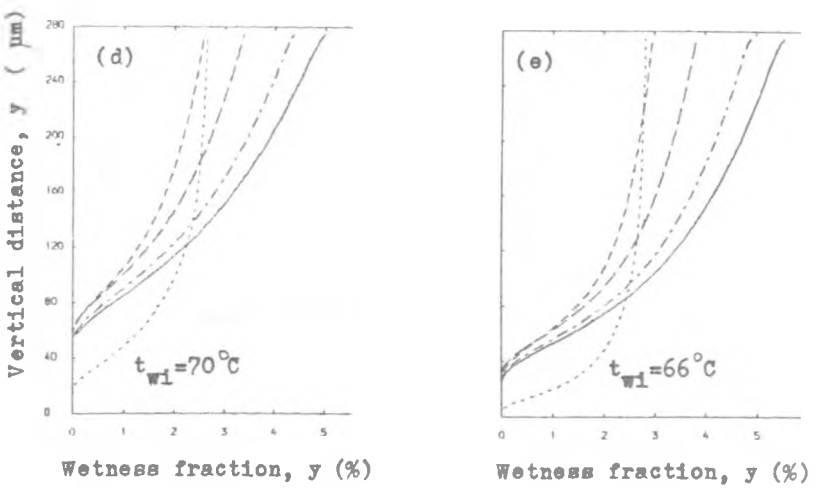

Fig. 7.71 : Variation of Wetness Fraction along y-axis for a range of Blade Surface Temperatures when d_1= 0.5 μm .

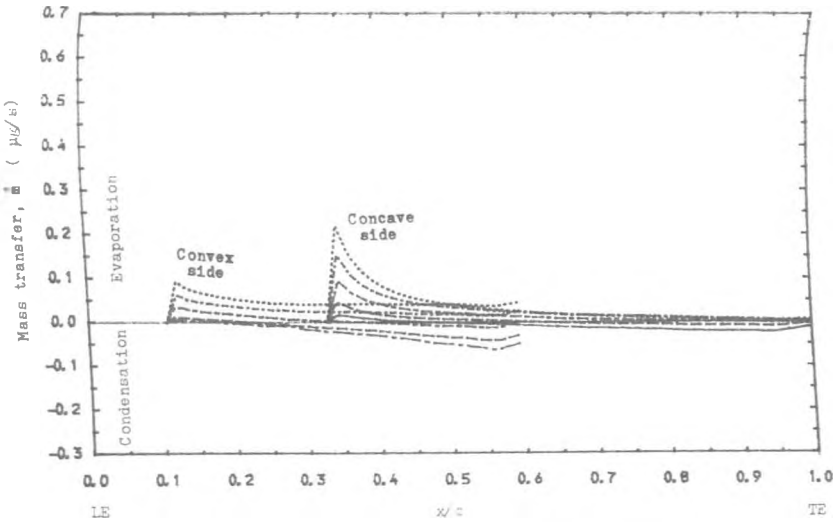

Fig. 7.72 : Variation of the Mass Transfer between Droplets and Vapour inside the Concave and Convex Boundary Layer at Different Distance from the Blade Surface when t_{wi} = 66 °C and d_i = 1.0 μm.

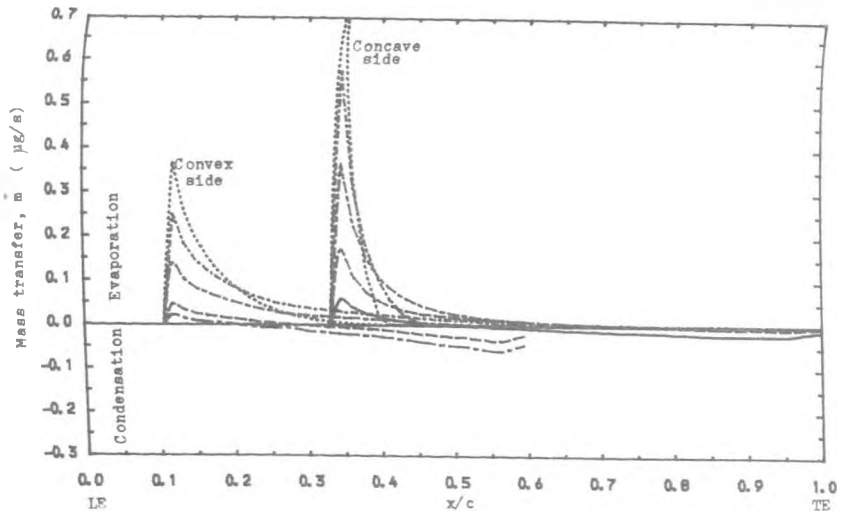

Fig. 7.74 : Variation of the Mass Transfer between Droplets and Vapour inside the Concave and Convex Boundary Layer at Different Distance from the Blade Surface when t_{wi} = 75 C and d_i = 1.0 μm .

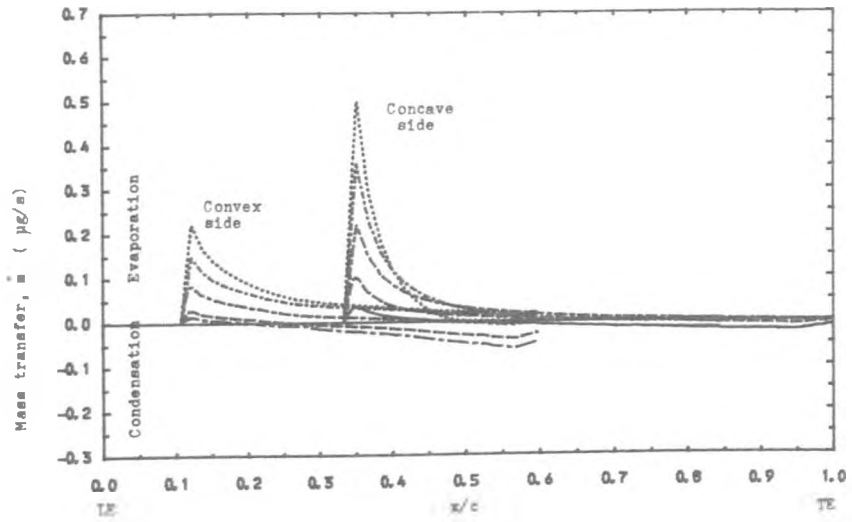

Fig. 7. 73 : Variation of the Mass Transfer between Droplets and Vapour inside the Concave and Convex Boundary Layer at Different Distance from the Blade Surface when t_{wi} = 70 °C and d_i = 1.0 μm .

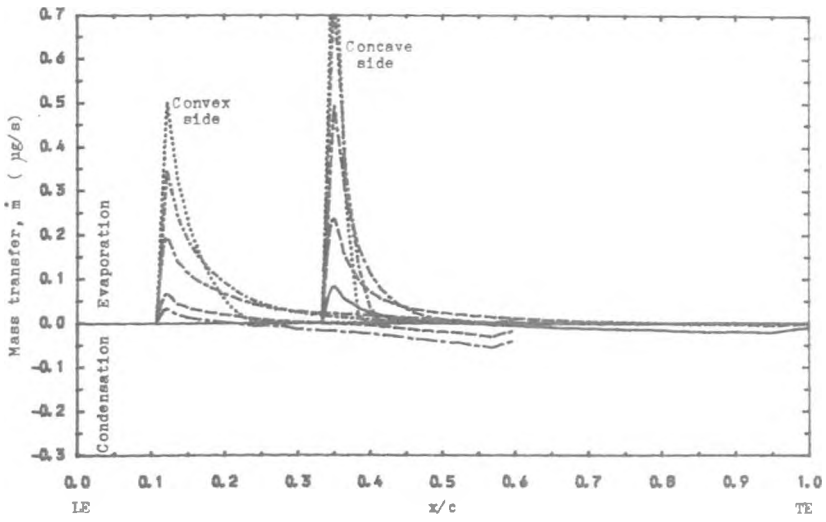

Fig. 7.75 : Variation of the Mass Transfer between Droplets and Vapour inside the Concave and Convex Boundary Layer at Different Distance from the Blade Surface when t_{wi} = 80 °C and d_i = 1.0 μm .

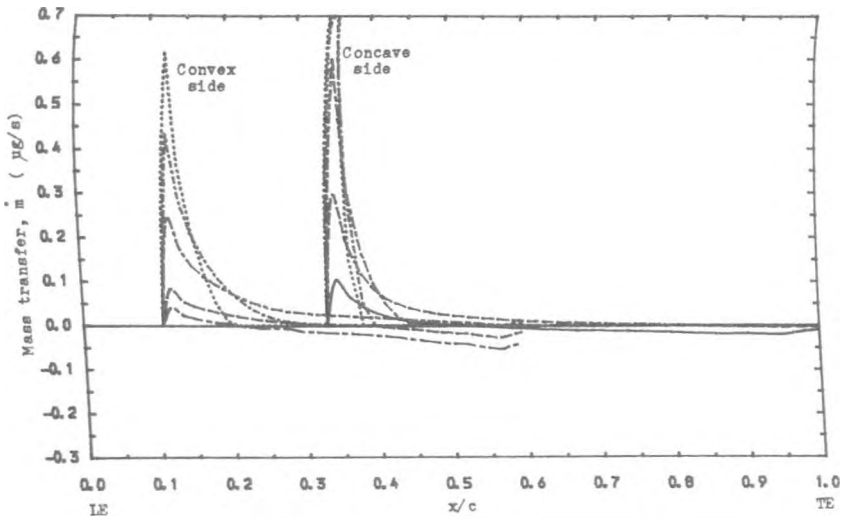

Fig. 7.76 : Variation of the Mass Transfer between Droplets and Vapour inside the Concave and Convex Boundary Layer at Different Distance from the Blade Surface when t_{wi}= 85 °C and d_i= 1.0 μm .

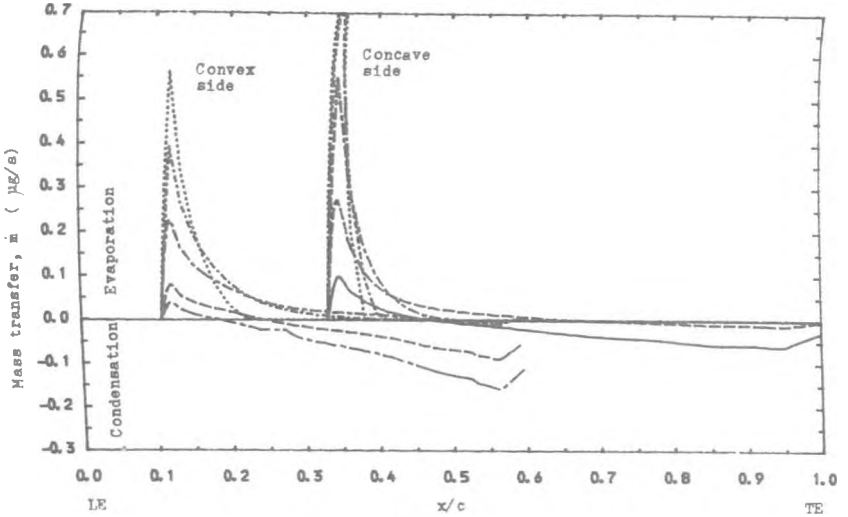

Fig. 7. 78 : Variation of the Mass Transfer between Droplets and Vapour inside the Concave and Convex Boundary Layer at Different Distance from the Blade Surface when t_{wi}= 70 °C and d_i= 0.5 μm .

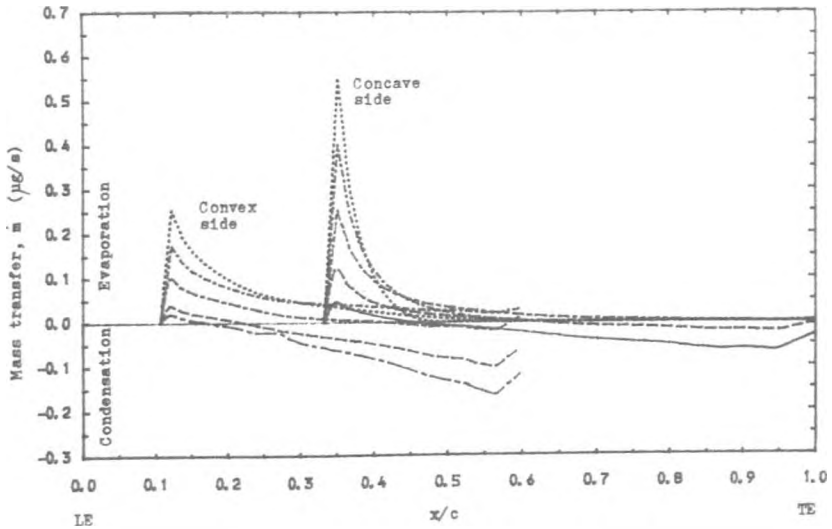

Fig. 7. 77 : Variation of the Mass Transfer between Droplets and Vapour inside the Concave and Convex Boudary Layer at Different Distance from the Blade Surface when t_{wi}= 66 °C and d_i= 0.5 μm .

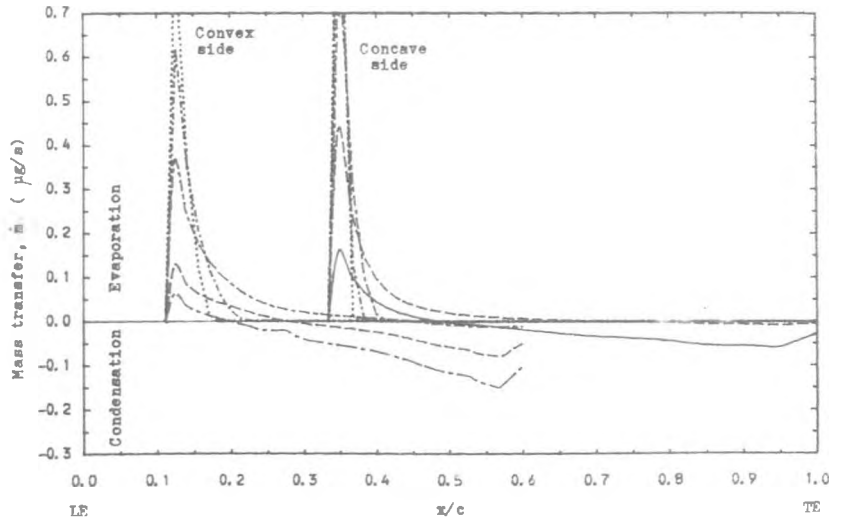

Fig. 7. 79 : Variation of the Mass Transfer between Droplets and Vapour inside the Concave and Convex Boundary Layer at Different Distance from the Blade Surface when t_{wi}=75 °C and d_i= 0.5 μm .

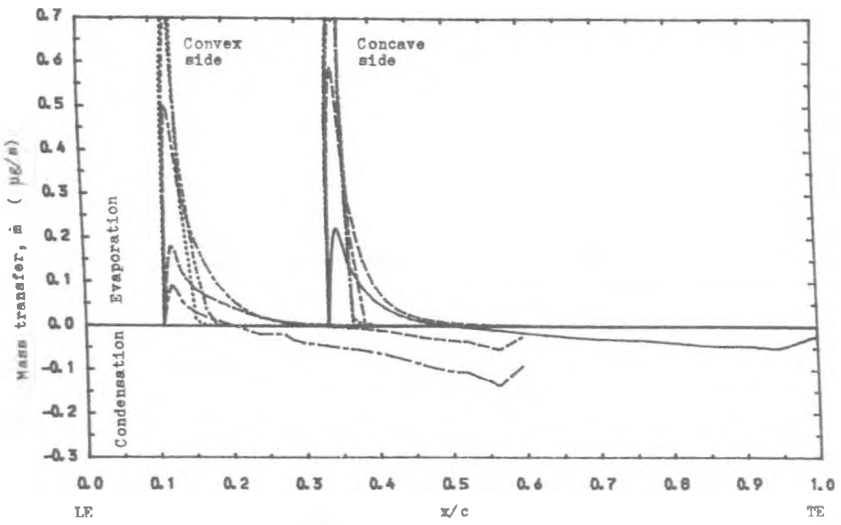

Fig. 7. 80 : Variation of the Mass Transfer between Droplets and Vapour inside the Concave and Convex Boundary Layer at Different Distance from the Blade Surface when t_{wi} = 80 °C and d_i = 0.5 µm .

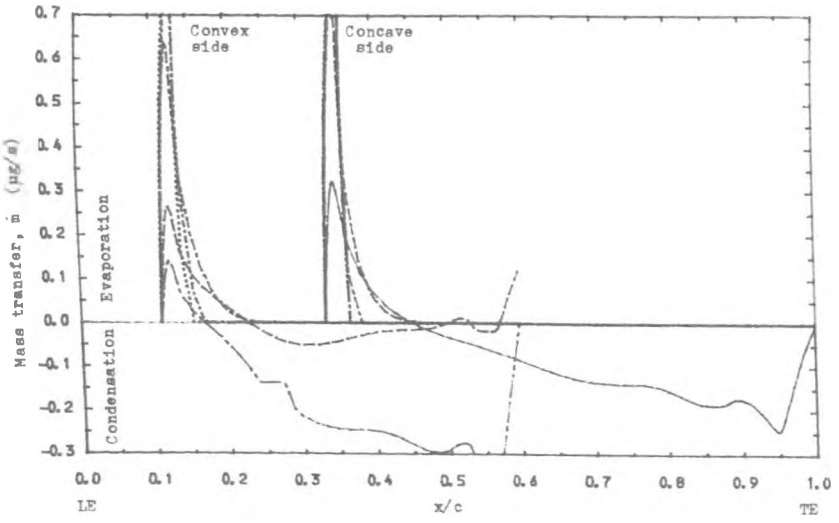

Fig. 7. 82 : Variation of the Mass Transfer between Droplets and Vapour inside tthe Concave and Convex Boundary Layer at Different Distance from the Blade Surface when t_{wi} = 66 °C and d_i = 0.1 µm .

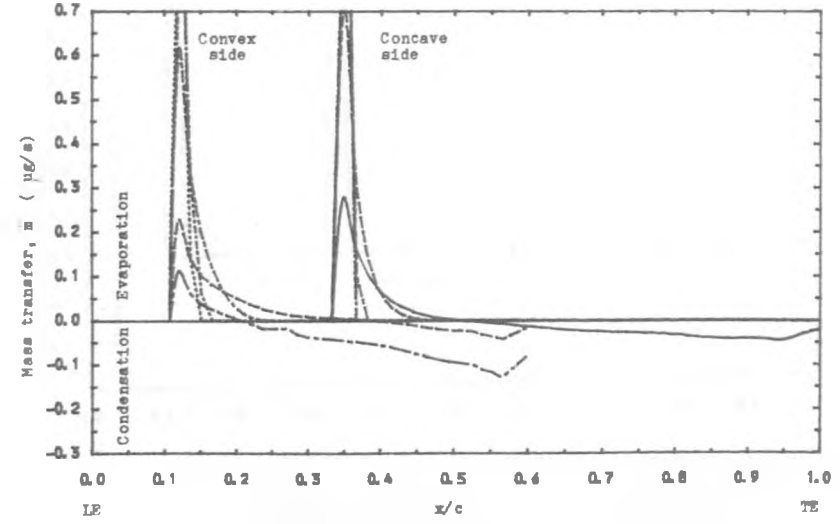

Fig. 7. 81 : Variation of the Mass Transfer between Droplets and Vapour inside the Concave and Convex Boundary Layer at Different Distance from the Blade Surface when t_{wi} = 85 °C and d_i = 0.5 µm .

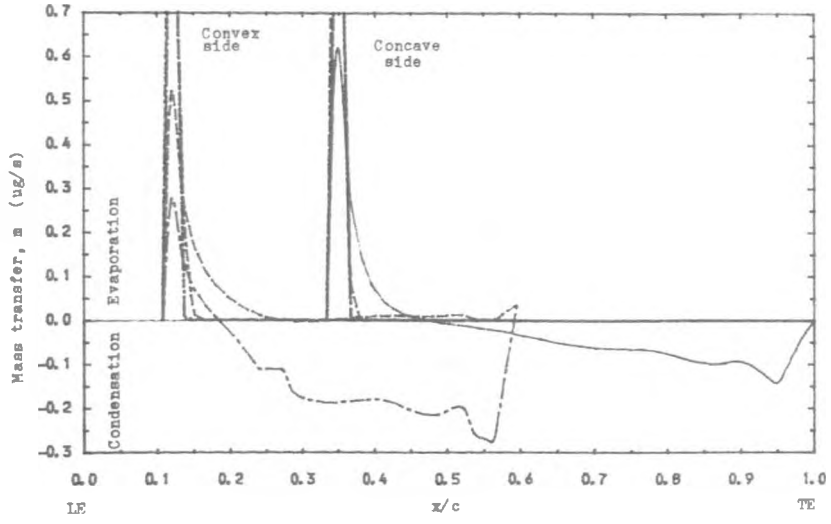

Fig. 7. 83 : Variation of the Mass Transfer between Droplets and Vapour inside the Concave and Convex Boundary Layer at Different Distance from the Blade Surface when t_{wi} = 70 °C and d_i = 0.1 µm .

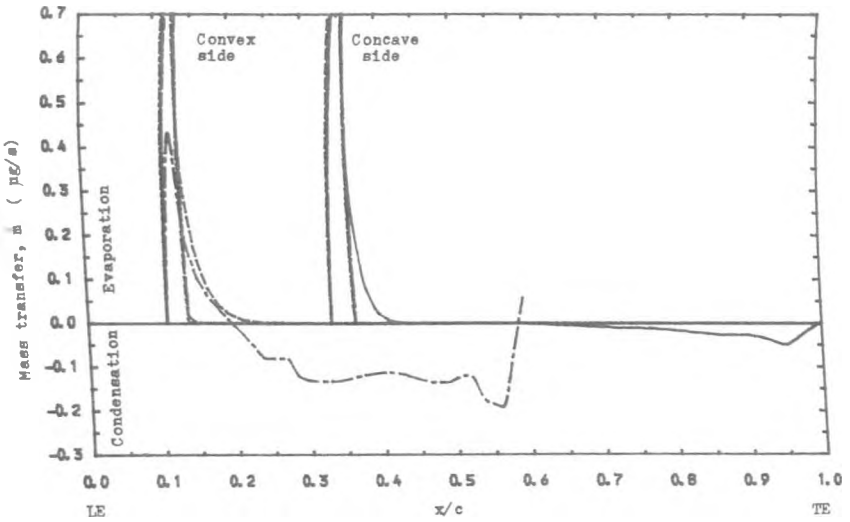

Fig. 7. 84 : Variation of the Mass Transfer between Droplets and Vapour inside the Concave and Convex Boundary Layer at Different Distance from the Blade Surface when t_{wi}= 75 °C and d_i= 0.1 µm .

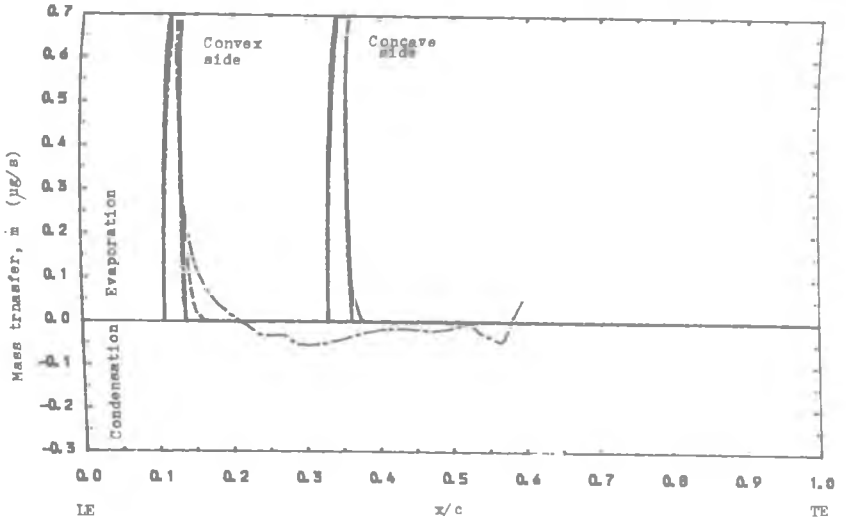

Fig. 7. 86 : Variation of the Mass Transfer between Droplets and Vapour inside the Concave and Convex Boundary Layer at Different Distance from the Blade Surface when t_{wi}= 85 °C and d_i= 0.1 µm .

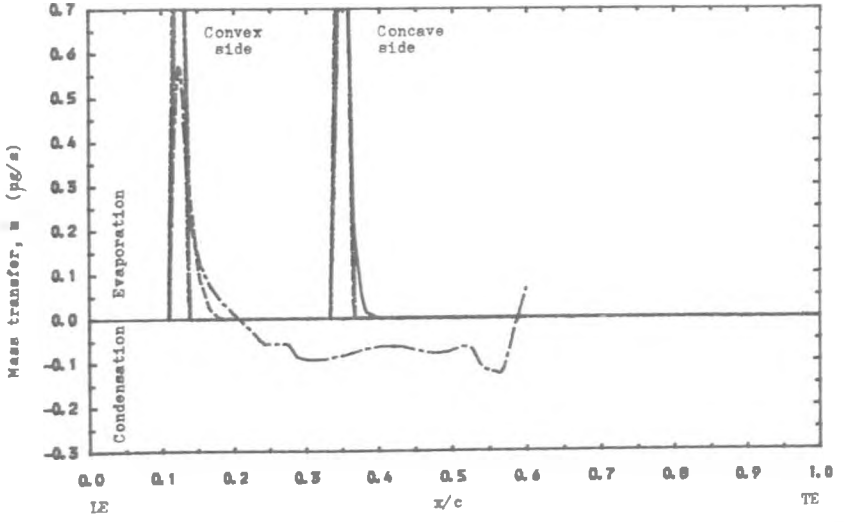

Fig. 7. 85 : Variation of the Mass Transfer between Droplets and Vapour inside the Concave and Convex Boundary Layer at Different Distance from the Blade Surface when t_{wi}= 80 °C and d_i= 0.1 µm .

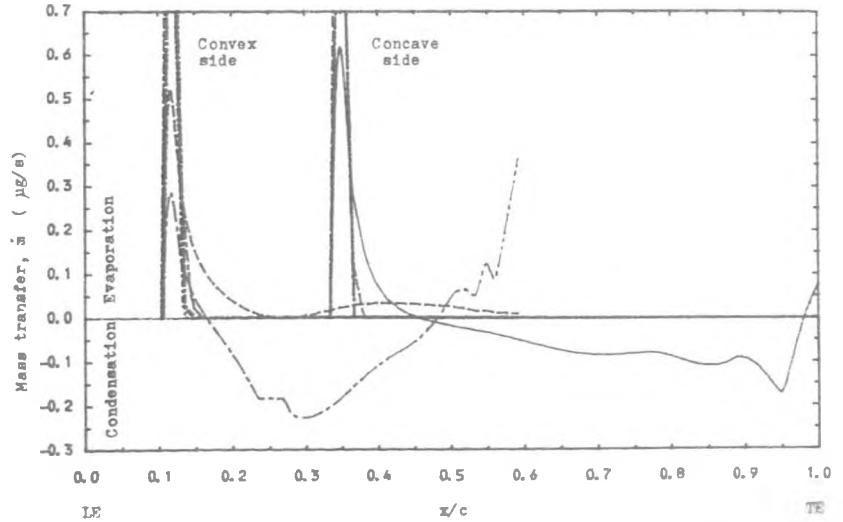

Fig. 7. 87 : Variation of the Mass Transfer between Droplets and Vapour inside the Concave and Convex Boundary Layer at Different Distance from the Blade Surface when t_{wi}= 66 °C and d_i= 0.05 µm .

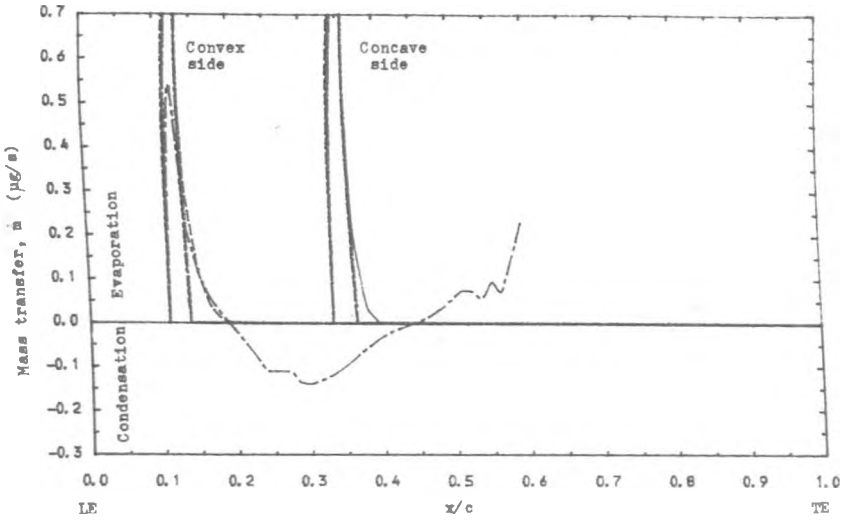

Fig. 7. 88 : Variation of the Mass Transfer between Droplets and Vapour inside the Concave and Convex Boundary Layer at Different Distance from the Blade Surface when t_{wi}= 70 °C and d_i= 0.05 μm .

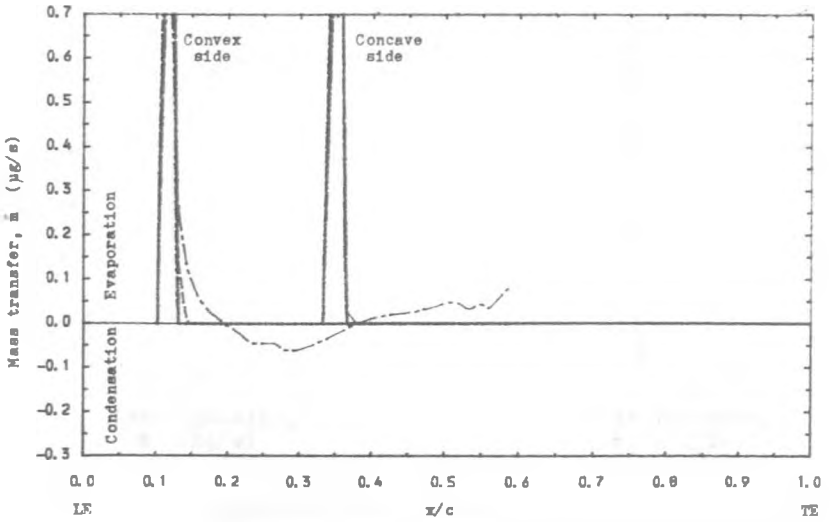

Fig. 7. 89 : Variation of the Mass Transfer between Droplets and Vapour inside the Concave and Convex Boundary Layer at Different Distance from the Blade Surface when t_{wi}= 75 °C and d_i= 0.05 μm .

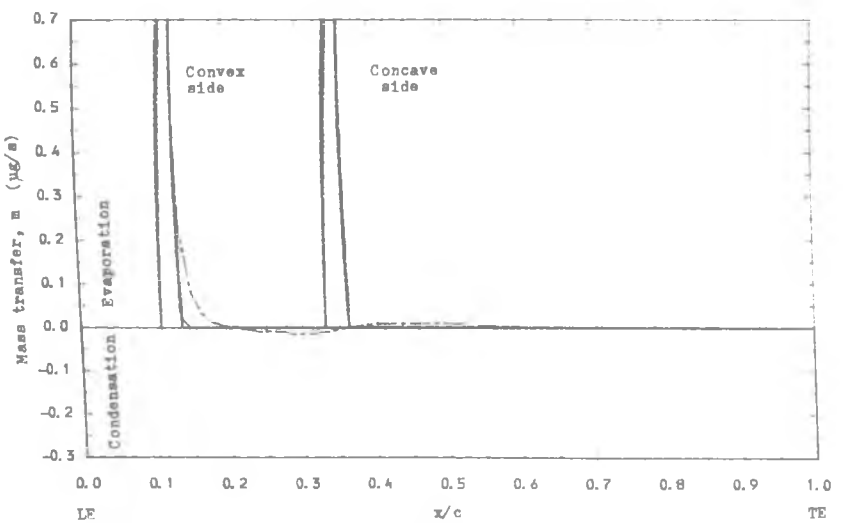

Fig.7. 90 : Variation of the Mass Transfer between Droplets and Vapour inside the Cocave and Convex Boundary Layer at Different Distance from the Blade Surface when t_{wi}= 85 °C and d_i= 0.05 μm .

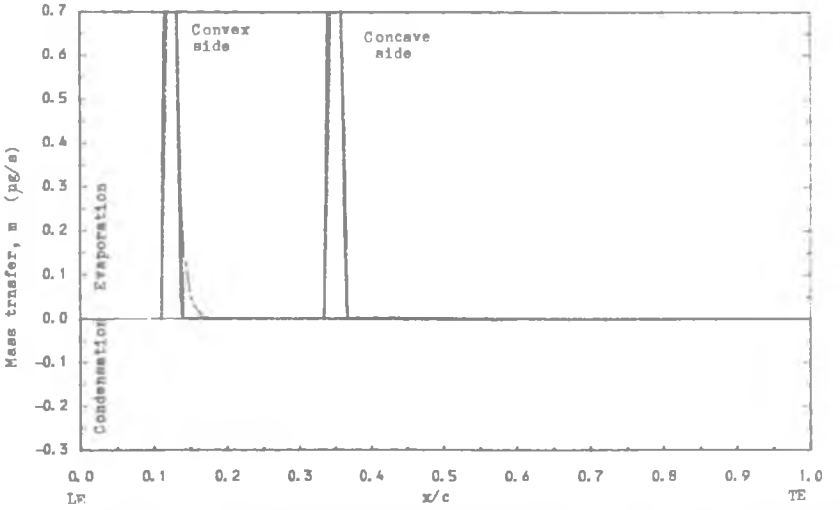

Fig. 7. 91 : Variation of the Mass Transfer between Droplets and Vapour inside the Concave and Convex Boundary Layer at Different Distance from the Blade Surface when t_{wi}= 85 °C and d_i= 0.05 μm .

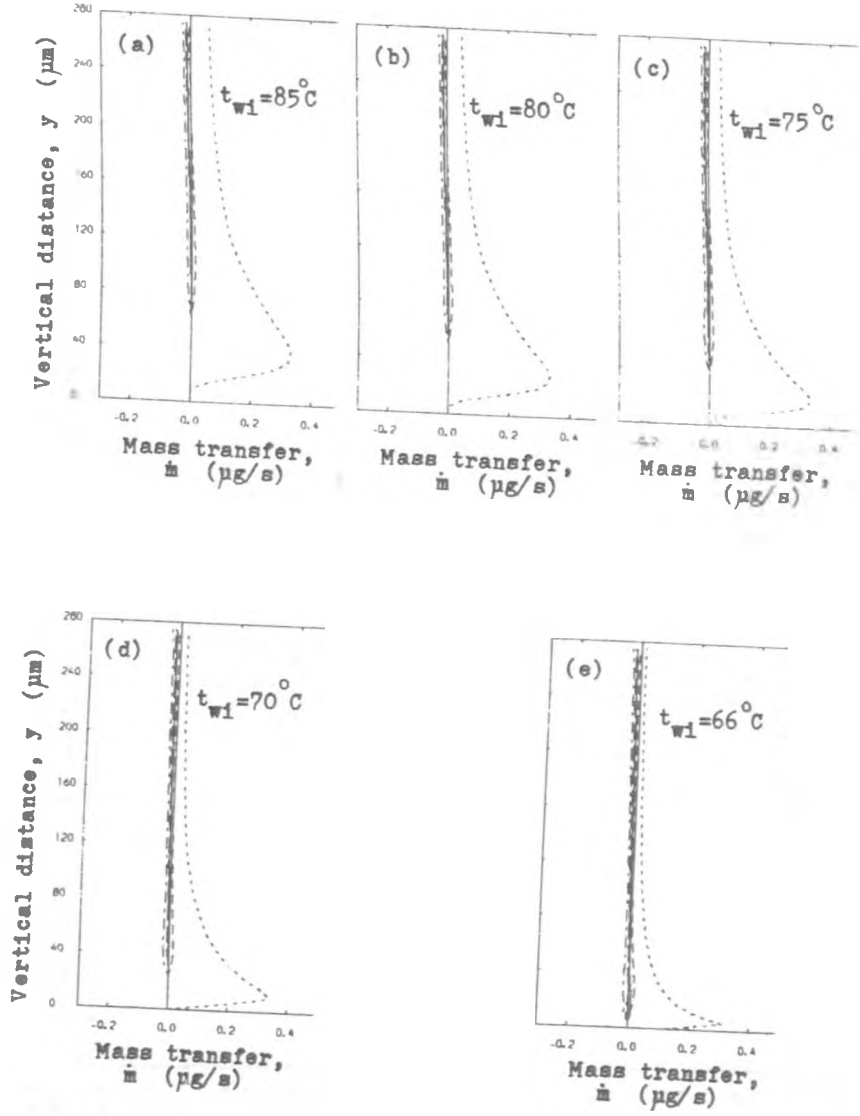

Fig. 7.92 : Change in Droplet Mass along y-axis for a range of Blade Surface Temperatures when d_1= 1.0 μm .

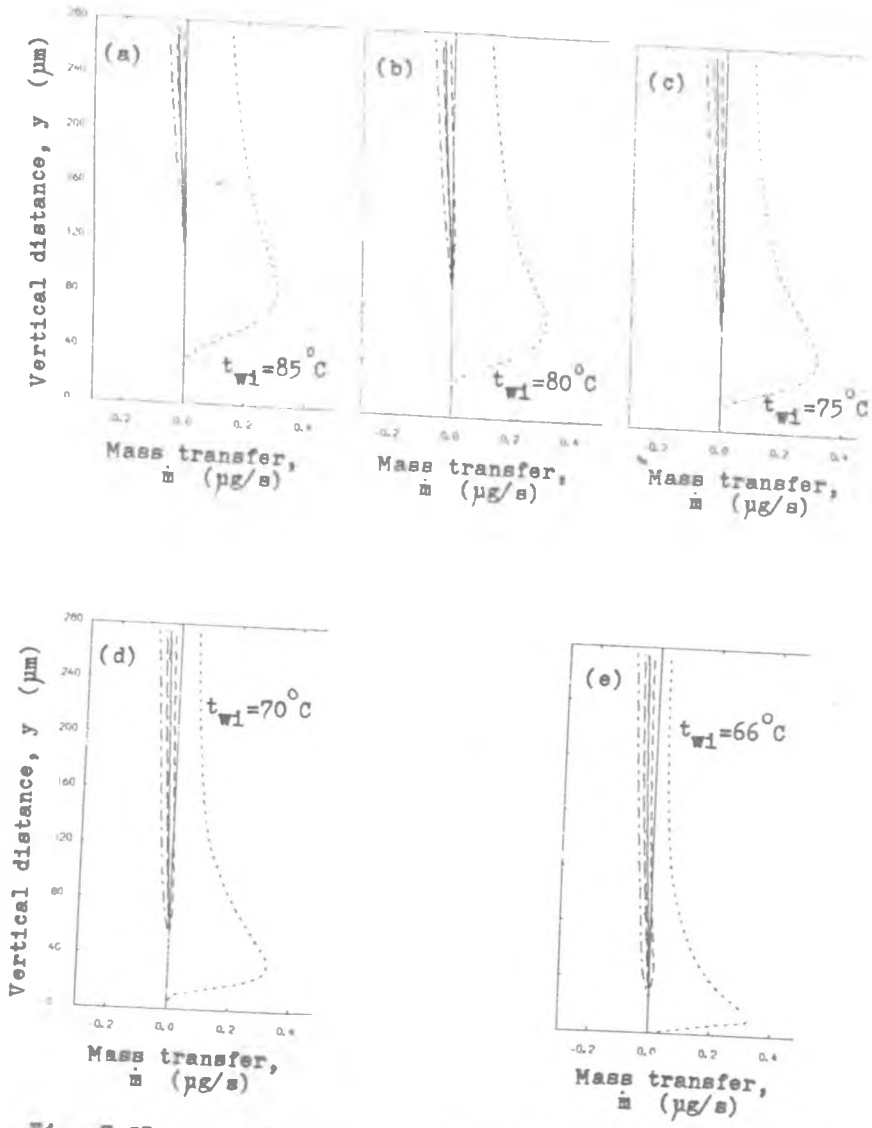

Fig. 7.93 : Change in Droplet Mass along y-axis for a range of Blade Surface Temperatures when d_1= 0.5 μm .

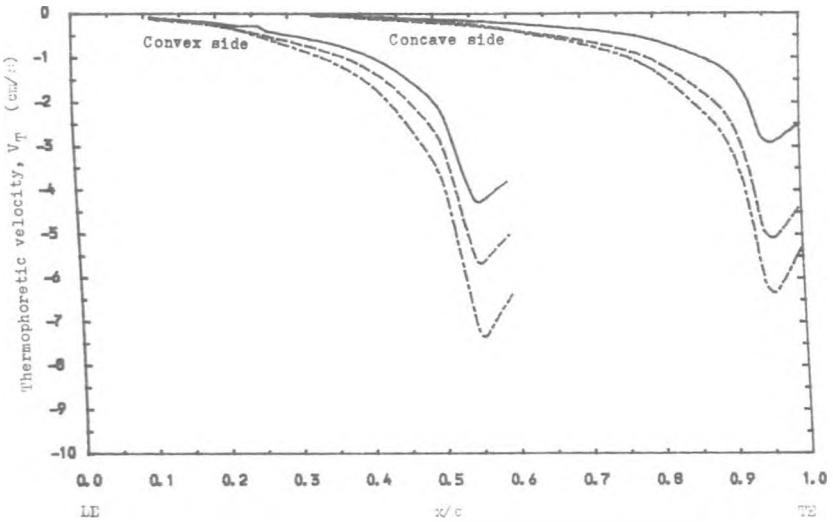

Fig. 7.94 : Variation of the thermophoretic Velocity of the Droplets inside the Concave and Convex Boundary Layer at Different Distance from the Blade Surface when t_{wi}= 66 °C and d_i= 1.0 μm.

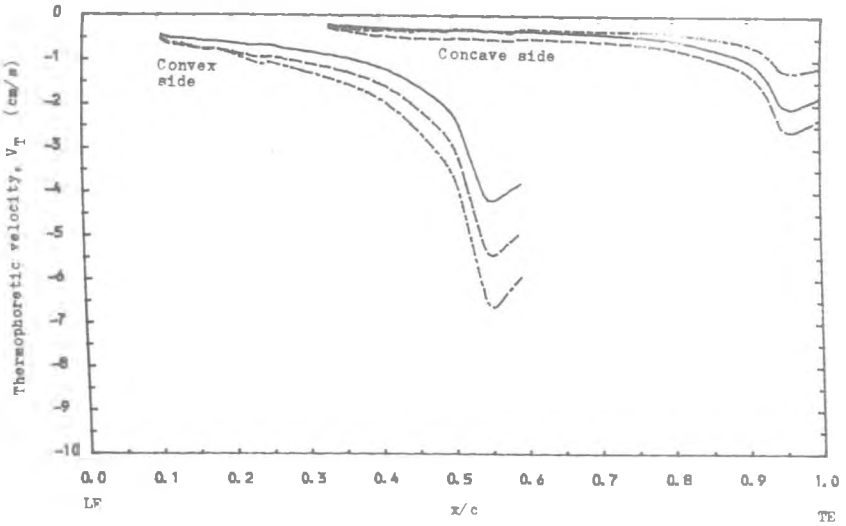

Fig. 7.96 : Variation of the Thermophoretic Velocity of the Droplets inside the Concave and Convex Boundary Layer at Different Distance from the Blade Surface when t_{wi}=75 °C and d_i= 1.0 μm .

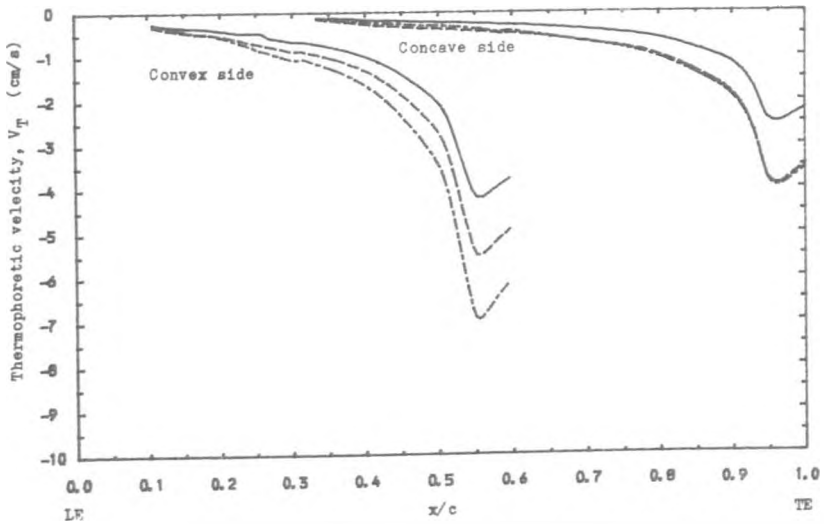

Fig. 7.95 : Variation of the Thermophoretic Velocity of the Droplets inside the Concave and Convex Boundary Layer at Different Distance from the Blade Surface when t_{wi}= 70 °C and d_i = 1.0 μm .

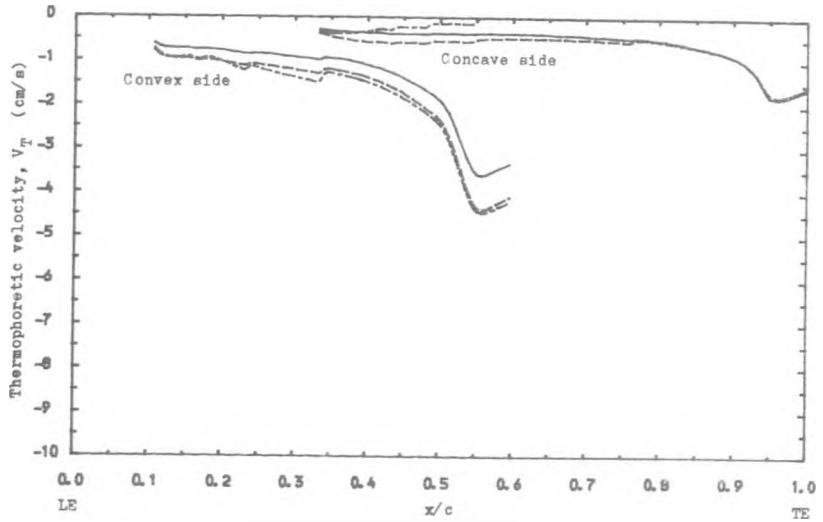

Fig. 7.97 : Variation of the Thermophoretic Velocity of the Droplets inside the Concave and Convex Boundary Layer at Different Distance from the Blade Surface when t_{wi}= 80 °C and d_i= 1.0 μm .

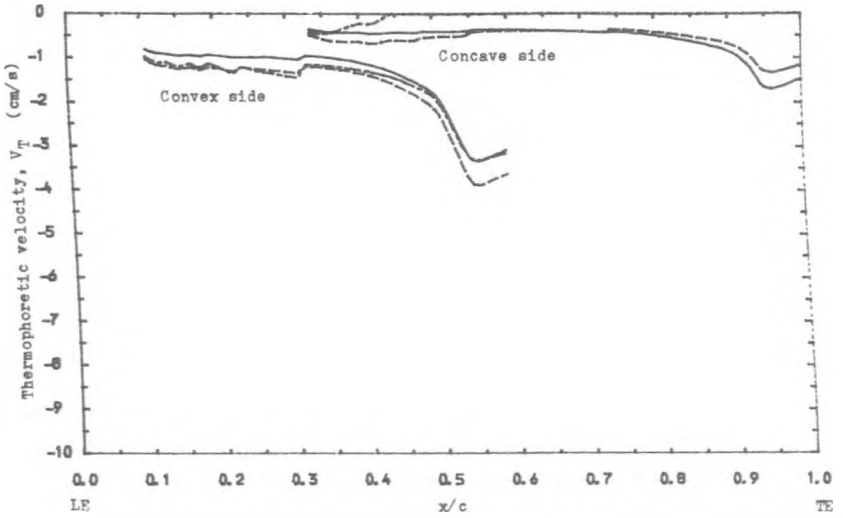

Fig. 7.98.: Variation of the Thermophoretic Velocity of the Droplets inside the Concave and Convex Boundary Layer at Different Distance from the Blade Surface when t_{w1}=85 °C and d_j= 1.0 μm .

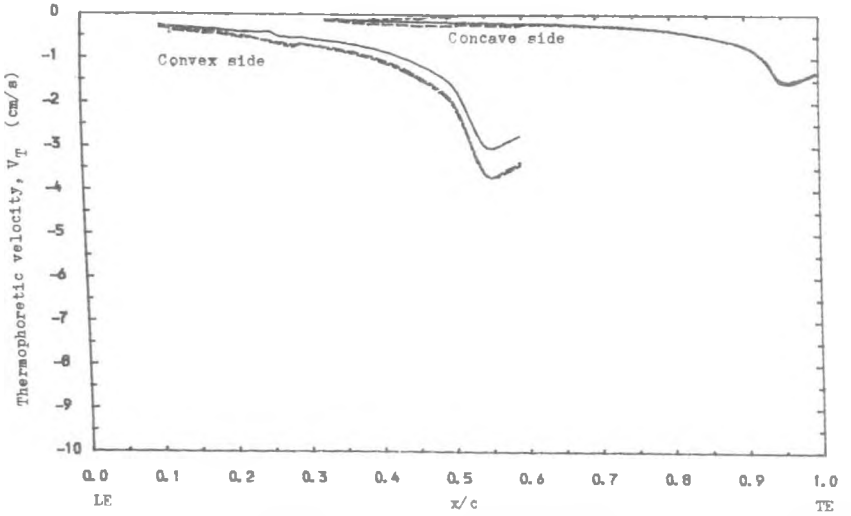

Fig. 7.100 : Variation of the Thermophoretic Velocity of the Droplets inside the Concave and Convex Boundary layer at Different Distance from the Blade Surface when t_{w1}= 70 °C and d_j= 0.5 μm .

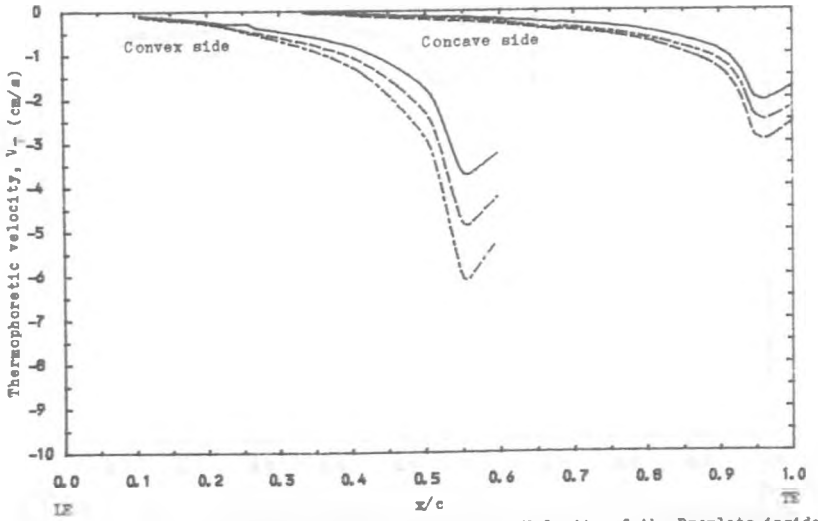

Fig. 7.99 : Variation of the Thermophoretic Velocity of the Droplets inside the Concave and Convex Boundary Layer at Different Distance from the Blade Surface when t_{w1}= 66 °C and d_j=1.0 μm .

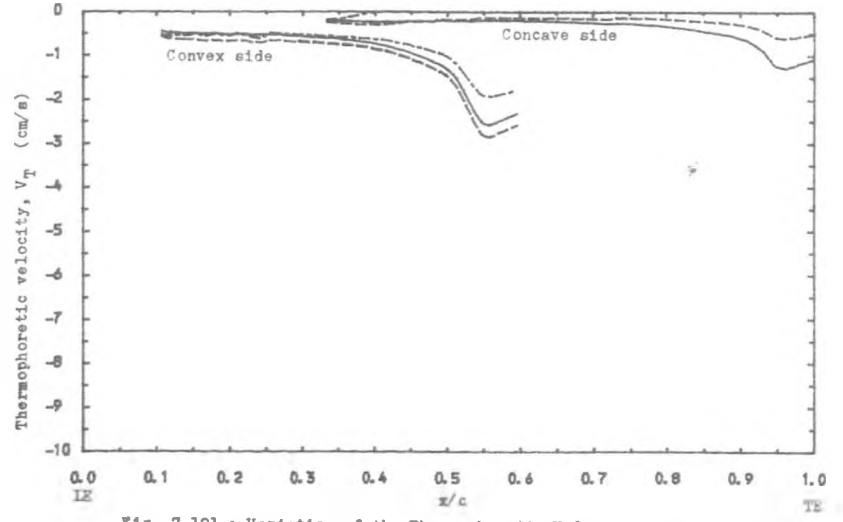

Fig. 7.101 : Variation of the Thermophoretic Velocity of the Droplets inside the Concave and Convex Boundary Layer at Different Distance from the Blade Surface when t_{w1}= 75 °C and d_j= 0.5 μm .

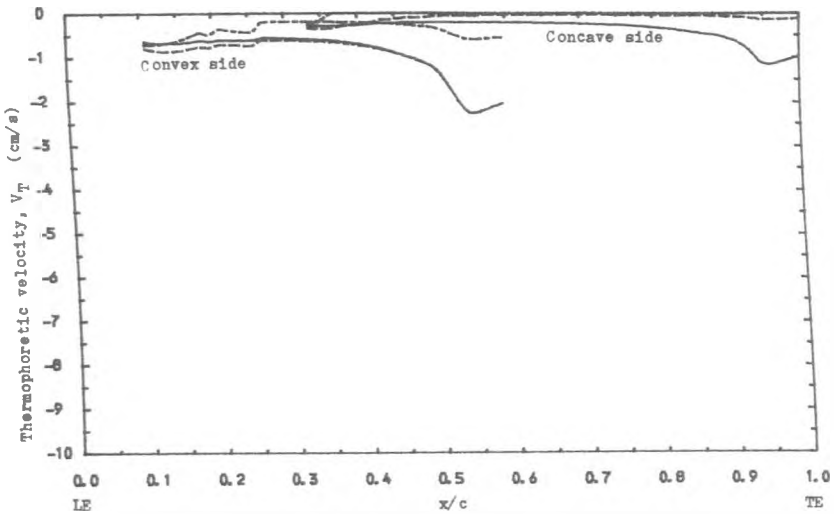

Fig. 7.102 : Variation of the Thermophoretic Velocity of the Droplets inside the Concave and Convex Boundary Layer at Different Distance from the Blade Surface when t_{wi}= 80 °C and d_i = 0.5 μm .

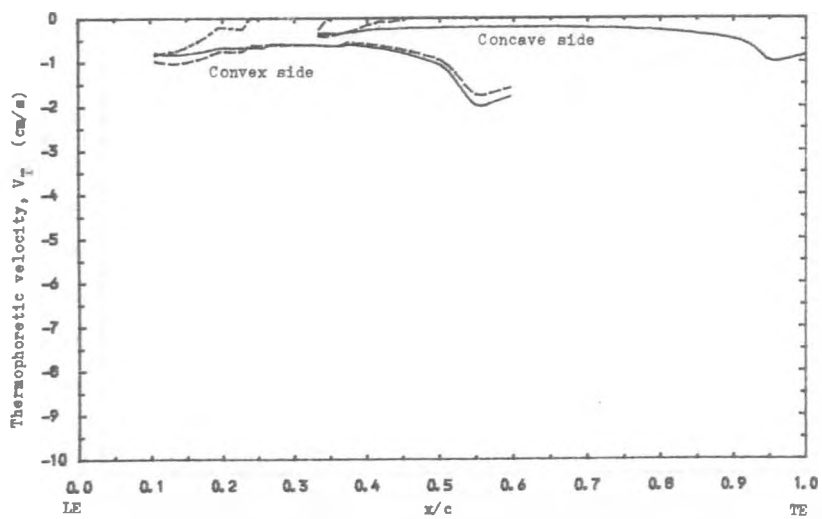

Fig. 7.103 : Variation of the Thermophoretic Velocity of the Droplets inside the Concave and Convex Boundary Layer at Different Distance from the Blade Surface when t_{wi}= 85 °C and d_i= 0.5 μm .

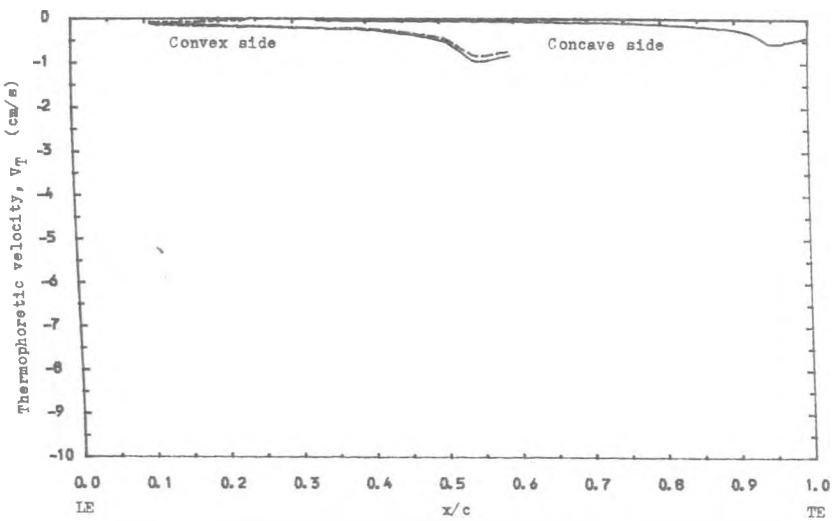

Fig. 7.104 : Variation of the Thermophoretic Velocity of the Droplets inside the Concave and convex Boundary Layer at Different Distance from the Blade Surface when t_{wi}= 66 °C and d_i= 0.1 μm .

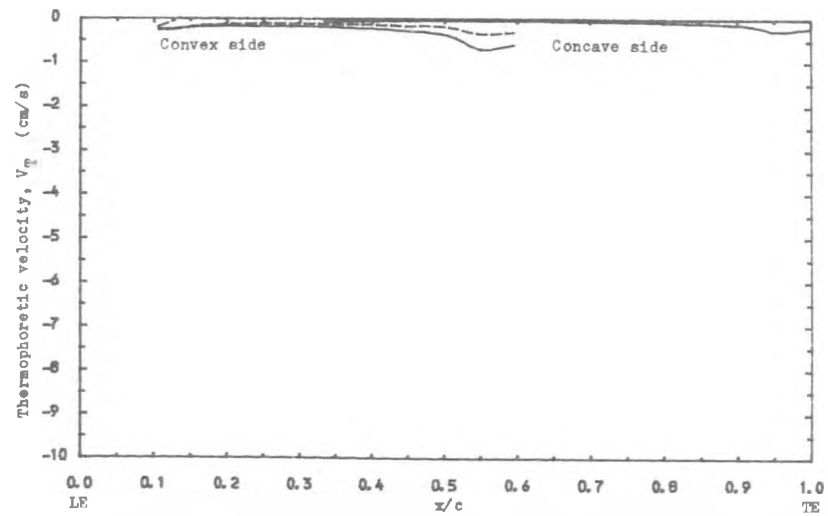

Fig. 7.105 : Variation of the Thermophoretic Velocity of the Droplets inside the Concave and Convex Boundary Layer at Different Distance from the Blade Surface when t_{wi}=70 °C and d_i= 0.1 μm .

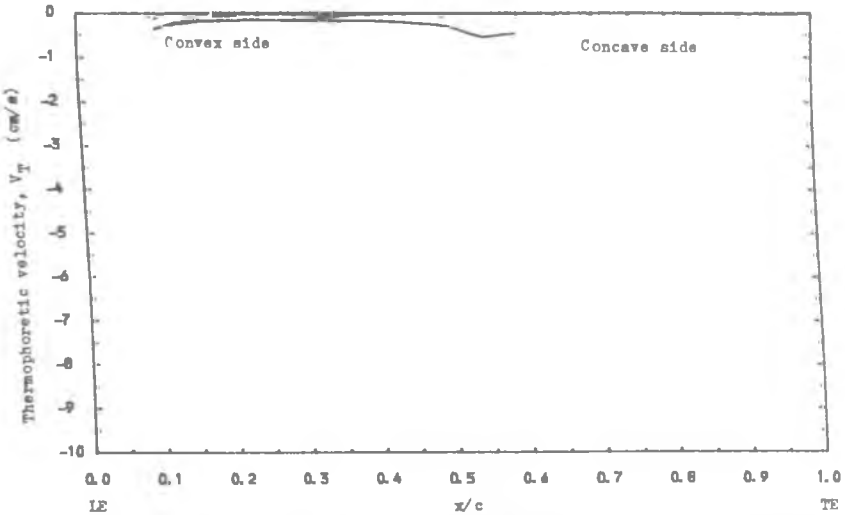

Fig. 7.106 : Variation of the Thermophoretic Velocity of the Droplets inside the Concave and Convex Boundary Layer at Different Distance from the Blade Surface when t_{wi}= 75 °C and d_i= 0.1 μm .

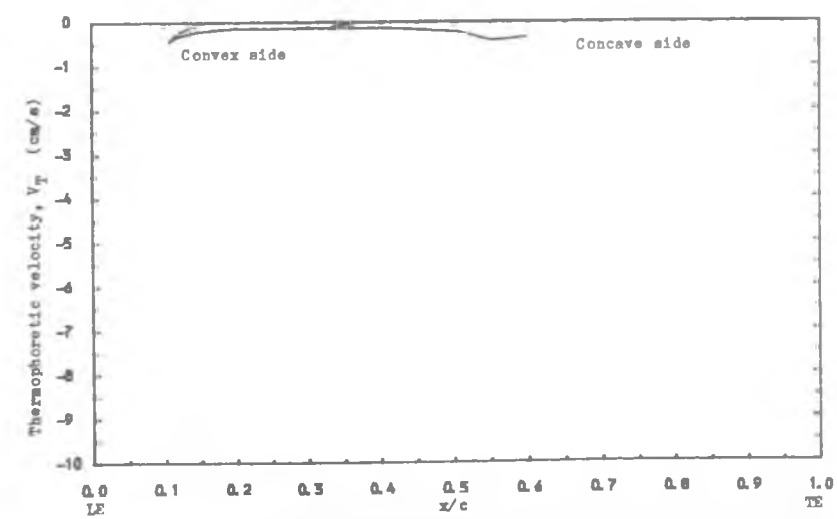

Fig. 7.107 : Variation of the Thermophoretic Velocity of the Droplets inside the Concave and Convex Boundary Layer at Different Distance from the Blade Surface when t_{wi}= 80 °C and d_i= 0.1 μm .

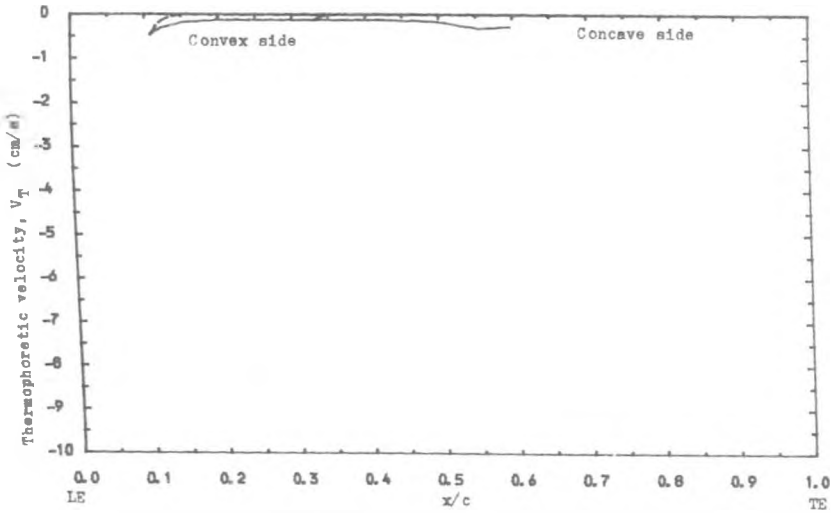

Fig. 7. 108 : Variation of the Thermophoretic Velocity of the Droplets inside the Concave and Convex Boundary Layer at Different Distance from the Blade Surface when t_{wi}= 85 °C and d_i= 0.1 μm .

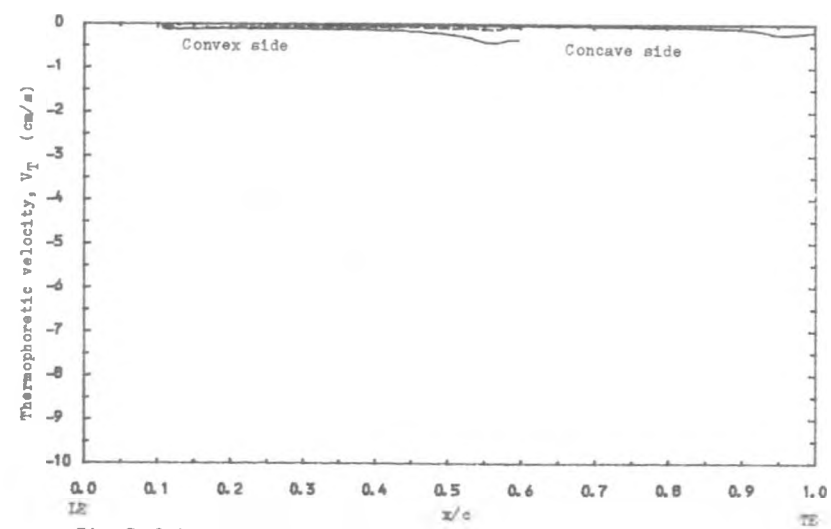

Fig. 7. 109 : Variation of the Thermophoretic Velocity of the Droplets inside the Concave and Convex Boundary Layer at Different Distance from the Blade Surface when t_{wi}= 66 °C and d_i= 0.05 μm .

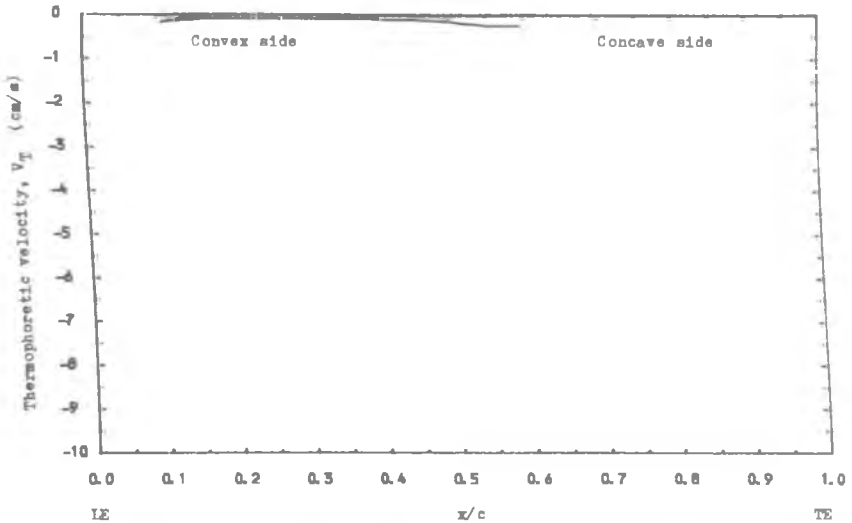

Fig. 7. 110 : Variation of the Thermophoretic Velocity of the Droplets inside the Concave and Convex Boundary Layer at Different Distance from the Blade Surface when t_{wi}= 70 °C and d_i= 0.05 μm .

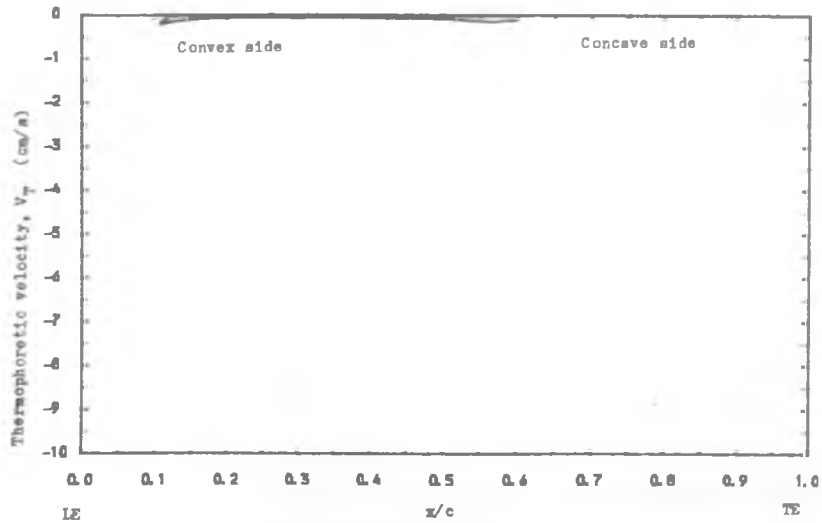

Fig. 7.111 : Variation of the Thermophoretic Velocity of the Droplets inside tthe Concave and Convex Boundary Layer at Different Distance from the Blade Surface when t_{wi}= 75 °C and d_i= 0.05 μm .

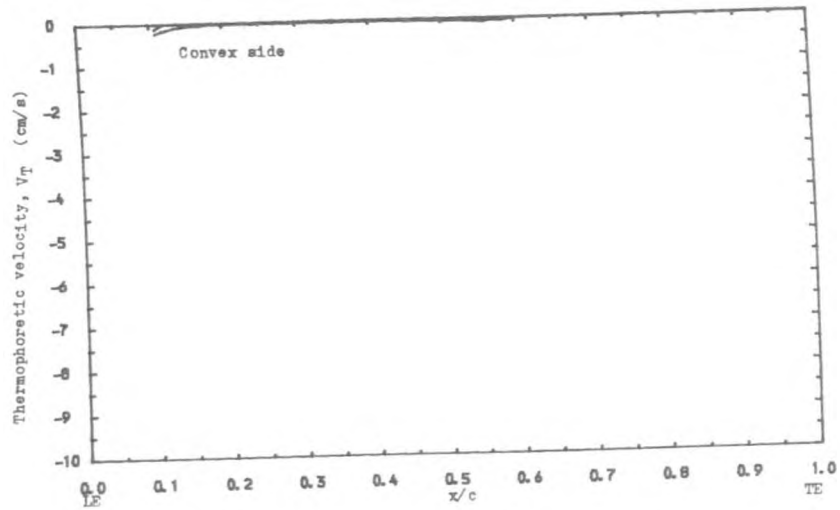

Fig. 7. 112 : Variation of the Thermophoretic Velocity of the Droplets inside the Concave and Convex Boundary Layer at Different Distance from the Blade Surface when t_{wi}= 80 °C and d_i= 0.05 μm .

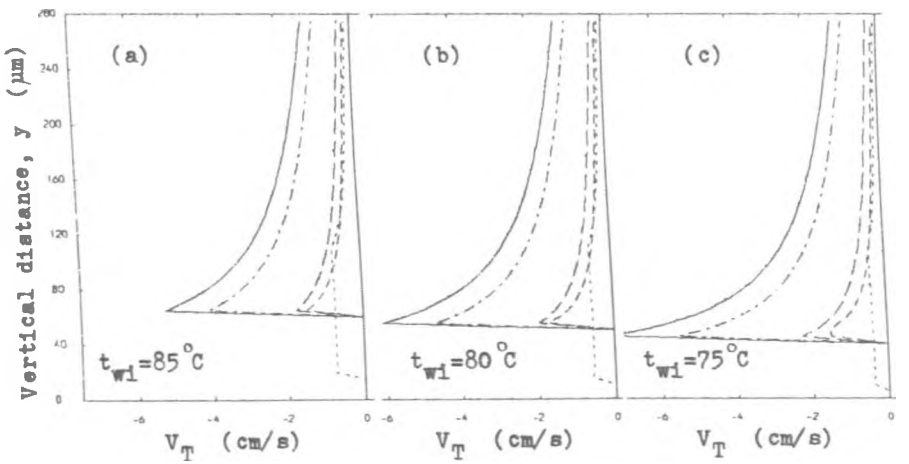

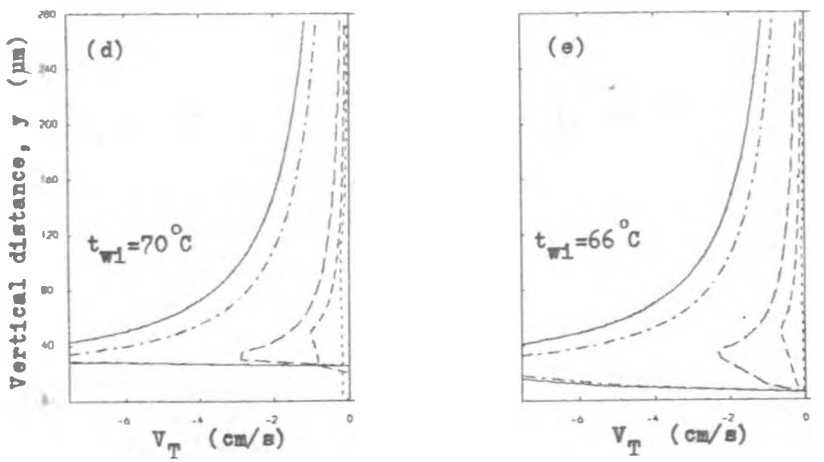

Fig. 7.113 : Variation of Thermophoretic Velocity along y-axis for a range of Blade Surface Temperatures when d_i= 1.0 μm .

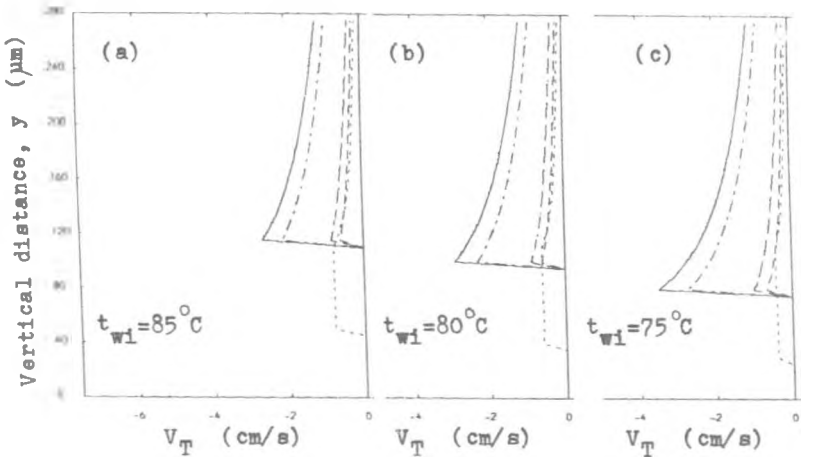

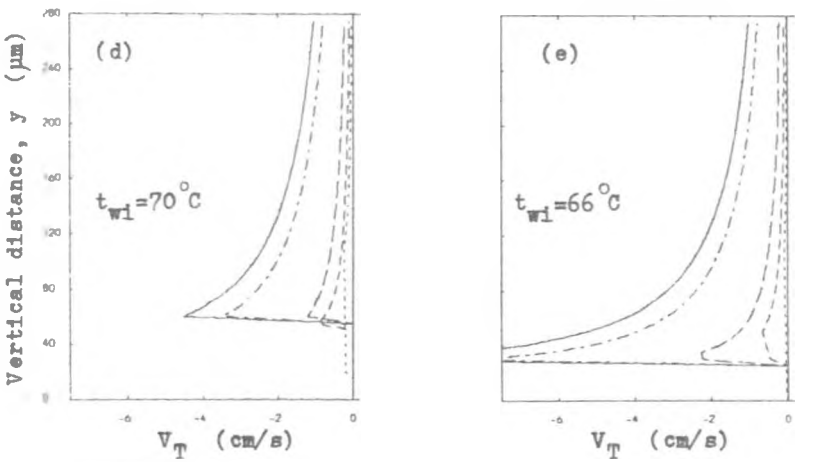

Fig. 7.114 : Variation of Thermophoretic Velocity along y-axis for a range of Blade Surface Temperatures when d_i= 0.5 μm .

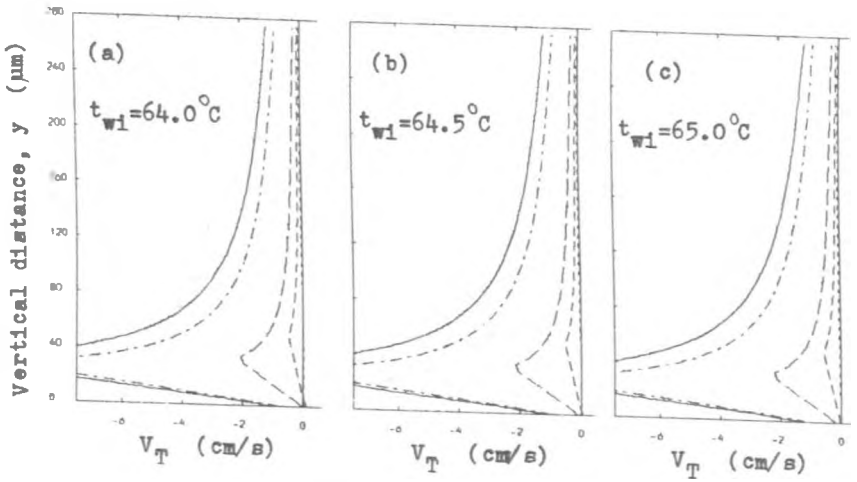

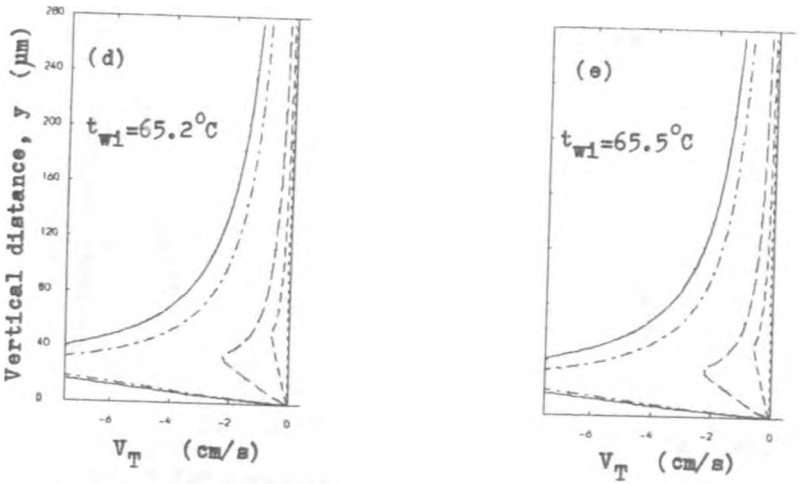

Fig. 7.115 : Variation of Thermophoretic Velocity along y-axis for a range of Blade Surface Temperature when d_i=1.0 μm .

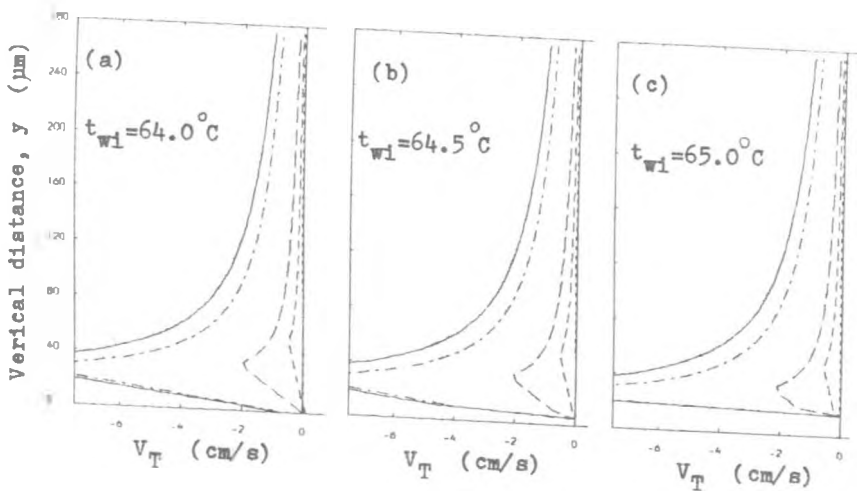

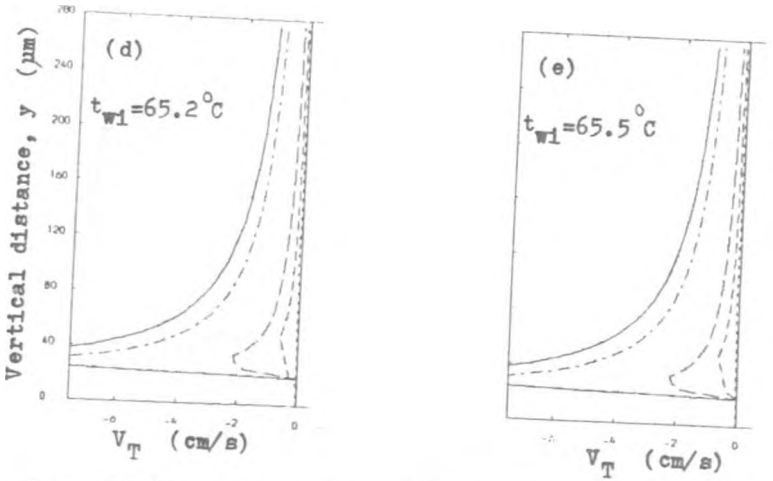

Fig. 7.116 : Variation of Thermophoretic Velocity along y-axis for a range of Blade Surface Temperatures when d_i= 0.5 μm .

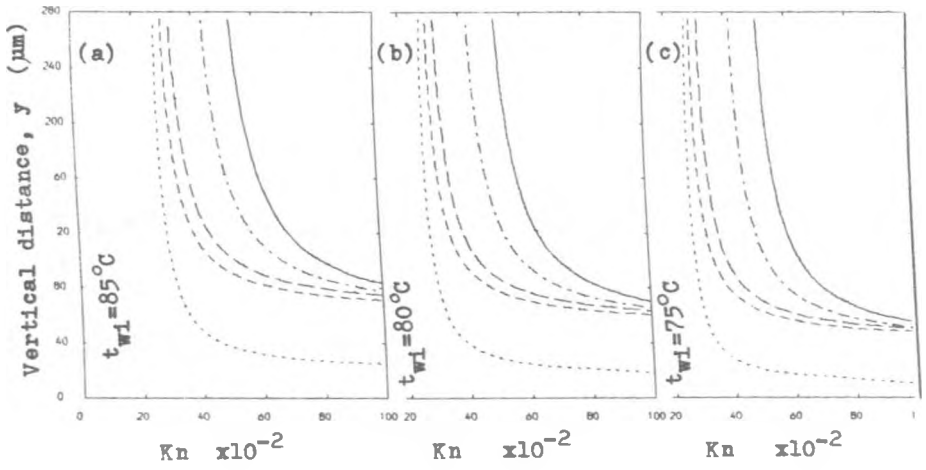

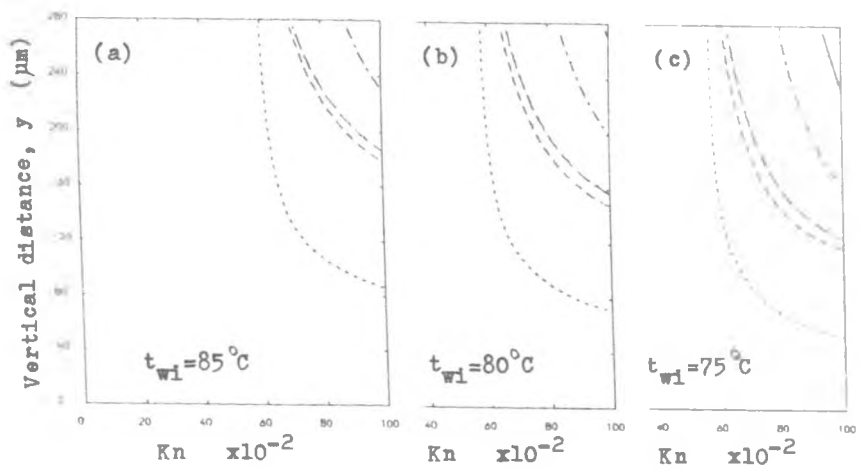

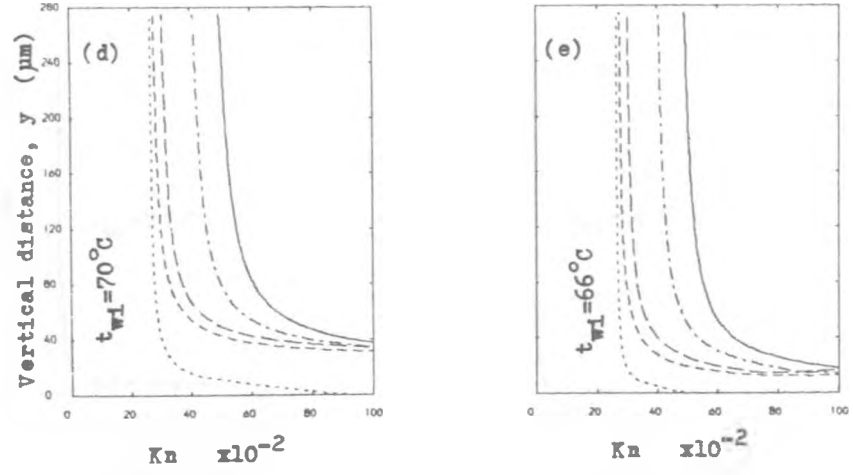

Fig. 7.117 : Variation in Knudsen Number along y-axis for a range of Blade Surface Temperatures when d_1=1.0 μm .

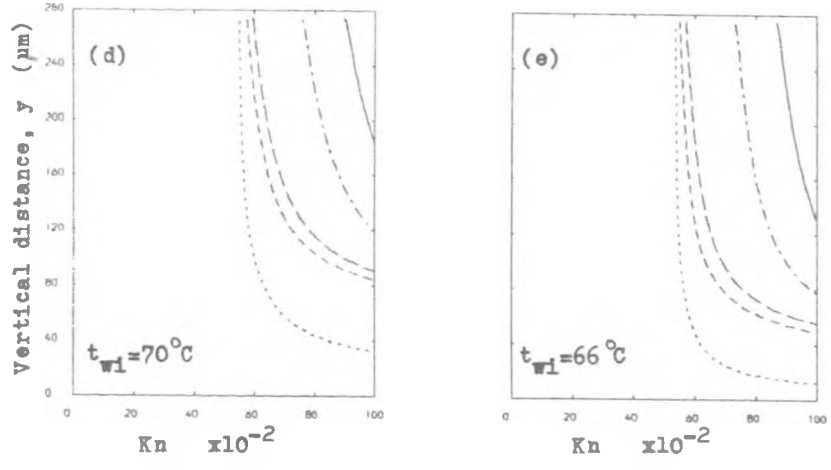

Fig. 7.118 : Variation in Knudsen Number along y-axis for a range of Blade Surface Temperatures When d_1=0.5μm.

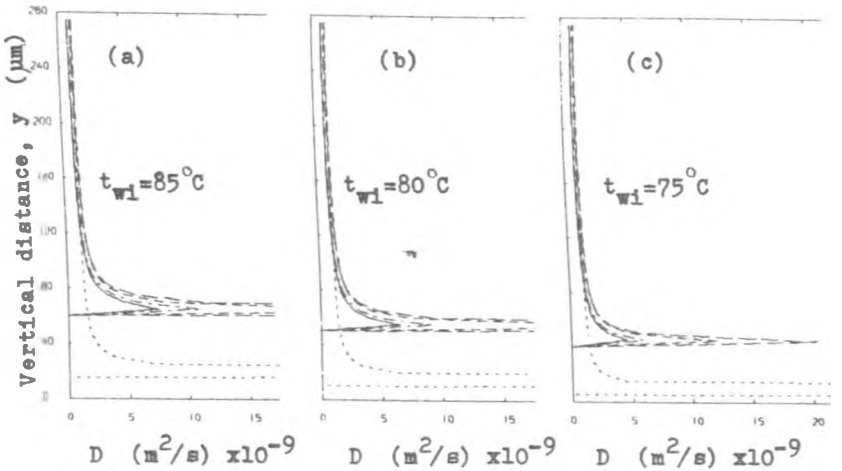

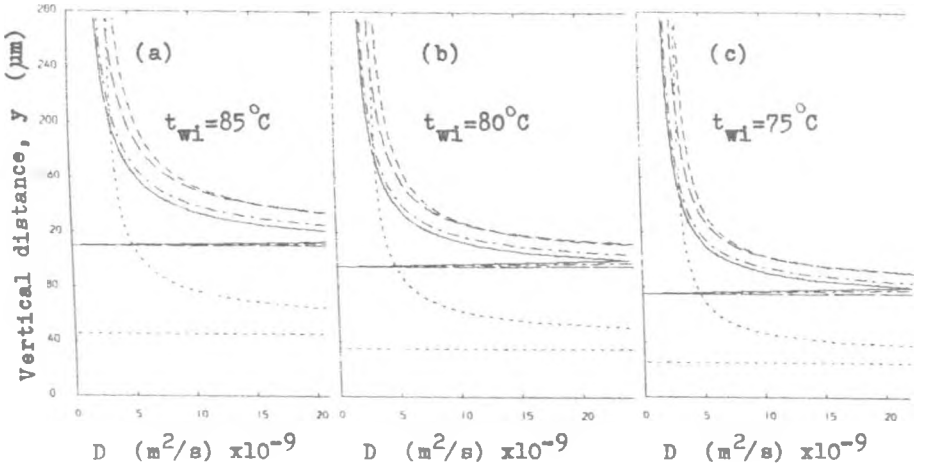

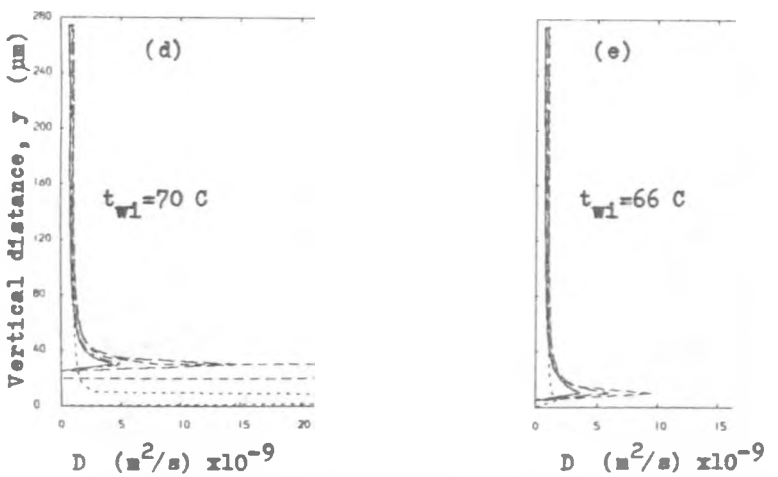

Fig. 7.119 : Variation in Diffusion Coefficient along y-axis for a range of Blade Surface Temperature when d_1= 1.0 μm .

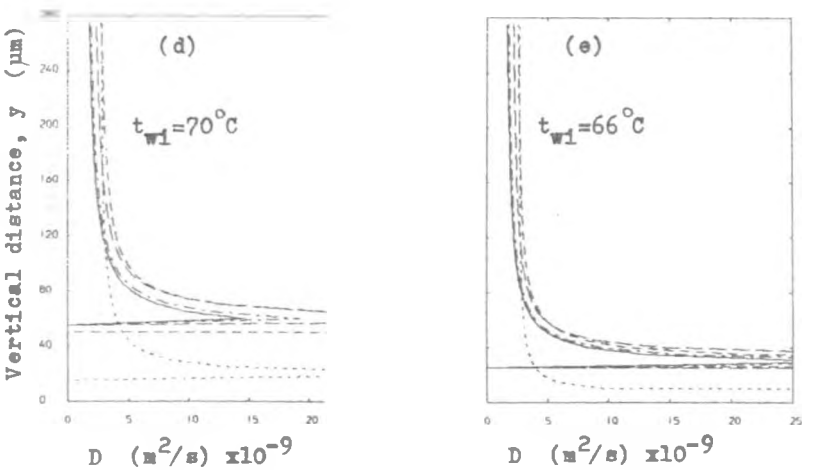

Fig. 7.120 : Variation in Diffusion Coefficient along y-axis for a range of Blade Surface Temperatures when d_1= 0.5 μm .

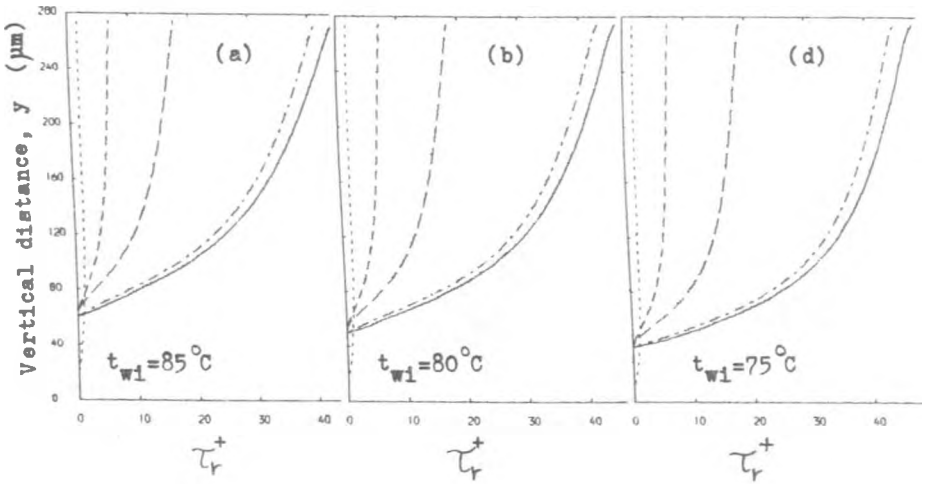

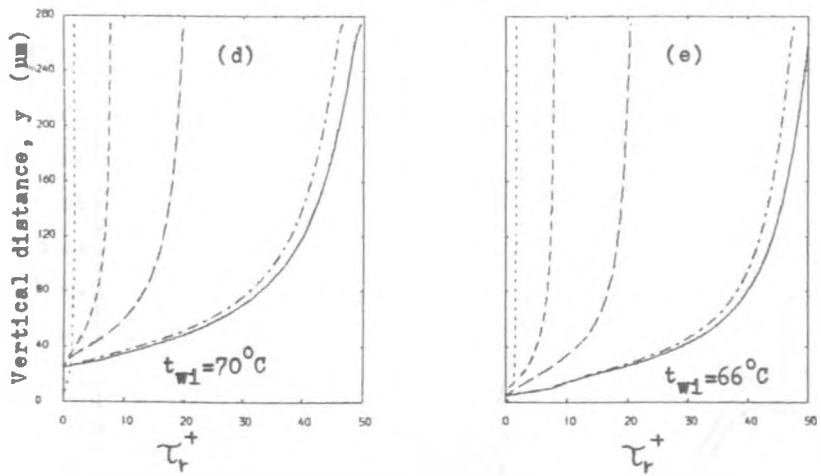

Fig. 7.121 : Variation in Dimensionless Relaxation Time along y-axis for a range of Blade Surface Temperatures when d_i= 1.0 μm .

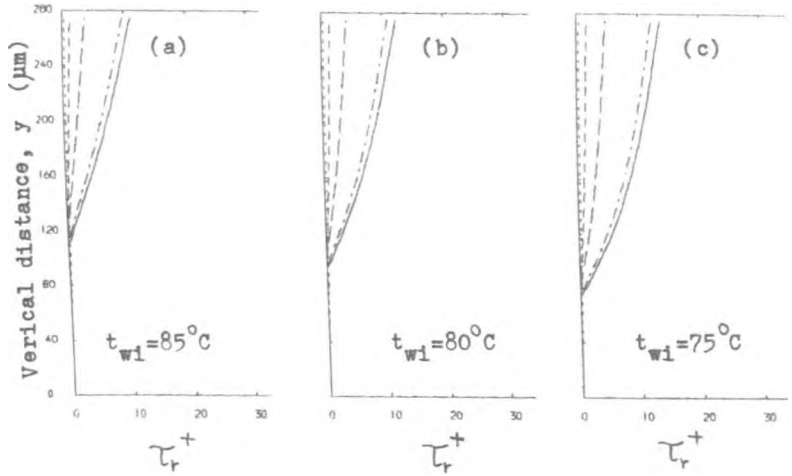

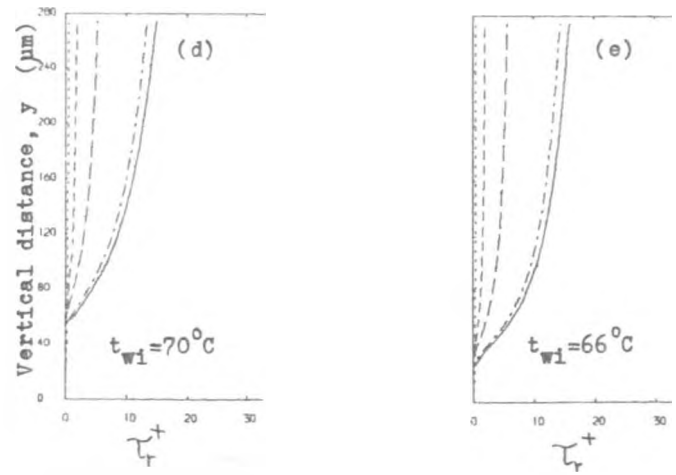

Fig. 7.122 : Variation in Dimensionless Relaxation Time along y-axis for a range of Blade Surface Temperatures when d_i= 0.5 μm .

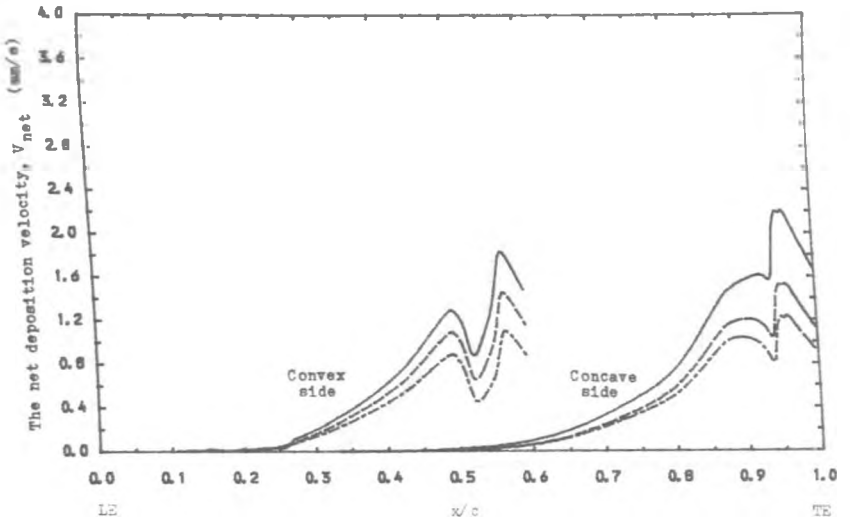

Fig. 7.123 : Variation of the Net Deposition Velocity inside the Concave and Convex Boundary Layer at Different Distance from the Blade Surface when t_{wi}= 66 °C and d_i= 1.0 μm.

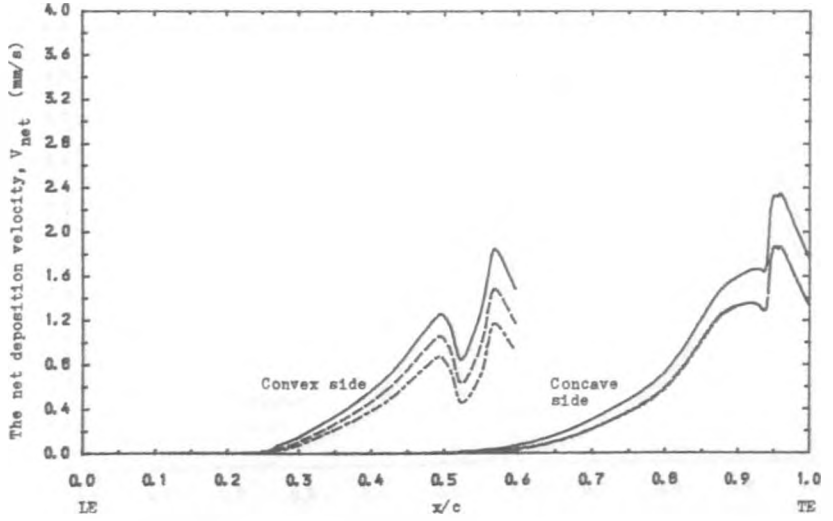

Fig. 7. 124 : Variation of the Net Deposition Velocity of Droplets inside the Concave and Convex Boundary Layer at Different Distance from the Blade Surface when t_{wi}= 70 °C and d_i= 1.0 μm .

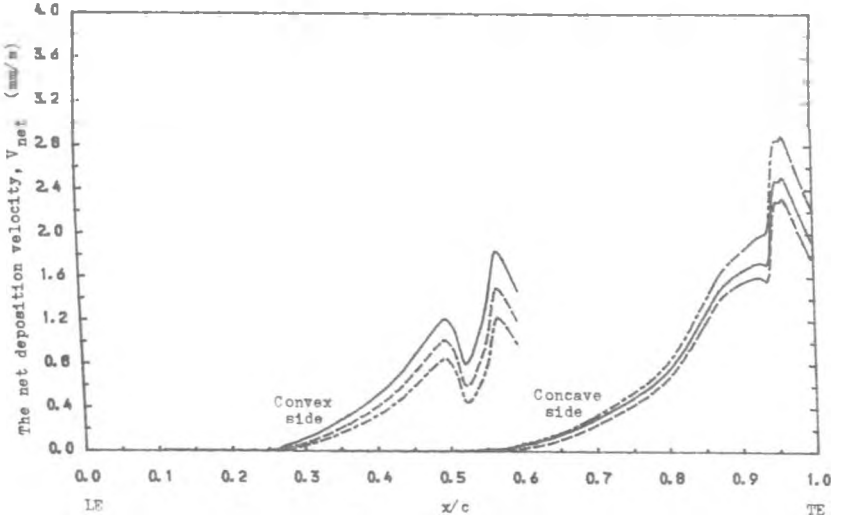

Fig. 7.125 : Variation of the Net Deposition Velocity of Droplets inside the Concave and Convex Boundary Layer at Different Distance from the Blade Surface when t_{wi}= 75 °C and d_i= 1.0 μm .

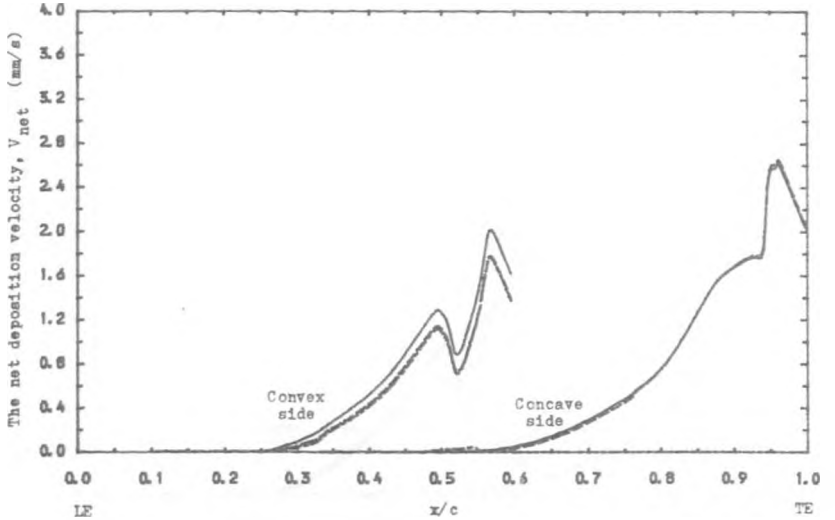

Fig. 7.126 : Variation of the Net Deposition Velocity of Droplets inside the Concave and Convex Boundary Layer at Different Distance from the Blade Surface when t_{wi}= 80 °C and d_i= 1.0 μm .

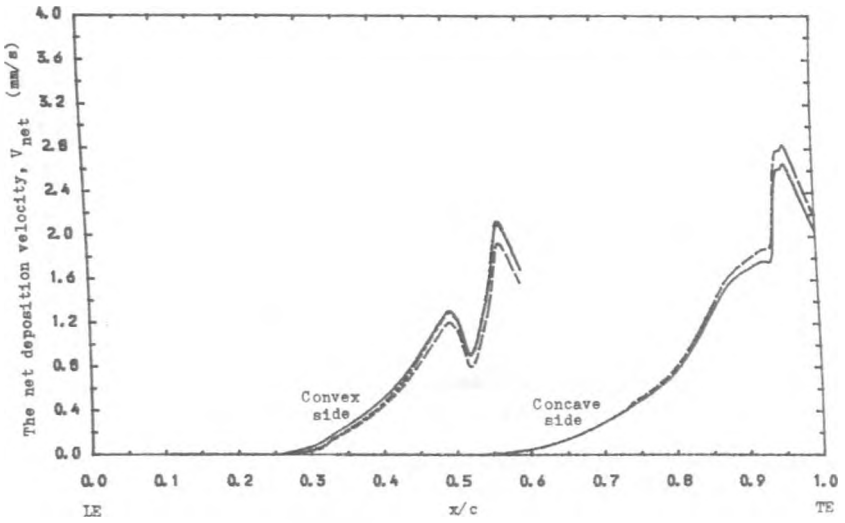

Fig. 7.127 : Variation of the Net Deposition Velocity of Droplets inside the Concave and Convex Boundary Layer at Different Distance from the Blade Surface when t_{wi}= 85 °C and d_i= 1.0 μm .

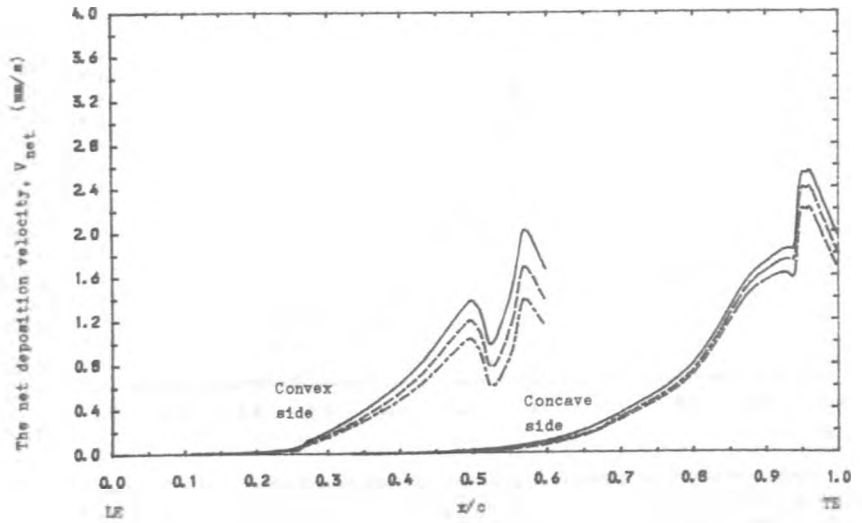

Fig.7.128 : Variation of the Net Deposition Velocity of Droplets inside the Concave and Convex Boundary Layer at Different Distance from the Blade Surface when t_{wi}= 66 °C and d_i= 0.5 μm .

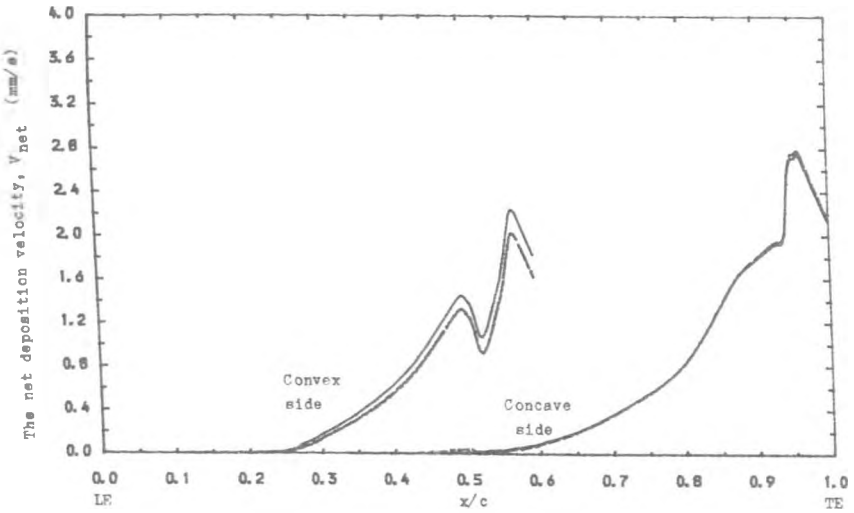

Fig. 7.129 : Variation of the Net Deposition Velocity of Droplets inside the Concave and Convex Boundary Layer at Different Distance from the Blade Surface when t_{wi}= 70 °C and d_i= 0.5 μm .

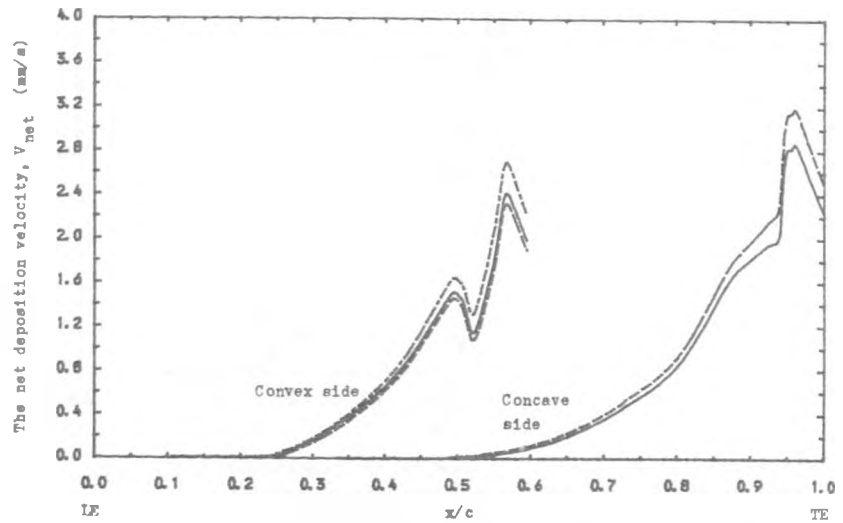

Fig. 7.130 : Variation of the Net Deposition Velocity of Droplets inside the Concave and Convex Boundary Layer at Different Distance from the Blade Surface when t_{wi}= 75 °C and d_i= 0.5 μm .

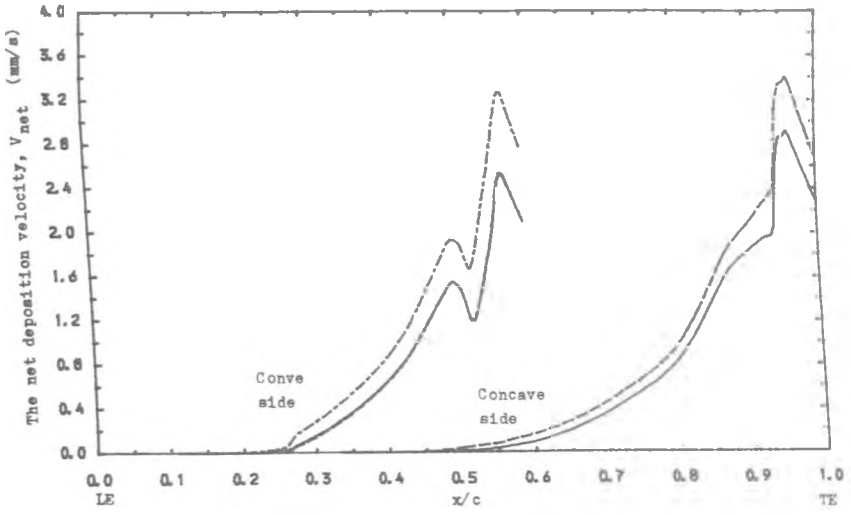

Fig. 7. 131 : Variation of the Net Deposition Velocity of Droplets inside the Concave and Convex Boudary Layer at Different Distance from the Blade Surface when t_{wi}= 80 °C and d_i= 0.5 μm .

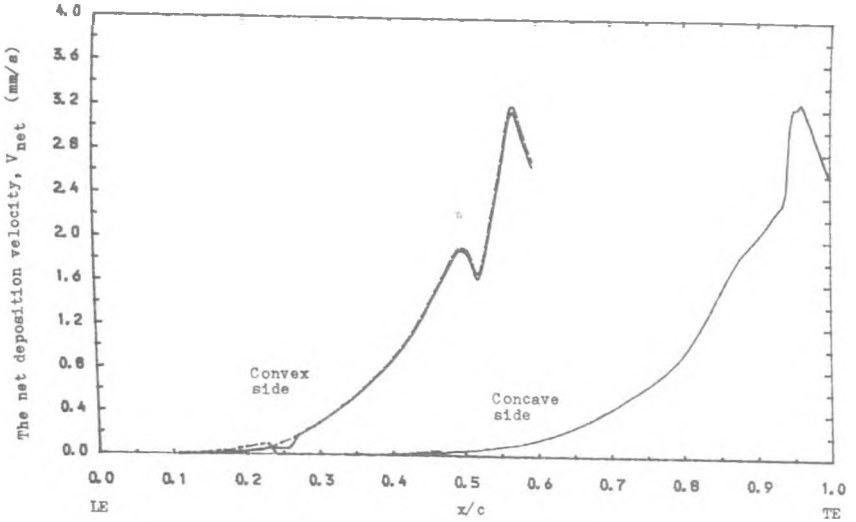

Fig.7. 133 : Variation of the Net Deposition Velocity of Droplets inside the Concave and Convex Boundary Layer at Different Distance from the Blade Surface when t_{wi}=66°C and d_i= 0.1 μm

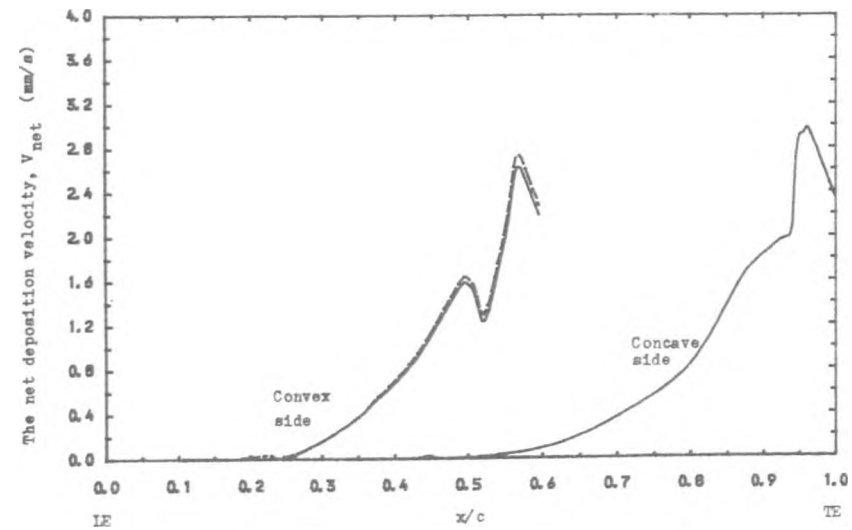

Fig .7.132 : Variation of the Net Deposition Velocity of Droplets inside the Concave and Convex Boundary Layer at Different Distance from the Blade Surface when t_{wi} = 85 °C and d_i= 0.5 μm .

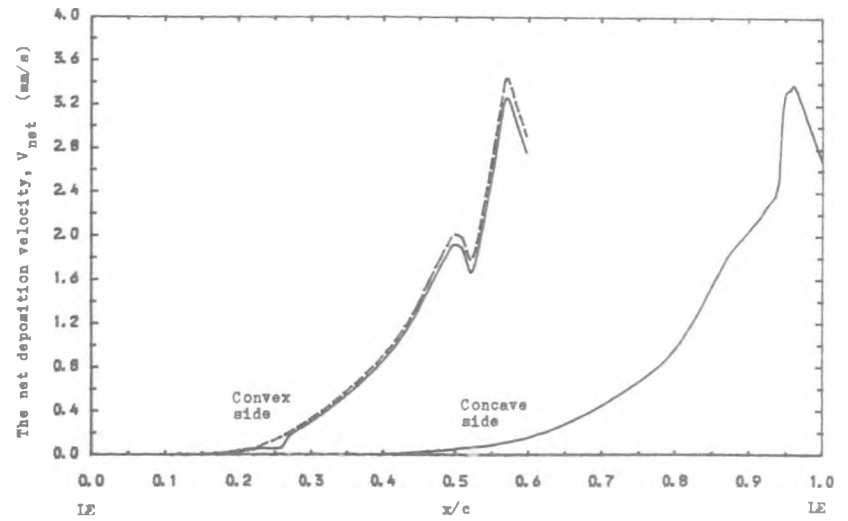

Fig. 7.134 : Variation of the Net Deposition Velocity of Droplets inside the Concave and convex Boundary Layer at Different Distance from the Blade Surface when t_{wi}= 70 °C and d_i= 0.1 μm .

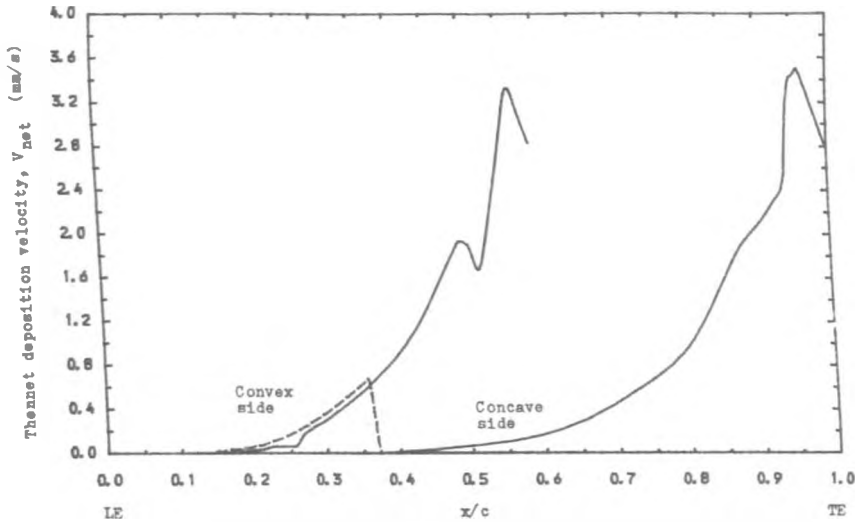

Fig. 7. 135 : Variation of the Net Deposition Velocity of Droplets inside tthe Concave and Convex Boundary Layer at Different Distance from the Blade Surface when t_{wi}= 75 °C and d_i= 0.1 μm .

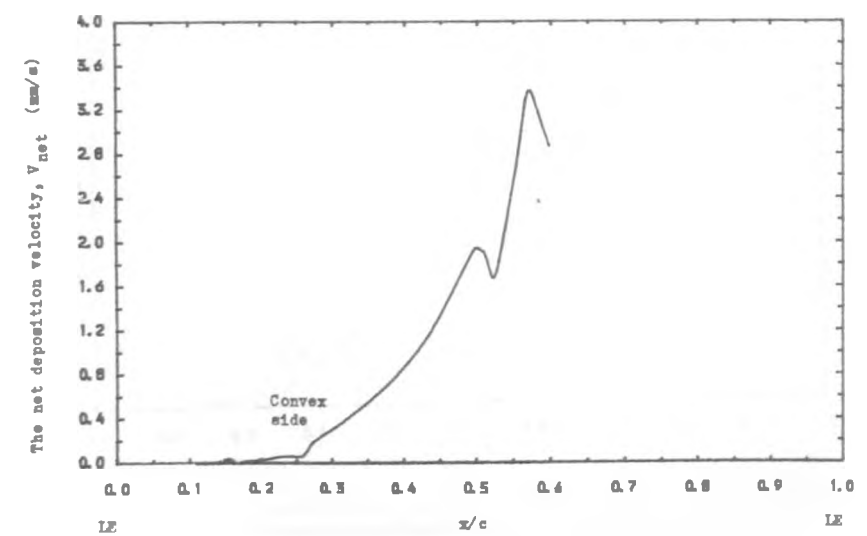

Fig. 7. 136 : Variation of the Net Deposition Velocity of Droplets inside the Concave and Convex Boundary Layer at Different Distance from the Blade Surface when t_{wi}= 80 °C and d_i= 0.1 μm .

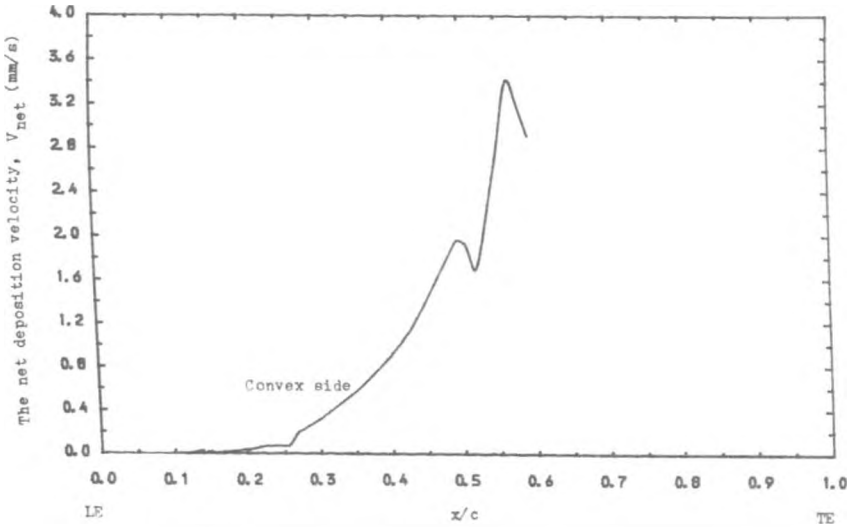

Fig. 7. 137 : Variation of the Net Deposition Velocity of Droplets inside the Concave and Convex Boundary Layer at Different Distance from the Blade Surface when t_{wi}= 85 °C and d_i= 0.1 μm .

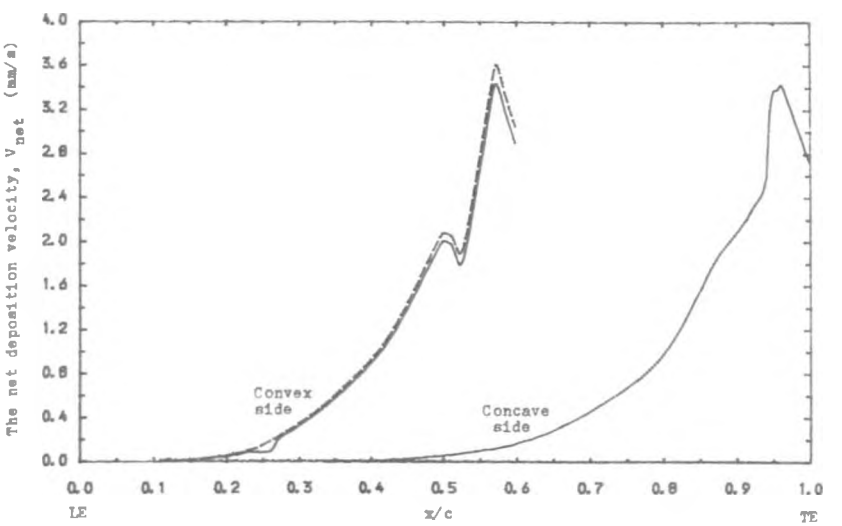

Fig. 7.138 : Variation of the Net Deposition Velocity of Droplets inside the Concave and Convex Boundary Layer at Different Distance from the Blade Surface when t_{wi}= 66 °C and d_i= 0.05 μm .

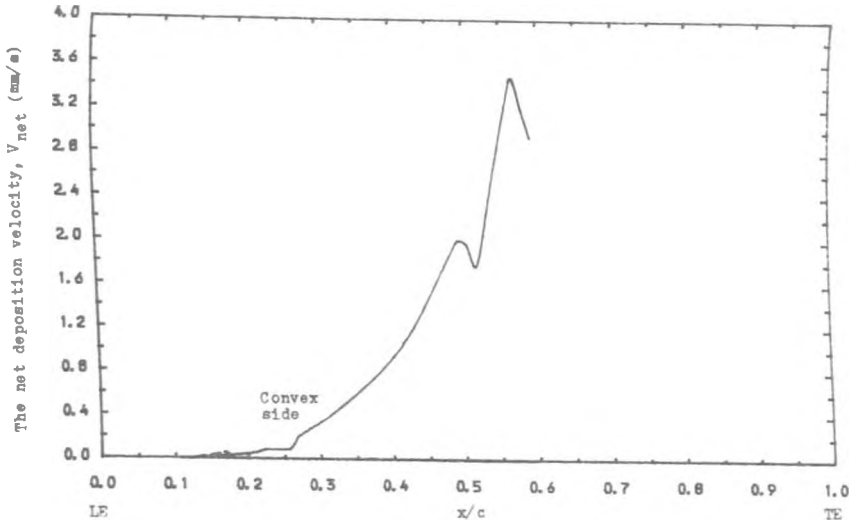

Fig.7.139 : Variation of the Net Deposition Velocity of Droplets inside the Concave and Convex Boundary Layer at Different Distance from the Blade Surface when t_{w1} = 70 °C and d_i = 0.05 μm .

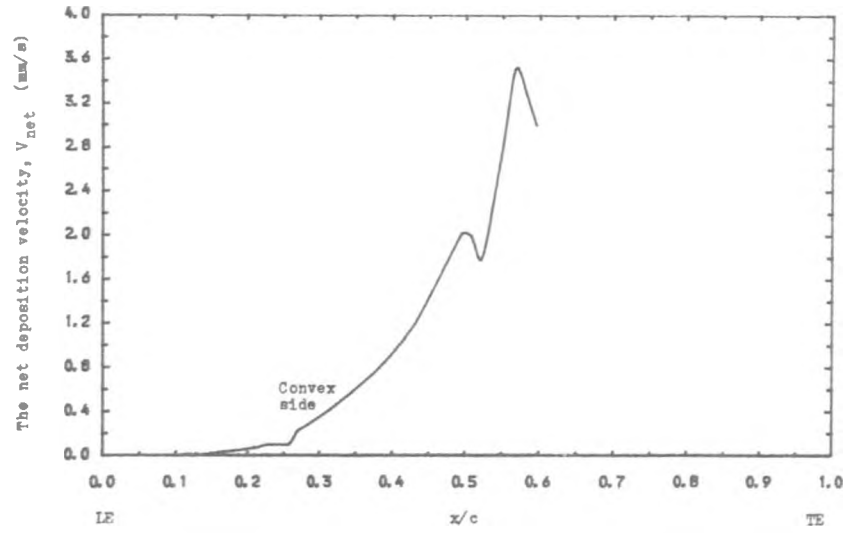

Fig.7.140 : Variation of the Net Deposition Velocity of Droplets inside the Concave and Convex Boundary Layer at Different Distance from the Blade Surface when t_{w1} = 75 °C and d_i = 0.05 μm .

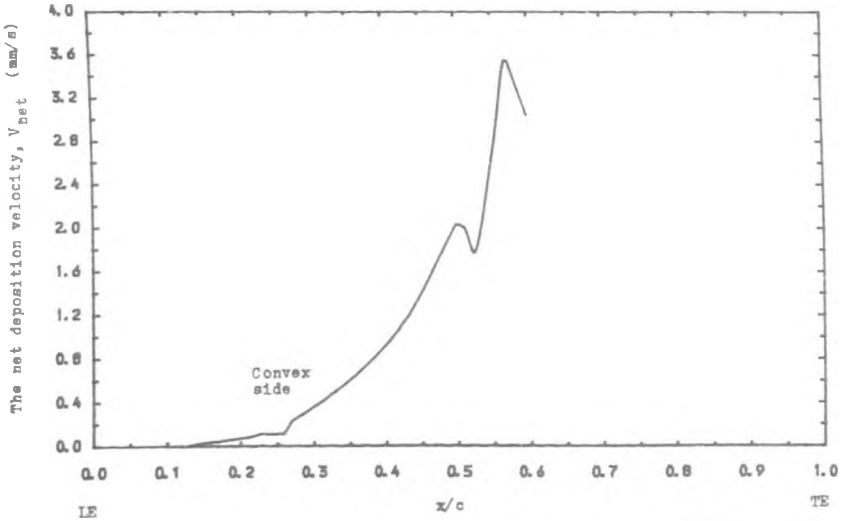

Fig. 7. 141 : Variation of the Net Deposition Velocity of Droplets inside the Concave and Convex Boundary Layer at Different Distance from the Blade Surface when t_{w1} = 80 °C and d_i = 0 05 μm .

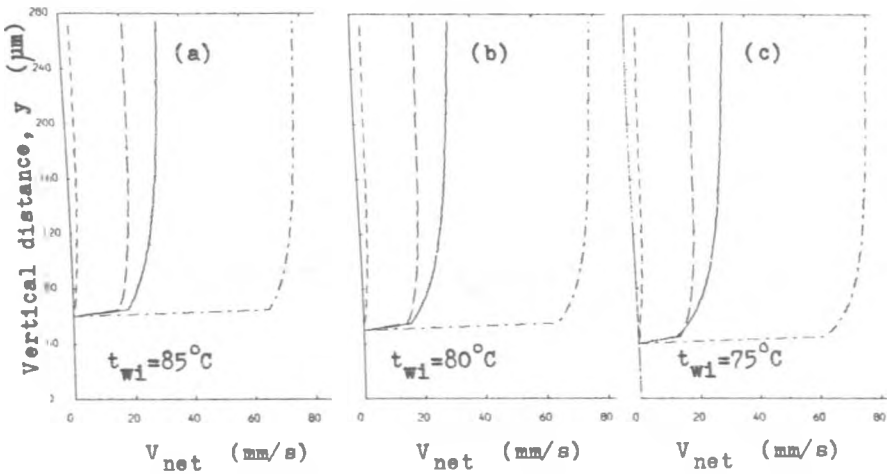

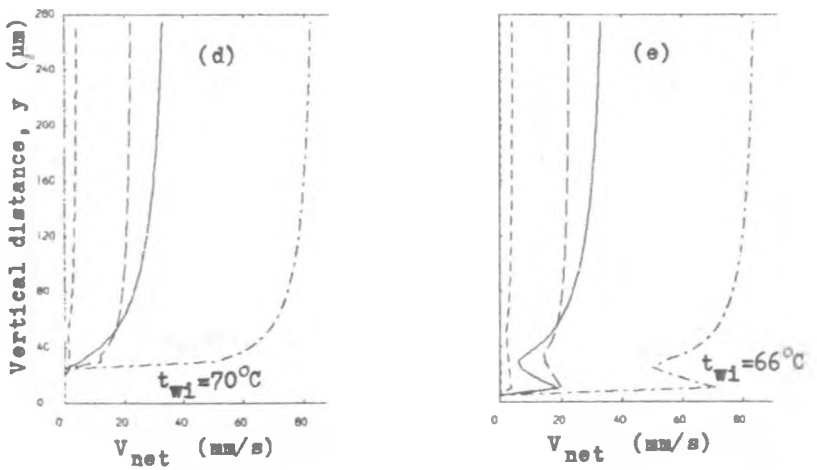

Fig. 7.142 : Variation in the Net Deposition Velocity along y-axis for a range of Blade Surface Temperatures when d_1= 1.0 μm .

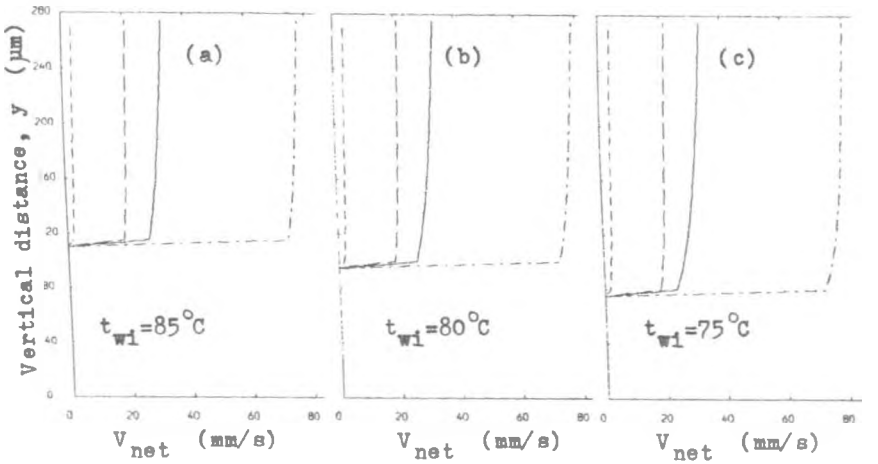

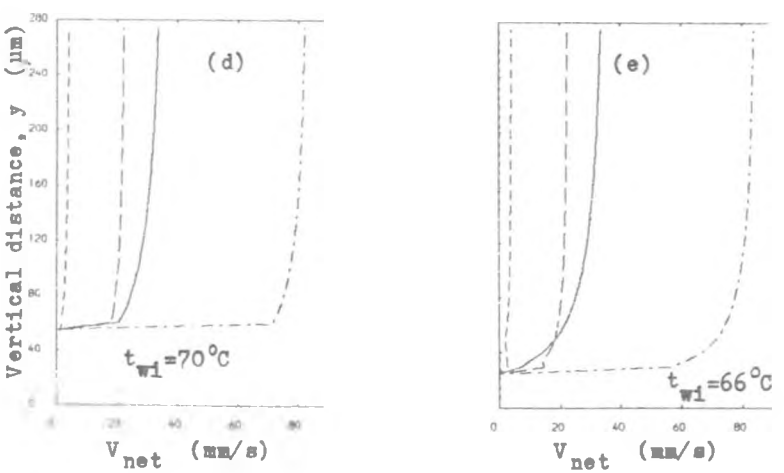

Fig. 7.143 : Variation in the Net Deposition Velocity along y-axis for a range of Blade Surface Temperatures when d_1= 0.5 μm .

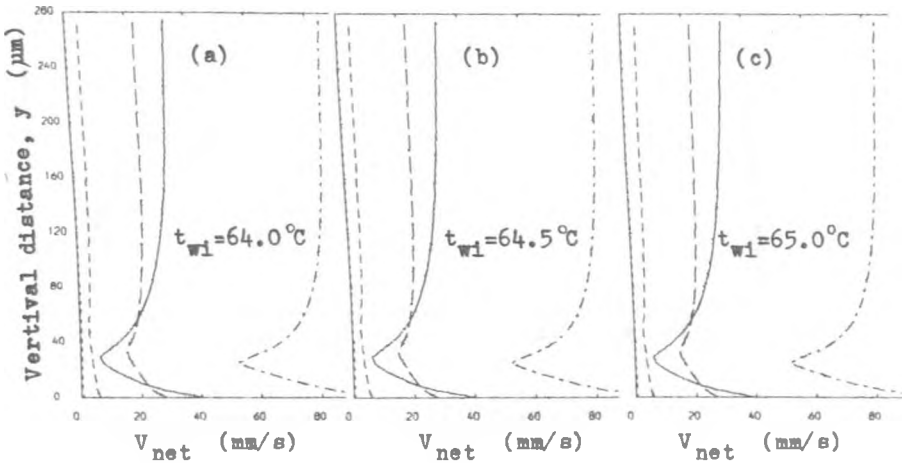

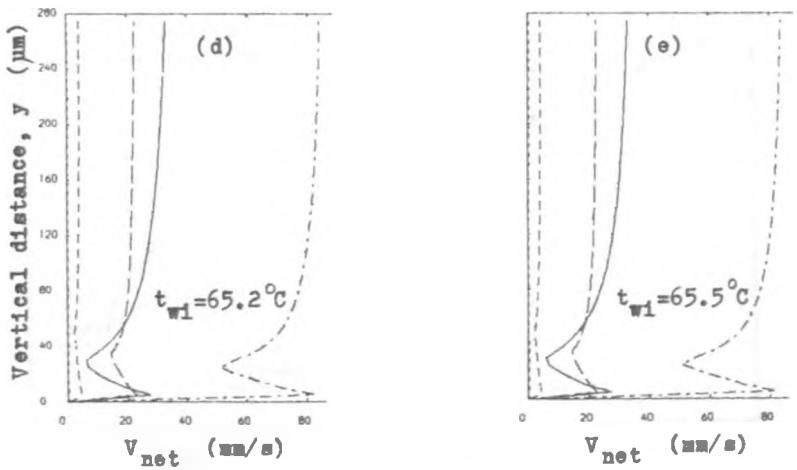

Fig. 7.144 : Variation in the Net Deposition Velocity along y-axis for a range of Blade Surface Temperatures when d_1= 1.0 μm .

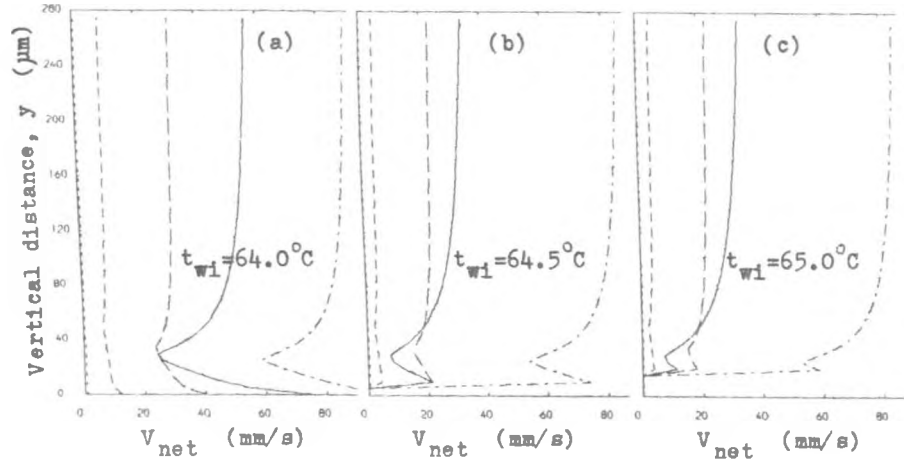

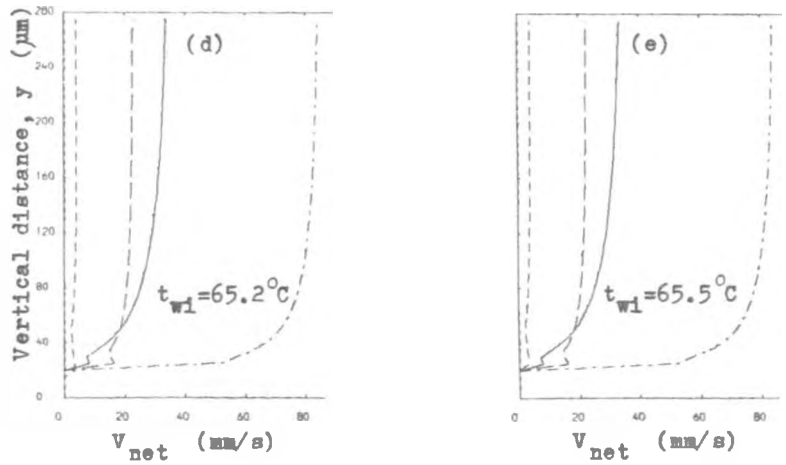

Fig. 7.145 : Variation in the Net Deposition Velocity along y-axis for a range of Blade Surface Temperatures when d_1= 0.5 μm .

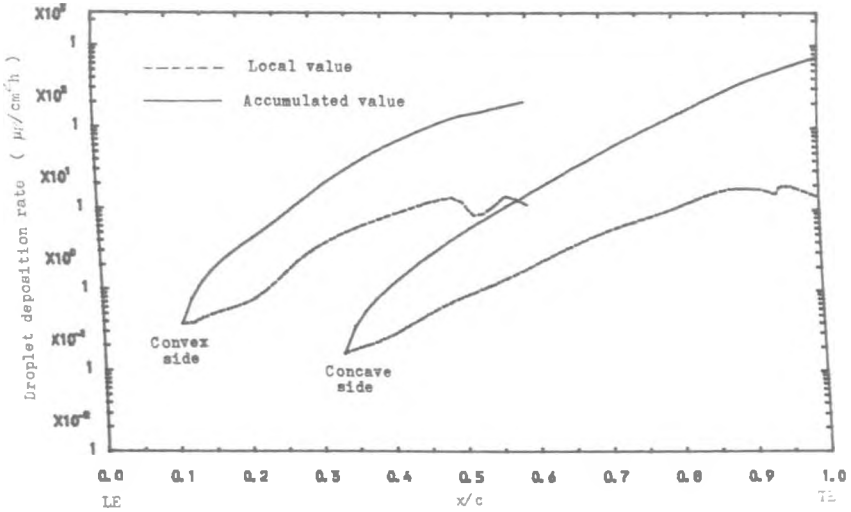

Fig. 7.146 : Distribution of Local and Accumulated Deposited Water on the Blade Surfaces when t_{wi}= 64.0 °C and d_i= 1.0 μm.

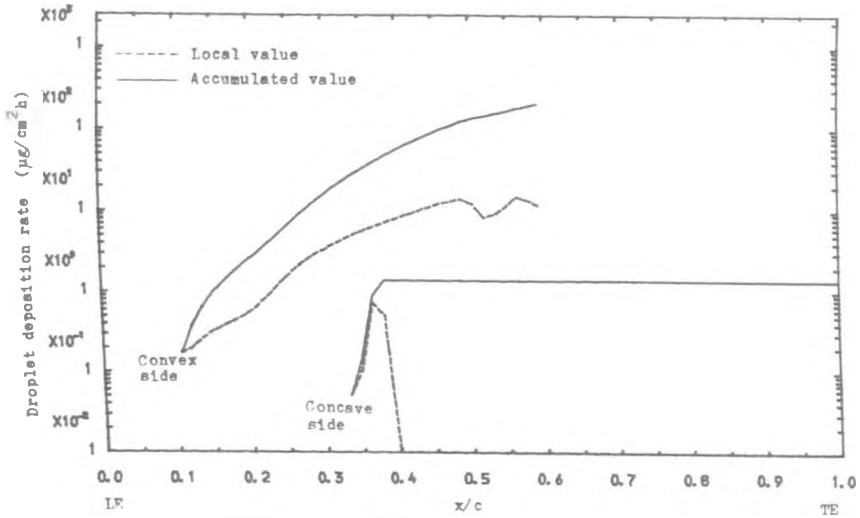

Fig.7.148 : Distribution of Local and Accumulated Deposited Water on the Blade Surfaces when t_{wi}= 65.0 °C and d_i= 1.0 μm .

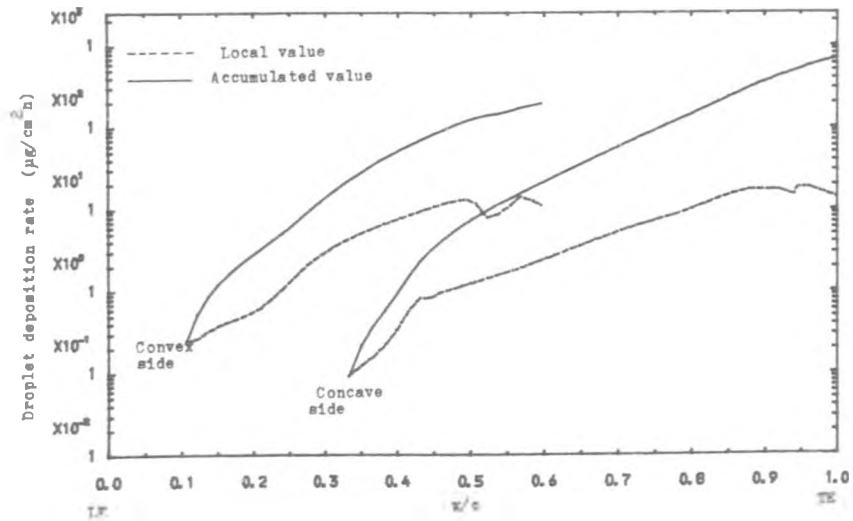

Fig. 7.147 : Distribution of Local and Accumulated Deposited Water on the Blade Surfaces when t_{wi}= 64.5 °C and d_i= 1.0 μm .

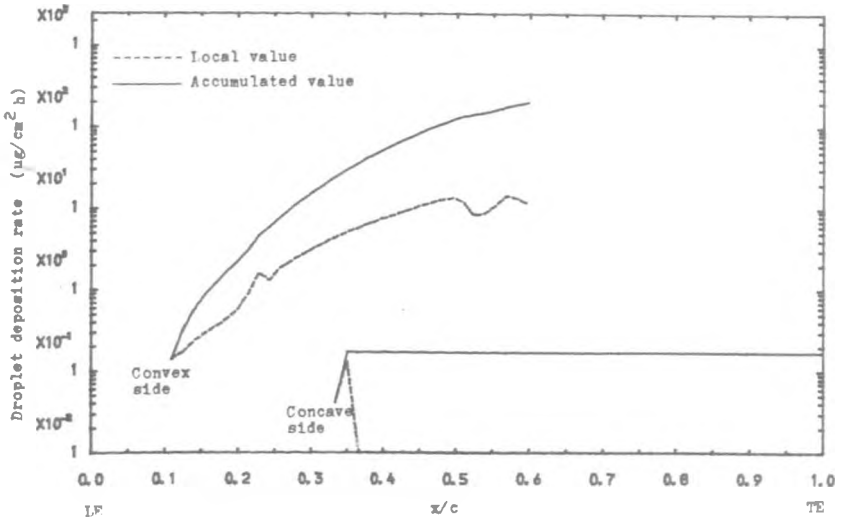

Fig.7.149 : Distribution of Local and Accumulated Deposited Water on the Blade Surface when t_{wi}= 65.2 °C and d_i= 1.0 μm .

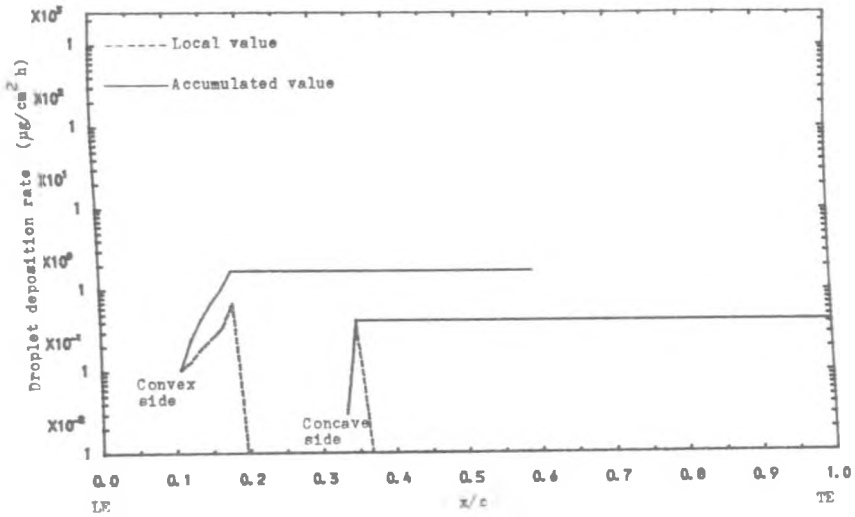

Fig. 7.150 : Distribution of Local and Accumulated Deposited Water on the Blade Surface when t_{wi}=65.5°C and d_i= 1.0 μm .

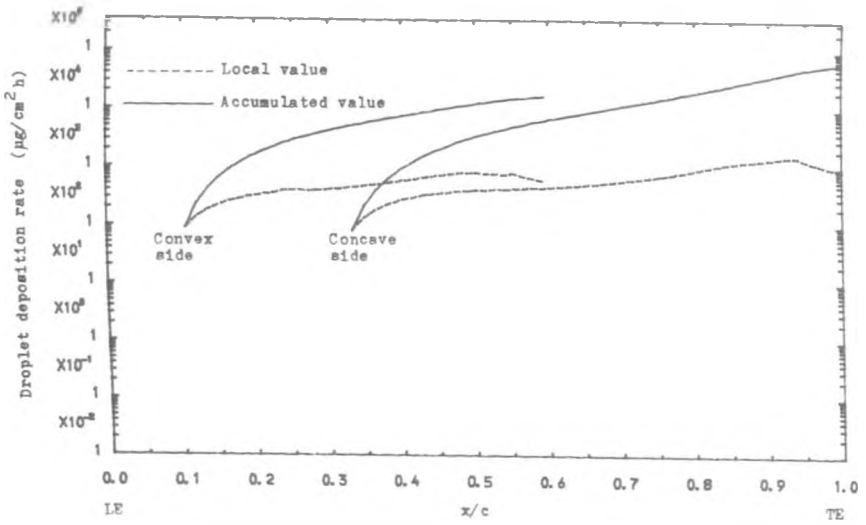

Fig.7.152 : Distribution of Local and Accumulated Deposited Water on the Blade Surface when t_{wi}= 32 °C and d_i= 0.5 μm .

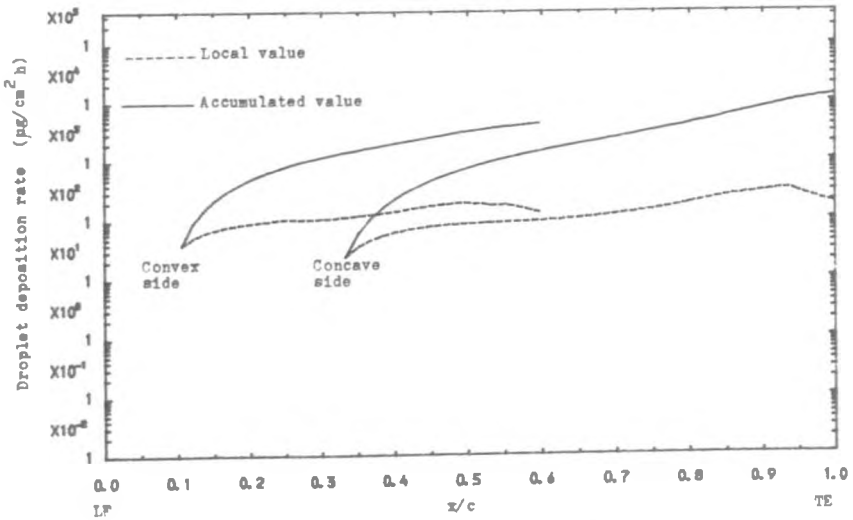

Fig. 7.151 : Distribution of Local and Accumulated Deposited Water on the Blade Surface when t_{wi}= 32 °C and d_i= 1.0 μm .

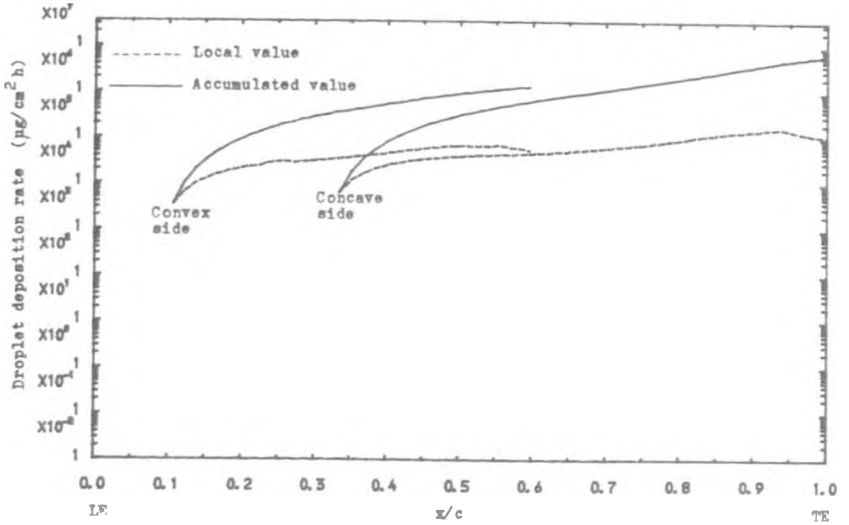

Fig.7.153 : Distribution of Local and Accumulated Deposited Water on the Blade Surface when t_{wi}= 32°C and d_i= 0.1 μm .

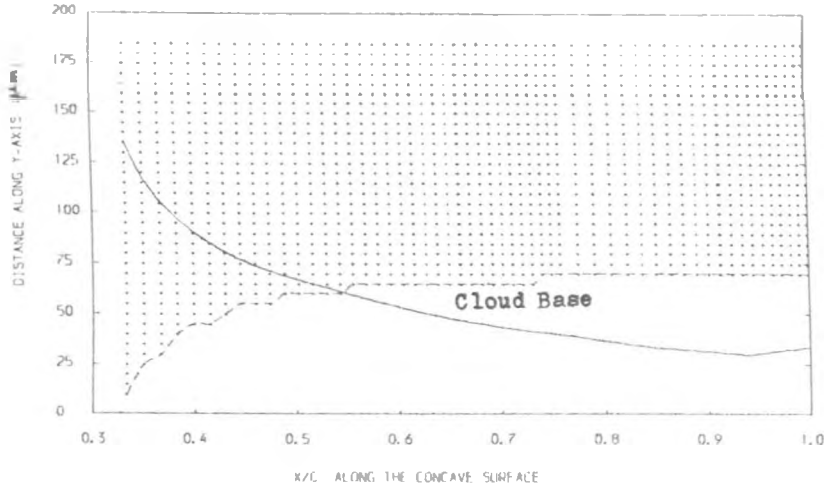

Fig. 7.154 : Profile of Fog Droplet Cloud Base and of Boundary Sublayer along the Concave Surface when t_{wi}= 85°C and d_i= 1.0 μm .

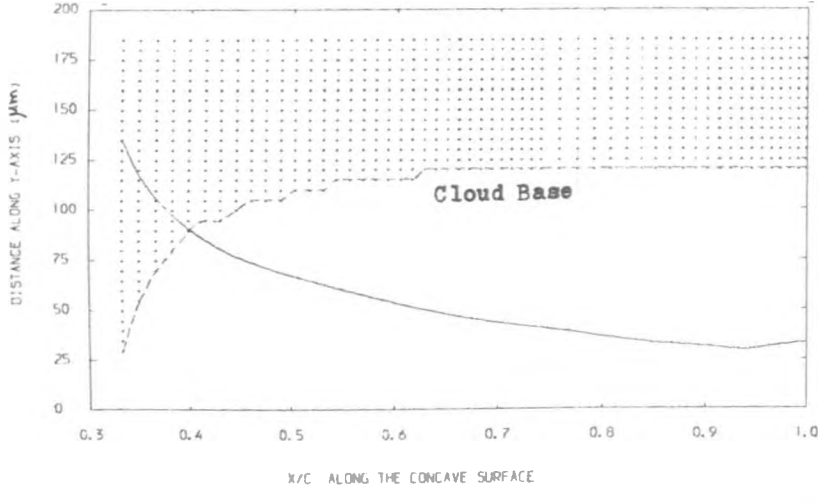

Fig. 7.155 : Profile of Fog Droplet Cloud Base and of Boundary Sublayer along the Concave Surface when t_{wi}= 85°C and d_i= 0.5 μm .

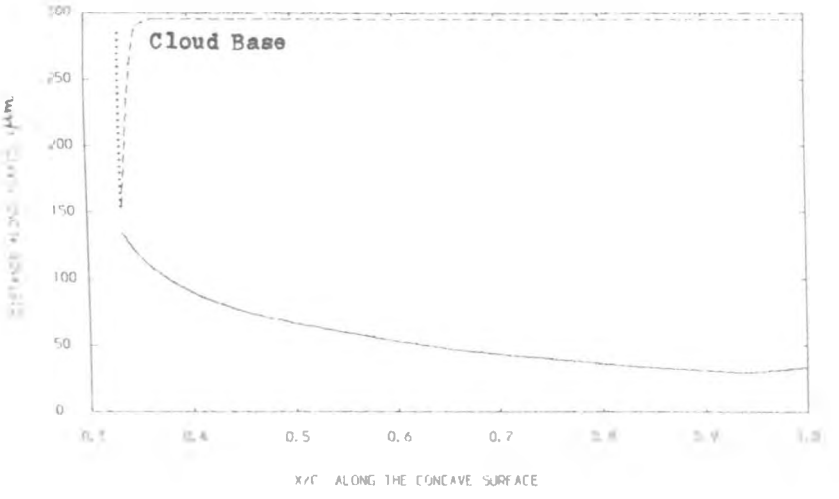

Fig. 7.156 : Profile of Fog Droplet Cloud Base and of Boundary Sublayer along the Concave Surface when t_{wi}= 85°C and d_i= 0.1 μm .

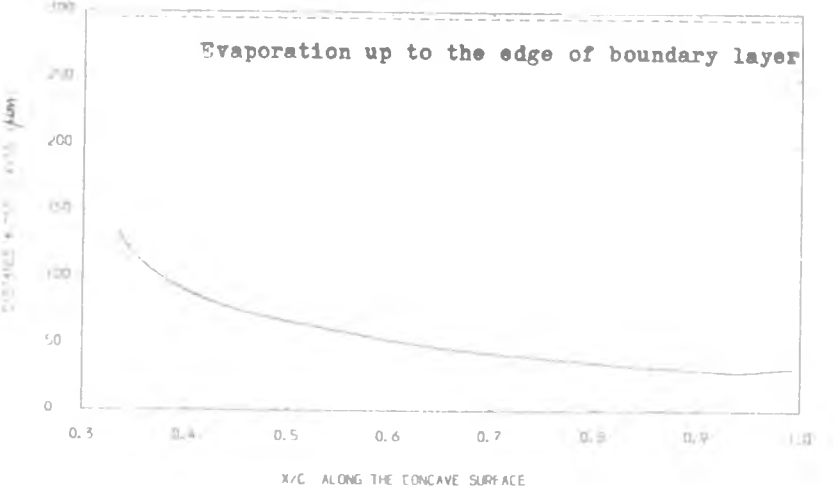

Fig. 7.157 : Profile of Fog Droplet Cloud Base and of Boundary Sublayer along the Concave Surface when t_{wi}= 85°C and d_i= 0.05 μm .

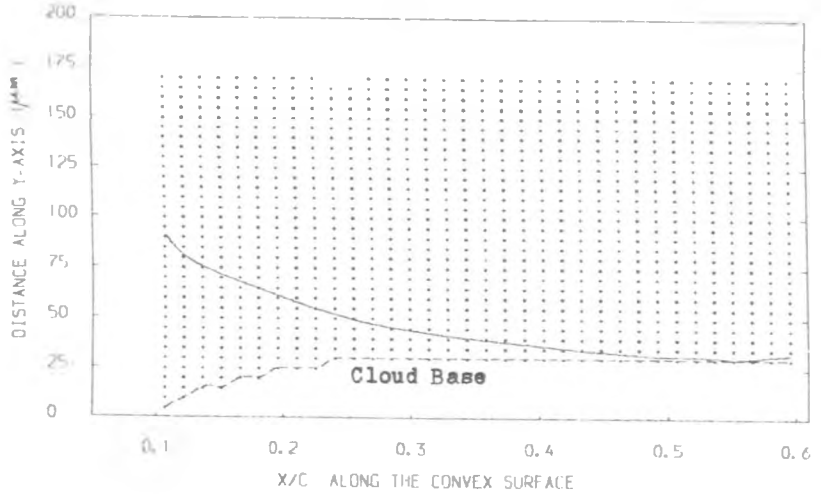

Fig.7.158 : Profile of Fog Droplet Cloud Base and of Boundary Sublayer along the Convex Surface when t_{wi}= 85°C and d_i= 1.0 μm .

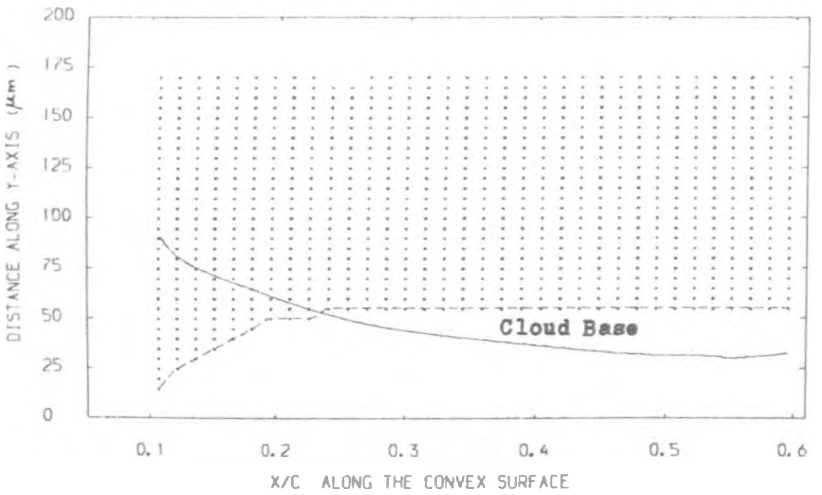

Fig. 7.159 : Profile of Fog Droplet Cloud Base and of Boundary Sublayer along the Convex Surface when t_{wi}= 85°C and d_i= 0.5 μm .

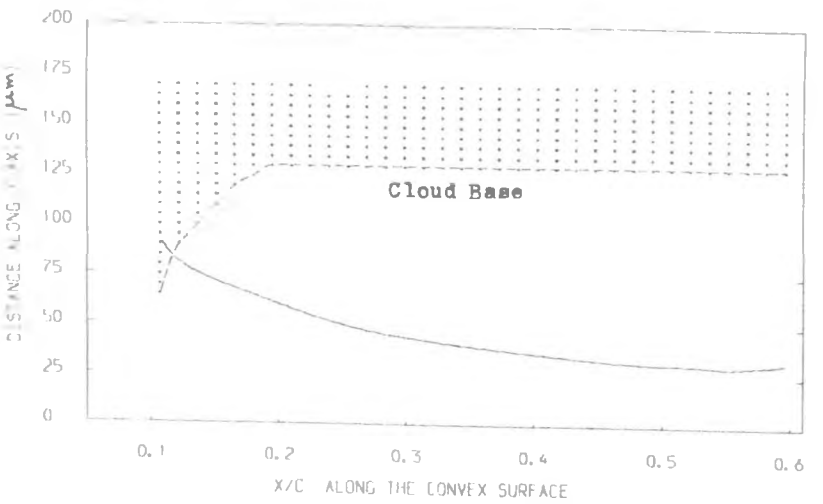

Fig. 7.160 : Profile of Fog Droplet Cloud Base and of Boundary Sublayer along the Convex Surface when t_{wi}= 85°C and d_i= 0.1 μm .

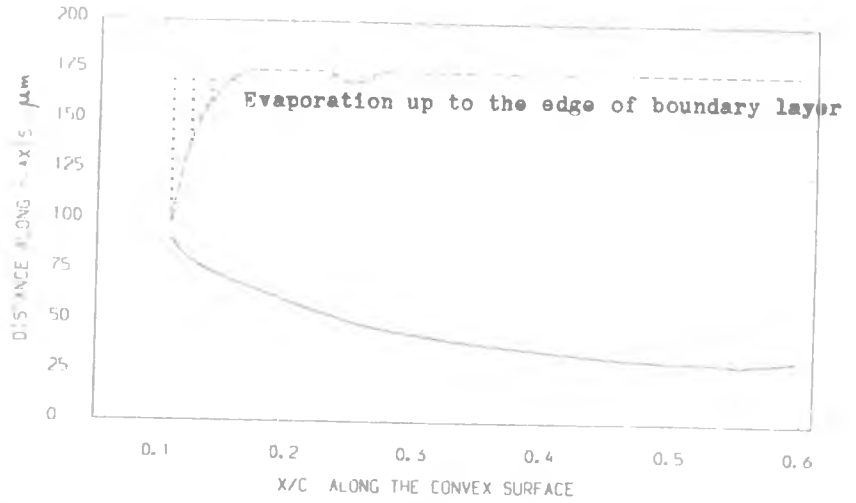

Fig. 7.161 : Profile of Fog Droplet Cloud Base and of Boundary Sublayer along the Convex Surface when t_{wi}= 85°C and d_i= 0.05 μm .

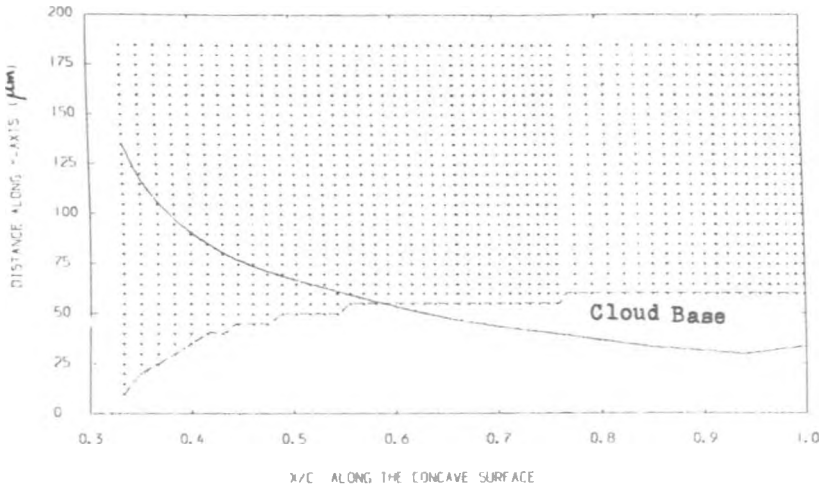

Fig. 7.162 : Profile of Fog Droplet Cloud Base and of Boundary Sublayer along the Concave Surface when t_{wi} = 80°C and d_i = 1.0 μm .

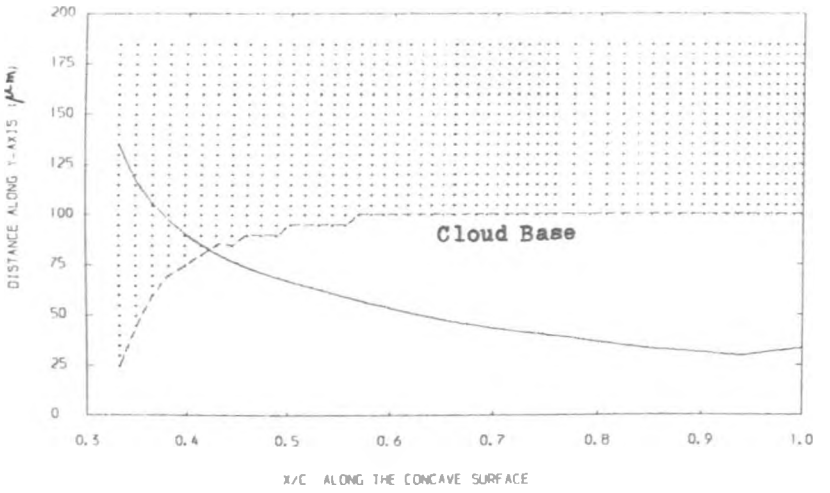

Fig. 7.163 : Profile of Fog Droplet Cloud Base and of Boundary Sublayer along the Concave Surface when t_{wi} = 80°C and d_i = 0.5 μm .

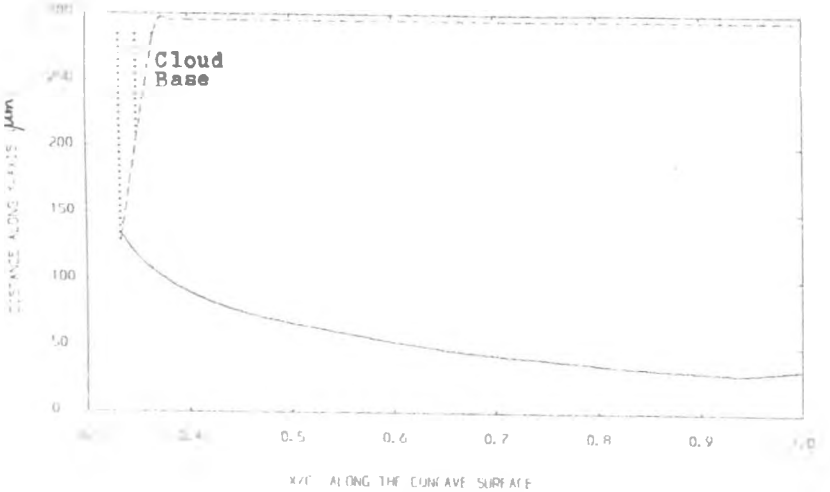

Fig. 7.164 : Profile of Fog Droplet Cloud Base and of Boundary Sublayer along the Concave Surface when t_{wi} = 80°C and d_i = 0.1 μm .

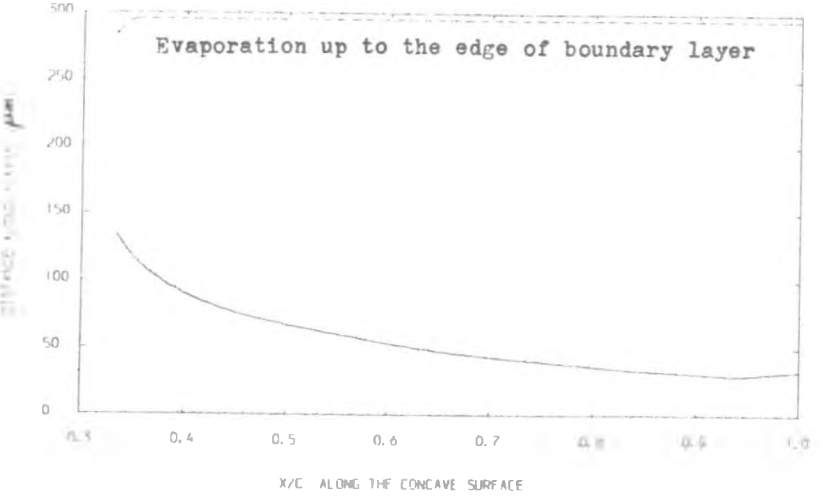

Fig. 7.165 : Profile of Fog Droplet Cloud Base and of Boundary Sublayer along the Concave Surface when t_{wi} = 80°C and d_i = 0.05 μm .

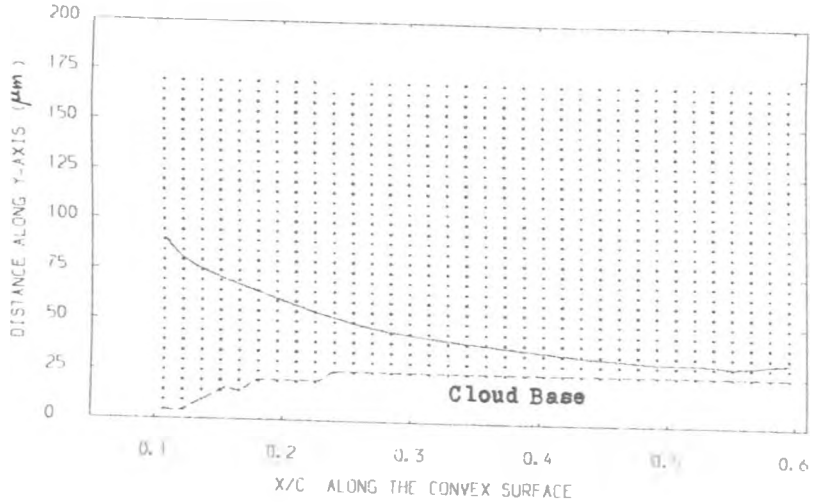

Fig. 7.166 : Profile of Fog Droplet Cloud Base and of Boundary Sublayer along the Convex Surface when t_{wi}= 80°C and d_i= 1.0 μm .

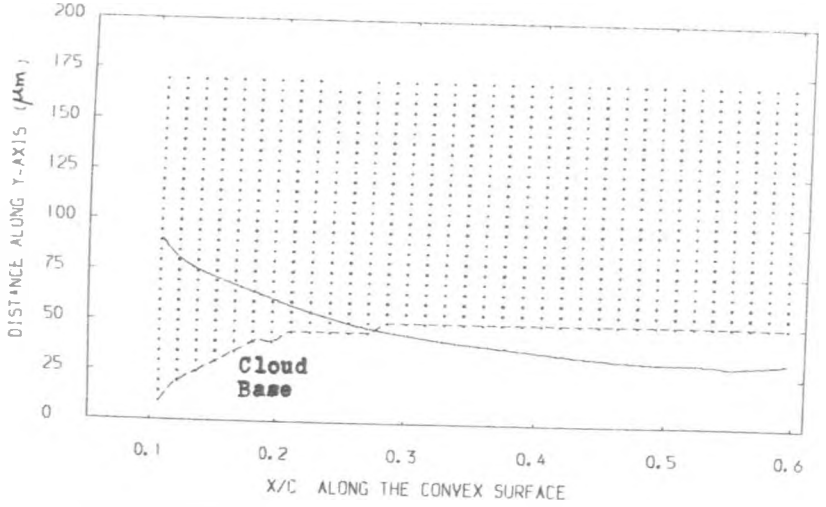

Fig. 7.167 : Profile of Fog Droplet Cloud Base and of Boundary Sublayer along the Convex Surface when t_{wi}= 80°C and d_i= 0.5 μm .

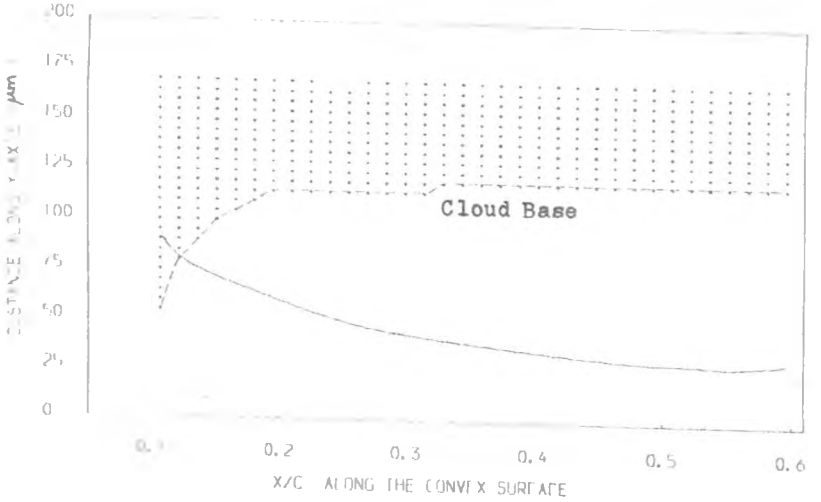

Fig. 7.168 : Profile of Fog Droplet Cloud Base and of Boundary Sublayer along the Convex Surface when t_{wi}= 80°C and d_i= 0.1 μm .

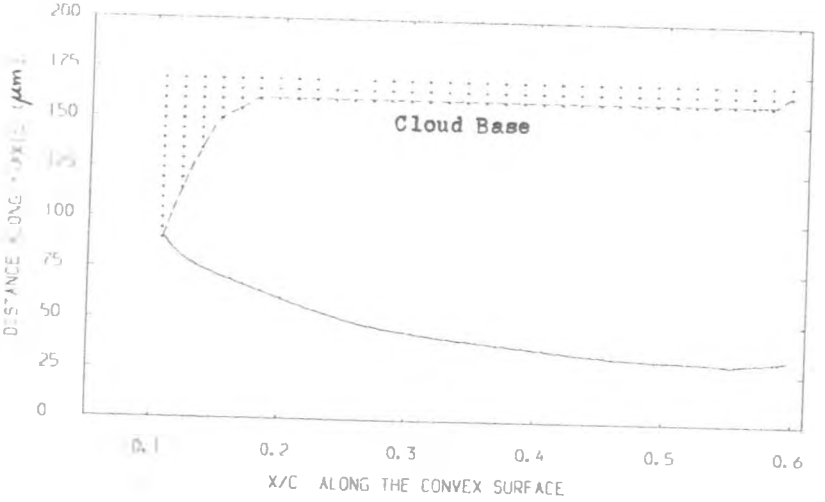

Fig. 7.169 : Profile of Fog Droplet Cloud Base and of Boundary Sublayer along the Convex Surface when t_{wi}= 80°C and d_i= 0.05 μm .

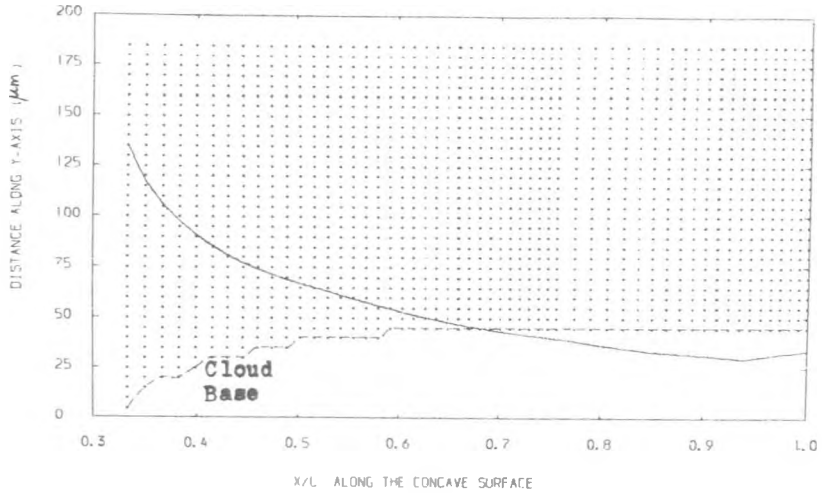

Fig. 7.170 : Profile of Fog Droplet Cloud Base and of Boundary Sublayer along the Concave Surface when t_{wi}= 75°C and d_i= 1.0 μm .

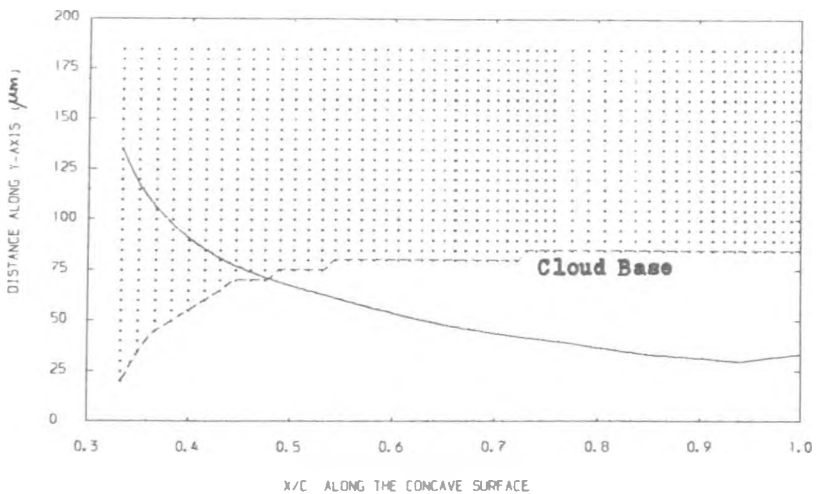

Fig. 7.171 : Profile of Fog Droplet Cloud Base and of Boundary Sublayer along the Concave Surface when t_{wi}= 75°C and d_i= 0.5 μm .

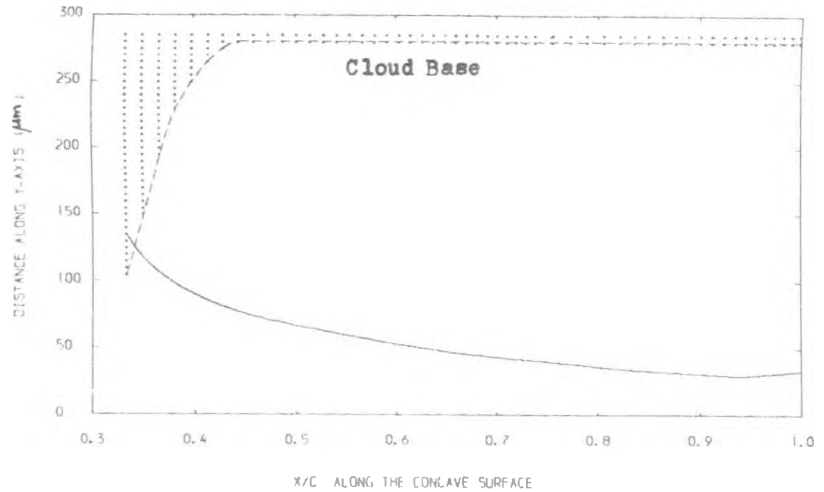

Fig. 7.172 : Profile of Fog Droplet Cloud Base and of Boundary Sublayer along the Concave Surface when t_{wi}= 75°C and d_i= 0.1 μm .

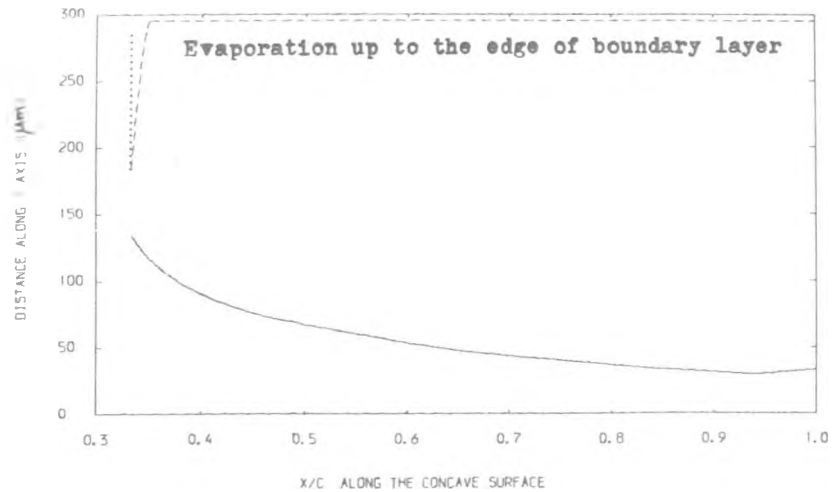

Fig. 7.173 : Profile of Fog Droplet Cloud Base and of Boundary Sublayer along the Concave Surface when t_{wi}= 75°C and d_i= 0.05 μm .

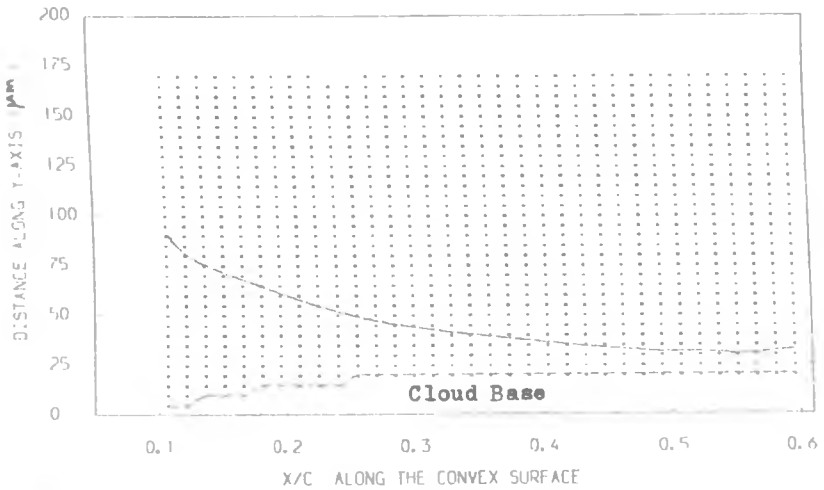

Fig. 7.174 : Profile of Fog Droplet Cloud Base and of Boundary Sublayer along the Convex Surface when t_{wi} = 75°C and d_i = 1.0 μm .

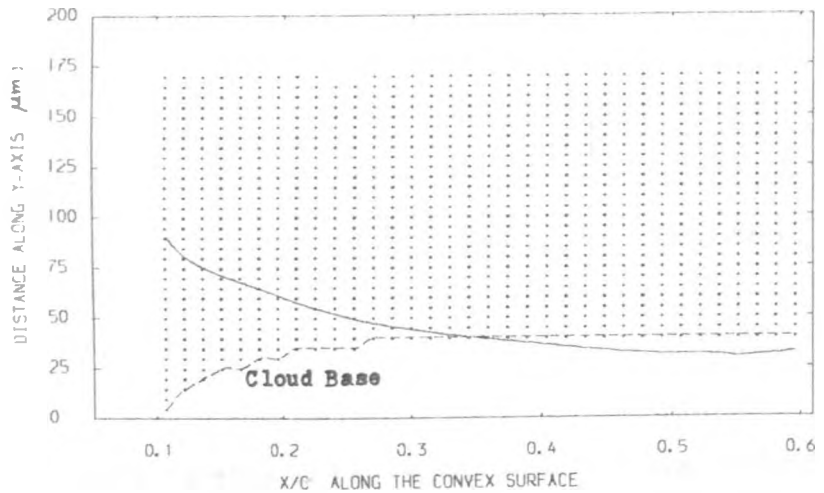

Fig. 7.175 : Profile of Fog Droplet Cloud Base and of Boundary Sublayer along the Convex Surface when t_{wi} = 75°C and d_i = 0.5 μm .

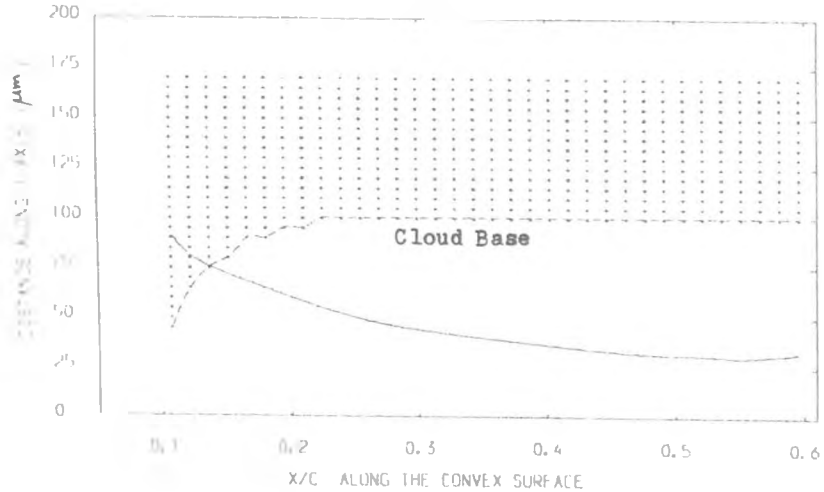

Fig. 7.176 : Profile of Fog Droplet Cloud Base and of Boundary Sublayer along the Convex Surface when t_{wi} = 75°C and d_i = 0.1 μm .

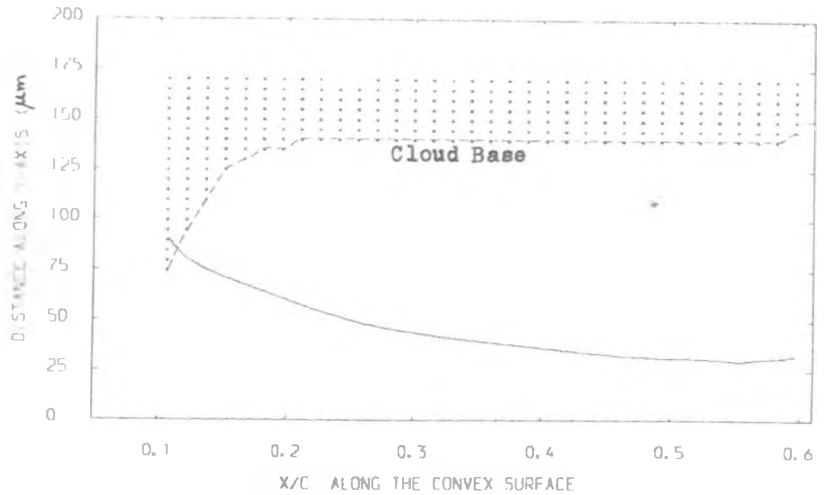

Fig. 7.177 : Profile of Fog Droplet Cloud Base and of Boundary Sublayer along the Convex Surface when t_{wi} = 75°C and d_i = 0.05 μm .

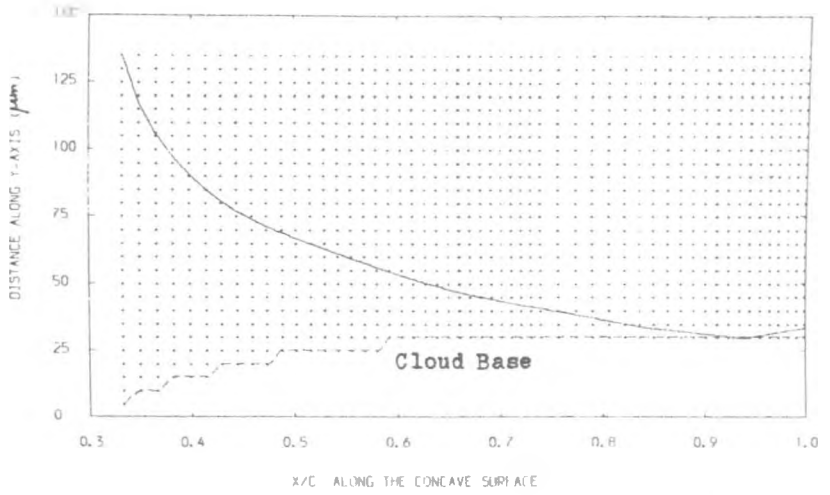

Fig. 7.178 : Profile of Fog Droplet Cloud Base and of Boundary Sublayar along the Concave Surface when t_{wi}= 70°C and d_i= 1.0 μm .

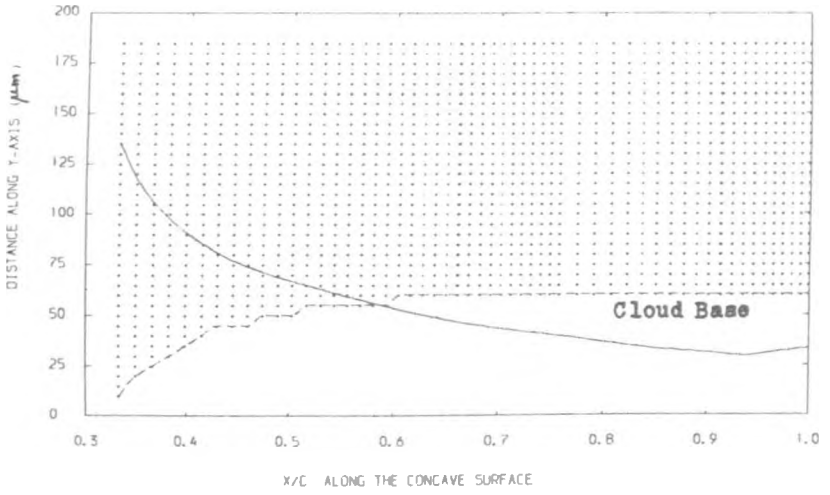

Fig. 7.179 : Profile of Fog Droplet Cloud Base and of Boundary Sublayer along the Concave Surface when t_{wi}= 70°C and d_i= 0.5 μm .

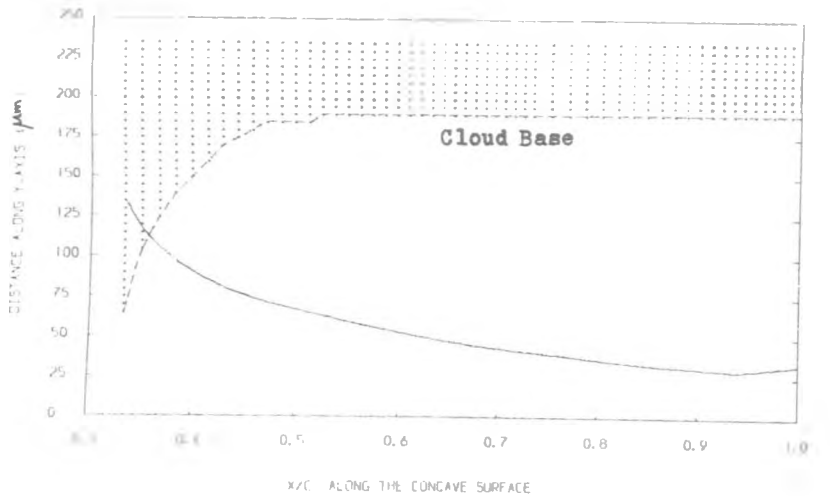

Fig. 7.180 : Profile of Fog Droplet Cloud Base and of Boundary Sublayer along the Concave Surface when t_{wi}= 70°C and d_i= 0.1 μm .

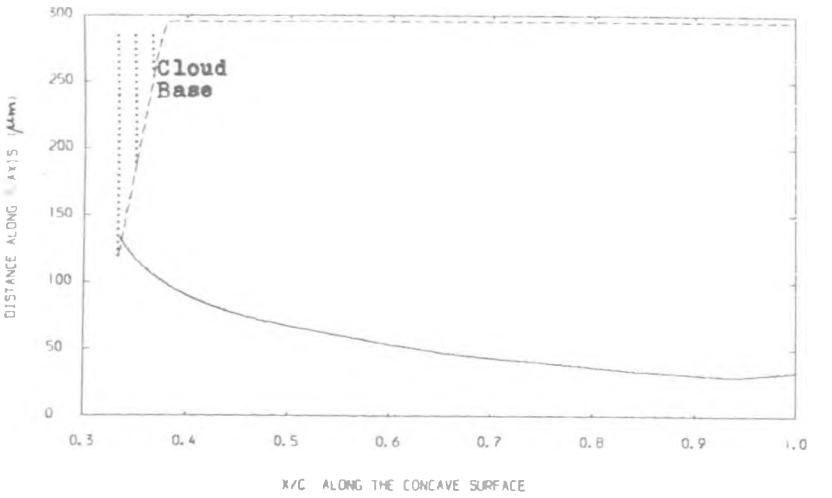

Fig. 7.181 : Profile of Fog Droplet Cloud Base and of Boundary Sublayer along the Concave Surface when t_{wi}= 70°C and d_i= 0.05 μm .

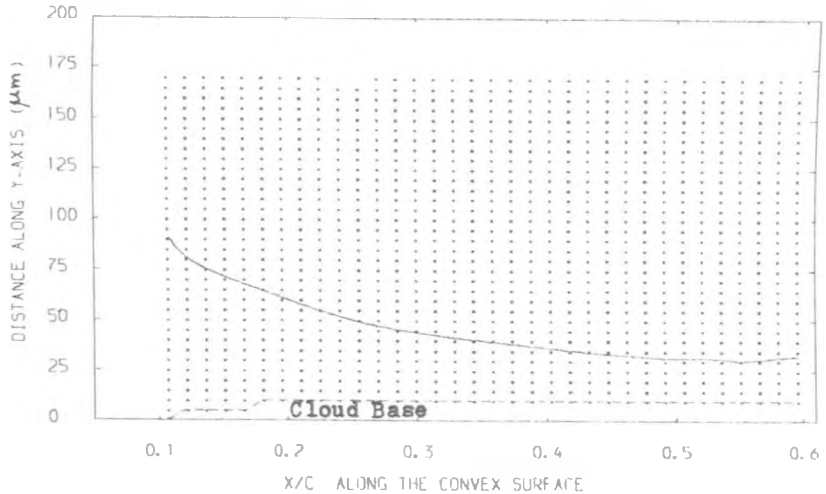

Fig. 7.182 : Profile of Fog Droplet Cloud Base and of Boundary Sublayer along the Convex Surface when t_{wi}= 70°C and d_1= 1.0 μm .

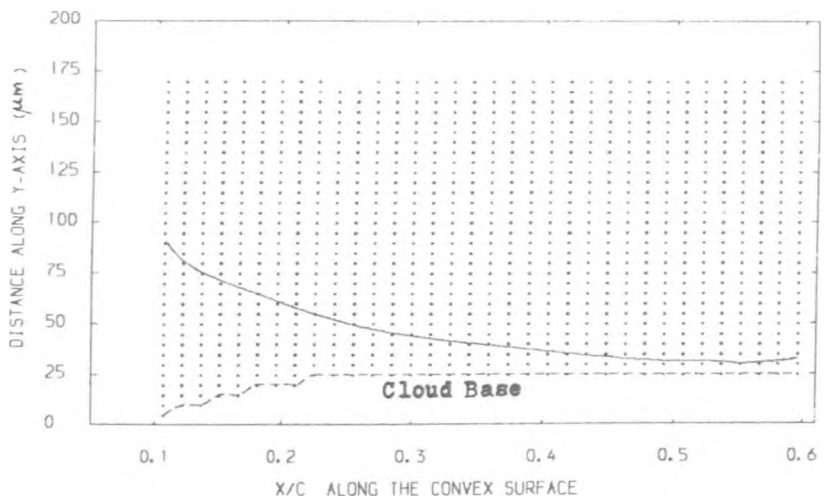

Fig. 7.183 : Profile of Fog Droplet Cloud Base and of Boundary Sublayer along the Convex Surface when t_{wi}= 70°C and d_1= 0.5 μm .

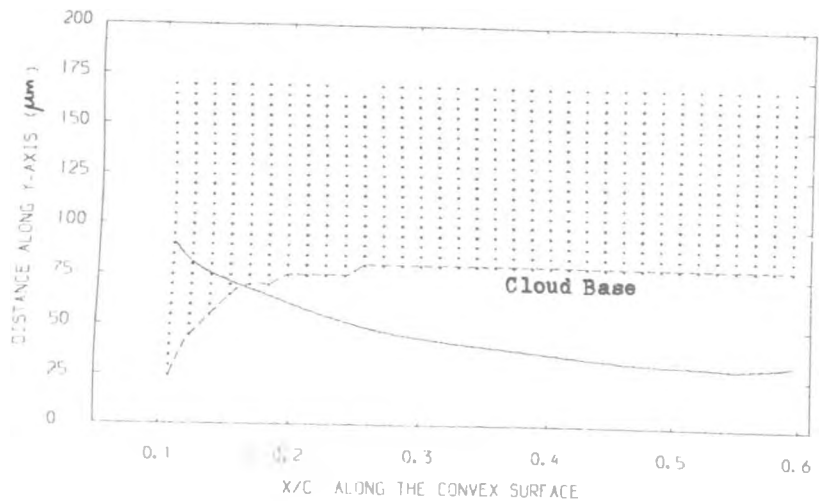

Fig. 7.184 : Profile of Fog Droplet Cloud Base and of Boundary Sublayer along the Convex Surface when t_{wi}= 70°C and d_1= 0.1 μm .

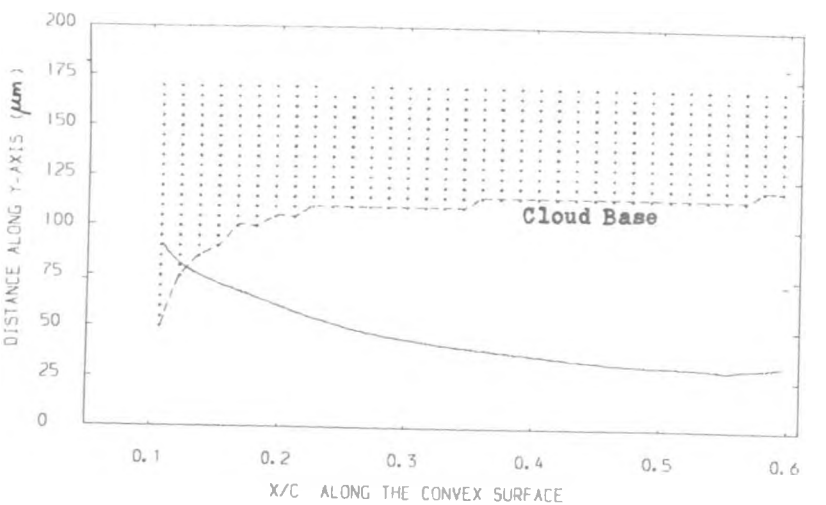

Fig. 7.185 : Profile of Fog Droplet Cloud Base and of Boundary Sublayer along the Convex Surface when t_{wi}= 70°C and d_1= 0.05 μm .

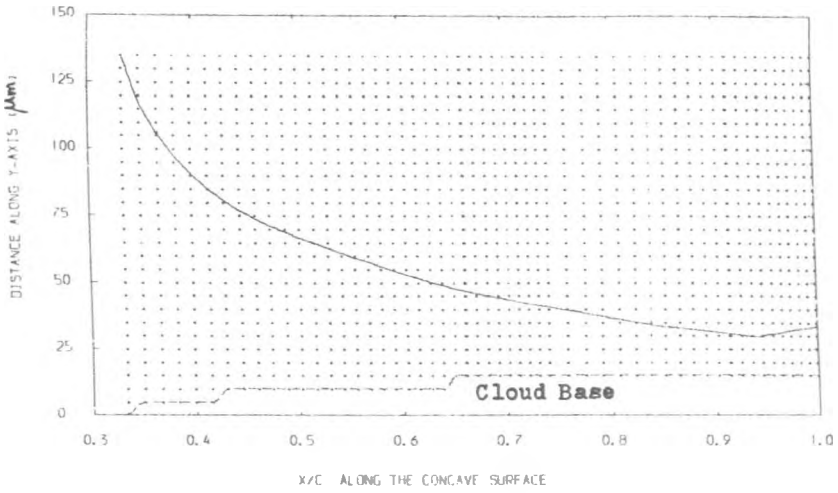

Fig 7.186 : Profile of Fog Droplet Cloud Base and of Boundary Sublayer along the Concave Surface when t_{wi} = 66°C and d_i = 1.0 μm .

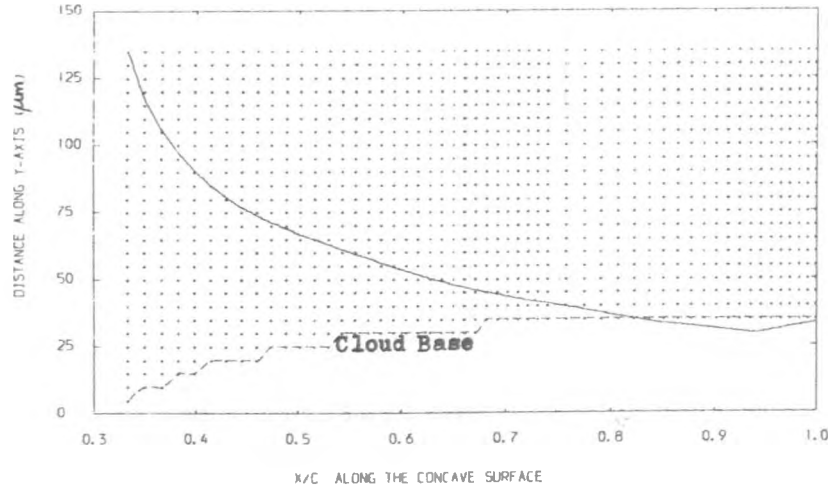

Fig. 7.187 : Profile of Fog Droplet Cloud Base and of Boundary Sublayer along the Concave Surface when t_{wi} = 66°C and d_i = 0.5 μm .

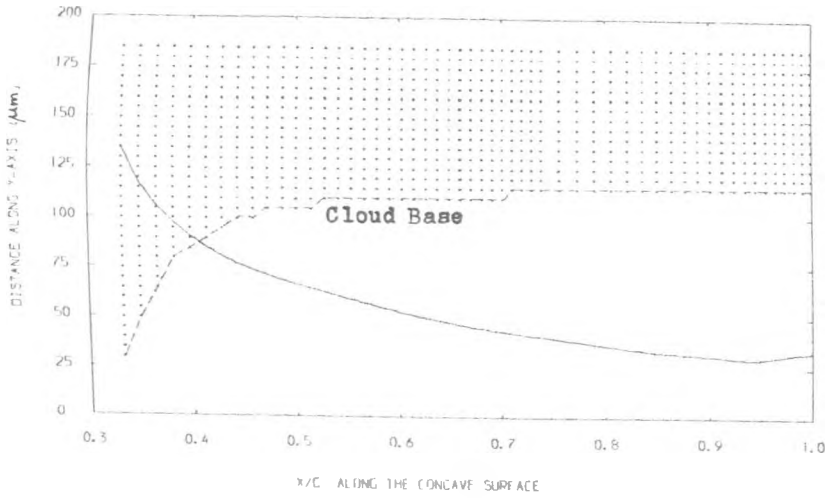

Fig 7.188 : Profile of Fog Droplet Cloud Base and of Boundary Sublayer along the Concave Surface when t_{wi} = 66°C and d_i = 0.1 μm .

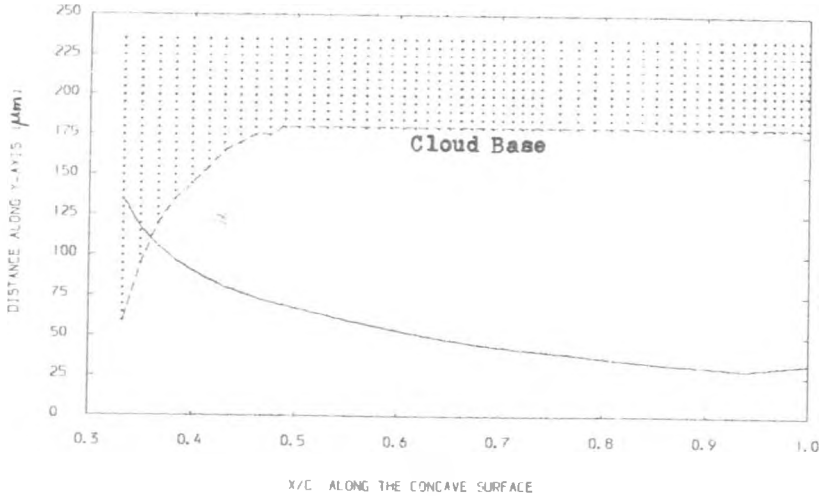

Fig. 7.189 : Profile of Fog Droplet Cloud Base and of Boundary Sublayer along the Concave Surface when t_{wi} = 66°C and d_i = 0.05 μm .

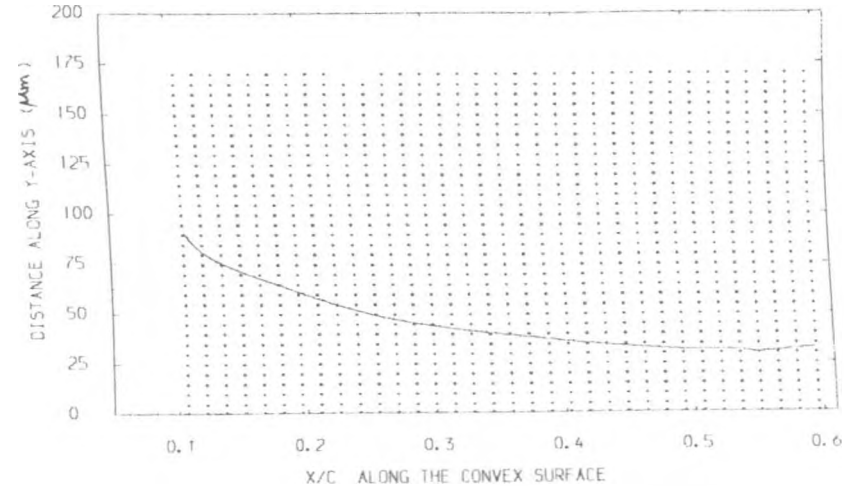

Fig. 7.190 : Profile of Fog Droplet Cloud Base and of Boundary Sublayer along the Convex Surface when t_{wi} = 66 °C and d_i = 1.0 μm .

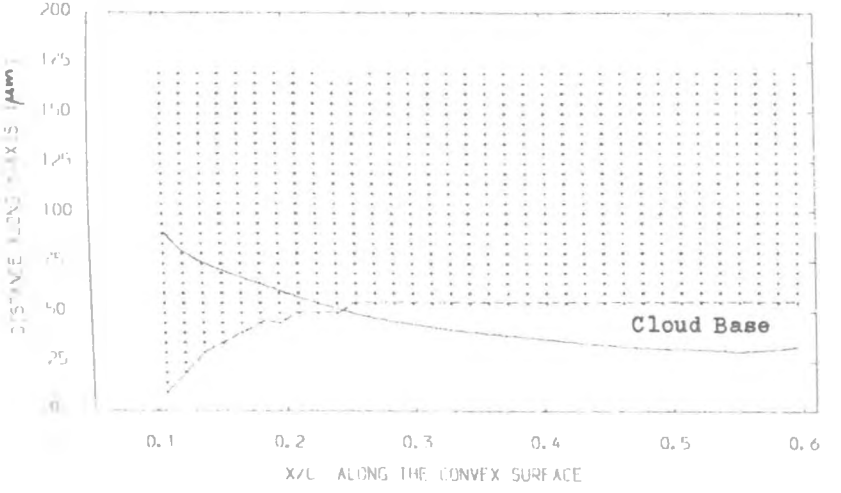

Fig. 7.192 : Profile of Fog Droplet Cloud Base and of Boundary Sublayer along the Convex Surface when t_{wi} = 66 °C and d_i = 0.1 μm .

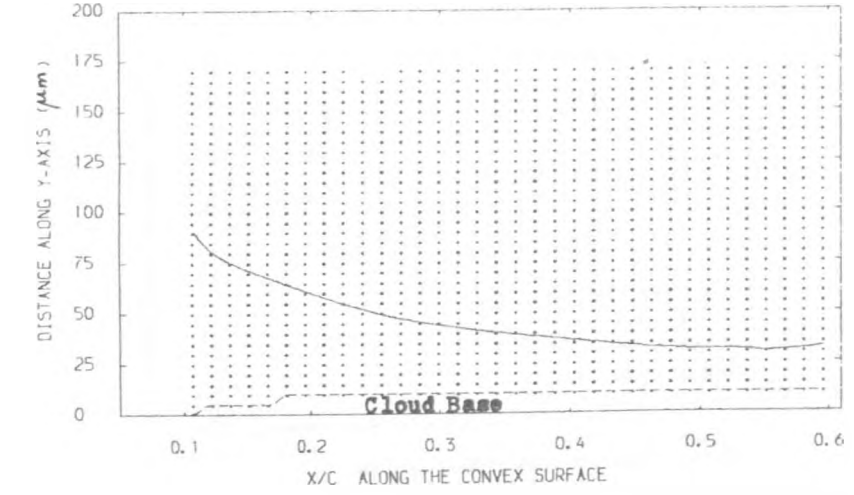

Fig. 7.191 : Profile of Fog Droplet Cloud Base and of Boundary Sublayer along the Convex Surface when t_{wi} = 66 °C and d_i = 0.5 μm .

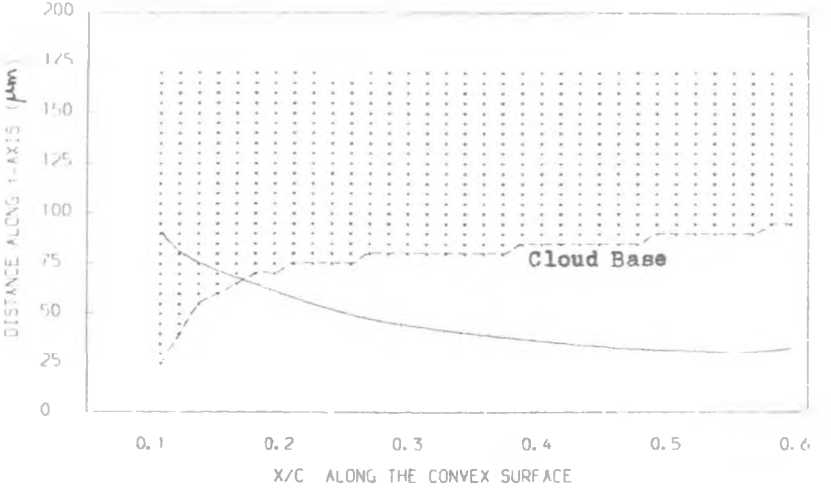

Fig. 7.193 : Profile of Fog Droplet Cloud Base and of Boundary Sublayer along the Convex Surface when t_{wi} = 66 °C and d_i = 0.05 μm .

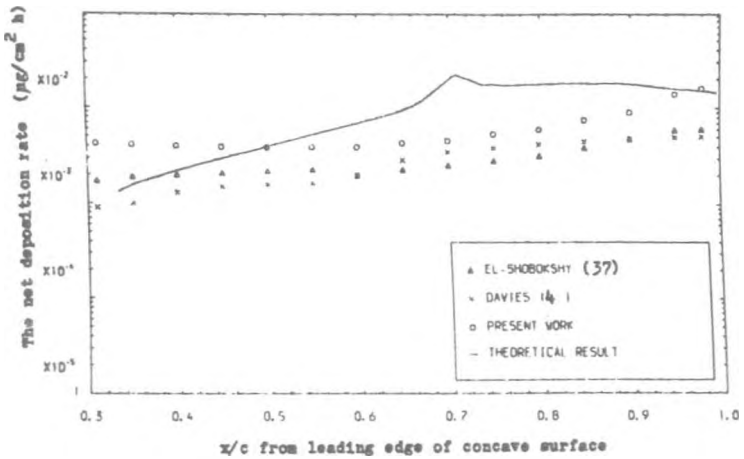

Fig. 7.195 : Distribution of Partical Deposition on Unheated Blade Surface when U_1= 11.2 m/s and d_{mm}= 0.186 μm .

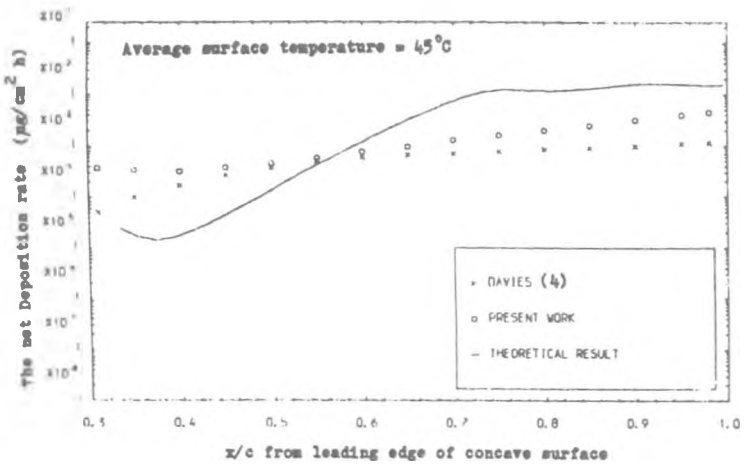

Fig. 7.197 : Distribution of Particle Deposition on the Heated Blade Surface when U_1= 13.0 m/s and d_{mm}= 0.186 μm .

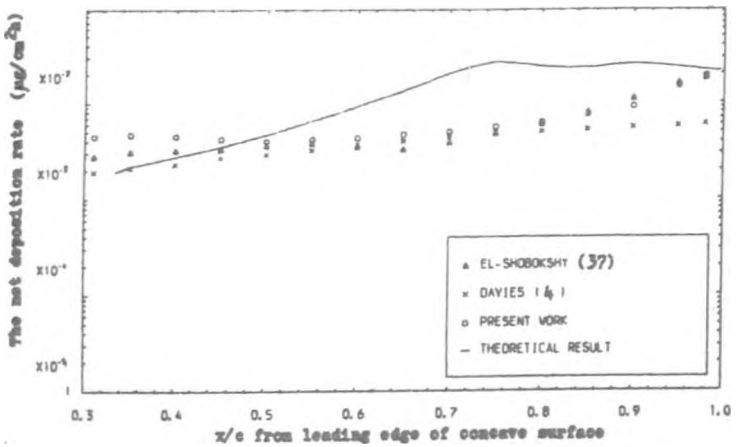

Fig. 7.194 : Distribution of Particle Deposition on Unheated Blade Surface when U_1= 13.0 m/s and d_{mm}= 0.186 μm .

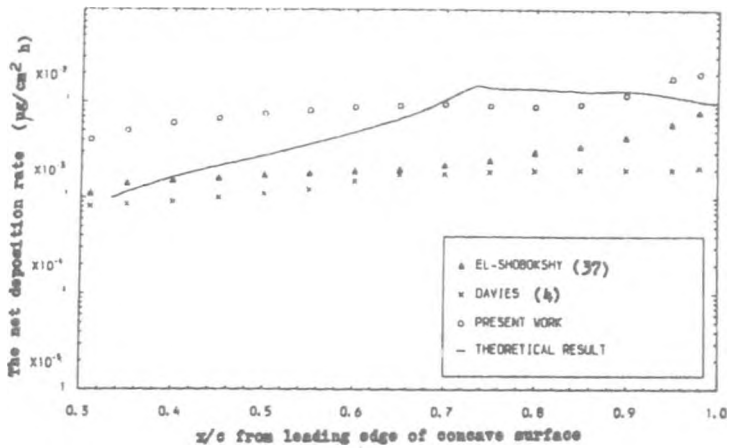

Fig. 7.196 : Distribution of Partical Deposition on Unheated Blade Surface when U_1= 9.5 m/s and d_{mm}= 0.186 μm .

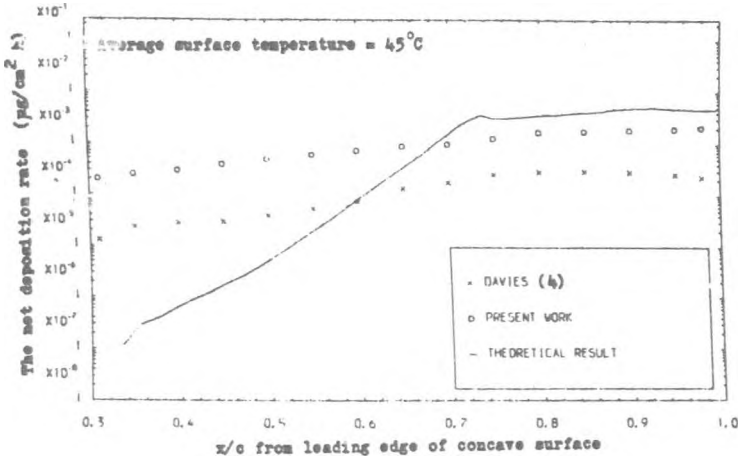

Fig. 7.199 : Distribution of Particle Deposition on the Heated Blade Surface when U_1= 9.5 m/s and d_{mm}= 0.186 μm .

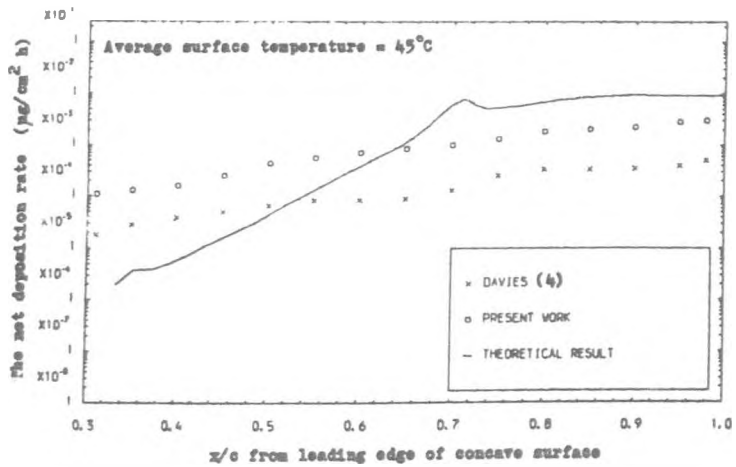

Fig. 7.198 : Distribution of Particle Deposition on the Heated Blade Surface when U_1= 11.2 m/s and d_{mm}= 0.186 μm .

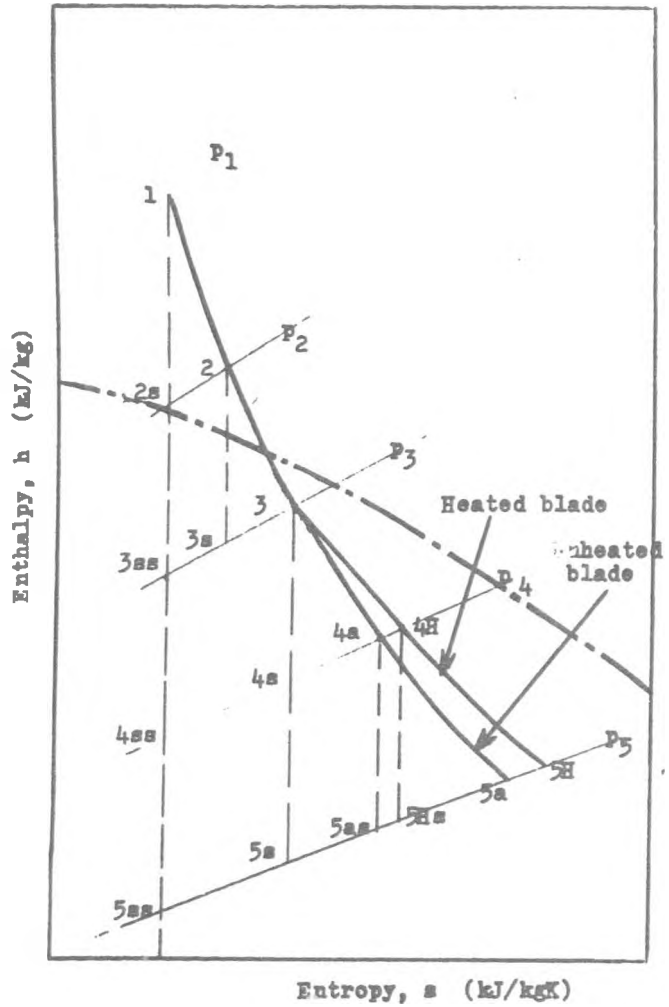

Fig. 8.1 : Thermodynamic Processes inside the Penultimate and Last Stages in the L.P. Turbine when the Blades of the Last Stator are Unheated and Internally Heated.

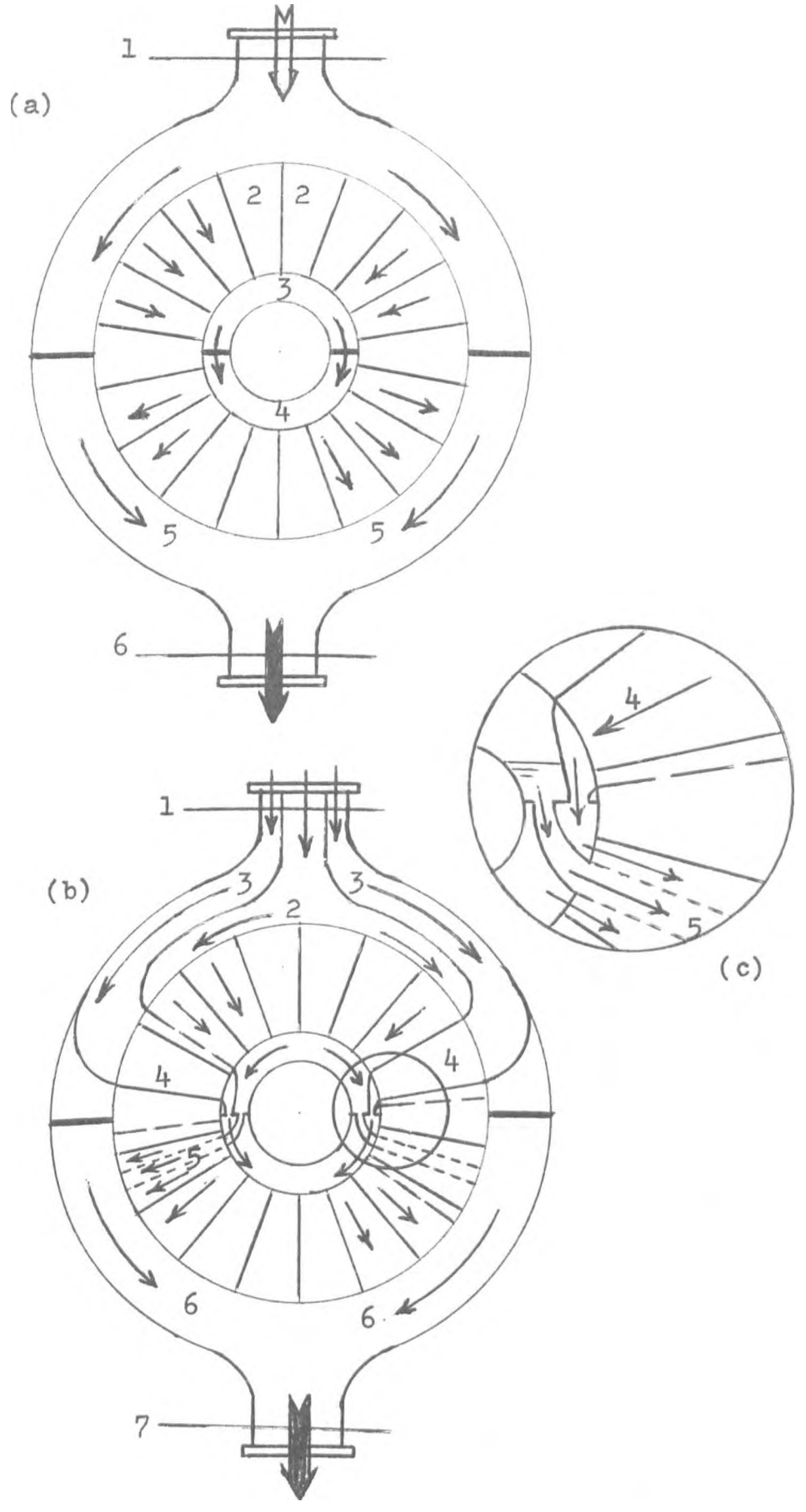

Fig. 8.2 : Paths of the Vapour and Condensate inside the Hollow Diaphragm .

(a) Suggestion from Ref.(106)

(b) New suggestion.

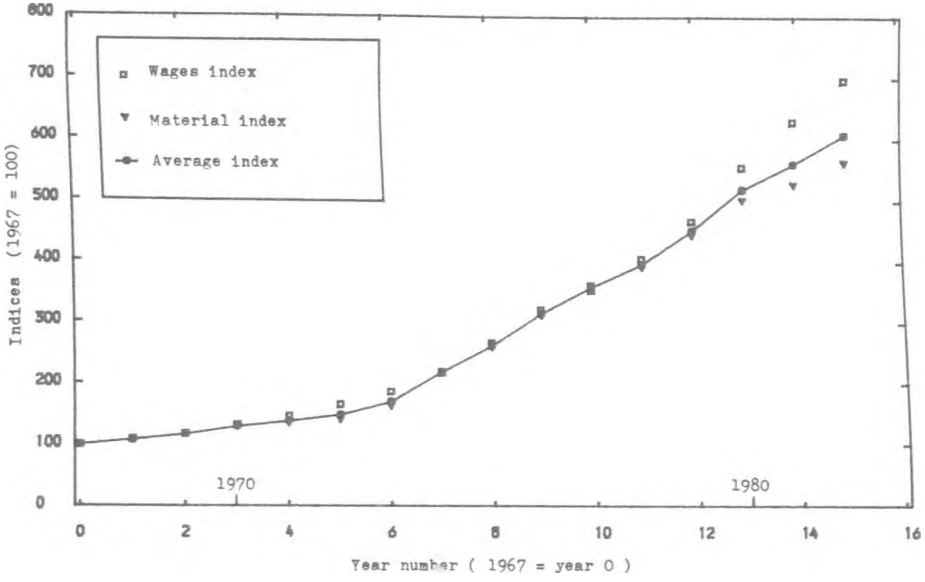

Fig. 8.4 : Indices of 'Wages' and ' Material and Fuel' for the Electrical Machinery Industries and the weighted average index over the period 1967 - 1983 .

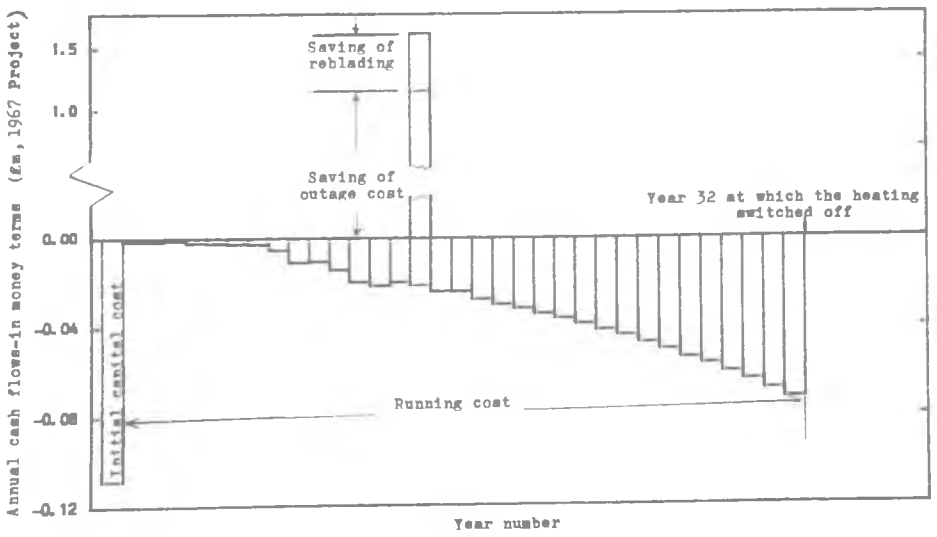

Fig. 8.3 : The Cash Flows (Costs and Benefits) over the Turbine Life .

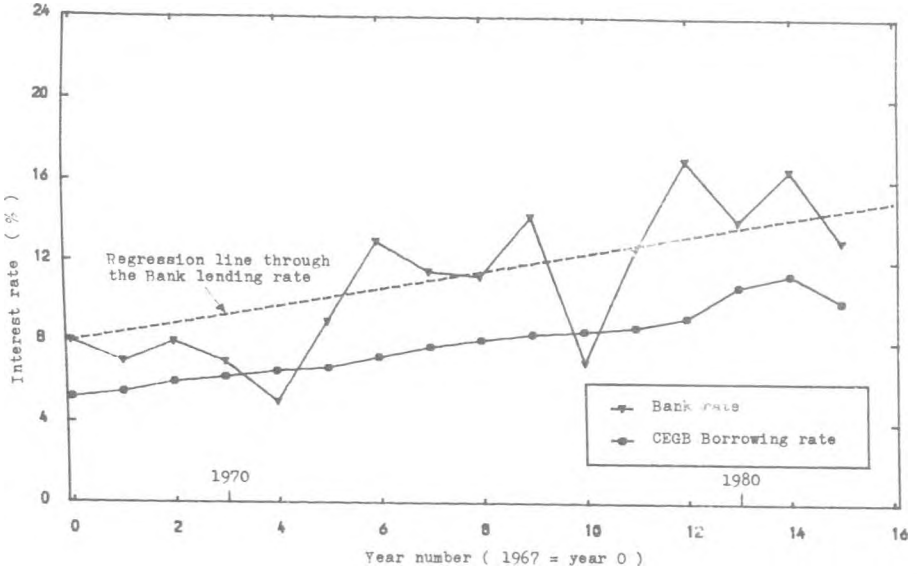

Fig. 8.6 : CEGB Borrowing Rates and Bank Lending Rates over the Period from 1967 to 1983 .

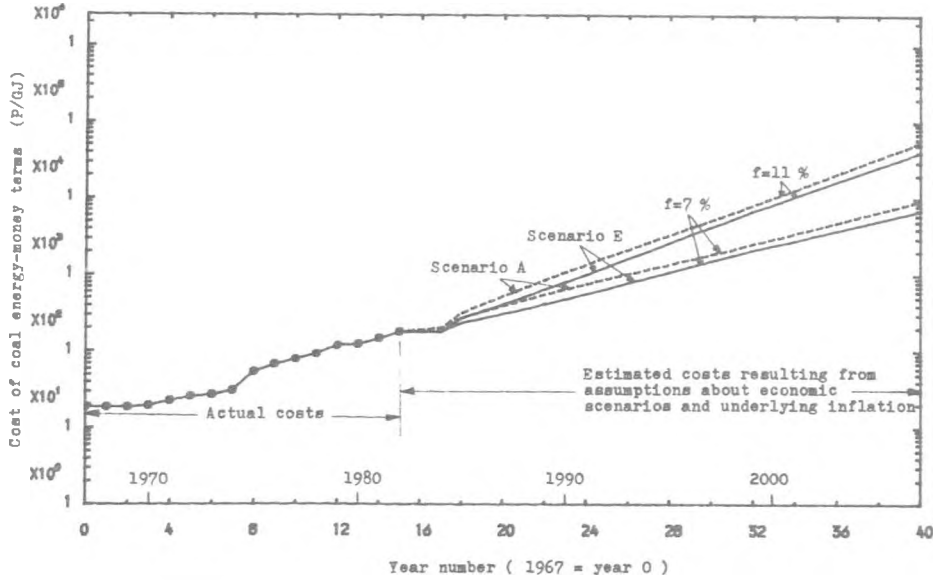

Fig. 8.5 : Cost of Coal Energy for the Period 1967-2007 .

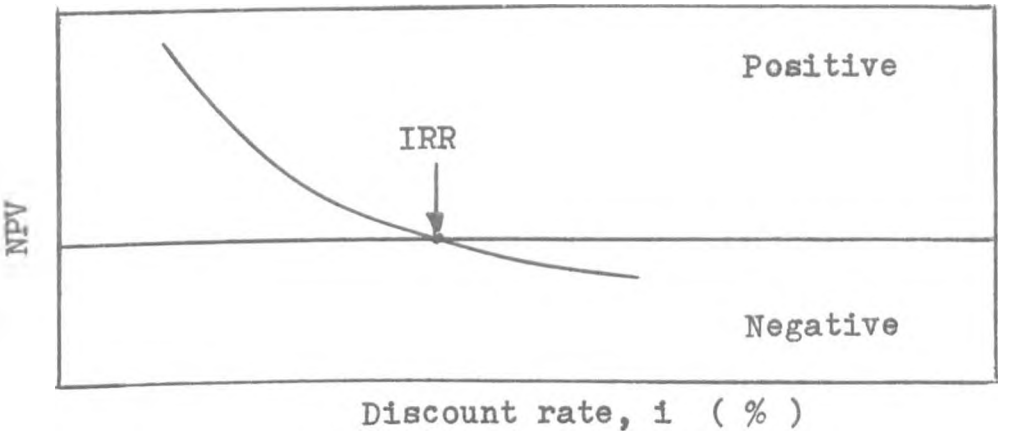

Fig. 8.7 : Variation of the Net Present Value (NPV) with the Discount Rate-for Determining the Yield (IRR) .

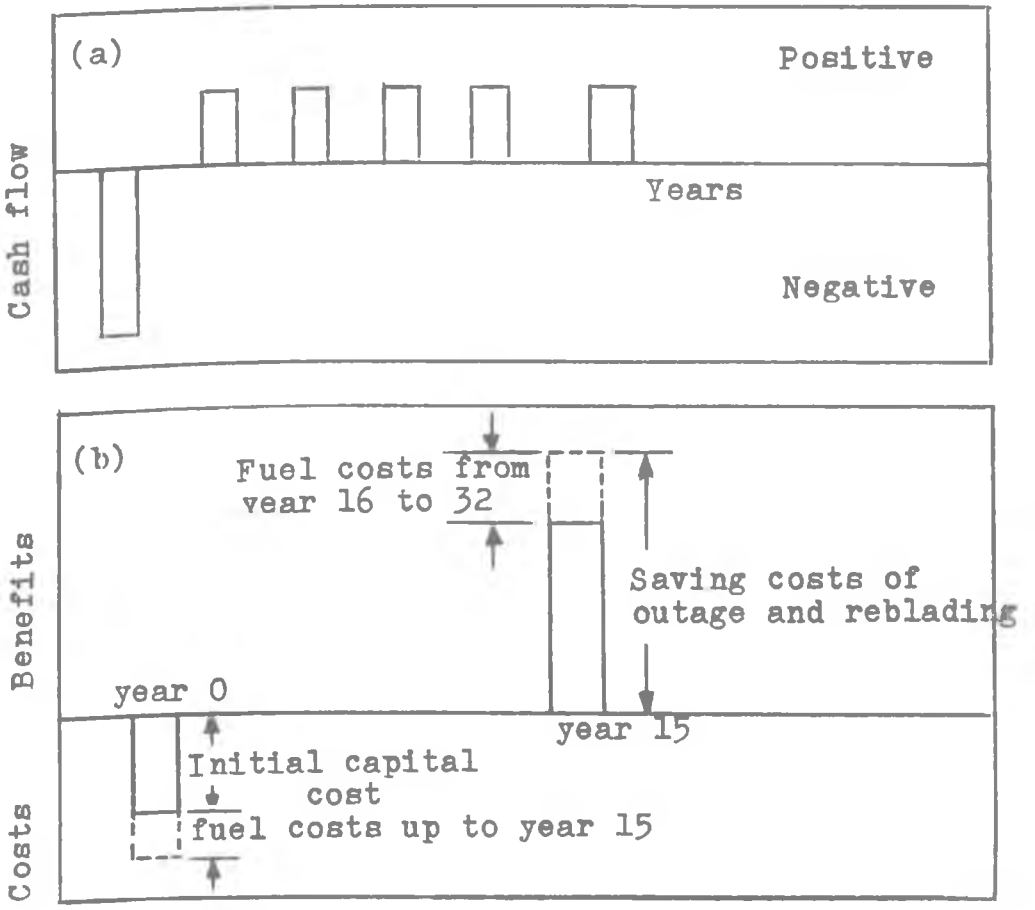

Fig. 8.8 : Distribution of the Cash Flows over the Life of the Project.
(a) For illustrated example .
(b) For the present project.

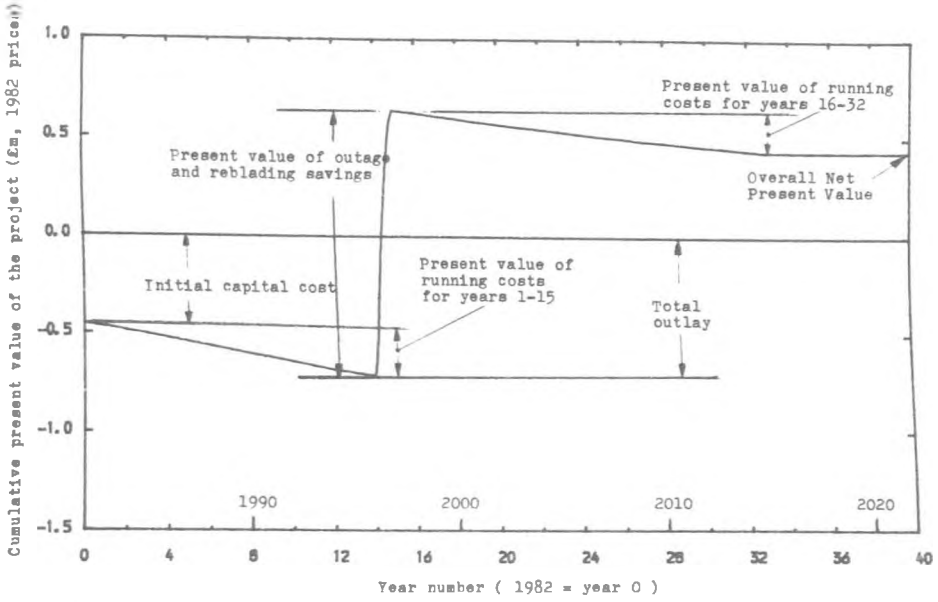

Fig. 8.10 : Cumulative Present Value of Project Case II over the Life of the Turbine (1982-2022).
Discount Rates; an assumed value of 9% for the whole life of the project.
Inflation; an assumed value of 7% for the whole life of the project.

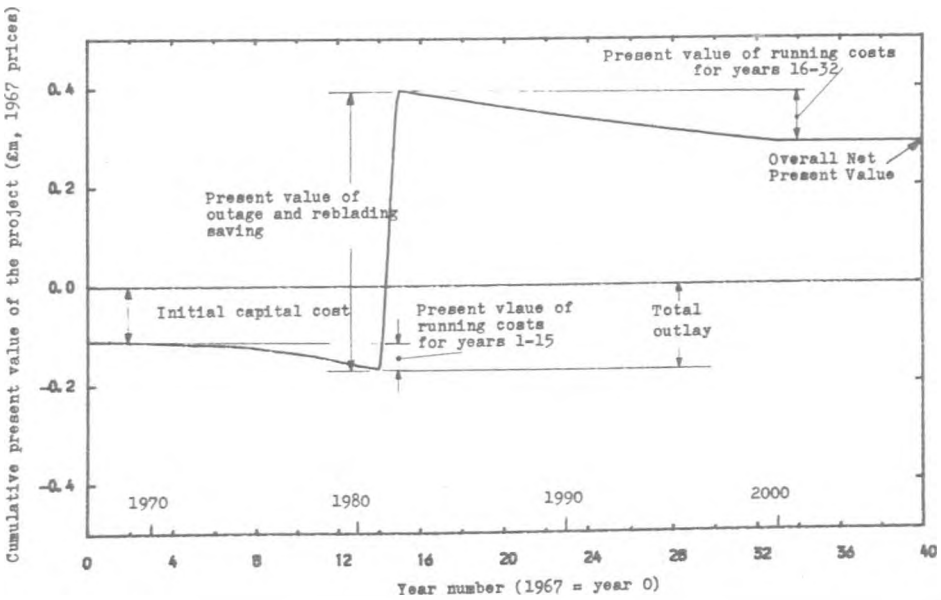

Fig. 8.9 : Cumulative Present Value of Project Case I over the Life of the Turbine (1967-2007).
Discount Rates; actual borrowing rates for years 0-15 and an assumed 9% for years 16 and thereafter .
Inflation; actual values for years 0-15 and an assumed value of 7% for year 16 and

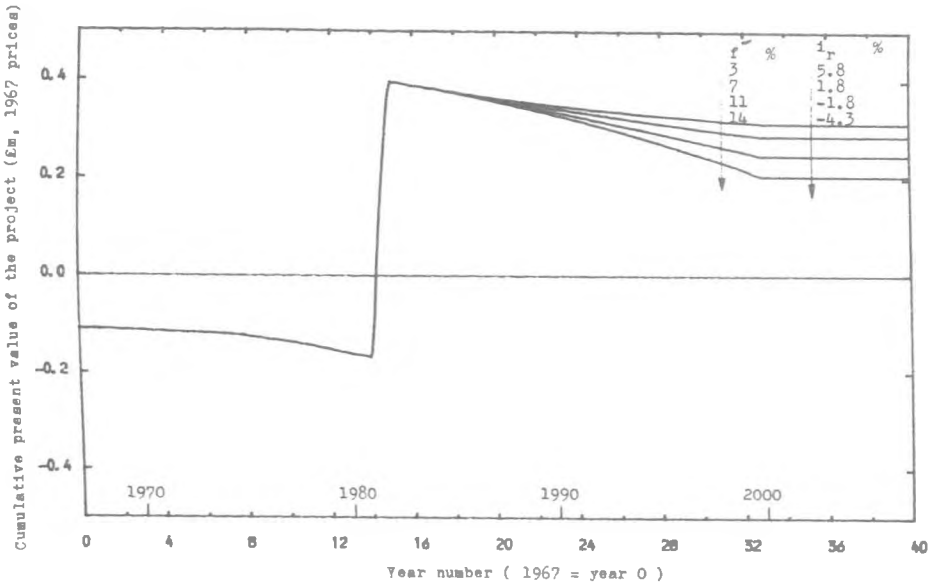

Fig. 8.12 : Cumulative Present Value of Project Case I over the Life of the Turbine (1967-2007), showing the Effect of Different Inflation when Interest Rate after year 15 is 9% .

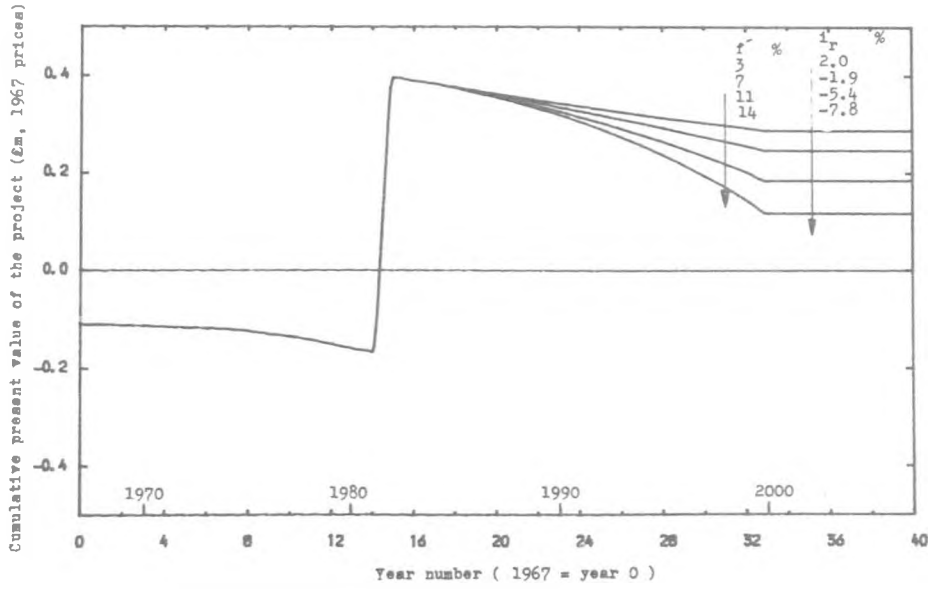

Fig. 8.11 : Cumulative Present Value of Project Case I over the Life of the Turbine (1967-2007), showing the Effect of Different Inflation when Interest Rate after year 15 is 5% .

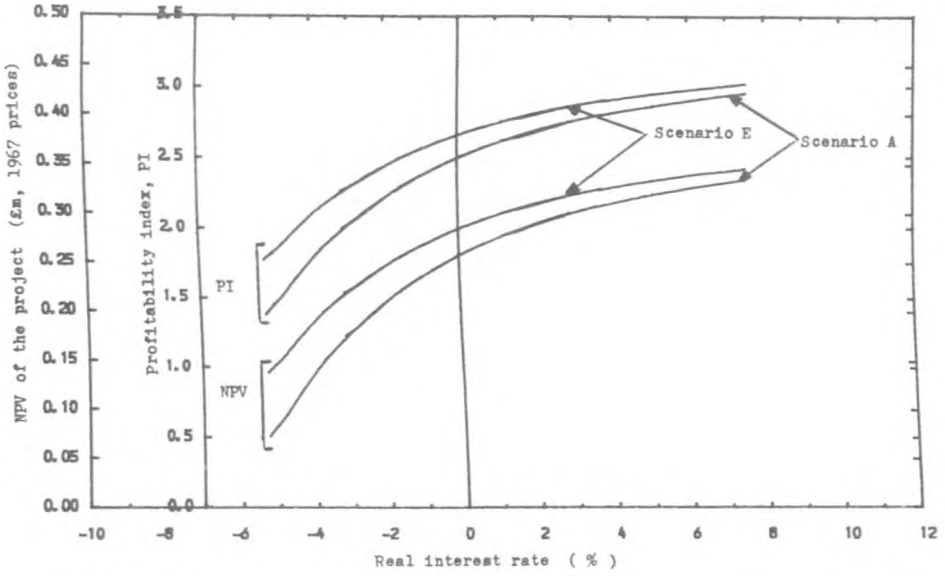

Fig. 8.14 : Variation of the Net Present Value and Profitability Index of Project Case I with the Real Rate of Interest for Economic Scenarios A and E .

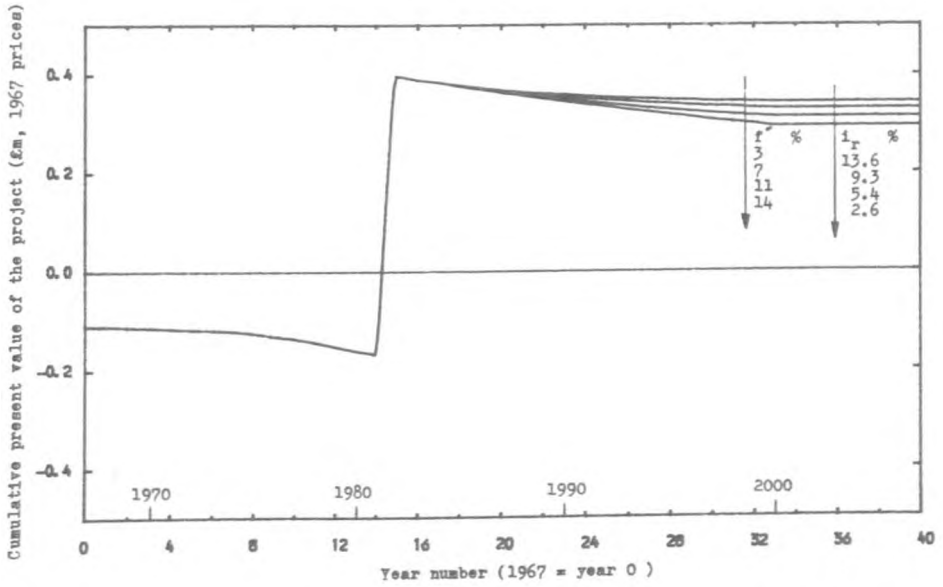

Fig. 8.13 : Cumulative Present Value of Project Case I over the Life of the Turbine (1967-2007), showing the Effect of Different Inflation when Interest Rate after year 15 is 17% .

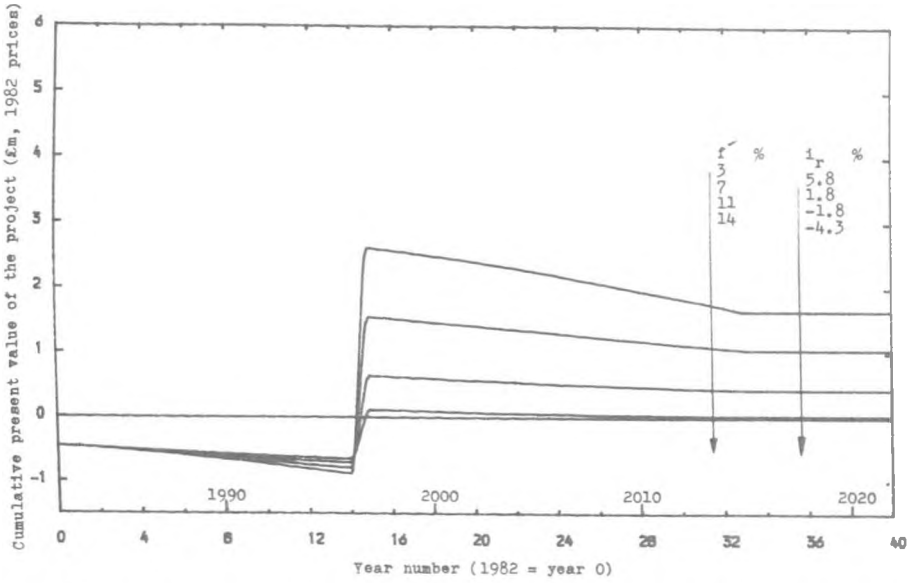

Fig. 8.16 : Cumulative Present Value of Project Case II over the Life of the Turbine (1982-2022), showing the Effect of Different Inflation when Interest Rate is 9% .

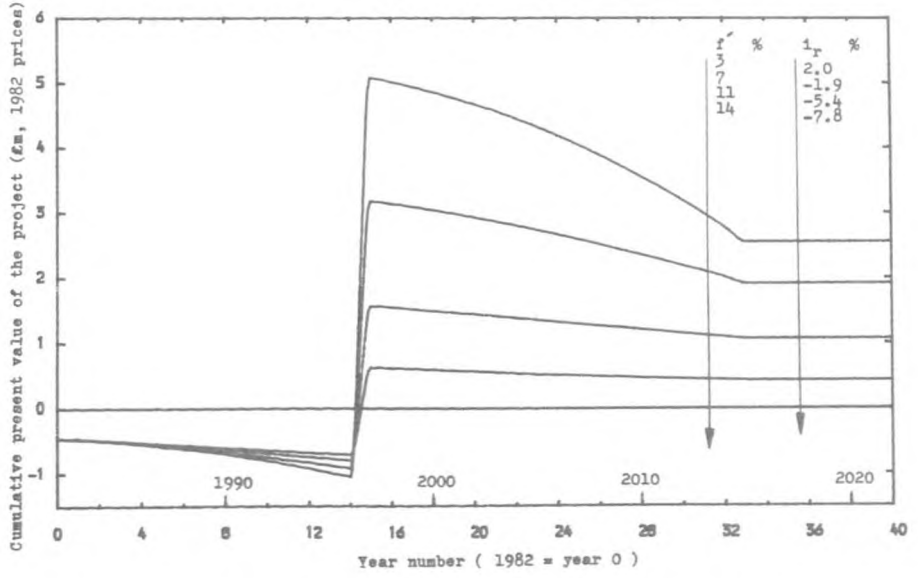

Fig. 8.15 : Cumulative Present Value of Project Case II over the Life of the Turbine (1982-2022), showing the Effect of Different Inflation when Interest Rate is 5% .

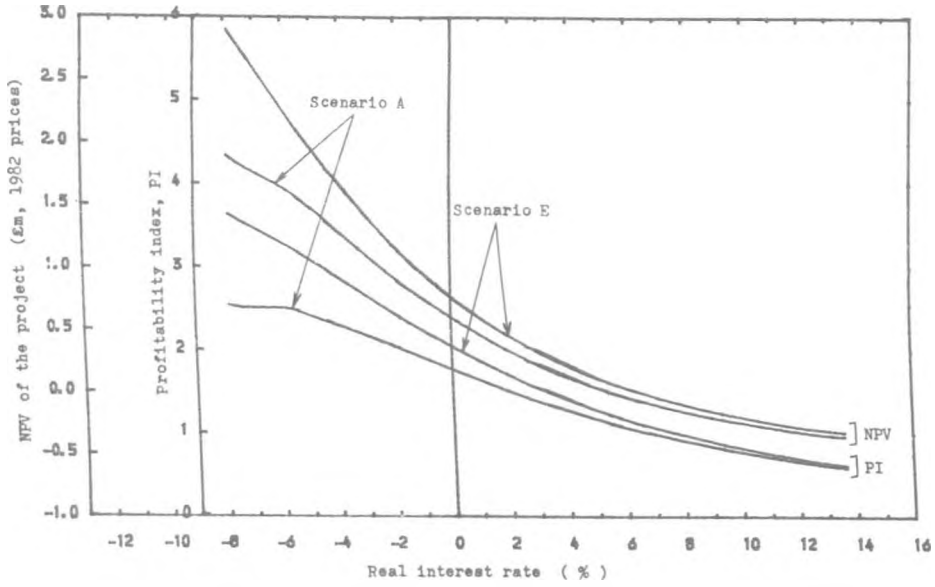

Fig. 8.18 : Variation of the Net Present Value and Profitability Index of Project Case II with the Real Rate of Interest for Economic Scenarios A and E .

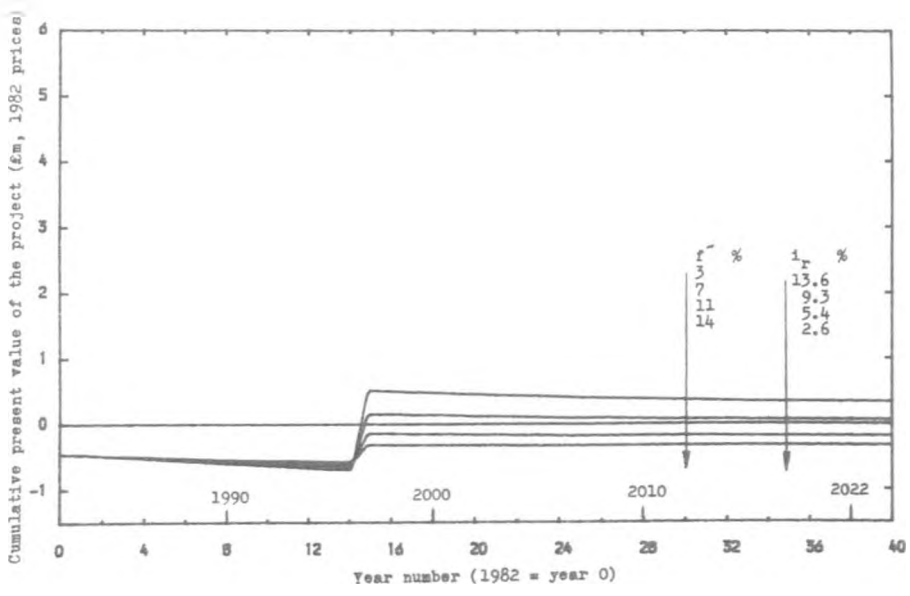

Fig. 8.17 : Cumulative Present Value of Project Case II over the Life of the Turbine (1982-2022), showing the Effect of Different Inflation when Interest Rate is 17% .

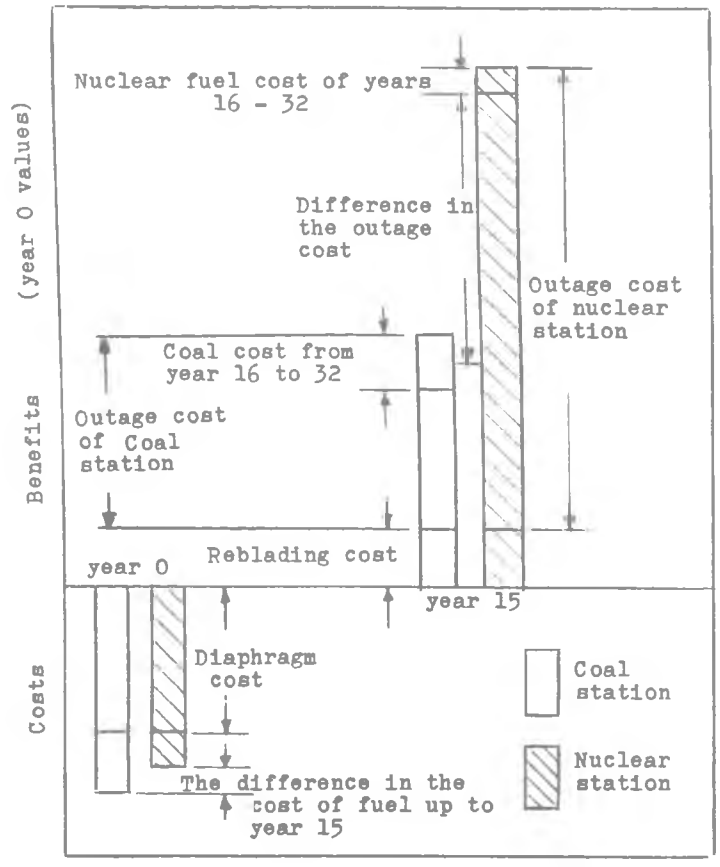

Fig. 8.19 : Distribution of Cash Flows of the Project for a Nuclear Station, Compared with a Coal Station .